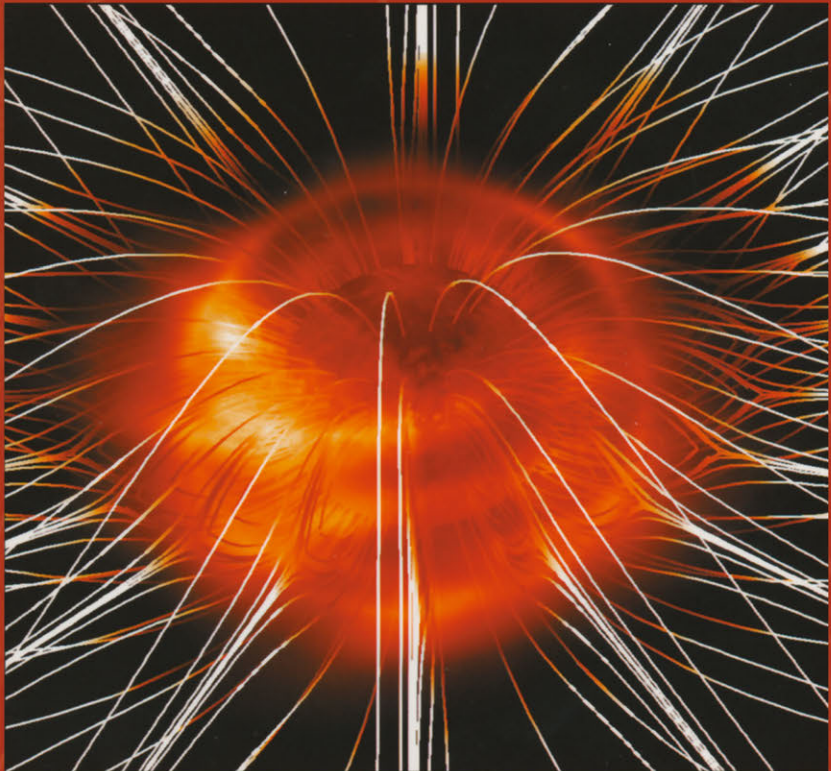


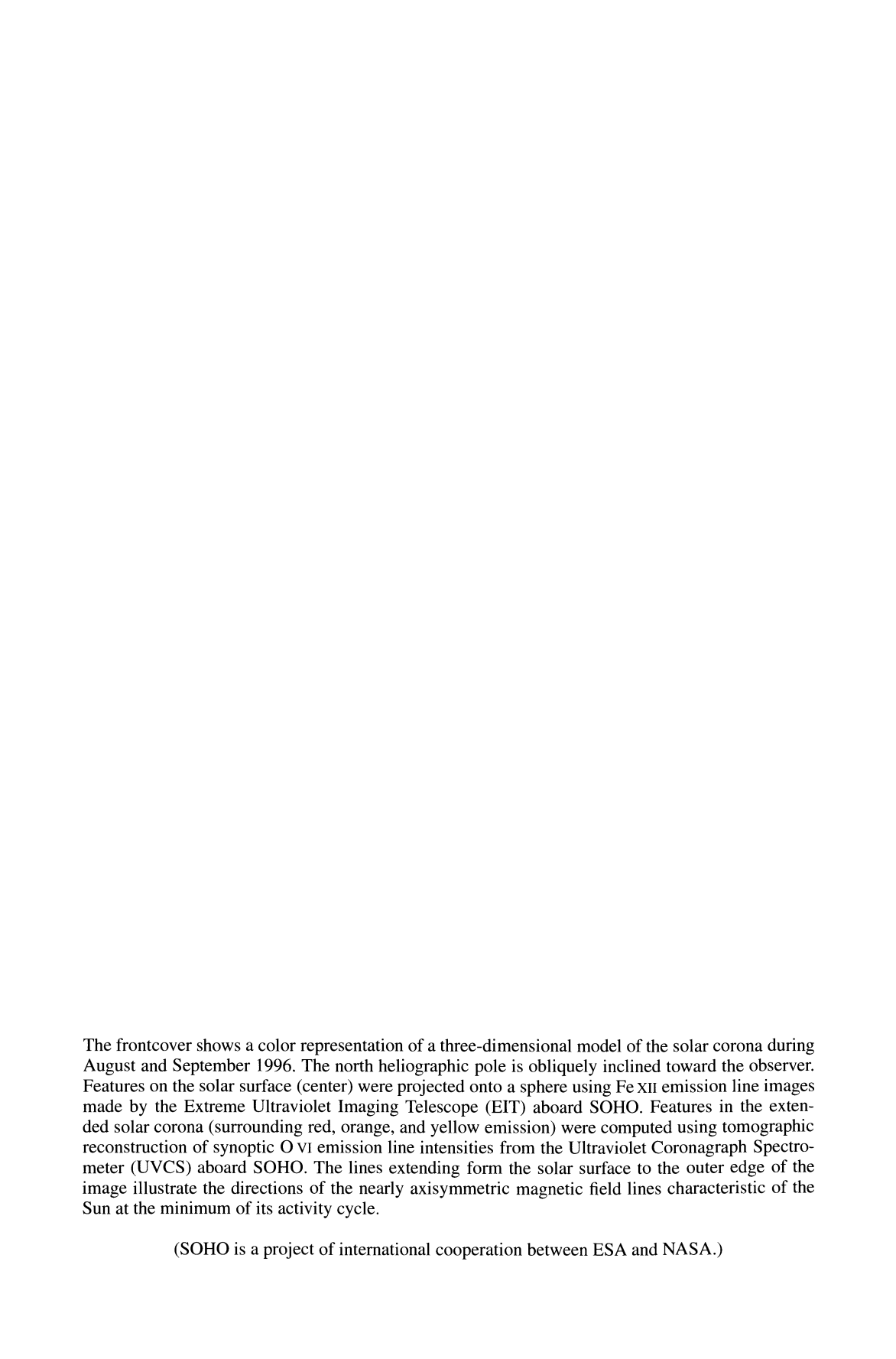
Coronal Holes and Solar Wind Acceleration



Edited by
John L. Kohl and Steven R. Cranmer

Springer-Science+Business Media, B.V.

CORONAL HOLES AND SOLAR WIND ACCELERATION



The frontcover shows a color representation of a three-dimensional model of the solar corona during August and September 1996. The north heliographic pole is obliquely inclined toward the observer. Features on the solar surface (center) were projected onto a sphere using Fe XII emission line images made by the Extreme Ultraviolet Imaging Telescope (EIT) aboard SOHO. Features in the extended solar corona (surrounding red, orange, and yellow emission) were computed using tomographic reconstruction of synoptic O VI emission line intensities from the Ultraviolet Coronagraph Spectrometer (UVCS) aboard SOHO. The lines extending from the solar surface to the outer edge of the image illustrate the directions of the nearly axisymmetric magnetic field lines characteristic of the Sun at the minimum of its activity cycle.

(SOHO is a project of international cooperation between ESA and NASA.)

CORONAL HOLES AND SOLAR WIND ACCELERATION

*Proceedings of the SOHO-7 Workshop, held at Asticou Inn
in Northeast Harbor, Maine, U.S.A., from
28 September–1 October, 1998*

Edited by

JOHN L. KOHL and STEVEN R. CRANMER

Harvard-Smithsonian Center for Astrophysics, Cambridge, MA, U.S.A.

Reprinted from *Space Science Reviews*, Volume 87, Nos. 1–2, 1999



Springer-Science+Business Media, B.V.

A C.I.P. Catalogue record for this book is available from the Library of Congress.

ISBN 978-90-481-5267-4 ISBN 978-94-015-9167-6 (eBook)
DOI 10.1007/978-94-015-9167-6

Printed in acid-free paper

All Rights Reserved
©1999 Springer Science+Business Media Dordrecht
Originally published by Kluwer Academic Publishers in 1999.
Softcover reprint of the hardcover 1st edition 1999
No part of the material protected by this copyright notice
may be reproduced or utilized in any form or by any means,
electronic or mechanical, including photocopying,
recording or by any information storage and retrieval
system, without written permission from the copyright
owner.

TABLE OF CONTENTS

| | |
|----------|----|
| Foreword | ix |
|----------|----|

INTRODUCTORY AND SUMMARY PRESENTATIONS

| | |
|--|-----|
| E. MARSCH / Solar Wind Models from the Sun to 1 AU: Constraints by <i>in situ</i> and Remote Sensing Measurements | 1 |
| W.I. AXFORD, J.F. MCKENZIE, G.V. SUKHORUKOVA, M. BANASZKIEWICZ, A. CZECHOWSKI and R. RATKIEWICZ / Acceleration of the High Speed Solar Wind in Coronal Holes | 25 |
| L.A. FISK, T.H. ZURBUCHEN and N.A. SCHWADRON / Coronal Hole Boundaries and their Interactions with Adjacent Regions | 43 |
| J.C. RAYMOND / Composition Variations in the Solar Corona and Solar Wind | 55 |
| E. LEER and E. MARSCH / Working Group 1 Report: Solar Wind Models from the Sun to 1 AU: Constraints by <i>in situ</i> and Remote Sensing Measurements | 67 |
| A.W. HOOD / Working Group 2 Report: Energy Input, Heating, and Solar Wind Acceleration in Coronal Holes | 79 |
| R. ESSER / Working Group 3 Report: Coronal Hole Boundaries and Interactions with Adjacent Regions | 93 |
| H.E. MASON and P. BOCHSLER / Working Group 4 Report: Composition and Elemental Abundance Variations in the Solar Atmosphere and Solar Wind | 105 |
| A.H. GABRIEL / SOHO after 30 Months: A Personal View | 123 |

WORKING GROUP PRESENTATIONS

| | |
|--|-----|
| J.-L. BERTAUX, E. KYRÖLÄ, E. QUEMERAIS, R. LALLEMENT, W. SCHMIDT, T. SUMMANEN, J. COSTA and T. MÄKINEN / SWAN Observations of the Solar Wind Latitude and its Evolution Since Launch | 129 |
| R. BETTA, S. ORLANDO, G. PERES and S. SERIO / On the Stability of Siphon Flows Confined in Coronal Loops | 133 |
| L.F. BURLAGE and A. SZABO / Fast and Slow Flows in the Solar Wind near the Ecliptic at 1 AU? | 137 |
| F. CHIUDERI-DRAGO, A. KERDRAON, E. LANDI and A. FLUDRA / EUV and Radio Observations of an Equatorial Coronal Hole | 141 |
| J.R. CLEGG, B.J.I. BROMAGE and P.K. BROWNING / The Solar Magnetic Field as a Coronal Hole Extension Forms: Effects of Magnetic Helicity and Boundary Conditions | 145 |
| S.R. CRANMER, G.B. FIELD and J.L. KOHL / Spectroscopic Constraints on Models of Ion-Cyclotron Resonance Heating in the Polar Solar Corona | 149 |

| | |
|---|-----|
| I. CUSERI, D. MULLAN and G. POLETTO / Coronal Heating: A Comparison of Ion-Cyclotron and Gravity Damping Models | 153 |
| R.B. DAHLBURG and G. EINAUDI / Compressible Aspects of Slow Solar Wind Formation | 157 |
| I.E.DAMMASCH, D.M. HASSLER, W. CURDT and K. WILHELM / Statistical Analysis of EUV and UV Lines Inside and Outside of Solar Coronal Holes | 161 |
| J.M. DAVILA and L. OFMAN / Two-Fluid 2.5D MHD Simulations of the Fast Solar Wind in Coronal Holes and the Relation to UVCS Observations | 165 |
| G. DEL ZANNA and B.J.I. BROMAGE / Characterization of Solar Coronal Holes and Plumes Using Spectroscopic Diagnostic Techniques Applied to SOHO/CDS Observations | 169 |
| D. DOBRZYCKA, A. PANASYUK, L. STRACHAN and J.L. KOHL / Comparison of Polar and Equatorial Coronal Holes Observed by UVCS/SOHO: Geometry and Physical Properties | 173 |
| D. DOBRZYCKA, L. STRACHAN, M.P. MIRALLES, J.L. KOHL, L.D. GARDNER, P. SMITH, M. GUHATHAKURTA and R. FISHER / Variation of Polar Coronal Hole Profiles with Solar Cycle | 177 |
| D.A. FALCONER, R.L. MOORE, J.G. PORTER and D.H. HATHAWAY / Large-Scale Coronal Heating, Clustering of Coronal Bright Points, and Concentration of Magnetic Flux | 181 |
| A. FLUDRA, G. DEL ZANNA and B.J.I. BROMAGE / EUV Observations Above Polar Coronal Holes | 185 |
| R.A. FRAZIN, A. CIARAVELLA, E. DENNIS, S. FINESCHI, L.D. GARDNER, J. MICHELS, R. O'NEAL, J.C. RAYMOND, C.-R. WU, J.L. KOHL, A. MODIGLIANI and G. NOCI / UVCS/SOHO Ion Kinetics in Coronal Streamers | 189 |
| C.P.T. GROTH, D.L. DE ZEEUW, T.I. GOMBOSI and K.G. POWELL / A Parallel Adaptive 3D MHD Scheme for Modeling Coronal and Solar Wind Plasma Flows | 193 |
| M. GUHATHAKURTA, E.C. SITTLER and D. McCOMAS / Semi-empirical MHD Model of the Solar Wind and its Comparison with Ulysses | 199 |
| P. HACKENBERG, G. MANN and E. MARSCH / Plasma Properties in Coronal Funnels | 207 |
| B. INHESTER, G. STENBORG, R. SCHWENN, N. SRIVASTAVA and B. PODLIPNIK / The Rotation of the Fe XIV Solar Corona During the Recent Solar Activity Minimum | 211 |
| J.E. INSLEY / A CDS Observation of the Relationship Between a Coronal Hole and Chromospheric Structure | 215 |

| | |
|---|-----|
| M. KAROVSKA, B.E. WOOD, J.W. COOK, R.A. HOWARD and G.E. BRUECKNER / Study of Dynamical Properties of Coronal Structures in the Polar Regions | 219 |
| R. KEPPENS and J.P. GOEDBLOED / Numerical Simulations of Stellar Winds | 223 |
| Y.-K. KO and C.P.T. GROTH / On the Electron Temperature and Coronal Heating in the Fast Solar Wind Constrained by <i>in situ</i> Observations | 227 |
| J.L. KOHL, S. FINESCHI, R. ESSER, A. CIARAVELLA, S.R. CRANMER, L.D. GARDNER, R. SULEIMAN, G. NOCI and A. MODIGLIANI / UVCS/SOHO Observations of Spectral Line Profiles in Polar Coronal Holes | 233 |
| M. KOJIMA, K. FUJIKI, T. OHMI, M. TOKUMARU, A. YOKOBE and K. HAKAMADA / The Highest Solar Wind Velocity in a Polar Region Estimated from IPS Tomography Analysis | 237 |
| E. LANDI, H.E. MASON and M. LANDINI / Observation of Transition Region Fine Structures with SOHO/SUMER | 241 |
| M. LANDINI, A. BRKOVIĆ, E. LANDI, I. RÜEDI and S. SOLANKI / Loop Models from SOHO Observations | 245 |
| P. LEMAIRE, K. BOCCIALINI, V. ALETTI, D. HASSLER and K. WILHELM / Search for Signatures of a Coronal Hole in Transition Region Lines near Disk Center | 249 |
| X. LI / A 16-Moment Fast Solar Wind Model | 253 |
| P. LIEWER, M. VELLI and B. GOLDSTEIN / Hybrid Simulations of Wave Propagation and Ion Cyclotron Heating in the Expanding Solar Wind | 257 |
| Y.-Q. LOU / Magneto-Gravity Waves Trapped in the Lower Solar Corona | 261 |
| L. MACCARI, G. NOCI, S. FINESCHI, A. MODIGLIANI, M. ROMOLI and J.L. KOHL / Ly- α Observation of a Coronal Streamer with UVCS/SOHO | 265 |
| W.H. MATTHAEUS, G.P. ZANK, R.J. LEAMON, C.W. SMITH, D.J. MULLEN and S. OUGHTON / Fluctuations, Dissipation and Heating in the Corona | 269 |
| M.P. MIRALLES, L. STRACHAN, L.D. GARDNER, P.L. SMITH, J.L. KOHL, M. GUHATHAKURTA and R.R. FISHER / Properties of Coronal Hole-Streamer Boundaries and Adjacent Regions as Observed by Spartan 201 | 277 |
| R.L. MOORE, D.A. FALCONER, J.G. PORTER and S.T. SUESS / Coronal Heating by Magnetic Explosions | 283 |
| L. OFMAN, M. ROMOLI, G. NOCI, G. POLETTO, J.L. KOHL, R.A. HOWARD, C. ST. CYR and C.E. DEFOREST / SOHO Observations of Density Fluctuations in Coronal Holes | 287 |
| S. PATSOURAKOS, J.-C. VIAL, J.-R. GABRYL, S. KOUTCHMY and U. SCHÜHLE / Outflow Velocities at the Base of a Polar Coronal Hole During the 1998 Total Eclipse | 291 |

| | |
|--|-----|
| S. POEDTS, A.D. ROGAVA and S.M. MAHAJAN / Velocity Shear Induced Phenomena in Solar Atmosphere | 295 |
| U. SCHÜHLE, W. CURDT, K. WILHELM, S.K. SOLANKI and K. STUCKI / Signatures of Coronal Hole Spectra Between 660 Ångstroms and 1460 Ångstroms Measured with SUMER on SOHO | 299 |
| N. SRIVASTAVA, R. SCHWENN, B. INHESTER, G. STENBORG and B. PODLIPNIK / Acceleration Profile of the Slow Solar Wind as Inferred from Gradual Mass Ejections Observed by LASCO | 303 |
| G. STENBORG, R. SCHWENN, N. SRIVASTAVA, B. INHESTER, B. PODLIPNIK, M. ROVIRA and C. FRANCILE / MICA: The Mirror Coronagraph for Argentina | 307 |
| L. STRACHAN, Y.-K. KO, A.V. PANASYUK, D. DOBRZYCKA, J.L. KOHL, M. ROMOLI, G. NOCI, S.E. GIBSON and D.A. BIESECKER / Constraints on Coronal Outflow Velocities Derived from UVCS Doppler Dimming Measurements and <i>in situ</i> Charge State Data | 311 |
| K. STUCKI, S.K. SOLANKI, I. RÜEDI, J.O. STENFLO, A. BRKOVIĆ, U. SCHÜHLE, K. WILHELM and M.C.E. HUBER / Coronal Hole Properties Observed with SUMER | 315 |
| S.T. SUESS, G. POLETTO, G. CORTI, G. SIMNETT, G. NOCI, M. ROMOLI, J. L. KOHL and B. GOLDSTEIN / Ulysses-UVCS Coordinated Observations | 319 |
| S.T. SUESS, A.H. WANG, S.T. WU and S.F. NERNEY / Streamer Evaporation | 323 |
| R.M. SULEIMAN, J.L. KOHL, A.V. PANASYUK, A. CIARAVELLA, S.R. CRANMER, L.D. GARDNER, R. FRAZIN, R. HAUCK, P.L. SMITH and G. NOCI / UVCS/SOHO Observations of H I Lyman Alpha Line Profiles in Coronal Holes at Heliocentric Heights above $3.0 R_{\odot}$ | 327 |
| C.-Y. TU, E. MARSCH and K. WILHELM / Ion Temperature as Observed in a Solar Coronal Hole | 331 |
| A.M. VASQUEZ, J.C. RAYMOND and A.A. VAN BALLEGOOIJEN / UVCS Observations and Modeling of Streamers | 335 |
| M. VELLI and P. LIEWER / Alfvén Wave Generation in Photospheric Vortex Filaments, Macrospicules, and ‘Solar Tornadoes’ | 339 |
| P.R. YOUNG and R. ESSER / Comparing Quiet Sun and Coronal Hole Regions with CDS/SOHO | 345 |
| L. ZANGRILLI, P. NICOLOSI, G. POLETTO and G. NOCI / On the Lyman α and O VI Line Profiles in Streamers and Coronal Holes | 349 |
| T.H. ZURBUCHEN, S. HEFTI, L.A. FISK, G. GLOECKLER and R. VON STEIGER / The Transition Between Fast and Slow Solar Wind from Composition Data | 353 |

FOREWORD

The SOHO-7 Workshop was held from 28 September through 1 October 1998 at the Asticou Inn in Northeast Harbor, Maine. The primary topic of this Workshop was the impact of SOHO observations on our understanding of the nature and evolution of coronal holes and the acceleration and composition of the solar wind. The presentations and discussions occasionally went beyond this topic to include the impact of the reported research on other solar structures and the heliosphere.

SOHO (the Solar and Heliospheric Observatory), a project of international cooperation between ESA and NASA, was launched in December 1995 and began its science operations during the first few months of 1996. To many solar and space physicists, it was a great advantage that SOHO began its comprehensive look at the Sun during the 1996 solar minimum. The qualitatively simple two-phase corona, with polar coronal holes expanding into the high-speed solar wind, and a steady equatorial streamer belt related somehow to the stochastic slow-speed solar wind, allowed various SOHO diagnostics to be initiated with a reasonably well-understood circumsolar geometry. The analysis of subsequent SOHO measurements made during the rising phase of solar cycle 23 will continue to benefit from what has been learned from the first two years of data.

Because of the comprehensive observations possible with SOHO of the photosphere, chromosphere, transition region, and corona, the capability exists of investigating the detailed physical processes responsible for the heating of the outer solar atmosphere and the acceleration of the solar wind. The steady high-speed flow above coronal holes is known to depart strongly from ideal thermal equilibrium, but the mechanisms that produce the observed non-Maxwellian velocity distributions and differentially flowing particle velocities are not yet known with certainty. The magnetic field above the poles is a complex superposition of large-scale open field lines and small-scale structures such as bright points, polar plumes, spicules, and macrospicules. This Workshop was planned with the specific goal of reviewing what has been learned with SOHO about coronal holes and solar wind acceleration. These proceedings thus contain a summary of the current "state of the art" of the observational and theoretical insight about these phenomena.

The SOHO-7 Workshop began on 28 September with a brief memoriam given by Russ Howard for Guenter Brueckner, who passed away on 11 July 1998. The Keynote Lecture, titled "*Solar Wind 2000*," was then given by George Gloecker for Johannes Geiss, who could not attend the Workshop. On 29 September, four hour-long invited introductory lectures were given on the four topics that were covered in greater depth by the Working Groups. These topics, along with the associated Introductory Lecturers, Discussion Leaders, and Reporters, are given as follows.



1. Solar Wind Models from the Sun to 1 AU: Constraints by “in situ” and remote sensing measurements

INTRODUCTORY LECTURER & DISCUSSION LEADER: **Eckart Marsch**
REPORTER: **Egil Leer**

2. Energy Input, Heating, and Solar Wind Acceleration in Coronal Holes

INTRODUCTORY LECTURER: **W. Ian Axford**
DISCUSSION LEADER: **Robert Rosner**
REPORTER: **Alan Hood**

3. Coronal Hole Boundaries and Interactions with Adjacent Regions

INTRODUCTORY LECTURER: **Lennard Fisk**
DISCUSSION LEADER: **Steve Suess**
REPORTER: **Ruth Esser**

4. Composition and Elemental Abundance Variations in the Solar Atmosphere and Solar Wind

INTRODUCTORY LECTURER: **John Raymond**
DISCUSSION LEADER: **Helen Mason**
REPORTER: **Peter Bochsler**

The remainder of 29 and 30 September were devoted to four parallel Working Group sessions. The Discussion Leaders all did a remarkable job of coordinating the large numbers of topics and guiding the participants to integrate their results with others presented in each Working Group. In order to accurately assess both the overall progress in the field and the specific needs of one’s colleagues, it is important to have a wide observational context from many instruments (both on and off SOHO) and a broad theoretical context from different analytical and computational approaches. The Working Group sessions at SOHO-7 fostered this type of interaction between old friends and new acquaintances, and probably produced several new collaborations.

At the final session on 1 October, the four Reporters gave hour-long summary talks that well encapsulated the “output” of the Working Groups. The four introductory talks, the four Working Group summary presentations by the Reporters, and a final overall summary report (by final session chair Alan Gabriel) are the first nine papers in this volume. Shorter contributions, based on many of the poster and Working Group session presentations, comprise the remainder of these proceedings.

Mention should be made of the historic and scenic location of the SOHO-7 Workshop. The Asticou Inn is on Mount Desert Island in Maine, and is surrounded by Acadia National Park. Visitors toured the Asticou’s beautiful gardens, enjoyed tea and popovers at Jordan Pond, and drove up Cadillac Mountain, the highest point on the Atlantic in North America. The varied options for hiking, biking, and boating around the island were enjoyed by many participants, and those inclined to more urban diversions were also well occupied by shopping and restaurants in the several towns on the island such as Bar Harbor.

The editors would like to acknowledge the Scientific Organizing Committee for their efforts in producing a seamless and productive Workshop: Peter Bochsler, Guenter Brueckner, Craig DeForest, Kenneth Dere, Ruth Esser, Lennard Fisk, Alan Gabriel, Antoinette Galvin, Martin Huber, John Kohl (chair), Piet Martens, Helen Mason, Art Poland, Giannina Poletto, and Klaus Wilhelm. The Local Organizing Committee worked extremely hard in preparing meeting materials, designing the Workshop web site, arranging transportation, preparing for the poster sessions, running the computer systems and audio-visual equipment, and dealing with registrations and the hotel arrangements; the editors would also like to extend thanks to these tireless people: Brenda Bernard, Steven Cranmer, Danuta Dobrzycka, Larry Gardner, Roger Hauck, John Kohl (chair), Mari Paz Miralles, John Raymond, Peter Smith, Leonard Strachan, and Raid Suleiman. Additional appreciation is also expressed to Joyce Janjigian, Marion Hauck, Nancy Kohl, and Chi-Rai Wu for their kind assistance with the Workshop. Finally, the editors and participants would like to thank the General Manager of the Asticou Inn, Joseph Joy, and the entire staff for their hospitality during our stay.

March 1999

JOHN L. KOHL AND STEVEN R. CRANMER
Cambridge, Massachusetts



The Asticou Inn (photo credit: Roger Hauck)

SOLAR WIND MODELS FROM THE SUN TO 1 AU: CONSTRAINTS BY IN SITU AND REMOTE SENSING MEASUREMENTS

E. MARSCH

Max-Planck-Institut für Aeronomie, D-37191 Katlenburg-Lindau, Germany

Abstract. There are three major types of solar wind: The steady fast wind originating on open magnetic field lines in coronal holes, the unsteady slow wind coming probably from the temporarily open streamer belt and the transient wind in the form of large coronal mass ejections. The majority of the models is concerned with the fast wind, which is, at least during solar minimum, the normal mode of the wind and most easily modeled by multi-fluid equations involving waves. The in-situ constraints imposed on the models, mainly by the Helios (in ecliptic) and Ulysses (high-latitude) interplanetary measurements, are extensively discussed with respect to fluid and kinetic properties of the wind. The recent SOHO observations have brought a wealth of new information about the boundary conditions for the wind in the inner solar corona and about the plasma conditions prevailing in the transition region and chromospheric sources of the wind plasma. These results are presented, and then some key questions and scientific issues are identified.

Key words: solar corona and wind, boundary conditions, radial profiles, kinetic and multifluid characteristics, future research topics

1. Introduction

The solar wind is the supersonic outflow of completely ionized gas from the solar corona. It consists of protons and electrons with an admixture of a few percent of alpha particles and heavy, much-less-abundant ions in different ionization stages. The hot corona at a typical temperature of 1–2 MK expands radially into interplanetary space. The flow becomes supersonic at a few solar radii (Parker 1958). The solar magnetic field lines are dragged away by the wind, because of its high conductivity, and transform into the heliospheric field lines, which attain the form of spirals due to solar rotation at a sidereal period of 25 days. Mass conservation and spherical geometry imply that for constant wind speed the density must decrease in proportion to r^{-2} . This yields an ever declining ram pressure of the expanding wind, which is finally brought into collision with the interstellar gas. Near 100 AU even the weak pressure of the local interstellar medium is capable of braking the dilute wind flow, and the heliosphere ends. The heating of the solar corona and the origin and acceleration of the solar wind are among the important unsolved problems of space plasma and solar physics.

2. Global Structure of the Corona and Wind

2.1. THE STRUCTURE OF THE MINIMUM-ACTIVITY CORONA

From the Helios, Ulysses, Yohkoh and SOHO missions it has become abundantly clear that two characteristic types of solar corona and wind exist, prevailing at



different heliographic latitudes and longitudes and phases of the solar cycle. This field and flow pattern is simple and conspicuous near solar minimum, when the steady fast wind emanates from the magnetically open polar coronal holes, whereas the unsteady slow wind originates from the equatorial streamer belt, which opens intermittently (Wang *et al.* 1998) to release abruptly plasma blobs and coronal mass ejections (CMEs), or perhaps more continuously from the boundary layers of the streamer belt forming the heliospheric current sheet, in which case the expansion of the magnetic flux-tubes, extending from high solar to low heliospheric latitudes (Wang and Sheeley 1990), would play a decisive role.

The large-scale structure of the corona changes over the 11-year solar cycle and becomes particularly simple near the minimum period, where it can be described essentially by a dipolar and quadrupolar component supplemented by contributions from the near-Sun current sheet, features which can clearly be inferred from Figure 1 showing coronal images obtained in the green Fe XIV 5303 Å emission line and in white light with the LASCO coronagraph on SOHO (e.g., Schwenn *et al.* 1997). Banaszkiewicz *et al.* (1998) provided a simple algebraic model for the field near minimum, which describes the global field properties and also allows one to derive the expansion factor of magnetic flux tubes required in models of the fast wind originating in the polar coronal holes.

2.2. THE THREE-DIMENSIONAL SOLAR WIND AND HELIOSPHERE

The large-scale structure of the heliosphere in three dimensions has been described in several articles in the book edited by Marsden (1995). The Ulysses observations analyzed by Woch *et al.* (1997) resulted in a polar plot of the wind speed and magnetic field magnitude and polarity. The general flow pattern is clearly visible in this plot, which provides a concise overview of the three-dimensional heliosphere and indicates the overall steadiness of the fast wind and the variability of the slow wind (intermingled with recurrent streams from low-latitude coronal holes).

A detailed study of the magnetic field as a function of distance, longitude and latitude in the inner heliosphere shows that the distant radial field is rather monopolar, with large compressive deviations occurring near the heliospheric current sheet. The combined image from LASCO in Figure 1 nicely illustrates the corona near solar activity minimum. The current sheet becomes more complicated and highly structured and warped during increased activity of the Sun, being associated with a complex multipole field and many small activity regions, as shown for the present epoch in the article of Bravo *et al.* (1998). Traditionally (see, e.g., Hoeksema 1995), one has described the evolution of the current sheet by means of plots of the source field polarity at $2.5 R_{\odot}$, as constructed from potential field extrapolations of the solar surface fields.

Barnes *et al.* (1995) clearly showed that the mass flux and helium abundance of the solar wind are remarkably stable and constant all over the solar surface with the exception of the equatorial streamer belt, where transients and coronal mass

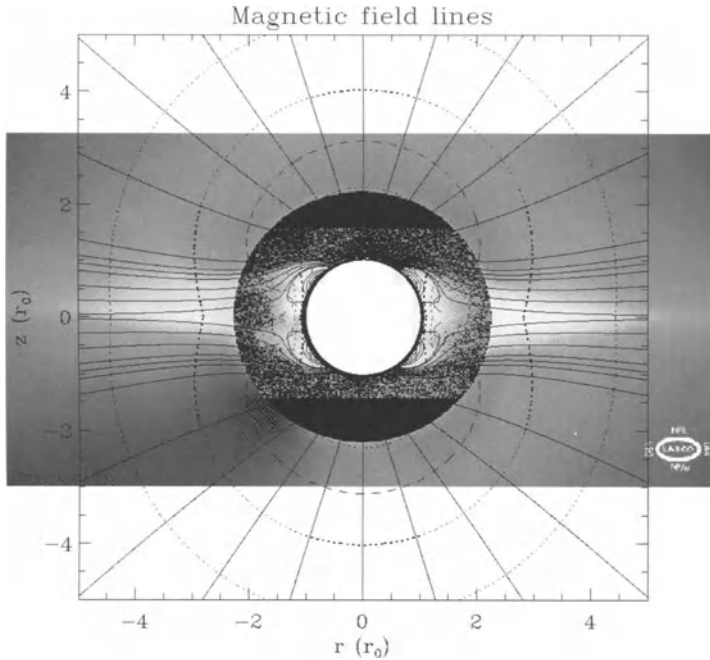


Figure 1. The solar corona as seen by the LASCO coronagraph on SOHO (after Schwenn *et al.* 1997) and magnetic field lines of a model (after Banaszkiewicz *et al.* 1998) with a dipolar, quadrupolar and current sheet contribution. The magnetic field direction is indicated by the continuous lines, and the strength by the dotted isocontours. Note the overall good agreement between the observed electron density distribution made visible by Thomson-scattered white light and the related morphology of the plasma-confining magnetic field.

ejections render the mass flux more variable. Yet, its daily average seems to be even invariant in time over a full magnetic solar cycle. Helios (Schwenn 1990) found 22 years earlier nearly the same mass flux as Ulysses! The SWAN experiment on SOHO allowed us recently to derive global averages of the mass flux from sky maps in Ly α . Bertaux *et al.* (1996) quoted a mean value of $2.2 \times 10^8 \text{ cm}^{-2} \text{ s}^{-1}$, consistent with in-situ values, assuming that 1/3 of space is filled by slow wind (within a latitudinal band of $\pm 20^\circ$) and 2/3 by fast wind.

3. Solar Wind Theory and Models

3.1. BASIC STATIONARY EQUATIONS FOR THE FAST SOLAR WIND

As will be shown below, the minimum effort in modeling the fast solar wind flow is to consider a combined electron-proton fluid with separate energy equations. Alpha

particles are a major player too (see, e.g., Hansteen *et al.* 1997), but heavier minor ions may be treated as test particles. As the observations indicate, the thermodynamics and energetics of the corona and wind are still badly understood. Increasing the sophistication of solar wind models, one may include the minor species and anisotropies in the temperatures as well as proper-frame energy flows, which are related to skewed velocity distributions and associated with heat conduction in collisional plasma. For the sake of simplicity we consider a steady coronal expansion and wind with mass density ρ , flow speed V , pressures $p_{e,p}$, and magnetic field B_r . In order to account for the nonradial expansion in coronal holes, a nonradial area function of the flow/flux tube must be introduced. The continuity equation for the mass flux, \dot{M} , then reads

$$\dot{M} = \rho V A = \int_{R_\odot}^{\infty} dr q(r) \quad (1)$$

The plasma source function, $q(r)$, is left here unspecified. It contains all the complexities of the ionization/recombination processes (Hansteen *et al.* 1997) in the chromosphere, where the plasma is produced and the mass flux determined (Peter and Marsch 1997). The flow-tube area function is $A(r) = f(r)r^2$, and $f(r)$ describes the non-spherical expansion. This function is traditionally modeled after Kopp and Holzer (1976), but more realistic functions are provided by Wang and Sheeley (1990) or recently Banaszkiewicz *et al.* (1998). The maximum of $f(r)$ may typically range at 10. For the evolution of the radial magnetic field component Gauss' law is used, implying that the magnetic flux, $F_B = A(r)B_r$, is constant.

As shown below (or see the review of Tu and Marsch 1995a), the fast streams are permeated by low-frequency Alfvén waves. These waves exert a wave-pressure-gradient force and can thus accelerate the flow (Belcher 1971; Alazraki and Couturier 1971; Hollweg 1973; Jacques 1978; Leer *et al.* 1982). Also direct acceleration, denoted by a_w , of the ions by cyclotron-resonant absorption of high-frequency waves (Hollweg 1978; Hollweg and Turner 1978; Dusenbery and Hollweg 1981; Marsch *et al.* 1982a; Isenberg and Hollweg 1983) may occur. The momentum equation including the Alfvén wave pressure, p_w , and cyclotron-wave acceleration, a_w , is

$$V \frac{d}{dr} V = -\frac{1}{\rho} \frac{d}{dr} (p + p_w) + a_w - \frac{GM_\odot}{r^2} \quad (2)$$

The thermal particle pressures are $p_e = nk_B T_e$ and $p_p = nk_B T_p$. Quasineutrality means $n_e = n_p = n$, and the mass density is $\rho = n(m_p + m_e)$. The wave pressure is

$$p_w = \frac{1}{8\pi} \langle \delta B^2 \rangle = \frac{1}{2} \rho \langle \delta V^2 \rangle \quad (3)$$

i.e., it is given by the mean value of the magnetic or kinetic fluctuation energy of the waves. The radial evolution of the Alfvén waves is described by the wave-energy exchange equation including wave dissipation, Q_w , which may be written as

$$V \frac{d}{dr} p_w = Q_w + \frac{1}{A} \frac{d}{dr} (AF_A) \quad (4)$$

Here the Alfvén speed is $V_A = B_r / \sqrt{4\pi\rho}$. The wave energy flux density may be written as $F_A = p_w(3V + 2V_A)$. Note that Q_w is a source for thermal energy of the particles but a sink for the wave energy.

Concerning the thermodynamics and energetics of the corona and wind, there is now agreement among solar physicists that the problem of solar wind acceleration and coronal heating must be treated in concert (Hammer 1982a, b; Hollweg 1986; Hollweg and Johnson 1988; Withbroe 1988; Hansteen and Leer 1995), and that the corona cannot simply be assumed as a given boundary when dealing with the wind acceleration but rather that both phenomena are intimately connected. For solar wind models this requires placing the boundary not at the bottom of a 10^6 K corona but even further down in the upper chromosphere or lower transition region (Axford and McKenzie 1997; Marsch and Tu 1997a, b). The price to be paid by including these complications is that radiative losses in EUV and X-ray emission and conductive losses in terms of an inward directed heat flux must be accounted for. The radiative loss function, $L = n_e^2 \Lambda(T_e)$, is proportional to the squared electron density and the function $\Lambda(T_e)$, which is given by atomic physics and determined by the collisionally excited, atomic radiation of the various highly ionized minor elements in the corona (Mariska 1992).

The coronal heating function is the great unknown in solar corona and wind theory. Therefore, the energy input has often been modeled *ad hoc* (e.g., Holzer and Axford 1970; Hammer 1982a, b; Withbroe 1988) by a simple exponential heating function such that

$$Q_p = Q_p(R_\odot) e^{-(r-R_\odot)/\lambda_m} \quad (5)$$

where the damping length λ_m is an adjustable free parameter of the model. The proton heating rate, Q_p , is determined by the energy flux required to maintain corona and wind, which in coronal holes requires the typical value of 5×10^5 erg/(cm² s) in compliance with the estimated overall energetics of the atmosphere and wind. The thermodynamics, i.e., the cooling of the plasma by radiation (loss function L) and conduction (heat flux $F_{e,p}$), and its heating by mechanical energy input at a volumetric rate $Q_{e,p}$ and by Alfvén wave dissipation at the rate Q_w , all these processes are described by the entropy or internal energy equations, which read (with $\gamma = 5/3$) as follows:

$$\begin{aligned} V \frac{dT_p}{dr} + (\gamma - 1) \frac{T_p}{A} \frac{d}{dr}(VA) &= -\nu_{ep}(T_p - T_e) \\ \frac{(\gamma - 1)}{nk_B A} \frac{d}{dr} \left[A \kappa_p \frac{\partial T_p}{\partial r} \right] + \frac{2Q_p}{3nk_B} \end{aligned} \quad (6)$$

$$\begin{aligned} V \frac{dT_e}{dr} + (\gamma - 1) \frac{T_e}{A} \frac{d}{dr}(VA) &= +\nu_{ep}(T_p - T_e) \\ \frac{(\gamma - 1)}{nk_B A} \frac{d}{dr} \left[A \kappa_e \frac{\partial T_e}{\partial r} \right] + \frac{2Q_e}{3nk_B} - L \frac{(\gamma - 1)}{nk_B} \end{aligned} \quad (7)$$

Here ν_{ep} is the Coulomb collision frequency between protons and electrons. In order to account for the observed temperature differences of electrons and protons we need to consider two separate energy equations (Hartle and Sturrock 1968; Holzer and Axford 1970), in which there are different heating sources and collisional couplings between the two species. The radiative loss only appears in the electron equation, since it is the electrons that lose thermal energy by collisional EUV-line excitations and soft X-ray emissions. Classical collisional conduction is included here for both species, with the thermal conductivity $\kappa_{e,p}$ being independent of the density $n_{e,p}$ and proportional to $T_{e,p}^{5/2}$. Modified heat-flux laws have in the past (Hollweg 1986) and again recently (Hu *et al.* 1997) been used in models for the outer corona and distant wind, mainly because of our lack of understanding of heat conduction processes in the collisionless solar wind in the presence of strong wave turbulence.

For the electrons Lie-Svendsen *et al.* (1997) solved the full Fokker-Planck kinetic equation and found very significant deviations from Fourier's law. The electron drift speed and heat flux was found to be carried entirely by the collisionless suprathermal tail electrons, which were able to surmount the electrostatic potential barrier produced essentially by the core electron pressure. The classical proton heat conduction law breaks down close to the corona and generally tends to overestimate the heat carried by protons. In an 8-moment approximation of the two-fluid equations, Olsen and Leer (1996) were able to demonstrate and quantify the validity range of Fourier's law for the protons in models with different coronal heating rates.

In order to describe the evolution of the Alfvénic fluctuations one must consider complicated spectral transfer equations. Also, dissipation and nonlinearity is to be accounted for. This forces one to consider turbulence models of the solar wind. Tu *et al.* (1984) and Tu (1987, 1988) were the first to modify the WKB theory to describe the cascading and damping of interplanetary fluctuations and the associated heating of the solar wind. The evolution of the fluctuations is described in those papers or in Tu and Marsch (1995a, b; 1997).

If the temperature is anisotropic, we have to further differentiate between the parallel and perpendicular degrees of freedom (e.g., Leer and Axford 1972), and consider the coupling processes between the parallel and perpendicular temperatures. Marsch and Richter (1984) have determined empirical estimates of the related effective anomalous collision frequency, which turns out to be about $10^{-3} \Omega_p$, a value required to explain the in-situ-observed temperature anisotropies. Detailed parametric studies of the fast solar wind in models including the proton temperature anisotropy have recently been carried out by Hu *et al.* (1997), who conclude that anisotropy has little influence on the dynamics yet imposes requirements on the heating mechanism of the solar wind.

The basic mechanism for the solar wind acceleration will only be satisfactorily understood once progress is made in the following fields. The input of mechanical energy, most likely in the form of waves and small-scale directed flows through the network (see references related to Working Group 2 organized by Axford, Rosner

and Priest, this volume), and the associated heating functions must be defined in terms of micro-physics and not simple parametric models. The transport phenomena associated with weak collisions and strong wave-particle interactions need to be described quantitatively and understood from first plasma-physics principles. The chromospheric plasma sources and the associated plasma production processes must be identified and clarified. None of the existing models fulfills these requirements. Yet, we shall briefly review them in the following section.

3.2. MODELS WITH HOT IONS IN THE INNER CORONA

Solar wind models which drive the high-speed wind by wave dissipation leading to hot protons in the corona were presented some time ago by Hollweg and Johnson (1988) and Isenberg (1990). McKenzie *et al.* (1995) developed more recently a theory for the high-speed solar wind with a simple dissipation-length characterization of wave heating of the coronal plasma close to the Sun, with the dissipation length λ_m ranging between 0.25 and 0.5 R_\odot . The significant features of the solution based on the model equations of the previous sections are: rapid acceleration with a sonic point at about 2 R_\odot , and very high maximum proton temperature, namely 8 to 10 MK. Such efficient near-Sun dissipation requires high-frequency Alfvén waves in the range above 1 Hz. McKenzie *et al.* (1997) have extended these calculations further to include also the proton temperature anisotropy.

Hansteen and Leer (1995) and Esser *et al.* (1997) have presented parameter studies on the effects of very hot protons in the inner corona on the nascent solar wind. A high T_p is a genuine property of these models, and thus flow velocities of up to 800 km/s are readily obtained within 10 R_\odot by a deposition of heat or momentum within a fraction of a solar radius above the Sun's surface. Li *et al.* (1997) studied recently in detail the influence of heavy ions on the fast wind in a three-fluid model. They conclude that preferential heating of heavy ions, in particular of alpha particles, has an impact on the bulk flow which must be considered in wind models.

None of the models discussed so far described the detailed physics of the heating mechanism. Tu and Marsch (1997) elaborated the ideas of Marsch (1992) and Axford and McKenzie (1992, 1997) that high-frequency Alfvén wave dissipation is responsible for the heating, a process well established in the distant solar wind. The key model assumptions are as follows. Proton-cyclotron damping of Alfvén waves, running into resonance in a rapidly declining magnetic field, gives fast heating close to the Sun (Marsch *et al.* 1982). The wave energy is then absorbed by the particles at the local dissipation frequency, i.e., at Ω_p , which declines with solar distance such that a growing part of the power spectrum is converted into heat. This dissipation builds up a large proton temperature. Input in the model is the unknown power spectrum for which assumptions have to be made, guided by what is observed in situ (see the subsequent Figure 2). The protons attain temperatures of 2–3 MK. Since proton heat conduction was included the temperature maximum was lower

than without conduction. For a more detailed study of the subtle effects of proton heat conduction see the recent work of Olsen and Leer (1996).

3.3. COULOMB COLLISIONS AND ALFVÉNIC TURBULENCE

Besides Coulomb collisions, kinetic wave-particle interactions induced by small-scale waves and fluctuations play a key role in particle scattering and related transport and largely shape velocity distributions, together with the mean large-scale interplanetary forces which are determined by the global set up of the heliosphere. The heliospheric current sheet region, where the electrons and ions are comparatively cold and their density is high, is the collisional domain of the wind. Plasma waves play in the collisionless coronal hole and associated wind a role similar to collisions. In the expanding inhomogeneous solar wind, the particle distributions develop velocity-space gradients which can drive plasma instabilities and lead to wave growth or damping. The kinetic wave modes of primary importance are the ion-cyclotron, ion-acoustic and whistler-mode waves, which are the high-frequency extensions of such fluid modes as the Alfvén, slow and fast magnetoacoustic waves.

Ulysses observations have revealed new aspects of the nature of Alfvénic fluctuations at high latitudes. Firstly, their amplitudes or the field component variances are very large (Smith *et al.* 1995). Secondly, they are intimately linked with discontinuities (Tsurutani *et al.* 1997), which occur at rates of about 150 per day. Thirdly, rotational discontinuities are an integral part of the Alfvén wave, such that phase glitches (of about 90°) often occur, which leads one to consider these directional fluctuations as phase-steepened nonlinear Alfvén waves (Riley *et al.* 1995). Vasquez and Hollweg (1998a, b) have recently provided a theoretical explanation of this interesting wave phenomenon.

The radial evolution of the power spectrum of Alfvénic fluctuations in the ecliptic plane is illustrated in Figure 2, after Tu and Marsch (1995b), which shows the power spectra of Alfvén waves at 0.29 and 0.87 AU and the obvious steepening and decline in intensity with increasing distance from the Sun. The spectra are normalized to the WKB amplitude evolution. Thus the dissipation becomes clearly visible. Wave energy is lost in the expanding wind to the particles and helps in maintaining non-adiabatic ion temperature profiles.

4. Boundary Conditions and Radial Gradients

4.1. FLOW VELOCITIES NEAR THE SUN

One of the key objectives of SOHO was to measure by Doppler spectroscopy the initial flow velocity profiles of the fast wind emanating from coronal holes. Yet, the measurement of the EUV lines emitted from plasma in the transition region and lower corona still do not give a fully conclusive picture of the flow pattern

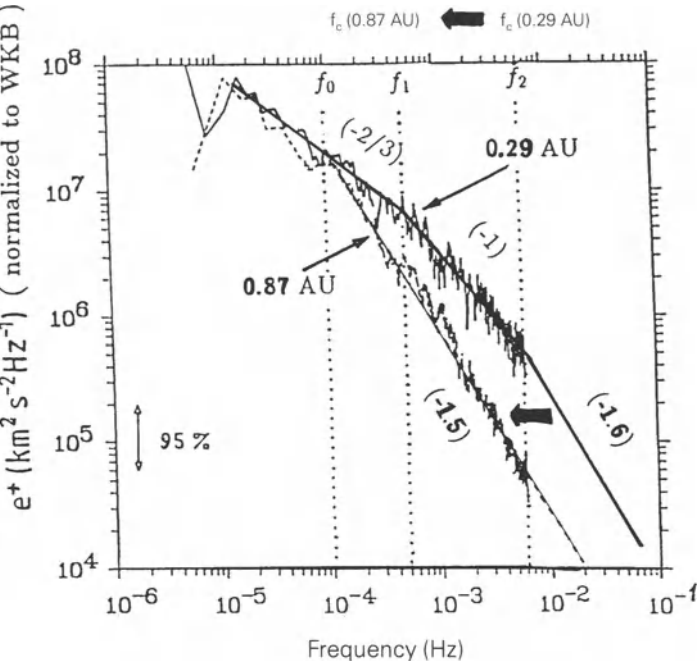


Figure 2. The power spectra of Alfvénic fluctuations for two solar distances. Each spectrum is normalized to the WKB solution to emphasize turbulence evolution and dissipation, which become obvious in the difference between the two curves. Spectral slopes are given in brackets (Tu and Marsch 1995b).

there, because the shifts observed may be due to waves and/or directed flows, and the interpretation of the data is not entirely free from ambiguities. Chae *et al.* (1998) and Brekke *et al.* (1997) analyzed Doppler shifts from many lines for the quiet Sun and over a temperature range of $\log(T/K) = 4\text{--}6$. Their results are composed in Figure 3 and show that near $\log(T/K) = 5$ there is a maximum of the shift, located at about 10 km/s average red-shift, which indicates downflows away from the observer, perhaps mostly of plasma confined in loops but not on open field lines. The interpretation of the decreasing red-shift at high temperatures ($> \log(T/K) = 5$) is still controversial.

Wilhelm *et al.* (1998) in coronal hole (CH) observations off limb found Mg IX 706 Å ions at higher red-shifts of up to 34 km/s. It is only very recently that Hassler *et al.* (1999) found systematic outflows (blue-shifts) in the polar CH and downflows (red-shifts) at lower latitudes in full-Sun disk observations. Hassler *et al.* (1999) investigated in particular the blue- and red-shifts of the hot EUV emission line Ne VIII 770.4 Å and found sizable line-of-sight (LOS) blue-shifts, on the average of up to 10 km/s, in a coronal hole in the polar cap region. Marsch and Tu (1997a)

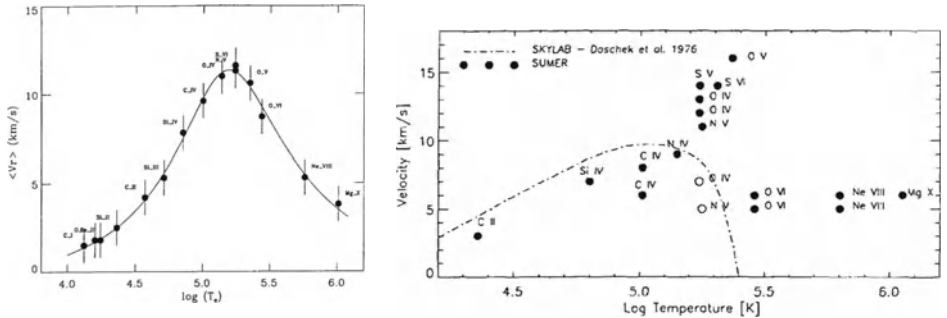


Figure 3. Average Doppler shifts observed in the quiet Sun according to Chae *et al.* (1998), on the left, and Brekke *et al.* (1997), on the right. Note that the maximum shift occurs in transition region lines and at temperatures of about 0.1 MK.

have modeled the outflow of the nascent solar wind in the coronal funnels rooted in the network lanes and got flow speeds of that order and higher.

With the LASCO and UVCS coronagraphs the near-Sun outflow velocity profiles of the expanding corona and wind have been inferred. From white-light coronagraph difference images Sheeley *et al.* (1997) derived the flow speed of the plasma. The moving coronal features, marking the slow wind flow, cluster in speed around a parabolic radial path characterized by a constant acceleration of about 4 m/s^2 . Habbal *et al.* (1997) reported velocities derived from UVCS oxygen-ion coronal images. A velocity of 100 km/s is observed at a distance of $1 R_\odot$ over the poles, whereas the acceleration is much slower in the streamer belt, where such a value is only reached beyond $3 R_\odot$. Furthermore, the slow wind seems to peel slowly off the streamer tops in an intermittent fashion (Sheeley *et al.* 1997), whereas evidence is accumulating that the fast wind accelerates rather rapidly.

Recent measurements with EISCAT seem to suggest that the full acceleration of the wind over the Sun's poles occurs within $10 R_\odot$ (Grall *et al.* 1996). The direct flow-velocity measurements of UVCS clearly indicate strong near-Sun acceleration (Corti *et al.* 1997), in which the outflow speed increases from 50 km/s at $1.5 R_\odot$ to 140 km/s at $2.3 R_\odot$ in the Doppler-dimming data obtained along a line of sight cutting through a plume.

4.2. ION TEMPERATURES IN THE CORONA

The SUMER instrument is able to measure the temperature gradient from the chromosphere through the Transition Region into the lower corona. The SUMER instrument design and characteristics, and its performance and first results are described by Wilhelm *et al.* (1995, 1997) and Lemaire *et al.* (1997). Using SUMER, Seely *et al.* (1997) made observations in coronal streamers and found the widths of many EUV emission lines of different ions to be much larger than the thermal width

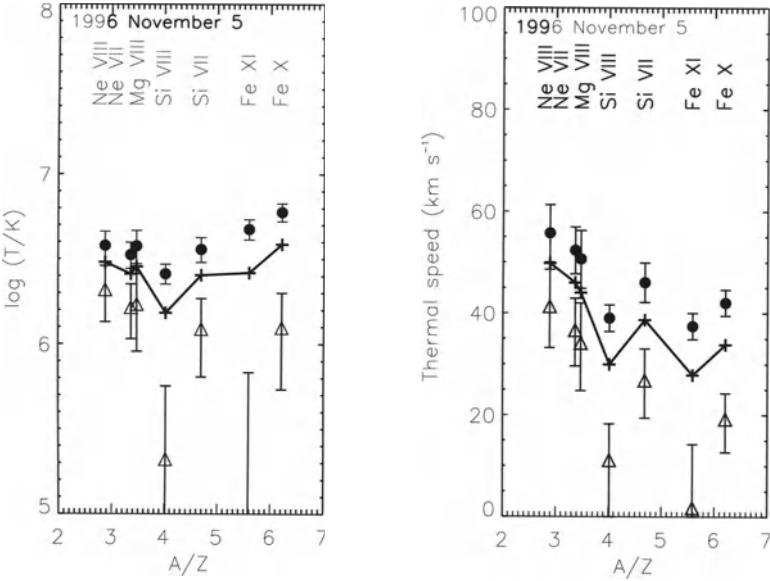


Figure 4. Minor ion temperatures and thermal speeds observed in a southern polar coronal hole. The left panel shows the logarithm of the ion temperature, $\log(T_i/\text{K})$ versus the A_i/Z_i ratio of the ions. The right panel shows the thermal speed of the ions. Diamonds represent the results for $\xi = 0 \text{ km/s}$, while triangles are for $\xi = 34 \text{ km/s}$. Solid curves with plus signs refer to a value of $\xi = 25 \text{ km/s}$. The error bars correspond to a ± 0.2 pixel variation of the Gaussian-fit standard deviation σ for each line (after Tu *et al.* 1998).

expected for a kinetic temperature equal to T_e or the line formation temperature. Arguments were put forward that the effective temperature in those lines is of a kinetic nature with no or weak contribution only of a “turbulent” velocity. After Seely *et al.* (1997) the kinetic temperature T_i for ions originating from such elements as Ne, Fe, Mg and Si would range between 2.5 and 6 MK for heights above the solar limb between 100 arcsec and 200 arcsec. Yet, these observations are of questionable relevance for the free-flowing solar wind.

Therefore, Tu *et al.* (1998) investigated the temperatures of minor ions also in a polar coronal hole, where the slits were oriented in the north-south direction and placed above the southern limb of the Sun. In Figure 4 the data are presented according to the mass-per-charge, m_i/e_i , or A_i/Z_i values of the various ions (with $m_i = A_i m_p$ and $e_i = Z_i e$ and the electric charge unit e). The purpose of this data presentation is to compare the different ion temperatures and discriminate them by their fundamental atomic parameters, without making assumptions about the local plasma state in the emission region.

More importantly, it was suspected that the coronal heating of the ions may be of a kinetic nature and caused primarily by cyclotron-resonance with high-frequency

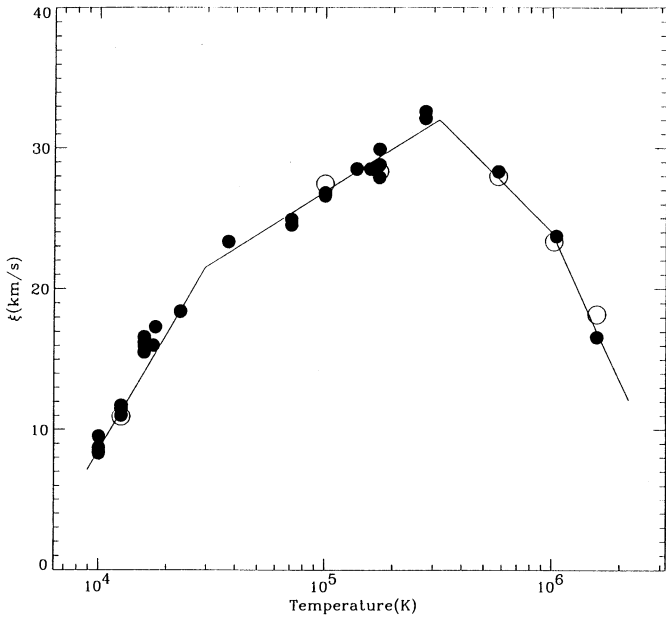


Figure 5. Turbulence speed in the transition region and lower corona as inferred from EUV emission line width, after Chae *et al.* (1998).

Alfvén waves. There is strong evidence, found in-situ by observations (Marsch *et al.* 1991a, b) of the fast solar wind originating from coronal holes, for ion-cyclotron resonant heating taking place in the interplanetary medium. This possibility was also demonstrated in models (Marsch *et al.* 1982; Isenberg and Hollweg 1983). Therefore, it is important to see if preferential heating occurs in the corona as well.

Figure 4 shows the ion temperatures and thermal speeds. The diamonds represent the upper limits of the temperatures and thermal speeds in the left and right panels, respectively. The triangles show the minimum temperatures and thermal speeds, which are calculated with a turbulent speed of $\xi = 34$ km/s. This value is very near the effective speed of Fe XI, which is 37 km/s and equal to the maximum possible value of ξ . The thermal speeds seem to increase generally with the ion gyrofrequency (or decrease with m_i/e_i), a result which may indicate that ion-cyclotron heating is responsible for the high ion temperatures.

4.3. TURBULENCE AMPLITUDES

One of the key parameters from the modeling point of view and as far as the energetics of corona and wind is concerned is the wave or turbulence amplitude. In

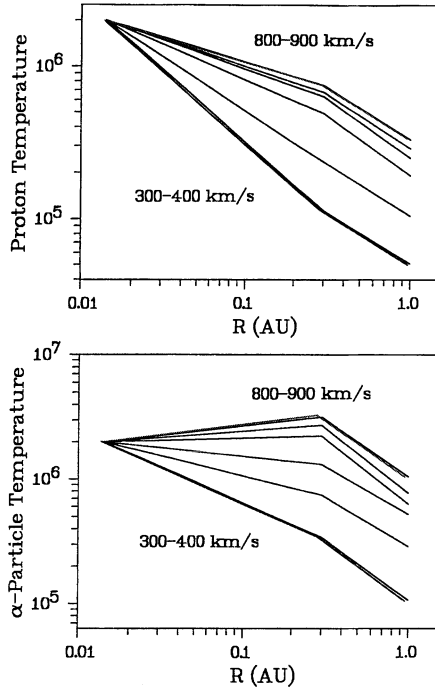


Figure 6. Temperatures of the protons (top) and alpha particles (bottom) versus distance from the Sun for different solar wind speeds as indicated. The profiles inside 0.3 AU are an extrapolation of the Helios observations, obtained by connecting the in-situ profiles with a coronal temperature of 2 MK at $3 R_\odot$.

Figure 5 the results from a paper by Chae *et al.* (1998) are shown. The turbulence amplitude ξ is given versus T_i , as derived from observations on the solar disk. Clearly, there seems to be an upper limit of $\xi = 30$ km/s, with a decline of ξ toward higher temperatures. It should be emphasized that this value would be sufficient to drive fast flows with gradual acceleration, but not flows where the acceleration is achieved essentially within the first $10 R_\odot$. That ξ declines with height is an observational bias of on-disk observations. Off-limb measurements (Wilhelm *et al.* 1998; Tu *et al.* 1998) indicate a further increase of the amplitude up to about 80 km/s near $1.35 R_\odot$, consistent with the expectations of WKB theory of undamped waves conserving their wave action (Jacques 1978), if we attribute the whole linewidth to turbulence. If the interpretation is in terms of a kinetic temperature, then Si VIII would be at 10 MK at $1.35 R_\odot$.

There has been evidence for the existence of hot minor ions in the distant solar wind already for a long time (see the reviews of Marsch 1991a, b). Helios observed in situ that alpha particles in the fast wind near 0.3 AU were hotter than 10 MK.

Similary, protons were found to almost be at the then canonical 1 MK coronal temperatures perpendicular to the magnetic field. These old observations comply nicely with the new SOHO results and indicate a region of the outer corona, beyond a distance range where the SOHO EUV instruments can measure, of extended ion heating. Depending on the wind speed the temperature profiles can then be smoothly connected with the ones obtained and extrapolated from Helios results. These are plotted in Figure 6, reproduced from Thieme *et al.* (1990).

4.4. OXYGEN DIFFERENTIAL SPEED AND TEMPERATURE

All recent SOHO observations indicate that the protons, and more so the heavy ions, are rather hot in coronal holes. The minor ion temperatures are strongly anisotropic, as clearly indicated by the oxygen line shapes derived from the UVCS instrument which were presented by Cranmer *et al.* (1999) and by Kohl *et al.* (1997) in their report about first results from the UVCS instrument, and recently in Li *et al.* (1997). For oxygen, T_{\perp} is much larger than T_{\parallel} , a signature which is familiar from the Helios proton in situ measurements. Some of the UVCS results are shown in Figure 7, which gives the proton (left) and oxygen (middle) temperature and the oxygen speed (right) as a function of heliocentric distance. Note the radially increasing relative speed of O^{+5} with respect to the protons and similarly the pronounced temperature difference, indicating strong preferential heating and acceleration of O^{+5} , effects which are interpreted as being the result of ion-cyclotron heating. The equivalent thermal velocity, corresponding to the Doppler width of the O VI 1032 Å line, is truly remarkable since it reaches 600 km/s. If this is interpreted as a kinetic broadening it would give a minor-ion coronal temperature of more than 100 MK! Strangely enough, because the Alfvén velocity is still higher, the local ion plasma beta is much smaller than unity, and thus minor ions still represent a cold plasma from the kinetic point of view.

4.5. ELECTRON TEMPERATURE AND DENSITY

The electron density and temperature in coronal holes are of paramount importance, since they not only characterize the collisional properties and the electron partial pressure in the coronal hole, but also determine the ionization state of hydrogen, helium and heavier elements and govern the radiative losses in the EUV and soft X-rays through collisional line excitation (see, e.g., Mariska 1992). Strictly speaking it is the detailed electron distribution function that matters; this is presently incapable of measurement close to the Sun, yet well known farther away, where nonthermal features prevail, such as the suprathermal tail, the strahl, and the core-halo structure (see Pilipp *et al.* 1987; Marsch 1991a; Marsden 1995, for the details).

Line ratio techniques have been used to determine the electron density and to establish with SOHO the electron density profiles for the first few 100 arcsec above the limb in various regions. Wilhelm *et al.* (1998) have used the Si VIII

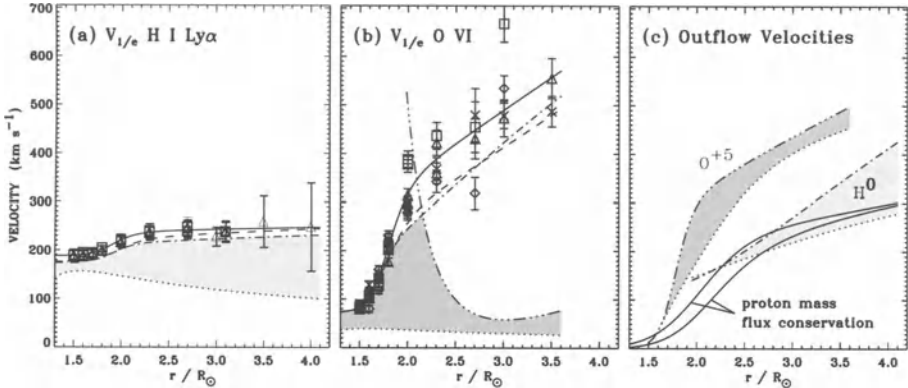


Figure 7. The proton (a) and O $^{+5}$ (b) ion thermal speeds and bulk speeds (c) observed in a southern polar coronal hole. Note the pronounced preferential heating and acceleration of oxygen with respect to the protons, a result that perhaps indicates cyclotron heating. For comparison the thermal speeds based on the electron temperature (dotted lines in [a] and [b]) are shown as well (Cranmer *et al.* 1999).

1445.73 Å / 1440.51 Å line ratio, yielding a density that starts at 10^8 cm $^{-3}$ at 20 arcsec (1 arcsec \approx 715 km) and drops to about 6×10^7 cm $^{-3}$ at an altitude of 300 arcsec in the polar CH. This profile smoothly continues into the radial profile of n_e as estimated by the UVCS measurements of oxygen O VI 1032 Å / 1037 Å line intensities and related emission measures (Corti *et al.* 1997). Given these densities, one can infer a corresponding flow speed of the plasma by exploiting the mass continuity equation and assuming a flow or flux tube geometry. This technique was applied by Fisher and Guhathakurta (1995) and also implies that the wind is strongly accelerated very close to the Sun.

One of the major surprises of SOHO is the fact that electrons are rather cold in CHs, evidence that comes from T_e estimates obtained from EUV emission line ratios. Wilhelm *et al.* (1998) used the Mg IX 749.55 Å / 706.07 Å line ratio and concluded that T_e hardly ever reaches the canonical value of 1 MK, but remains below it and rapidly falls off with height in the CH. Similarly, David *et al.* (1998) derived, in a synergistic effort of the SUMER and CDS instruments using the line pair O VI 173 Å / 1032 Å, the electron temperature profiles in an equatorial streamer at the west limb and in a coronal hole at the polar north limb. Again, their data shown in Figure 8 demonstrates that electrons cool off rapidly and only have a T_e of about 0.5 MK at $1.3 R_\odot$.

These low electron temperatures are consistent with the Helios velocity distribution measurements almost a full solar cycle ago, which clearly indicated that interplanetary electrons are cold and their radial temperature gradients flat in the fast flows associated with the CHs (see the review by Marsch 1991a). There was strong

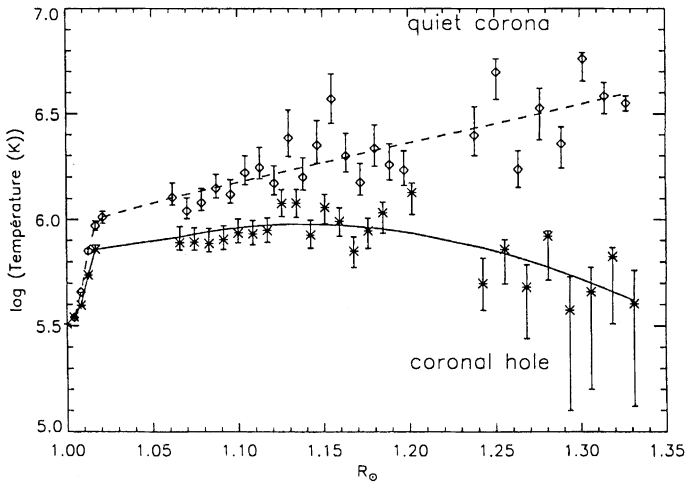


Figure 8. Electron temperature gradients in the inner corona as obtained from EUV line-ratio diagnostics with the CDS/SUMER spectrometers on SOHO (David *et al.* 1998). Note that the electrons cool off rapidly in coronal holes and more slowly in the streamers.

evidence that interplanetary electrons cool off strongly in fast wind, or even started at low temperatures at the Sun, a speculation which now seems to be consistent with the coronal data from SOHO.

5. Kinetic and Multifluid Characteristics

5.1. INTRODUCTION

At all heliospheric latitudes the radial evolution of the internal state of the wind resembles a complicated irreversible process, in the course of which free (as compared with LTE and MHD equilibrium conditions) particle kinetic energy is converted into wave and turbulence energy on a wide range of scales. This implies interplanetary production of entropy, which is illustrated in Marsch and Richter (1984), who calculated the total entropy of the wind (electrons, protons and alpha particles included) based on an equivalent bi-Maxwellian. This specific entropy clearly increases with distance from the Sun for all wind speeds. The entropy is produced by collisions, heat flux degradation, micro-turbulent wave-particle interactions, and stream mixing or viscous heating by wind velocity shear. Turbulent fluctuations lead to intermittent wave-particle scattering and unsteady anomalous transport, mixed with the weak effects of the rare Coulomb collisions. Spherical expansion and large-scale inhomogeneity force the wind to attain a complex state of dynamic statistical equilibrium between the particle species and field fluctuations.

5.2. VELOCITY DISTRIBUTIONS AND KINETIC PROPERTIES

The in-situ observed distributions of ion and electrons come in various shapes and vary widely with the solar wind speed, heliographic coordinates and the phase of the solar cycle. Typical proton distributions, ranging from Maxwellian in the heliospheric current sheet to highly nonthermal in fast solar wind streams, have temperature anisotropies with $T_{\perp} > T_{\parallel}$ and field-aligned beams with a drift speed larger than the local Alfvén speed. Ion differential streaming also occurs, which is probably generated in the inner corona and from thereon fades away with heliocentric distance (Marsch 1991a), as is known from Helios data. In the ecliptic plane, sometimes differential ion streaming is still seen with Ulysses beyond 1 AU at shocks and stream interaction regions (Neugebauer *et al.* 1994). At high latitudes, differential streaming is also evident well beyond 1 AU (Neugebauer *et al.* 1996).

The shape variations of the ion distribution functions in fast wind have been investigated systematically. Whereas high-energy extensions are a universal property of the protons, they are not seen in the alpha particles which tend to move faster than the protons and surf on the ubiquitous Alfvén waves (for a review of this phenomenon see Marsch 1991a, b). Some typical proton distributions are presented in Figure 9, together with the radial profile of the average magnetic moment $\mu_p = T_{p\perp}/B$ of the particles as a function of radial distance from the Sun. The radially increasing μ_p indicates continuous ion heating perpendicular to the field in the interplanetary medium.

Heavy ions have often been used to trace wave effects in the wind and as test particles to probe the plasma. One of the most prominent features of minor ions is that they all travel at the same speed (by about V_A faster than the protons) and show temperature scaling in proportion to their masses, with the exception of helium (Neugebauer 1981). Ulysses observations showed, now with very good statistical significance, that all ions heavier than helium have the same speed and the same thermal widths of their velocity distribution functions (von Steiger *et al.* 1995) for wind speeds above 400 km/s. Recent measurements from SOHO confirm these features (Hefti *et al.* 1998), but on much better time resolution of typically 5 minutes only to obtain a statistically reliable minor ion energy distribution.

The electron distribution functions in velocity space are determined by the large-scale interplanetary magnetic field and electrostatic potential (related to the electron pressure gradient), by Coulomb collisions in the thermal energy range, and by various kinds of wave-particle interactions at all energies. They can be decomposed into two components, a cold and almost isotropic collisional core and hot variably skewed halo population, and may be described by two convecting bi-Maxwellians as illustrated in Figure 10. On open field lines the halo usually develops a high-energy extension with a very narrow pitch-angle distribution, the so-called strahl.

Observations of the ICE and Ulysses spacecraft, while being radially aligned, allowed one to characterize the radial gradients of electron thermal parameters

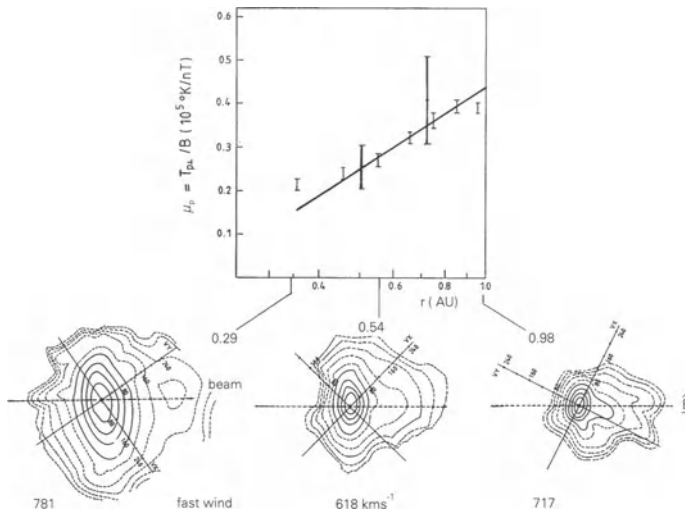


Figure 9. Proton magnetic moment versus heliocentric distance (top) and selected velocity distribution functions measured in high-speed wind (Marsch 1991a). Solid isodensity contours correspond to 20% steps of the maximum and the last broken contour is at 0.1%. Note the large temperature anisotropy in the core and the proton beam along the magnetic field. The magnetic moment increases, thus indicating interplanetary heating. The solid line shows Tu's (1988) model results.

(Phillips *et al.* 1995). The core temperature was found to vary widely between isothermal and adiabatic, while the halo behaves more isothermally. The halo density falls off more steeply in dense plasma. McComas *et al.* (1992) have studied the halo electron parameters in the range from 1 to 4 AU and found that the halo represents always about 4% of the total distribution. The break point energy in the electron spectrum scales on average like 7 times the core temperature, a result predicted by Scudder and Olbert (1979a, b) for electrons mediated by Coulomb collisions. There is no simple way to model these characteristics other than by a kinetic theory, or by at most two electron fluids, an approach that no one has yet attempted for the electrons in the solar corona and wind.

In the context of the freezing-in of the ionization state of heavy ions in the corona (Geiss *et al.* 1995; Ko *et al.* 1997) non-Maxwellian electron distribution functions have been invoked frequently to explain the deviation from a Saha-type ionization equilibrium. The most convenient form of such distributions is the so-called κ -distribution, which is a generalized Lorentzian with overpopulated high-energy tails. Maksimovic *et al.* (1997) have fitted thousands of Ulysses electron energy-distributions by κ -distributions, and come up with typical values for the κ -parameter between 2 and 3 in fast and from 3 to 4 in slow solar wind. The problem with the κ -

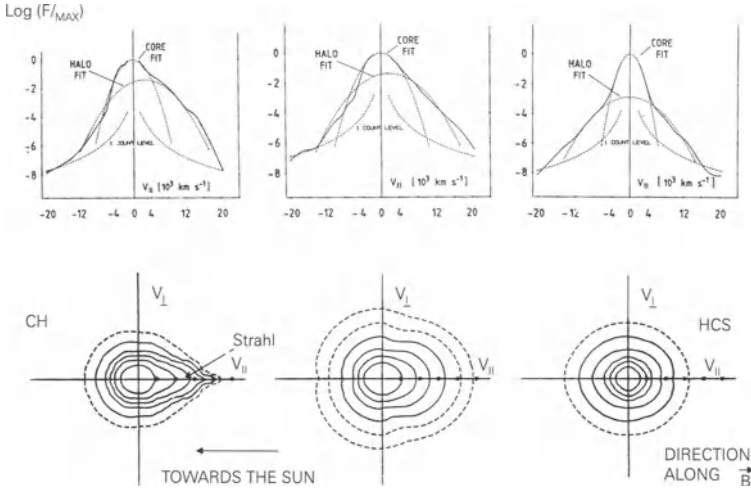


Figure 10. Electron velocity distribution functions as energy spectra (top) and velocity space contours (bottom) for fast (left), intermediate and slow (right) wind (after Pilipp *et al.* 1987). Note the core-halo structure and the strahl of suprathermal electrons in fast solar wind.

function is that it cannot represent adequately the detailed pitch-angle distributions as measured by Helios and shown in Figure 10.

It has been argued for a long time that whistler waves might be the primary agent for the regulation of the electron heat flux. Feldman *et al.* (1976a, b) suggested a simple heat conduction law, in which the heat flux (F_e) is carried mainly by the halo electrons and scales essentially in proportion to the halo particle flux times the halo temperature. This proportionality has now experimentally been verified to a high degree by Scime *et al.* (1994), demonstrating that solar wind heat conduction has not much to do with the local temperature gradient but with the thermal energy convected by halo electrons. The halo drift speed itself is closely tied to the Alfvén velocity or the local magnetic field, which is evidence for a wave regulation of the heat flux. Radial profiles, as measured with Helios, of $F_{e,p}$ and their sum including ion differential motion can be found in the paper of Marsch and Richter (1984), which indicates that F_p is not negligible but amounts to 30% of F_e near 0.3 AU and may likely become comparable in coronal holes.

6. Conclusions and Open Questions

In the past years considerable progress has been made in characterizing the coronal plasma state and in determining the radial profiles of key parameters in the polar

coronal holes. This success is largely due to the unprecedented and concerted effort of all the SOHO corona instruments. The new empirical constraints have to be accepted and digested by the theorists concerned with modeling the fast wind. Certainly, the single fluid descriptions are outdated and multi-fluid models are necessary. It is also obvious that a thorough understanding of the microstate of the coronal plasma as diagnosed by means of EUV-line shapes and in-situ-measured ion compositions will require a new approach, going beyond the MHD paradigm and classical transport but involving instead kinetic physics and concepts familiar from space plasmas in the heliosphere. It is time to abandon the simple heating functions so common in models, and to face the difficult problem of identifying the traits of the real heating processes in the data and of developing the associated microphysics. This involves waves at frequencies much higher than considered in conventional MHD models. Kinetic physics will open new avenues for research on the coronal heating and solar wind acceleration problem.

Even after SOHO, many important questions concerning corona and wind remain open. We list a few here: What heats the two types of corona, being either closed with dense plasma in magnetic confinement, or open with dilute plasma escaping on magnetic field lines? What determines the solar wind mass flux? Is it the properties of the plasma source region in the upper chromosphere or the temperature conditions in the corona? Do we understand transport in the weakly collisional corona, or do we have to invoke kinetic physics to explain solar wind acceleration? What is the role of waves? Clear unambiguous evidence for waves is not easily established in the remote-sensing spectroscopic data. Can stationary multi-fluid models describe adequately the fast steady wind? Is the slow wind a boundary-layer phenomenon, or does it originate in the transiently opening streamer belt around the Sun, releasing plasmoids like droplets from a leaking water tap? These are some of the key questions awaiting an answer from the community of space and solar physicists.

References

- Alazraki, G., and Couturier, P.: 1971, Solar wind acceleration caused by the gradient of Alfvén wave pressure, *Astron. Astrophys.*, **13**, 380.
- Axford, W. I., and McKenzie, J. F.: 1992, The origin of high speed solar wind streams, in *Solar Wind Seven*, ed. E. Marsch and R. Schwenn, (Pergamon Press: Oxford, England), pp. 1–4.
- Axford, W. I., and McKenzie, J. F.: 1997, The solar wind, in *Cosmic Winds and the Heliosphere*, ed. J. R. Jokipii, C. P. Sonett, and M. S. Giampapa, (University of Arizona Press: Tucson, USA), pp. 31–66.
- Banaszkiewicz, M., Axford, W. I., and McKenzie, J. F.: 1998, An analytic solar magnetic field model, *Astron. Astrophys.*, **337**, 940–944.
- Barnes, A., Gazis, P. R., and Phillips, J. L.: 1995, Constraints on solar wind acceleration mechanisms from Ulysses plasma observations: The first polar pass, *Geophys. Res. Lett.*, **22**, 3309–3311.
- Belcher, J.: 1971, Alfvénic wave pressure and the solar wind, (*Astrophys. J.*, **168**, 509).
- Bertaux, J.-L., Quemerais, E., and Lallement, R.: 1996, Observations of a sky Lyman α groove related to enhanced solar wind mass flux in the neutral sheet, *Geophys. Res. Lett.*, **23**, 3675–3678.

- Bravo, S., Stewart, G. A., and Blanco-Cano, X.: 1998, The varying multipolar structure of the Sun's magnetic field and the evolution of the solar magnetosphere through the solar cycle, *Solar Phys.*, **179**, 223–235.
- Brekke, P., Hassler, D. M., and Wilhelm, K.: 1997, Doppler shifts in the quiet-Sun transition region and corona observed with SUMER on SOHO, *Solar Phys.*, **175**, 349–374.
- Chae, J., Yun, H. S., and Poland, A. I.: 1998, Temperature dependence of UV line average Doppler shifts in the quiet Sun, *Astrophys. J. Supp.*, **114**, 151.
- Corti, G., Poletto, G., Romoli, M., Michels, J., Kohl, J., and Noci, G.: 1997, Physical parameters in plume and interplume regions from UVCS observations, in *Proceedings of the Fifth SOHO Workshop*, ESA-SP-404, pp. 289–294.
- Cranmer, S. R., Kohl, J. L., Noci, G., et al.: 1999, An empirical model of a polar coronal hole at solar minimum, *Astrophys. J.*, **511**, 481.
- David, C., Gabriel, A. H., Bely-Dubau, F., Fludra, A., Lemaire, P., and Wilhelm, K.: 1998, Measurement of the electron temperature gradient in solar coronal holes, *Astron. Astrophys.*, **336**, L90.
- Dusenberry, P. B., and Hollweg, J. V.: 1981, Ion-cyclotron heating and acceleration of solar wind minor ions, *J. Geophys. Res.*, **86**, 153–164.
- Esser, R., Habbal, S. R., Coles, W. A., and Hollweg, J. V.: 1997, Hot protons in the inner corona and their effect on the flow properties of the solar wind, *J. Geophys. Res.*, **102**, 7063–7074.
- Feldman, W. C., Asbridge, J. R., Bame, S. J., Gary, S. P., and Montgomery, M. D.: 1976a, Electron parameter correlations in high-speed streams and heat flux instabilities, *J. Geophys. Res.*, **81**, 2377–2382.
- Feldman, W. C., Asbridge, J. R., Bame, S. J., Gary, S. P., Montgomery, M. D., and Zink, S. M.: 1976b, Evidence for the regulation of solar wind heat flux at 1 AU, *J. Geophys. Res.*, **81**, 5207–5211.
- Fisher, R., and Guhathakurta, M.: 1995, Physical properties of polar coronal rays and holes as observed with the Spartan 201-01 coronagraph, *Astrophys. J.*, **447**, L139–L142.
- Geiss, J., Gloeckler, G., and von Steiger, R.: 1995, Origin of the solar wind from composition data, *Space Science Reviews*, **72**, 49–60.
- Grall, R. R., Coles, W. A., Klinglesmith, M. T., Breen, A. R., Williams, P. J. S., Markkanen, J., and Esser, R.: 1996, Rapid acceleration of the polar solar wind, *Letters of Nature*, **379**, 429–432.
- Habbal, S. R., Woo, R., Fineschi, S., O'Neal, R., Kohl, J., Noci, G., and Korendyke, C.: 1997, Origins of the slow and the ubiquitous fast solar wind, *Astrophys. J.*, **489**, L103.
- Hammer, R.: 1982a, Energy balance of stellar corona: I. Methods and examples, *Astrophys. J.*, **259**, 767–778.
- Hammer, R.: 1982b, Energy balance of stellar corona: II. Effect of coronal heating, *Astrophys. J.*, **259**, 779–791.
- Hansteen, V., and Leer, E.: 1995, Coronal heating, densities, and temperatures and solar wind acceleration, *Journal of Geophys. Res.*, **100**, 21577–21593.
- Hansteen, V., Leer, E., and Holzer, T.: 1997, The role of helium in the outer solar atmosphere, *Astrophys. J.*, **482**, 498.
- Hassler, D. M., Dammasch, I. E., Lemaire, P., Brekke, P., Curdt, W., Mason, H. E., Vial, J.-C., and Wilhelm, K.: 1999, Solar coronal hole outflow velocities and the chromospheric network, *Science*, **283**, 5040, 810–813.
- Hartle, R. E., and Sturrock, P. A.: 1968, Two-fluid model of the solar wind, *Astrophys. J.*, **151**, 1155–1170.
- Hefti, S., Grünwaldt, H., Ipavich, F. M., et al.: 1998, Kinetic properties of solar wind minor ions and protons measured with SOHO/CELIAS, *J. Geophys. Res.*, in press.
- Hoeksema, J. T.: 1995, The large-scale structure of the heliospheric current sheet during the Ulysses epoch, *Space Science Reviews*, **72**, 137–148.
- Hollweg, J. V.: 1978, Some physical processes in the solar wind, *Rev. Geophys. Space Phys.*, **16**, 689–720.
- Hollweg, J. V.: 1986, Transition region, corona, and solar wind in coronal holes, *J. Geophys. Res.*, **91**, 4111–4125.
- Hollweg, J. V., and Turner, J. M.: 1978, Acceleration of solar wind He^{++} , 3, Effects of resonant and nonresonant interactions with transverse waves, *J. Geophys. Res.*, **83**, 97–113.

- Hollweg, J. V., and Johnson, W.: 1986, Transition region, corona, and solar wind in coronal holes: Some two-fluid models, *J. Geophys. Res.*, **93**, 9547–9554.
- Holzer, T. E., and Axford, W. I.: 1970, The theory of stellar winds and related flows, *Ann. Rev. Astron. Astrophys.*, **8**, 31–61.
- Hu, Y. Q., Esser, R., and Habbal, S. R.: 1997, A fast solar wind model with anisotropic proton temperature, *J. Geophys. Res.*, **102**, 14661–14676.
- Isenberg, P. A., and Hollweg, J. V.: 1983, On the preferential acceleration and heating of solar wind heavy ions, *J. Geophys. Res.*, **88**, 3923–3935.
- Isenberg, P. A.: 1990, Investigations of a turbulence driven wave model, *J. Geophys. Res.*, **95**, 6437.
- Jacques, S. A.: 1978, Solar wind models with Alfvén waves, *Astrophys. J.*, **226**, 632–649.
- Ko, Y.-K., Fisk, L., Geiss, J., Gloeckler, G., and Guhathakurta, M.: 1997, An empirical study of the electron temperature and heavy ion velocities in the south polar coronal hole, *Solar Phys.*, **171**, 345–361.
- Kohl, J. L., Noci, G., Anonucci, E., Tondello, G., Huber, M. C. E., Gardner, L. D., Nicolosi, P., Strachan, L., Fineschi, S., Raymond, J. C., Romoli, M., Spadaro, D., Panasyuk, A., Siegmund, O. H. W., Benna, C., Ciaravella, A., Cranmer, S. R., Giordano, S., Karovska, M., Martin, R., Michels, J., Modigliani, A., Naletto, G., Pernechele, C., Poletto, G., and Smith, P. L.: 1997, First results from the SOHO Ultraviolet Coronagraph Spectrometer, *Solar Phys.*, **175**, 613–644.
- Kopp, R. A., and Holzer, T. E.: 1976, Dynamics of coronal hole regions, I. Steady polytropic flows with multiple critical points, *Solar Phys.*, **49**, 43–56.
- Leer, E., and Axford, W. I.: 1972, A two fluid model with anisotropic proton temperature, *Solar Phys.*, **23**, 238–250.
- Leer, E., Holzer, T. E., and Flå, T.: 1982, Acceleration of the solar wind, *Space Sci. Rev.*, **33**, 161–200.
- Lemaire, P., Wilhelm, K., Curdt, W., Schühle, U., Marsch, E., Poland, A. I., Jordan, S. D., Thomas, R. J., Hassler, D. M., Vial, J. C., Kühne, M., Huber, M. C. E., Siegmund, O. H. W., Gabriel, A., Timothy, J. G., and Grewing, M.: 1997, First results of the SUMER telescope and spectrometer on SOHO, II. Imagery and data management, *Solar Phys.*, **170**, 105–122.
- Li, X., Esser, R., and Habbal, S. R.: 1997, Influence of heavy ions on the high-speed solar wind, *J. Geophys. Res.*, **102**, 17419–17432.
- Lie-Svendsen, O., Hansteen, V. H., and Leer, E.: 1997, Kinetic electrons in high-speed solar wind streams: Formation of high-energy tails, *J. Geophys. Res.*, **102**, 4701–4718.
- Mariska, J. T.: 1992, *The Solar Transition Region* (Cambridge Astrophysics Series **23**, Cambridge, University Press).
- Marsch, E., Goertz, C. K., and Richter, K.: 1982, Wave heating and acceleration of solar wind ions by cyclotron resonance, *J. Geophys. Res.*, **87**, 5030–5044.
- Marsch, E., and Richter, A. K.: 1984, Helios observational constraints on solar wind expansion, *J. Geophys. Res.*, **89**, 6599–6612.
- Marsch, E.: 1991a, Kinetic physics of the solar wind plasma, in *Physics of the Inner Heliosphere*, Vol. II, eds. R. Schwenn and E. Marsch, (Springer-Verlag: Heidelberg), pp. 45–133.
- Marsch, E.: 1991b, MHD Turbulence in the Solar Wind, in *Physics of the Inner Heliosphere*, Vol. II, eds. R. Schwenn and E. Marsch, (Springer Verlag: Heidelberg), pp. 159–241.
- Marsch, E.: 1992, On the possible role of plasma waves in the heating of chromosphere and corona, in *Solar Wind Seven*, ed. E. Marsch and R. Schwenn, (Pergamon Press: Oxford, England), pp. 65–68.
- Marsch, E., and Tu, C.-Y.: 1997a, Solar wind and chromospheric network, *Solar Physics*, **176**, 87–106.
- Marsch, E., and Tu, C.-Y.: 1997b, The effects of high-frequency Alfvén waves on coronal heating and solar wind acceleration, *Astron. Astrophys.*, **319**, L17–L20.
- Marsden, R. G.: 1995, *The High Latitude Heliosphere*, (vol. **72** of Space Science Reviews, Kluwer Academic Publishers, Dordrecht, The Netherlands).
- Maksimovic, M., Pierrard, V., and Lemaire, J. F.: 1997, A kinetic model of the solar wind with Kappa distribution functions in the corona, *Astron. Astrophys.*, **324**, 725–734.
- McComas, D. J., Bame, S. J., Feldman, W. C., Gosling, J. T., and Phillips, J. L.: 1992, Solar wind halo electrons from 1–4 AU, *Geophys. Res. Lett.*, **19**, 1291–1294.
- McKenzie, J. F., Banaszkiewicz, M., and Axford, W. I.: 1995, Acceleration of the high speed solar wind, *Astron. Astrophys.*, **303**, L45–L48.

- McKenzie, J. F., Axford, W. I., and Banaszkiewicz, M.: 1997, The fast solar wind, *Geophys. Res. Lett.*, **24**, 2877–2880.
- Neugebauer, M.: 1981, Observations of solar wind helium, *Fundam. Cosmic Phys.*, **7**, 131–199.
- Neugebauer, M., Goldstein, B. E., Bame, S. J., and Feldman, W. C.: 1994, Ulysses near-ecliptic observations of differential flow between protons and alphas in the solar wind, *J. Geophys. Res.*, **99**, 2505–2511.
- Neugebauer, M., Goldstein, B. E., Bame, S. J., and Feldman, W. C.: 1996, Ulysses observations of differential alpha-proton streaming in the solar wind, *J. Geophys. Res.*, **101**, 17047–17055.
- Olsen, E. L., and Leer, E.: 1996, Thermally-driven one-fluid electron-proton solar wind; 8-moment approximation, *Astrophys. J.*, **462**, 982–996.
- Parker, E. N.: 1958, Dynamics of the interplanetary gas and magnetic fields, *Astrophys. J.*, **128**, 664–684.
- Peter, H., and Marsch, E.: 1997, Ionization layer of hydrogen in the solar chromosphere and the solar wind mass flux, in *Proceedings of the Fifth SOHO Workshop*, ESA-SP-404, pp. 591–594.
- Pilipp, W. G., Miggennieder, H., Montgomery, M. D., Mühlhäuser, K.-H., Rosenbauer, H., and Schwenn, R.: 1987, Characteristics of electron velocity distribution functions in the solar wind derived from the Helios plasma experiment, *J. Geophys. Res.*, **92**, 1075–1092.
- Phillips, J. L., Feldman, W. C., Gosling, J. T., and Scime, E. E.: 1995, Solar wind plasma electron parameters based on aligned observations by ICE and Ulysses, *Adv. Space Res.*, **16** (9), 95–100.
- Riley, P., Sonett, C. P., Balogh, A., Forsyth, R. J., Scime, E. E., and Feldman, W. C.: 1995, Alfvénic fluctuations in the solar wind: A case study using Ulysses measurements, *Space Sci. Rev.*, **72**, 197–200.
- Schwenn, R.: 1990, Large scale structure of the interplanetary medium, in *Physics of the Inner Heliosphere*, Vol. 1, ed. R. Schwenn and E. Marsch, (Springer Verlag: Berlin, Heidelberg, New York), pp. 99–181.
- Schwenn, R., Inhester, B., Plunkett, S. P., Epple, A., Podlipnik, B., Bedford, D. K., Bout, M. V., Brueckner, G. E., Dere, K. P., Eyles, C. J., Howard, R. A., Koomen, M. J., Korendyke, C. M., Lamy, P. L., Llebaria, A., Michels, D. J., Moses, J. D., Moulton, N. E., Paswaters, S. E., Simnett, G. M., Socker, D. G., St. Cyr, O. C., Tappin, S. J., and Wang, D.: 1997, First view of the extended green line emission corona at solar activity minimum using the LASCO-C1 coronagraph on SOHO, *Solar Phys.*, **175**, 667–684.
- Scime, E. E., Bame, S. J., Feldman, W. C., Gary, S. P., and Phillips, J. L.: 1994, Regulation of the solar wind electron heat flux from 1 to 5 AU: Ulysses observations, *J. Geophys. Res.*, **99**, 23401–23410.
- Scudder, J. D., and Olbert, S.: 1979a, A theory of local and global processes which affect solar wind electrons, 1. The origin of typical 1 AU velocity distribution functions – Steady state theory, *J. Geophys. Res.*, **84**, 2755–2772.
- Scudder, J. D., and Olbert, S.: 1979b, A theory of local and global processes which affect solar wind electrons, 2. Experimental support, *J. Geophys. Res.*, **84**, 6603–6620.
- Seely, J. F., Feldman, U., Schühle, U., Wilhelm, K., Curdt, W., and Lemaire, P.: 1997, Turbulent velocities and ion temperatures in the solar corona obtained from SUMER line widths, *Astrophys. J.*, **484**, L87–L90.
- Sheeley, N. R., Jr., Wang, Y.-M., Hawley, S. H., Brueckner, G. E., Dere, K. P., Howard, R. A., Koomen, M. J., Korendyke, C. M., Michels, D. J., Paswaters, S. E., Socker, D. G., St. Cyr, O. C., Wang, D., Lamy, P. L., Llebaria, A., Schwenn, R., Simnett, G. M., Plunkett, S., and Biesecker, D. A.: 1997, Measurements of flow speeds in the corona between 2 and 30 R_{\odot} , *Astrophys. J.*, **484**, 472–478.
- Smith, E. J., Neugebauer, M., Balogh, A., Bame, S. J., Lepping, R. P., and Tsurutani, B. T.: 1995, Ulysses observations of latitude gradients in the heliospheric magnetic field: Radial component and variances, *Space Science Reviews*, **72**, 165–170.
- Thieme, K. M., Marsch, E., and Schwenn, R.: 1990, Spatial structures in high-speed streams as signatures of fine structures in coronal holes, *Annales Geophysicae*, **8** (11), 713–724.
- Tsurutani, B. T., Ho, C. M., Arballo, J. K., Lakhina, G. S., Glassmeier, K.-H., and Neubauer, F. M.: 1997, Nonlinear electromagnetic waves and spherical arc-polarized waves in space plasmas, *Plasma Phys. Control Fusion*, **39**, A237–A250.

- Tu, C.-Y., Pu, Z.-Y., and Wei, F.-S.: 1984, The power spectrum of interplanetary Alfvénic fluctuations: Derivation of the governing equations and its solution, *J. Geophys. Res.*, **89**, 9695–9702.
- Tu, C.-Y.: 1987, A solar wind model with the power spectrum of Alfvénic fluctuations, *Solar Phys.*, **109**, 149–186.
- Tu, C.-Y.: 1988, The damping of interplanetary Alfvénic fluctuations and the heating of the solar wind, *J. Geophys. Res.*, **93**, 7–20.
- Tu, C.-Y., and Marsch, E.: 1995a, MHD structures, waves and turbulence in the solar wind: Observations and theories, *Space Science Reviews*, **73**, 1–210.
- Tu, C.-Y., and Marsch, E.: 1995b, Comment on “Evolution of energy-containing turbulent eddies in the solar wind” by W. H. Matthaeus, S. Oughton, D. H. Pontius Jr., and Y. Zhou, *J. Geophys. Res.*, **100**, 12323–12328.
- Tu, C.-Y., and Marsch, E. (1997): Two-fluid model for heating of the solar corona and acceleration of the solar wind by high-frequency Alfvén waves, *Solar Physics*, **171**, 363–391.
- Tu, C.-Y., Marsch, E., Wilhelm, K., and Curdt, W.: 1998, Ion temperatures in a solar polar coronal hole observed by SUMER on SOHO, *Astrophys. J.*, **503**, 475–482.
- von Steiger, R., Geiss, J., Gloeckler, G., and Galvin, A. B.: 1995, Kinetic properties of heavy ions in the solar wind from SWICS/Ulysses, *Space Science Reviews*, **72**, 71–76.
- Vasquez, B. J., and Hollweg, J.: 1998a, Formation of spherically polarized Alfvén waves and imbedded rotational discontinuities from a small number of entirely oblique waves, *J. Geophys. Res.*, **103**, 335.
- Vasquez, B. J., and Hollweg, J.: 1998b, Formation of imbedded rotational discontinuities with nearly field aligned normals, *J. Geophys. Res.*, **103**, 349.
- Wang, Y. M., and Sheeley, N. R., Jr.: 1990, Solar wind speed and coronal flux-tube expansion, *Astrophys. J.*, **355**, 726.
- Wang, Y. M., Sheeley, N. R., Jr., Walters, J. H., Brueckner, G. E., Howard, R. A., Michels, D. J., Lamy, P. L., Schwenn, R., and Simnett, G. M.: 1998, Origin of streamer material in the outer corona, *Astrophys. J.*, **498**, L165.
- Wilhelm, K., Curdt, W., Marsch, E., Schühle, U., Lemaire, P., Gabriel, A., Vial, J. C., Grewing, M., Huber, M. C. E., Jordan, S. D., Poland, A. I., Thomas, R. J., Kühne, M., Timothy, J. G., Hassler, D. M., and Siegmund, O. H. W.: 1995, SUMER – Solar Ultraviolet Measurements of Emitted Radiation, *Solar Phys.*, **162**, 189–231.
- Wilhelm, K., Lemaire, P., Curdt, W., Schühle, U., Marsch, E., Poland, A. I., Jordan, S. D., Thomas, R. J., Hassler, D. M., Huber, M. C. E., Vial, J.-C., Kühne, M., Siegmund, O. H. W., Gabriel, A., Timothy, J. G., Grewing, M., Feldman, U., Hollandt, J., and Brekke, P.: 1997a, First results of the SUMER telescope and spectrometer on SOHO, *Solar Phys.*, **170**, 75–104.
- Wilhelm, K., Marsch, E., Dwivedi, B. N., Hassler, D. M., Lemaire, P., Gabriel, A. H., and Huber, M. C. E.: 1998, The solar corona above polar coronal holes as seen by SUMER on SOHO, *Astrophys. J.*, **500**, 1023–1038.
- Withbroe, G. L.: 1988, The temperature structure, mass and energy flow in the corona and inner solar wind, *Astrophys. J.*, **325**, 442–467.
- Woch, J., Axford, W. I., Mall, U., Wilken, B., Livi, S., Geiss, J., Gloeckler, G., and Forsyth, R. J.: 1997, SWICS/Ulysses observations: The three-dimensional structure of the heliosphere during solar minimum, *Geophys. Res. Lett.*, **24**, 2885–2888.

ACCELERATION OF THE HIGH SPEED SOLAR WIND IN CORONAL HOLES

W. I. AXFORD, J. F. MCKENZIE and G. V. SUKHORUKOVA

Max-Planck-Institut für Aeronomie, D-37191 Katlenburg-Lindau, Germany

M. BANASZKIEWICZ, A. CZECHOWSKI and R. RATKIEWICZ

Space Research Centre, Polish Academy of Sciences, Warsaw, Poland

Abstract. We outline a theory for the origin and acceleration of the fast solar wind as a consequence of network microflares releasing a spectrum of high frequency Alfvén waves which heat (by cyclotron absorption) the corona close to the Sun. The significant features of our model of the fast wind are that the acceleration is rapid with the sonic point at around two solar radii, the proton temperatures are high (~ 5 million degrees) and the minor ions are correspondingly hotter, roughly in proportion to their mass. Moreover we argue that since the energy flux needed to power the quiet corona in closed field regions is about the same as that needed to drive the fast solar wind, and also because at deeper levels ($< 2 \times 10^5$ K) there is no great difference in the properties of supergranules and network in closed and open field regions, the heating process (i.e., dissipation of high frequency waves) must be the same in both cases.

1. Introduction

The high speed solar wind is long-lasting and relatively steady in its characteristics. It is associated with coronal holes and unipolar magnetic fields. The energy, mass and magnetic field fluxes are constants of the motion in this case and may be determined at any distance from the Sun. As a consequence, there is little in the way of free parameters to be chosen and indeed we find that, given a realistic magnetic field geometry and constraining the plasma density at the base of the corona to be about $10^8/\text{cm}^3$, one is forced to a solution in which the plasma is heated strongly close to the Sun. It reaches temperatures of the order of 5–10 million degrees per amu and accelerates rapidly with the sonic point being at about $2 r_S$, up to ~ 750 km/sec.

Observations of the proton temperature/pressure distributions by the Helios spacecraft, of the preferred heating and acceleration of heavy species, and of the rapid heating required, suggest that the heating is in some way associated with cyclotron absorption of waves emitted directly from the coronal base, i.e., from the chromospheric network. The precise nature of the waves and the dissipation process involved is not understood at present, although, by elimination, we deduce that the source should lie in small-scale, flare-like events occurring in the network. Cyclotron absorption can lead to large temperature anisotropies in the corona which, in the case of protons, should be quenched by plasma instabilities but, in the case of minor species, can persist since they do not contribute significantly to the overall pressure anisotropy.



The characteristics of the chromospheric network underlying coronal holes and the neighboring quiet coronal regions are indistinguishable. Furthermore the energy fluxes in the form of high speed solar wind, in the case of coronal holes, and radiation from the transition region and elsewhere, in the case of the magnetically closed corona, are about the same. It is therefore reasonable to argue that the heating mechanisms should also be the same in each case, namely high-frequency Alfvén waves emitted from the network. The principal alternative suggestion that the quiet, closed-field corona is heated by the dissipation of twisted, force-free magnetic fields as nano-flares does not appear to be viable, since the low-frequency Alfvén waves that arise from the necessary twisting of the field in closed regions should be easily detected as outgoing waves in the high speed solar wind; these are not present with anything like the energy flux required.

On extending these ideas to include phenomena occurring in the network itself we find that it is unlikely that there should be a significant FIP effect in the high speed wind, apart from the special case of helium, and that the charge states of ions in the wind are probably determined by a high energy tail of the electron distribution since the electron temperatures expected are otherwise too low to be effective.

2. The Magnetic Field

At solar minimum, when the fast wind is dominant at all latitudes in excess of 20° of the ecliptic, it is possible to construct a simple, analytic model for the solar magnetic field. This consists of an equatorial current which causes open field regions plus a dipole and quadrupole (Banaszkiewicz *et al.* 1998). The current sheet is supported by hydrostatic pressure. The boundary of the coronal hole determines the last closed field line, which in the above model occurs at 60° latitude on the solar surface. In the open field regions within $\sim 10 r_s$ the field must be potential, since $\beta \ll 1$ and currents cannot flow to infinity. In the closed regions the field may be force-free giving an azimuthal field in the axisymmetric case and a changed stress balance. The magnetic field configuration is shown in Figure 1(a). The dipole and quadrupole moments and the strength of the current sheet have been chosen to fit observations at 1 AU and close to the Sun. Those are therefore fixed parameters which determine the latitudinal variations of the magnetic field at the surface and the expansion factor, as shown in Figure 1(b). In general, the expansion factor varies between around 7 (at the coronal hole boundary) to 10 at the pole and is not equal to ones which are of the Kopp-Holzer form (Kopp and Holzer 1976). It is of interest to note that this model predicts a modification of the Parker spiral, which agrees reasonably well with Ulysses results (Smith *et al.* 1997) as shown in Figure 1(c). The field will appear underwound at large distances reflecting that open field lines coming from solar latitudes in excess of 60° rotate more slowly with increasing latitude.

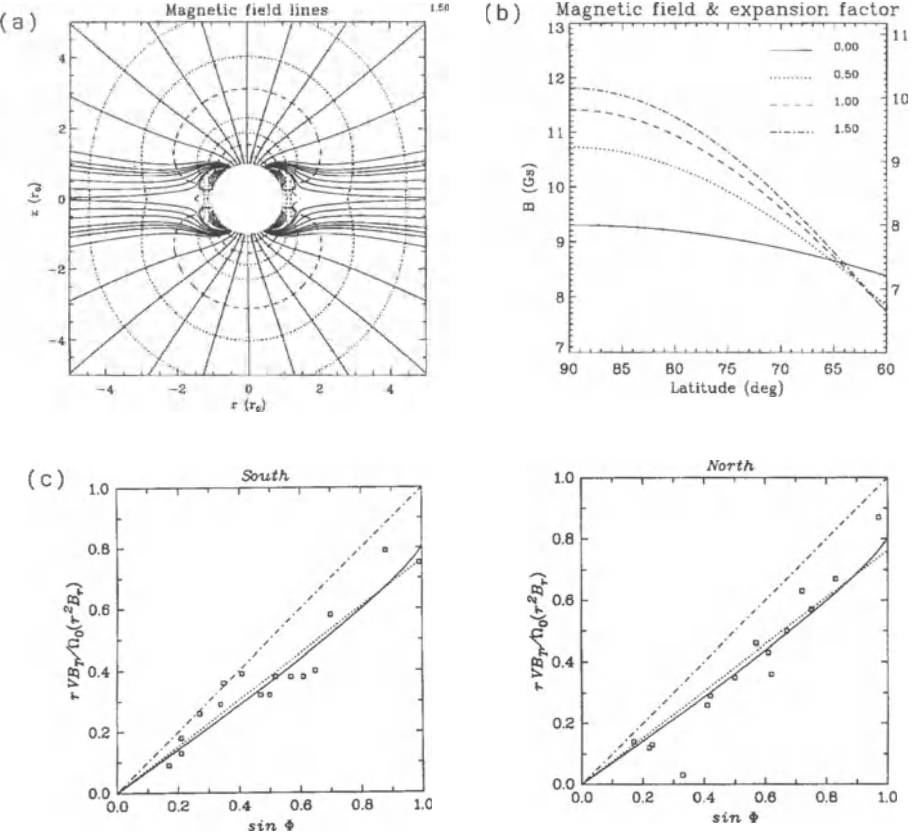


Figure 1. (a) The dipole-current sheet-quadrupole model of the solar magnetic field. The dashed lines indicate surfaces of constant field. (b) The variation of the surface field strength and expansion factor f within the polar coronal hole (latitudes $> 60^\circ$). (c) A comparison between our model magnetic field (solid line) and Ulysses observations (squares) and their best fit line (Smith *et al.* 1997). The dash-dot line corresponds to solid body rotation at the equatorial rate.

3. Fast Wind Model

In his original model of the solar wind Parker (1958) realized that without heating, solutions of the steady flow equations with $\gamma = 5/3$ (which indeed it is for hydrogen) do not give rise to flows exhibiting a subsonic-supersonic transition. To overcome this difficulty γ was chosen such that the corona is not gravitationally bound and has sufficient enthalpy to yield the required asymptotic flow speed V_∞ at large radial distances, thus requiring that, for a coronal base temperature T_0 of 10^6 K, $\gamma < 1.03$. Hence Parker favored an isothermal flow ($\gamma = 1$) out to a distance well beyond the critical (sonic) point followed by an adiabatic ($\gamma = 5/3$) flow. In this case an “isothermal” base temperature $\sim 2 \times 10^6$ K is needed to achieve a fast solar wind

with $V_\infty \sim 750$ km/sec. However, isothermal flows are not physical and evade the issue of the required heating close to the Sun. Hartle and Sturrock (1968) attempted to model a solar wind driven by heat conduction, using a spherically symmetric two-fluid (electrons and protons) solar wind in which the electron temperature is determined by classical (Spitzer-Härm) heat conduction from a million degree corona. Within two solar radii electron-proton energy exchange is important but beyond $7 r_S$, $T_p \propto r^{-4/3}$ (adiabatic cooling) and $T_e \propto r^{-2/7}$ (constant heat flux). At 1 AU, $V_\infty \sim 250$ km/sec, $T_p \sim 3 \times 10^3$ K and $T_e \sim 3 \times 10^5$ K. Clearly this model cannot reproduce the properties of the fast wind and in fact it shows that heat conduction from a corona with $T_e \leq 10^6$ K cannot supply more than $\sim 10\%$ of the required energy flux in the fast solar wind.

At the base of the corona the flow is subsonic and gravitationally bound (total energy density $E_0 < 0$), whereas at large distances from the Sun the flow is supersonic and $E_\infty > 0$. In a flow with $\gamma = 5/3$ this can only be achieved by adding heat so that $E(r)$ changes from $E_0 < 0$ to $E_\infty > 0$. By choosing an exponential heating function $Q(r)$ with some length scale L , Holzer and Axford (1970) showed that one can obtain solutions in which the Mach number is small near the Sun, exhibit a sonic point, and join smoothly to adiabatic solutions ($Q = 0$). A maximum temperature ($T_p + T_e$) of the order of 10^7 K is acquired. A thermally driven model of this sort will give rise to a high speed wind but it is inevitable that the coronal temperature is very high and the acceleration is rapid. We shall return to this question subsequently.

Belcher (1971) and Alazraki and Couturier (1971) pointed out that Alfvén waves may play an important role in solar wind dynamics. Non-dissipative Alfvén waves can drive fast, low density winds. However, the observed wave energy flux at 1 AU, extrapolated back to the Sun adiabatically, is only about 4% of that required to drive the fast solar wind. Hence purely adiabatic Alfvén waves are not the cause of the solar wind. An attempt to model the high speed wind was made by Leer *et al.* (1982) but with their assumptions a fast wind accompanied by rapid acceleration and high proton temperatures could not be achieved. The reasons seem to be associated with a single fluid heat conduction, unrealistic geometry and an aversion to having rapid heating close to the Sun.

A combination of the above considerations led Axford and McKenzie (1993) and McKenzie *et al.* (1995, 1997) to suggest a picture in which plasma heating near the Sun is taken to be due to the dissipation of high frequency Alfvén waves (for example, by cyclotron damping). By including wave pressure gradients consistent with the assumed heating function and also anisotropic proton temperatures they constructed a model of the fast solar wind in which the base density is low ($\sim 10^8$ cm $^{-3}$), the acceleration is rapid (the sonic point is $\lesssim 2 r_S$) and the maximum proton temperature is high ($\sim 5 \times 10^6$ K), as depicted in Figure 2. A few comments about this model are in order. The first is that the expansion factor is not an arbitrarily chosen one of the Kopp-Holzer type but is based on a more “correct” (in the sense that it satisfies Maxwell’s equations) magnetic field geometry which provides a

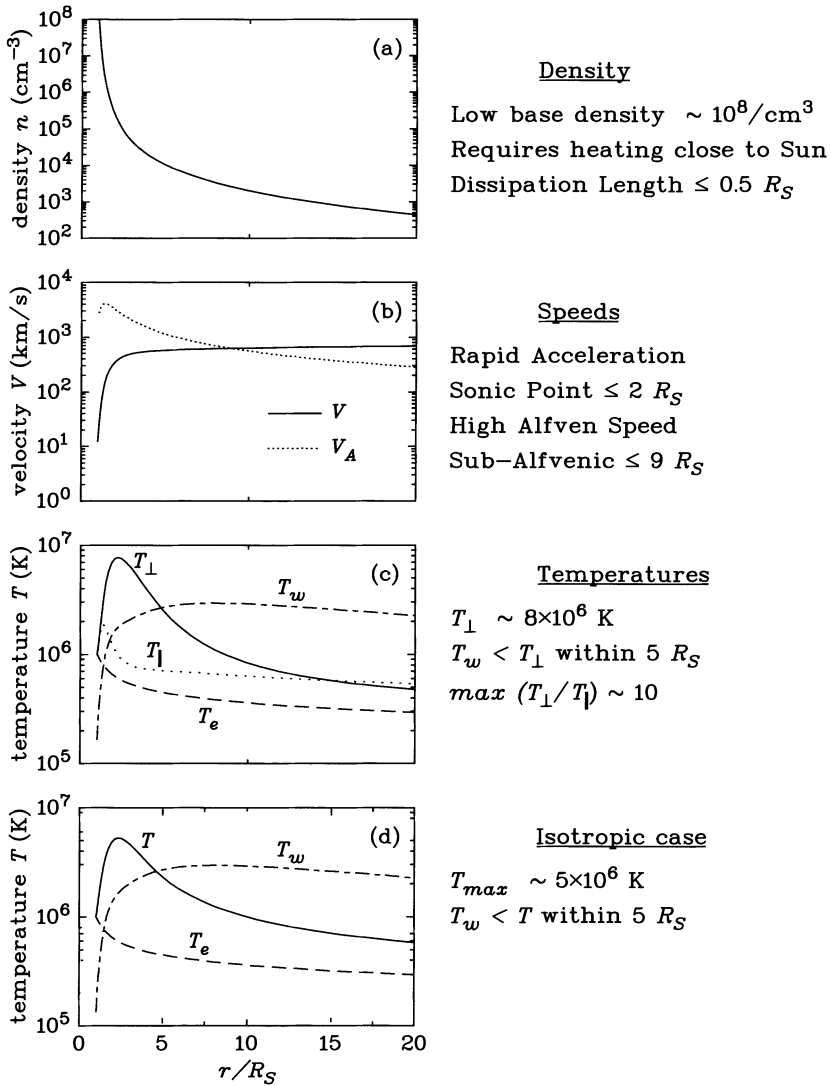


Figure 2. The radial variation of the density, flow and Alfvén speeds, and temperatures from the McKenzie *et al.* (1997) model of the fast solar wind. The wave temperature T_w is the wave pressure divided by the density.

reasonably accurate representation of the solar magnetic field at solar minimum. The electrons are governed by classical heat conduction and it is argued that, as far as the protons are concerned, heat conduction and viscosity are suppressed by wave scattering processes (e.g., Williams 1995). The mass and energy fluxes are fixed by

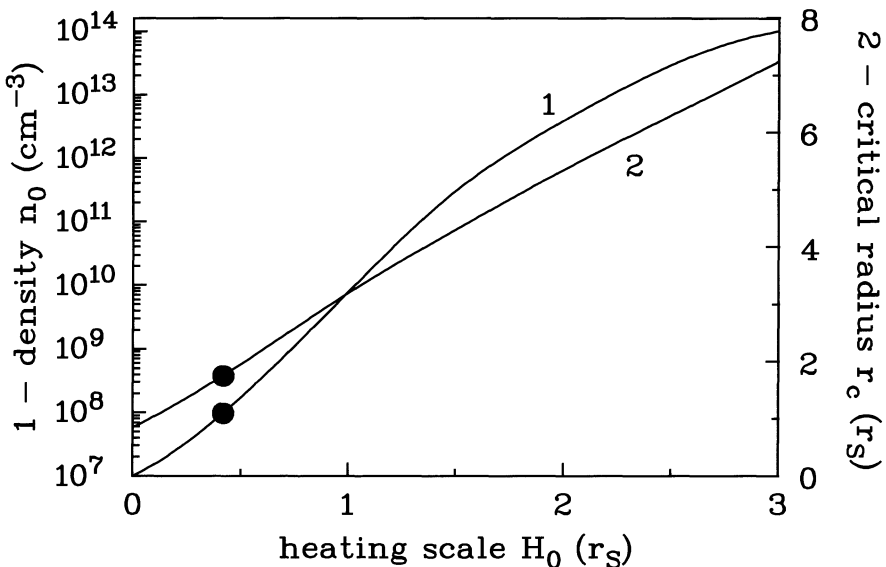


Figure 3. The coronal base density (n_0) and corresponding critical point radius (r_c) for wave dissipation length scales (H_0). The solution shown in Figure 2 corresponds to $n_0 = 10^8/cm^3$ and $r_c \simeq 2r_s$.

their observed in situ values at 1 AU. Thus the only remaining free parameter is the form of the heating (chosen to be exponential) for which we find that in order to obtain a base density of $\sim 10^8\text{ cm}^{-3}$ its length scale is about $0.35\text{ }r_s$. The variation of the coronal base density and the corresponding critical point radius with the wave dissipation length scale (H_0) is shown in Figure 3, in which the points (filled circles) denote the density and critical radius for $H_0 = 0.35\text{ }r_s$. In view of the high Alfvén wave speeds near the Sun, this is consistent with the idea of the dissipation of high frequency waves generated in the chromospheric network.

We do not know the wave spectrum in the corona but it involves much higher frequencies than is observed at large distances in the solar wind. We assume that the dissipation is mainly due to cyclotron damping. Higher frequencies may be directly emitted or generated by cascading from low to high frequencies in the corona (cf. Isenberg and Hollweg 1983; Tu 1987). It is no more arbitrary to specify a heating function rather than a source wave spectrum because the plasma responds directly to the heating and only weakly to the remnant wave pressure gradient (e.g., compare our approach—McKenzie *et al.* 1995 and 1997—with that of Marsch and Tu 1997).

It is of interest to calculate speed and temperature profiles for the case in which not all of the waves are dissipated close to the Sun because, as mentioned above, there is a remnant undamped low frequency wave energy flux at large distances

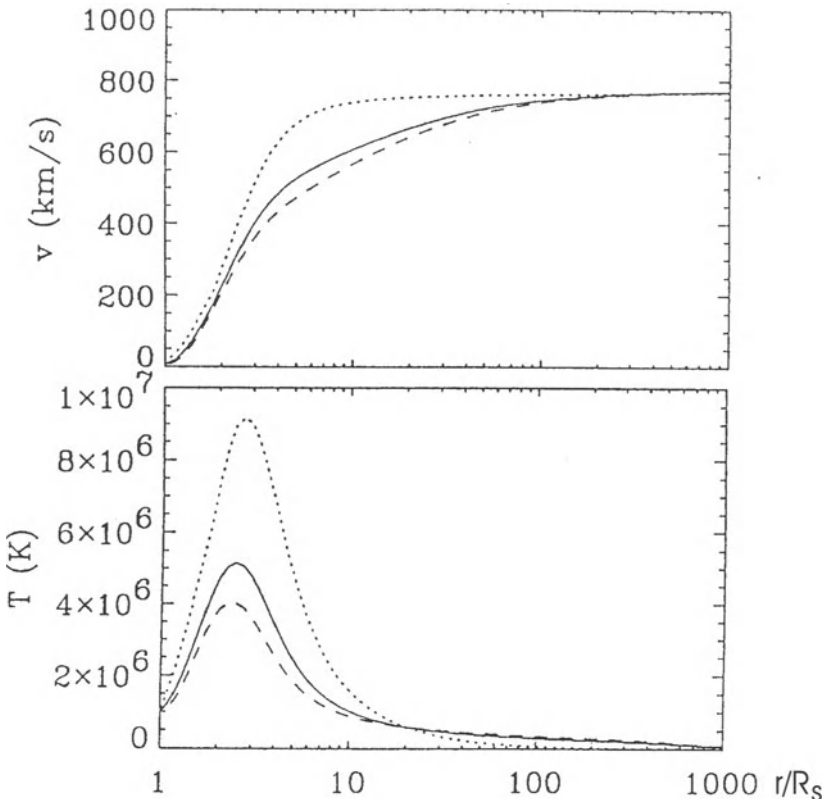


Figure 4. The effect of a fraction of undamped waves on the fast solar wind model. Dotted line (all waves damped), full line (5% undamped), dashed line (10% undamped).

which is of the order of or less than about 4% of the observed streaming energy flux. Figure 4 shows the speed and temperature profiles which indicate that in the presence of some undamped waves at large distances the acceleration is not quite so rapid and the maximum temperatures are reduced somewhat.

A comparison between the radial variation of the flow derived from the density profiles from white light coronagraph observations (using our expansion factor in the continuity equation) and our model calculations shows that the case of no undamped waves provides quite a good fit, as indeed it also does with the UVCS results (see Figure 5) (Giordano *et al.* 1998).

On the basis of Figure 5 we conclude that our model with rapid acceleration and high proton temperatures is in reasonable agreement with observations as has also been pointed out by Guhathakurta (these Proceedings). Figure 6 shows the radial variation of the radial V_r and latitudinal V_{pol} speeds for different latitudes. Because the latitudinal variation of V_r is small, only the polar field line case is given.

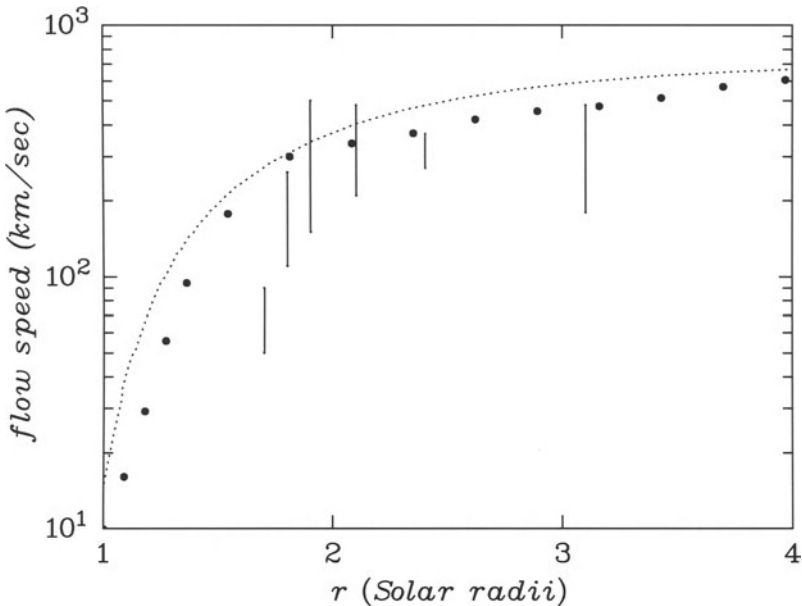


Figure 5. A comparison between flow profiles deduced from white light coronagraph observations (dots; using our model for B) (Fisher and Guhathakurta 1995), the UVCS O VI profile (squares) and our fast wind model with no undamped waves (dotted line).

4. “Furnace” Model of Microflares and High Frequency Waves in the Supergranular Network

The open field lines in coronal holes originate mostly in the supergranular network. This must be the main source of the energy, mass and magnetic fluxes in the fast solar wind. Gabriel (1976) realized that the coronal magnetic field must be squeezed into magnetic “trunks” by the supergranulation convection pattern (indicated by the broken curves in Figure 7[a]) and assumed a unipolar potential field in pressure balance with the surrounding chromosphere. There is no free energy in such a configuration. Dowdy *et al.* (1986) introduced the idea of a static magnetic “junkyard” indicated by the closed loops (Figure 7[b]), which are independently heated from below. Axford and McKenzie (1992, 1993) extended these ideas to include magnetic flux (full curves in Figure 7[c]) being continuously fed in from the sides by the convection and giving rise to reconnection and microflares in the junkyard, releasing energy (in waves) and plasma (blueshifts) into open field lines. It also creates loops carrying hot trapped plasma (bright points) which are gradually pulled downwards as this plasma cools and recombines (redshifts). Fresh loops are pushed into the network by the convection to maintain the process.

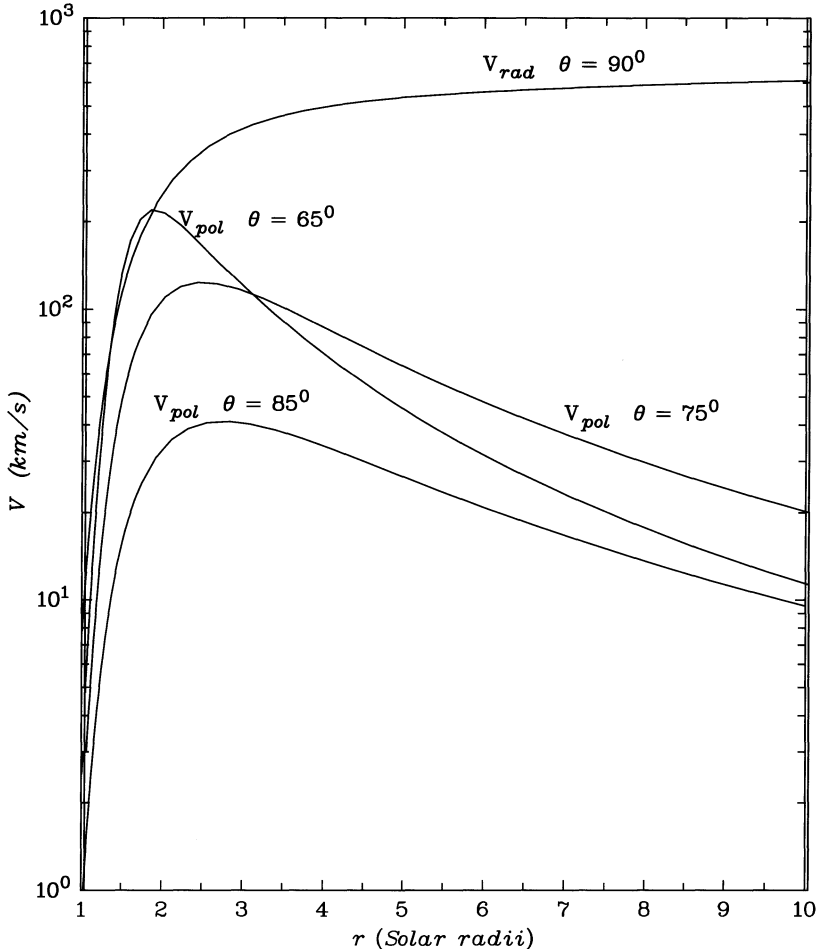


Figure 6. The radial variation of V_r and V_{pol} corresponding to different latitudes θ on the solar surface.

The larger loops may protrude above the level of the coronal base giving limb brightening. The loops may also arrange themselves into a quasi-stable pattern (“anemone”) which is associated with polar plumes. The fast solar wind energy, mass and magnetic fluxes must originate in the entire network and not just from restricted regions (e.g., such as plumes), otherwise the flux densities required become too large. The waves and plasma escaping on open field lines of the coronal hole produce the fast solar wind. The same processes acting in closed field regions supply the hydrostatic quiet corona with energy and plasma. Note that the energy

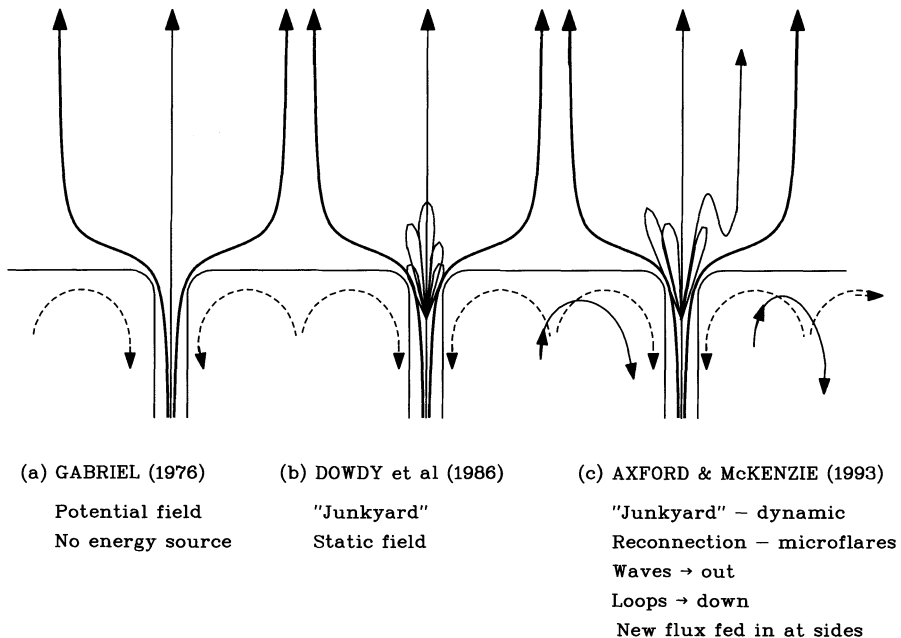


Figure 7. The development of a dynamic “furnace” model.

fluxes required to drive the fast wind and heat the closed quiet corona are about the same.

Most of the magnetic flux in coronal holes and the quiet closed corona emerges from “funnels” in the chromospheric supergranular network. Figure 8 provides a diagrammatic illustration of the connection between the fast and slow winds and their origin in these funnels. Characteristically the network is $\sim 30,000$ km across, with lifetimes of ~ 40 hours, and takes about 1 hour to reform. The flow speeds are between 5 and 10 km/sec. If the width λ of the network in the funnels is ~ 3000 km, then the magnetic field strength is ~ 100 Gauss and the Alfvén speed $V_A \sim 2 \times 10^4$ km/sec. We assume that the field is split evenly between unipolar and loops. The following numbers are appropriate to conditions in the furnace:

$$n \sim 10^8 \text{ cm}^{-3}, F_N \sim 10^{15}/\text{cm}^2\text{sec}, \Phi_N \sim 10^7 \text{ ergs}/\text{cm}^2\text{sec}$$

$$V \sim 100 \text{ km/sec}, V_W \sim 50 \text{ km/sec}, \lambda/3V_A \sim 0.05 \text{ sec.}$$

(Here F_N is the particle flux, Φ_N the energy flux, V the flow speed, V_W the wave amplitude.)

The magnetic flux replenishment time is $(\sim B^2 H_c / 4\pi \Phi_N) \sim 20$ minutes. This must be supplied as emerging loops (~ 10 Gauss) brought in by the supergranular convection (~ 10 km/sec).

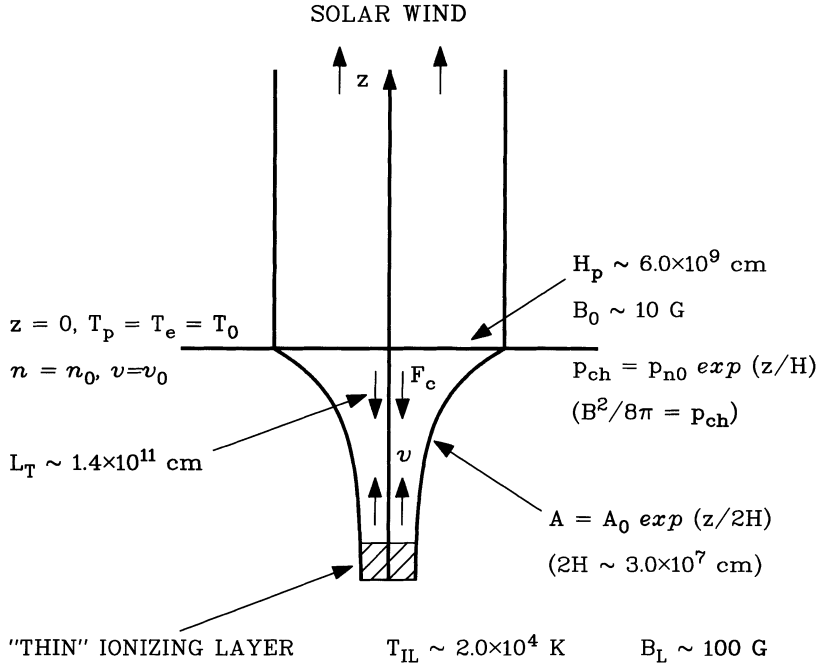


Figure 8. A diagrammatic sketch of the connection between the solar wind, the magnetic funnel and the ionization layer at its foot.

The main result of reconnection/flaring is to launch large amplitude Alfvén waves into the corona (the process is illustrated in Figure 9). The frequency spectrum of the waves is controlled by the Alfvén speed and the size (L_B) of the “microflares.” This yields a time scale

$$T_R \sim L_B / \varepsilon V_A \sim 10^{-3} - 1 \text{ sec} \text{ (with } \varepsilon \sim 0.1 - 1, L_B \sim 10 - 10^3 \text{ km).}$$

We expect most of the power to come from small events which would probably be invisible. There may also be a steady energetic particle component associated with the flaring. Bright points in soft X-rays, EUV and UV are associated with remnant loops and need not contain much of the energy released. However, they could be a rough proxy for the size of the events. Indeed, Hudson (1991) and Krucker and Benz (1998) find that most of the power radiated is contained in the smallest of such loops. Unfortunately, it seems that the most interesting things happening in coronal holes are in the dark regions and are not easily visible.

Although the processes taking place in the funnel are clearly unsteady and time varying, we have modeled (McKenzie *et al.* 1998a) the flow in the funnel on the basis of steady flow to indicate qualitatively the connection between the funnel,

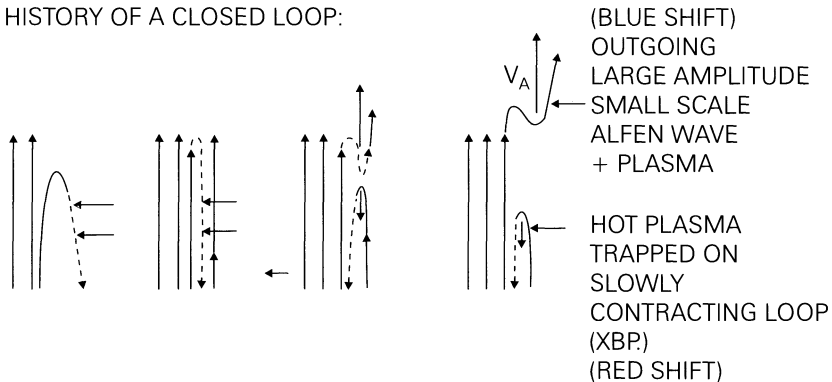


Figure 9. The history of a closed loop being pushed into a unipolar field and undergoing reconnection. Note that the loop tends to migrate into the “network.”

the ionization layer at its foot and the fast solar wind. The family of solutions for the temperature, speed and density in the funnel for different heat fluxes into it are shown in Figure 10. The main point to note is that if the downward heat flux is sufficiently large, the flow remains subsonic and the temperature drops rapidly at the bottom where the density increases sharply.

The ionization layer at the bottom of the funnel, brought about by electron impact driven by downward heat conduction, is very thin (\sim few tens of km) and can be modeled as a weak deflagration.

5. Quiet Coronal Heating

The energy flux needed to power the radiation emitted by the quiet corona in closed field regions is about the same as that needed to produce the fast solar wind on open field lines ($\sim 10^6$ ergs/cm 2 sec). At deeper levels, where the temperature is less than 2×10^5 K, there is no great difference in the morphology between the supergranules and network in closed and open field regions. This suggests that the same heating process is involved in both cases, namely network microflaring and the emission of high frequency ($\gtrsim 1$ Hz) Alfvén waves. The quiet corona structure must then be such that the source heats the plasma (probably by cyclotron resonant absorption) until an equilibrium is achieved with increased density and temperature.

In the Gold/Parker model of coronal “nanoflares,” very low frequency waves are generated from the twisting and shuffling of coronal field lines (Gold 1964; Parker 1988). The resulting stored energy (in a force-free configuration) is released intermittently by magnetic reconnection. On open field lines such low frequency waves are not found in the fast solar wind with more than a few percent of the

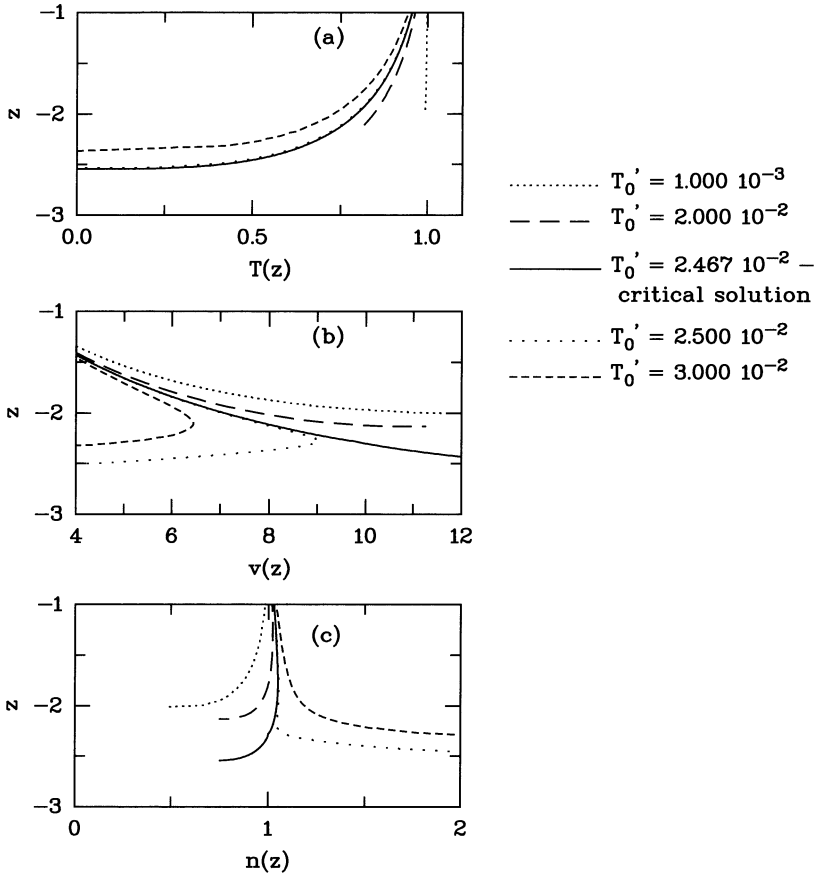


Figure 10. The structure of the funnel flow showing temperature (a), speed (b) and density (c) as functions of the depth into the funnel, normalized to their values at the base, for different temperature gradients T_0' .

necessary energy flux. Since the energy source is inadequate, this casts doubts on the validity of this theory of coronal heating.

6. Minor Ions

Observations (Schmidt *et al.* 1980) of minor ions indicating that $T_{\perp} > T_{\parallel}$, $T_i \sim AT_p$, and $u_i = u_p + V_A$ lend support to the idea that ion cyclotron resonant processes play an important role in the acceleration and heating of minor ions in the solar wind. Minor ions are accelerated by the electric field, ZeE , friction with protons ($\propto Z^2/\sqrt{A}$), the wave force, and their own pressure gradient ($d(n_i k T_i)/dr$), all

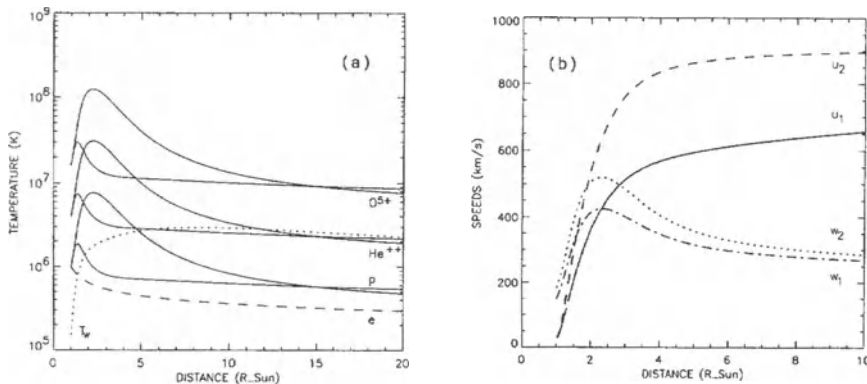


Figure 11. (a) Temperature profiles T_p , T_α , $T_{O^{5+}}$ (solid lines), T_e (dashed line) and T_w (dotted). For the ions both perpendicular (upper lines) and parallel (lower lines) temperatures are shown. (b) The flow speeds u_1 (solid line) and u_2 (dashed line) for the $p + \alpha$, O^{5+} system with $K = 2$. Also shown the ion thermal (v_{th}) and wave (v_w) speeds $w \equiv (v_{th}^2 + v_w^2)^{1/2}$ for $p + \alpha$ (dash-dot) and O^{5+} (dot).

of which must overcome gravity (GMn_iAm_p/r^2). Moreover, unless the ions are heated proportionally to their mass (augmented by some factor K) they will be “disadvantaged.” Li *et al.* (1997) have extended the ideas of a three-fluid model (Yeh 1970; Weber 1973) but assuming proton heat conduction (without including viscosity and using a Kopp-Holzer geometry). Recently Czechowski *et al.* (1998) have constructed a self-consistent model in which helium is placed on an equal footing with protons, including all of the above accelerating forces and with an augmented heating. Figures 11(a) and (b) show the temperature and speed profiles of electrons, protons, He^{++} and O^{5+} . The significant features are the high minor ion temperatures and rapid flow speeds. In order to yield flow speeds of the order of the Alfvén speed relative to the protons at large distances the excess heating factor K must be as high as 2.

7. The FIP Effect

If ionization is incomplete, especially of high FIP species, it is possible to preferentially separate low-FIP species by the plasma $\mathbf{E} \times \mathbf{B}$ drift. This process occurs in the equatorial ionosphere. In the upper chromosphere there is an abundance of Lyman α , which easily ionizes “metals” at the interface in the neutral chromosphere adjacent to the corona. With \mathbf{B} horizontal and $\mathbf{E} \times \mathbf{B}$ upwards, the metals are preferentially carried upwards, as indicated in Figure 12. This process does not work well in network funnels where the fast solar wind originates and \mathbf{B} is almost vertical. However, the rate of ionization also matters in funnels (see McKenzie *et al.*

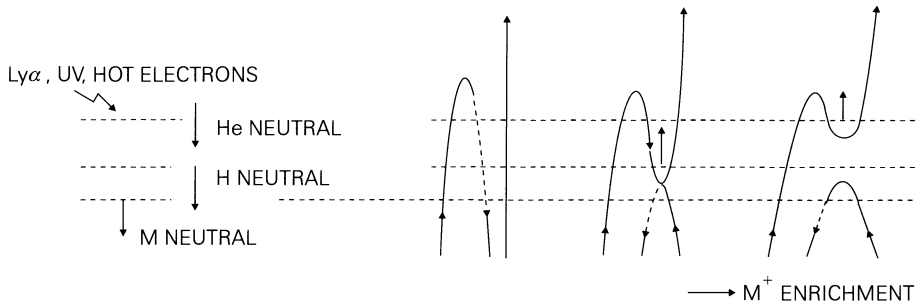


Figure 12. An illustration of how reconnection and upward $\mathbf{E} \times \mathbf{B}$ drifts can lead to the enhancement of metals.

al. 1998b) where it is possible that He atoms are carried upwards mainly as neutrals and can therefore be lost through the sides of the funnels before there is time for them to be ionized.

Steady state models cannot produce a FIP effect (e.g., McKenzie *et al.* 1998b) since they do not have the possibility of removing excess protons or hydrogen atoms at the base of the funnel, except as mentioned above for the case of helium. In fact, measurements in high speed winds are consistent with there being no FIP effect (Geiss 1995).

As far as the highly ionized states are concerned, it appears they must be produced by a high energy tail in the electron distribution function, because the core temperature is quite low $\lesssim 10^6$ K and is therefore ineffective.

8. The Slow Solar Wind (SSW)

We stress that the slow solar wind (SSW) is unsteady, filamentary in nature, exhibits large variations in density and composition, and is generally collision dominated. Therefore it is not possible to describe it with a steady-state model (Axford 1980). About 90% of the SSW is on field lines which connect to the base of the quiet corona. The plasma is filamentary with each filament continually switching its footprint to allow quiet coronal plasma to be disgorged from previously closed flux tubes, each with differing characteristics. The time scales involved are of the order of hours. The FIP effect is presumably associated with emerging horizontal flux tubes. The remaining 10% of the SSW is on closed field regions in the form of “bubbles” which are ejected along the current sheet (Borrini *et al.* 1981), following reconnection at the tips of streamers. These show no heat conduction and low He abundance.

9. Conclusions

1. It seems to be possible to account for the properties of the fast solar wind reasonably well on the basis of high frequency hydromagnetic wave dissipation in the corona.
2. A reasonable magnetic field model is used, which appears to agree well with observations. Together with white light coronagraph observations of electron density it results in a flow speed profile which is in good agreement with the model.
3. The implications of the model are that the acceleration is rapid and the temperature of the protons reaches ~ 5 MK.
4. Minor ions are accelerated by heating proportional to their atomic mass. High-Z ions must be produced by a high energy tail in the electron distribution. No FIP effect is expected in the fast wind.
5. The source of the fast wind lies in the chromospheric network with network “micro”-flares supplying the wave energy.
6. The quiet corona must be heated by the same process that heats the fast solar wind. The Gold/Parker approach based on small coronal “nano”-flares does not appear viable.
7. Coronal plumes are a special problem. It is not clear whether they contribute significantly to the fast wind or not.
8. The slow solar wind is inherently filamentary and unsteady. It originates in the predominately closed corona as a consequence of magnetic field reconnection.

References

- Alazraki, G., and Couturier, P.: 1971, Solar wind acceleration caused by the gradient of Alfvén wave pressure, *Astron. Astrophys.*, **13**, 380–389.
- Axford, W. I.: 1980, Very hot plasmas in the solar system, in *Highlights of Astronomy*, ed. P. A. Wayman, **5**, pp. 351–359.
- Axford, W. I., and McKenzie, J. F.: 1992, The origin of high speed solar wind streams, in *Solar Wind Seven*, eds. E. Marsch and R. Schwenn (Oxford: Pergamon Press), pp. 1–5.
- Axford, W. I., and McKenzie, J. F.: 1997, The solar wind, in *Cosmic Winds and the Heliosphere*, eds. J. R. Jokipii, C. P. Sonett, and M. S. Giampapa (Tucson: University of Arizona Press), pp. 31–36.
- Banaszkiewicz, M., Axford, W. I., and McKenzie, J. F.: 1998, An analytic solar magnetic field model, *Astron. Astrophys.*, **337**, 940–944.
- Belcher, J. W.: 1971, Alfvénic wave pressure in the solar wind, *Astrophys. J.*, **168**, 509–524.
- Borrini, G., Gosling, J. T., Bame, S. J., Feldman, W. C., and Wilcox, J. M.: 1981, Solar wind helium and hydrogen structures near the heliospheric current sheet: A signal of coronal streamers at 1 AU, *J. Geophys. Res.*, **86**, 4565–4573.
- Czechowski, A., Ratkiewicz, R., McKenzie, J. F., and Axford, W. I.: 1998, Heating and acceleration of minor ions in the solar wind, *Astron. Astrophys.*, **335**, 303–308.
- Dowdy, J. F., Jr., Rabin, D., and Moore, R. L.: 1986, On the magnetic structure of the quiet transition region, *Solar Phys.*, **105**, 35–45.
- Fisher, R., and Guhathakurta, M.: 1995, Physical properties of polar coronal rays and holes as observed with the Spartan 201-01 coronagraph, *Astrophys. J.*, **447**, L139–L142.

- Gabriel, A. H.: 1976a, A magnetic model of the solar transition region, *Phil. Trans. Roy. Soc.*, **A281**, 339–352.
- Gabriel, A. H.: 1976b, Structure of the quiet chromosphere and corona, in *The Energy Balance and Hydrodynamics of the Solar Chromosphere and Corona*, ed. R. Bonnet and P. Delache (Clermont-Ferrand: G. de Bussal), pp. 375–418.
- Geiss, J., Gloeckler, G., von Steiger, R., Balsiger, H., Fisk, L. A., Galvin, A. B., Ipavich, F. M., Livi, S., McKenzie, J. F., Ogilvie, K. W., and Wilken, B.: 1995, The southern high-speed stream: Results from the SWICS instrument on Ulysses, *Science*, **268**, 1033–1036.
- Giordano, S., Antonucci, E., and Dodero, M. A.: 1998, Velocity of the fast solar wind in coronal holes, *Adv. Space Res.*, submitted.
- Gold, T.: 1964, Magnetic energy shedding in the solar atmosphere, in *Proc. AAS-NASA Symp. on The Physics of Solar Flares*, pp. 389–395.
- Guhathakurta, M.: 1999, these proceedings.
- Hartle, R. E., and Sturrock, P. A.: 1968, Two-fluid model of the solar wind, *Astrophys. J.*, **151**, 1155–1170.
- Holzer, T. E., and Axford, W. I.: 1970, The theory of stellar winds and related flows, *Ann. Rev. Astron. Astrophys.*, **8**, 31–60.
- Hudson, H. S.: 1991, Solar flares, microflares, nanoflares, and coronal heating, *Solar Phys.*, **133**, 357–369.
- Isenberg, P. A., and Hollweg, J. V.: 1983, On the preferential acceleration and heating of solar wind heavy ions, *J. Geophys. Res.*, **88**, 3923–3935.
- Kopp, R. A., and Holzer, T. E.: 1976, Dynamics of coronal hole regions, 1, Steady polytropic flow with multiple critical points, *Sol. Phys.*, **49**, 43.
- Krucker, S., and Benz, A. O.: 1998, Energy distribution of heating processes in the quiet solar corona, *Astrophys. J.*, **501**, L213–L216.
- Leer, E., Holzer, T. E., and Flå, T.: 1982, Acceleration of the solar wind, *Space Sci. Rev.*, **33**, 161–200.
- Li, X., Esser, R., Habbal, S. R., and Hu, Y.-Q.: 1997, Influence of heavy ions on the high-speed solar wind, *J. Geophys. Res.*, **102**, 17,419–17,432.
- Marsch, E., and Tu, C.-Y.: 1997, Solar wind and chromospheric network, *Solar Phys.*, **176**, 87–106.
- McKenzie, J. F., Axford, W. I., and Banaszkiewicz, M.: 1997, The fast solar wind, *Geophys. Res. Lett.*, **24**, 2877–2880.
- McKenzie, J. F., Banaszkiewicz, M., and Axford, W. I.: 1995, Acceleration of the high speed solar wind, *Astron. Astrophys.*, **303**, L45–L48.
- McKenzie, J. F., Sukhorukova, G. V., and Axford, W. I.: 1998a, The source region of the fast solar wind, *Astron. Astrophys.*, **330**, 1145–1148.
- McKenzie, J. F., Sukhorukova, G. V., and Axford, W. I.: 1998b, Structure of a photoionization layer in the solar chromosphere, *Astron. Astrophys.*, **332**, 367–373.
- Parker, E. N.: 1958, Dynamics of the interplanetary gas and magnetic fields, *Astrophys. J.*, **128**, 664–676.
- Parker, E. N.: 1988, Nanoflares and the solar wind X-ray corona, *Astrophys. J.*, **330**, 474–479.
- Rosner, R., Tucker, W. H., and Vaiana, G. S.: 1978, Dynamics of the quiescent solar corona, *Astrophys. J.*, **220**, 643–665.
- Schmidt, W. K. H., Rosenbauer, H., Shelley, E. G., and Geiss, J.: 1980, On temperature and speed of He^{2+} and O^{6+} ions in the solar wind, *Geophys. Res. Lett.*, **7**, 697–700.
- Smith, E. J., et al.: 1997, Radial and azimuthal components of the heliospheric magnetic field: Ulysses observations, *Adv. Space Res.*, **20**, 47–53.
- Tu, C.-Y.: 1987, A solar wind model with the power spectrum of Alfvénic fluctuations, *Solar Phys.*, **109**, 149–186.
- Weber, E. J.: 1973, Multi-ion plasma in astrophysics, *Astrophys. Space Sci.*, **20**, 391–465.
- Williams, L. L.: 1995, Heat flux and viscosity of protons in the collisionless solar wind, *Astrophys. J.*, **453**, 953–958.
- Yeh, T.: 1970, A three-fluid model of solar winds, *Planet. Space Sci.*, **18**, 199–215.

CORONAL HOLE BOUNDARIES AND THEIR INTERACTIONS WITH ADJACENT REGIONS

L. A. FISK, T. H. ZURBUCHEN and N. A. SCHWADRON

Department of Atmospheric, Oceanic and Space Sciences, University of Michigan, Ann Arbor, USA

Abstract. Coronal hole boundaries are the interfaces between regions where the coronal magnetic field contains a significant component which is open into the heliosphere and regions where the field is primarily closed. It is pointed out that there are constraints on the magnetic field which opens into the heliosphere that must be satisfied in the corona: it must come into pressure equilibrium in the high corona, and the component of the field which connects to the polar regions of the Sun must differentially rotate. A model is presented in which satisfying these constraints determines which field lines are open and which are closed, and thus where the polar coronal hole boundaries occur. Some of the consequences of this model are discussed.

Key words: coronal holes, solar wind, Ulysses

1. Introduction

The subject of this paper is coronal hole boundaries and their interactions with adjacent regions. It is perhaps appropriate to begin then by defining a coronal hole boundary. The definition here will be quite simple: a coronal hole boundary is the interface between a region in the corona where the magnetic field contains a significant component which is open into the heliosphere, and a region where the magnetic field is primarily closed. This is not to say that on the side with a significant open field there are no loops and other closed structures—presumably there are—but there is nonetheless a significant open field component. Of course from this open field, the solar wind flows, reduces the coronal density, and thus forms a coronal hole. We will also concentrate here on solar minimum conditions, and in particular on the well developed and somewhat stable polar coronal holes and their extensions.

Wang, Sheeley, and co-workers, in a series of papers (Nash *et al.* 1988; Wang *et al.* 1988; Wang and Sheeley 1993; Wang *et al.* 1996) have argued that the positioning of coronal holes arises from the superposition of an axial symmetric polar magnetic field and a non-axial symmetric equatorial field. It is thus the global magnetic field structure of the Sun that specifies coronal hole boundaries. These models are intrinsically static since the field configuration is determined from a potential field model. However, the evolution of the coronal hole and its boundaries under the influence of differential rotation can be modeled by assuming that the corona is in continuous relaxation to a potential field configuration, presumably due to reconnection. This model provides an explanation for the apparent rigid rotation of the polar coronal holes.

In this paper we argue a somewhat different point of view. Namely, the differential rotation of the photosphere results in motions of the coronal magnetic field.



However, field lines in the corona which open into the heliosphere must relax to being essentially in pressure equilibrium in the high corona. It is then the motions due to differential rotation combined with the need to relax to pressure equilibrium which determine which field lines are open into the heliosphere and which are closed, and therefore where the coronal hole boundaries occur. The general concepts of this approach and additional details are discussed in Fisk *et al.* (1999).

There are important differences in the consequences of the model presented here and those of, e.g., Wang and Sheeley. In this model no reconnection is required within the polar coronal hole; indeed, differential rotation and the absence of reconnection cause the field line motions described here. Reconnection does determine the coronal hole boundaries, but even here, as we shall discuss, it occurs at low latitudes removed from the photospheric boundary of the polar coronal hole. Moreover, the heliospheric magnetic field which results from the model presented here is fundamentally different from that which results from a traditional potential field model for the corona.

2. Relevant Observations

Lets us begin then by reviewing some of the observations of open field lines, which are summarized in Table I. The Table has been divided into three categories of observations, or of inferences from the observations. The first are heliospheric, of the properties of open field lines and of the solar wind; the second are solar observations, and the third category includes some solar and heliospheric observations which will support the arguments that we will make. The first heliospheric observation is the well known one that at least near solar minimum the polarity of the heliospheric magnetic field is essentially uniform in each hemisphere, and with the polarity of the corresponding solar pole. The regions of uniform polarity are separated by an equatorial current sheet. The current sheet is the expected extension of the streamer belt. It is wavy, but even more important it is tilted relative to the solar rotation axis, and that tilt becomes less as we approach solar minimum (Shultz 1973; Smith *et al.* 1978; Suess *et al.* 1993).

The second observation is that the radial component of the heliospheric magnetic field is essentially uniform with latitude, as has been documented in detail by Smith and Balogh (1995), from Ulysses observations. A uniform field strength with latitude is what should be expected, which is a point that has been made convincingly by Suess (1999). If we extrapolate back the magnetic field strength and the solar wind plasma pressure, we easily conclude that the beta of the plasma—the ratio of thermal to magnetic energy—is very small, 10^{-2} or less in coronal holes, at a few solar radii from the Sun. The radius of curvature of the open field lines is relatively large at this point. The open field lines are essentially radial. A low beta plasma cannot support any net magnetic forces. The only alternative is then no pressure gradients in the magnetic field strength. That is to say the magnetic field becomes uniform in strength in the corona, and thus creates a magnetic field in the

Table I
Observations relevant to this theory

| Observations | Comments |
|---|---|
| Heliospheric | |
| Magnetic field is divided into two regions of uniform polarity separated by an equatorial current sheet (e.g., Smith <i>et al.</i> 1978). | Current sheet is the expected extension of streamer belt; it is wavy and tilted relative to solar rotation axis. |
| Radial component of magnetic field is uniform with latitude (Smith and Balogh 1995). | |
| Extrapolation of solar wind parameters—magnetic field strength and plasma pressure—back to high corona yields a plasma with a very small β (Suess 1999). | Implies force-free conditions. Field is essentially radial, which implies magnetic pressure must be essentially constant. |
| No strong time variations in heliospheric magnetic field near solar minimum (Smith and Balogh 1995). | |
| Solar wind occurs in two types: fast and steady, and slow and variable (e.g., Phillips <i>et al.</i> 1995). | Fast wind from polar coronal holes occurs at higher latitudes; slow wind from band about equatorial current sheet. |
| Magnetic field lines from polar coronal holes expand non-radially. | Polar coronal holes at base of corona have smaller solid angle than regions of high speed wind in heliosphere. |
| Fast and slow wind have different origins (Geiss <i>et al.</i> 1994). | Slow wind has strong FIP bias; fast wind does not. |
| Solar | |
| Photosphere differentially rotates (e.g., Snodgrass 1983). | 20–25% slower rotation, or more, at poles. |
| Characteristic scale size for organization of magnetic field in photosphere is supergranules, or $\lambda \sim 30,000$ km; characteristic time scale for reconfiguration of network is $\tau \sim 1\text{--}2$ days (Schrijver <i>et al.</i> 1997). | Limits rate at which field lines should diffuse in photosphere or corona; effective diffusion coefficient is λ^2/τ . |
| Supporting | |
| Corona rotates more rigidly than photosphere (e.g., ref. in Bird and Edenhofer 1990). | |
| Low energy energetic particles propagate easily in heliographic latitude (e.g., Roelof <i>et al.</i> 1997). | |

heliosphere which is uniform strength, as is observed. We will make considerable use here of the uniformity of the field strength of open field lines in the corona, at several solar radii.

We should note also that there are no large time variations in the heliospheric magnetic field (Smith and Balogh 1995). At least at this point in the solar cycle, the total magnetic energy in the magnetic field in the heliosphere is relatively constant. Coronal mass ejections do occur, bringing out new magnetic flux, but during solar minimum this is not a large effect, and in general we are dealing with a heliospheric magnetic field strength which is constant in time and a radial component, or equivalently a strength back in the corona, which is constant in latitude and longitude.

The next observation is that the solar wind comes in two types: fast and slow. The fast wind occurs at the higher latitudes, above 30 degrees or so in heliographic latitude. The slow solar wind occurs at low latitudes. The fast wind extends downward in latitude below 30 degrees heliographic latitude, and then as it flows outward it overtakes and interacts with the slow wind. The geometry in a rough sense is simply that the slow wind originates from a band that surrounds the equatorial current sheet which in turn is tilted in heliographic latitude.

The fast wind is considered to originate from the polar coronal holes. The polar coronal holes occupy a much smaller solid angle in the low corona than does the fast solar wind. There must therefore be a considerable nonradial expansion of the open field lines from the polar coronal holes, from a small surface area in the low corona, to the larger surface area in the heliosphere.

The origin of the slow solar wind is less clear, which is a point we will discuss later. However, whatever is the origin of the slow wind it is different from the origin of the fast wind. As has been described in detail by, e.g., Geiss *et al.* (1994), the slow wind is enhanced in elements with low first ionization potential (FIP), whereas in the fast wind, there is little or no such enhancement. Enhancements based on first ionization potential must occur in the chromosphere where the particles can be neutral. Clearly, there is then a difference in the origin in the low corona and chromosphere between the fast and slow wind, and thus between the open field lines on which the fast and slow wind flows.

For solar observations, we will make use first of the well known fact that the photosphere differentially rotates, with the poles, to the extent that the photospheric rotation rate can be determined at high latitudes, rotating 20–25% slower than the solar equator (e.g., Snodgrass 1983). The second solar observation is more of an inference than an observation. The characteristic scale size for the organization of the magnetic field in the photosphere is the size of supergranules, $\lambda \sim 30,000$ kilometers. As has been seen by the SOHO MDI observations, this network of supergranules appears to be reconfigured on a time scale of $\tau \sim 1\text{--}2$ days, through the continuous emergence of new flux (Schrijver *et al.* 1997). New loops emerge and reconnection occurs. This reconfiguration is somewhat of a random process. And should result in a diffusion of magnetic field lines, with a characteristic diffusion coefficient of λ^2/τ . We will use this diffusion coefficient later to argue that random motions of the field lines must be sufficiently slow so that, for the time scales with which we will be interested, the rotational motions of the Sun are more important

than these diffusive motions. The magnetic field lines, in effect, simply remain attached to the differentially rotating photosphere.

Finally, there is a category in Table I called supporting observations, which will support the conclusions that we will draw here, and which we will return to below in more detail. The solar observation that is supporting is that the corona tends to rotate more rigidly than the underlying differentially rotating photosphere. If we look at coronal green lines, prominences, or the boundaries of well defined coronal holes, or particularly their extensions, they tend to rotate more rigidly than the photosphere, at least during the declining activity phase (e.g., ref. in Bird and Edenhofer 1990). Finally there are some heliospheric observations of the configuration of the heliospheric magnetic field and the important Ulysses observation that low energy energetic particles propagate easily in heliographic latitude (Roelof *et al.* 1997).

3. Surface of Constant Pressure

Consider now the following spherical surface which is illustrated in Figure 1. The surface is placed at several solar radii from the Sun. The surface is permeated only by open magnetic field lines. That is, the surface is safely above any closed loop structures. We will also place this surface well inside the Alfvén point, which typically occurs at 10–15 solar radii, in which case the dynamic pressure of the solar wind is not important. From the list of heliospheric observations in Table I, and the inferences from them, the plasma at this surface is a very low beta plasma, i.e., thermal pressure very much less than the magnetic field pressure. The magnetic field, then, must be in a force-free configuration; no thermal pressure forces to balance the magnetic forces. We assume, however, that the radius of curvature of the magnetic field which permeates this surface is large compared to the radius of the surface. That is, the field lines through this surface are essentially radial, in which case the magnetic field strength must be nearly constant.

We marked on the surface several regions. First is the location of the equatorial current sheet, which for simplicity we take to be a plane, that is, no warps, and which is tilted relative to the solar rotation axis. If we define an axis “ M ” that is normal to this plane, and use M to define a spherical coordinate system, then the equatorial current sheet lies at a polar angle, θ_M , of 90 degrees.

The slow solar wind is considered to come from a band about the equatorial current sheet. Again, for simplicity we take this band to be uniform, and to reach to a polar angle of θ_{M_1} . The fast solar wind comes from the region $\theta_M < \theta_{M_1}$.

The field lines which carry the fast solar wind have a non-radial expansion underneath the surface in Figure 1; they connect to the polar regions of the Sun and form the polar coronal hole. The field lines which carry the slow solar wind have an unspecified origin at this time, to which we will return.

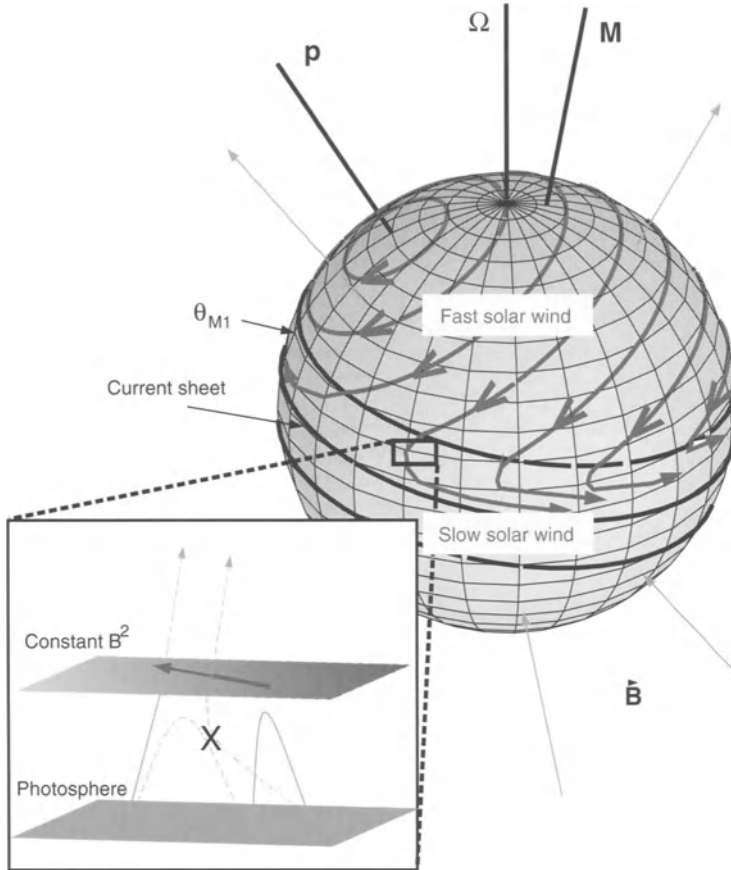


Figure 1. The surface of constant magnetic pressure. The surface is located at several solar radii from the Sun, and is penetrated only by open magnetic field lines. The surface is located in a region of low beta plasma, and the field lines are primarily radial. The location of the equatorial current sheet and the interface between the regions of fast and slow solar wind, θ_{M1} , are marked. The M -axis is normal to the plane defined by the equatorial current sheet, and is offset from the solar rotation axis Ω . The field line located at p connects to the solar heliographic pole. The arrows on the surface are the trajectories of the field lines which penetrate through the surface, and are described in the text.

The Sun is of course not this regular. However, we do know that the boundary between the fast and slow solar wind is tilted relative to the rotation axis; otherwise the two flows would not interact. This tilt of the interface is the important issue.

Consider now any motions of the magnetic field on this surface. There is no reconnection occurring on the surface, and thus the inductance equation is simply:

$$\frac{\partial \mathbf{B}}{\partial t} = \nabla \times (\mathbf{u} \times \mathbf{B}) \quad (1)$$

This equation can be then be manipulated into the following form:

$$\frac{\partial B^2/2}{\partial t} = -\nabla \cdot (B^2 \mathbf{u}_\perp) - \mathbf{u}_\perp \cdot [(\nabla \times \mathbf{B}) \times \mathbf{B}] \quad (2)$$

where \mathbf{u}_\perp is the velocity normal to the magnetic field direction.

The first assumption is that the magnetic field is essentially constant in time. The flux of open magnetic field near solar minimum is not changing, in which case the time derivative of B^2 is zero. We are also assuming that the magnetic field is essentially force free; it is a low beta plasma. That is, $(\nabla \times \mathbf{B}) \times \mathbf{B}$ must be essentially zero. We also assume that the field is essentially radial, in which case force-free is equivalent to constant field magnitude, and the motions normal to the field must lie on the surface we have just defined.

With these assumptions, then, any motions on the surface of constant magnetic pressure must satisfy

$$\nabla \cdot \mathbf{u}_\perp = 0 \quad (3)$$

This is a rather obvious point. Any motions which result in a divergence would also result in an accumulation of magnetic field strength, which cannot be supported in our force-free field conditions.

At the equatorial current sheet the polar component of \mathbf{u}_\perp must be zero. We are not mixing polarities across the current sheet. We are not annihilating magnetic fields at the current sheet and reducing the field strength in time. We thus have a boundary condition at the current sheet that \mathbf{u}_\perp must be zero, and $\mathbf{u}_\perp = 0$ is a solution to equation 3. It is not unreasonable then to ask whether \mathbf{u}_\perp is zero everywhere. This, however, is unlikely. The surface in Figure 1 should be roughly stationary in the frame co-rotating at the equatorial rotation rate of the Sun. The current sheet is a low latitude structure. Similarly this boundary, θ_{M_1} , between the fast and slow solar wind is at low latitudes, and the axis in this figure, the M axis, is drawn normal to the plane of the current sheet. All these structures, then, are rotating essentially with the equatorial rotation rate. However, the magnetic field lines which penetrate this surface in the fast solar wind region attach back to the polar region of the Sun, which differentially rotates 20 to 25% slower than the equatorial region.

We argued earlier that if we consider the rate at which field lines are likely to diffuse across the solar surface, we are constrained by the fact that the characteristic dimension for the photosphere magnetic field is the size of supergranules, some 30,000 kilometers, and the characteristic time is the observed time during which the supergranule network is reconfigured, which is 1 to 2 days. If we compare the resulting diffusion time with the time during which the field lines differentially rotate, we find that at high latitudes the differential rotation time is much faster. This is not surprising. In general a systematic convection wins over a random diffusion, unless the diffusion is extremely fast. The point is, however, that the field lines which penetrate the surface in Figure 1 in the fast wind region are attached to the

photosphere in the polar region. They are thus forced to differentially rotate and move along this surface. That is, \mathbf{u}_\perp will not be zero along this surface.

We can estimate what these velocities are likely to be along the surface in Figure 1, as was done by Fisk (1996) in discussing the heliospheric magnetic field that results from these motions along this surface. The M axis is essentially the axis of symmetry of the expansion of the magnetic field from the polar coronal hole. We have some field strength for open field lines on the solar surface, and they expand non-radially to a uniform field strength on the surface in Figure 1. There is then a simple one-to-one mapping of every open field line on the solar surface to this outer surface. This is best illustrated in Figure 2. The center sphere depicts the solar surface. The outer shell is the surface in Figure 1. The M axis is the same, as is the rotation axis. The field lines expand about M , symmetrically and non-radially from the solar surface to the outer surface. Figure 2 is again in the frame which co-rotates with the equatorial rotation rate. The M axis is fixed because it is normal to the equatorial current sheet. However, the solar surface in the polar region is differentially rotating. And the field lines which are attached to this differentially rotating surface are forced to move along the outer surface on the trajectories shown. This situation is easiest to see if we examine the field line which comes from the solar pole. It of course does not differentially rotate, and in this co-rotating frame, it expands non-radially and comes out at the fixed location marked p on the outer surface. All other field lines differentially rotate about this field line on the solar surface, and about p on the outer surface. Because the M axis is offset from the rotation axis, and the non-radial expansion is considerable, the excursions of the field lines in latitude and longitude on the outer surface are considerable.

We have drawn these trajectories in Figure 2 as circles. In reality they will be more complicated. The expansion is not really symmetric about M , the field strength on the solar surface may be uneven, etc. However, circles are easy to deal with, and they should indicate the general trends of the motions.

The field line trajectories in Figure 2, which are for the magnetic field in the fast solar wind region in the polar coronal hole, are also shown in Figure 1. In the slow solar wind region, there must also be trajectories, because we have a requirement that $\nabla \cdot \mathbf{u}_\perp = 0$ everywhere on the surface. The motion in the θ direction across the interface from fast to slow solar wind must be continuous. The motion in the θ direction at the current sheet must be zero. We are not mixing polarities across the current sheet or eliminating flux here. The solution for \mathbf{u}_\perp in the slow solar wind region is then completely determined, and is discussed in detail in Fisk *et al.* (1999). The solution is shown schematically in Figure 1 with the arrows in the slow solar wind region.

The physics here is fairly simple. In the fast solar wind region, differential rotation drives the motions of the field lines. In the slow solar wind region, our requirement that there is no magnetic pressure buildup drives the motions. In other words, if we did not have the predicted motions, the deposition of magnetic flux at

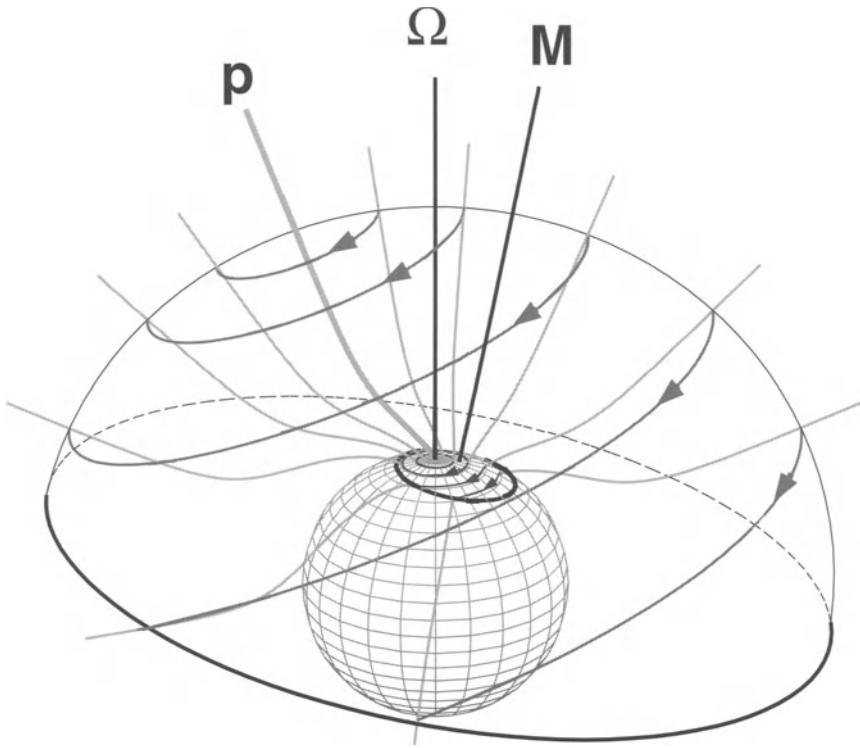


Figure 2. An illustration of the motions of the magnetic field in the corona, in the polar coronal hole, as predicted in the model of Fisk (1996) (after Zurbuchen *et al.* 1997). The outer surface, which is defined in the text, is penetrated only by field lines which open into the heliosphere, and which have essentially constant magnetic pressure. The figure is drawn in the frame co-rotating with the equatorial rotation rate. The M axis is the axis of symmetry for the expansion of the magnetic field from a polar coronal hole. The Ω axis is the solar rotation axis. The open lines are field lines, with p marking the field line that connects to the heliographic pole. The curves with arrows are the trajectories of the field lines, the motions of which are driven by differential rotation of the photosphere.

low latitudes, resulting from the differential rotation, would cause a flux build-up that cannot be supported. Since we are not allowing flux through the current sheet, the only recourse is motion in longitude, back to the other side of the Sun.

Let us return now to the coronal hole boundary problem. The base of an open field line in the polar coronal hole moves by differential rotation. This forces motion of the field lines on the surface in Figure 1. Eventually it reaches low latitudes. No buildup in the magnetic forces is allowed. Thus the field line must turn to make the return trip to the other side of the Sun. It then becomes entangled with other field lines, perhaps with large loops, and presumably reconnects. Failure to perform this reconnection would yield a very unnatural and insupportable bend in the field line. The top end of the field line must move to avoid magnetic pressure buildup.

The bottom end must find a way to follow. As the field line traverses back to the other side of the Sun at low latitudes, it presumably does so through a series of reconnections, which are illustrated schematically in the insert in Figure 1.

Now we are back to the main subject. When the polar field line reconnects, it produces a large scale closed loop. In other words, the polar field line is opened into the heliosphere until it moves to low latitudes, after which it reconnects. We have thus defined the boundary of the coronal hole. It occurs when the non-radial expansion of the polar field brings the upper end of the field line to low latitudes, and it is forced to reconnect in order that it can make the return trip back to the other side of the Sun.

The process on the other side of the Sun is more difficult—the side opposite to the one shown in Figure 1. Field lines at low latitudes are transported in longitude, and then on the back side of Figure 1 they must reconnect to polar field lines to continue the motion across the polar hole. A low latitude field line thus has to find a high latitude field line with which to reconnect. Perhaps this is a multi-step process in which the reconnection occurs with some intermediate latitude loop and then with a polar field line. The point is, however, if such reconnection does not occur, there would be an unacceptable buildup or depletion of magnetic flux and pressure on the surface in Figure 1.

In this model, then, the constraint which determines which field lines are open and which are closed is the requirement that the magnetic pressure is constant on the surface in Figure 1. Differential rotation will drive motions of the field lines on this surface. Field lines are continuous down into the photosphere. Thus, at low latitudes the motions on this surface must be accompanied by corresponding motions at the solar surface which only can be accomplished if polar field lines which were opened become closed, and there is continuous reconnection among low latitude loops as the field lines move in longitude.

4. Some Consequences

Consider now some of the consequences of this model. First of all, there is a clear difference between the origin of the fast solar wind and the slow solar wind. The fast wind originates on a single continuously open field line. The slow wind originates on field lines which are continuously reconnecting, jumping from low latitude loop to low latitude loop. This model for the corona, in which there are clear distinctions between the continuously open field lines from the polar coronal hole and randomly open field lines at low latitude, was proposed by Axford (1977). We should expect in these models, as is observed, that the slow wind is much more variable than the fast wind. It is also possible, as was done by Schwadron *et al.* (1999), to construct a first ionization or FIP enhancement mechanism which takes advantage of the fact that in this model the material which forms the slow solar wind started as material which was stored on closed loops. Recall that the slow wind is FIP enhanced, whereas the fast wind is not (Geiss *et al.* 1994).

This model also suggests that the corona should appear to rigidly rotate. The field lines which are open and those which are closed, and thus where the density is enhanced and where it is not, is determined by the global properties: the need for the open field lines to both move on the surface in Figure 1, to not cross the current sheet, and to be in pressure equilibrium. These flow patterns are fixed in the frame which co-rotates with the equatorial rotation rate. The pattern thus rotates rigidly as will the underlying density structure of the corona implied by this pattern.

The coronal hole boundary, in particular, should tend to rigidly rotate, since it forms when the field lines encounter the low latitude interface in Figure 1, θ_{M1} , which is sufficiently low in latitude to rotate effectively at the equatorial rotation rate.

The configuration of the heliospheric magnetic field is a major consequence of this model. The trajectories on the field lines in Figure 1 are simply the footpoints of the heliospheric magnetic field. Unlike the standard Parker spiral for the heliospheric magnetic field, where the footpoints remain at a single latitude and simply co-rotate rigidly with the Sun, here the footpoints make large excursions in latitude and longitude. This creates a much more complicated field configuration in the heliosphere, as has been discussed in detail by Fisk (1996) and Zurbuchen *et al.* (1997).

The large excursions in latitude do provide a natural explanation for perhaps the most curious observation from Ulysses. It is well known that low energy particles—of order an MeV or less—are accelerated in the stream-stream interaction regions in the solar wind, the Co-rotating Interaction Regions, at low latitudes. These accelerated particles, however, are seen up to the highest latitudes observed by Ulysses, up to 80 degrees or so (Roelof *et al.* 1997). In a Parker spiral, the field lies on cones of constant latitude. It is hard to image how these low energy or low rigidity particles can propagate across the magnetic field in latitude. In the model here, however, the magnetic field in the heliosphere, as a result of the motion of the footpoints, can make a direct connection from low to high latitudes, and provides an easy path for the low energy particles to propagate in latitude.

Finally, we should mention that there has always been evidence in heliospheric observations for the motion of the open field lines in the corona. There are periods of time—over hours, days—when the heliospheric field is essentially radial, that is, when it is substantially underwound. In many cases this is unlikely to be a heliospheric effect caused by solar wind interactions. Rather, the more reasonable explanation is that the footpoints of the heliospheric field are in motion back in the corona.

5. Summary

In summary, we have argued that there are constraints that must be imposed on the field lines which open into the heliosphere: they must be in pressure equilibrium in the high corona, they must be anchored into the differentially rotating photosphere,

and they must not cross the tilted equatorial current sheet. The tilt of the current sheet is determined by the underlying photospheric magnetic field. When you satisfy these constraints, there are inferences for when and where field lines must be open and when and where they must be closed, and that process of closing previously open field lines, and vice versa, is what determines the location and properties of coronal hole boundaries.

Acknowledgements

This work was supported, in part, by NASA contracts NAG5-2810, NAG5-7111 and JPL contract 955460. THZ and NAS were also supported, in part, by NASA grant NAG5-6471 and NSF grant ATM 9714070.

References

- Axford, W. I.: 1977, in *Study of Travelling Interplanetary Phenomena*, eds. M. A. Shea, *et al.*, (Dordrecht: D. Reidel), p. 145.
- Bird, M. K., and Edenhofer, P.: 1990, in *Physics of the Inner Heliosphere I*, ed. R. Schwenn and E. Marsh, (Springer-Verlag: Berlin).
- Fisk, L. A.: 1996, *J. Geophys. Res.*, **101**, 15547.
- Fisk, L. A., Zurbuchen, T. H., and Schwadron, N. A.: 1999, *Astrophys. J.*, in press.
- Geiss, J., Gloeckler, G., and von Steiger, R.: 1994, *Space Sci. Rev.*, **72**, 49.
- Nash, A. G., Sheeley, Jr., N. R., and Wang, Y.-M.: 1988, *Solar Phys.*, **117**, 359.
- Parker, E. N.: 1958, *Astrophys. J.*, **128**, 664.
- Phillips, J. L., *et al.*: 1995, *Geophys. Res. Lett.*, **22**, 3301.
- Roelof, E. C., *et al.*: 1997, *J. Geophys. Res.*, **102**, 251.
- Schrijver, *et al.*: 1997, *Astrophys. J.*, **487**, 424.
- Schwadron, N. A., Fisk, L. A., and Zurbuchen, T. H.: 1999, *Astrophys. J.*, in press.
- Shultz, M.: 1973, *Astrophys. Space Sci.*, **34**, 371.
- Smith, E. J., and Balogh, A.: 1995, *Geophys. Res.*, **101**, 24349.
- Smith, E. J., Tsurutani, B. T., and Rosenberg, R. L.: 1978, *J. Geophys. Res.*, **83**, 717.
- Snodgrass, H. B.: 1983, *Astrophys. J.*, **270**, 288.
- Suess, S. T., McComas, D. J., and Hoeksema, J. T.: 1993, *Geophys. Res. Lett.*, **20**, 161.
- Suess, S. T.: 1999, *Adv. in Space Res.*, in press.
- Wang, Y.-M., Sheeley, Jr., N. R., Nash, A. G., and Shampline, L. R.: 1988, *Astrophys. J.*, **327**, 427.
- Wang, Y.-M., and Sheeley, Jr., N. R.: 1993, *Astrophys. J.*, **414**, 916.
- Wang, Y.-M., Hawley, S. H., and Sheeley, Jr., N. R.: 1996, *Science*, **271**, 464.
- Zurbuchen, T. H., Schwadron, N. A., and Fisk, L. A.: 1997, *J. Geophys. Res.*, **102**, 24175.

Address for correspondence: L. A. Fisk, Department of Atmospheric, Oceanic and Space Sciences, University of Michigan, 2455 Hayward Street, Ann Arbor, MI 48109-2143

COMPOSITION VARIATIONS IN THE SOLAR CORONA AND SOLAR WIND

J. C. RAYMOND

Harvard-Smithsonian Center for Astrophysics

Abstract. Order of magnitude variations in relative elemental abundances are observed in the solar corona and solar wind. The instruments aboard SOHO make it possible to explore these variations in detail to determine whether they arise near the solar surface or higher in the corona. A substantial enhancement of low First Ionization Potential (FIP) elements relative to high FIP elements is often seen in both the corona and the solar wind, and that must arise in the chromosphere. Several theoretical models have been put forward to account for the FIP effect, but as yet even the basic physical mechanism responsible remains an open question. Evidence for gravitational settling is also found at larger heights in quiescent streamers. The question is why the heavier elements don't settle out completely.

Key words: corona, solar wind, composition

1. Introduction

Abundance variations are frequently observed in the solar wind and the solar corona. Factor of 3 changes in conveniently measured abundance ratios, such as O:Mg and Ne:Mg are common, and factor of 10 departures from photospheric abundance are sometimes observed. We care about these anomalies because

1. Abundance variations provide a means for connecting features in the corona with structures in the solar wind.
2. Knowledge of the composition is *required* to correctly apply many diagnostics, such as X-ray band ratios used to derive electron temperatures (Li *et al.* 1998).
3. The radiative cooling rate enters into models used to understand coronal heating, and it depends on elemental abundances.
4. Composition is a unique signature of the connection between the chromosphere and corona and of the physical processes involved in heating and accelerating the solar corona and solar wind. Unfortunately, like some of the viewgraphs on which this review is based, that signature is difficult to read.

The predominant pattern observed in both the solar wind and in the corona is the FIP effect—the enhancement of elements whose neutral atom has an ionization potential below 10 eV (low-FIP) relative to the high-FIP elements. The 10 eV dividing line is likely to be associated with the energy of a Ly α photon. The abundant low-FIP elements are Na, Si, Al, Ca, Fe and Ni, while He, N, O, Ne and Ar are high-FIP. The intermediate FIP elements C and S show intermediate enhancement. The FIP enhancement is typically a factor of 3–4 in the slow solar wind and less than 2 in the fast wind. Most observations give relative rather than absolute abundance determinations, so a longstanding question is whether the low-FIP elements are enhanced or the high-FIP elements are depleted. The element



Space Science Reviews 87: 55–66, 1999.

©1999 Kluwer Academic Publishers.

fractionation must occur where the low-FIP elements are ionized and the high-FIP elements are neutral. SOHO measurements show the FIP effect and its variation among different coronal and solar wind structures. They also reveal an abundance anomaly interpreted as gravitational settling of the heavy elements in quiescent structures at high altitudes.

A number of comprehensive reviews of both observations and theoretical explanations of coronal and solar wind composition are available (Meyer 1985; Saba 1995; Feldman 1992; Henoux 1995). A volume of *Space Science Reviews* edited by R. von Steiger presenting abundance results from a recent ISSI workshop is due to appear shortly. This paper summarizes the measurements, concentrating on recent results from SOHO and Ulysses. It discusses the analysis and the uncertainties involved, particularly for absolute abundance determinations. It briefly summarizes the currently available theoretical models.

2. Measurements

2.1. PHOTOSPHERIC COMPOSITION

While it is interesting to observe variations in the coronal or solar wind composition from point to point and time to time for their own sake, any interpretation of the cause of the variations will eventually require knowledge of how the fractionation mechanism affects the composition, i.e., how the coronal and solar wind compositions compare with the photospheric values. Photospheric abundances for most elements are determined from absorption line profiles and the assumption of Local Thermodynamic Equilibrium. Thus they are sensitive primarily to the photospheric temperature structure and to the oscillator strengths of the transitions observed. Errors may arise as a result of averaging over the fluctuations in photospheric temperature associated with granulation. This is most likely to affect elements for which only a minority ionization stage can be observed (see the discussion of the Li abundance by Kurucz 1995) or elements for which only transitions among highly excited states can be observed in the optical.

Abundance errors will also result from errors in the oscillator strengths. While the oscillator strengths are among the easier atomic parameters to compute, and they are more accurately known than collisional excitation cross sections, ionization rates or recombination rates, there have occasionally been major recalibrations of the abundance scale due to changes in the oscillator strengths of complex elements such as iron. The oscillator strengths are likely to be reliable to about the 20% level for complicated species and better for simple ions. Some elements are not easily observed at optical wavelengths, and their abundances are obtained from meteorite composition scaled to elements that can be observed in the solar photosphere.

Anders and Grevesse (1989) presented a comprehensive abundance analysis. A recent study by Boyarchuk *et al.* (1998) confirmed the Anders and Grevesse values

for the preferred atmospheric model, but found offsets of order 0.1 the logarithm for abundances based on other model atmospheres.

Feldman (1992) presents a fairly recent compilation of photospheric abundances, and we will use that set of abundances for reference. Most of these values are from Anders and Grevesse (1989) with a few updated values. The Ne abundance is taken from local galactic and flare measurements. It is unfortunate that the Ne abundance is especially difficult to determine, because neon is frequently used as the indicator for high-FIP abundances.

2.2. SOLAR WIND ABUNDANCES

Variations in the ratio of He to H in the solar wind have long been known, and as instrumental capabilities improved other elements were seen to vary. The He to H ratio is fairly constant at about 0.05 in the fast solar wind, or about half solar (e.g., von Steiger *et al.* 1995). In the slow wind, the helium abundance is even lower, and it varies on short time scales. Especially low helium abundances are associated with the interplanetary current sheet. During Coronal Mass Ejections (CMEs), the helium abundance can reach 30% and enhanced heavy element abundances are sometimes seen (Galvin 1997). CELIAS measurements of abundances in the 6 January 1997 CME show a systematic enhancement of heavy elements in the CME and erupted filament material, with Fe/O about an order of magnitude above the photospheric value with no FIP signature (Wurz *et al.* 1998), though this result may depend upon the charge state assumed in analyzing the data.

The FIP effect has been observed under a wide range of solar wind conditions, usually based on relative abundances such as the Mg/O or Fe/O ratios. Absolute abundance determinations are more difficult due to the large dynamic range needed to compare proton fluxes with fluxes of trace elements. The Mg/O enrichment is typically a factor of 3.3 in the slow solar wind, and less than half as great in the fast wind (Geiss *et al.* 1995). The enhancement is quite constant in the fast wind, and strongly variable in the slow wind. Besides the clear correlation with solar wind speed, the Mg/O ratio is correlated with the freeze-in temperatures derived from the ionization state of the wind.

Measurements were made of the Fe/O ratio with the CELIAS experiment on SOHO while solar minimum conditions prevailed (Aellig *et al.* 1998). The average ratio of 0.11 ± 0.03 indicates a factor of 3 FIP bias, and as with the Ulysses measurements, the enhancement ranges from about 0.12 at the lowest speeds to 0.06 when the speed exceeds 500 km/s (Ipavich *et al.* 1992; Geiss *et al.* 1995). The high time resolution of the CELIAS instrument shows strong variability on a time scale of hours. The anticorrelation of FIP bias with wind speed and correlation with freeze-in temperature hold in a general way at the shorter time scales, but Aellig *et al.* present a remarkable example of a 6 hour offset between a sharp jump in the Fe/O ratio and the corresponding jump in the other variables.

Abundance anomalies are also observed in Solar Energetic Particles (Reames 1990, 1992). A mass bias attributed to the Q/A dependence of the acceleration process is superimposed on the FIP bias (Meyer 1985). The strength of the FIP effect varies from one event to another. A strong FIP bias is taken to mean that the particles were accelerated by CME-driven shocks in the coronal regions associated with the slow solar wind, while a weaker FIP bias could mean that they arise in the flare or in shock acceleration in fast solar wind regions. The abundance of ^3He can be enhanced by orders of magnitude in events associated with impulsive solar flares, and these events also show enhancements of heavy elements.

2.3. CORONAL ABUNDANCES

2.3.1. *X-ray Observations*

There have been indications of abundance variations in the solar corona for many years. X-ray observations of solar flares suggested changes in the Ca abundance from line-to-continuum ratios (Sylwester *et al.* 1984). As this method compares the emission of the dominant He-like ion with bremsstrahlung continuum produced by electrons at similar energies, it is relatively insensitive to uncertainties in atomic rates and to uncertainty in the instrumental calibration. Because the bremsstrahlung is largely produced by collisions with protons, it yields an absolute abundance measurement. Fludra and Schmelz (1995) concluded that low-FIP elements were enhanced by factors of 1.5–2, while oxygen was depleted by a factor of 4 from one set of observations. Sylwester *et al.* (1998) derived an average calcium abundance of 5.8×10^{-6} from over 100 flares, or about twice the photospheric value. The abundances are likely to depend on the fraction of flare plasma provided by evaporation of chromospheric material.

Another approach to solar flare abundances is a comparison of the Fe XXV emission line flux produced in the flare to the fluorescent Fe K α emission produced when X-rays from the flare ionize material at the solar surface (Phillips *et al.* 1994). This method compares the coronal iron abundance to the abundance in the photosphere, again cancelling out instrumental calibration uncertainties. This method has not been applied to a large number of flares, but it seems to show photospheric iron abundances in the flare plasma.

The most widely used approach to deriving coronal abundances from X-ray spectra is to pair lines of different elements that are formed at the same temperature to obtain the relative abundances of those elements. Ne IX and Fe XVII are particularly convenient in that these are the dominant ions of their respective elements over a large, and largely overlapping, temperature range, the lines are strong and close together in wavelength, and they represent a high- and a low-FIP element (Schmelz *et al.* 1996; Phillips *et al.* 1997). The results have been somewhat controversial due to differences in the Fe XVII ionization balance calculations used and due to disagreement about the importance of resonance scattering in the Fe XVII 15.01 Å line.

In general, X-ray abundance studies employ strong emission lines of relatively simple ions. The collisional excitation rates for these transitions should be accurate to about 20% or better. Phillips and Feldman (1997) have investigated the analysis of abundances, ionization state and temperature based on S, Ca and Fe K line measurements from YOHKOH. They find consistency at the 50% level.

2.3.2. UV Observations

An extensive series of papers has explored the FIP effect in a wide variety of coronal structures based on the relative intensities of the Mg VI and Ne VI multiplets near 400 Å (e.g., Widing and Feldman 1989; Sheeley 1996). The lines are formed at the same temperature in coronal equilibrium (about 2×10^5 K), and their wavelengths are so close that instrumental sensitivity can be safely assumed to be the same for the two sets of lines. Order of magnitude variations in the line ratios, and by inference the relative abundances of Mg and Ne, were reported. Though there was initially skepticism about abundances derived from a single pair of ions, density effects and departures from ionization equilibrium seem unable to account for the large line ratio variations observed (Jordan *et al.* 1997). In general unipolar field regions were FIP-enhanced, while small bipolar regions were not. It seems plausible that impulsive events lift chromospheric material more or less unchanged, while fractionation over a longer time scale enhances the low-FIP elements in large scale features. Spicer *et al.* (1998) used Mg VI and Ne VI to investigate the FIP effect in prominences. They found intermediate FIP enhancements between the photospheric and coronal abundance sets.

Young and Mason (1997) have extended the Ne:Mg study by observing a set of two ions of Ne and three ions of Mg with the CDS instrument on SOHO, along with an O IV density-sensitive line ratio to help compensate for density dependence of the Ne and Mg line intensities. The range of ions eliminates the possibility that a shift in ionization state might give a spurious abundance, and it provides consistency checks on the atomic rates. Young and Mason found that the Ne:Mg ratio within the active region they observed depends upon the type of the feature observed. The “spike” feature which they identified as a larger, older magnetic loop showed an Mg/Ne enhancement as large as a factor of 9, while the apparently younger, newly emerged loops showed a photospheric abundance ratio.

Coronal abundance studies have also been performed with the SUMER spectrometer on SOHO. Doschek *et al.* (1998) compared the FIP-sensitive ratios of silicon and magnesium to neon in coronal holes and the quiet Sun. They observed lines from two ions of Ne, four ions of Mg and two ions of Si to avoid ionization balance uncertainties, but atomic rate uncertainties and radiometric calibration uncertainties limited the analysis to a factor of 2 accuracy, close to the strength of the effect being sought. Doschek *et al.* showed that the apparent factor of 2 FIP bias in coronal hole interplume regions is probably real. No difference was observed between coronal hole and quiet Sun abundances. The ions observed are formed over the 5×10^5 to 1.5×10^6 K range, so the abundances pertain to the upper transition

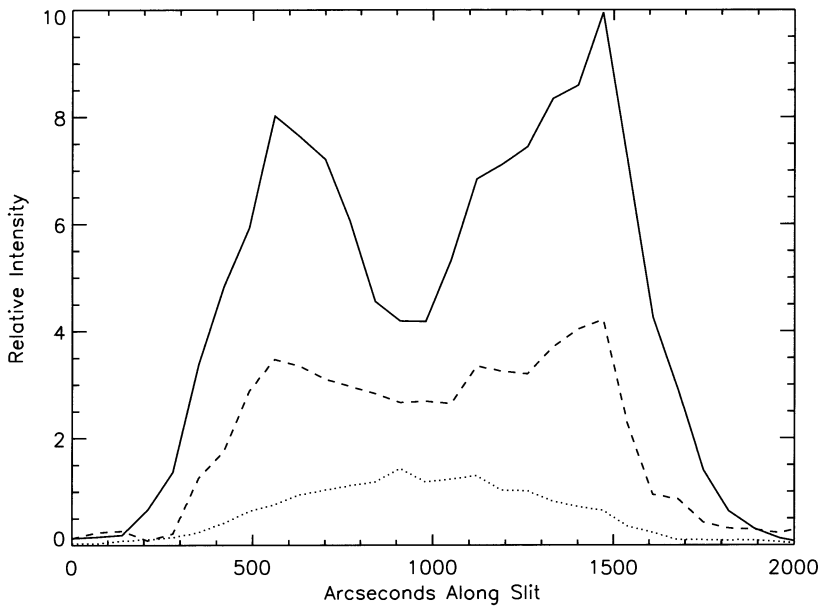


Figure 1. Relative intensities of O VI λ 1032 (solid line), Si XII λ 499 (dashed line) and Ly β (dotted line) along the UVCS spectrograph slit for the equatorial streamer observed in July 1996. While Ly β peaks near the center of the streamer, the other lines peak near the streamer edges.

region and corona. On the other hand, a set of SUMER observations $22''$ above the limb in a coronal hole analyzed by Feldman *et al.* (1998) showed no FIP effect at all.

At greater heights, the UVCS instrument on SOHO has obtained abundances in coronal streamers. Because the UVCS spectral range includes several of the H I Lyman lines, and because the coronagraph effectively rejects stray light from the solar disk (Kohl *et al.* 1996), it is possible to obtain absolute abundances. Raymond *et al.* (1997) analyzed an equatorial streamer observed in July 1996, while the sun was still at solar minimum. At $1.5 R_{\odot}$ the line intensities show the surprising behavior shown in Figure 1. While the H I Lyman line intensities peak at the streamer center (along with the white light brightness, as reported by Gibson *et al.* 1998 for the same streamer one solar rotation later), the line intensities of the other elements peak at the edges of the streamer. Both high and low ionization states (e.g., Si XII and O VI are shown in the figure) behave in this manner, so it is not a result of variation in ionization state. Doppler dimming studies show that the outflow speed is small, and variation in the relative importance of collisional excitation and radiative scattering cannot account for the different behavior. Thus substantially different abundances in the center and legs of the streamer are required (Noci *et al.* 1997).

Table I.
Elemental Abundance Estimates

| Element | Photosphere | Corona | Center | Leg | Active |
|---------|-------------|--------|-------------|-------------|-------------|
| H | 12.00 | 12.00 | 12.00 | 12.00 | 12.00 |
| He | 10.99 | 11.00 | ≤ 10.7 | ≤ 11.0 | ≤ 11.1 |
| N | 8.00 | 7.59 | ≤ 7.40 | ≤ 7.60 | ≤ 7.60 |
| O | 8.93 | 8.39 | 7.80 | 8.40 | 8.50 |
| Ne | 8.11 | 7.54 | ≤ 8.4 | ≤ 8.6 | ≤ 8.6 |
| Mg | 7.58 | 7.57 | 7.1 | 7.4 | 7.7 |
| Al | 6.47 | 6.44 | 5.7 | 5.9 | 6.3 |
| Si | 7.55 | 7.59 | 6.7 | 7.1 | 7.5 |
| S | 7.21 | 6.94 | 6.2 | 6.6 | 6.6 |
| Ar | 6.65 | 6.33 | — | 6.1 | 6.2 |
| Ca | 6.36 | 6.47 | — | 6.1 | 6.2 |
| Fe | 7.51 | 7.57 | 7.0 | 7.5 | 7.4 |
| Ni | 6.25 | 6.33 | — | — | 6.3 |

Analysis of the line intensities from the UVCS spectra yields the abundances listed in Table I. The photospheric and coronal abundances from Feldman's (1992) compilation are given for comparison. Spectra were extracted for the 500'' near the streamer center where the O VI intensity is lowest ("Center"), for the brighter of the two O VI peaks ("Leg") and for a complex set of streamers on the other limb of the Sun above a pair of active regions to the north and south of the solar equator ("Active"). It is apparent from the table that a factor of 3 FIP bias is present in all three spectra. What is surprising is the sense of the FIP bias. Instead of an enhancement of the low-FIP elements with respect to the photosphere, the high-FIP elements are depleted by a factor of 3 in the Leg and Active spectra, and in the streamer core the low-FIP elements are down by a factor of 3 and the high-FIP elements are depleted by a factor of 10, a more extreme value than is generally encountered even in the slow solar wind. A plausible explanation for these observations is that the FIP bias is imposed at the chromospheric level for both streamer legs and streamer core. Because the streamer is so quiescent (it remained largely unchanged for several solar rotations), gravitational settling reduces the abundances of the heavier elements in the streamer core. This is completely plausible if the streamer core is considered to be an arcade of closed magnetic loops. If the streamer core is open (Noci *et al.* 1997), material may be flowing out through the core and the low abundance in the streamer center may require a change in the drag due to variation of the ion-ion collision rate with changing density.

SUMER observations in the core of an equatorial streamer reconcile the depletions derived from UVCS at $1.5 R_{\odot}$ with the view that in general high-FIP elements are at normal abundance and low-FIP elements are enhanced (Feldman *et al.* 1998).

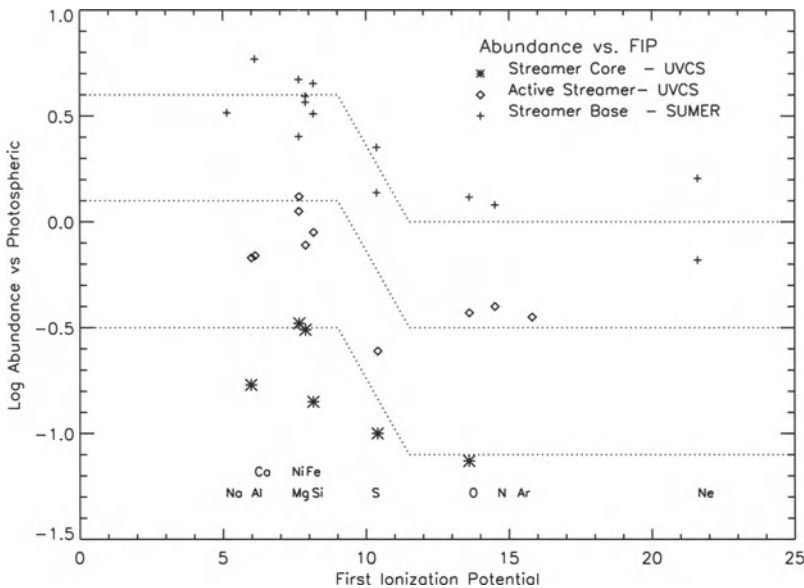


Figure 2. Elemental abundances plotted against First Ionization Potential from UVCS data (Streamer Core and Active Streamer; Raymond *et al.* 1997) and SUMER (Streamer Base; Feldman *et al.* 1998). The UVCS data were obtained at $1.5 R_{\odot}$ and the SUMER data pertain to heights below $1.03 R_{\odot}$. For comparison with the three sets of data, the dotted lines show for a FIP bias of 4 matched to the high-FIP elements for each data set.

Close to the surface, the SUMER spectra showed high-FIP abundances close to photospheric and low-FIP elements enhanced by a factor of 4. Emission lines of different elements declined at different rates with height above the limb, however, with Fe lines dropping more quickly than lines of other elements. This confirms the gravitational settling interpretation of the UVCS data. Figure 2 shows the UVCS abundances obtained for a streamer core and an active region streamer, along with the SUMER abundances for the base of an equatorial streamer.

Few abundance measurements are available so far for CMEs near the Sun. UVCS observations of prominence ejecta in the 11 December 1997 event include lines of Si III, C III, N V, S V] and O VI (Ciaravella *et al.* 1998). Most of the observed lines arise from high-FIP ions, making study of the FIP effect difficult, but the Si/C and S/O ratios appear consistent with photospheric values.

The uncertainties in the abundances derived from UV spectra of the corona include uncertainties in (1) collisional excitation rates, (2) radiometric calibration, (3) the separation of stray light and scattering contributions to the line intensities, and (4) the ionization state of the plasma. Uncertainties in excitation rates of the lines generally used should be in the 10%–30% range. Both SUMER and UVCS were carefully calibrated in the laboratory and their radiometric calibration has been

monitored with observations of stars above 912 Å. Thus the uncertainties should be no more than 15% at long wavelengths. At shorter wavelengths it is less clear what uncertainty to assign, but cross calibration of the UVCS instruments will provide an estimate. Stray light levels should be quite small for SUMER spectra close to the limb and for the UVCS spectra discussed above. For SUMER spectra at larger heights and for UVCS offset pointings (below $1.4 R_{\odot}$) corrections must be made based on the apparent intensities of lines from the chromosphere. Separation of collisional and radiative scattering contributions of the H I Lyman lines and the O VI doublet is straightforward. For instance, the O VI doublet intensity ratio is 2:1 for the collisional component and 4:1 for disk photons scattered by O VI ions in the corona (provided the outflow speed is small). Some uncertainty may arise from the details of the chromospheric Ly α and Ly β profiles and the relative radiometric calibration at these wavelengths. Perhaps the largest worry is the ionization state of the plasma, as the abundances shown in Figure 2 are derived from one or two ions of each element. While all three data sets shown indicated remarkably isothermal gas along the line of sight, it is likely that ionization balance uncertainties dominate the error. The scatter in abundances at a single FIP for a given data set in Figure 2 could be real (for instance First Ionization Time rather First Ionization Potential would shift points along the x axis, and mass segregation could shift some elements relative to others in the y direction), but discrepancies such as different abundances of an element derived for different ions suggest that this is the current level of uncertainty in the atomic rates and intensity measurements.

3. Theoretical Models

A number of theories have been put forward to explain the FIP effect. All these models rely upon the differing behavior of ions and neutrals in the part of the chromosphere where low-FIP elements are ionized and high-FIP elements are neutral. Some models are based purely on diffusion in a region of strong gradients in temperature, density and ionization state, while other models employ electric or magnetic fields to separate ions from neutrals.

The diffusion models generally treat the heavy elements as test particles in a static or rising hydrogen plasma. Early models produced very strong abundance anomalies (Shine, Gerola and Linsky 1975; Roussel-Dupre 1981). Recent models impose flows of a few hundred meters per second in the chromosphere and produce stronger FIP enhancements in slower flows, reminiscent of the difference between fast and slow solar wind (Peter 1996, 1998) or assume that transient heating evaporates chromospheric material (Wang 1996). In these models the First Ionization Time, rather than First Ionization Potential, is the crucial parameter, in harmony with the measured abundance patterns. A potential difficulty with such steady-flow models is that flux conservation should force the coronal abundances to be the same as those at the lower boundary (McKenzie, Sukhorukova and Axford 1998).

If the diffusion zone is at the bottom of a closed magnetic loop, the FIP bias may increase over the course of time (Zurbuchen *et al.* 1998; Schwadron, Fisk and Zurbuchen 1999). This picture fits in with the observed tendency for the FIP effect to be stronger in older magnetic structures (e.g., Young and Mason 1997). The FIP-enhanced material enters the slow solar wind when reconnection opens the magnetic loops. Thus Schwadron, Fisk and Zurbuchen (1999) propose that wave heating of the ions gives low FIP elements larger scale heights, and that material trapped in magnetic loops develops a FIP bias on a gravitational settling time scale of order a day.

An example of a model based on magnetic separation is the von Steiger and Geiss (1989) model, in which material flows up along a magnetic flux tube. Ions are closely confined by the magnetic field, but neutrals diffuse across field lines and fall out of the flow. The angle of the flux tube from vertical is an important parameter for the strength of the FIP enhancement. Vauclair and Meyer (1985) studied FIP fractionation in a model in which predominantly horizontal magnetic field rises through the chromosphere, lifting ions more efficiently and leaving some neutrals behind. Henoux and Somov (1992) present a model in which twisting of a vertical, diverging flux tube produces vertical currents that lift the ions. A promising model has recently been presented by Arge and Mullan (1998). They use a 2D two-fluid MHD numerical simulation of a magnetic interaction region—a region where opposing magnetic fields are pressed together as in magnetic reconnection models, but without the rapid reconnection and heating sought in flare models. If the magnetic interaction occurs in the chromosphere, it can concentrate ions (low FIP elements) in the field reversal region, and this material could be subsequently ejected by magnetic forces or thermal pressure.

At present it is difficult to choose among the theoretical models for the FIP effect, or even to be certain that one among them captures all the dominant physical processes. The common theme of the loss of efficient collisional coupling in a region of partial ionization must be correct, and all the models can produce a reasonably strong FIP effect. However, all the models have one or more free parameters that are adjusted to match the observed enhancements. Some potential difficulties that FIP effect models must address include

1. Self-consistent models show that protons diffuse downward on average in a static chromosphere-transition region (Fontenla, Avrett and Loeser 1990); this would drive the FIP bias in the wrong direction.
2. The steady chromosphere assumed in many models may not exist, and shocks in a cooler atmosphere provide the UV emission previously attributed to the upper chromosphere (Wikstol *et al.* 1997).
3. The mass circulation associated with spicules is 100 times larger than the net outflows assumed in the diffusion models (Athey 1976).
4. Little is known about the actual magnetic structure and dynamics at small scales in the chromosphere.

The theoretical picture of gravitational settling high in the corona is also unsettling. This may be a result of the smaller number of models put forward so far. The gravitational settling time for streamer material at $1.5 R_{\odot}$ is about a day, and the thermal scale height for the heavier elements is so small that species such as iron ought to be depleted by orders of magnitude. Thus either there is a mechanism that mixes fresh material into the streamer with a time scale of order a few days, or there is non-thermal support available for the ions. It is easy to imagine that material flows along magnetic flux tubes, or that reconnection mixes material into the streamer core from along its edges. However, a natural mechanism for supporting the ions in a static or slowly rising flow is readily available, in that non-thermal line widths of order 30 km/s are typical of the low corona (e.g., Mariska *et al.* 1979). At larger heights, lines such as O VI and Mg X reach velocity widths comparable to the widths of the Lyman lines by heights of 4 or 5 R_{\odot} in streamers (Kohl *et al.* 1997). Lenz, Lou and Rosner (1998) have constructed models of closed magnetic loops including diffusion and a self-consistent treatment of the electric field. They find that elements of differing mass settle in a manner consistent with the SOHO observations for loops of order 10^9 cm in length, but the abundances of heavy elements are far too small for 10^{10} cm loops compared with SOHO observations. Models incorporating wave-particle interactions, constrained by the observed line widths, are badly needed, along the lines of the models being developed for coronal holes (Cranmer *et al.* 1999). More detailed observations will be needed to test the model, and in particular to examine the physics of wave-particle interaction assumed in these calculations and in models of the fast solar wind. As pointed out by Zurbuchen *et al.* (1998) and Schwadron, Fisk and Zurbuchen (1999) the FIP bias and gravitational settling may be intertwined.

This work was supported by NASA Grant NAG5-3192 to the Smithsonian Astrophysical Observatory. It has benefited from useful comments by T. Zurbuchen, A. van Ballegooijen and R. Frazin.

References

- Aellig, M. R., Hefti, S., Grünwaldt, H., Bochsler, P., Wurz, P., Ipavich, F. M., and Hovestadt, D.: 1998, *JGR*, submitted.
- Anders, E., and Grevesse, N.: 1989, *N. Geochim. Cosmochim. Acta*, **53**, 197.
- Arge, C. N., and Mullan, D. J.: 1998, *Solar Physics*, **182**, 293.
- Athay, R. G.: 1976, in *The Solar Chromosphere and Corona: Quiet Sun*, ed. C. J. Macris (Dordrecht: Reidel), p. 36.
- Boyarchuk, A. A., Antipova, L. I., Boyarchuk, M. E., and Savanov, I. S.: 1998, *Astronomy Reports*, **42**, 517.
- Ciaravella, A., *et al.*: 1998, in preparation.
- Cranmer, S. R., Field, G. B., and Kohl, J. L.: 1999, this volume.
- Doschek, G. A., Laming, J. M., Feldman, U., Wilhelm, K., Lemaire, P., Schüle, U., and Hassler, D. M.: 1998, *ApJ*, **504**, 573.
- Feldman, U.: 1992, *Phys. Script.*, **46**, 202.
- Feldman, U., Schüle, E., Widing, K. G., and Laming, J. M.: 1998, *ApJ*, **505**, 999.

- Fludra, A., and Schmelz, J. T.: 1995, *ApJ*, **227**, 936.
- Fontenla, J. M., Avrett, E. A., and Loeser, R.: 1990, *ApJ*, **355**, 700.
- Galvin, A. B.: 1997, in *Coronal Mass Ejections*, N. Crooker, J. A. Joselyn and J. Feynmann, eds. (Washington: AGU), p. 253.
- Geiss, J. *et al.*: 1995, *Science*, **268**, 1033.
- Gibson, S. E., Fludra, A., Bagenal, F., Biesecker, D., Del Zanna, G., and Bromage, B.: 1998, preprint.
- Henoux, J. C.: 1995, *Adv. Sp. Res.*, **15**, No. 7, 23.
- Henoux, J. C., and Somov, B. V.: 1992, in Proceedings of the First SOHO Workshop, ESA SP-348, p. 325.
- Ipavich, F. M., Galvin, A. B., Geiss, J., Ogilvie, K. W., and Gliem, F.: 1992, in *Solar Wind Seven, COSPAR Colloquium Series*, 3, E. Marsch and R. Schwenn, eds., p. 369.
- Jordan, C., Doschek, G. A., Drake, J. J., Galvin, A., and Raymond, J. C.: 1997, *Tenth Cambridge Workshop on Cool Stars, Stellar Systems and the Sun*, R. Donahue and J. Bookbinder, eds., p. 91.
- Kohl, J. L., *et al.*: 1996, *Solar Physics*, **162**, 313.
- Kohl, J. L., *et al.*: 1997, *Solar Physics*, **175**, 613.
- Kurucz, R. L.: 1995, *ApJ*, **452**, 102.
- Lenz, D. D., Lou, Y.-Q., and Rosner, R.: 1998, *ApJ*, **504**, 1020.
- Li, J., Raymond, J. C., Acton, L. W., Kohl, J. L., Romoli, M., Noci, G., and Naletto, G.: 1998, *ApJ*, **506**, 431.
- Mariska, J. T., Feldman, U., and Doschek, G. A.: 1979, *A&A*, **73**, 361.
- McKenzie, J. F., Sukhorukova, G. V., and Axford, W. I.: 1998, *A&A*, **332**, 367.
- Meyer, J.-P.: 1985, *ApJ Suppl.*, **57**, 173.
- Noci, G., *et al.*: 1997, *Adv. Sp. Res.*, **20**, 2219.
- Peter, H.: 1996, *A&A*, **312**, L37.
- Peter, H.: 1998, *A&A*, **335**, 691.
- Phillips, K. J. H., and Feldman, U.: 1997, *ApJ*, **477**, 502.
- Phillips, K. J. H., Pike, C. D., Lang, J., Watanabe, T., and Takahashi, M.: 1994, *ApJ*, **435**, 888.
- Phillips, K. J. H., Greer, C. J., Bhatia, A. K., Coffey, I. H., Barnsley, R., and Keenan, F. P.: 1997, *A&A*, **324**, 381.
- Raymond, J. C., *et al.*: 1997, *Solar Physics*, **175**, 645.
- Reames, D. V.: 1990, *ApJ Suppl.*, **73**, 235.
- Reames, D. V.: 1992, in *Proceedings of the First SOHO Workshop*, ESA SP-348, p. 315.
- Roussel-Dupre, R.: 1981, *ApJ*, **250**, 408.
- Saba, J.: 1995, *Adv. Sp. Res.*, **15** no. 7, 13.
- Schmelz, J. T., Saba, J. L. R., Ghosh, D., and Strong, K. T.: 1996, *ApJ*, **473**, 519.
- Schwadron, N. A., Fisk, L. A., and Zurbuchen, T. H.: 1999, preprint.
- Sheeley, N. R., Jr., *et al.*: 1997, *ApJ*, **484**, 472.
- Shine, R., Gerola, H., and Linsky, J. L.: 1975, *ApJL*, **202**, 101.
- Spicer, D. S., Feldman, U., Widing, K. G., and Rilee, M.: 1998, *ApJ*, **494**, 450.
- Sylwester, J., Lemen, J. R., and Mewe, R.: 1984, *Nature*, **310**, 665.
- Sylwester, J., Lemen, J. R., Bentley, R. D., Fludra, A., and Zolcinski, M.-C.: 1998, *ApJ*, **501**, 397.
- Vauclair, S., and Meyer, J.-P.: 1985 in *Proc. 19th Int. Cosmic Ray Conf.*, p. 233.
- von Steiger, R., and Geiss, J.: 1989, *A&A*, **225**, 222.
- von Steiger, R., Wimmer-Schweingruber, R. F., Geiss, J., and Gloeckler, G.: 1995, *Adv. Sp. Res.*, **15**, 3.
- Wang, Y.-M.: 1996, *ApJ*, **464**, L91.
- Widing, K. G., and Feldman, U.: 1989, *ApJ*, **334**, 1046.
- Wikstol, O., Judge, P. G., and Hansteen, V.: 1997, *ApJ*, **483**, 972.
- Wurz, P., *et al.*: 1998, *GRL*, **25**, 2557.
- Young, P. R., and Mason, H. E.: 1997, *Solar Physics*, **175**, 523.
- Zurbuchen, T. Z., Fisk, L. A., Gloeckler, G., and Schwadron, N.A.: 1998, *Space Science Reviews*, **85**, 397.

WORKING GROUP 1 REPORT: SOLAR WIND MODELS FROM THE SUN TO 1 AU: CONSTRAINTS BY “IN SITU” AND REMOTE SENSING MEASUREMENTS

E. LEER

*Institute of Theoretical Astrophysics, University of Oslo, PO Box 1029, N-0316 Oslo, Norway,
egil.leer@astro.uio.no*

E. MARSCH

Max Planck Institut für Aeronomie, 37191 Katlenburg-Lindau, Germany, marsch@linmpi.mpg.de

1. Summary

The goal of Working Group 1 was to discuss constraints on solar wind models. The topics for discussion, outlined by Eckart Marsch in his introduction, were: (1) what heats the corona, (2) what is the role of waves, (3) what determines the solar wind mass flux, (4) can stationary, multi-fluid models describe the fast and slow solar wind, or (5) do we need time dependent fluid models, kinetic models, and/or MHD models to describe solar wind acceleration.

The discussion in the working group focused on observations of “temperatures” in the corona, mainly in coronal holes, and whether the observations of line broadening should be interpreted as thermal broadening or wave broadening. Observations of the coronal electron density and the flow speed in coronal holes were also discussed. There was only one contribution on observations of the distant solar wind, but we can place firm constraints on the solar wind particle fluxes and asymptotic flow speeds from observations with Ulysses and other spacecraft. Theoretical work on multi-fluid models, higher-order moment fluid models, and MHD models of the solar wind were also presented.

2. The Coronal Temperature

2.1. THE ELECTRON TEMPERATURE

The electron temperature in coronal holes seems to be quite low. F. Chiuderi Drago reported on observations of an equatorial coronal hole, observed around the central meridian transit on 19 October 1996, with the EIT and CDS instruments and with the radio-heliograph at Nancay, France. The observed radio brightness temperatures observed at the four frequencies, 164, 236, 327, and 408 MHz, were compared to the radio brightness temperatures computed for different transition region/corona models. The best agreement between the observed and calculated brightness was found for a coronal temperature around 9×10^5 K.

Low coronal hole electron temperatures were also reported by Fludra *et al.* On the basis of weekly observations of the North and South polar coronal holes with



CDS/SOHO, they found that the electron temperature increases from 7.5×10^5 K at the limb to 9.0×10^5 K at $r = 1.2R_s$.

These results support earlier findings that the electron temperature in coronal holes is around a million degrees or so. With such low electron temperatures we can conclude that the coronal electron pressure is rather low, and the polarization electric field cannot play an important role in accelerating the solar wind.

2.2. THE PROTON TEMPERATURE

In contrast to the low coronal hole electron temperatures, the proton temperatures deduced from the UVCS/SOHO observations of the 1216 Å Ly α line in coronal holes are quite high. J. Kohl reported on observations of the width and intensity of the Ly α line in both the North and South hole during a 5 month period from November 1996 to April 1997. The width of the line corresponds to a random motion perpendicular to the magnetic field that increases from 190 km s^{-1} at $r = 1.5R_s$ to 250 km s^{-1} at $r \approx 3.0R_s$. These velocities are in good agreement with the values found by Antonucci *et al.* on the basis of UVCS observations from 21 May 1996. Antonucci placed an upper limit of 160 km s^{-1} on the amplitude of waves (with wave motion perpendicular to the magnetic field) that may be present in the corona.

Observations of the width of the Ly α line in coronal holes were also discussed by Suleiman *et al.* By increasing the time of integration they were able to measure the line width in the solar wind acceleration region with a better accuracy than Kohl *et al.* (1998). Their observations show that the line width increases out to $r = 2.8R_s$, where it reaches a maximum. Beyond $r \approx 2.8R_s$ the line width decreases. The azimuthal velocity, deduced from the observed line-width, is reduced from 210 km s^{-1} at $r = 2.8R_s$ to 110 km s^{-1} at $r = 5.0R_s$. This is close to the r^{-1} dependence we find if we assume that the neutral hydrogen atoms conserve their angular momentum in $r > 2.8R_s$.

In order to drive high speed wind a significant fraction of the energy flux must be deposited in the supersonic region of the flow. Alfvén waves are very well suited for energy transport through the inner corona. These waves propagate with a speed of 1000 km s^{-1} or more, so they can transport a significant energy flux into the solar wind even when the velocity amplitude is relatively small. However, the wave velocity amplitude derived by Antonucci *et al.*, $\delta u \leq 160 \text{ km s}^{-1}$, may be too low to drive solar wind with the mass flux and flow speed measured in high speed wind. But a velocity amplitude of say $\delta u \geq 200 \text{ km s}^{-1}$, should be sufficient to drive the wind. If the width of the Ly α line, measured in coronal holes, is interpreted as thermal motion rather than a wave amplitude, it is difficult to drive high speed wind.

Kohl emphasized that there may be significant differences between the plume and inter-plume regions, and that the high density, low “temperature” plume regions may contribute significantly to the Ly α line profile in coronal holes. Therefore, the

out-flowing plasma may have a higher “temperature” and lower density than the values deduced from remote sensing observations of large coronal holes. It was mentioned that the UVCS/Spartan observations were interpreted as the sum of a “cold” and a “hot” component (Kohl *et al.* 1996).

3. Electron Density Profiles and Flow Speed

M. Guhathakurta presented observations of the electron density using LASCO/SOHO, CDS/SOHO, Mark III/Spartan, and *in situ* Ulysses observations. These observations are combined with magnetic field observations to construct a 2D semi-empirical MHD model of the corona/solar wind system. The model gives fast and slow solar wind. In coronal holes the electron density decreases rapidly in the inner corona, starting from a density around $n_e = 2 \times 10^{14} \text{ m}^{-3}$. The flow speed profile shows a rapid acceleration close to the sun: The flow reaches 300 km s^{-1} at $r = 2R_s$. The rapid acceleration of the solar wind, close to the sun, in large coronal holes seems to be a general trend in recent studies. From a theoretical point of view it is not easy to construct self-consistent models of the corona/solar wind system with electron densities as high as 10^{14} m^{-3} at $T = 10^6 \text{ K}$ with a mass flux and an asymptotic flow speed that are observed in quasi-static high speed streams.

The Mark III/Spartan observations, in $1.16R_s < r < 5R_s$, are crucial for deducing the density profile and for deriving the flow speed in this study. If there are significant differences between plume and inter-plume regions one may consider trying to apply a tomography technique to derive (variations in) the electron density.

Such a technique was used by M. Kojima when analyzing Inter-Planetary Scintillation (IPS) observations to obtain the solar wind flow speed. Kojima presented IPS observations during the Ulysses years, and showed that there is quite good agreement between the flow speeds obtained from the IPS observations and the asymptotic solar wind speed measured with Ulysses. With the IPS method one can also find the solar wind over the poles of the sun. Both Ulysses and the IPS observations give an asymptotic flow speed that increases with increasing latitude, and during 1996 the asymptotic speed was higher in the Northern than in the Southern hemisphere.

Karovska presented a study of “polar jets,” using LASCO/SOHO pictures taken every 10 minutes over 40 hours. Three jets were observed. The initial velocity is around 500 km s^{-1} , and the speed decreases with height. These jets are rather strong density enhancements; they are narrower than the plumes.

4. Theoretical Models

Most model studies of the solar wind are based on a five moment fluid model; density, velocity (3 components), and temperature. The heat flux is a function of these quantities, and in a collision dominated flow it is determined by the temperature and the temperature gradient. The solar wind electrons may be described as a

collision dominated gas (cf. Lie-Svendsen *et al.* 1997), but the protons may become collisionless already in the corona. In models with significant proton heating the proton heat flux is an important quantity. In higher-order fluid models one solves for the heat flux, along with the density, flow speed, and temperature.

4.1. HIGHER-ORDER FLUID MODELS

The eight-moment model (density, flow velocity [3 components], temperature, and heat flux density [3 components]) velocity distribution function is taken to be close to a Maxwellian. Olsen and Leer (1996) used this model to study the solar wind acceleration region, and found that the proton heat flux deviates from a “classical” value in coronal holes.

The eight-moment model does not allow for temperature anisotropies. In the region where collisions are not frequent such anisotropies will develop, and a set of fluid equations based on a distribution function that is close to a bi-Maxwellian, may be more reasonable. This set of equations reduces to the gyro-tropic transport equations in the limit of a very large background magnetic field (cf. Burgers 1969; Demars and Schunk 1979; Gombosi and Nagy 1988).

Leer presented a study (by Olsen and Leer) of the solar wind acceleration region, from the very inner corona, $r = 1R_s$, and out to $r = 20R_s$, based on the gyro-tropic equations. It was shown that ion-cyclotron heating of protons close to the sun results in a large perpendicular proton temperature locally, but the collisionless proton distribution function is cooled perpendicular to the field and “heated” along the field as the gas expands outwards. In the outer corona the parallel temperature is higher than the perpendicular temperature. Such a proton distribution function is not consistent with the Ly α observations by Kohl *et al.* (1998). They find that the perpendicular proton temperature is higher than the parallel temperature. If one allows for a significant Alfvén wave energy flux, and a gradual transfer of wave energy into the the flow, the solar wind can be accelerated to high flow speeds without having the high parallel proton temperature.

Li presented a study of a gyro-tropic fluid model of the solar wind extending from the inner corona and out to the orbit of Earth. A spiraling background magnetic field was taken into account. By adding energy to the flow in the form of “heat” and as direct acceleration he showed that one can construct models that describe the solar wind quite well.

The gyro-tropic fluid model can be derived from a 16-moment fluid model in the limit of very large background magnetic field. The 16-moment model then reduces to a 6-moment description: density, flow speed, temperatures parallel and perpendicular to the magnetic field, and flux of parallel and perpendicular thermal motion along the field. One does not make any assumptions about the heat flux; the heat fluxes are treated on an equal footing with the other flow parameters. In this description the velocity distribution function is assumed to be a specified function of these six parameters. One can therefore use the solution to construct

the distribution function. This type of model seems to describe, quite well, both the collision dominated protons in the very inner corona and the collisionless protons in the solar wind.

The proton heat flux is an important parameter in models with significant coronal proton heating. It may determine the temperature structure of the corona and therefore also the density structure, and the heat flux into the transition region.

Li also reported work on traditional solar wind models with different coronal heating processes. In the corona the proton heat flux is taken to be proportional to the temperature gradient, whereas in the solar wind it is smaller than the classical value. Low frequency Alfvén waves are assumed to carry most of the energy flux needed to accelerate the solar wind, and nonlinear cascade processes are used to transport energy to the ion cyclotron part of the spectrum. The interaction of these waves with the protons, and their effects on the proton anisotropy, were studied.

The evolution of the proton distribution function in the corona may give information about the proton heating process. As protons and neutral hydrogen are coupled, at least out to $r = 2\text{--}3 R_s$, it is of great interest to determine the temperature anisotropy of neutral hydrogen. The width of the Ly α line provides information about the temperature across the magnetic field, whereas the Doppler dimming of the line provides information about the temperature along the field.

There was some debate on how well the temperature anisotropy in the proton gas can be determined. As the proton anisotropy may provide information about the coronal heating process, and place constraints on models, this point requires attention from the observers.

The theorists should focus on the coupling of neutral hydrogen atoms to the background electron-proton flow. Model calculations indicate that neutrals “follow” the protons, reasonably well, out to $r = 5R_s$ (Allen *et al.* 1998) whereas Suleiman’s observations indicate that there may be no interaction between neutrals and protons beyond $r \approx 2.8R_s$.

4.2. MHD MODELS

L. Ofman presented studies of one-fluid and two-fluid MHD models of electron-proton solar wind in coronal holes (cf. Ofman and Davila 1998). In these models the initial electron density and the electron and proton temperature are specified at the coronal base. A spectrum of Alfvén waves is also specified. The Alfvén waves are the main source of energy for the solar wind. The waves suffer Ohmic dissipation, and the Alfvén waves also generate acoustic waves that steepen and transfer energy as heat. (In the two-fluid model only the electron gas is heated by Ohmic dissipation.)

The wave fluctuations along the line of sight, in these models, are comparable to the velocity fluctuations observed with UVCS/SOHO. The density fluctuations at $r = 2\text{--}3 R_s$ are some 20–30%. The effect of the waves on the background flow depends on the wave frequency.

These MHD models are well suited to study the force and energy balance in the coronal plasma. In order to draw conclusions about the solar wind one must also impose reasonable boundary conditions. The choice of electron density at the coronal base (i.e., of coronal base pressure) plays a role in determining how much of the energy flux deposited in the corona is lost as gravitational and as kinetic solar wind energy flux. In MHD models the lateral variation of the electron density at the base is consistent with the variations of the field strength, but the absolute value of the electron density is so important that it must be chosen very carefully.

Ofman's models focus on the outflow from large coronal holes, whereas the model studies presented by R. Dahlburg deal with streamers and current sheaths. In an MHD model with very low speed in the current sheath and fast wind on the outside, the fast wind transfers momentum to the slow wind, breaks up the current sheath, and accelerates the plasma in the sheath to flow speeds characteristic of slow solar wind.

P. Liewer presented studies of "hybrid" solar wind where the electrons are treated as a fluid. The particle motion of ions is described in the code, and the propagation of Alfvén waves/ion cyclotron waves and their interaction with the ions are studied.

W. Matthaeus discussed the MHD fluctuations in the solar wind and whether we can learn about the coronal spectrum from these observations. He also discussed the energy transfer from fluctuations with wave-normal along the magnetic field to wave-normal across the field, and how energy may be transferred to the coronal plasma.

The presentations of Liewer and Matthaeus deal with the "coronal heating problem." In both of these studies the focus is on proton/ion heating. Observations of the Ly α line may give some information about the heating of protons, but lines from heavy ions may also be used to study coronal heating.

5. Minor Ions

Helium may be so abundant in the corona that it can affect the force and energy balance of the flow, but minor elements like oxygen, magnesium, silicon, and iron are so few that they can only act as "tracers." Observations of the O VI lines at 1032 and 1037.6 Å are an important part of the UVCS/SOHO effort, and Kohl reported on observations of large perpendicular O VI temperatures, and rather small parallel temperatures (cf. Kohl *et al.* 1998). The perpendicular temperature can be deduced from the line profiles, and the pumping of the 1037.6 line by the C II lines at 1037 Å and 1036.3 Å allows for determination of the width of the O VI distribution function along the field as well as the flow speed of O VI. (A detailed description of these effects are given by Li *et al.* 1998.)

The evolution of the distribution function of a collisionless O VI gas in an expanding geometry leads to a focusing along the magnetic field. Pitch-angle scattering will reduce this focusing, but the perpendicular temperature will decrease with distance from the sun unless there is significant heating to balance the adiabatic

cooling. The observation of a steadily increasing perpendicular O VI temperature is consistent with a steady input of energy in the perpendicular direction as r increases. The outflow velocity of O VI also increases.

The increase of the perpendicular O VI temperature is more rapid than the increase of the Mg X temperature in the inner corona. If ion-cyclotron waves are heating the oxygen ions we would also expect a significant heating of Mg X since these two ions have gyro-frequencies that are so close that they should absorb in more or less the same part of the wave spectrum.

The observations of the O VI and Mg X ions may help us understand the heating of the corona. Some model calculations have been carried out to study the effects of ion-cyclotron waves on minor ions (e.g., Cranmer *et al.* 1999), but more theoretical work should go into studies of minor ions in reasonable background solar wind models where Alfvén waves (i.e., also ion cyclotron waves) are a significant energy source.

It should be pointed out that minor ions, in low density coronal holes, can lose energy only by escaping from the sun. Thus, there is no energy loss from the heavy ions before they reach quite high temperatures. Hence, a high ion temperature should not be taken as a “proof” of preferential heating of minor ions, (e.g., Hansteen *et al.* 1997), but the anomalously high temperature to mass ratio for O VI can be taken as an indication that the O VI ions are preferentially heated.

All ions participate in low frequency wave motion. The width of lines from ions, observed above the limb of the sun, can therefore be used to place an upper limit on the wave amplitude in the corona. Tu presented a study (cf. Tu *et al.* 1998) where they use SUMER/SOHO observations of UV lines from Mg X, Ne VIII, Mg VIII, Si VIII, and Fe XII to measure the temperature of these ions and place upper limits on the wave amplitude. The observations show that the temperature increases with increasing mass to charge ratio, and that the upper limit on the wave amplitude in the inner corona is around 35 km s^{-1} (at $r = 1.15R_s$).

6. The Solar Wind Mass Flux

One of the themes that Eckart Marsch suggested be discussed in Working Group 1 was the solar wind mass flux. This subject did not receive a lot of attention, but it was discussed in the joint session with Working Group 2. According to the Oslo group the solar wind mass flux is determined by the energy flux deposited in the corona. According to the Lindau group the mass flux is determined by ionization and recombination processes in the chromospheric network. Let us here present arguments for these different points of view. We start with Oslo/Leer:

6.1. CORONAL ENERGY INPUT AND THE SOLAR WIND MASS FLUX

In an open coronal region a significant fraction of the energy flux may be lost in the solar wind. We can write the energy balance in an expanding corona as

$$F_E = F + F_q + F_{SW} = \text{Constant} \quad (1)$$

where F is the energy flux from the sun. This energy flux is gradually transferred to the coronal plasma. F_q is the heat conductive flux (positive outwards), and F_{SW} is the solar wind energy flux. We introduce $(-\dot{M})$ for the solar wind mass flux and write the energy conservation equation as

$$F_0 = -F_{q0} + (-\dot{M})\left(\frac{GM_s}{r_0} + \frac{1}{2}u_\infty^2\right). \quad (2)$$

The energy flux from the Sun, F_0 , deposited in the corona, is lost as inward heat conductive flux, $-F_{q0}$, and as solar wind energy flux. The structure of the corona and the solar wind depend on the amplitude of the energy flux, F_0 , and where it is deposited. Heating very close to the sun leads to a large inward heat flux (and a large radiation loss from the lower transition region). Generally, we have that most of the energy flux deposited in the extended corona is lost in the solar wind, but there is a difference between electron and proton heating. Heating of the electrons leads to a larger inward heat flux, larger transition region pressure, lower coronal temperature, and a solar wind with relatively low asymptotic flow speed. In order to drive high speed solar wind streams most of the energy must be deposited in the proton (ion) gas in the extended corona. In these cases the inward heat flux is relatively small, and most of the energy flux is lost in the solar wind. The energy balance in a flow tube can be written as

$$f_0 = -f_{q,0} + f_{SW} \approx f_{SW} \quad (3)$$

where

$$f_{SW} = (\rho u)_0 \left(\frac{1}{2}u_\infty^2 + \frac{GM_s}{R_s} \right) \quad (4)$$

As the asymptotic flow speed is comparable to the escape speed for the sun,

$$\frac{1}{2}u_\infty^2 \approx \frac{GM_s}{R_s} \quad (5)$$

we find that the mass flux is approximately proportional to the energy flux deposited in the extended corona:

$$(\rho u)_0 \approx \frac{f_0 R_s}{2GM_s} \quad (6)$$

The energy per electron-proton pair required to produce the solar wind, $\epsilon \approx 2GM_s m_p / R_s$, is around 4000 eV. This is a factor 300 larger than the energy required to ionize hydrogen. Hence, the solar wind mass flux is determined by the coronal energy input rather than by ionization processes in the chromosphere. This result is supported by model studies where formation of the corona and acceleration

of the solar wind is treated as *one* problem (cf. Hansteen and Leer 1995; Hansteen *et al.* 1997).

6.2. IONIZATION PROCESSES IN THE NETWORK AND THE SOLAR WIND MASS FLUX

The view held by the Lindau group/Marsch is that the solar wind mass flux is determined by ionization and recombination processes in the network.

Peter and Marsch (1997) have developed a two-fluid model for neutral hydrogen and protons in the upper solar chromosphere and analyzed the ionization layer of hydrogen, which they found to be only a few 10 km thick. One main result of their model is that the proton flux in the distant solar wind and the flux of ionizing UV photons in the Ly α line and recombination continuum are essentially equal, given that some reasonable assumptions on the flux tube geometry of the plasma are made. The related area function is $A(r) = f(r)r^2$, and $f(r)$ describes the non-spherical expansion and contains the geometry of the magnetically open coronal funnels in which the fast solar wind plasma is believed to originate (cf. Axford and McKenzie 1997; Marsch and Tu 1997). Then the continuity equation gives the mass flux, $-\dot{M}$, along a given magnetic field line. The mass flux reads generally

$$-\dot{M} = \rho(r)V(r)A(r) = \int_{R_s}^{\infty} dr' A(r')q(r') \quad (7)$$

The plasma source function, $q(r)$, is left unspecified. It contains all the complexities of the ionization/recombination processes (cf. Hansteen *et al.* 1997) in the chromosphere, where the plasma is produced. In a steady state, whatever these processes are, the resulting mass flux is determined entirely within the thin ionization layer and does not depend upon coronal plasma conditions. McKenzie *et al.* (1998) came to a similar conclusion from their analysis of a pure photoionization layer in the solar chromosphere. They provided additional insight into the problem by analyzing their equations in the phase plane of the hydrogen density and photon flux and found that there is a unique critical solution linking the bottom to the top of the ionization layer. All these authors hold the opinion that the equation (1) should be interpreted differently. We write it in terms of u_{∞} such that

$$u_{\infty} = \sqrt{2F_E/(-\dot{M})} \quad (8)$$

This simple expression was derived and discussed by Leer and Holzer (1980). The total energy flux F_E in coronal holes, where inward heat conduction by cold electrons and radiative losses by dilute electrons are negligible, is essentially given by the energy flux F put in to heat the corona minus the gravitational binding energy of a proton to the Sun. The remaining energy is converted into terminal kinetic energy, and thus the corresponding speed u_{∞} is fully determined by the two flow-tube constants F_E and $-\dot{M}$.

7. Conclusion

Observations with UVCS and SUMER indicate that heavy ions are preferentially heated in the corona. As the temperature across the magnetic field is much larger than the temperature along the field, over quite some distance, we must conclude that there is significant perpendicular heating. Ion-cyclotron waves may be one possible heating mechanism, but one should also investigate other mechanisms that may transfer heat into the perpendicular direction.

The rather low electron temperatures in coronal holes indicate that there is more energy input into the protons than into electrons. We can therefore conclude that the electrons do not play an important role in the force and energy balance of the corona and of the solar wind; the coronal density scale height is determined by the proton temperature rather than the electron temperature, and the polarization electric field plays only a minor role in accelerating the solar wind. In the original work by Parker it is the electrons that supply the energy flux (through heat conduction) necessary to drive the outflow, and this energy flux is transferred to the protons via the electric field.

In order to describe the quasi-steady outflow from coronal holes we can use steady-state models. The electron gas can be described using “classical” hydrodynamic equations, but collisions are so infrequent among the solar wind protons that the fluid equations, describing collision-dominated gas, cannot be used. A kinetic description of the solar wind protons is quite an undertaking, but it seems that a gyro-tropic fluid description can be used to describe both the collision-dominated proton flow in the very inner corona and also the collisionless protons in the outer corona and in the solar wind.

It may be possible to give a fairly good description of high speed solar wind using “hydrodynamics.” The energy transport and transfer of energy to the gas can better be described using MHD equations, and such a description may be necessary to describe variable, low speed wind. For Coronal Mass Ejections the magnetic field plays such an important role that an MHD model must be used.

Acknowledgments

Egil Leer acknowledges support from the Norwegian Research Council under contract 121076/420 and from NASA grant W-18.786.

References

- Allen, L. A., S. R. Habbal, and Y. Q. Hu: 1998, Thermal coupling of protons and neutral hydrogen in the fast solar wind, *J. Geophys. Res.*, **103**, 6551.
- Axford, W. I., and J. F. McKenzie: 1997, The solar wind, in *Cosmic Winds and the Heliosphere*, edited by J. Jokipii, C. Sonett, and M. Giampapa, (Tucson, USA. Arizona University Press), 31.
- Burgers, J.: 1969, *Flow Equations for Composite Gasses*, (Academic Press Inc., New York).

- Cranmer, S., G. Field, and J. Kohl: 1999, Spectroscopic constraints on models of ion-cyclotron resonance heating in the polar solar corona and high speed solar wind, *Astrophys. J.*, **518**, in press (20 June 1999).
- Demars, H., and R. Schunk: 1979, Transport equations for multispecies plasmas based on individual bi-Maxwellian distributions, *J. Phys. D: Appl. Phys.*, **12**, 1051.
- Gombosi, T., and A. Nagy: 1988, Time-dependent polar wind modeling, *Adv. Space Res.*, **8**, 59.
- Hansteen, V. H., and E. Leer: 1995, Coronal heating, densities, and temperatures and solar wind acceleration, *J. Geophys. Res.*, **100**, 21577.
- Hansteen, V. H., E. Leer, and T. E. Holzer: 1997, The role of helium in the outer corona, *Astrophys. J.*, **482**, 498.
- Kohl, J. L., *et al.*: 1998, UVCS/SOHO empirical determination of anisotropic velocity distributions in the solar corona, *Astrophys. J.*, **501**, L127.
- Kohl, J. L., L. Strachan, and L. D. Gardner: 1996, Measurement of hydrogen velocity distributions in the extended solar corona, *Astrophys. J.*, **465**, L141.
- Leer, E., and T. E. Holzer: 1980, Energy addition in the solar wind, *J. Geophys. Res.*, **85**, 4681.
- Li, X., S. Habbal, J. Kohl, and G. Noci: 1998, The effect of temperature anisotropy on observations of Doppler dimming and pumping in the inner corona, *Astrophys. J.*, **501**, L133.
- Lie-Svendsen, Ø., V. H. Hansteen, and E. Leer: 1997, Kinetic electrons in high-speed solar wind streams: Formation of high-energy tails, *J. Geophys. Res.*, **102**, 4701.
- Marsch, E., and C. T. Tu: 1997, Solar wind and chromospheric network, *Sol. Phys.*, **176**, 87.
- McKenzie, J. F., G. Sukhorukova, and W. I. Axford: 1998, Structure of a photoionization layer in the solar chromosphere, *Astron. Astrophys.*, **332**, 332.
- Ofman, L., and J. Davila: 1998, Solar wind acceleration by large-amplitude nonlinear waves: Parameter study, *J. Geophys. Res.*, **103**, 23677.
- Olsen, E. L., and E. Leer: 1996, An 8-moment approximation two-fluid model of the solar wind, *J. Geophys. Res.*, **101**, 15591.
- Peter, H., and E. Marsch: 1997, Ionization layer of hydrogen in the solar chromosphere and the solar wind mass flux, in *Proceedings of the Fifth SOHO Workshop*, ESA-SP-404, 591.
- Tu, C.-Y., E. Marsch, K. Wilhelm, and W. Curdt: 1998, Ion temperatures in a polar coronal hole observed by SUMER on SOHO, *Astrophys. J.*, **503**, 475.

WORKING GROUP 2 REPORT: ENERGY INPUT, HEATING, AND SOLAR WIND ACCELERATION IN CORONAL HOLES

A. W. HOOD

University of St. Andrews

Abstract. Theories and observations of energy input, heating and acceleration mechanisms in the low corona were presented and discussed. The main topics of discussion were large-scale solar wind simulations, theoretical heating mechanisms, observational constraints, confronting theory with observations and observational issues.

Key words: coronal heating, solar wind acceleration, coronal holes

1. Introduction

This group consisted of a large number of delegates with fairly diverse interests and some topics overlapping with some of the other groups. The outstanding observations from SOHO have played a key role in the theoretical models of the solar wind. For example, it was not appreciated that there was such a rapid acceleration of the solar wind so close to the Sun prior to SOHO and the theorists have responded with heating and acceleration mechanisms to explain these key observational facts. Basically the discussions were divided into four main topics.

Firstly, large scale simulations of the solar wind were presented. The main aim of these simulations is to reproduce the observed physical variables both at 1 AU, from in situ observations, and in the low corona, from SOHO observations. The complexity of the equations means that some assumptions must be made about, for example, the heating mechanism. The next section deals essentially with theoretical models of coronal heating, both low down in the corona and higher up in the fast solar wind streams. The third topic concerned the observational constraints on the various heating mechanisms. Here SOHO is already playing an important role but more can still be done. The fourth topic was confronting theory with observations. For example, the plume phenomenon was presented but how big a role (if at all) do plumes play in the energy input, heating and acceleration of the fast solar wind? In addition, our understanding of the transition region and its relationship with the chromospheric network has been modified by recent SUMER observations. The final topic concerned some observational issues relating to streamers, the quiet Sun, the redshift observed in transition region lines and observed blue shifts in coronal holes.

2. How to Construct Numerical Models of the Solar Wind

The basic fast solar wind equations are well agreed, depending on the level of sophistication required. Essentially the equations are conservation laws for the



Space Science Reviews 87: 79–92, 1999.
©1999 Kluwer Academic Publishers.

conservation of mass, momentum, energy and magnetic flux. In the momentum equation an additional wave pressure can be included to provide an additional acceleration to the wind and in the energy equation an additional heating term is included. The heating term is assumed to be due to the damping of waves that are generated by either convective motions, photospheric footpoint motions or magnetic reconnection. The models are either 1D, in which the magnetic field plays a passive role in channelling the plasma flow, or multi-dimensional, where the magnetic field can respond to the flow. Finally, the equations are chosen either to model a single fluid or a multi-fluid plasma. In the low β coronal hole region, the magnetic field is essentially potential and simply acts as an expanding rigid tube. However, this approximation must be revised when the flow velocity approaches the local Alfvén speed.

Many of the differences between the various numerical models can be attributed to the particular choices of boundary conditions. The position of the coronal base is also important. In addition, there are various constants of the motion, such as mass flux, that act as control parameters and these may be chosen (i) by using observed values at 1 AU or from SOHO observations or (ii) may be given by the solution. Finally, there is a heating term and the functional form of that may either be specified, determined from a theoretical model or determined by detailed observations. Three solar wind models illustrate these ideas.

Axford and McKenzie (1998) choose a potential magnetic field as a dipole and equatorial current sheet plus a quadrupole component. This component is quite large in order to flatten the magnetic field and generate the rapid coronal hole expansion. The magnetic flux, $\Phi = BA$, where B is the field strength and A , the cross-sectional area, are determined from observations. The mass flux, $J = mnVA$ is determined from observations at 1 AU. The model is a two fluid model and includes both parallel and perpendicular temperatures, T_{\parallel} and T_{\perp} and a wave pressure gradient, but the wave pressure usually remains small. The coronal base is taken as $T = 10^6$ K. Finally, there is a wave energy input of the functional form

$$e^{-(r-R_0)/L}, \quad r > R_0,$$

where r is the radial coordinate, R_0 is the radius of the Sun and L is a decay length that is free to be chosen. In fact L is selected to obtain a base density of 10^8 cm^{-3} . The model predicts a good flow speed profile and locates the critical sonic point at about $2 R_0$ (see Figure 1). In a simple extension, this solar wind model is patched onto a lower atmosphere that connects it to the chromosphere.

Hansteen (1998) approaches the modeling in a different way. The base boundary conditions are placed in the chromosphere, where the ultimate source of plasma for the solar wind is located. Initially, the atmosphere is assumed to be at chromospheric temperatures with the result that the density falls off extremely rapidly. Then, a mechanical heating term of the form

$$F_m = \begin{cases} F_{m0} \exp [-(r - r_m)/L], & r > r_m, \\ F_{m0}, & r < r_m, \end{cases}$$

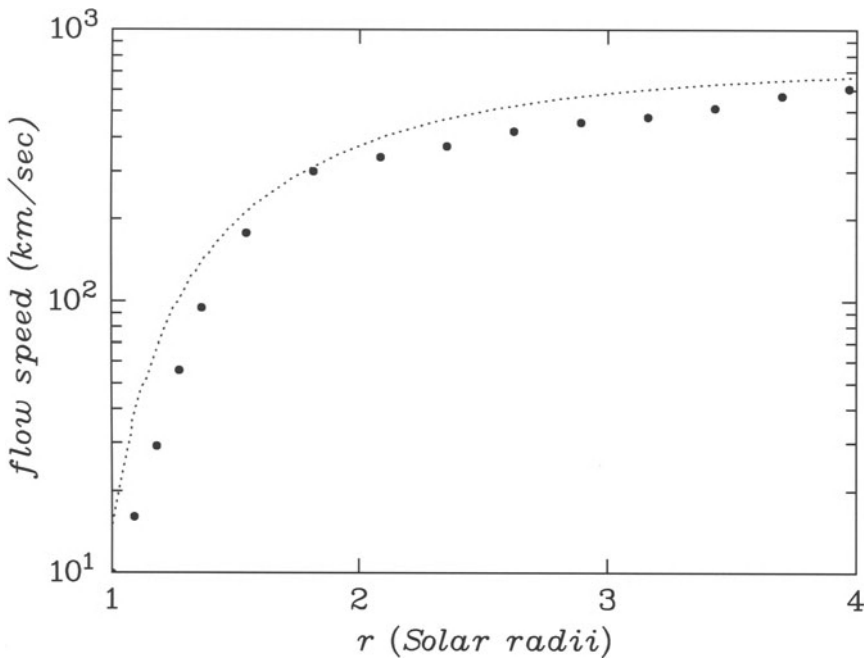


Figure 1. The flow speed as a function of radius for various values of the heating compared with the observed speed (dots).

is switched on, where r_m is the height at which the heating begins to decay and again L is a dissipation length. The atmosphere rapidly heats and forms a corona and a fast solar wind. On reaching a steady state, the mass flux and total energy, that are constants of the system of equations (a set of 6 fluid equations for the various states of hydrogen and helium), are given by the solution and are now solely dependent on the parameters of the imposed heating function. The hot coronal plasma conducts heat back down to the chromosphere, where evaporation occurs, and out into the solar wind. The optically thin radiation is important in the transition region, falling off in importance as the density drops off with height. The importance of the various terms in the energy balance are illustrated schematically in Figure 2.

The final state depends on the amount of heat deposited but not critically on the value of r_m , as long as r_m is greater than a few chromospheric scale heights. Between 85% and 90% of the energy deposited in the corona goes into driving the solar wind.

Both of the above models make use of a coronal heating term but do not give any physical reason for the particular form used. Whatever the coronal heating mechanism actually is, there will be a definite radial functional form that must be

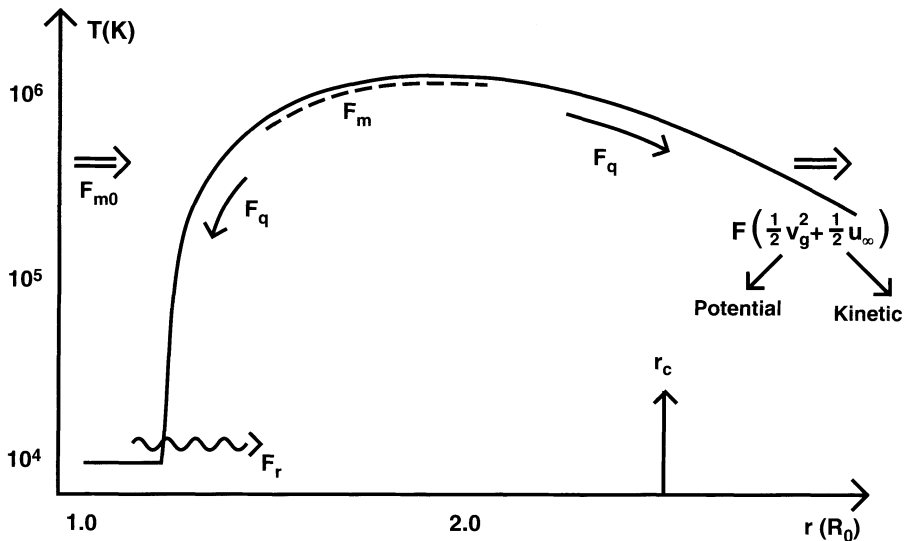


Figure 2. The importance of the various energy terms is schematically illustrated and shows the inclusion of a dense chromosphere at the base of the model.

used. The aim of the theoretical models is to explain how the energy is deposited at the correct height to explain the rapid acceleration of the solar wind so close to the Sun.

Guhathakurta and Sittler (1998) used a semi-empirical method to try to determine the functional form of the heating function. The magnetic field is prescribed by a multi-polar expansion, with an equatorial current sheet. The field is then matched to the Ulysses observations. Observations at 1 AU are used to fix the mass flux and the total energy of the wind. Next, detailed observations are used to determine the temperature and the solar wind equations are used to obtain an effective temperature given by

$$T_{\text{eff}} = T + T_w,$$

where T_w is the temperature obtained by treating the frequency integrated velocity wave amplitude as if it were a thermal speed. Finally, the functional form of the heating function can be estimated from the thermal energy equation. This approach is extremely interesting but the task is difficult and requires extremely detailed observations for the temperature variations with height. This is available from the SOHO observations of SUMER, CDS and UVCS and more detailed investigations of existing data are definitely required. This possibility of tying down of the functional form of the heating is important as it severely restricts the possible theories of coronal heating.

Keppens and Goedbloed (1998) described a fully 3D non-linear code and applied it to a thermal, magneto-centrifugally driven stellar outflow. The code describes, in a self-consistent manner, both the closed field region of the equatorial plane and the open field of the polar coronal holes. The single fluid equations model the plasma wind that satisfies the additional restrictions of passing through the 3 critical points of the system.

What is clear from the above fast solar wind models is the need to obtain a detailed description of the actual heating mechanism.

3. Theoretical Heating Mechanisms

It is generally agreed that the plasma in the open field of the coronal holes must be heated by some form of wave heating mechanism. However, the source of these waves, their subsequent evolution and possible observational signatures require further investigation.

Cuseri *et al.* (1998) invoked the gravity damping mechanism of Alfvén waves, proposed by Khabibrakhmanov and Mullan (1994), in the proton energy equation and show that there is preferential heating of the perpendicular proton temperature and acceleration of the heavier ions. Including this form of heating predicts good agreement with the observed plasma properties at 1 AU.

Assume that the heating and driving of the solar wind is by high frequency waves such as ion-cyclotron modes but that the wave spectrum is unknown. Cranmer *et al.* (1998) show that the minor ions should absorb power from these modes and so disturb the wave spectrum. The fact that the heating appears to behave as though they do not modify the spectrum suggests that there is a mechanism generating the high frequency waves faster than they want to be damped by the ions themselves. Now, using the theory of ion-cyclotron resonance, when the wave frequency satisfies the resonance condition,

$$\omega - \mathbf{k} \cdot \mathbf{v} = \Omega_{\text{ion}},$$

and

$$\Omega_{\text{ion}} = \frac{Z_{\text{ion}}}{A_{\text{ion}}} \left(\frac{eB_r}{m_p c} \right),$$

together with the observations of the minor ions, one can deduce the form of the wave spectrum. Using that spectrum, it is possible then to infer how the major species must behave.

However, neither Cuseri *et al.* nor Cranmer consider the actual generation of the waves. They have assumed that the waves are present in the solar wind and with a sufficient energy flux.

Davila and Ofman (1998) use a two fluid, MHD, coronal hole model in which motions on the coronal boundary base drive Alfvén waves into the corona. The

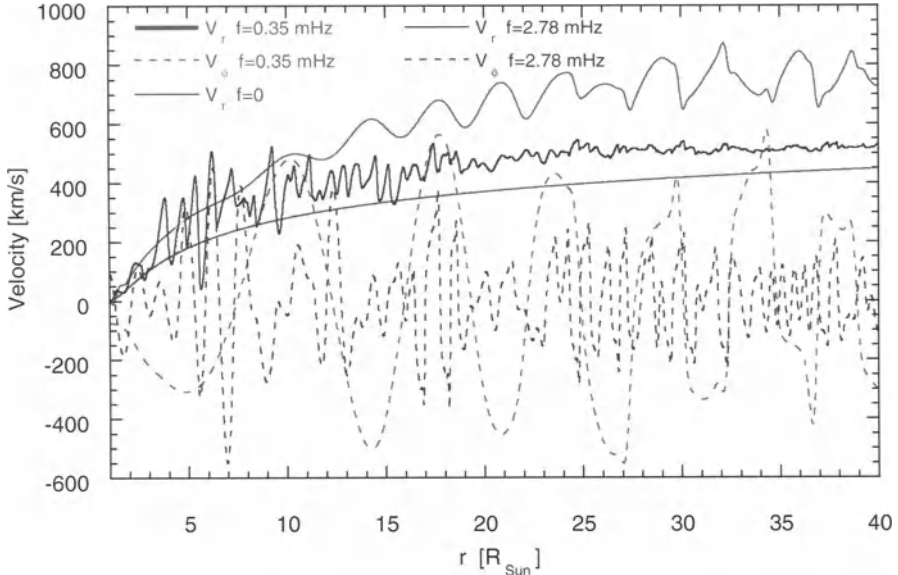


Figure 3. The radial dependence of the solar wind velocity components v_ϕ and v_r at the center of the coronal hole for a frequency $f = 2.78$ mHz. Parker's solar wind solution without waves ($f = 0$) is shown as the smooth curves, from Ofman and Davila (1998).

driven motions excite many modes. Starting from a hot corona and a Parker wind initially, the Alfvén waves are started and they nonlinearly generate compressional waves in the radial direction. The inhomogeneity of the background plasma density means that the Alfvén waves also phase-mix with height. Results suggest that high frequency waves contribute to acceleration near the Sun whereas low frequency waves contribute further out. This is illustrated in Figure 3 (Ofman and Davila 1998).

The conversion of Alfvén waves into either slow or fast mode magnetoacoustic waves is important for the rapid damping of waves and heating. If nonlinearities are necessary, then the initial wave amplitudes must be fairly large. However, Poedts *et al.* (1998) showed that a shear flow, along the radial magnetic field in coronal holes, results in a transformation of Alfvén waves into fast mode waves and vice versa. The effect occurs in the linear regime and the fast waves can convert part of their energy into the background wind, causing an acceleration of the plasma.

Liewer *et al.* (1998) consider a hybrid model of Alfvén/cyclotron wave propagation and ion heating in the solar wind. They assume a 4% helium and hydrogen plasma and solve in a computational box that moves with the solar wind. An important element of the method is to account for the expansion of the computational

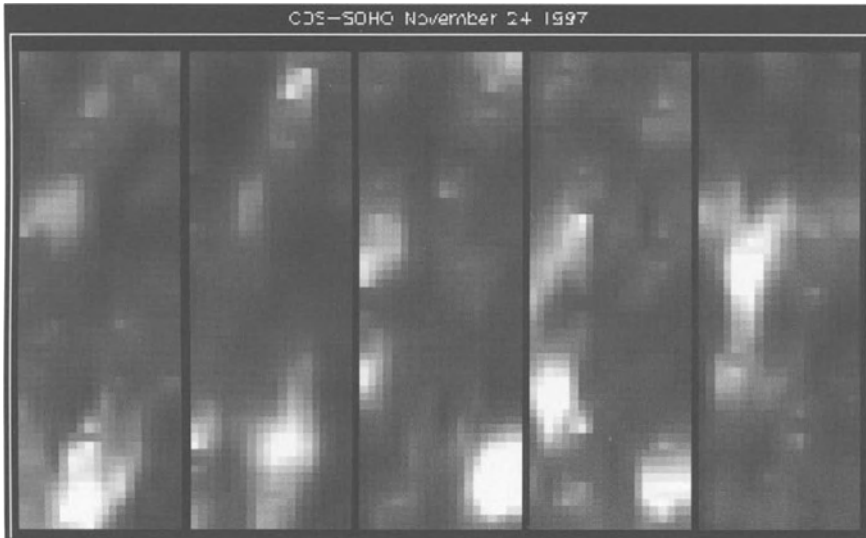


Figure 4. Bright features in the chromospheric network brighten and fade with time. Solar rotation causes individual features to cross the field of view.

box, to simulate the radial expansion of the solar wind. Results clearly demonstrate that there is a preferential heating and acceleration of the helium ions resulting in

$$v_{\parallel}^{\text{He}} > v_{\parallel}^{\text{H}}.$$

In addition, the perpendicular temperature of the helium ions is larger than their parallel temperature.

4. Observational Constraints on Heating

One of the many important new results from SOHO is the discovery of the UV blinks seen by CDS. Harrison presented their basic properties. A simple description of a blinker is a brightening of emission in the transition region plasma, lasting between 10 and 15 minutes. There are estimated to be the order of 3,000 UV blinks on the Sun at any time, with each releasing energy of the order of 10^{19} J. It appears that the blinks are located at the supergranular cell corners and are probably sites of magnetic reconnection. This is backed up by SUMER observations that show bi-directional jets, indicative of the plasma jets expected theoretically from reconnection sites. However, more detailed comparisons with the magnetograms of MDI would show whether the convergence of opposite magnetic polarities occurs at the same time and location as the UV blinks. A typical blinker is clearly seen in the time sequence of CDS images in Figure 4.

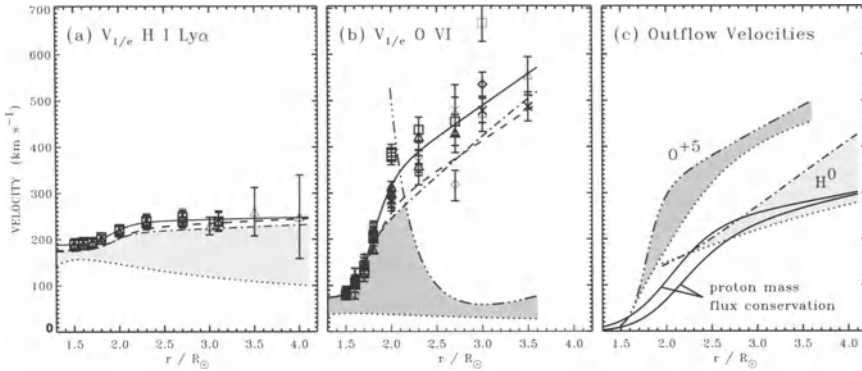


Figure 5. (a) Line widths and empirical most-probable speeds (parallel and perpendicular to the radial magnetic field) for H⁰ atoms derived from H I Ly α profiles. Also plotted are the most-probable speeds corresponding to thermal distributions T_e (dotted line) and the perpendicular speeds for the two consistent models (dashed, dot-dashed lines). The shaded region denotes the possible values of the parallel most-probable speed. (b) Same as (a) but for O VI, 1032, 1037 Å. The dash-triple-dotted line denotes an empirical upper limit on the parallel most-probable speed of O⁵⁺ ions. (c) The empirical outflow velocity over the poles corresponding to the two consistent models in (a) and (b) for H⁰ and O⁵⁺. Solid lines denote proton mass flux conservation assuming super-radial coronal hole expansion (upper line) and radial expansion (lower line). Shaded regions correspond to those in (a) and (b).

Damasch *et al.* (1998) presented some SUMER observations of Ne VIII inside a coronal hole. Firstly, the rest wavelength of Ne VIII may be wrong in the literature. Secondly, there are large, localized, blue-shifted outflows at the supergranular cell corners and a small but general background blue-shift in the coronal hole. It would be interesting to investigate the relationship between the large outflows and coronal plumes. Are they co-spatial or not?

More restrictions on theories can be placed using the UVCS observations obtained by Kohl *et al.* (1998). An empirical coronal hole model is constructed, using the detailed measurements of densities, outflow velocities and microscopic velocities below 5 R_0 where the main acceleration of the solar wind occurs. Various physical quantities, for example density, are determined from the observations. Synthetic observables, e.g., line profiles and intensities, are then determined from these models and compared with the data. The model is then adjusted in an iterative manner until there is optimal agreement between model and observations. Since no assumptions are made in advance about heating and acceleration mechanisms, the results can be used to constrain theoretical models. Figure 5 shows that the outflow velocity of the O⁵⁺ is consistently higher than either the proton or the H⁰ velocities in both the parallel and perpendicular directions. See Kohl *et al.* (1998) and Cranmer *et al.* (1999a) for a more detailed description. One possible mechanism (see Cranmer *et al.* 1998, 1999b) for explaining the acceleration of the heavier ions, in

preference to the protons, is the dissipation of high frequency Alfvén waves through the ion-cyclotron resonance due to finite Larmor motions.

Fludra *et al.* (1998) presented some regular CDS observations of coronal holes up to a height of $1.2 R_\odot$. Thus, temperatures are obtained from Mg X and Mg IX line ratios, and densities from the density sensitive lines of Si IX. The electron temperature above polar coronal holes increases with height from 7.5×10^5 K at the limb to 9.0×10^5 K at $1.2 R_\odot$. These values remain steady on a timescale of up to nine months. The electron density, on the other hand, decreases with height from 2×10^8 cm $^{-3}$ at $1 R_\odot$ to 6×10^7 cm $^{-3}$ at $1.2 R_\odot$. Two bright plumes observed have a lower temperature than the interplume region and a marginally higher density, in contrast to the results of DeForest.

Bromage *et al.* (1998) investigated the difference between the open field region of an equatorial coronal hole and the closed field region of the neighboring quiet Sun. Using CDS, with the slit crossing both coronal hole and quiet Sun plasma, allowed a direct comparison of the plasma. In addition, a small bright feature in the coronal hole was also observed and this may have been a coronal plume, viewed almost directly from above. Calculations of the temperatures showed that

$$T_{\text{plume}} = 7.6 \times 10^5 \text{ K} < T_{\text{CH}} = 8.0 \times 10^5 \text{ K} < T_{\text{QS}} = 9.7 \times 10^5 \text{ K} .$$

The plume density, 2.1×10^8 cm $^{-3}$, was higher than the coronal hole value, 1.7×10^8 cm $^{-3}$, but why these values are lower than the typical values in polar coronal holes is not clear.

SUMER also observed a small equatorial coronal hole with the slit again sampling both the quiet Sun and the coronal hole regions. Lemaire *et al.* (1998) found that the line widths in the coronal hole were greater than in the quiet Sun, suggesting a higher turbulence level in the open field region. In contrast, the intensities were higher in the quiet Sun.

Matthaeus investigated turbulence in the solar wind and found that there is an anisotropy in the cascade to shorter length scales. If the magnetic fluctuations, δB , are much smaller than the background radial field, B_0 , then there is a transfer of energy into larger perpendicular wavenumbers, k_\perp , while the parallel cascade to larger k_\parallel is suppressed.

5. Confronting Theory with Observations

DeForest presented the latest EIT/SOHO and TRACE observations of plumes. While plumes may well not contribute significantly to the fast solar wind, they are major features of coronal holes. Plumes and inter-plume regions require detailed theoretical modeling. Detailed observational properties of plumes have been deduced. Plumes occur in magnetic flux concentrations situated at the corners of network cells. The magnetic field has a peak value of about 300 G but about 10% of the flux present in the footprint is of the opposite polarity. Presumably this minority

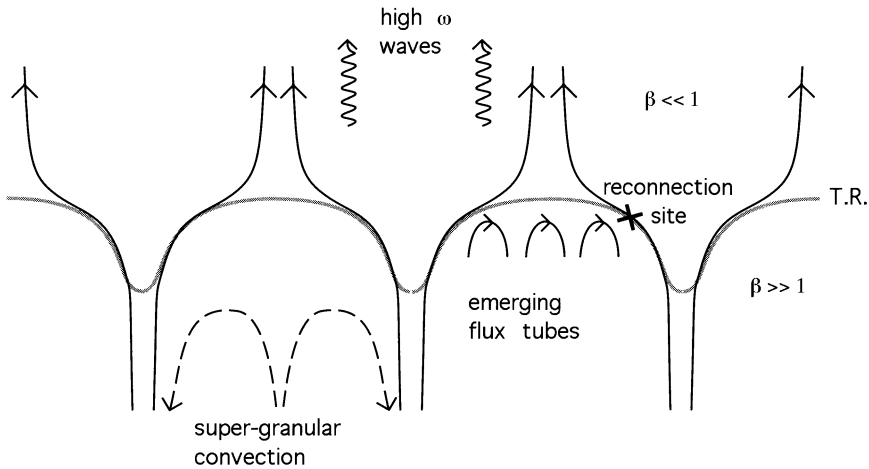


Figure 6. Cartoon model showing the height variation of the transition region, labelled by T.R., across the chromospheric network.

magnetic flux can reconnect with the dominant polarity and the energy released can help to drive the plume phenomena. The lifetime of an individual plume is hard to define since there is an overall change in the brightness of a plume on a timescale of a few hours but the same region can brighten and fade many times in the same flux concentration. In addition, there are smaller sub-structures in plumes that vary in intensity over a few minutes. Waves have been observed with an outward velocity of about 100 km/s and a period of 12 minutes. Basically, plumes appear to be density structures being denser than the surrounding coronal holes by a factor in the range 2 to 10. If the coronal hole magnetic field is almost uniform, then the Alfvén speed is lower in a plume than in the surrounding coronal hole. Fast magnetoacoustic waves will be refracted towards the plume and the Alfvén speed gradient will result in phase-mixing of Alfvén waves. Plumes are cooler, being about 10^6 K, compared to the inter-plume plasma temperature of 1.5×10^6 K. Finally, 50% of the plasma in the coronal hole comes from the flux concentrations at the supergranular cell corners.

Velli introduced a discussion on the production of high frequency waves due to motions at the photospheric level. Wilhelm presented some SUMER observations that suggest that the transition region is lower inside the strong field region of the chromospheric network than in the cell centres. This led to the cartoon description of the low atmosphere shown in Figure 6. Low frequency disturbances in the cell centres will propagate as slow magnetoacoustic waves and will be channelled into the inter-plume regions. New emerging flux regions are carried by the convection from the cell centres into the cell edges. Reconnection will occur and generate outflows at the local Alfvén speed. These will propagate up into the corona as high

frequency waves. However, these cartoon models seem reasonable but there is, as yet, no detailed proof. There is, for example, no description of either reconnection or tearing modes in a gravitationally stratified atmosphere.

6. Observational Issues

Frazin presented some UVCS observations of the velocities in two streamers. One equatorial streamer, observed at solar minimum, had a higher velocity than that in a mid-latitude streamer seen in 1998. No explanation was offered but theorists should try to explain this. One would imagine that the mid-latitude streamer is surrounded by the fast solar wind and so would have a higher velocity. On the other hand, the plasma at the base of this streamer may, in fact, be cooler resulting in a lower outflow speed.

EIT observations of the quiet Sun (Falconer *et al.* 1998) split the corona into several distinct regions as either large or small and bright or dim. Comparison with magnetograms show that the bright regions, which are hotter, have an average field strength that is about 50% stronger than the dim regions. This again suggests that the heating of the corona is magnetic in nature. However, observations of the chromospheric network show no obvious differences between the open, cooler regions of coronal holes and the hotter closed field regions of the quiet Sun.

One outstanding observational problem is to explain the predominant redshift that is observed in transition region lines. It is inconceivable that all the plasma is draining down from the corona and that none is flowing up, and hence blue shifted, to replenish the plasma. Poland and Chae (1998) proposed a neat solution to the problem. He solved the energy balance equation for a plasma that is flowing up and one that is flowing down magnetic field lines. In the downflow model the enthalpy flux essentially balances the optically thin radiation, leaving only a small contribution from the thermal conduction, and so produces a gradual temperature gradient. In the upflow model, on the other hand, the thermal conduction balances the enthalpy flux and this produces a very steep temperature gradient. These results are shown in Figure 7. Thus, the temperature gradients are much steeper for the upflow than the downflow. This means that there is more plasma emitting at transition region temperatures in the downflow. Hence, there will be a predominant red shift observed. However, Wilhelm showed some SUMER observations of regions where there were upflows and downflows both present. Is there a problem to be solved at all? More examples of observed upflows and downflows in transition region lines would be extremely useful. Jones (1998) presented evidence of a blue wing asymmetry in the He I 1083 nm line in a coronal hole. This blue shift provides direct evidence of a general outflow from the coronal hole.

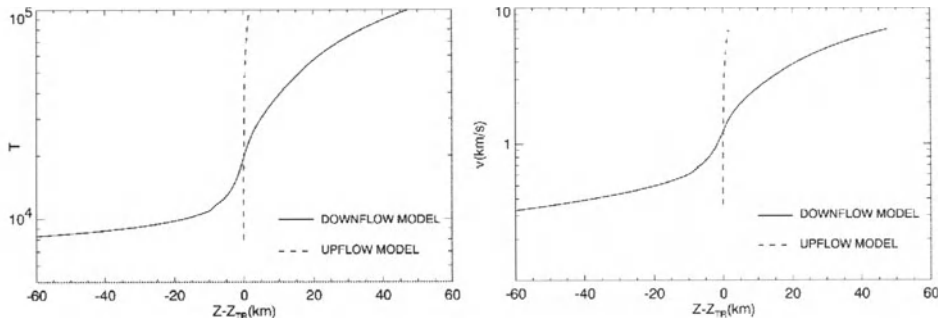


Figure 7. Temperature and velocity variations with height. The important point is that there is more material in the transition region temperature range for the downflow case and thus it is much more visible.

7. Conclusions

So what has been learnt from our discussions? There is some debate on the validity of the large scale numerical simulations of the solar wind. Since the MHD equations are essentially conservation laws, using the observations at 1 AU as boundary conditions does allow us to determine some of the constants of the equations. However, the actual form of the heating function is arbitrary and is normally expressed as a simple exponential. This seems reasonable since the results give reasonable agreement with the observations. However, the actual functional form should be determined by a theoretical model of the heating mechanism. Where is the base and what are the boundary conditions at the base? In earlier models of coronal loops, during the 1980s, it was critical to incorporate the transition region and this probably remains true for solar wind models. However, a detailed connection to the chromosphere is complicated and requires further work.

Theoretical heating mechanisms based on either wave mechanisms or small scale reconnection events must now predict the actual form of the heating to be included in the large scale simulations along the lines of the Ofman approach (Ofman and Davila 1998). Coming from the other direction, SOHO observations are beginning to constrain the theoretical models.

Many properties of plumes are now known. However, we still do not know how important plumes are for the solar wind. Are they simply a nuisance and just obscure the observations of the fast solar wind? Is the energy source responsible for plume formation also important for energy input to the solar wind? And what about UV blinkers? If they are small scale reconnection events, what is their role in heating and energy input? While they are obviously important in active regions are they important in the coronal holes? Then there is the general point that the chromospheric network does not appear to show any differences between active

regions and coronal holes. Does this mean that the same heating mechanism is occurring in the closed and open magnetic field regions?

SOHO has certainly improved our understanding of many different facets of the solar corona. However, there are still many unsolved problems remaining to be tackled. With more analysis of the data from SOHO and new TRACE observations, these problems can be successfully solved.

8. Acknowledgments

Many thanks to group leader Bob Rosner for useful comments on this manuscript and for controlling the sessions in an ordered manner.

References

- Axford, W. I., and McKenzie, J. F.: 1998, 'Acceleration of the high speed solar wind in coronal holes,' this volume.
- Bromage, B., Clegg, J. R., and Thompson, B.: 1998, 'Birth of a large low-latitude coronal hole,' this volume.
- Cranmer, S. R., Field, G. B., and Kohl, J. L.: 1998, 'The impact of ion-cyclotron wave dissipation on heating and accelerating the solar wind,' this volume.
- Cranmer, S. R., *et al.*: 1999a, 'An empirical model of a polar coronal hole at solar minimum,' *Astrophys. J.*, **511**, 481.
- Cranmer, S. R., Field, G. B., and Kohl, J. L.: 1999b, 'Spectroscopic constraints on models of ion-cyclotron resonance heating in the polar solar corona and high speed solar wind,' *Astrophys. J.*, **518**, in press.
- Cuseri, I., Mullan, D. J., Noci, G., and Poletto, G.: 1998, 'Heating and acceleration of the solar wind via the gravity damping of Alfvén waves,' this volume.
- Dammasch, I. E., Hassler, D. M., Curdt, W., and Wilhelm, K.: 1998, 'Statistical analysis of EUV lines inside and outside of coronal holes,' this volume.
- Davila, J., and Ofman, L.: 1998, 'Fast solar wind acceleration and heating by nonlinear waves,' this volume.
- Falconer, D. A., Moore, R. L., Porter, J. G., and Hathaway, D. H.: 1998, 'Accumulation of small coronal bright points in the quiet magnetic network,' this volume.
- Fludra, A., Del Zanna, G., and Bromage, B.: 1998, 'Characteristics of polar coronal holes and their evolution from EUV observations,' this volume.
- Guhathakurta, M., and Sittler, Jr. E.: 1998, 'MHD model of the large-scale corona and the interplanetary medium from $1 R_\odot$ to 4 AU using SOHO and Ulysses observations,' this volume.
- Hansteen, V. H.: 1998, 'Time dependent heating of the corona and the solar wind,' this volume.
- Jones, H. P.: 1998, 'He I 1083 nm asymmetry and EUV line shifts in coronal holes,' this volume.
- Khabibrakhmanov, I. K., and Mullan, D. J.: 1994, 'Gravitational damping of Alfvén waves in stellar atmospheres and winds,' *Astrophys. J.*, **430**, 814–823.
- Keppens, R., and Goedbloed, J. P.: 1998, 'Numerical simulations of stellar winds,' this volume.
- Kohl, J. L., Fineschi, S., Esser, R., Ciaravella, A., Cranmer, S. R., Gardner, L. D., Modigliani, A., Suleiman, R., and Noci, G.: 1998, 'UVCS/SOHO observations of spectral line profiles in polar coronal holes,' this volume.
- Lemaire, P., Bocchialini, K., Aletti, V., Hassler, D., and Wilhelm, K.: 1998, 'Search for signatures of a coronal hole in transition region lines near disk center,' this volume.
- Liewer, P. C., Velli, M., and Goldstein, B. E.: 1998, 'Hybrid simulations of wave propagation and ion heating in the solar wind using a 1D expanding box model,' this volume.

- Ofman, L., and Davila, J. M.: 1998, *J Geophys. Res.*, **103**, 23677.
Poedts, S., Rogava, A., and Mahajan, S. M.: 1998, 'Velocity shear induced effects in the solar wind,' this volume.
Poland, A. I., and Chae, J.: 1998, 'Energetics of the lower transition region,' this volume.

Address for correspondence: School of Mathematical and Computational Sciences, University of St. Andrews, KY16 9SS, U.K.

WORKING GROUP 3 REPORT: CORONAL HOLE BOUNDARIES AND INTERACTIONS WITH ADJACENT REGIONS

R. ESSER

Harvard-Smithsonian Center for Astrophysics, Cambridge, MA 02138, USA

Abstract. Summarized below are the discussions of working group 3 on “Coronal hole boundaries and interactions with adjacent regions” which took place at the 7th SOHO workshop in Northeast Harbor, Maine, USA, 28 September to 1 October 1998. A number of recent observational and theoretical results were presented during the discussions to shed light on different aspects of coronal hole boundaries. The working group also included presentations on streamers and coronal holes to emphasize the difference between the plasma properties in these regions, and to serve as guidelines for the definition of the boundaries. Observations, particularly white light observations, show that multiple streamers are present close to the solar limb at all times. At some distance from the sun, typically below $2 R_S$, these streamers merge into a relatively narrow sheet as seen, for example, in LASCO and UVCS images. The presence of multiple current sheets in interplanetary space was also briefly addressed. Coronal hole boundaries were defined as the abrupt transition from the bright appearing plasma sheet to the dark coronal hole regions. Observations in the inner corona seem to indicate a transition of typically 10 to 20 degrees, whereas observations in interplanetary space, carried out from Ulysses, show on one hand an even faster transition of less than 2 degrees which is in agreement with earlier Helios results. On the other hand, these observations also show that the transition happens on different scales, some of which are significantly larger.

The slow solar wind is connected to the streamer belt/plasma sheet, even though the discussions were still not conclusive on the point where exactly the slow solar wind originates. Considered the high variability of plasma characteristics in slow wind streams, it seems most likely that several types of coronal regions produce slow solar wind, such as streamer stalks, streamer legs and open field regions between active regions, and maybe even regions just inside of the coronal holes. Observational and theoretical studies presented during the discussions show evidence that each of these regions may indeed contribute to the solar slow wind.

Key words: coronal holes, streamer belt, fast and slow solar wind, coronal and interplanetary observations

1. Introduction

The topic of the coronal hole boundaries was introduced to the general audience of the SOHO 7 workshop in a one hour lecture by L. Fisk which concentrated on the magnetic nature of the slow and fast solar wind, pointing out that an expansion of magnetic field lines from the differentially rotating photosphere into the corona would lead to reconnection of field lines from the polar regions with closed field lines in the equatorial regions (Fisk *et al.* 1999, this volume). The working group then began with a general overview by S. Suess who presented a list of key questions to stimulate and guide the discussions. During the following days this list was used to focus contributions of the members of the working group, even though the questions were not necessarily addressed in the original order. An overview of the key questions is given below:



1. Do we know what coronal hole boundaries are?
 - a. What do they look like in interplanetary and coronal observations (e.g., Ulysses, Yohkoh, SOHO, Spartan)?
 - b. What is the thickness of the boundaries?
2. Do coronal hole boundaries diverge faster than radially; what does the divergence look like?
3. Where does the slow solar wind come from?
4. What is the quiet sun; is there a need for that term?
5. What are the streamer properties (e.g., compared to coronal hole properties)?

The working group then continued with presentations of about 10 minutes each on different aspects of the key questions, mainly transition from fast to slow solar wind (coronal hole to adjacent regions), and on the origin(s) of the slow solar winds. Contributions relevant to point 5 were not presented separately but rather together with contributions on the other topics whenever they were complementary to some of the boundary observations. Point 4 was only addressed extremely briefly towards the end of the workshop, and the discussion was not conclusive.

These contributions included observations from a large number of SOHO instruments, as well as instruments from other spacecraft (e.g., Ulysses, Spartan and ACE), in addition to ground based observations (e.g., Interplanetary Scintillation (IPS) observations, spectral line observations), and theoretical studies. The presentations were complemented by shorter contributions from the other members of the working group. The contributions were generally of high quality and well prepared which resulted in an active participation of almost all members of the working group. The discussions were lively, yet focused, throughout the whole workshop. In the following I have made an attempt to summarize the different contributions grouped into regions observed, as well as topics. I tried to be as complete as possible but some contributions might have been overlooked. Some contributions might be relevant for more than one session or subsession, and, therefore, are referred to in several places. Note that most of the contributions will also be published as separate papers in this volume. The studies described in this summary are mostly for conditions at or close to solar minimum. Focus was on the boundaries of the large polar coronal holes and their occasional extensions towards the equatorial regions.

2. Coronal Hole Boundaries

Both disk, limb and observations in the extended corona, as well as in interplanetary space of coronal hole boundaries were presented at the workshop. In the inner corona, the streamer region surrounding the equatorial plane is usually a very complex region with an ensemble of several loop like structures being present at almost all times, even close to solar minimum. This can be seen in white light

images taken close to the coronal base (e.g., Koutchmy *et al.* 1978). This complex region seems to merge into a structure that at least at times looks like only one streamer, as for example in the LASCO (Brueckner *et al.* 1995) and UVCS (Kohl *et al.* 1995) images taken at distances above 1.5 to 2 R_S . Even though, it is not uncommon that sector transitions observed in interplanetary space show multiple field reversals, as was pointed out by several participants (see Mariani and Neubauer 1990 for a more detailed description). In interplanetary space the solar wind has been characterized as a two-state phenomenon (e.g., Schwenn 1990): the high speed, quasistationary solar wind, and the highly variable low speed streams with a rather sharp separation between the two types. This narrow transition, which is visible in coronal observations as a sharp intensity drop, was defined as the boundary region.

2.1. OBSERVATIONS IN INTERPLANETARY SPACE

Knowledge of the fast-slow solar wind boundaries in interplanetary space have, until the more recent polar passages of Ulysses, been derived from spacecraft observations carried out in or near the ecliptic plane, or from remote sensing measurements which can probe the solar wind at latitudes and distances not yet accessible by spacecraft. The properties of the boundaries derived from in situ measurements could thus be studied only for the fast solar wind originating from smaller equatorial coronal holes or from the occasional extensions of the large polar coronal holes to low latitudes. These streams, often called corotating streams, have a broad range of different sizes and are typically characterized by high temperatures, low densities and high speeds (Burlaga 1999, this volume). The boundaries separating the two stages of the solar wind were shown theoretically (Dessler and Fejer 1963) and observationally (Gosling *et al.* 1978, and references therein) to be discontinuities where the characteristics of the plasma change quite abruptly near the leading edge of the fast stream from the typical slow wind to the distinctly different high speed values.

Detailed observations of the fast to slow solar wind transition were carried out during the line up experiments of the Helios I and II space probes (Rosenbauer *et al.* 1977; Schwenn 1990, and references therein). These observations show that this transition, from slow to fast wind, occurs within 2 degrees. The possibility of the two spacecraft encountering the same stream was basically zero when the latitudinal separation of the two probes was larger than 5 degrees. These observations had also shown that it is not only the speed of the wind that changes extremely rapidly across the boundary, but all other plasma characteristics such as particle temperatures, electron density and helium abundance as well. Using data from the IMP spacecraft these results were confirmed by Mitchell *et al.* (1981). The picture of the solar wind as a bimodal phenomenon emerged from these observations (e.g., Schwenn 1990).

Interplanetary Scintillation observations which have been carried out over several solar cycles have probed the solar wind plasma as a function of latitude and radial distance long before Ulysses reached the polar regions (e.g., Kojima *et al.* 1998,

and references therein). These observations confirm the bimodal speed structure of the solar wind, with a low speed region ($\approx 400 \text{ km s}^{-1}$) concentrated around the equator (< 30 degrees), and a high speed solar wind (750 to 850 km s^{-1}) in the polar regions with a narrow transition between the two. IPS data also show that electron density fluctuations ($\delta N_e/N_e$) show a similar rapid transition between high and low speed wind, with the high speed wind having the higher fractional density fluctuations (Asai *et al.* 1998).

The distribution of slow and fast wind throughout the heliosphere has been mapped from measurements of the Ly- α intensity back-scattered from interstellar neutral hydrogen (Bertaux *et al.* 1997; Kyrölä *et al.* 1998). New results from the SWAN instrument on SOHO were presented at the workshop (Bertaux *et al.* 1999, this volume). The distribution of interstellar H atoms in the heliosphere is mainly determined by their destruction due to ionization charge exchange with solar wind protons. For example, close to the neutral sheet where the slow solar wind is concentrated and has a higher mass flux, more of the H atoms get destroyed, thus producing a grove of depressed neutral hydrogen. The remaining hydrogen atoms scatter the solar radiation and measurements of the scattered Ly- α radiation are capable of providing full sky 3-D pictures of the solar wind mass flux. Solar wind properties derived from the modeling of the back-scattered radiation are in very good agreement with observations obtained from Ulysses, which makes the back-scatter observations extremely useful tools in studying the long term properties of the solar system. While Ulysses only provides snapshots of the out of ecliptic heliosphere, the Ly- α observations, as well as the IPS observations, can be carried out over long time intervals, thus monitoring the behavior during solar minimum and maximum.

The most detailed analysis so far of a slow-fast solar wind boundary was recently made possible by one of the fast crossings of the northern coronal hole boundary by Ulysses in March 1995 when the spacecraft was at 1.35 AU (McComas *et al.* 1998). The crossing was unique in the sense that the spacecraft made a smooth and complete transition from the low latitude (≤ 20 degrees) dense/slow solar wind to the tenuous/fast high latitude solar wind. These observations, carried out by the SWOOPS instrument (Bame *et al.* 1992) and the Imperial College/JPL magnetometer (Balogh *et al.* 1992) and presented at the workshop by S. Suess, revealed that the transition from slow to fast wind occurs over several spatial scales. The shortest scale is that of the tangential discontinuity itself which is of the order of or smaller than $10^5 \text{ km} \approx 0.03$ degrees. Many of the plasma properties change abruptly over that scale, like the halo electron and proton densities, the magnetic field and the plasma beta. The density of the alpha particles, on the other hand, seems to be unaffected by the transition from one stream to the other. The marked difference of the alpha abundance in the low and high speed wind is thus mostly a result of the decrease of the proton density across the boundary. The proton and alpha temperatures begin to increase right at the interface, but reach their final high-speed values over a scale almost one order of magnitude larger (0.3 degrees).

The compression region extends over 2×10^7 km (about 6 degrees). The speed increase can be characterized by two scales. The first one, right at the interface, has an extension of a few degrees and the increase of the speed in that region is about $32 \text{ km s}^{-1} \text{ deg}^{-1}$ which is in very good agreement with the Helios results, for example. The final speed, on the other hand, is approached on a much larger scale, almost asymptotically. That region extends over almost 28 degrees, and the gradient changes about five times more slowly than in the interaction region. How typical this particular crossing is for other slow-fast wind transitions remains to be seen.

Measurements from SWICS on ACE (Gloeckler 1998) reveal that the slow and fast solar wind are also fundamentally different in elemental and charge state composition with a relatively narrow transition region between the two. For example, the ratios Fe/O, Mg/O and O⁷⁺/O⁶⁺ all decrease across the boundary from the slow to the fast wind (Zurbuchen *et al.* 1999, this volume). The authors place emphasis on the fact that the transitions on the trailing edges of fast streams happen significantly more slowly than on the leading edges which is in agreement with the Ulysses results described above. They also note that the transitions of the elemental and charge state compositions sometimes do not happen exactly simultaneously. Since the in situ charge states reflect conditions in the inner corona, and can thus be considered a link between the inner corona and interplanetary space, these measurements indicate also that plasma conditions in the regions where these ions come from, the source regions of the slow and fast streams, are very different with a relatively narrow transition between them.

2.2. OBSERVATIONS CLOSE TO THE SUN

Coronal holes have been known to be the sources of high speed streams for a very long time (Krieger *et al.* 1973); regions outside coronal holes were thought to produce the slow solar wind. When observed in coronal lines formed at temperatures at or greater than 10^6 K, coronal holes emerge as regions of depressed emission. At cooler temperatures, on the other hand, coronal holes are no longer readily distinguishable from the surrounding regions, which are often called quiet regions. A study by Harvey (1999, this volume) which was presented by H. Jones illustrated how coronal holes are identified using full disk magnetograms and He I $\lambda 10830$ line intensities from the National Solar Observatory at Kitt Peak. Coronal holes can be distinguished as areas of low He I absorption and predominantly unipolar magnetic fields. Flow speeds recently derived from chromospheric/transition region and coronal observations indicate that the fast solar wind acceleration process takes place at heights in the solar atmosphere much lower than previously thought (e.g., Grall *et al.* 1996; Dupree *et al.* 1996; Strachan *et al.* 1993, 1997). Several observations comparing outflow properties in coronal holes and surrounding regions were discussed at the workshop. Following the earlier study by Dupree *et al.* (1996), Jones *et al.* (1999, this volume) presented observations of blue-wing line

asymmetries of the He I $\lambda 10830$ lines in coronal holes. These observations indicate outwardly directed flows consistent with an origin of the high speed solar wind in the low transition region. Since the He I $\lambda 10830$ line forms over a relatively large temperature/density range it is difficult to determine the exact height in the solar atmosphere. The estimated flow speeds are of the order of 8 km s^{-1} . Jones *et al.* (1999, this volume) coordinated their observations with CDS observations of He I $\lambda 584$, He II $\lambda 304$, and O V $\lambda 630$ which are cool transition region lines. Using two different techniques to derive line of sight velocities, they conclude that these observations are consistent with blue shifts in the coronal hole regions relative to other areas in the CDS field of view.

Observations carried out with SUMER by Warren *et al.* (1997), on the other hand, show no evidence for blue shifts in transition region lines below temperatures of $2.9 \times 10^5 \text{ K}$. At temperatures above $6.3 \times 10^5 \text{ K}$, however, they find, using the Ne VIII $\lambda 770$ line, a transition to blue shifts corresponding to 5 to 12 km s^{-1} (Hassler *et al.* 1999) which are of the same order as the outflow velocities derived by Dupree *et al.* (1996). In order to compare these different observations to determine discrepancies/agreements one would have to look into the details of the line formation and observational techniques. Compared to the Ne VIII line which has not very well determined atomic data/rest wavelength (Hassler *et al.* 1999, and references therein), the He I $\lambda 10830$ line has very well known atomic physics, can be calculated quite accurately, and is very sensitive to outflows (Sasselov and Lester 1994). For example, Dupree *et al.* (1993) show that including outflows in atmospheric models reproduces the asymmetry in the He I $\lambda 10830$ line, but has no observable effect on other observed spectral lines. In the Dupree *et al.* (1996) study the outflow seems to be predominantly in the center of the supergranular cells, whereas Hassler *et al.* (1999) find their outflows in the boundary, particularly in the places where the boundaries cross. To resolve this discrepancy one would have to investigate how accurately these types of observations actually resolve the spatial information. One also has to keep in mind that these lines form at different heights in the solar atmosphere. In any case, at this point, it seems that more people agree that there are indications for outflows at much lower heights in the solar atmosphere in coronal holes than in the regions surrounding them.

Zangrilli *et al.* (1999, this volume), analyzing the profiles of H I Ly- α and the O VI doublet $\lambda 1031.9$ and $\lambda 1037.6$ observed by the UVCS instrument in the extended corona from 1.5 to $2 R_S$, find that there is a significant difference in the latitudinal behavior of the lines. The full width at half maximum (FWHM) of the H I Ly- α line is wider in the streamer region and decreases towards the polar regions, while the opposite is true for the O VI lines which have a minimum FWHM in the center of the streamer, and their FWHM increases steadily towards the poles. The gradients at the boundaries are rather sharp. The transition between the streamer and hole regions is about 10 to 20 degrees wide in their observations. Using observations from the UVCS/Spartan 201 flights from 1993 to 1995 (Kohl *et al.* 1994) Miralles *et al.* (1999, this volume) find that the line width in the streamer peaks between

2.1 and $2.5 R_S$ with a value corresponding to $T_{\text{kinetic}} = 3 \times 10^6$ K. They also find that the minimum in the Ly- α intensity is located between the streamer and the coronal hole. Hassler *et al.* (1999, this volume) carried out SUMER observations in Fe XII $\lambda 1242$, Mg X $\lambda 625$, O V $\lambda 630$, and N V $\lambda 1238$ which are representative of different heights in the transition region. Their analysis shows an inverse relation in intensity and line width, with the edges of the streamers being the brightest regions. Using a mid latitudinal streamer from 1998 and an equatorial streamer from 1996 observed by UVCS as examples, Frazin *et al.* (1999, this volume) pointed out that not all streamers have the same properties. The difference in the O VI line widths between the two streamers is almost a factor of 2.5 at $4 R_S$. It is not clear whether this difference is due to the fact that these streamers were observed at different times in the solar cycle, or whether it is a result of the different locations of these streamers.

Results from CDS/SOHO observations of plumes, coronal holes and surrounding quiet sun regions were presented by Del Zanna and Bromage (1999, this volume). Using line ratio techniques they derive electron densities in the hole to be of the order of 2×10^8 cm $^{-3}$ which is about a factor of two to three lower than in the quiet sun region. The peak of the emission in coronal holes is at lower temperatures about 8×10^5 K than in the quiet sun where it is closer to 10^6 K.

A study by Bromage *et al.* (1999, this volume; and 1997) focused on the large “Elephant’s Trunk coronal hole” visible on the solar disk in August 1996. Their observations show the difference in size of the coronal hole at different temperatures/heights. The four lines they use, He I $\lambda 584.3$, Mg IX $\lambda 368.1$, Mg X $\lambda 624.9$ and Si XII $\lambda 520.7$, observed with the SUMER instrument, span a temperature range from $\log T = 4.5$ to $\log T = 6.3$. The intensity profiles of these lines clearly show a sharp boundary between this extended coronal hole and the adjacent regions. From the increase of the extension of the coronal hole with increasing temperature/height, they also derive evidence for a faster than radial expansion of the hole.

3. Coronal Hole Expansion

Observational and theoretical studies presented at the workshop all seem to indicate a faster than radial expansion of the coronal hole boundaries in the inner corona (for an alternative view see Woo and Habbal 1999, and references therein), even though, different studies did not necessarily agree on the more detailed expansion geometry.

A rather detailed study of the latitudinal distribution of the H I Ly- α and O VI ($\lambda\lambda 1032$ and 1037) line intensities measured with the UVCS instrument was carried out by Dobrzycka *et al.* (1999). These observations, ranging in height from 1.5 to $2.25 R_S$ (in the equatorial regions to $3 R_S$), cover the time period from 10 August to 8 September 1996. This time period includes the large extension of the Northern coronal hole also described in the observations by Bromage *et al.* (1997, 1999), see

above, which even though carried out at rather low heights in the solar atmosphere, indicate a more than radial expansion. From the observations and analysis of the polar region of that coronal hole, Dobrzycka *et al.* (1999) find that the super radial expansion is even more pronounced at larger distances. The expansion factors they derive, ranging from 6 to 7.5, agree rather well with earlier results derived from white light intensity measurements (Kopp and Holzer 1976; Munro and Jackson 1977). Dobrzycka *et al.* (1999) also find that the diverging geometry is different on the East and West limb, and the size and the geometry of the holes change over periods of days.

Using both observations and models Guhathakurta and Sittler (1999, this volume; see also Sittler and Guhathakurta 1999) conducted a study of the coronal expansion and solar wind. Their 2-D semiempirical MHD model assumes azimuthal symmetry and conservation of mass, momentum and energy. The model is constrained by the electron density distribution derived from line-of-sight integrated pB measurements carried out with LASCO and Mark III/Spartan 201 as well as from Ulysses in situ measurements. In their model the solar magnetic field geometry is determined by coronal observations, the field strength by in situ measurements of the radial component of the magnetic field, and magnetic flux conservation. In order to match the model results with coronal and in situ densities, the authors have to assume a more than radial expansion. In their study they find that the expansion is extremely rapid below 2 to 3 R_S , even more rapid than in the Kopp and Holzer (1976) geometry, and the expansion is basically finished before the flow reaches 2.5 R_S . They also find that the divergence varies as a function of latitude.

Using a variety of different models and observations Gibson *et al.* (1999, this volume; see also Gibson *et al.* 1997; Gibson and Charbonneau 1998, and references therein) construct a 3-D coronal magnetic field that matches the observed white light features. Comparing the predictions of different models to observed plasma parameters they identify the model assumptions that best fit the data. Their conclusion is that to fit model predictions with observation, a more than radial expansion has to exist in the inner corona. Using observations from MDI, EIT and LASCO from the time interval surrounding the large coronal hole extension (August 1996) to model the coronal magnetic field, Clegg *et al.* (1999a, b) show that the open magnetic fields over the northern polar hole are highly divergent which is made possible because the polar crown arcade is asymmetric to the surface normal allowing a shallow open field angle for the polar coronal hole.

4. Origin and Acceleration of the Slow Solar Wind

Dahlburg *et al.* (1998, 1999) consider a plasma element assumed to consist of a neutral sheet embedded in a magnetic wake and situated beyond the underlying cusp region of the streamer. Studying the effect of 2-D disturbances on this wake, and the effect of 3-D disturbances on the subsequently developing 2-D equilibrium,

they find that the wake configuration can explain (1) the development of plasmoids, (2) the acceleration of the slow solar wind which in this case happens due to a transfer of kinetic energy from the fast solar wind regions outside the wake to the central regions of the wake, and (3) the development of turbulence which finally limits the further acceleration of the slow wind and also leads to the destruction of the plasmoids. In this model the slow solar wind accelerates from the regions on top of the streamer cusp.

Wang *et al.* (1998) consider the origin and acceleration of the density irregularities, plasma “blobs,” detected by LASCO (Sheeley *et al.* 1997). These blobs, characterized by low speeds and continuously emitted from the tip of the helmet streamer at about 3 to 4 R_S , are assumed to be “leaves in the wind” that move outward with speeds similar to the more homogeneous plasma surrounding them. The blobs are then the visible manifestation of a reconnection process. During this process a closed field line of the helmet streamer reconnects with an adjacent open field line. Plasma trapped along the leg of the helmet streamer is ejected as a result of this foot point exchange. The plasma blobs and the surrounding plasma are thus representative of closed magnetic field plasma. The plasma blobs observed with LASCO start at 3 to 4 R_S with speeds ranging from 0 to 100 km s⁻¹, and accelerate to speeds of 250 to 400 km s⁻¹. In the Wang *et al.* (1998) model the plasma sheet is made up by continuous reconnection events which is consistent with the filamentary structure of that region. Wang *et al.* (1998) notice that during solar minimum the densest and slowest solar wind at 1 AU is concentrated around the interplanetary sector boundary. The width of that region is about 3 degrees, similar to the width of the plasma sheet in the corona. Slow solar wind plasma with speeds below 500 km s⁻¹, on the other hand, can be found in a region much wider than that, 20 to 30 degrees. They conclude that the densest/slowest solar wind component originates from within the helmet streamer as described above, but that the much more common slow solar wind component must originate from a region outside the helmet streamers, most likely the region just inside the coronal hole boundaries (Wang and Sheeley 1990).

Srivastava *et al.* (1999, this volume) presented a study of gradual CMEs observed by the LASCO C1 coronagraph. These balloon type events originate at about 1.5 R_S and cause a change in the nearby large scale streamers. The velocity profiles of these events are very similar to the ones observed for the density blobs described above. They start with speeds less than 100 km s⁻¹, often less than 50 km s⁻¹, and their terminal speeds which they reach beyond 20 R_S range from 300 to 400 km s⁻¹. The maximum acceleration occurs between 4 to 6 R_S . Since the magnitude of the speed of these events is comparable to that of the plasma blobs, the authors conclude that slowly evolving balloon type events drift away in the slow solar wind.

A theoretical model by Noci *et al.* (1997) suggests that the slow solar wind originates in the unipolar regions which exists between streamers close to the coronal base. They argue that as the plasma flows upwards between the loops, it traverses a region where the flux tubes widen. As the plasma continues to flow

upwards, the loops start to merge into the narrow region of the current sheets, and the flux tubes become narrower and narrower with height. They conclude that it is the narrowing of the flux tubes that pushes the point where the flow becomes supersonic upwards, causes the wind to slow down below that point, and also determines the depletion of the abundances of heavy ions as observed with UVCS (Raymond *et al.* 1997).

Using a tomographic method to analyze IPS data Kojima *et al.* (1998) were able to produce synoptic velocity maps of the solar wind as a function of Carrington longitude. Identifying the regions with the lowest flow speeds, they traced these streams back to a source surface located at $2.5 R_S$ assuming constant and radial flows. To make the connection between the source surface and the corona, magnetic field lines were calculated from a potential field model (Hakamada 1999) using magnetic field data from Kitt Peak National Observatory. The magnetic data, together with observations of the Fe XIV line intensity measurements from Sacramento Peak National observatory, were then used to identify active region loops. Tracing the flow back from the source surface to the corona along the field lines of the model, they were able to show that at least some of the lowest speed streams originate in the unipolar region between two or more closed loop structures, which is in agreement with the theoretical argument made by Noci *et al.* (1997). Kojima *et al.* (1999, this volume) also found that these regions have very high super radial expansion factors, of the order of 2000 (defined as the ratio between the region that the stream occupies in interplanetary space, and the region on the solar surface from where it originates).

5. Concluding Remarks

The discussions and presentations described above clearly showed that a lot of progress has been made due to SOHO observations, and coordinated efforts between ground based and SOHO observations, as well as between observations and theoretical approaches. Partial answers were found during the workshop to some of the important questions presented in the introduction. On the other hand, it was also quite evident that a lot of work remains still to be done. In the future, progress could be made by trying to understand the discrepancies between different observational approaches, such as between the line observations used to determine solar wind flow speeds in the upper chromosphere/transition region. In addition to these observational efforts more detailed theoretical studies will also have to be carried out. The interaction region between the high and low speed solar wind is highly complex, even more so than the rest of the solar wind. In this region shear flows, turbulence, instabilities and wave-particle interactions will almost certainly play significant roles. In order to gain a basic understanding of the plasma in the interaction region emphasis should be placed on theoretical studies investigating these fundamental physical processes.

Acknowledgements

This work is supported by the National Aeronautics and Space Administration under grants NAG5-6192 and NAG5-7055 to the Smithsonian Astrophysical Observatory.

References

- Asai, K., Kojima, M., Tokumaru, M., Yokobe, A., Jackson, B. V., Hick, P. L., and Manoharan, P. K.: 1998, *J. Geophys. Res.*, **103**, 1991.
- Balogh, A., Beek, T. J., Forsyth, R. J., Hedgecock, P. C., Marquedant, R. J., Smith, E. J., Southwood, D. J., and Tsurutani, B. T.: 1992, *Astron. Astrophys. Suppl.*, bf 92, 221.
- Bame, S. J., McComas, D. J., Barraclough, B. L., Phillips, J. L., Sofaly, K. J., Chavez, J. C., Goldstein, B. E., and Sakurai, R. K.: 1992, *Astron. Astrophys. Suppl.*, **92**, 237.
- Bertaux, J. L., Quemerais, E., Lallement, R., Kyrölä, E., Schmidt, W., Summanen, T., Goutail, J. P., Berthe, M., Costa, J., and Holzer, T. E.: 1997, *Sol. Phys.*, **175**, 737.
- Bertaux, J. L., Kyrölä, E., Quemerais, E., Lallement, R., Schmidt, W., Summanen, T., Costa, J., and Makinen, T.: 1999, this volume.
- Bromage, B. J. I., Clegg, J. R., and Thompson, B.: 1999, this volume.
- Bromage, B. J. I., Del Zanna, G., DeForest, C., Thompson, B., and Clegg, J. R.: 1997, in *Proceedings of Fifth SOHO Workshop*, ESA Publication SP-404, p. 241.
- Brueckner, G. E., et al.: 1995, *Sol. Phys.*, **162**, 357.
- Burlaga, L. F.: 1999, this volume.
- Clegg, J. R., Bromage, B. J. I., and Browning, P. K.: 1999a, *J. Geophys. Res.*, submitted.
- Clegg, J. R., Browning, P. K., and Bromage, B. J. I.: 1999b: this volume.
- Dahlburg, R. B., and Karpen, J. T.: 1999, this volume.
- Dahlburg, R. B., Karpen, J. T., Einaudi, G., and Boncinelli, P.: 1998, in *ESA Proceedings SP-421*, p. 199.
- Del Zanna, G., and Bromage, B. J. I.: 1999, this volume.
- Dessler, A. J., and Fejer, J. A.: 1963, *Planet. Space Sci.*, **11**, 505.
- Dobrzycka, D., et al.: 1999, *J. Geophys. Res.*, in press.
- Dupree, A. K., Sasselov, D. D., and Keener, S. R.: 1993, *Bulletin A.A.S.*, **25**, 1321.
- Dupree, A. K., Penn, M. J., and Jones, H. P.: 1996, *Ap. J. Lett.*, **467**, L121.
- Fisk, L., et al.: 1999, this volume.
- Frazin, R. A., Modigliani, A., Ciaravella, A., Dennis, E., Fineschi, S., Gardner, L. D., Michels, J., O'Neil, R., Raymond, J. C., Noci, G., and Kohl, J. L.: 1999, this volume.
- Gibson, S. E.: 1999, this volume.
- Gibson, S. E., and Charbonneau, P.: 1998, *J. Geophys. Res.*, **103**, 14511.
- Gibson, S. E., Bagenal, F., Biesecker, D., Guhathakurta, M., Hoecksema, J. T., and Thompson, B. J.: 1997, in *Proceedings of the Fifth SOHO Workshop*, SP-404, p. 407.
- Gloeckler, G.: 1998, *Space Sci. Rev.*, in press.
- Gosling, J. T., Asbridge, J. R., Bame, S. J., and Feldman, W. C.: 1978, *J. Geophys. Res.*, **83**, 1401.
- Grall, R. R., et al.: 1996, *Nature*, **379**, 429.
- Guhathakurta, M., and Sittler, E. C., Jr.: 1999, this volume.
- Hakamada, K.: 1999, *Sol. Phys.*, in press.
- Harrison, R. A., et al.: 1995, *Sol. Phys.*, **162**, 233.
- Harvey, K. L.: 1999, this volume.
- Hassler, D. M., Dammasch, I. E., Lemaire, P., Warren, H., and Wilhelm, K.: 1999, this volume.
- Hassler, D. M., Dammasch, I. E., Lemaire, P., Brekke, P., Curdt, W., Mason, H. E., Vial, J.-C., and Wilhelm, K.: 1999, *Science*, in press.
- Jones, H. P., Andretta, V., and Penn, M. J.: 1999, this volume.
- Kojima, M., Fujiki, K., Ohmi, T., Tokumaru, M., and Yokobe, A.: 1999, this volume.
- Kojima, M., Tokumaru, M., Watanabe, H., Yokobe, A., Asai, K., Jackson, B. V., and Hick, P. L.: 1998, *J. Geophys. Res.*, **103**, 1981.

- Kohl, J. L., *et al.*: 1995, *Sol. Phys.*, **162**, 313.
- Kohl, J. L., Gardner, L. D., Strachan, L., and Hassler, D. M.: 1994, *Space Sci. Rev.*, **70**, 253.
- Kopp, R. A., and Holzer, T. E.: 1976, *Sol. Phys.*, **49**, 43.
- Koutchmy, S., Lamy, P., Stellmacher, G., Koutchmy, O., Dzubenco, N. I., Ivanchuk, V. I., Popov, O. S., Rubo, G. A., and Vsekhsvjatsky, S. K.: 1978, *Astron. Astrophys.*, **69**, 35.
- Krieger, A. S., Timothy, A. F., and Roelof, E. C.: 1973, *Sol. Phys.*, **29**, 505.
- Kyrölä, E., Summanen, T., Schmidt, W., Makinen, T., Bertaux, J. L., Lallement, R., Quemerais, E., and Costa, J.: 1998, *J. Geophys. Res.*, **103**, 14,523.
- Mariani, F., and Neubauer, M.: 1990, in *Physics of the Inner Heliosphere, I*, eds. R. Schwenn and E. Marsch, (Springer Verlag: Berlin, Heidelberg, New York), p. 183.
- McComas, D. J., Riley, P., Gosling, J. T., Balogh, A., and Forsyth, R.: 1998, *J. Geophys. Res.*, **103**, 1955.
- Miralles, M. P., Strachan, L., Gardner, L. D., Smith, P. L., Kohl, J. L., Guhathakurta, M., and Fisher, R. R.: 1999, this volume.
- Mitchell, D. G., Roelof, E. C., and Wolfe, J. H.: 1981, *J. Geophys. Res.*, **86**, 165.
- Munro, R. H., and Jackson, B. V.: 1977, *Astrophys. J.*, **213**, 874.
- Noci, G., *et al.*: 1997, in *Proceedings of Fifth SOHO Workshop*, ESA Publication SP-404, p. 75.
- Raymond, J. C., *et al.*: 1997, *Sol. Phys.*, **175**, 645.
- Rosenbauer, H., Schwenn, R., Marsch, E., Meyer, B., Miggenrieder, H., Montgomery, M., Mühlhäuser, K. H., Philipp, W., Voges, W., and Zink, S. K.: 1977, *J. Geophys. Res.*, **42**, 561.
- Sasselov, D. D., and Lester, J. B.: 1994, *Astrophys. J.*, **423**, 777.
- Schwenn, R., Montgomery, M. D., Rosenbauer, H., Miggenrieder, H., Muhlhauser, K. H., Bame, S. J., Feldman, W. C., and Hansen, R. T.: 1978, *J. Geophys. Res.*, **83**, 1011.
- Schwenn, R., Inhester, B., Podlipink, B., Srivastava, N., Stenborg, G.: 1999, this volume.
- Schwenn, R.: 1990, in *Physics of the Inner Heliosphere, I*, eds. R. Schwenn and E. Marsch, (Springer Verlag: Berlin, Heidelberg, New York), p. 99.
- Sheeley, N. R., Jr., *et al.*: 1997, *Astrophys. J.*, **484**, 472.
- Sittler, E., and Guhathakurta, M.: 1999, *Astrophys. J.*, in press.
- Srivastava, N., Schwenn, R., Inhester, B., Stenborg, G., and Podlipink, B.: 1999, this volume.
- Strachan, L., Gardner, L. D., Smith, P. L., and Kohl, J.: 1997, in *Robotic Exploration Close to the Sun*, AIP Conference Proceedings, ed. S. R. Habbal, (Woodbury, NY: AIP), p. 113.
- Strachan, L., Kohl, J. L., Weiser, H., Withbroe, G. L., and Munro, R. H.: 1993, *Astrophys. J.*, **412**, 410.
- Wang, Y.-M., Sheeley, N. R., Jr., Walter, J. H., Brueckner, G. E., Howard, G. E., Michels, D. J., Lamy, P. L., Schwenn, R., and Simenett, G. M.: 1998, *J. Geophys. Res. Lett.*, **498**, L165.
- Wang, Y.-M., and Sheeley, N. R., Jr.: 1990, *Astrophys. J.*, **355**, 726.
- Warren, H. P., Mariska, J. T., and Wilhelm, K.: 1997, *Astrophys. J. Lett.*, **490**, L187.
- Woo, R., and Habbal, S. R.: 1999, *Astrophys. J. Lett.*, **510**, L69.
- Zangrilli, L., Nicolosi, P., and Poletto, G.: 1999, this volume.
- Zurbuchen, T. H., Hefti, S., Fisk, L. A., Gloeckler, G., Schwadron, N. A., and von Steiger, R.: 1999, this volume.

Address for correspondence: Ruth Esser, Harvard-Smithsonian Center for Astrophysics, 60 Garden Street, Mail Stop 50, Cambridge, MA 02138, USA. Email: Resser@cfa.harvard.edu

WORKING GROUP 4 REPORT: COMPOSITION AND ELEMENTAL ABUNDANCE VARIATIONS IN THE SOLAR ATMOSPHERE AND SOLAR WIND

HELEN E. MASON

Department of Applied Mathematics and Theoretical Physics, Silver Street, Cambridge CB3 9EW, UK

PETER BOCHSLER *

Space Physics Group, Department of Physics, University of Maryland, College Park, MD 20742, USA

Abstract. This paper contains a summary of the topics treated in the working group on abundance variations in the solar atmosphere and in the solar wind. The FIP bias (overabundance of particles with low First Ionization Potentials over photospheric abundances) in coronal holes and coronal hole associated solar wind amounts to values between 1 and 2. The FIP bias in the slow solar wind is typically a factor 4, consistent with optical observations in streamers. In order to distinguish between different theoretical models which make an attempt to explain the FIP bias, some observable parameters must be provided. Unfortunately, many models are deficient in this respect. In addition to FIP fractionation, gravitational settling of heavy elements has been found in the core of long lived streamers. The so-called electron ‘freeze in’ temperatures derived from in situ observed ionization states of minor ions in the fast wind are significantly higher than the electron temperatures derived from diagnostic line ratios observed in polar coronal holes. The distinction between conditions in plumes and interplume lanes needs to be further investigated. The ‘freeze in’ temperatures for the slow solar wind are consistent with the electron temperatures derived for streamers.

Key words: element abundances, in situ observations, UV data

Abbreviations: SOHO: Solar and Heliospheric Observatory, FIP: First Ionization Potential

1. Introduction

The discussions in this working group focused on physical parameters and elemental abundance variations in high speed solar wind, coronal holes (plumes and interplumes), the slow solar wind, streamers and coronal mass ejections. The key issue addressed was the consistency between in situ measurements of the solar wind and optical measurements of the solar atmosphere. We assessed what had been learnt so far from SOHO and other space missions, and we carefully considered the underlying assumptions of various analyses. An illustration for the important differences between fast and slow wind has been provided by Ulysses/SWICS (Geiss *et al.* 1995). Three key parameters shown in this superposed epoch plot (Figure 1) of daily averages characterize the two principal solar wind flow regimes, the Mg/O abundance ratio which is established in the chromosphere, the O⁷⁺/O⁶⁺ freeze-in temperature which is fixed in the corona and the helium bulk speed which is the least conservative property.

* Also: Physikalisches Institut, University of Bern, CH-3012 Bern, Switzerland

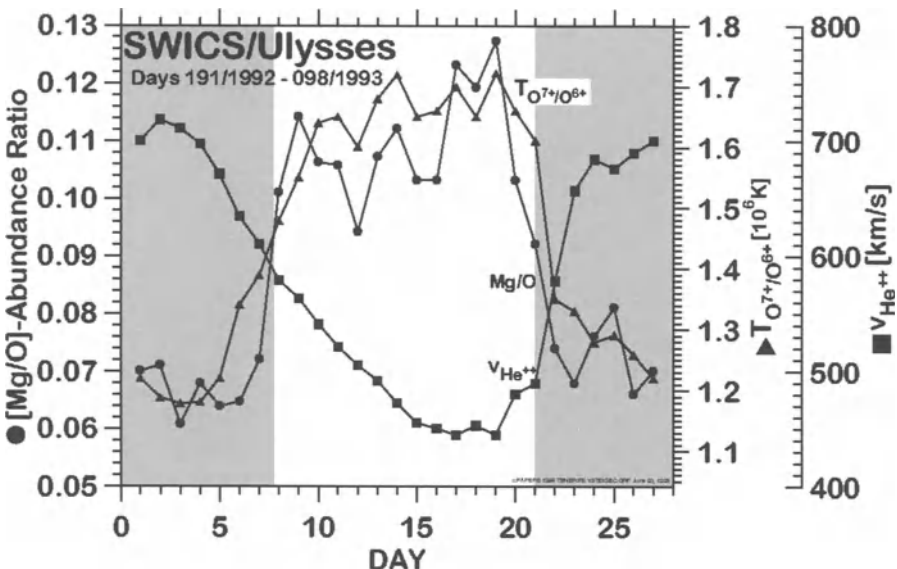


Figure 1. Variations of the Mg/O abundance ratio, the O^{7+}/O^{6+} freeze-in temperature and the helium speed among two different solar wind regimes (adapted from Geiss *et al.* 1995)

The Mg/O abundance ratio demonstrates the variation of the First Ionization Potential (FIP) bias. The O^{7+}/O^{6+} freeze in temperature varies from 1.2×10^6 K to 1.7×10^6 K, averaging at around 1.5×10^6 K for the slow wind and is more steady at 1.2×10^6 K in the fast wind. While the FIP bias is generally assumed to be established in the chromosphere, the freeze-in temperature is imprinted high in the corona at distances of typically $1 R_\odot$, and the velocity and other kinetic properties of minor species are significantly affected by wave-particle interactions and stream-stream interactions throughout the heliosphere. Yet, despite these differences in physical processes and despite their very different sites of operation, there is a strong correlation between the corresponding phenomena, at least on large scales.

2. Coronal Temperatures

2.1. STREAMERS AND SLOW SOLAR WIND

Fludra *et al.* (1998, 1999) used SOHO/CDS spectra to compare the temperature and electron density distribution above the limb in the equatorial region and polar coronal holes. The temperatures which they found for the equatorial regions ($1.1 - 1.4 \times 10^6$ K) are given in Table I together with a corresponding electron density decrease with respect to altitude in Table II. These temperatures at low latitudes are

consistent with the freeze-in temperatures ($1.2\text{--}1.7 \times 10^6$ K) reported from in situ measurements with Ulysses/SWICS and SOHO/CELIAS in slow solar wind (e.g., Geiss *et al.* 1995; Aellig 1998)

2.2. SUPRATHERMAL ELECTRONS IN STREAMERS

Aellig (1998) has simulated the freeze in temperatures of oxygen and iron ions superposing core and halo velocity distributions for the electrons. While recombination rates are generally rather insensitive to temperature variations, ionization rates strongly depend on temperatures. For example, a species such as O⁶⁺ which has an ionization potential of 739 eV is sensitive to the presence of suprathermal halo electrons. On the other hand, the ionic abundances of species from Fe⁹⁺ to Fe¹¹⁺ with much lower ionization potentials are insensitive to suprathermals. The authors use this fact to show that a core of cold electrons when combined with a halo of hot electrons (Figure 2) will produce quite different charge state combinations of oxygen and iron ions than a pure core distribution. For the streamer observed with CELIAS/CTOF and analyzed by Aellig (1998), consistency could be found between the freeze in temperature of O^{7+}/O⁶⁺ and Fe^{10+}/Fe⁹⁺ with one single, core Maxwellian velocity distribution. It should be noted that the oxygen temperatures in Figure 2 are smaller than the canonical values quoted more than a decade ago (2.1×10^6 K). The reason for this is two-fold: advances in measurement techniques which do not just look at the E/Q spectra and advances in atomic data, with improved ionization balance calculations.}}

2.3. CORONAL MASS EJECTIONS

The temperature of coronal mass ejecta observed with UVCS (Ciaravella *et al.* 1999), was found to lie in a broad range around 1.6×10^5 K (see Table I). Figure 3 shows emission measures (in units of cm⁻⁵) as function of the temperature for various spectral lines observed with UVCS at a heliocentric distance of $1.7 R_\odot$ during the CME, which occurred on the North West limb on 11 December 1997.

Ipavich presented a poster showing the charge state distribution of iron ions in the 3 May 1998 CME-ejecta as observed with the ACE/SWICS instrument. A very wide distribution was observed combining at the same time strongly charged species such as Fe¹⁶⁺, indicative of coronal electron temperatures of 3×10^6 K, and weakly ionized iron, i.e., Fe²⁺–Fe⁸⁺. Such exotic cases should not be taken as evidence for a “mixed” flow of cold and hot plasma through one flow tube. Probably, a complicated thermal history, involving plasmoids or other protective magnetic bubbles (e.g., Neukomm and Bochsler 1996) must be invoked to explain this observation.

Table I
Coronal Temperatures

| Instrument Method | Distance from Solar Centre (R_{\odot}) | Temperature (10^6 K) | | | | Ref. | |
|--|--|-------------------------|-----------|-------|-----------------|------|-----|
| | | Quiet Sun | CME | Plume | Inter- plume | | |
| SUMER: Mg IX | 1.03 | | | 0.73 | 0.78 | W98 | |
| | 1.1 | 2.0 | | | | | |
| | 1.30 | | | 0.58 | 0.88 | | |
| | 1.60 | | | 0.33 | | | |
| CDS: Si XII/Mg X Mg X/Mg IX | 1.0 | 1.1 | | | | 0.75 | F98 |
| | 1.2 | 1.4 | | | | 0.9 | |
| | | | | | | | |
| CDS/SUMER: O VI | 1.0 | | | | 0.85 | D98 | |
| | 1.15 | | | | 1.0 | | |
| | 1.3 | | | | 0.4 | | |
| CDS: DEM | on disk | 1.0 | | 0.76 | 0.8 | DZ98 | |
| CDS: | 1.0 | | | 1.0 | 1.0 | Y99 | |
| UVCS DEM | 1.7 | | 0.06–0.30 | | | C99 | |
| IN SITU Fe ⁹⁺ –Fe ¹²⁺ (Halo/core $\leq 15\%$) | | 1.2–1.7 | | | | A98 | |
| IN SITU Fe ²⁺ –Fe ¹⁶⁺ | | | 0.1–3.0 | | | I99 | |
| IN SITU O ⁷⁺ /O ⁶⁺ Fe ⁹⁺ –Fe ¹²⁺ | | | | | 1.2 | G95 | |

References: A98: Aellig (1998); C99: Ciaravella *et al.* (1999); D98: David *et al.* (1998); DZ98: Del Zanna and Bromage (1998, 1999); F98: Fludra *et al.* (1998, 1999); G95: Geiss *et al.* (1995); I99: Ipavich *et al.* (1999); W98: Wilhelm *et al.* (1998); Y99: Young *et al.* (1999).

2.4. CORONAL HOLES, POLAR PLUMES, AND FAST SOLAR WIND

Wilhelm reported on some measurements of electron temperature and electron density above a polar coronal hole (Wilhelm *et al.* 1998) obtained with SOHO/SUMER.

Table II
Coronal Electron Densities

| Instrument: method | Distance from Sun Center (R_{\odot}) | Electron Density (10^8 cm^{-3}) | | | | Ref. |
|-----------------------|--|---|-------|-----------------|-----------------|------|
| | | Quiet Sun | Plume | Inter- plume | Coronal hole | |
| SUMER: Si VIII | 1.03 | | 1.3 | 0.8 | | W98 |
| | 1.1 | 0.6 | | | | |
| | 1.30 | | 0.2 | 0.07 | | |
| | 1.60 | | 0.1 | | | |
| CDS: Si IX | 1.0 | 0.5 | | | 2.0 | F98 |
| | 1.1 | | | | 0.6 | |
| | 1.15 | 1.0 | | | | |
| CDS: Si IX | on disk | | | | 2.0 | DZ98 |

References: F98: Fludra *et al.* (1998, 1999); DZ98: Del Zanna and Bromage (1998, 1999); W98: Wilhelm *et al.* (1998).

These were obtained during a successful roll manoeuvre of SOHO on 3 September 1997, placing the SUMER slit in the east-west direction. It was possible to step the slit off limb and to distinguish between a plume and an inter-plume lane. The Si VIII diagnostic line ratios were used to obtain electron density values shown in Table II, and the Mg IX line ratios gave electron temperature values shown in Table I. The plumes were found to be significantly cooler than the inter-plume lanes. These values can be compared to the temperature of $2 \times 10^6 \text{ K}$ and density of $6 \times 10^7 \text{ cm}^{-3}$ obtained from SUMER in the quiet Sun at $1.1 R_{\odot}$. The electron temperature in polar coronal holes as a function of height above the limb has been derived by David *et al.* (1998) from SOHO/CDS and SOHO/SUMER observations using diagnostic line ratios from O VI (Figure 4 and Table I). These temperatures are consistent with SUMER Mg IX line ratios.

Del Zanna presented results from a differential emission measure analysis of SOHO/CDS spectra for the quiet Sun, a coronal hole and a polar plume. His results are also shown in Table I and Table II. They are consistent with the electron temperature derived for the coronal hole regions by David *et al.* (1998) and by Bodmer and Wilhelm (1999). The coronal hole electron number densities were found to be $2 \times 10^8 \text{ cm}^{-3}$, a factor of 2–3 lower than the quiet Sun values. Results obtained by Fludra *et al.* (1998) with SOHO/CDS are also given in Table I and Table II. They found that the temperature and electron number density distributions stayed the same for the north and south coronal holes over the time period of

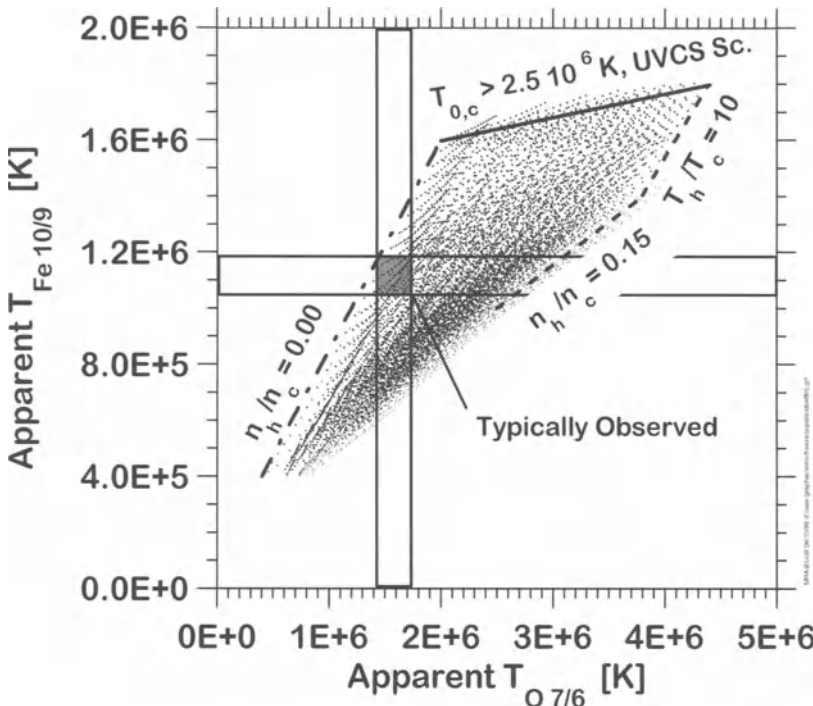


Figure 2. Comparison of typically observed (full square) and simulated freeze-in temperatures in the slow solar wind. The simulations have been performed with varying admixtures of hot halo electrons. Depending on the amount of hot electrons, the apparent O^{+7}/O^{+6} freeze-in temperature increases whereas the apparent Fe^{10+}/Fe^{9+} temperature remains essentially unaltered (from Aellig 1998). $T_{o,c}$ denotes the base temperature which has been deduced by extrapolating backwards from the in situ freeze in temperature determinations, according to given power laws. The method used, based on UVCS observations, is described in the paper by Aellig. $T_{o,c}$ is greater than 2.5×10^6 K for all points above the line shown.

observation (nine months). The coronal hole results above the limb are dominated by plume material. Two bright plumes have been analyzed and these show a marked drop in temperature and an increase in electron number density. The darkest areas, possibly free from plumes, selected inside the coronal holes, on the disk, had a temperature of 8.2×10^5 K and an electron density of about $1 \times 10^8 \text{ cm}^{-3}$

Young *et al.* (1999) also studied a polar coronal hole region with SOHO/CDS. They found a sharply peaked emission measure distribution for both the coronal hole background and a polar plume at around $1.0\text{--}1.1 \times 10^6$ K; see Table I. The temperature was found to rise with height in the coronal hole background, but stay constant in the plume out to about $1'$ above the limb.

The freeze in temperature from in situ measurements of O^{+7}/O^{+6} and Fe^{10+}/Fe^{9+} in the fast solar wind above the coronal hole is found to be 1.2×10^6 K (Geiss *et al.* 1995), given in Table I. This is significantly higher than the electron temperatures derived by Wilhelm *et al.* (1998) and David *et al.* (1998), which optical SOHO

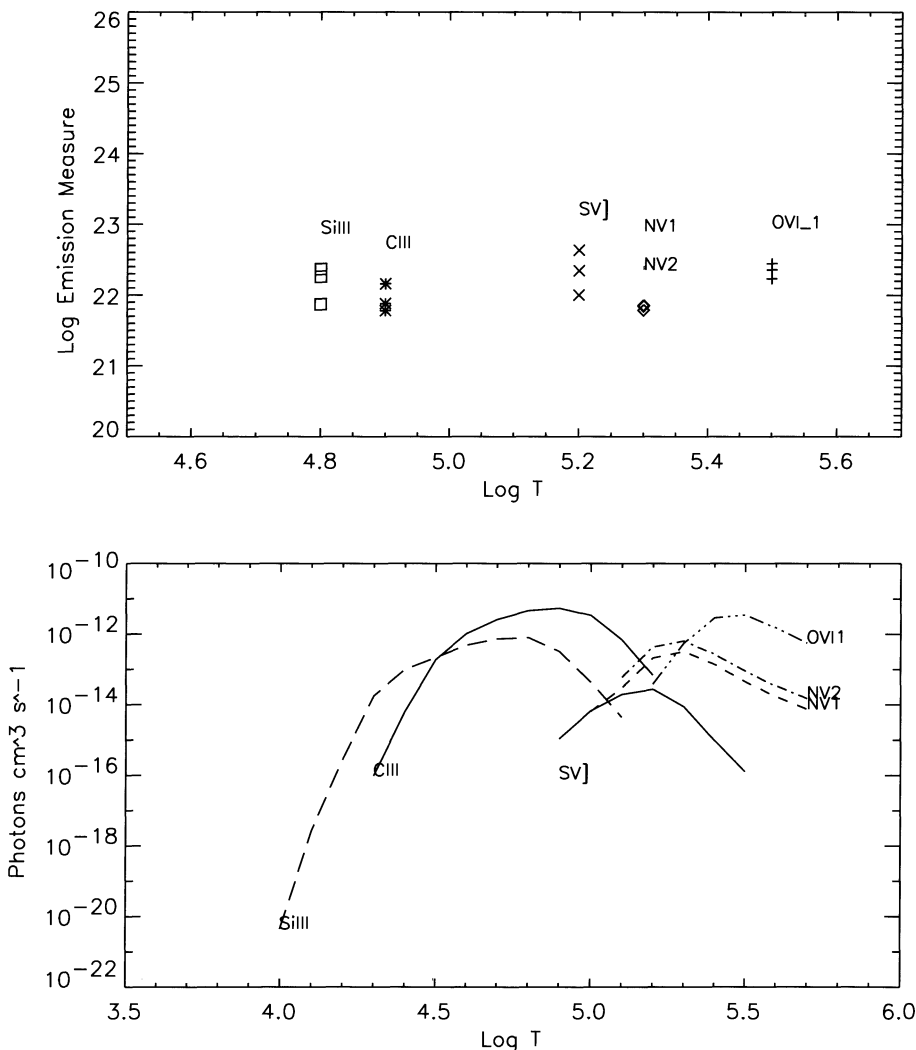


Figure 3. Emission measure as a function of the temperature derived from UVCS observations, for the CME which occurred on the north west limb on 11 December 1997 (taken from Ciaravella *et al.* 1999). The three symbols for each line correspond to three different knots of plasma ejected during the prominence eruption which caused the CME. In the lower panel the radiative losses as function of the temperature are plotted.

observations indicate. The type of analysis described in Aellig (1998) might help to resolve the discrepancy in temperature (electron and freeze in) for the fast solar wind.

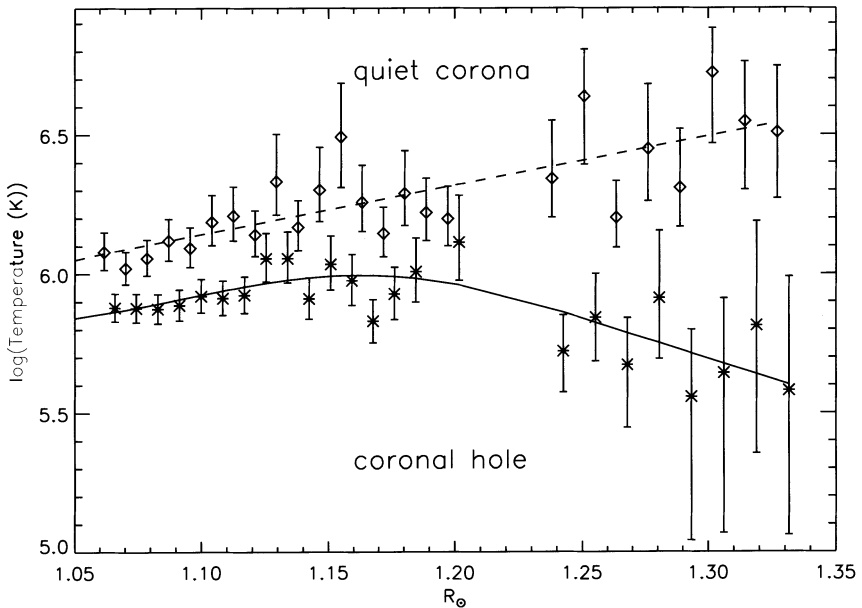


Figure 4. Electron temperature in the quiet corona and polar coronal hole as a function of height above the limb (taken from David *et al.* 1998)

3. FIP Effect

3.1. STREAMERS, ACTIVE REGIONS AND THE SLOW SOLAR WIND

Gabriel *et al.* (1999) presented a comparison of the oxygen to hydrogen abundance ratios, from a polar coronal hole and an equatorial closed-field region, over the range 1.05–1.3 R_{\odot} . They used a combination of SOHO/CDS, SOHO/SUMER, SOHO/LASCO and eclipse observations. They found a substantial enhancement (up to a factor 10) in the abundance of oxygen in the coronal hole region relative to the equatorial region. These authors also analyzed some iron lines, but the spread in the results was very large and somewhat inconclusive.

Feldman *et al.* (1998) have carried out a detailed analysis of the FIP bias for different solar regions using spectral emission lines from a range of ions observed with SUMER. Their results for a solar streamer are given in Figure 5. The authors deduced an overall FIP bias of 4 and attributed unrealistically small experimental uncertainties (smaller than the estimated errors in the atomic parameters used) to this value.

Wilhelm reported on SOHO/SUMER observations of the FIP effect across streamers on the east and west sides of the Sun. The FIP bias was found to range between 1–3 for the central streamer, but around 20 near the northern and southern boundaries, where the temperatures were higher. Dwivedi *et al.* (1998) studied the

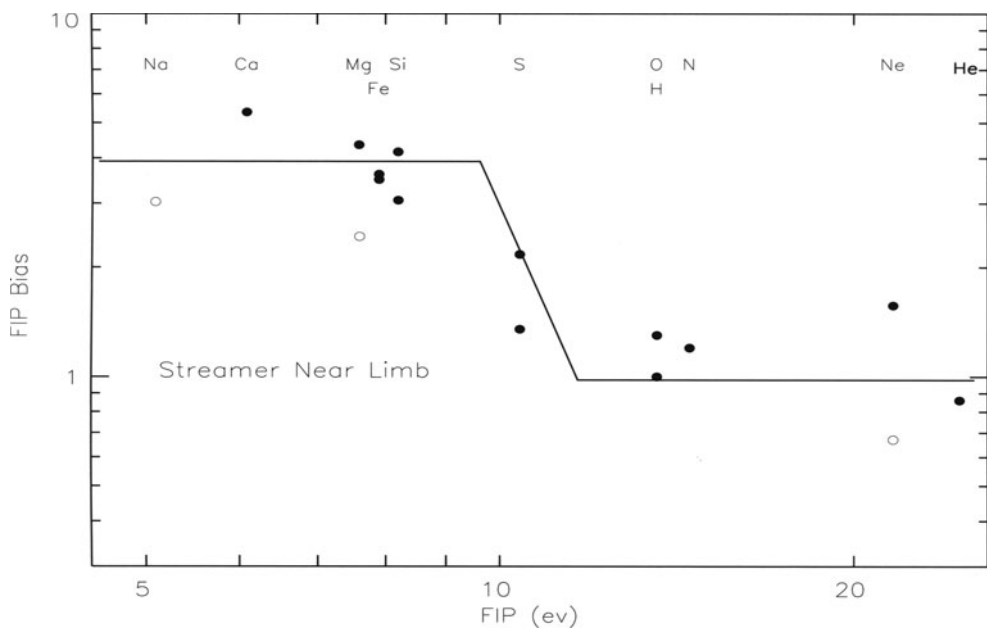


Figure 5. FIP bias versus FIP for the corona above the quiet equatorial region. Li-like Ne VIII, Na IX and Mg X are represented by open circles (taken from Feldman *et al.* 1998).

Ne VI and Mg VI lines from SOHO/SUMER in an active region on the east limb, on 20 June 1996. Since neon has a FIP of 21.6 eV and magnesium has a FIP of 7.6 eV, both line intensities exhibiting similar temperature dependences and the atomic masses differing by not more than 20%, these two elements are ideally suited and frequently used to study the FIP bias. Their SUMER measurements covered heights from 40 to 120 arcsec above the limb. They found a very high FIP bias ranging from 8 to 16, which corresponds to a significant enhancement of Mg/Ne relative to photospheric values. Their results indicated that the high FIP bias might be related to processes in the loop system above active regions, rather than to simple limb distance effects in the quiet Sun.

Young and Mason (1998) have studied the variation in the Mg/Ne abundance ratio from the SOHO/CDS observations for several different solar regions. Figure 6 illustrates their results. The emission measure curves for magnesium and neon are derived from spectral lines from the ions Ne IV–Ne VII and Mg V–Mg VIII, which cover a wide temperature range. The $T^{1.5}$ dependency of the emission measure curves has been removed. Since these emission measure curves are derived using photospheric values, the Mg/Ne FIP bias can easily be seen from these plots.

The active region brightening, thought to be a small emerging structure, shows a photospheric abundance ratio. The quiet Sun, network and cell-center show a factor around 2.0 enhancement in Mg/Ne. An active region ‘spike,’ possibly characteristic of the leg of a large, long lived, active region loop structure, shows a Mg/Ne enhancement of around a factor 10. The same Mg/Ne abundance enhancement of a ‘spike’ relative to an emerging flux region was obtained for a different active region analyzed in detail by Young and Mason (1997). The CDS results are subject to an uncertainty of a factor 2 in the relative calibration of the two wavelength bands NIS1 and NIS2.

Evidence for gravitational settling in long lived structures has been presented by Raymond *et al.* (1997, 1998) and is confirmed by Feldman *et al.* (1998). This is discussed in more detail elsewhere in this volume (Raymond 1999). That gravitational settling could affect coronal abundances had been suspected a long time ago from the in situ observations of occasionally strong helium enrichments in coronal mass ejecta with He/H up to 0.3 (Hirshberg *et al.* 1970). Recently, more detailed studies have become available with improved time and mass resolution of new particle instrumentation (Wurz *et al.* 1998; Neukomm 1998), indicating that mass dependent fractionation in low-latitude coronal mass ejecta is a fairly common phenomenon.

3.2. CORONAL HOLES AND THE FAST SOLAR WIND

The FIP bias found by Feldman *et al.* (1998) in a coronal hole (see Figure 7) is between 1 and 1.5. Del Zanna used SOHO/CDS spectra to obtain elemental abundances in the quiet Sun (cell center, network) and a coronal hole (cell center, network). He derived a differential emission measure for the distribution of plasma as a function of temperature and derived some elemental abundance ratios. The abundance ratio of Mg/Ne for the quiet Sun cell-center was found to be consistent with photospheric values and the network values were found to be slightly sub-photospheric. The lowest Mg/Ne abundance ratio was found in the coronal hole network. This was about 2.5 lower than the quiet Sun cell center and could represent the signature of the fast solar wind originating from the chromospheric network. The highest Mg/Ne ratio was found in polar plumes, which supports the idea that plumes are not the source of the fast solar wind. It seems that neon is depleted in polar plumes, while values for other elements are near photospheric. The error in this ratio is estimated at around 0.1 in the log, but this may be conservative. Problems in the analysis arise through uncertainties in the atomic data and from the calibration of CDS. Until these uncertainties can be eliminated, most weight should be given to relative changes in the ratio between different regions, rather than absolute values for the Mg/Ne ratio.

Wilhelm reported on SOHO/SUMER results for FIP bias measurements in the northern polar coronal hole (Wilhelm and Bodmer 1998; Bodmer and Wilhelm 1999). It was found that neon is less abundant relative to magnesium in the plume

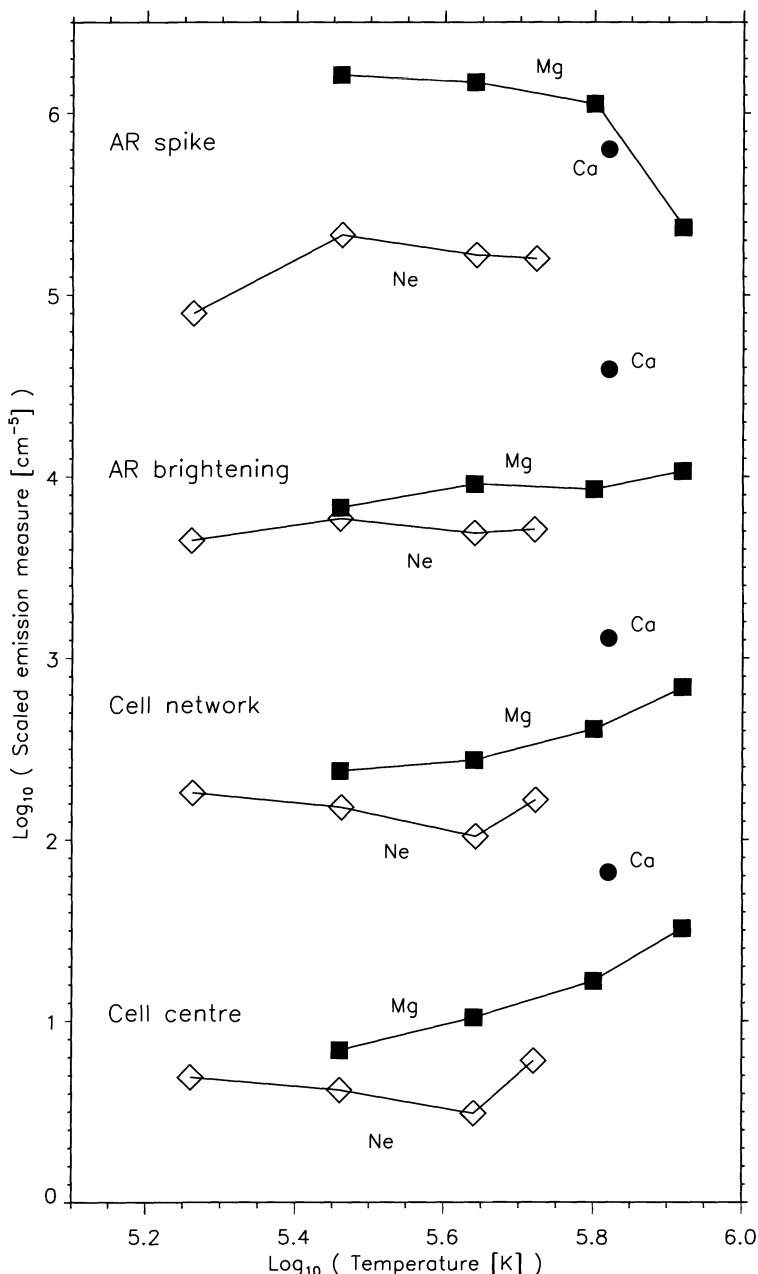


Figure 6. The emission measure curves for magnesium and neon ions (with the $T^{1.5}$ dependency removed) derived from SOHO/CDS observations. These show the relative Mg/Ne abundance ratio for various solar features. Each set of curves has been scaled to aid display. For reference, the Ne IV log emission measures (at $\log_{10} T = 5.25$) are 26.5, 27.5, 25.7 and 25.3 for the spike, brightening, network and cell-center, respectively. Also displayed are emission measures derived from Ca X. (taken from Young and Mason 1998)

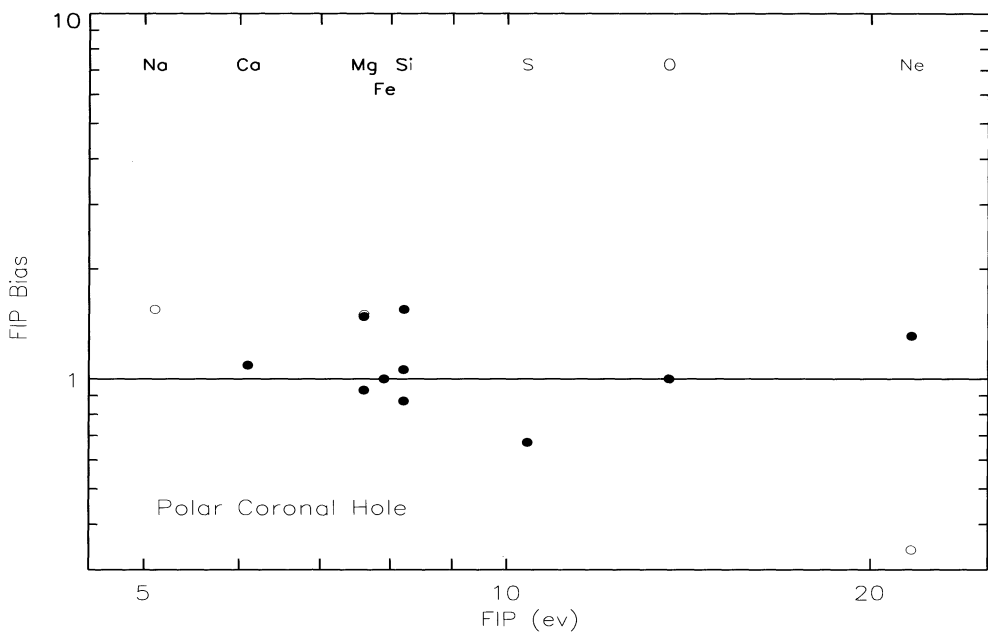


Figure 7. FIP bias versus FIP for the corona above a polar coronal hole. Li-like Ne VIII, Na IX and Mg X are represented by open circles (taken from Feldman *et al.* 1998).

compared to the inter-plume region by about a factor of 3 at heights of 35,000 and 70,000 km above the limb. There was some uncertainty in the analysis since the temperature range spanned by the neon ion (Ne VIII) did not overlap with that spanned by the magnesium ions (Mg VIII, Mg IX, Mg X). The overall result is consistent with Del Zanna's conclusions and would provide further evidence that the plumes do not contribute significant flux to the fast solar wind. Wilhelm has seen no evidence for any outward velocity flow in polar plumes from the SOHO/SUMER observations. Mason presented evidence obtained with SUMER to indicate that the fast solar wind emanates from the chromospheric network junctions (Hassler *et al.* 1999). The observation of Ne VIII line profiles (formed at 600,000 K) relative to a chromospheric line showed marked relative velocity blue shifts of up to 10 km s^{-1} at boundary intersections of the chromospheric network.

3.3. FIP THEORIES

In assessing theoretical models for generating the FIP bias, we considered certain basic questions:

1. Are Magnetic Fields essential?
2. Time dependent or stationary?

The theoretical model of the Michigan group presented by Zurbuchen (Zurbuchen *et al.* 1998) was discussed. This is based on an idea by Fisk (1996), who proposed that the footpoints of the heliospheric magnetic field in the fast wind move with the solar wind source surface. Reconnections could be a mechanism for magnetic field transport in the corona, leading to magnetic field connections of different heliospheric latitudes. Consistent with the picture presented in the introductory lecture by Axford, slow solar wind emerges from closed magnetic field regions which are continuously opened by reconnection. Hence, as has been emphasized before by McKenzie and Axford the slow solar wind is a time-dependent flow of plasma, fed from many distinct sources. The FIP bias detected in the slow solar wind would be a characteristic of long-lived closed, magnetic structures. Figure 8 illustrates the major properties of the Michigan model presented by Zurbuchen. It is based on fractionation in loops caused by wave-particle interactions. In a static loop, matter is settling depending on its mass and temperature. The typical scale height of this settling process in LTE is $\ll 500$ km. In the Michigan model, however, magneto-hydrodynamic waves are heating heavy particles in the loop which dramatically increases the scale height of selected heavy species. Since the waves can only interact with charged particles at the footpoint of the loop where matter is only partially ionized, this automatically leads to a strong enrichment of low FIP elements at large scale heights, thus, producing a FIP effect. The details are discussed in Schwadron *et al.* (1998) and Zurbuchen *et al.* (1998). Large low density loops would likely be the source of the slow solar wind. Observables would be the size and lifetime of such coronal loop structures. Since the FIP effect is tightly bound to the operation of waves in large loop-like structures, a completely different approach would have to be found to explain a weaker FIP effect in the fast, coronal-hole associated solar wind. However, the members of the working group felt that at this time the evidence for a weak FIP bias in high-speed solar wind was controversial. One application of the Michigan model to the isotopic fractionation of He is given in Zurbuchen *et al.* (1998). In fact, ACE/SWICS observations (Gloeckler *et al.* 1998) have revealed extreme enrichments of ^3He in the 3 May 1998 coronal mass ejecta. The only likely explanation for this phenomenon involves some selective heating mechanism as invoked to explain the even stronger enrichments found in impulsive flare related solar energetic particles (e.g., Fisk 1978, or Riyopoulos 1991). It remains to be seen whether this process is really able to operate at solar wind energies. In this context it is noteworthy that no enrichment of ^{26}Mg was observed at solar wind energies in the ^3He -enriched event (Wimmer-Schweingruber *et al.* 1998).

Wang presented his two-component model for the slow component of the solar wind, based on the observation of *blobs* by SOHO/LASCO (Wang *et al.* 1998). The blobs, or outward moving density inhomogeneities, are concentrated around the thin plasma layer that surrounds the heliospheric current sheet and that constitutes the outer streamer belt. They contribute only a small, fluctuating component (few

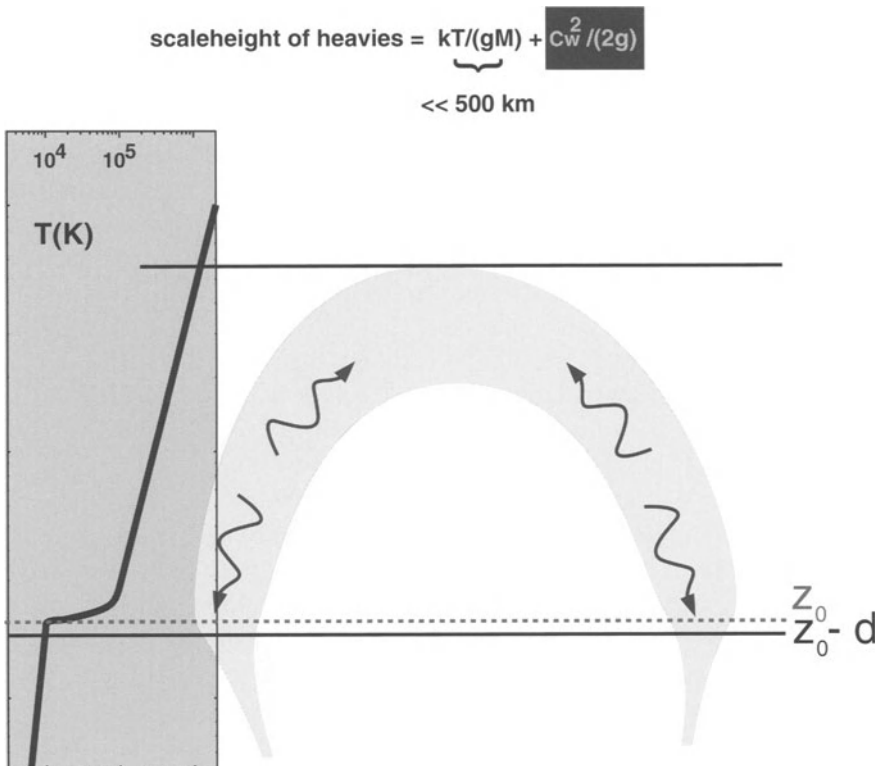


Figure 8. This figure illustrates the model proposed by Zurbuchen *et al.* (1998) for the FIP bias.

(%) to the total density within the plasma sheet. They are emitted from the elongated tips of helmet streamers at $3\text{--}4 R_\odot$ from the Sun center. Wang suggests that both the blobs and the plasma sheet represent closed-field material injected into the solar wind (slow I). They result from the footpoint exchanges between the helmet streamer loops and the neighboring open field lines. Wang *et al.* conclude that a major component of the slow solar wind (slow II) must originate outside the helmet streamers, just inside the coronal holes.

No consensus emerged about the level of sophistication required from FIP models to reproduce the available observations. Whereas some members advocated a very simple ion neutral separation mechanism involving only the first ionization potential as an ordering parameter, others felt that there was observational evidence for the requirement of more sophisticated models involving, for example First Ionization Time (FIT), FIT and diffusion (to replenish material in the chromosphere from below), time-dependent heating and evaporation of loops, including stochastic element (e.g., in a size distribution of loops). The following suggestions were made as most important tests for FIP models:

1. to predict Kr, Xe, Al elemental abundances (which do not follow the simple FIP pattern),
2. to explain why FIP-bias in IS/SW-SEP of very quickly ionizing elements (e.g., Al) is 4 and not infinity,
3. to explain why He/H in coronal hole associated solar wind is invariant at 4.5%.

3.4. CHALLENGE TO OBSERVATIONS

The working group felt that the most important issue for future observations was to produce decisive evidence for the existence of a FIP bias in coronal hole associated solar wind. Observations of quickly ionizing species (e.g., with CELIAS/MTOF) in the solar wind should soon be evaluated and related to the best available photospheric abundance ratios. Reliable comparisons between legs/cores of streamers and plumes/lanes in coronal holes should be produced for a standardized set of elements with high precision photospheric and solar wind abundance ratios.

4. Summary

A lot of questions were raised in our working group, to which the answers were not obvious. We decided to draw up a list of action items for future work. These are listed below.

1. Resolve the apparent observational discrepancy between electron temperatures inferred from diagnostic line ratios in coronal holes and in-situ minor ion charge state distributions in coronal hole associated solar wind flows.
2. Assess the role of superthermal (halo) electrons in ionizing minor species in the coronal hole type solar wind.
3. Combine outflow speeds near $1 R_{\odot}$ (and electron densities) to model charge state distributions at coronal hole boundaries.
4. Is there any FIP bias in coronal hole abundances and coronal hole associated wind?
5. Origin of low-speed solar wind (blobs released from closed structures, boundary of closed loops).
6. Role of plumes versus lanes in coronal hole associated solar wind.
7. Joint observations on ‘standard’ solar plumes.
8. Combine ‘in situ’ particle data with all optical observations on stable streamer structure which prevailed during the first half of 1996.
9. Helium abundance.

5. Acknowledgements

We would like to thank all the members of Working Group 4 for their active participation, in particular Peter Smith, John Raymond and Fred Ipavich. We thank

Peter Young for help in production of the manuscript. PB acknowledges the support of the Swiss National Science Foundation and the Space Physics Group at the University of Maryland. HEM acknowledges the financial support of the UK-PPARC.

References

- Aellig, M. R.: 1998, 'Solar wind iron freeze-in temperatures and fluxes measured with SOHO/CELIAS/CTOF,' Thesis, University of Bern.
- Bodmer, R., and Wilhelm, K.: 1999, 'Ne/Mg ratios above a polar coronal hole from UV/EUV observations by SUMER/SOHO,' *SOHO-7 Workshop*, in press.
- Ciaravella, A., Raymond, J. C., Thompson, B., Li, J., O'Neal, R., Kohl, J., and Noci, G.: 1999, 'Physical and dynamical parameters of a CME observed with SOHO,' *SOHO-7 Workshop*, in press.
- David, C., Gabriel, A. H., Bely-Dubau, F., Fludra, A., Lemaire, P., and Wilhelm, K.: 1998, 'Measurement of the electron temperature gradient in a solar coronal hole,' *Astron. Astrophys.*, **336**, L90.
- Del Zanna, G., and Bromage, B. J. I.: 1998, 'The elephant's trunk: spectroscopic diagnostics applied to SOHO/CDS observations of the August 1996 equatorial coronal hole,' *J. Geophys. Res.*, in press.
- Del Zanna, G., and Bromage, B. J. I.: 1999, 'Characterisation of solar coronal holes and plumes using spectroscopic diagnostic techniques applied to SOHO/CDS observations,' *SOHO-7 Workshop*, in press.
- Dwivedi, B. N., Curdt, W., and Wilhelm, K.: 1998, 'Analysis of EUV off-limb spectra obtained with SUMER/SOHO - Ne VI/Mg VI emission lines,' *Astrophys. J.*, submitted.
- Feldman, U., Schuhle, U., Widing, K. G., and Laming, J. M.: 1998, 'The Coronal Composition Above the Solar Equator and the North Pole As Determined from Spectra Acquired by the SUMER Instrument on SOHO,' *Astrophys. J.*, **505**, 999.
- Fisk L. A.: 1978, '³He-rich flares: A possible explanation,' *Astrophys. J.*, **224**, 1048.
- Fisk, L. A.: 1996, 'Motion of the footpoints of heliospheric magnetic field lines at the Sun: implications for recurrent energetic particle events at high heliospheric latitudes,' *J. Geophys. Res.*, **101**, 15547.
- Fludra, A., Del Zanna, G., Alexander, D., and Bromage, B. J. I.: 1998, 'Electron density and temperature of the lower solar corona,' *J. Geophys. Res.*, in press.
- Gabriel, A. H., Bely-Dubau, F., David, C., Lamy, P., and Quemerais, E.: 1999, 'Enhanced abundance of oxygen and iron in polar coronal holes from CDS, SUMER and LASCO,' *SOHO-7 Workshop*, in press.
- Geiss, J., Gloeckler, G., and von Steiger, R.: 1995, 'Origin of the Solar Wind from Composition data,' *Space Sci. Rev.*, **72**, 49.
- Gloeckler G., Hefti S., Zurbuchen T. H., Schwadron N. A., Fisk L. A., Ipavich F. M., Geiss J., Bochsler P., and Wimmer-Schweingruber R. F.: 1998, 'Unusual composition of the solar wind in the 2–3 May 1998 CME observed with SWICS on ACE,' *Geophys. Res. Lett.*, submitted.
- Hassler, D. M., Dammasch, I. E., Lemaire, P., Brekke, P., Curdt, W., Mason, H. E., Vial, J.-C., and Wilhelm, K.: 1999, 'Solar wind outflow and the chromospheric magnetic network,' *Science*, in press.
- Hirshberg, J., Alksne, A., Colburn, D. S., Bame, S. J., and Hundhausen, A. J.: 1970, 'Observation of a solar flare induced interplanetary shock and helium-enriched driver gas,' *J. Geophys. Res.*, **75**, 1.
- Ipavich, F. M., Gloeckler G., Zurbuchen, T. H., Hefti, S., Bochsler, P., Fisk, L. A., Kallenbach, R., Paquette, J. A., and Wimmer-Schweingruber, R. F.: 1999, 'Temporal Behavior of Solar Wind Fe and O in High Speed Stream Onsets,' personal communication.
- Neukomm, R. O., and Bochsler, P.: 1996, 'Diagnostics of closed magnetic structures in the solar corona using charge states of helium and of minor ions,' *Astrophys. J.*, **465**, 462.

- Neukomm, R. O.: 1998, 'Composition of Coronal Mass Ejections derived with SWICS/Ulysses,' Thesis, University of Bern.
- Raymond, J. C., *et al.*: 1997, 'Composition of coronal streamers from the SOHO UVCS,' *Sol. Phys.*, **175**, 645.
- Raymond, J. C., *et al.*: 1998, 'Elemental Abundances in Coronal Structures,' in *Solar Composition and its evolution: From Core to Corona*, Proceedings of the ISSI Workshop, 26–30 January 1998, Bern, eds. C. Fröhlich, M. C. E. Huber, S. K. Solanki, R. von Steiger, *Space Sciences Series of ISSI* (Kluwer), p. 283.
- Raymond, J. C., *et al.*: 1999, 'Composition Variations in the Solar Corona and Solar Wind,' *SOHO-7 Workshop*, in press.
- Riyopoulos, S.: 1991, 'Subthreshold stochastic diffusion with application to selective acceleration of ^3He in solar flares,' *Astrophys. J.*, **381**, 578.
- Schwadron, N. A., Fisk, L. A., and Zurbuchen, T. H.: 1998, 'On the solar wind: II. Element Fractionation,' *Astrophys. J.*, in press.
- Wang, Y.-M., Sheeley, N. R., Walters, J. H., Brueckner, G. E., Howard, R. A., Michels, D. J., Lamy, P. L., Schwenn, R., and Simnett, G. M.: 1998, 'Origin of streamer material in the outer corona,' *Astrophys. J.*, **498**, L165.
- Wilhelm, K., Marsch, E., Dwivedi, B. D., Hassler, D. M., Lemaire, P., Gabriel, A. H., and Huber, M. C. E.: 1998, 'The Solar Corona above Polar Coronal Holes as Seen by SUMER on SOHO,' *Astrophys. J.*, **500**, 1023.
- Wilhelm, K., and Bodmer, R.: 1998, 'Solar EUV and UV emission lines observations above a polar coronal hole,' in *Solar Composition and its evolution: From Core to Corona*, Proceedings of the ISSI Workshop, 26–30 January 1998, Bern, eds. C. Fröhlich, M. C. E. Huber, S. K. Solanki, R. von Steiger, *Space Sciences Series of ISSI* (Kluwer), p. 71.
- Wimmer-Schweingruber, R. F., Bochsler, P., Gloeckler, G., Ipavich, F. M., Geiss, J., Kallenbach, R., Fisk, L. A., Hefti, S., and Zurbuchen, T. H.: 1998, 'On the bulk isotopic composition of magnesium and silicon during the May 1998 CME: ACE/SWIMS,' *Geophys. Res. Lett.*, submitted.
- Wurz, P., Ipavich, F. M., Galvin, A. B., Bochsler, P., Aelrig, M. R., Kallenbach, R., Hovestadt, D., Grünwaldt, H., Hilchenbach, M., Axford, W. I., Balsiger, H., Bürgi, A., Coplan, M. A., Geiss, J., Gliem, F., Gloeckler, G., Hefti, S., Hsieh, K. C., Klecker, B., Lee, M. A., Livi, S., Managadze, G. G., Marsch, E., Möbius, E., Neugebauer, M., Reiche, K. U., Scholer, M., Verigin, M. I., and Wilken, B.: 1998, 'Elemental composition of the January 6, 1997, CME,' *Geophys. Res. Lett.*, **25**, 2557.
- Young, P. R., and Mason, H. E.: 1997, 'The Mg/Ne abundance ratio in a recently emerged flux region observed by CDS,' *Solar Phys.*, **175**, 523.
- Young, P. R., and Mason, H. E.: 1998, 'Atomic physics for atmospheric composition measurements,' in *Solar Composition and its evolution: From Core to Corona*, Proceedings of the ISSI Workshop, 26–30 January 1998, Bern, eds. C. Fröhlich, M. C. E. Huber, S. K. Solanki, R. von Steiger, *Space Sciences Series of ISSI* (Kluwer), p. 315.
- Young, P. R., Klimchuk, J. A., and Mason, H. E.: 1999, 'SOHO/CDS Observations of a polar plume,' *Astron. Astrophys.*, in press.
- Zurbuchen, T. H., Fisk, L. A., Gloeckler, G., and Schwadron, N. A.: 1998, 'Element and isotopic fractionation in closed magnetic structures,' *Space Sci. Rev.*, in press.

Address for correspondence: H. E. Mason, Department of Applied Mathematics and Theoretical Physics, Silver Street, Cambridge CB3 9EW, UK

SOHO AFTER 30 MONTHS: A PERSONAL VIEW

A. H. GABRIEL
Institut d'Astrophysique Spatiale, Orsay

1. Introduction

The success of the seventh SOHO workshop is well-evidenced by the fact that the future eighth workshop has already decided to adopt a similar format, with only small modifications. The stimulating discussions we have heard have been well summarized in the four excellent reports which precede this contribution. For this reason, I am fortunate in being able to treat in a rather flexible manner my invitation from the Scientific Committee to write this summary report. I do not pretend to offer a balanced summary of the entire workshop. I will instead select a number of points which seem to me to be important and indicate some personal opinions on the future needs.

SOHO was launched near solar minimum. The first 18 months saw the corona in a configuration essentially typical of this phase, whilst the following year has shown a progressive change towards a more active configuration. The tremendous advantage of this phasing is now becoming clear. We were able to understand quite rapidly, at least qualitatively, many aspects of the two-component corona, and can now begin to follow them through the more complex geometry which is evolving. I refer of course to the coronal holes and the closed field regions, which are somewhat related in turn to the fast and slow wind regions at greater distances. This rapid contact with a number of basic principles has been particularly important when we consider the small proportion of the data collected which has been analyzed in depth. The SOHO operations plan we have chosen, with its daily evaluation and planning exercise, places enormous demands on the scientific community involved, so that in-depth analysis has inevitably been limited to a relatively small fraction of the data. Our understanding of the SOHO Sun is therefore based today on these limited studies, combined with a much wider field of "quick-look" evaluation of the results. We need to remember that the remaining 90% or more of the data interpretation may well modify later some of the preliminary conclusions being adopted at present.

It is useful to recall here the three primary scientific objectives announced for the SOHO mission. These were the study of the solar interior, the heating mechanisms for the corona, and the acceleration of the solar wind. We will not here consider the solar interior, since the subject is not included in the scope of the seventh workshop. It is now clear that the heating mechanism of the corona is closely linked through the physics to the acceleration of the wind. Nevertheless, the two effects are different and can in some respects be discussed and investigated separately. Today we can see that SOHO has been able to make more rapid advances on the



wind processes than has been possible for the heating. This is understandable, to the extent that the wind is more directly linked to physical observables. To decide on the heating mechanism may require detailed in-depth analysis, necessitating more precise instrument calibration, which will take more time to realize.

In spite of these limitations, this workshop has shown that we are now stimulating a very fruitful exchange between the observations and theoretical modeling. SOHO is producing some quite stringent constraints on the range of models that can be accepted. SOHO has also provided new and unexpected observations that have stimulated the development of models involving physical processes not previously believed to be important.

2. Coronal Holes and the Fast Wind

It is in the acceleration of the fast solar wind that SOHO gave us the most rapid quantitative results and several surprises. Data from LASCO and UVCS show the essential configuration of the inner heliosphere at minimum and, by Doppler dimming, some close-in velocities. We find that acceleration takes place much closer to the Sun than previously believed and that this is particularly true in the fast wind over the poles. Radial temperature profiles close to the Sun are important in modeling the initial acceleration processes. Electron temperatures, measured by CDS and SUMER, are found to be low and to reach a maximum of less than 1 MK at around $1.2 R_\odot$. These low temperatures pose some difficulties in comparison with values in the wind, as well as the "freezing-in" temperatures, measured at 1 A.U., which would indicate maximum values in the corona of over 1.2 MK. One explanation offered for these discrepancies is that we measure spectroscopically the "core" temperature, whereas there exists a higher "halo" temperature, responsible for the freeze-in effects. This explanation is not fully convincing and requires further study. It might be worth questioning the precision of our existing ionization balance theory, used in the freezing-in modeling. The recombination rates used are subject to uncertainties and have never been effectively tested with real data. A further uncertainty arises concerning the existence of polar plumes in these regions. Several observers claim that the plumes are denser and colder than the surrounding inter-plume material and attempts to measure radial Doppler velocities in plumes have shown very low limiting velocities, inconsistent with the solar wind. The implicit suggestion is that the spectroscopic measurements are of more intense cooler material, whilst the rarer (and perhaps hotter) wind material escapes detection. This is a very important question which must be confronted with more detailed analysis. Many observations, often conflicting, pretend to interpret the geometry of plumes and to identify the surface structures at their base. These are in my view based on an inadequate and subjective examination of an insufficient database of observations and are quite unconvincing. There are also considerable doubts concerning the identity of plume-like structures observed by different means: UV

or white-light structures below $1.3 R_o$ and very fine structures visible at greater distances, often only when using contrast-enhancing techniques. It is not clear whether plumes play an important role in determining coronal physics. However, since they influence observations of this key region, an interpretation of their geometry and physical properties becomes a high priority for the immediate future.

If the electron temperature remains low, this is not the case for the ions, for which UVCS measurements show much higher kinetic "temperatures." Evidently we cannot directly separate true temperatures from turbulent motions, although the increase of these "temperatures" with the mass of minor ions is too steep to be either a global temperature or a simple turbulence. The popular explanation today is that the ions are heated by ion cyclotron resonance. This can explain the different temperatures from different species, as well as the observed higher transverse than longitudinal temperature. Whatever the mechanism, the measurement of such Doppler line profiles, particularly for hydrogen must place an upper limit on the energy traversing this region in Alfvén waves, and thereby available to drive the supersonic flow. The interpretation of UVCS hydrogen profiles is not a simple and direct procedure, and there is some discussion as to whether these measurements allow sufficient wave energy to produce the wind driving mechanism.

Many theorists are developing models for the solar wind and its acceleration. The most uncertain parameter in all of these models is the coronal heating function. For linear Alfvén waves, there is the usual difficulty of dissipation. For high amplitude waves, non-linear mixing into magneto-acoustic modes becomes possible, but observational constraints tend to exclude the existence of sufficiently high amplitudes. Some theoretical studies predict other mechanisms for damping linear waves, including gravity damping and "sheer flow" processes. If ion cyclotron heating is important, then high-frequency waves are required. UVCS "temperatures" can be used in order to deduce the spectrum required for such waves, and then to work out their effect on the mainly hydrogen and helium wind constituents. It might be reasonable to consider heating by high-frequency waves close to the Sun and then by Alfvén waves further out.

3. Closed Fields, Streamers and the Slow Wind

In a typical solar minimum configuration, the magnetic field in equatorial regions is closed, in the region below $2 R_o$. Further out beyond $3 R_o$, the field is open and characterized by a current sheet in the equatorial plane, with a reversal of field direction. These two regions, although related, are clearly very different physically. The outer region is the classical "streamer," although the entire equatorial configuration is sometimes loosely referred to by this term. The inner closed field region inhibits wind flow, although there may be a slow outward migration of the plasma. In the streamer region, there is an outward flow, which is believed to be a major component of the observed slow solar wind. Observations of the flow-rate in the

streamer of small inhomogeneities or “blobs” show acceleration consistent with the 1 A.U. slow wind velocities seen by Ulysses. It is assumed that the blobs are merely “feathers in the wind.” They are witnesses of the background flow rate, but do not themselves constitute a large fraction of the flow.

There are three or more different attempts to interpret theoretically how material escapes from the inner closed region into the streamer. In one case the movement of photospheric footpoints leads to reconnection further out and a continuous exchange of material from closed to open field lines. An alternative model depends on a multipole component to the Sun’s field, which allows open field-lines to exist, even in the near-equatorial regions. Other models involve instabilities in the current sheet leading to repeated reconnection, with the expulsion of plasmoids. Some workers believe that there are inner and outer slow wind regions, the latter originating in the outermost layers of the polar open field coronal hole. It is not clear which further measurements will help to choose between these models. Although there may be other sources of the slow wind, e.g., open field lines from active regions, it is generally believed that the streamer is a primary source. Observations of the velocity and acceleration of CME’s show values much more variable and generally larger than that of the slow wind blobs. More recent studies of smaller CME’s suggest a complete spectrum of velocities, with the smaller CME’s traveling at speeds comparable with the wind. These considerations can be considered consistent with the observation at 1 A.U. of variability and turbulence in the slow solar wind.

4. Observation of Heating Processes

Heating by reconnection, following the twisting of coronal magnetic fields by random footpoint motions, is the basis of the Gold/Parker microflare mechanism. It is difficult to conceive of such a process in the open-field regions of coronal holes. An alternative process, valid in or out of holes, involves reconnection lower down in the transition region. It is now widely accepted that the Gabriel 1976 model of the expansion of basically monopolar fields above the transition region network is only a part of the complete picture. Observations of magnetic fields from MDI show a continual emergence of small dipoles in the supergranule cells, which migrate towards the network boundaries, where they reconnect with the ambient field. The resulting forest of low-lying loops provides the previously unexplained excess Differential Emission Measure at temperatures below 0.3 MK. Observation of explosive events with SUMER as high-velocity Doppler shifts may be related to the transient brightenings or “blinkers” observed by CDS. Both these events occur in transition region lines and coincide spatially with the network boundary regions. A possible scenario is that these phenomena correspond with reconnection and a heating source for the corona.

There are however some difficulties in this interpretation. The local energy release is limited to material at transition region temperatures. No brightenings are

seen at coronal temperatures. If this is the principal coronal heating mechanism, the Second Law of Thermodynamics requires that some reasonable portion of the energy is released at the temperature maximum. One way out of this difficulty is to suppose that the reconnection energy, released at 0.3 MK, is conveyed by a non-thermal process from this region to the corona at over 1 MK, where it becomes thermalized. A non-thermal process has been proposed, in the form of the upward propagation of a kink in the field lines, resulting from the local explosive reconnection. Such a process is in effect a very high amplitude local Alfvén wave. Although the mean energy might be modest, this high local value could provide the non-linearity required for effective dissipation and heating, through mode-mixing.

5. Comparison of Open and Closed Regions

Numerous studies are reported of abundance variations between different solar structures. In general, the FIP effect is manifested in the corona in the slow-flowing closed-field regions, as also in the slow wind arising from such regions. The faster flows in open-field regions greatly reduce the FIP effect, which is also the case for the fast solar wind. This is complicated by the effect of gravitational settling, which is also manifested in non-flowing regions. Most of these abundance studies are made by comparing two or more minor species, having different FIP values or masses.

Some interesting questions arise when we try to compare physical parameters between polar open-field and equatorial closed-field regions. Starting with electron density, some measurements reported at the workshop, based on density sensitive line ratios, indicate ratios of only 2 to 3 between closed and open regions. These values might be credible in the transition region, but are much too low for the corona. Decades of ground-based eclipse measurements of Thompson scattering intensities give electron density ratios around 10 between such regions. This figure is fully supported by SOHO measurements based on LASCO/C2. If temperatures and abundances remained constant between the two regions, this would translate into a factor of 100 between the regions for collisionally excited spectral line intensities. Such factors are never seen. A typical observed ratio for O VI is around 7 or 8. The explanation lies partly in a temperature effect through ionization balance, but mostly in abundance differences. This type of observation concerns not the ratio of two minor species, but rather one minor species (oxygen) to hydrogen (or more strictly to free electrons). These observations can be interpreted as a ratio of the *absolute* abundance of oxygen between these two regions of a factor of 10. This must be mainly due to gravitational settling. There are some indications of even larger ratios in the case of iron.

6. Observational Limitations

The sophisticated diagnostics offered by the SOHO spectroscopic instruments go way beyond what has been previously practiced. To exploit these possibilities, a large amount of preparatory atomic theory has been developed in the years leading up to the launch. We must express our appreciation for this effort, the results of which we are now taking for granted in our analysis. This is a good moment to mark our appreciation of the work of Brunella Monsignori Fossi, who died tragically before she could see her work applied to the SOHO data.

The precision of the diagnostics based on spectroscopic line ratios will vary according to each case. I believe that we need to take this more fully into account and to avoid over-interpreting some of the data. Optically allowed excitation rates used in some electron temperature diagnostics may be better than 10% reliable. On the other hand inter-system and forbidden transitions, often used in electron density measurements can be only 20% to 30%. Of course, densities measured to this accuracy would be very welcome. However, further dangers can arise if we use density-dependent ratios near to the limit of their density range of sensitivity. I feel that some of the numbers that are being quoted would benefit from a more realistic error analysis.

There are also difficulties in understanding all of the parameters involved in the most valuable Doppler dimming method for obtaining velocities from the UVCS data. The UVCS team are well aware of these questions and are continually working on improvements to the technique. These remarks are in no way meant to criticize. They are merely to alert those less close to the methods that we may not yet be at the limit of what we will obtain from these techniques.

I would stress again the fact that only a small fraction of the data has so far been fully analyzed. Some of the results presented are the outcome of very detailed analysis. Others are the result of rapid analysis of a single observation. Solar activity is now rising and the magnetic configuration is becoming more complex. Some observations are no longer possible in this cycle; for example, tangential studies of a large polar coronal hole. Others, involving activity and flares, are now becoming more attainable. But we have accumulated a large data base in the archive, so that there is no difficulty in obtaining new sets to analyze, even for the solar minimum configuration.

Finally, and on behalf of all of those who participated, I would like again to thank John Kohl and all of the team of SOHO-7 for organizing an extremely successful workshop.

Address for correspondence: Institut d'Astrophysique Spatiale, Université Paris XI, 91405 Orsay Cedex, France

SWAN OBSERVATIONS OF THE SOLAR WIND LATITUDE DISTRIBUTION AND ITS EVOLUTION SINCE LAUNCH

JEAN-LOUP BERTAUX¹, ERKKI KYRÖLÄ², ERIC QUEMERAIS¹,
ROSINE LALLEMENT¹, WALTER SCHMIDT², TUULA SUMMANEN²,
JORGE COSTA¹ and TEEMU MÄKINEN²

¹ Service d'Aéronomie du CNRS, BP. 3, 91371 Verrières-le-Buisson, France

² Finnish Meteorological Institute, P.O. Box 503, FI 00101, Helsinki, Finland

Abstract. SWAN is the first space instrument dedicated to the monitoring of the latitude distribution of the solar wind by the Lyman alpha method. The distribution of interstellar H atoms in the solar system is determined by their destruction during ionization charge-exchange with solar wind protons. Maps of sky Ly- α emission have been recorded regularly since launch. The upwind maximum emission region deviates strongly from the pattern that would be expected from a solar wind that is constant with latitude. It is divided in two lobes by a depression aligned with the solar equatorial plane, called the Lyman-alpha groove, due to enhanced ionization along the neutral sheet where the slow and dense solar wind is concentrated. The groove (or the anisotropy) is more pronounced in 1997 than in 1996, but it then decreases between 1997 and 1998.

1. The SWAN Lyman- α Full-Sky Intensity Maps

In the solar system, the gas of interstellar H atoms is illuminated by solar Ly- α . Only those atoms which have survived ionization (mainly by the solar wind in charge exchange collisions) may be observed through their resonance scattering of solar photons. The resulting Ly- α sky pattern is governed by three different effects:

1. The volumetric 3D distribution of H atoms which have not yet been destroyed by the solar wind. This is what we are interested in to determine the distribution of solar wind as a function of latitude.
2. The solar Ly- α angular distribution (2D).
3. The exact position of SOHO in the solar system, because the location of the emission is within a few AU from the Sun and SOHO.

The main features of the SWAN maps are a region of maximum near the upwind direction (254° , $+6^\circ$), and a minimum in the opposite direction (Bertaux *et al.* 1997a). Each map also shows a secondary minimum of emission along the solar equator. This minimum divides the region of maximum intensity into two bright areas, one north and one south, forming a groove in the sky indicative of depleted H atoms more ionized by the slow solar wind concentrated along the neutral sheet. This minimum, which was already detected with Prognoz observations in 1976, was called the Ly- α groove (Bertaux *et al.* 1996).

A quantitative analysis (Kyrölä *et al.* 1998) of the SWAN intensities shows an overall excellent agreement with Prognoz results, which were taken at a similar phase of the solar cycle (near minimum). There is a clear dichotomy of the solar



Table I
SW Bulk Properties at minimum activity

| Wind Type | Fast Wind | Slow Wind |
|--|------------------------|-------------------|
| Average velocity (km/s) | 750 | 350–400 |
| Heliographic latitude (deg) | −90 to −20, +20 to +90 | −20 to +20 |
| Fraction of space occupied by the wind | 2/3 | 1/3 |
| Average proton flux ($\text{cm}^{-2} \text{s}^{-1}$) | 2.0×10^8 | 2.8×10^8 |

wind, the slow solar wind being concentrated near the heliographic equator (within $\pm 20^\circ$) with a higher ionization and solar wind proton number flux, and the fast solar wind ubiquitous above 20° latitude in both hemispheres. This dichotomy is illustrated in Table I which gives the proton number fluxes derived from the SWAN analysis. It is clear that, when weighted by the solid angle covered by the two regions (fast and slow solar wind), the average solar wind flux is only 2.3×10^8 protons $\text{cm}^{-2} \text{s}^{-1}$, and not 3 or 3.5×10^8 protons $\text{cm}^{-2} \text{s}^{-1}$ as used to be found frequently in the literature. This latter estimate was biased by the fact that most measurements were taken by space probes in the ecliptic plane. Note that this table is corrected for an unfortunate error present in an earlier presentation of this table, where the latitude spans and solid angles of the slow and fast solar wind were inadvertently inverted (Bertaux *et al.* 1997b).

2. The Evolution of the Groove from Year to Year

The parallax effect, a major source of the changing sky pattern, may be eliminated by comparing and dividing SWAN maps recorded at 1 year intervals, since SOHO is exactly at the same place in the solar system. Then, one may detect directly changes in the solar wind latitude distribution from year to year. The top half of Figure 1 is an example of such a ratio map: intensity recorded on 13 November 1997 divided by the map of 13 November 1996. All values are above 1, most likely because of global enhancement of solar Ly- α during the ascending phase of the solar cycle. A large region with enhanced ratio around 1.2 shows up near the 180° meridian (in ecliptic longitude). This is due to an active region on the sun in 1997 giving more illumination at that solar longitude, as proven by the fact that ratio maps taken earlier and later show the displacement of this bulge with the 26 day rotation period. This bulge is cut in two by the heliographic equator, along which the bulge enhancement is smaller. Similarly, on the left side, there is a region of smaller ratio near the heliographic equator with respect to the surrounding regions at higher latitudes. Altogether, this elongated region with reduced enhancement is aligned with the Ly- α groove along the heliographic equator (which cuts the ecliptic

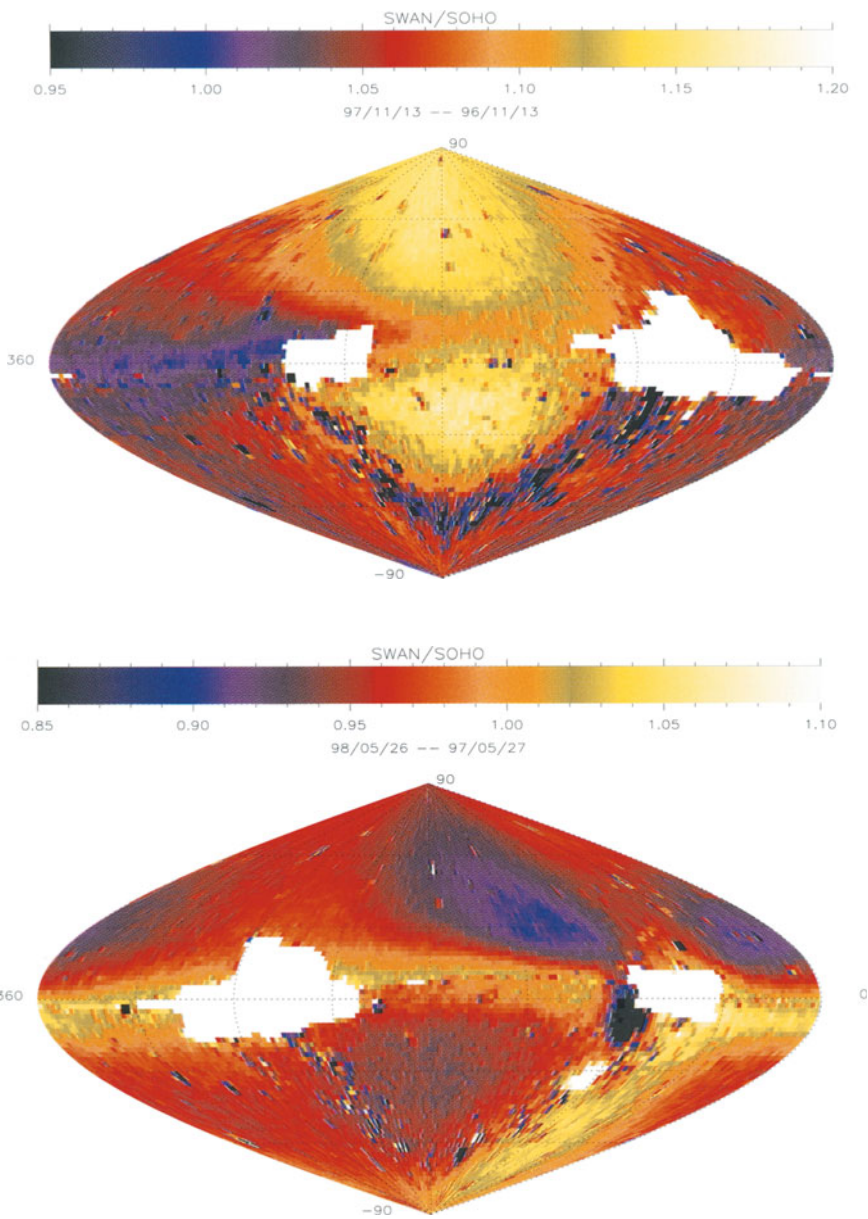


Figure 1. Top: Ratio of the map obtained on 13 November 1997 divided by the map of 13 November 1996. Maps are in ecliptic coordinates. The intensity is globally higher in 1997. The big yellow blob is due to a big solar spot in 1997 with larger solar Ly- α , seen rotating with the 26 day solar rotation. Along the solar equator, the intensity has increased less than at other places; the groove is more pronounced in 1997 than in 1996. **Bottom:** Ratio of the 26 May 26 1998 map to the 26 May 1997 map. The intensity is slightly lower in 1998 than in 1997. Along the solar equator, the intensity is higher in 1998 than in 1997, showing that the groove has been replenished with H atoms.

around 75° and 255° of longitude. It shows that the groove was more pronounced (deeper) in November 1997 than in November 1996.

Six months later, the situation is different. The bottom half of Figure 1 shows a similar map with 26 May 1998 intensities divided by those of 26 May 1997. A black area near the ecliptic at 90° longitude is due to comet Hale-Bopp, which was present in 1997 but not in 1998. Otherwise, the pattern is dominated by a region along the heliographic equator of enhanced ratio with respect to the surrounding region. This is a reverse situation with respect to November 1997. It indicates that the groove in May 1998 was less pronounced than in May 1997. The groove is carved in the incoming interstellar H atoms by the slow solar wind, which flows along the Heliospheric Neutral Sheet (HCS). Around solar minimum, the HCS is less inclined to the solar equator, and less warpy. These are the best conditions to produce, in spite of the solar rotation, a permanent flow of slow solar wind along the heliographic equator, and correspondingly a deep Ly- α groove. When the solar cycle is on the ascending phase, the inclination of the HCS to the solar equator is increasing, and also its warps; two factors that will distribute the slow solar wind over a larger range of solar latitudes, resulting in a groove that will be less pronounced. Since the solar minimum occurred in May 1996 (according to sunspot records) while the groove became more pronounced until November 1997, it seems that there is a substantial lag time between the solar minimum and the minimum inclination of the HCS.

As for the future, we hope we will be able to monitor the continuation of the replenishment of the groove as we reach the solar maximum, when the groove is expected to fade or disappear because of the increasing inclination of the neutral sheet where the slow solar wind is concentrated.

References

- Bertaux, J.-L., Quemerais, E., and Lallement, R.: 1996, "Observations of a Ly- α groove related to enhanced solar wind mass flux in the neutral sheet," *GRL*, **23**, 3675.
Bertaux, J.-L., Quemerais, E., Lallement, R., Kyrölä, E., Schmidt, W., Summanen, T., Berthe, M., Goutail, J. P., and Costa, J.: 1997a, "First Results from SWAN," *Sol. Phys.*, **175**, 737.
Bertaux, J.-L., Quemerais, E., Lallement, R., Kyrölä, E., Schmidt, W., Summanen, T., Mäkinen, T., and Holzer, T.: 1997b, "The First 1.5 year of Observations from SWAN Lyman alpha solar wind mapper on SOHO," *ESA SP-404*, 29.
Kyrölä, E., Summanen, T., Schmidt, W., Mäkinen, T., Bertaux, J.-L., Lallement, R., Quemerais, E., and Costa, J.: 1998, "Preliminary retrieval of solar wind latitude distribution from SWAN/SOHO observations," *JGR*, **103**, 14523.

ON THE STABILITY OF SIPHON FLOWS CONFINED IN CORONAL LOOPS

RITA BETTA¹, SALVATORE ORLANDO², GIOVANNI PERES³ and
SALVATORE SERIO^{1,3}

¹ *Osservatorio Astronomico, Piazza del Parlamento, 1, I-90134 Palermo, Italy*

² *ESA Solar System Division, Space Science Dept., ESTEC (SO), Postbus 299, NL-2200 AG Noordwijk, The Netherlands*

³ *Dipartimento di Scienze Fisiche e Astronomiche, Sezione di Astronomia, Università di Palermo, Piazza del Parlamento 1, I-90134 Palermo, Italy*

Abstract. We use a time-dependent hydrodynamic model to study the dynamics of siphon flows triggered by differences of pressure or heat deposition asymmetries between the two footpoints of a coronal loop. We show that steady pressure driven flows in a uniformly heated loop are unstable, whereas those driven by asymmetries in the heating function may be stable. We also show that, in these cases, relatively cool loops might be filled far above their static pressure scale height.

1. Introduction

Siphon flows in coronal loops have been extensively modeled (Orlando *et al.* 1995, and references therein) and should in principle be a very common feature of observed loop structures. However, we do not have clear evidence of the existence of siphon flows; there are only rare examples, such as the siphon flow detected in the infrared by Rüedi *et al.* (1992), or the flows confined in cool loops observed in UV lines (Kjeldseth-Moe and Brekke 1998, and references therein).

The present paper aims on the one hand to investigate whether the lack of siphon flow observations may be due to some suppressing instability, and, on the other hand, to pinpoint possible observable signatures of the presence of siphon flows confined in coronal loops. We have therefore carried out a numerical study of the stability of siphon flows using a 1D hydrodynamic model, considering the effects of both symmetric and asymmetric heat deposition.

2. The Hydrodynamic Loop Model

We solve the time-dependent equations of mass, momentum and energy balance along a semi-circular flux tube. Many physical effects, such as gravity, viscosity, ionization, thermal conduction and radiative losses are considered. The equations are solved with a finite-difference scheme (Peres *et al.* 1982; Betta *et al.* 1997). The model allows for asymmetric solutions since the equations are solved along the whole loop. We use a regridding algorithm which allows for high spatial resolution in both transition regions between the chromosphere and the corona.



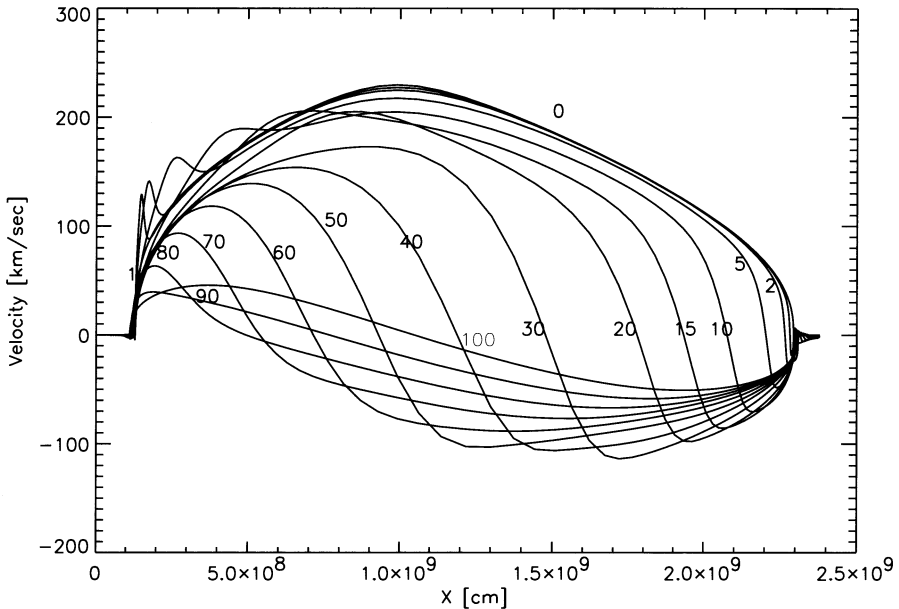


Figure 1. Velocity evolution along a loop uniformly heated with pressure at the base of 6 dyn cm^{-2} . The pressure difference between the two footpoints at $2 \times 10^4 \text{ K}$ is 0.05 dyn cm^{-2} . Time is marked on each curve.

Boundary conditions are fixed at the two footpoints: pressure, temperature and density are constant, and velocity is zero at the left footpoint; and temperature is constant in time at the last point where velocity and density are computed.

3. Siphon Flows Driven by a Pressure Difference

Initial distributions of temperature, density and velocity along the loop have been derived using the code developed by Orlando *et al.* (1995). We have considered a grid of subsonic solutions with loop lengths ranging from $2 \times 10^9 \text{ cm}$ to 10^{10} cm , and pressure ranging from 0.01 to 6 dyn cm^{-2} . The Mach number varies from 0.06 to 0.9. The pressure difference has been maintained at the two feet at the base of the chromosphere.

The evolution of the flow inside the loop during the first 100 seconds is shown in Figure 1 for a typical simulation. The flow is subsonic but the plasma velocity is very close to the sound speed (the maximum Mach number is 0.87). The two fronts of material from the two feet of the loop toward the top rapidly stop; after 10 minutes velocities are below 3 km/s everywhere along the loop.

We have found the same qualitative behavior for all the subsonic siphon flows of the grid considered. The density increases everywhere since two fronts of material

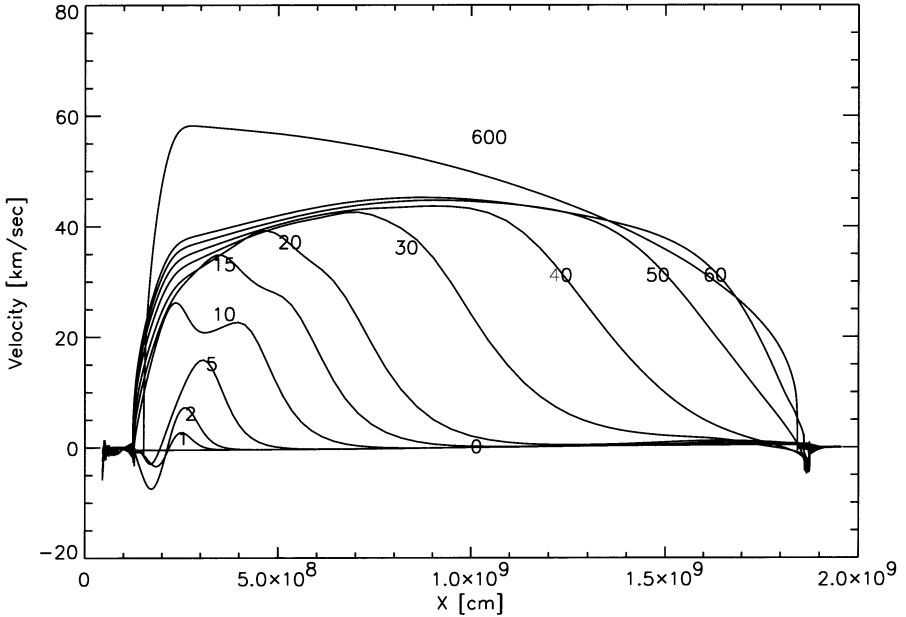


Figure 2. Velocity evolution along a loop with base pressure 35 dyn cm^{-2} and heat deposited along $1/20$ of the loop length near the left foot. Time since the beginning of the heating is marked on each curve.

gradually fill in the whole loop. After a time approximatively comparable to $2-3$ times the characteristic decay time, $\tau \approx 120L_9/\sqrt{T_7}$, where L_9 is the half-length of the loop in 10^9 cm units and T_7 is the temperature at the top in 10^7 K units, the atmosphere approaches a final steady thermodynamic configuration. The temperature at the loop top T_{top} and the pressure at the base p satisfy the scaling laws of Rosner, Tucker, and Vaiana (1978); $T_{\text{top}} \approx 1.4 \times 10^3(pL)^{1/3}$.

4. Asymmetric Heat Deposition

Let us consider what happens when asymmetric heat is localized only at one ‘leg’ of the loop. The initial configuration of the atmosphere is in steady state equilibrium; velocities are zero everywhere and temperature, density and pressure are computed with the code developed by Serio *et al.* (1981). The total power released is the same needed to maintain the loop atmosphere in hydrostatic and thermodynamic equilibrium. We use a Gaussian spatial function for the heat term, constant in time, in the low corona at the left ‘leg;’ the width of the Gaussian function is chosen as $1/20$ of the half-length.

We have studied the plasma evolution with such a heat source for all the loops of the grid examined above; the initial conditions have been selected as the final steady

configurations reached after the siphon flow disruption discussed in the previous section. In Figure 2 we plot snapshots of the velocity when the heat source is localized at the left ‘leg’ of the loop. The atmosphere gradually evolves towards a new configuration, and a continuous steady flow of material between one footpoint and the other arises, with the maximum velocity ranging from 20 to 60 km/s. The transient phase lasts for a time ranging between τ and 3τ . The maximum Mach number is between 0.15 and 0.20.

The temperature increases where the heat source is localized and slightly decreases elsewhere. If the loop length is $> 10^{10}$ cm an inversion of the temperature profile is seen at the top.

5. Conclusions

According to our model results, if the heat is uniform along the loop, we obtain that, after having explored the space of parameters for subsonic siphon flow solutions with a time-dependent hydrodynamic code, steady siphon flows cannot easily be detected by any instrument since they quickly disappear (~ 1 hour). During the transient phase (i.e., a few minutes) an increase of the emission and plasma upflows could be measured in lines typically formed in the transition region and in the corona, due to plasma evaporation.

On the other hand siphon flows that are steady (i.e., 20–60 km/s) can be obtained when the heat source is asymmetrically localized along the loop.

References

- Betta, R., Peres, G., Reale, F., and Serio, S.: 1997, *A&A Suppl. Ser.*, **122**, 585.
- Kjeldseth-Moe, O., and Brekke, P.: 1998, *Solar Phys.*, **182**, 73.
- Orlando, S., Peres, G., and Serio, S.: 1995, *A&A*, **294**, 861.
- Peres, G., Rosner, R., Serio, S., and Vaiana, G. S.: 1982, *ApJ*, **252**, 791.
- Rüedi, I., Solanki, S. K., and Rabin, D.: 1992, *A&A*, **261**, L21.
- Rosner, R., Tucker, W. H., and Vaiana, G. S.: 1978, *ApJ*, **220**, 643.
- Serio, S., Peres, G., Vaiana, G. S., Golub, L., and Rosner, R.: 1981, *ApJ*, **243** 288.

FAST AND SLOW FLOWS IN THE SOLAR WIND NEAR THE ECLIPTIC AT 1 AU?

L. F. BURLAGA and A. SZABO

Laboratory for Extraterrestrial Physics, NASA-Goddard Space Flight Center, Greenbelt, MD 20771

Abstract. At 1 AU in 1998, when solar activity was increasing, the distribution of hour averages of the solar wind speed was approximately lognormal. There was no distinct separation between fast and slow flows. The density, temperature and magnetic field strength also had lognormal distributions. It was possible to identify distinct structures such as corotating streams and magnetic clouds during some intervals. We suggest that coexistence of a simple statistical structure and deterministic physical structures is the consequence of the dynamical evolution and interactions of the flows between the sun and 1 AU and a relatively complex source signal.

1. Introduction

Much of the SOHO 7 Workshop discussed the origin of fast and slow flows. The concept of distinct fast and slow flows in the solar wind appears in the early literature (Hundhausen 1972). The fast wind consists of both quasi-stationary corotating flows and non-stationary transient flows. Corotating flows originate in coronal holes (Hundhausen 1977). Slow flows can originate near the streamer belt (Borrini *et al.* 1981; Gosling *et al.* 1981).

Observations from Helios 1 and 2 (Rosenbauer *et al.* 1977; Schwenn 1990), Ulysses (McComas *et al.* 1995) and Voyager 2 (Burlaga and Ness 1998; Richardson and Paularena 1997) provide evidence for fast flows from coronal holes and slow flows from the streamer belt.

2. Observations

We shall discuss hour averages of the magnetic field strength (B), the density (N), the bulk speed (V) and the proton temperature (T) from the WIND spacecraft made in the solar wind upstream of Earth from day 1 through day 75, 1998.

The plasma data for one solar rotation are shown in Figure 1. One can see several types of flows, some of which are interacting. There is a large corotating stream from days 70 to 75 and a magnetic cloud on days 64 to 65. Three intervals of relatively slow flows (< 325 km/s) are indicated in Figure 1 by vertical lines but these intervals are neither uniquely defined nor physically distinct. The slow speed interval on days 64–65 is produced by the dynamical expansion of a magnetic cloud as it moves from the sun to earth. There is a compound stream on days 59 to 65 consisting of a magnetic cloud, a narrow corotating stream and a post-shock flow, all of which are interacting. Finally, there are flows from day 50 to 57 that do not fit into the standard categories for solar wind flows.

The speed profile measured by WIND from day 1 to 75, 1998 is shown in Figure 2. This speed profile is complex. One cannot partition the time series into fast flows



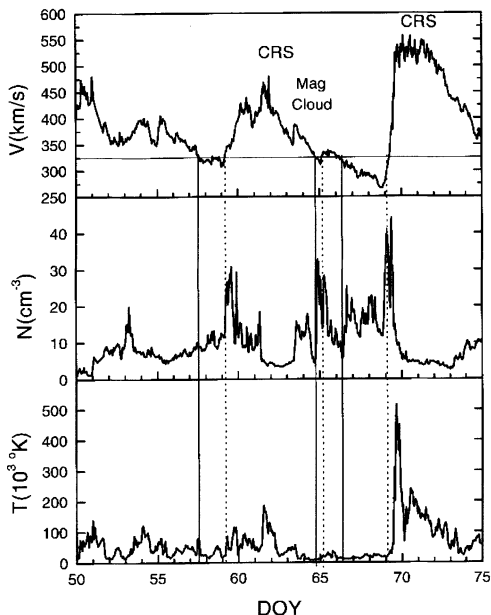


Figure 1. The solar wind speed (top panel), density (middle panel) and proton temperature (bottom panel) for day of year (DOY) 50 to 75, 1998, measured upstream of Earth.

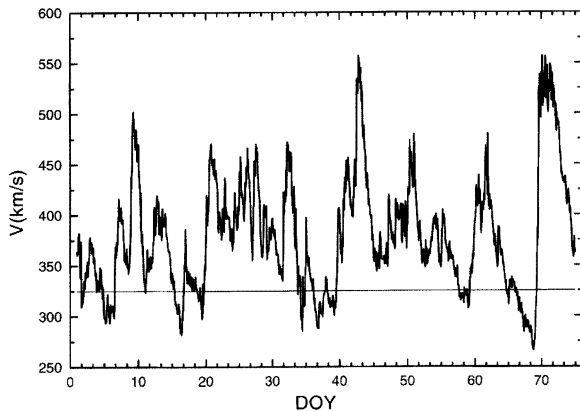


Figure 2. The profile of hour averages of the bulk speed from day of year (DOY) 1 to 75, 1998

and slow flows. The distribution of the hour averages of the solar wind speed from day 1 to 75, 1998 is shown by the solid dots in the lower-right panel of Figure 3. The curve in this panel is a non-linear least squares fit of the data to a lognormal distribution, viz., $F = A \exp\{-(\ln B - \mu)^2/(2w^2)\}$. The distribution of speeds is lognormal to good approximation.

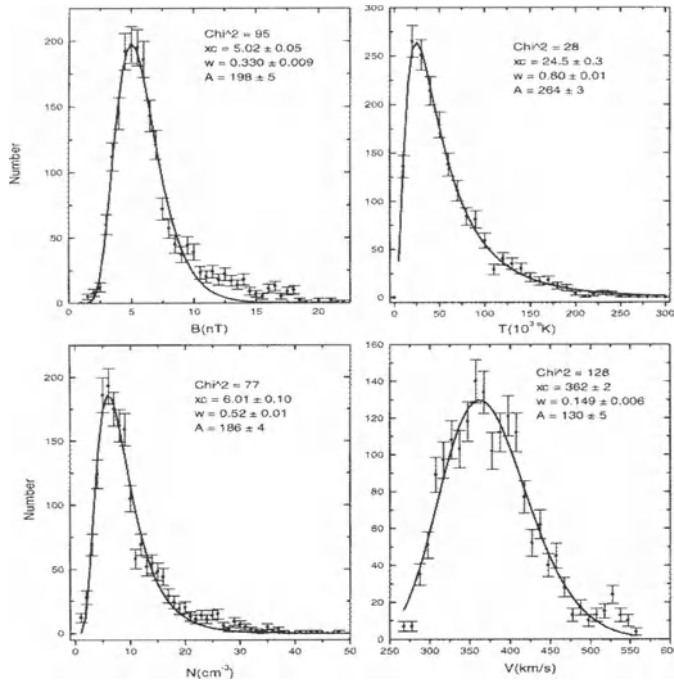


Figure 3. Distributions of the magnetic field strength (B), proton temperature (T in units of 1000 K), proton number density (N), and bulk speed (V). Each distribution is described to good approximation by a lognormal distribution, shown by the solid curves in each panel, although small deviations are present in the tails.

The distributions of the magnetic field strength, the density and the proton temperature are also shown in Figure 3 with a nonlinear least squares fit to each. The lognormal distribution provides a good fit to most of the magnetic strength observations, although there is an excess of strong fields in the tail of the distribution. The approximately lognormal distribution of magnetic field strengths at 1 AU was initially reported by Burlaga and King (1981). An excess of strong fields relative to a lognormal distribution has previously been reported by Burlaga (1992) and described by a multifractal distribution.

The distribution of the hour averages of the solar wind proton temperatures from day 1 to 75, 1998 is lognormal to very good approximation (Figure 3). Since fast corotating flows are always hot and slow flows are characteristically cold, a wind consisting of fast and slow flows would be associated with a bimodal temperature distribution, rather than the lognormal distribution that is observed. The distribution of the hour averages of the densities is also approximately lognormal, although there is possibly a small excess of high densities.

The lognormal distributions suggest the presence of multiplicative dynamical processes. They give an approximate description of the tails of the measured dis-

tributions. It is possible that they are an approximation to a basic multi-scaling symmetry in the solar wind (Burlaga 1995).

3. Summary and Discussion

We have shown that the distribution of the hour averages of the solar wind speeds, densities, temperatures and magnetic field strengths observed by WIND upstream of the earth from day 1 to 75, 1998 are approximately lognormal.

We suggest that there are three factors involved in producing the lognormal distributions. First, the source signal near the ecliptic during the ascending phase of solar activity contains a complex mixture of flow patterns, including corotating streams, magnetic clouds, other transient ejecta, transient and quasi-stationary flows from the streamer belt, and some flows that do not fall into familiar categories. Second, individual flows evolve and interact with neighboring flows between the sun and 1 AU. Finally, the individual flows can have a complex internal structure.

The approximate lognormal distributions of the fluid parameters of the solar wind at 1 AU have to be considered when discussing the sources of "fast" and "slow" solar wind, particularly when using data from spacecraft such as ACE and WIND.

The plasma data used in this paper are from the Solar Wind Experiment (SWE) on WIND (PI K. W. Ogilvie), provided by A. J. Lazarus and J. T. Steinberg via the MIT Space Plasma Group web site. The magnetic field data are from the Magnetic Field Instrument (MFI) on WIND (PI R. P. Lepping).

References

- Borrini, G., Gosling, J. T., Bame, S. J., Feldman, W. C., and Wilcox, J. M.: 1981, *J. Geophys. Res.*, **86**, 4565.
- Burlaga, L. F.: 1992, *J. Geophys. Res.*, **97**, 4283.
- Burlaga, L. F.: 1995, *Interplanetary Magnetohydrodynamics*, (Oxford U. Press: New York).
- Burlaga, L. F., and King, J. H.: 1981, *J. Geophys. Res.*, **84**, 6684.
- Burlaga, L. F., and Ness, N. F.: 1997, *J. Geophys. Res.*, **102**, 19,731.
- Burlaga, L. F., and Ness, N. F.: 1998, *Space Sci. Rev.*, **83**, 105.
- Gosling, J. T., Borrini, G., Asbridge, J. R., Bame, S. J., Feldman, W. C., and Hansen, R. T.: 1981, *J. Geophys. Res.*, **86**, 5438.
- Hundhausen, A. J.: 1972, *Coronal Expansion and Solar Wind*, (Springer-Verlag, New York, USA).
- Hundhausen, A. J.: 1977, in *Coronal Holes and High Speed Wind Streams*, ed. J. B. Zirker, (Colo. Assoc. Univ. Press, Boulder), p. 225.
- McComas, D. J., et al.: 1995, *J. Geophys. Res.*, **10**, 19,893.
- Rosenbauer, H., Marsch, E., Meyer, B., Miggrenrieder, H., Montgomery, M., Mulhauser, K. H., Pilipp, W., Voges, W., and Zink, S. K.: 1977, *J. Geophys. Res.*, **42**, 561.
- Richardson, J. D., and Paularena, K. I.: 1997, *Geophys. Res. Lett.*, **24**, 1435.
- Schwenn, R.: 1990, in *Physics of the Inner Heliosphere*, vol. 1, ed. R. Schwenn and E. Marsch, (Springer-Verlag, Berlin-Heidelberg), p. 99.

EUV AND RADIO OBSERVATIONS OF AN EQUATORIAL CORONAL HOLE

F. CHIUDERI-DRAGO¹, A. KERDRAON², E. LANDI¹ and A. FLUDRA³

¹ Dip. di Astronomia e Scienza dello Spazio, Università di Firenze, Italy

² Observatoire de Paris-Meudon, France

³ Rutherford Appleton Laboratory, Chilton, Didcot, Oxfordshire OX11 0QX, UK

Abstract. An equatorial coronal hole has been observed on 18 and 19 October 1996 with SOHO-CDS and with the Nancay Radioheliograph (RH). The CDS EUV line intensities are used to determine the coronal hole Differential Emission Measure (*DEM*); in turn this is used to compute the radio brightness temperature T_b at the observed frequencies, leaving the coronal electron temperature and density as free parameters. EUV line intensities, calculated from the derived models, show a good agreement with EUV observations.

Key words: plasma diagnostics, coronal holes, radio observations

1. The Observations

An equatorial coronal hole was observed around its central meridian transit on 18 and 19 October 1996 by the Coronal Diagnostic Spectrometer (CDS) on board SoHO, and by the Nancay Radioheliograph (RH) at the following frequencies: 164, 236, 327 and 410 MHz. For the technical performance of this instrument see Kerdraon and Delouis (1997).

The lines observed by CDS inside the coronal hole are listed in Table I. The temperature coverage of the CDS observation spans from 10^4 K (chromosphere) to 10^6 K (corona). Lines from O IV and Si IX allow density diagnostics in the transition region and in the corona. The emission detected by CDS has been averaged over the coronal hole area, which was determined using the Mg IX intensity.

2. DEM Determination

Values of the *DEM* ($\varphi(T) = N^2 dh/dT$) have been determined from CDS line intensities as a function of $\log T_{\text{eff}}$, defined for each line as

$$\log T_{\text{eff}} = \frac{\int G(T) \varphi_o(T) \log T dT}{\int G(T) \varphi_o(T) dT} \quad (1)$$

and fitted with a spline routine up to a temperature $T_c \simeq 1 \times 10^6$ K using the iterative *DEM* diagnostic technique described by Landi and Landini (1997, 1998). The resulting *DEM* is shown in Figure 1 (left). Since the line intensities used in the present work are emitted in the innermost region of the corona, where the solar wind



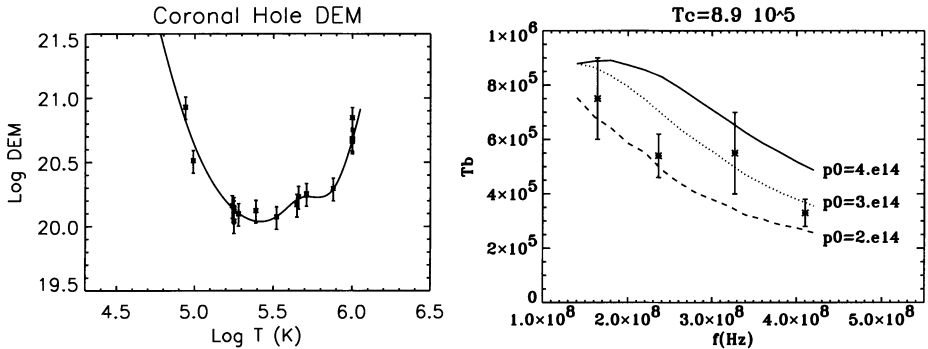


Figure 1. Left: Coronal hole *DEM* from CDS line intensities. Right: Fit of the radio observations with models at different p_0 .

speed is close to zero, the assumption of ionization equilibrium used in calculating the *DEM* should be valid at these heights.

3. Brightness Temperature Calculation

The radio brightness temperature T_b is related to the plasma parameters through the transfer equation:

$$T_b = \int T e^{-\tau} d\tau ; \quad d\tau = 0.2 \times \frac{\varphi(T)}{\nu^2 n T^{3/2}} dT \quad (2)$$

The electron density profile, necessary to compute the refraction index $n = \sqrt{1 - (N/N_{cr})}$ ($N_{cr} = 1.24 \times 10^{-8} \cdot \nu^2$ is the critical density), has been determined from the *DEM* and the assumption of hydrostatic equilibrium, getting:

$$N^2(T) = T^{-2} \times \left(C - 2\alpha \int_{T_0}^T T \varphi(T) dT \right) \quad (3)$$

where $\alpha = \mu m_H g_\odot / k_B \simeq 1.98 \times 10^{-4}$ (c.g.s. units) and C is an integration constant related to the pressure at the temperature T_0 ; $T_0 = 5 \times 10^4$ K is assumed.

The radio brightness temperature values have been calculated by integrating equations 2 using the *DEM* and $N(T)$ from equation 3 up to a temperature T_c , taken as the base of the corona, and adding the contribution of an isothermal corona in hydrostatic equilibrium at $T = T_c$.

4. Results

The computed T_b as a function of frequency are calculated for two values of the coronal temperature and different values of $C = (N_0 T_0)^2 = p_0^2$. The pressure

Table I
List of ions whose lines have been observed by the CDS instrument

| Sect. | wavelength (Å) | Obs. lines | Sect. | wavelength (Å) | Obs. lines |
|-------|----------------|-------------------|-------|----------------|---------------|
| 1 | 519.1–522.2 | Si XII | 2 | 542.3–545.4 | Ne IV |
| 3 | 552.9–556.0 | O IV | 4 | 556.5–559.5 | Ne VI, Ca X |
| 5 | 561.4–564.4 | Ne VI, Ne VII | 6 | 341.0–342.9 | Si IX, Fe XI |
| 7 | 571.4–574.5 | Ne V, Ca X, C III | 8 | 349.0–350.8 | Mg VI, Si IX |
| 9 | 582.8–585.8 | He I | 10 | 598.0–602.1 | O III |
| 11 | 606.2–609.3 | He II, O IV | 12 | 367.0–368.8 | Mg VII, Mg IX |
| 13 | 623.4–626.5 | Mg X, O IV | 14 | 628.2–631.3 | O V |

$p_0 = 2 \times 10^{14}$ (cm $^{-3}$ K) is the minimum compatible with the adopted *DEM* and with $T_c = 1 \times 10^6$ K; a lower pressure would provide negative values of N^2 at $T < T_c$ (see equation 3). The best fit of radio observations (Figure 1) are obtained assuming $T_c = 8.9 \times 10^5$ K and a pressure $p_0 = (2\text{--}3) \times 10^{14}$ (cm $^{-3}$ K) at $T_0 = 5 \times 10^4$ K, from which a density $N_c = (1.2\text{--}2.8) \times 10^8$ cm $^{-3}$ at $T = T_c$ is inferred.

Theoretical electron density profiles $N(T)$ determined from equation 3 are compared in Figure 2 with the densities derived from CDS O IV and Si IX line ratios (taken from CHIANTI; Landi *et al.* 1999). The CDS density values appear to be in disagreement with the hydrostatic equilibrium assumption. This may be the effect of inhomogeneities in the emitting plasma, due to the network structure of the low transition region which may lead to an overestimate of the O IV densities. In fact, the Si IX density agrees with the value required by radio data, while the O IV value is about three times larger. The slight temperature dependence of the O IV line ratio is not able to account for this difference.

The theoretical line intensities derived from the same models used for the T_b calculations show that the best agreement with the CDS observed values is found by assuming $p_0 = 3 \times 10^{14}$ cm $^{-3}$ K both for $T_c = 1 \times 10^6$ K and 8.9×10^5 K; the 10% variation in the coronal temperature does not affect significantly the results.

5. Discussion

Earlier studies (Chiuderi Drago 1980, and references therein) found coronal hole temperatures inferred from radio observations much lower than those obtained from EUV lines. In the present work we show that a radio-inferred coronal hole electron temperature lower than 10 6 K is consistent also with the CDS EUV observations. This is also in agreement with EUV temperatures found in polar coronal holes (Fludra *et al.* 1998; David *et al.* 1997). Such coronal hole temperatures are lower than those found from Yohkoh observations (Hara *et al.* 1994). Coronal emission measures on the contrary are rather similar; our models give a coronal emission

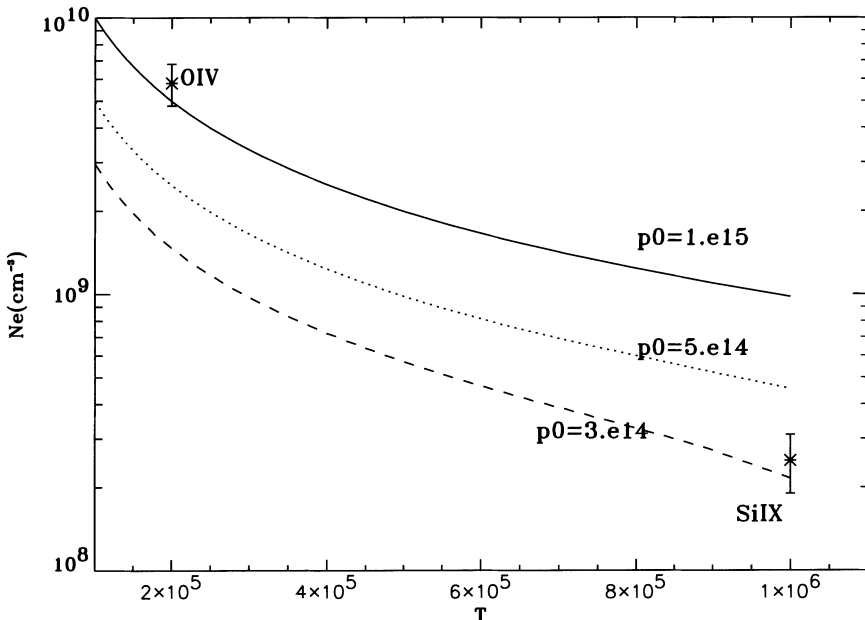


Figure 2. Fit of CDS densities with theoretical density profiles.

measure of $1.7 \times 10^{26} \text{ cm}^{-5}$ at $T_c = 8.9 \times 10^5 \text{ K}$ and $1.2 \times 10^{26} \text{ cm}^{-5}$ at $T_c = 1 \times 10^6 \text{ K}$.

A disagreement is found between theoretical density profiles and CDS O IV and Si IX densities; it appears that these density determinations do not agree with a hydrostatic equilibrium atmosphere. The very high density found from the O IV line ratio is possibly due to inhomogeneities in the transition region emitting plasma.

References

- Chiuderi Drago, F.: 1980, *Solar Phys.*, **65**, 237.
- David, C., Gabriel, A. H., Bely-Dubau, F., Fludra, A., Lemaire, P., and Wilhelm, K.: 1998, *A&A*, **336**, L90.
- Fludra, A., Del Zanna, G., Alexander, D., and Bromage, B.: 1998, *J. Geophys. Res.*, in press.
- Hara, H., Tsuneta, S., Acton, L. W., and Ogawara, Y.: 1994, *Pub. Astr. Soc. Jap.*, **46**, 493.
- Kerdraon, A., and Delouis, J. M.: 1997, in *Coronal Physics from Radio and Space Observations*, ed. G. Trottet, 483, 192.
- Landi, E., and Landini, M.: 1997, *A&A*, **327**, 1230.
- Landi, E., and Landini, M.: 1998, *A&A*, in press.
- Landi, E., Landini, M., Dere, K., Young, P., and Mason, H.: 1999, *A&ASS*, in press.

THE SOLAR MAGNETIC FIELD AS A CORONAL HOLE EXTENSION FORMS: EFFECTS OF MAGNETIC HELICITY AND BOUNDARY CONDITIONS

J. R. CLEGG and B. J. I. BROMAGE

Centre for Astrophysics, University of Central Lancashire, Preston, England, PR12HE

P. K. BROWNING

Dept. of Physics, UMIST, PO Box 88, Sackville St., Manchester, England, M601QD

Abstract. An analytical solution is presented for linear force fields within a spherical shell, representing the solar corona. Allowing for a global magnetic helicity, we find magnetic fields over the entire corona with realistic inner boundary conditions obtained from transformation and extrapolation of photospheric magnetograms and considering alternative outer boundary conditions. Such fields are found for the well known coronal hole extension event of August 1996.

Key words: force-free, corona, magnetic fields

1. Introduction

The inner solar corona is known to be a region where the structure of the magnetic field rather than flow advection dominates the plasma evolution. A sequence of force-free magnetic equilibria have been found to model the global fields associated with the coronal hole extension from the “Whole Sun Month.” This paper considers the sensitivity of such models to variations in the outer boundary conditions and to the amount of magnetic helicity present.

In an earlier paper (Clegg *et al.* 1999), a potential field approximation was used. In transforming from line-of-sight measurements, to provide a radial field component as an inner boundary condition, the assumption about the photospheric field vector can significantly affect the field reconstruction. The difficulty arises because the photosphere is not a low beta plasma like the corona, and while an assumed radial vector provides a good approximation (Wang and Sheeley 1992), it is better to correct for any small transverse field there. Secondly, the boundary condition across the far solar surface is obtained from combining the visible disc with extrapolations from a time series of MDI data, rather than by synoptic measurements.

It is evident that a current free corona is unrealistic and in particular the potential field solution cannot adequately reproduce the observations of streamers shown in the LASCO coronagraphs, which coincide because of the high plasma conductivity. As a first step, force-free equilibria can be found which are solutions to the elliptical equation

$$\nabla \times \mathbf{B} = \alpha \mathbf{B} \quad (1)$$

where $\alpha = \alpha(\mathbf{r}) = \mathbf{j} \cdot \mathbf{B}/B^2$ depends on transverse field gradients or shear across the photosphere which can inject a magnetic helicity into the corona. In this study



α is taken to be uniform, a simple free modeling parameter affecting the magnetic helicity content of the global field, and the resulting linear problem is amenable to analysis.

2. Field Solution and Boundary Conditions

A general solution is found to the linear force-free field problem (1) between two spherical shell boundaries enclosing the inner corona, which has bounded magnetic field energy. Introducing a scalar field P where

$$\mathbf{B} = \nabla \times [\nabla \times (P\hat{\mathbf{r}}) + \alpha P\hat{\mathbf{r}}] \quad (2)$$

substituting into (1), separating variables and using orthogonality to derive the unknown coefficients from the boundary conditions at $r = a$ (inner surface) and $r = b$ (outer surface), the solution, with $\mu = \cos \theta$, is

$$P(r, \mu, \phi) = \sum_{n=0}^{\infty} \sum_{m=0}^n P_n^m(\mu) \cdot [(a_{nm} \sin m\phi + b_{nm} \cos m\phi).g_b(r) + (c_{nm} \sin m\phi + d_{nm} \cos m\phi).g_a(r)] \quad (3)$$

$$g_a(r) = \frac{r^{1/2}}{b^{1/2}} \left(\frac{J_{-n-1/2}(\alpha a).J_{n+1/2}(\alpha r) - J_{n+1/2}(\alpha a).J_{-n-1/2}(\alpha r)}{J_{-n-1/2}(\alpha b).J_{n+1/2}(\alpha a) - J_{n+1/2}(\alpha b).J_{-n-1/2}(\alpha a)} \right) \quad (4)$$

and $g_b(r)$ is obtained by interchanging b and a in (4), and

$$\begin{bmatrix} a_{nm} \\ b_{nm} \end{bmatrix} = N_{nm} \cdot \int_0^{2\pi} \int_{-1}^1 a^2 \cdot B_r(a, \mu, \phi) \begin{bmatrix} P_n^m(\mu) \cdot \sin m\phi \\ P_n^m(\mu) \cdot \cos m\phi \end{bmatrix} \cdot d\mu \cdot d\phi \quad (5)$$

where $N_{nm} = [C(2n+1)(n-m)!]/[2\pi n(n+1)(n+m)!]$ with $C = 1/2$ for $m = 0$, otherwise $C = 1$, and c_{nm} , d_{nm} are found from (5) by replacing a with b . The expression (2) then gives the field.

At $r = b = 2.5 R_s$, $g_b(b) = 0$ and $B_r(b, \mu, \phi)$ is entirely specified by the outer boundary coefficients c_{nm} and d_{nm} . However, $B_\theta(b, \mu, \phi)$ and $B_\phi(b, \mu, \phi)$ are affected by a_{nm} and b_{nm} (related to the inner boundary) as well as by c_{nm} and d_{nm} , and these components cannot be made to vanish for all (μ, ϕ) , except when $\alpha = 0$. For this special case (only), a “source surface” condition $\mathbf{B} = B_r(b).\hat{\mathbf{r}}$ is possible provided

$$\begin{bmatrix} c_{nm} \\ d_{nm} \end{bmatrix} = \begin{bmatrix} a_{nm} \\ b_{nm} \end{bmatrix} \cdot \left(\frac{(2n+1)}{(n+1) \cdot a^{-2n-1} b^{2n+1} + n} \right) \cdot \left(\frac{1}{b^{-n-1} a^{n+1}} \right) \quad (6)$$

There is no reason why (6) cannot be applied *arbitrarily* to the problem with $\alpha \neq 0$ but it is understood that the condition is not then a “source surface.” Instead a

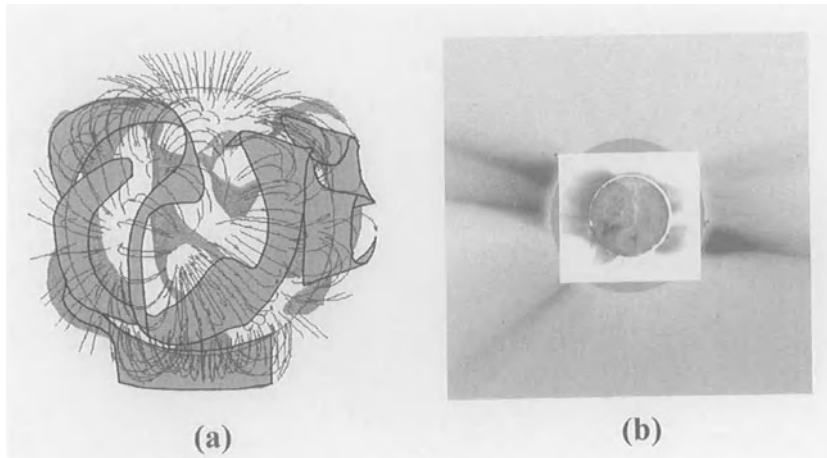


Figure 1. (a) The inversion surface of the radial field over the whole sun to $1.5R_s$ for 23:59, 27 August 1996. The near-side (light tone) and associated field is shown, with the far-side surface (dark tone) viewed through the sun. There is a northern polar hole and crown arcade. A prominence arcade (slightly twisted ribbon) runs alongside the eastern boundary of the extended coronal hole. (b) LASCO C1/C2 and EIT for 27 August 1996.

modification was used where c_{nm} and d_{nm} are obtained through (6) with a_{nm}^* and b_{nm}^* defined through a remapping $B_r(a, \mu, \phi) \rightarrow B_r(a, \mu, \phi \pm \phi_o(\mu))$, where the phase shift $\phi_o(\mu)$ falls to zero at the poles. This choice is motivated by the uncertain longitude of the streamer belt seen in coronagraphs, itself closely related to the neutral sheet “disc,” particularly its tilt (see Fisk, this workshop) and warp (Vibert *et al.* 1997), although its structure becomes complex towards $r = a$, Figure 1.

3. Results and Conclusions

The field reconstructions, Figure 2 and Figure 3, show the principle structures expected from EIT images. A latitudinal variation in magnetic helicity in the corona is implied by reconstructing fields with different (globally) uniform values of α and comparing fields away from the equator with LASCO. Here, a positive value of α increases the triangulation of the arcades to the north, and a negative value of α improves the representation of the southeast (SE) limb emission peak. In addition, a small differential lag in the position of the outer boundary condition can increase the superradial polar field-line expansion.

The authors are grateful for the provision of data by the SOHO MDI, EIT and LASCO consortiums. SOHO is a project of international co-operation between ESA and NASA. We thank PPARC for support.

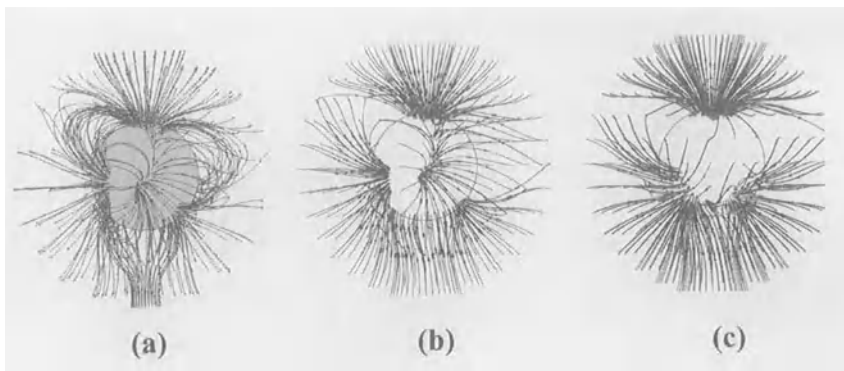


Figure 2. (a) Potential field lines over the visible corona on 27 August 1996, (b) subset of “open” field lines, and (c) as seen through to the far side. The streamer position, but not its shape, is realistic. Notice the superradial polar field-line expansion, a consequence of the $m = 0$ contribution, a characteristic of solar minimum.

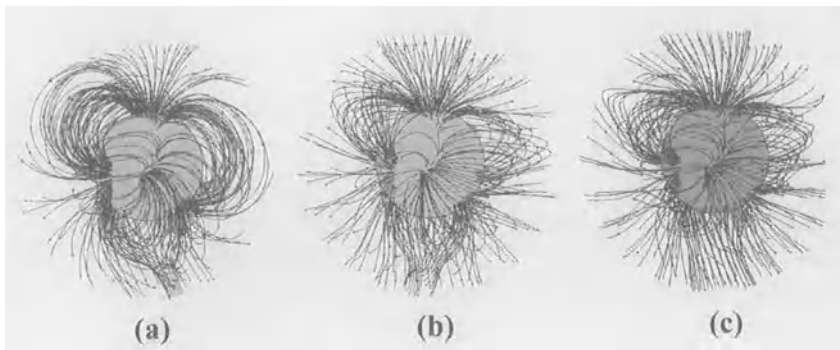


Figure 3. (a) $\alpha = -0.05$ (dim. units) twists the A.R. loops in the *south* to coincide with the LASCO SE emission peak, (b) $\alpha = 0.4$ shapes the arcade in the *north*, (c) $\alpha = 0.3$ and a phase shift $\phi_o = \pi/8$ at $2.5R_s$, displacing the lobe in the neutral line; polar superradial field-line expansion increases.

References

- Clegg, J. R., Bromage, B. J. I., and Browning, P. K.: 1999, ‘‘Modelling the coronal magnetic field with a new method for obtaining boundary conditions on the far side of sun,’’ *JGR*, in press.
 Vibert, D., Lamy, P., and Llebaria, A.: 1997, ‘‘Streamer belt at solar min: simulation & comparison with LASCO C2 images,’’ *Proc. 5th SOHO Workshop, Oslo*, p. 713.
 Wang, Y.-M., and Sheeley, N. R., Jr.: 1992, ‘‘On potential field models of the solar corona,’’ *Ap.J.*, **392**, 310.

SPECTROSCOPIC CONSTRAINTS ON MODELS OF ION-CYCLOTRON RESONANCE HEATING IN THE POLAR SOLAR CORONA

S. R. CRANMER, G. B. FIELD and J. L. KOHL

Harvard-Smithsonian Center for Astrophysics, Cambridge, MA 02138, USA

Abstract. Using empirical velocity distributions derived from UVCS and SUMER ultraviolet spectroscopy, we construct theoretical models of anisotropic ion temperatures in the polar solar corona. The primary energy deposition mechanism we investigate is the dissipation of high frequency (10–10000 Hz) ion-cyclotron resonant Alfvén waves which can heat and accelerate ions differently depending on their charge and mass. We find that it is possible to explain the observed high perpendicular temperatures and strong anisotropies with relatively small amplitudes for the resonant waves. There is suggestive evidence for steepening of the Alfvén wave spectrum between the coronal base and the largest heights observed spectroscopically. Because the ion-cyclotron wave dissipation is rapid, even for minor ions like O⁵⁺, the observed extended heating seems to demand a constantly replenished population of waves over several solar radii. This indicates that the waves are generated gradually throughout the wind rather than propagated up from the base of the corona.

Key words: Alfvén waves, corona, ion cyclotron resonance, spectroscopy, UV radiation

1. Introduction

Ultraviolet spectroscopy of the solar corona provides detailed empirical knowledge about the plasma conditions in the acceleration region of the solar wind. Specifically, the shapes of emission lines probe ion velocity distributions along the transverse line of sight. In this paper we present a preliminary analysis of measurements from the UVCS instrument aboard SOHO. These observations are interpreted in the context of a specific theoretical mechanism for preferential ion heating: the dissipation of high frequency Alfvén waves via resonance with ion-cyclotron Larmor motions. A more detailed analysis is presented by Cranmer *et al.* (1999a).

The high speed solar wind displays a marked departure from ideal thermal equilibrium. Spacecraft measurements at distances greater than 0.3 AU have found strong temperature anisotropies correlated with the local magnetic field direction, as well as a preferential energization (i.e., faster flow speed and higher temperature) of higher-mass ions (e.g., Feldman and Marsch 1997). Similar plasma properties have also been found in the extended polar corona with UVCS/SOHO (Kohl *et al.* 1995). Above 2–3 R_{\odot} , O⁵⁺ ions are measured to have perpendicular kinetic temperatures approaching 2×10^8 K and $T_{\perp}/T_{\parallel} \approx 10\text{--}100$ (Kohl *et al.* 1997, 1998a; Cranmer *et al.* 1999b). The O⁵⁺ and Mg⁹⁺ ion kinetic temperatures are significantly greater than “mass-proportional” when compared with H⁰ (i.e., $T_{\text{ion}}/T_H > m_{\text{ion}}/m_H$; see also Kohl *et al.* 1998b).

2. Steady State Models

In this work we model the ion velocity distributions as bi-Maxwellians and solve the perpendicular energy conservation equation for $T_{\perp i}$. The derived perpendicular



Space Science Reviews 87: 149–152, 1999.

©1999 Kluwer Academic Publishers.

temperatures are relatively insensitive to variations in parallel temperature and ion outflow velocity, so we constrain these quantities empirically (see also Cranmer *et al.* 1999a). Ion heat conduction is neglected, but Coulomb collisions between the ion and proton distributions are taken into account (Barakat and Schunk 1981). The magnetic field strength and superradial flux tube divergence over the poles are constrained using the model of Banaszkiewicz *et al.* (1998). The empirical electron temperature T_e of Ko *et al.* (1997) is adopted, and the proton temperature is modeled as $T_p = T_e(r/R_\odot)^{0.75}$. We use the solar minimum electron density n_e of Guhathakurta and Holzer (1994) and compute the proton outflow velocity u_p using mass flux conservation. The ion outflow speed u_i is set equal to the proton outflow speed, and a test with $u_i = 2u_p$ produced no more than a 30 km s^{-1} change in the resulting most probable speed $w_{\perp i} = (2kT_{\perp i}/m_i)^{1/2}$. The parallel random ion motions are assumed to be in thermal equilibrium with the protons, and the lower boundary condition at $r = R_\odot$ is simply $T_{\perp i} = T_{\parallel i} = T_p$.

We model the powerful wave-particle energy exchange arising from the resonance between high frequency, parallel propagating Alfvén waves and the cyclotron gyromotions of positive ions (e.g., Hollweg and Turner 1978; Marsch *et al.* 1982; Isenberg 1984; Tu and Marsch 1997). We use the “quasilinear” approximation for the wave damping rate, and have verified its consistency for minor ions in the corona. We assume the magnetic fluctuation spectrum is maintained in a self-similar power law form [$P(\omega) \propto \omega^{-\eta}$] over the resonant frequencies of interest, and that the radial evolution of wave power is governed by the linear conservation of wave action (Isenberg and Hollweg 1982).

3. Comparison with Spectroscopic Measurements

Cranmer *et al.* (1999a) present a detailed analysis of measurements made by the SUMER and UVCS instruments, and compare them to models similar to those described above (but with $T_{\parallel i}$ computed self-consistently as well). The relevant SUMER observations are the $1/e$ emission line widths presented by Tu *et al.* (1998) and Hassler *et al.* (1997) between 1.01 and $1.06 R_\odot$. These are modeled effectively using shallow power law wave spectra with $\eta \approx 0.5–1$. Steeper slopes cannot produce the observed dependence of line width on the charge-to-mass ratio Z/A of the ions. For lines of Fe and Si, which have been observed in more than one ionization state, lower charge states have broader widths; this is consistent with those ions having a weaker Coulomb collision rate ($\propto Z^2/A$; Spitzer 1962).

Measurements of emission lines at higher heights with UVCS have revealed unexpectedly broad profiles of O VI $\lambda\lambda 1032, 1037$ over the poles. The most-probable speeds $w_{\parallel i}$, $w_{\perp i}$ and outflow velocities u_i have been modeled empirically by Kohl *et al.* (1998a) and Cranmer *et al.* (1999b), and in Figure 1 we plot a comparison between the empirical values of $w_{\perp i}$ and model integrations from 1 to $3.5 R_\odot$. The normalization of the wave power law $P(\omega)$ was varied for each value of η to match the empirically derived $w_{\perp i}$ at $3 R_\odot$. Interestingly, the best

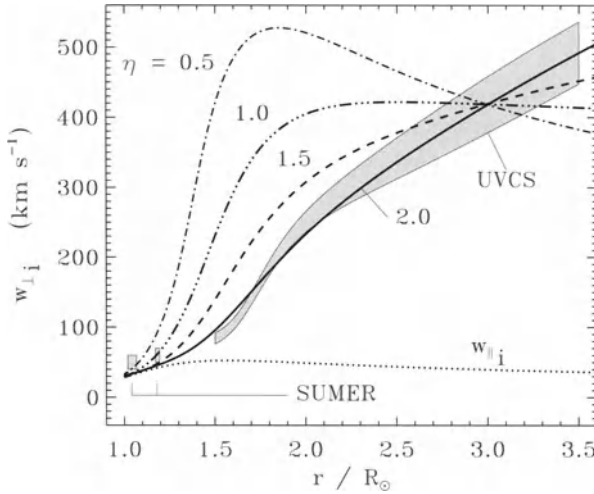


Figure 1. Radial dependence of the perpendicular most-probable speed $w_{\perp i}$ for O⁵⁺ ions. Empirical constraints from SUMER and UVCS are denoted by gray regions bordered by thin solid lines. Also plotted is the assumed parallel most-probable speed (dotted line) and model results for a range of spectral power law exponents η .

agreement with the observed radial variation comes from a model with a *steep* power law ($\eta \approx 2$), in contrast to the shallower value constrained by the SUMER measurements at lower heights.

The magnitude of the resonant wave power required to heat the O⁵⁺ ions is small when compared with the mean magnetic field and the thermal ion energy (see Marsch *et al.* 1982), and is also several orders of magnitude smaller than simple extrapolations of *in situ* wave power down to the corona. There is thus ample room for some resonant damping of the wave amplitudes to occur and still have enough power to heat the minor ions (Cranmer *et al.* 1999a). We find that resonant damping times are very short when compared to macroscopic wind flow times, so waves will damp rapidly if not otherwise maintained at their modeled amplitudes. Thus, a purely self-consistent model of their propagation (from, e.g., the base of the corona) and decay should not be able to deposit heat *gradually* into the extended corona as seems to be required. Such a self-damped model would produce a strong impulse of heating at low heights, followed by an extended region of ineffective and negligible energy deposition. It seems clear that some kind of additional wave generation over several solar radii is required to produce agreement with the observations.

It remains to be seen if the majority ions in the solar corona (protons and He²⁺) can be heated by the same mechanisms that power the minor species. Quasilinear theory may not be sufficient to model their stronger ion-cyclotron damping, and the required gradual production of waves proposed above may not be rapid enough to stop the dissipation arising from proton and He²⁺ resonances.

4. Conclusions

The generation and maintenance of a high-frequency coronal Alfvén wave spectrum remains a major unresolved issue. Standard MHD turbulent cascade may not be sufficient to replenish the resonant wave power on time scales short enough to compete with the ion-cyclotron damping. Kinetic microinstabilities arising from nonequilibrium velocity distributions may play an important role (Schwartz 1980). The existence of a self-organized power-law spectrum points to fundamentally nonlinear processes, and even the observed (*in situ*) onset of dissipation near the cyclotron frequency does not guarantee the dominance of parallel propagating wave resonances (e.g., Goldstein *et al.* 1995; Leamon *et al.* 1998). If ion-cyclotron wave dissipation is indeed the solution to the problem of extended coronal heating in the fast solar wind, then this solution gives rise to many new questions concerning the kinetic physics of the plasma and the origin of its fluctuation spectrum.

This work is supported by the National Aeronautics and Space Administration under grant NAG5-3192 to the Smithsonian Astrophysical Observatory, by Agenzia Spaziale Italiana, and by the ESA PRODEX program (Swiss contribution).

References

- Banaszkiewicz, M., Axford, W. I., and McKenzie, J. F.: 1998, *A&A*, **337**, 940.
 Barakat, A. R., and Schunk, R. W.: 1981, *J. Phys. D*, **14**, 421.
 Cranmer, S. R., Field, G. B., and Kohl, J. L.: 1999a, *Ap. J.*, **518**, in press (20 June 1999).
 Cranmer, S. R., *et al.*: 1999b, *Ap. J.*, **511**, 481.
 Feldman, W. C., and Marsch, E.: 1997, in *Cosmic Winds and the Heliosphere*, ed. J. R. Jokipii, C. P. Sonett, and M. S. Giampapa (Tucson: University of Arizona Press), 617.
 Goldstein, M. L., Roberts, D. A., and Matthaeus, W. H.: 1995, *Ann. Rev. Astron. Astrophys.*, **33**, 283.
 Guhathakurta, M., and Holzer, T. E.: 1994, *Ap. J.*, **426**, 782.
 Hassler, D. M., Wilhelm, K., Lemaire, P., and Schühle, U.: 1997, *Solar Phys.*, **175**, 375.
 Hollweg, J. V., and Turner, J. M.: 1978, *J. Geophys. Res.*, **83**, 97.
 Isenberg, P. A.: 1984, *J. Geophys. Res.*, **89**, 6613.
 Isenberg, P. A., and Hollweg, J. V.: 1982, *J. Geophys. Res.*, **87**, 5023.
 Ko, Y.-K., Fisk, L. A., Geiss, J., Gloeckler, G., and Guhathakurta, M.: 1997, *Solar Phys.*, **171**, 345.
 Kohl, J. L., *et al.*: 1995, *Solar Phys.*, **162**, 313.
 Kohl, J. L., *et al.*: 1997, *Solar Phys.*, **175**, 613.
 Kohl, J. L., *et al.*: 1998a, *Ap. J. Letters*, **501**, L127.
 Kohl, J. L., *et al.*: 1998b, *Ap. J. Letters*, **510**, L59.
 Leamon, R. J., Smith, C. W., Ness, N. F., Matthaeus, W. H., and Wong, H. K.: 1998, *J. Geophys. Res.*, **103**, 4775.
 Marsch, E., Goertz, C. K., and Richter, K.: 1982, *J. Geophys. Res.*, **87**, 5030.
 Schwartz, S. J.: 1980, *Rev. Geophys. Space Phys.*, **18**, 313.
 Spitzer, L., Jr.: 1962, *Physics of Fully Ionized Gases*, 2nd ed. (New York: Wiley).
 Tu, C.-Y., and Marsch, E.: 1997, *Solar Phys.*, **171**, 363.
 Tu, C.-Y., Marsch, E., Wilhelm, K., and Curdt, W.: 1998, *Ap. J.*, **503**, 475.

CORONAL HEATING: A COMPARISON OF ION-CYCLOTRON AND GRAVITY DAMPING MODELS

I. CUSERI

Università di Firenze, I-50125 Firenze, Italy

D. MULLAN

Bartol Research Institute, University of Delaware, Newark, DE 19716

G. POLETTO

Osservatorio di Arcetri, Largo E. Fermi, 5, I-50125 Firenze, Italy

Abstract. SOHO/UVCS data indicate that minor ions in the corona are heated more than hydrogen, and that coronal heating results in T_{\perp} larger than T_{\parallel} . Analogous behavior has been known from *in situ* measurements in solar wind for many years. Here we compare and contrast two mechanisms which have been proposed to account for the above behavior: ion-cyclotron resonance and gravity damping.

Key words: sun: corona; sun: wind; Alfvén waves; ion-cyclotron resonance

1. The Models

Recent findings from UVCS/SOHO (see, e.g., Kohl *et al.* 1998), where minor ions in the solar corona appear to be much hotter than hydrogen Ly- α , are reminiscent of *in situ* data obtained many years ago in the solar wind. A further similarity between solar wind data and the recent coronal data is the presence of temperature anisotropy: $T_{\perp} > T_{\parallel}$. The mechanism at work is apparently mass-dependent, and prefers to pump energy into the direction perpendicular to the radial direction.

One mechanism which has been proposed to explain these findings is ion-cyclotron resonance (ICR) (e.g., McKenzie *et al.* 1995, 1997; Marsch and Tu 1997; Tu and Marsch 1997; Cranmer *et al.* 1999). A second mechanism—gravity damping (GD) of Alfvén waves—was proposed by Khabibrakhmanov and Mullan (1994, 1997); Alfvén waves do work on the plasma, and a fraction f of this work may be converted (via collisions) into thermal energy. Cuseri *et al.* (1999) used GD to construct a two-fluid solar corona/wind model in the limit $f \rightarrow 1$ (see Figure 1). Many of the physical conditions in the inner corona and in the wind around 1 AU are reproduced both with the GD model and with the ICR model. Since ICR and GD both account for several aspects of the corona and wind, we ask: are there any observational signatures which might lead us to determine if either process is preferred in coronal/wind heating? This issue will be discussed in the next Section.

2. Comparison of the ICR and GD processes

A major empirical difficulty with the ICR mechanism is that, in coronal plasma, the requisite resonances occur at high frequencies (100–1000 Hz). There are no data



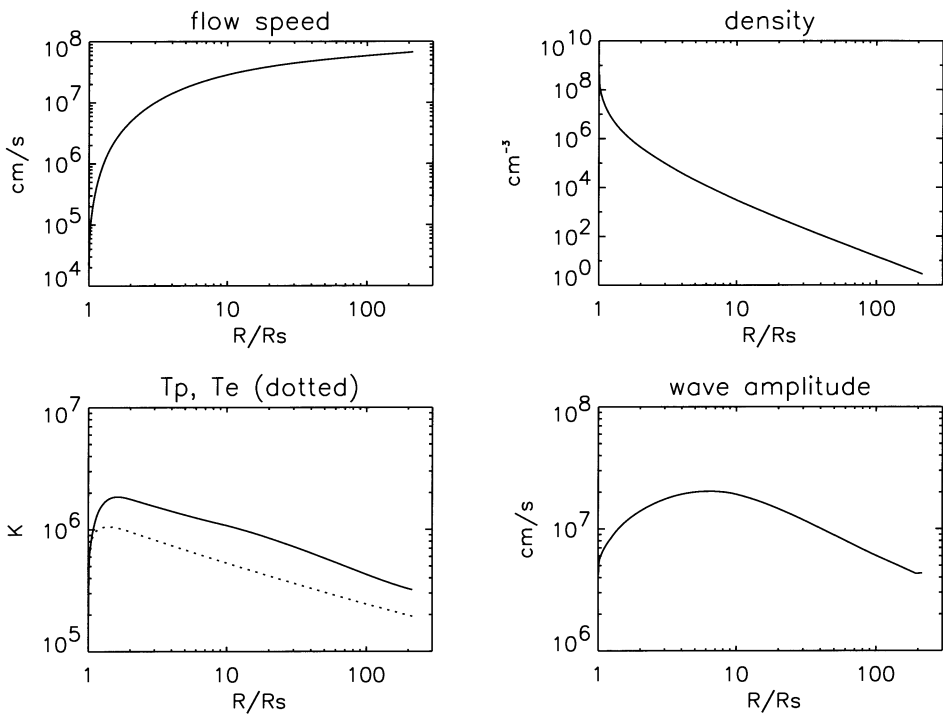


Figure 1. Flow speed, electron density, temperatures and wave amplitude vs. heliocentric distance for a model based on dissipation of Alfvén waves by gravity damping.

to provide quantitative, or qualitative, information about the spectra of relevant waves in the corona. Hence, ICR models rely on assumptions concerning the power spectra (see e.g., Tu and Marsch 1997) and/or on *ad hoc* heating functions. As a result, these models cannot yet *prove* that ICR is the principal mechanism at work in the corona/wind; at most, consistency can be demonstrated.

In contrast to our inability to measure the properties of resonant waves *in the corona*, waves *in the wind* at 1 AU which might resonate with plasma particles *are* susceptible to measurement. The power spectrum of magnetic fields in the solar wind typically exhibits a change in slope at frequencies $\nu_{bf} = 0.1\text{--}1$ Hz (Leamon *et al.* 1998). Since the proton gyro-frequency ν_{pc} is of order 0.1 Hz, it seems at first sight as if the near coincidence between ν_{bf} and ν_{pc} might be interpreted as evidence for ICR damping. But closer inspection reveals that this interpretation is incorrect: the WIND data in fact “contradict the expectations and predictions of parallel-propagating cyclotron-damped Alfvén wave theory” (Leamon *et al.* 1998). Moreover, if ICR damping were the dominant process at work in the wind, the magnetic structures in the wind which would be preferentially damped at $\nu \geq \nu_{pc}$

would be those *parallel* to the mean field. But this does *not* occur; instead, the damping applies preferentially to structures *transverse* to the mean field (Leamon *et al.* 1998).

On the other hand, the GD mechanism relies on non-resonant interactions with low-frequency waves; these waves are known to exist in the solar atmosphere. Observations of solar surface motions reveal clearly that the velocity power spectrum peaks at periods of 100–1000 seconds (Milano *et al.* 1997). Such surface motions undoubtedly couple with magnetic fields to create Alfvén waves of comparable period. The power available in these motions is sufficient to supply the coronal energy budget (Berger and Title 1996).

A significant difference between ICR and GD models lies in the predicted electron temperatures (T_e). ICR tends to lead to inefficient heating of electrons (see Cuseri *et al.* 1999). For example, in the Tu and Marsch (1997) model, where the boundary T_e is taken to be 7×10^5 K, T_e is found to reach a maximum of only $\approx 8 \times 10^5$ K. In subsequent models (Marsch and Tu 1997) where the base value of T_e is taken to be 4×10^5 K, no values of $T_e(r)$ are reported. On the other hand, GD leads to effective deposition of energy near the coronal base; in such conditions, efficient Coulomb coupling ensures that electrons are heated significantly. Cuseri *et al.* (1999) found that T_e increased from a boundary value of 2×10^5 K to more than 10^6 K.

The T_e data are hard to interpret: some SOHO data suggest $T_e < 10^6$ K between 1 and $1.3 R_\odot$ (e.g., David *et al.* 1998; Wilhelm *et al.* 1998; Doscheck *et al.* 1998). On the other hand, Yohkoh data (Foley *et al.* 1997) and *in situ* charge state observations (Ko *et al.* 1997) suggest $T_e > 10^6$ K. There is no unanimous explanation at present for the discrepancy between the reported values of T_e .

Both the ICR and GD models can successfully reproduce the Hydrogen Ly- α width vs. height profile. However, no attempt has been made by either model so far to reproduce the width of minor ion lines. Models of the heating and acceleration of heavy ions in the corona/wind are still scanty; the models which do exist assume *ad hoc* heating functions for the heavy ions (see, e.g., Li *et al.* 1997; Czechowski *et al.* 1998). As a result, these models cannot identify the mechanism at work in the corona/wind plasma. We suggest that the ability to reproduce the profile of the minor ions' effective temperature* vs. height will be a factor which may enable us to discriminate between the two mechanisms.

A further discriminant concerns the source regions of the wind. In weak field regions, the photospheric velocity amplitudes of Alfvén waves are determined by the granule flow speeds. In such conditions, the rate of energy deposition due to GD scales as $1/V_A$ (Cuseri *et al.* 1999). Thus, wind driving should be more efficient in regions of *low* Alfvén speed (as long as the ions are magnetized), and solar wind should emerge preferentially from supergranule cell interiors. Observationally, the site where the wind originates is controversial; Dupree *et al.* (1996) provided

* The effective temperature T_{eff} is defined as $T_{\text{eff}} = T + C m_i \langle v_A \rangle^2 / 2k$, where C depends on the degrees of freedom of the wave and $\langle v_A \rangle$ is the wave amplitude.

evidence for systematic outflows from the *cell centers* in coronal holes. On the other hand, Hassler *et al.* (1998), using SUMER data, found enhanced outflows from localized regions of the *network*. However, they have not identified with certainty these localized outflows as the main source of solar wind; they also report blue shifts which are present throughout the coronal hole, and the mass flux from cells is not necessarily small compared to the mass flux from the localized sources in the network.

References

- Berger, T. E., and Title, A. M.: 1996, *ApJ*, **463**, 365.
 Cranmer, S. R., Field, G. B., and Kohl, J. L.: 1999, *ApJ*, **518**, in press (20 June 1999).
 Cuseri, I., Mullan, D. J., Noci, G., and Poletto, G.: 1999, *ApJ*, in press (1 April 1999).
 Czechowski, A., Ratkiewicz, R., McKenzie, J. F., and Axford, W. I.: 1998, *A&A*, **335**, 303.
 David, C., Gabriel, A. H., Bely-Dubau, F., *et al.*: 1998, *A&A*, **336**, L90.
 Doschek, G. A., Laming, J. M., Feldman, U., *et al.*: 1998, *ApJ*, **504**, 573.
 Dupree, A. K., Penn, M. J., and Jones, H. P.: 1996, *ApJ*, **467**, L121.
 Foley, C. R., Culhane, J. L., and Acton, L. W.: 1997, *ApJ*, **491**, 933.
 Hassler, D. M., Dammasch, I. E., Lemaire, P., *et al.*: 1998, in *Proc. of Solar Wind 9*, ed. S. Habbal, in press.
 Khabibrahmanov, I. K., and Mullan, D. J.: 1994, *ApJ*, **430**, 814.
 Khabibrahmanov, I. K., and Mullan, D. J.: 1997, *ApJ*, **488**, 898.
 Kohl, J., Noci, G., Antonucci, E., *et al.*: 1998, *ApJ*, **501**, L127.
 Ko, Y.-K., Fisk, L. A., Geiss, J., *et al.*: 1997, *Solar Phys.*, **171**, 345.
 Leamon, R. J., *et al.*: 1998, *JGR*, **103**, 4775.
 Li, X., Esser, R., Habbal, S. R., and Hu, Y-Q.: 1997, *JGR*, **102**, 17419.
 Marsch, E., and Tu, C.-Y.: 1997, *A&A*, **319**, L17.
 McKenzie, J. F., Banaszkiewicz, M., and Axford, W. I.: 1995, *A&A*, **303**, L45.
 McKenzie, J. F., Axford, W. I., and Banaszkiewicz, M.: 1997, *GRL*, **24**, 2877.
 Milano, L. J., *et al.*: 1997, *ApJ*, **490**, 442.
 Tu, C.-Y., and Marsch, E.: 1997, *Solar Phys.*, **171**, 363.
 Wilhelm, K., Marsch, E., Dwivedi, B. N., *et al.*: 1998, *ApJ*, **500**, 1023.

Address for correspondence: G. Poletto, Osservatorio di Arcetri, Largo E. Fermi, 5, I-50125 Firenze, Italy

COMPRESSIBLE ASPECTS OF SLOW SOLAR WIND FORMATION

R. B. DAHLBURG

*Laboratory for Computational Physics and Fluid Dynamics, Naval Research Laboratory,
Washington, DC 20375-5344, USA*

G. EINAUDI*

*Dipartimento di Fisica, Università di Pisa è Istituto Nazionale Fisica Materia, Sez. A, 56100 Pisa,
Italia*

Abstract. Recently we have shown how the slow solar wind can be formed within a coronal helmet streamer. The solar wind is modeled by a “wake-neutral” sheet, whose subsequent linear and nonlinear evolution provides clues to the development of the wind. In this paper we describe the first results of our extension of this model to the compressible regime. In particular, we show that traveling density enhancements are formed, similar to those observed by LASCO. The compressible equations are solved by an extension to MHD of the SPECLS algorithm.

Key words: slow solar wind, magnetohydrodynamics, turbulence

1. Introduction

Recent UVCS observations indicate that the slow solar wind originates in streamer stalks (Habbal *et al.* 1997). Furthermore, density enhancements which accelerate up to the slow solar wind velocity have been observed within streamer stalks by LASCO (Sheeley *et al.* 1997; Wang *et al.* 1998) These features can be accounted for by considering the evolution of the plasma within the streamer stalk, which can be modeled as a magnetohydrodynamic wake-neutral sheet (Dahlburg *et al.* 1998b; Einaudi *et al.* 1999) Moving plasmoids are then formed as the magnetic field reconnects. A further acceleration is caused by the transfer of energy by nonlinear stresses (Dahlburg 1998). The process is quenched by a transition to turbulence, leading to greater unsteadiness in the slow component of the solar wind.

In this paper we describe the first results of our extension of this model to the compressible regime. The “blobs” observed by LASCO are density enhancements which must, in our model, be correlated with the magnetic islands which develop due to resistive instability. Our new linear compressible model provides information on density and temperature structures, as well as the velocity and magnetic fields.

2. Low Mach Number Disturbance Morphology

We model the solar wind as a wake-neutral sheet, i.e.,

$$B_{0x}(y) = \tanh y, \quad U_{0x}(y) = 1 - \operatorname{sech} y. \quad (1)$$

* Also at Berkeley Research Associates, Springfield, VA, USA



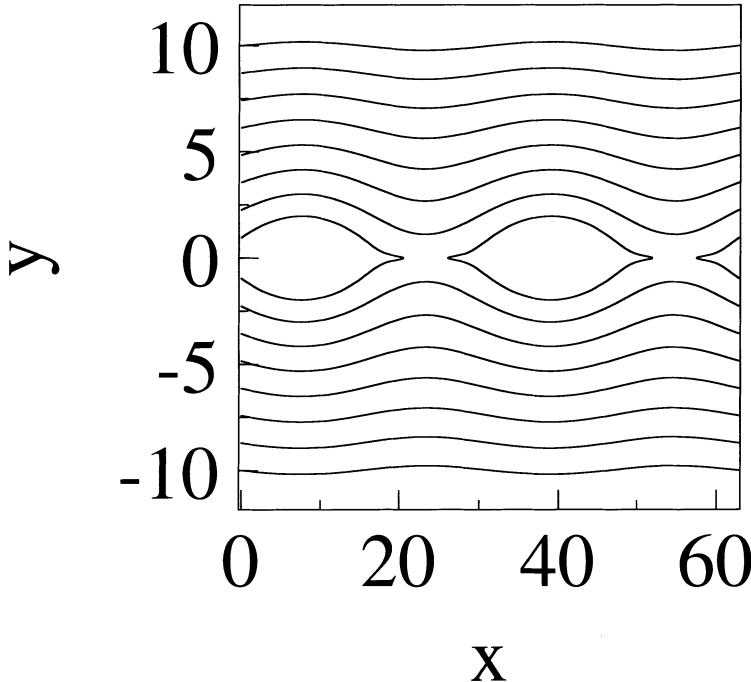


Figure 1. Two periods of the magnetic field. The plasmoids travel to the right.

Here $B_{0x}(y)$ mimics the magnetic field above a streamer, while the wake flow represents the fast wind for $y > 1$ and the slow wind for $y < 1$. For simplicity the thermodynamic basic state is chosen to ensure an ideal equilibrium:

$$\rho = 1, \quad p = 1 - \frac{1}{2} \tanh^2 y. \quad (2)$$

The linear equations for this system are quite extensive, and will be given elsewhere. We solve these equations using the SPECLS algorithm (Macaraeg *et al.* 1988), which we have modified for the MHD problem. The SPECLS algorithm is based on a Chebyshev collocation scheme.

We examine the eigenfunction for a low M case. Note that for the wake-neutral sheet, the Alfvén Mach number (M_A) is related to M as follows: $M_A = \gamma^{1/2} M$, where γ is the adiabatic index. Figure 1 shows the magnetic field, and Figure 2 shows the mass density enhancement for a typical case with $M = 0.1$, i.e., for a situation close to the Sun. In this case a mode develops which travels toward the right of the figures. We note that mass density enhancements do form which are strongly correlated with the magnetic islands. The perturbed temperature is anticorrelated with the perturbed mass density in x , implying that the density enhancements are somewhat cooler than the ambient temperature. As expected, the temperature peaks at the magnetic X-point.

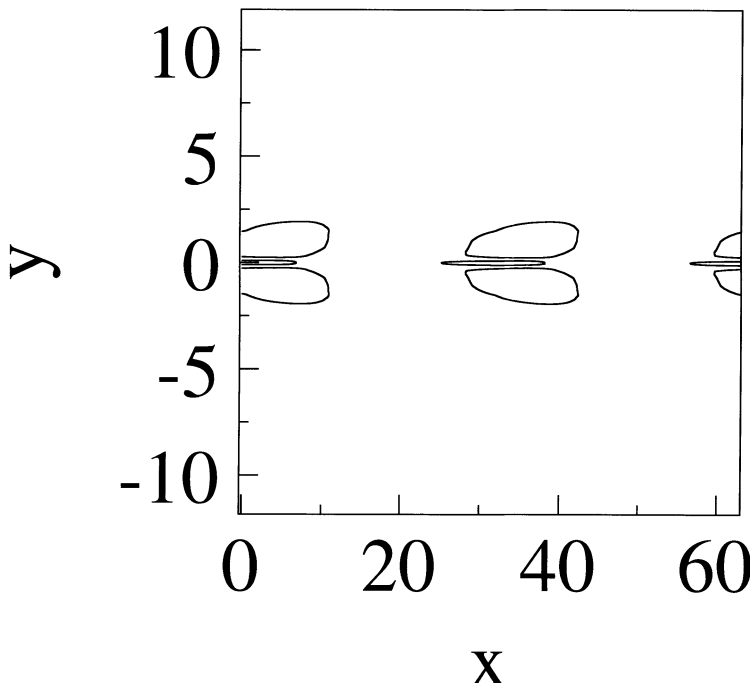


Figure 2. Two periods of the mass density enhancement.

The velocity field is shown in Figure 3. Note that the region in the center of the wake is disturbed, whereas the region exterior to the wake remains laminar. Hence, disturbances of this kind could promote unsteady behavior in the slow solar wind (Dahlburg *et al.* 1998).

Future directions include investigating the influence of the Mach number, with a particular emphasis on supersonic cases (cf. Chen *et al.* 1989). We also are at present developing a nonlinear model.

RBD was supported by the NASA SPTP. GE was supported by ASI. Computer time was provided by the DOD HPC program. We thank Dr. C. L. Streett for supplying us with a copy of the SPECLS code.

References

- Chen, J., Cantwell, B. and Mansour, N.: 1989, 'The Effect of Mach Number on the Stability of a Plane Supersonic Wake,' *AIAA Rept.*, **89-0285**.
 Dahlburg, R. B.: 1998, 'On the Nonlinear Mechanics of Magnetohydrodynamic Stability,' *Phys. Plasmas*, **5**, 133–139.

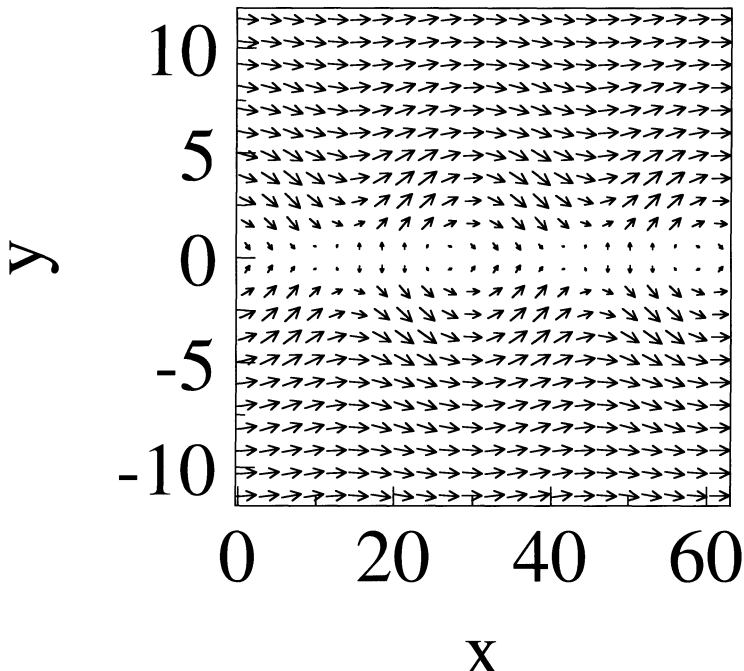


Figure 3. Two periods of the velocity for the low Mach number case.

- Dahlburg, R. B., Boncinelli, P. and Einaudi, G.: 1998a, 'The Evolution of a Plane Jet in a Neutral Sheet,' *Phys. Plasmas*, **5**, 79–93.
 Dahlburg, R. B., Karpen, J. T., Einaudi, G. and Boncinelli, P.: 1998b, 'Slow Solar Wind Acceleration,' in *Solar Jets and Coronal Plumes*, ed. T. -D. Guyenne, ESA-421, 199–205.
 Einaudi, G., Boncinelli, P., Dahlburg, R. B. and Karpen, J. T.: 1999, 'Formation of the Slow Solar Wind in a Coronal Streamer,' *J. Geophys. Res.*, **104**, 521–534.
 Habbal, S. R., *et al.*: 1997, 'Origins of the Slow and Ubiquitous Fast Solar Wind,' *Astrophys. J.*, **489**, L103–L106.
 Macaraeg, M. G., Streett, C. L. and Hussaini, M. Y.: 1988, 'A Spectral Collocation Solution to the Compressible Stability Eigenvalue Problem,' *NASA Tech. Paper*, **2858**.
 Sheeley, N. R., *et al.*: 1997, 'Measurements of Flow Speed in the Corona Between 2 and 30 R,' *Astrophys. J.*, **484**, 472–478.
 Wang, Y.-M., *et al.*: 1998, 'Origin of Streamer Material in the Outer Corona,' *Astrophys. J.*, **498**, L165–L168.

Address for correspondence: R. B. Dahlburg, Code 6440, Naval Research Laboratory, Washington, DC 20375-5344, USA

STATISTICAL ANALYSIS OF EUV AND UV LINES INSIDE AND OUTSIDE OF SOLAR CORONAL HOLES

I. E. DAMMASCH¹, D. M. HASSSLER², W. CURDT¹ and K. WILHELM¹

¹ Max-Planck-Institut für Aeronomie, D-37191 Katlenburg-Lindau, Germany

² Southwest Research Institute, 1050 Walnut St., Boulder, CO 80302, USA

Abstract. Two studies performed with SUMER (the Solar Ultraviolet Measurements of Emitted Radiation spectrometer on SOHO) in September 1996 are presented. Spatial scans, a long exposure time and a broad spectral window provide reliable line profiles for various regions of the Sun (off-limb corona, coronal hole, quiet Sun, bright and dark regions on disk) and for different formation temperatures (Si II, 14 000 K; C IV, 100 000 K; Ne VIII, 630 000 K). Line intensity, position and width distributions are presented together with the line positions relative to the wavelength seen above the limb.

1. Introduction

The transition region of the Sun has been the object of many studies using remote sensing techniques in EUV and UV emission lines. The temperature of the solar atmosphere increases from chromospheric values of 10 000 K to coronal levels of 1×10^6 K across the transition region. Also, the entire mass flow of the solar wind has to cross this region and evidence of outflow should be discernible with sensitive observational methods.

We will use SUMER (the Solar Ultraviolet Measurements of Emitted Radiation spectrometer) observations obtained in September 1996 from the SOHO (Solar and Heliospheric Observatory) spacecraft to study the statistical properties of some emission lines and search for Doppler shifts indicative of the initial stages of solar wind acceleration.

2. Observations and Data Analysis

The dates and some of the SUMER observational parameters are compiled in Table I. For both sequences the $1'' \times 300''$ slit was used with a step size of $3''$ and a sampling time of 150 s. The central portion of the detector A was read out covering the lines Si II ($\lambda 1533$), C IV ($\lambda 1548$) in first order and Ne VIII ($\lambda 770$) in second order in the 512 spectral pixels telemetered to the ground.

The fields of view of SUMER are shown in Figure 1 superimposed on an EIT/SOHO image taken on 21 September 1996 at 19:00 UT. In addition to the standard SUMER data handling methods, we have set the average Doppler shifts just above the limb to zero based on the assumption that for optically thin conditions there should be no line-of-sight component there. Near the limb, both C IV and



Table I
Summary of the observational parameters

| Date 1996 | Time (UT) | Field of View ('') | Steps | Remarks |
|--------------|---------------|--------------------------------|-------|--------------------------------------|
| 21 Sept. | 00:16 – 07:27 | 121 E – 397 W 630 N – 930 N | 173 | off-limb, coronal hole, quiet Sun |
| 22 Sept. | 00:40 – 08:11 | 476 E – 66 W 262 N – 562 N | 181 | quiet Sun |

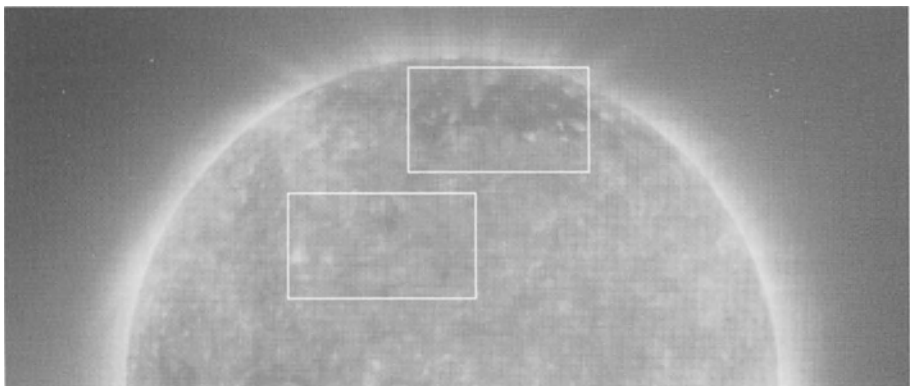


Figure 1. The Sun on 21 September 1996 at 19:00 UT at the EUV wavelength of 171 Å (Courtesy of EIT consortium) and the positions of the SUMER raster scans.

Ne VIII may exhibit some opacity effects, but the strong limb brightenings indicate no major deviation from the assumption of an optically thin medium.

3. Results

The statistical results of the quiet Sun scan on 22 September 1996 are summarized in Figure 2, in which the probability of intensities are shown on a logarithmic-linear scale; the line shifts and line widths, however, on linear-linear scales. All curves follow Gaussian distributions, which are broadest in the transition region (C IV) in each case. From simulation studies (Wilhelm *et al.* 1995), we have estimated the widths resulting from count statistics and detector effects, in order to demonstrate that the observed distributions are significantly wider. This was verified by de-convolution calculations. Similar intensity distributions have been reported by Wilhelm *et al.* (1998) and Griffiths *et al.* (1999). We show here that the line shifts and the total line widths are also normally distributed.

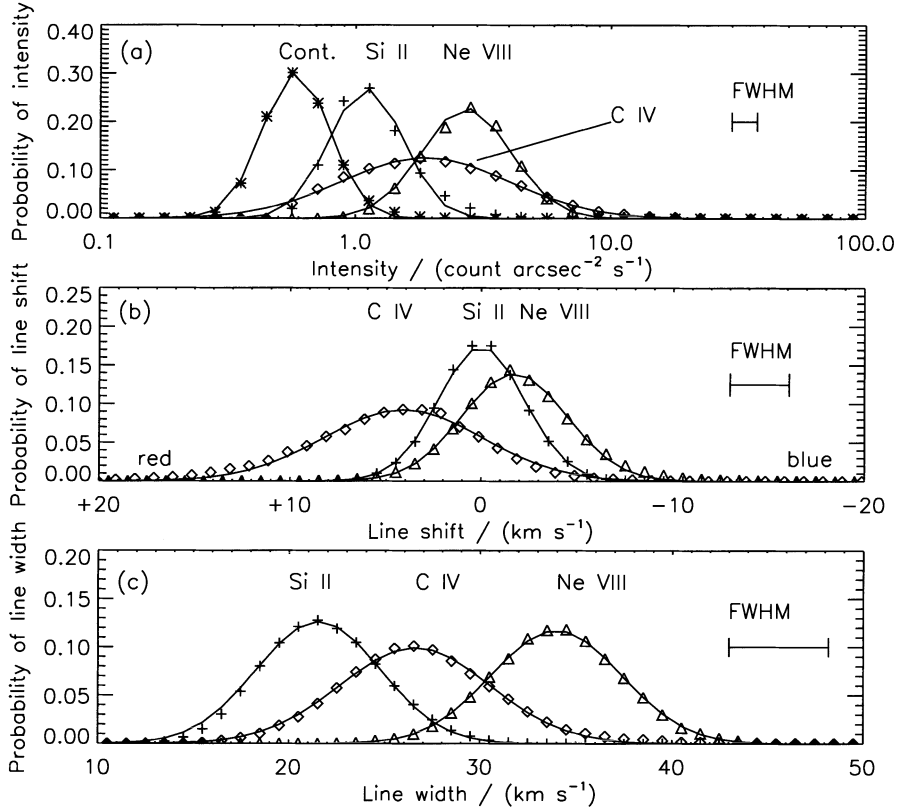


Figure 2. (a) Probability of intensity versus intensity for the lines Si II, C IV, Ne VIII and the continuum near 1543 Å; (b) Probability of line shifts versus shift; (c) Probability of line widths versus width. All results are for quiet Sun conditions. Note the different scales in (a), (b), and (c). The full widths at half maximum (FWHM) resulting from count statistics and detector effects are shown on the right-hand side.

In Figure 3, we present the most relevant findings concerning the line shifts of C IV and Ne VIII. C IV does not exhibit a strong difference in the quiet Sun and the coronal hole, whereas Ne VIII does with relative blue shifts of about -4 km s^{-1} . Moreover, the change of the slope has the opposite sign leading to an average red shift on the disk for C IV and a blue shift for Ne VIII.

4. Conclusions

Probabilities of intensities on a logarithmic scale, and line shifts and line widths on linear scales follow Gaussian distributions. These distributions are always broadest for C IV, i.e., the central transition region contains the widest variations with respect

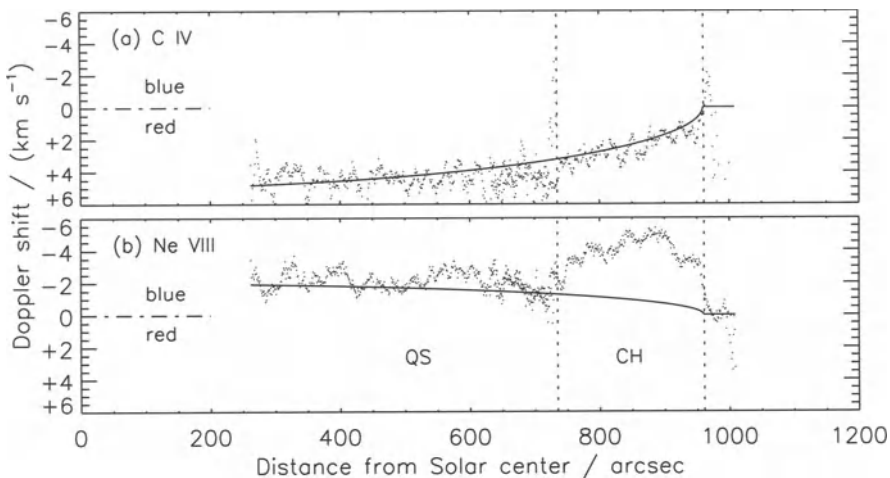


Figure 3. (a) The line shifts obtained for C IV under the assumption of zero shift just above the limb. Regions in which quiet Sun and coronal hole conditions prevail are shown as well as fits based on a cosine dependence. (b) The corresponding line shift for Ne VIII.

to radiation, speed and effective ion temperature. C IV is redshifted on the solar disk (+ 5 km s⁻¹), and Ne VIII is blueshifted on the solar disk (-2 km s⁻¹). This is in good agreement with results of Peter (1999). Inconsistencies with earlier findings may be resolved by a new determination of the Ne VIII rest wavelength, to be published by Dammasch *et al.* (1999). A significant blueshift of Ne VIII in the coronal hole which was already detected by Warren *et al.* (1997) and Hassler *et al.* (1999) is confirmed here. The upflow speed estimated for Ne VIII is at least -9 km s⁻¹, probably more when effects of blends with Si I lines are removed quantitatively.

The SUMER project is financially supported by DLR, CNES, NASA, and the ESA PRODEX program (Swiss contribution).

References

- Dammasch, I. E., Wilhelm, K., Curdt, W., and Hassler D. M.: 1999, *A&A*, in press.
- Griffiths, N. W., Fisher, G. H., Woods, D. T., and Siegmund, O. H. W.: 1999, *Ap.J.*, in press.
- Hassler, D. M., Dammasch, I. E., Lemaire, P., Brekke, P., Curdt, W., Mason, H. E., Vial, J. C., and Wilhelm, K.: 1999, *Science*, in press.
- Peter, H.: 1999, *Ap.J.*, in press.
- Warren, H. P., Mariska, J. T., and Wilhelm, K.: 1997, *Ap.J.*, **490**, L187.
- Wilhelm, K., *et al.*: 1995, *SPIE*, **2517**, 2.
- Wilhelm, K., Lemaire, P., Dammasch, I. E., Hollandt, J., Schühle, U., Curdt, W., Kucera, T., Hassler, D. M., and Huber, M. C. E.: 1998, *A&A*, **334**, 685.

TWO-FLUID 2.5D MHD SIMULATIONS OF THE FAST SOLAR WIND IN CORONAL HOLES AND THE RELATION TO UVCS OBSERVATIONS

J. M. DAVILA and L. OFMAN*
NASA GSFC, Code 682, Greenbelt, MD 20771, USA

Abstract. Recent SOHO/UVCS observations indicate that the perpendicular proton and ion temperatures are much larger than electron temperatures. In the present study we simulate numerically the solar wind flow in a coronal hole with the two-fluid approach. We investigate the effects of electron and proton temperatures on the solar wind acceleration by nonlinear waves. In the model the nonlinear waves are generated by Alfvén waves with frequencies in the 10^{-3} Hz range, driven at the base of the coronal hole. The resulting electron and proton flow profile exhibits density and velocity fluctuations. The fluctuations may steepen into shocks as they propagate away from the sun. We calculate the effective proton temperature by combining the thermal and wave velocity of the protons, and find qualitative agreement with the proton kinetic temperature increase with height deduced from the UVCS Ly- α observations by Kohl *et al.* (1998).

1. Introduction

In order to consider fully the solar wind acceleration by transverse Alfvén waves, nonlinear effects must be included. This is necessary in order to couple the transverse motions and the gradients of the magnetic pressure into the longitudinal motions.

Recently, Ofman and Davila (1997, 1998) have found that nonlinear compressional MHD waves are generated in a model coronal hole via Alfvén waves. They have used a monochromatic Alfvén wave source. In the present study we extend this model to two-fluid electron-proton plasma with a broad band Alfvén wave source and Ohmic electron heating due to the waves.

We consider the effects of waves on the observed line width temperature, and find that the proton temperature increases with heliocentric distance in qualitative agreement with UVCS observations of Ly- α lines (Kohl *et al.* 1998).

2. Two Fluid Coronal Hole Model

Neglecting electron inertia ($m_e \ll m_p$; $\mathbf{V} = \mathbf{V}_p$; $\rho = m_p n$) and relativistic effects ($V \ll c$), assuming quasi-neutrality ($n = n_e = n_p$), and neglecting minor ions and viscosity, we get the two-fluid MHD equations

$$\frac{\partial \rho}{\partial t} + \nabla \cdot (\rho \mathbf{V}) = 0, \quad (1)$$

$$\rho \left[\frac{\partial \mathbf{V}}{\partial t} + (\mathbf{V} \cdot \nabla) \mathbf{V} \right] = -(\nabla p_e + \nabla p_p) - \frac{GM_{\odot}\rho}{r^2} + \frac{1}{c} \mathbf{J} \times \mathbf{B}, \quad (2)$$

* Raytheon ITSS

$$\frac{\partial \mathbf{B}}{\partial t} = -c \nabla \times \mathbf{E}, \quad \mathbf{E} = -\frac{1}{c} \mathbf{V} \times \mathbf{B} + \eta \mathbf{J} + \frac{1}{n e c} \mathbf{J} \times \mathbf{B} - \frac{\nabla p_e}{n e}, \quad (3)$$

$$\nabla \times \mathbf{B} = \frac{4\pi}{c} \mathbf{J}, \quad \mathbf{V}_e = \mathbf{V} - \frac{\mathbf{J}}{n e}, \quad (4)$$

$$\frac{\partial p_p}{\partial t} = -\gamma_p p_p \nabla \cdot \mathbf{V} - \mathbf{V} \cdot \nabla p_p, \quad (5)$$

$$\frac{\partial p_e}{\partial t} = -\gamma_e p_e \nabla \cdot \mathbf{V}_e - \mathbf{V}_e \cdot \nabla p_e + S_e, \quad (6)$$

In the above equations we use the following normalization: $r \rightarrow r/R_s$; $t \rightarrow t/\tau_A$; $V \rightarrow V/V_A$; $B \rightarrow B/B_0$; $\rho \rightarrow \rho/\rho_0$; $p_p \rightarrow p_p/p_{p0}$; $p_e \rightarrow p_e/p_{e0}$. $S = \tau_r/\tau_A$ the Lundquist number, $\tau_r = 4\pi a^2/\nu c^2$ the resistive time scale, and $\tau_A = a/V_A$ the Alfvén time scale. In coronal holes for the relevant scales of $\mathcal{O}(0.01\text{--}1 R_\odot)$ the Hall term and the electron pressure terms are small in the Ohm's law compared to the other terms, and $\mathbf{V}_p \approx \mathbf{V}_e$. The Ohmic heating term in the electron energy equation is $S_e = (\gamma_e - 1)j^2/S$.

We assume an initial density profile given by

$$\rho_0(\theta, r) = \left[1 - (1 - \rho_r) e^{-[(\theta - \pi/2)/\theta_c]^4} \right] \rho(r)/\rho_r, \quad (7)$$

where $\rho_r = 0.111$. $\rho(r, t = 0)$ and the initial flow profile $V_r(r, t = 0)$ are given by Parker's (1963) solution. The boundary conditions at $r = 1$ are incoming characteristics approximated by zero order extrapolation (Steinolfson and Nakagawa 1976) with $v_r > 0$ and $B_r(1, \theta) = B_{r0}$, $V_\theta = B_\theta = 0$, $T_p = T_{p0}$, and $T_e = T_{e0}$, an open boundary at $r = r_{max}$ and $\theta = \theta_{max}$, and symmetry at $\theta = \pi/2$. We use a broad-band Alfvén wave source at $r = 1R_\odot$ with frequencies in the range of 1.4–6.9 mHz.

3. Numerical Results

In Figure 1 we show the results of the two-fluid run with the physical parameters $\gamma_p = 1.1$, $\gamma_e = 1.05$, $T_{p0} = 2 \times 10^6$ K, $T_{e0} = 0.8 \times 10^6$ K, $n_0 = 10^8$ cm $^{-3}$, $B_0 = 7$ G, $V_A = 1527$ km/s, $V_d = 0.0075V_A = 11.45$ km/s. The Lundquist number is set to $S = 10^4$.

The 2D distribution of the electron temperature in the model coronal hole is shown in the top left panel. The electron temperature in the center of the coronal hole decreases from 0.8×10^6 K at the base of the corona to about 0.6×10^6 K at $10R_\odot$. Two regions of somewhat higher electron temperature are evident in the model coronal hole in the boundary between the low and the high density regions. The higher temperature is the result of the Ohmic heating due to phase-mixing of the Alfvén waves in the inhomogeneous regions. The proton temperature (bottom left panel) is not directly affected by the Ohmic heating and decreases nearly monotonically from 2×10^6 K at $r = 1R_\odot$ to 1.1×10^6 K at $10R_\odot$.

The Alfvénic velocity component v_ϕ (top right panel) fluctuates out-of-phase with B_ϕ (not shown) as the waves propagate in the coronal hole. The Alfvén wave

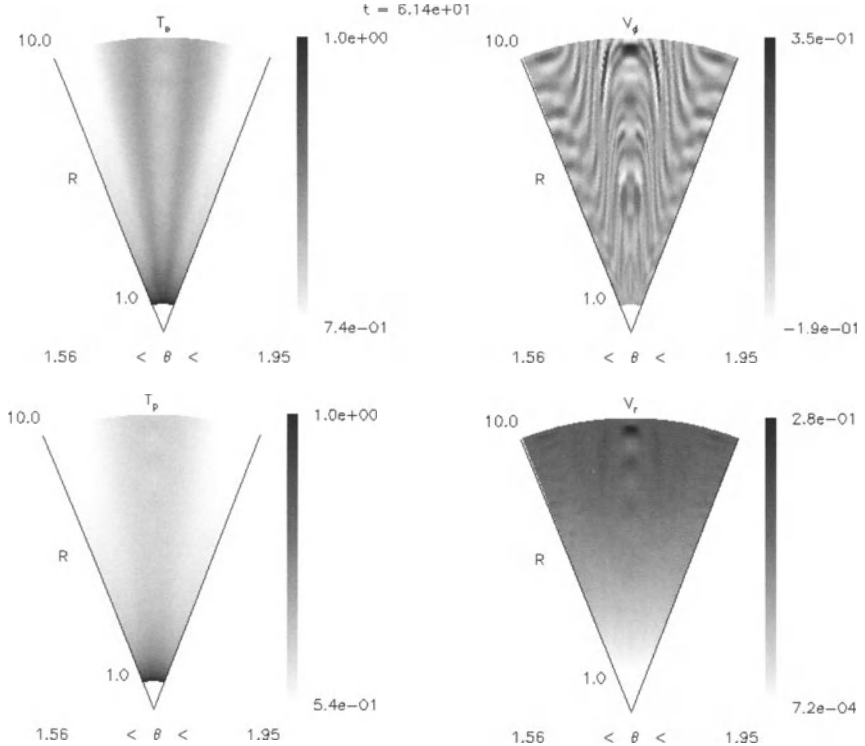


Figure 1. Temperatures and velocities of the model coronal hole (see text).

speed is faster in the central low-density region of the coronal hole than outside, and nonuniform due to the coronal structure and the broad band driver. The v_r reached about 430 km/s near $r = 10R_\odot$ and has not approached the asymptotic speed. The wave energy flux in the present run ($1.7 \times 10^4 \text{ erg cm}^{-2} \text{ s}^{-1}$) is smaller than the required flux to obtain the fast solar wind ($\sim 10^5 \text{ erg cm}^{-2} \text{ s}^{-1}$).

In Figure 2 we show the effect of v_ϕ on the line-width temperature. The dashed line shows the time-averaged proton temperature obtained from the model. The solid line shows the effective line-width temperature given by $T_{p,\text{eff}} = T_p + m_p \langle V_\perp^2 \rangle / 2k_b$, due to the contribution of wave motions integrated over the line of sight in space and over about 5 hours in time. It is evident that the effective line-width temperature increases with r in qualitative agreement with the increase of proton temperature with height, deduced from the SOHO/UVCS Ly- α observations (Kohl *et al.* 1998).

4. Conclusions

The SOHO/UVCS observations suggest that $T_p > T_e$ in coronal holes. We use the two-fluid 2.5D MHD model to investigate the self-consistent acceleration and heating of a two-temperature electron-proton plasma by broad band nonlinear waves. We find that the variations in the Alfvén wave pressure in the radial component of

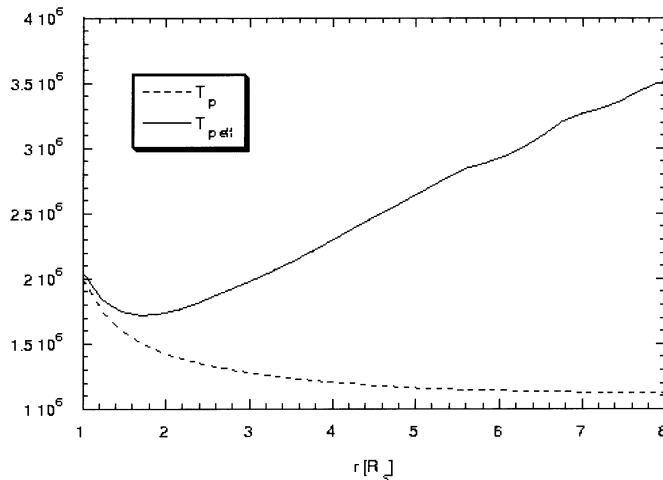


Figure 2. Effective and model proton temperatures.

the momentum equation couple to the variations in v_r , which nonlinearly steepen and generate large amplitude compressional waves.

We calculate the effective line-width proton temperature using the v_ϕ from the 2.5D two-fluid MHD model, and find an increase of the line-width proton temperature with heliocentric distance. This effect is in qualitative agreement with UVCS observations of the increase of the proton kinetic temperature deduced from the Ly- α line width observations (Kohl *et al.* 1998).

Our findings suggest that the nonlinear MHD waves may play an important role in the acceleration and heating of the fast solar wind.

Acknowledgements

LO would like to thank the support of the NASA SR&T and the SOHO Guest Investigator programs.

References

- Kohl, J. L., *et al.*: 1998, *Astrophys. J.*, **501**, 127.
- Ofman, L., and Davila, J. M.: 1997a, *Astrophys. J.*, **476**, 357.
- Ofman, L., and Davila, J. M.: 1997b, *Astrophys. J.*, **476**, L51.
- Ofman, L., and Davila, J. M.: 1998, *J. Geophys. Res.*, **103**, 23677.
- Parker, E.N.: 1963, *Interplanetary Dynamical Processes*, (New York: Interscience).
- Steinolfson, R. S., and Nakagawa, Y.: 1976, *Astrophys. J.*, **207**, 300.

CHARACTERIZATION OF SOLAR CORONAL HOLES AND PLUMES USING SPECTROSCOPIC DIAGNOSTIC TECHNIQUES APPLIED TO SOHO/CDS OBSERVATIONS

G. DEL ZANNA and B. J. I. BROMAGE

Centre for Astrophysics, University of Central Lancashire, Preston PR1 2HE UK

Abstract. Results from a series of SOHO/Coronal Diagnostic Spectrometer (CDS) observations of coronal holes and plumes are presented, including analysis of a low-latitude plume observed in August 1996. Spectroscopic diagnostic techniques using the CHIANTI atomic database are applied to derive the plasma parameters: electron density, temperature, and element abundances. The results are compared with quiet sun values. Coronal electron densities in the holes are found to be about $2 \times 10^8 \text{ cm}^{-3}$, a factor of two to three lower than in the quiet sun. The plasma thermal distribution exhibits differences between coronal holes, the quiet sun and plumes. For example, the peak of the emission in coronal holes is at a lower temperature ($T \simeq 8 \times 10^5 \text{ K}$) than in the quiet sun ($T \simeq 1 \times 10^6 \text{ K}$), while plumes are cooler ($T \simeq 7.6 \times 10^5 \text{ K}$) and show a different distribution, closer to an isothermal state.

Key words: solar corona, spectroscopic diagnostics, plumes

1. Introduction

SOHO/Coronal Diagnostic Spectrometer (CDS) (Harrison *et al.* 1995) observations of coronal holes were carried out in August 1996 and October 1997, in order to characterize them in terms of density, temperature and element abundances (for previous work, see e.g., the reviews of Habbal, Esser, and Arndt 1993; Withbroe 1988; Mason 1995). The CDS instrument provides a large range of spectral lines in the EUV which allow a more precise determination of these physical parameters than was possible with the earlier (mostly Skylab) data.

During the last week of August, a large equatorial coronal hole (named the Elephant's Trunk) appeared (Bromage *et al.* 1998), and some observing sequences were carried out near sun center, where projection effects of quiet sun material are reduced. This coronal hole has already been studied by Del Zanna and Bromage (1998). Here a detailed analysis is presented of a low latitude plume that formed in the Elephant's Trunk, and the results are compared to on-disc observations of polar coronal holes and plumes. Spectroscopic diagnostic techniques that make use of the CHIANTI atomic database (Dere *et al.* 1997) have been applied to the calibrated data in order to estimate (assuming ionization equilibrium) densities, temperatures, and relative element abundances, as described in Del Zanna and Bromage (1998). Briefly, density-sensitive ratios of lines emitted from the same ion were used to estimate electron densities, while ratios of lines emitted by the same element and a close ionization stage were used to estimate coronal temperatures, assuming an isothermal plasma. The multithermal plasma distribution along the line of sight was then studied with a differential emission measure (DEM) analysis,



Table I

Table of parameters deduced from the 27 August 1996 plume observation (a), compared to the values for the coronal hole network (b) and quiet sun (c) in Del Zanna and Bromage (1998). The densities, in cm^{-3} , are deduced from the following ratios: O IV [625.9 Å / 608.4 Å] ; Mg VII [319.0 Å / 367.7 Å] ; Si IX [349.9 Å / 341.9 Å] (Si IXa) ; Si IX [349.9 Å / 345.1 Å] (Si IXb). The isothermal temperatures are deduced from [Mg X 624.9 Å / Mg IX 368.0 Å] and [Mg IX 368.0 Å / Mg VII 367.67 Å] ratios.

| | N_e (O IV) | N_e (Mg VII) | N_e (Si IXa) | N_e (Si IXb) | T_e (K) (Mg X/IX) | T_e (K) (Mg IX/VII) |
|-----|-------------------------|--------------------|----------------------|----------------------|------------------------|--------------------------|
| (a) | $1.8 \pm 1 \ 10^{10}$ | $6 \pm 1 \ 10^8$ | $2.2 \pm 1 \ 10^8$ | $1.9 \pm 1 \ 10^8$ | $8.0 \pm 0.1 \ 10^5$ | $8.0 \pm 0.1 \ 10^5$ |
| (b) | $1.1 \pm 0.1 \ 10^{10}$ | $5 \pm 1 \ 10^8$ | $1.7 \pm 0.2 \ 10^8$ | $1.4 \pm 0.3 \ 10^8$ | $8.9 \pm 0.1 \ 10^5$ | $8.4 \pm 0.1 \ 10^5$ |
| (c) | $1.6 \pm 0.5 \ 10^{10}$ | $8.4 \pm 4 \ 10^8$ | $3.6 \pm 0.3 \ 10^8$ | $3.3 \pm 0.3 \ 10^8$ | $1.0 \pm 0.1 \ 10^6$ | $9.2 \pm 0.1 \ 10^5$ |

which was also used to deduce relative element abundances. Spectra have been spatially averaged, distinguishing between coronal hole areas and quiet sun, using isothermal temperature maps, and between cell center and network areas using the O V 629.7 Å intensity.

2. Observations and Results

On 27 August 1996, a series of CDS observations of the Elephant's Trunk was carried out. The results are presented in Del Zanna and Bromage (1998), and compared to a quiet sun observation on a region near the disc center westward of the coronal hole. The results concerning a full CDS/NIS spectrum observation of the equatorial plume are presented here. The upper transition region lines (Mg VI, Mg VII, Ca X, Mg VIII, Mg IX) show the presence of a small plume, directed almost toward the observer, that tends to 'spread out' when observed in lines emitted at higher temperatures. The plume is not visible in the high-FIP (first ionization potential) Ne lines, nor in the high-temperature (e.g., Fe XII) lines. It displayed increased Mg/Ne intensity ratios, typical of plumes (e.g., Widing and Feldman 1992). An averaged spectrum of a small region at the base of the plume was obtained (parameters shown in Table I) and a DEM analysis performed (Figure 1).

This plume showed almost an isothermal distribution at coronal heights, with a peak in the DEM at $T \simeq 7.6 \times 10^5$ K, close to the isothermal temperatures deduced from line ratios. The coronal hole DEM distribution peaks at a higher temperature ($T \simeq 8 \times 10^5$ K), while the quiet sun one peaks at $T \simeq 9.8 \times 10^5$ K and is much less isothermal. The very low emission measures at temperatures above 10^6 K are consistent with the fact that in August 1996, during solar minimum, the Sun was very quiet.

Since it was not possible to deduce absolute element abundances, the photospheric abundance of oxygen (Grevesse and Anders 1991) was assumed fixed, and all the others scaled accordingly. Only the following elements presented differ-

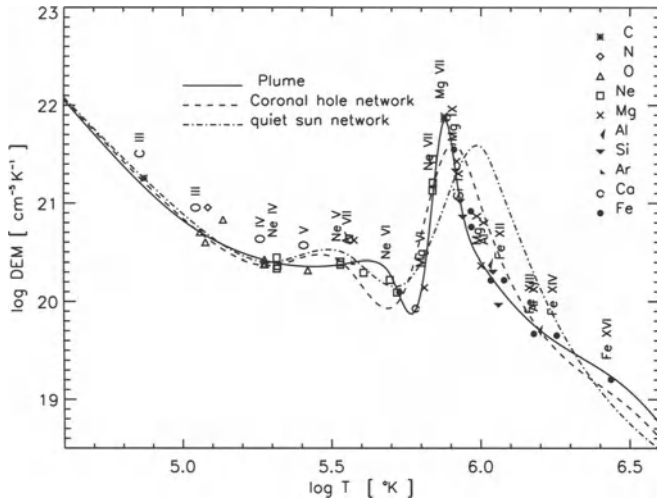


Figure 1. The DEM distribution of the plume area (solid line) with the observed points. A coronal hole network and a quiet sun network DEMs of nearby regions (Del Zanna and Bromage 1998) are overplotted for comparison. Note the narrowness of the peak of the plume DEM.

ent abundances (the numbers in parentheses are the fraction of their photospheric values): Ne (0.7), Si (0.8), Fe (0.8), Al (2.5), Ar (2.5), Ca (3.2).

A series of SOHO observations (JOP 42) was performed on a faint polar plume in the northwest region of the sun on 23 August 1996. A preliminary analysis has shown that this plume exhibited the same main characteristics as the equatorial plume (i.e., lower temperature, increased Mg/Ne and O/Ne intensities, visibility in only a few lines emitted over a limited temperature range) thus confirming the identification of the low-latitude feature as a plume.

On 10 October 1997, a northwest region of the polar coronal hole was observed by CDS. This area contains a quiet sun region in the lower part, a polar plume (visible in Mg VI–IX lines) and a bright point (visible in all lines). Densities and temperatures of these various areas have been derived (Table II). The coronal hole and quiet sun temperatures and densities are similar to the values deduced from the August 1996 observations. The plume had a transition region density a factor of two higher than in the coronal hole, while the bright point showed an increased coronal density ($N_e \simeq 8 \times 10^8 \text{ cm}^{-3}$). At transition region (O IV) heights the averaged density is $N_e \simeq 1 \times 10^{10} \text{ cm}^{-3}$ in the network, with consistently higher values in the cell-center areas. The density in the coronal hole region is about a factor of two lower than in the quiet sun areas.

3. Conclusions

CDS observations of an equatorial and a polar coronal hole both show average coronal electron densities $N_e \simeq 2 \times 10^8 \text{ cm}^{-3}$, about a factor of two lower than in

Table II

Table of parameters deduced from the 10 October 1997 averaged spectra of the selected regions. The coronal hole (CH) and quiet sun (QS) regions have been subdivided into network (Net) and cell centers (CC). The densities, in cm^{-3} , and isothermal temperatures (in K) are deduced from the ratios listed in Table I.

| | plume | CH Net | CH CC | QS Net | QS CC | BP |
|---------------------------------|---------------|---------------|---------------|---------------|---------------|---------------|
| N_e (O IV) (10^{10}) | 1.5 ± 0.3 | 1.6 ± 0.3 | 2.7 ± 0.9 | 3.5 ± 0.4 | 6 ± 0.6 | 4.5 ± 1 |
| N_e (Mg VII) (10^8) | 6 ± 1 | 3 ± 1.5 | 2.0 ± 2 | 5.3 ± 1 | 4 ± 2 | 4.7 ± 2 |
| N_e (Si IXa) (10^8) | 2.2 ± 1 | 2.2 ± 1 | 1.7 ± 1.5 | 4.7 ± 0.9 | 4.5 ± 1 | 8.4 ± 2 |
| T_e (Mg X/Mg IX) (10^5) | 8.2 ± 0.1 | 9.6 ± 0.1 | 9.8 ± 0.1 | 11 ± 1 | 11 ± 1 | 9.9 ± 0.1 |
| T_e (Mg IX/Mg VII) (10^5) | 7.7 ± 0.1 | 8.1 ± 0.1 | 8.3 ± 0.1 | 9.1 ± 0.1 | 9.2 ± 0.1 | 8.7 ± 0.1 |

the quiet sun areas, and average isothermal temperatures $T \simeq 8.5 \times 10^5$ K, about 10% lower than the quiet sun, although the precise values obtained depend on the line ratio used and the region examined.

The DEM distribution of a low-latitude plume, that formed inside the Elephant's Trunk, indicates an almost isothermal plasma distribution at coronal heights, with a peak in the emission measure at $T \simeq 7.6 \times 10^5$ K, close to the isothermal temperatures that are deduced from line ratios. The Elephant's Trunk and the quiet sun showed different thermal distributions, with peaks of the emission measure at $T \simeq 8 \times 10^5$ K and $T \simeq 9.7 \times 10^5$ K, respectively.

An examination of two other polar plumes seen with CDS in the north polar hole on 23 August 1996 and 10 October 1997 has revealed that the low-latitude plume shows all the characteristics of polar plumes: visibility only in lines emitted in a restricted range of temperatures (i.e., close to an isothermal state), a lower isothermal temperature, and enhanced Mg/Ne and O/Ne intensities, compared to the ambient coronal hole regions. The low-latitude plume exhibited lower Ne and higher Ca abundances, compared to the photospheric values. None of the plumes examined produced significant emission in high-temperature lines at their base. More details on plumes can be found in Del Zanna and Bromage (1999).

References

- Bromage, B. J. I., et al.: 1998, submitted to *Science*.
 Dere, K. P., Landi, E., Mason, H. E., Monsignori Fossi, B. C., and Young, P. R.: 1997, *Astron. Astrophys. Suppl.*, **125**, 149.
 Del Zanna, G., and Bromage, B. J. I.: 1999, in preparation.
 Del Zanna, G., and Bromage, B. J. I.: 1998, *J. Geophys. Res.*, in press.
 Grevesse, N., and Anders, E.: 1991, "Solar element abundances," in *Solar Interior and Atmosphere*, ed. A. N. Cox, W. C. Livingston, and M. S. Matthews, (Tucson: Univ. Arizona Press), p. 1227.
 Habbal, S. R., Esser, and Arndt, M. B.: 1993, *Astrophys. J.*, **413**, 435.
 Harrison, R. A., et al.: 1995, *Solar Physics*, **162**, 233.
 Mason, H. E.: 1995, *Adv. Space Res.*, **15**, 53.
 Widing, K. G., and Feldman, U.: 1992, *Astrophys. J.*, **392**, 715.
 Withbroe G. L.: 1988, *Astrophys. J.*, **325**, 442.

COMPARISON OF POLAR AND EQUATORIAL CORONAL HOLES OBSERVED BY UVCS/SOHO: GEOMETRY AND PHYSICAL PROPERTIES

D. DOBRZYCKA* A. PANASYUK, L. STRACHAN and J. KOHL
Harvard-Smithsonian Center for Astrophysics, Cambridge, MA 02138, USA

Abstract. We analyzed UVCS/SOHO data and compared the H I Ly α (121.6 nm) and O VI (103.2 nm, 103.7 nm) emission in the polar and equatorial coronal holes. We found that the emission lines have similar characteristics in these two types of coronal holes. Both types show evidence for superradially diverging boundaries. The latitudinal distribution of the O VI line ratio may indicate that the equatorial coronal hole has O $^{+5}$ outflow velocities lower than in the polar coronal holes.

Key words: corona, coronal holes, solar wind, plasma physics, line profiles

1. Introduction

Coronal holes formed over the north and south heliographic poles are relatively stable structures observed to exist permanently for several years around solar minimum. During active phases of the solar cycle, smaller coronal holes also form at lower latitudes. We present our analysis of the Ultraviolet Coronagraph Spectrometer (UVCS/SOHO) data acquired during the period of the Whole Sun Month (WSM) campaign (10 August to 08 September 1996) when the Sun was near the minimum of solar activity. At that time the north and south polar coronal holes were easily observed structures and at the end of August 1996 a trans-equatorial coronal hole appeared on the east limb and then crossed the west limb in September 1996. It appeared as an extension of the north polar coronal hole to low latitudes and assumed a shape similar to an "Elephant's Trunk." The UVCS/SOHO data allow us to compare characteristics of the H I Ly α (121.6 nm) and O VI (103.2 nm, 103.7 nm) emission lines in the polar and equatorial coronal holes.

2. Observations

We used the UVCS/SOHO standard synoptic observations obtained with both the Ly α and O VI spectrometer channels. The spectrometer slits were 40' long with slit widths of 14'' and 84'' respectively. In the standard synoptic sequence the slits are scanned radially at several heights and at eight position angles (*PA*, measured counterclockwise from the north heliographic pole). Images of the large-scale corona can be made by interpolating between the slit positions. In particular, for each day of our observations we created complete latitudinal scans for specific heights in the corona: 1.75 R_{\odot} , 1.85 R_{\odot} , 2.0 R_{\odot} , 2.1 R_{\odot} , and 2.25 R_{\odot} . The latitudinal scans were sampled in bins 2.25° wide in position angle.

* Also: Copernicus Astronomical Center, Bartycka 18, 00-716 Warszawa, Poland



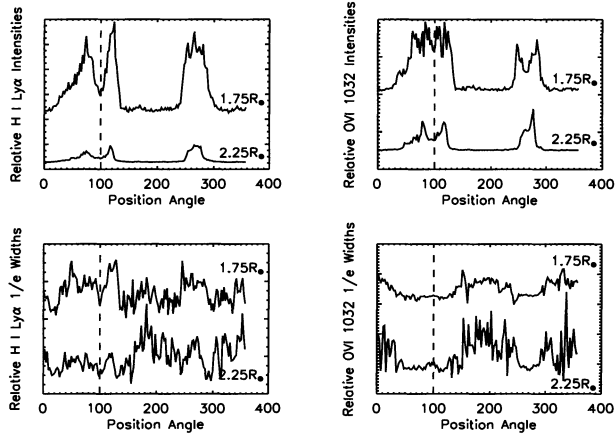


Figure 1. Properties of the H I Ly α and O VI (103.2 nm) line profiles—intensities and 1/e half widths—from 21 August 1996. They are plotted, in arbitrary units, as a function of position angle at two different heights: $1.75 R_{\odot}$ and $2.25 R_{\odot}$. The dashed line shows the position of the Elephant’s Trunk coronal hole ($PA = 100^{\circ}$) on that day.

For the data reduction we followed the standard techniques described in Kohl *et al.* (1997). We used the UVCS Display and Analysis Software (DAS) for flat field correction, wavelength and intensity calibration and removal of image distortion. We also derived the 1/e half widths by fitting a Gaussian function to the observed profiles. The uncertainties of the Ly α and the O VI (103.2 nm, 103.7 nm) line intensities due to radiometric calibration, photon counting statistics, and background subtraction are estimated to be 12%–15% (Gardner *et al.* 1996). The main uncertainties of the 1/e half widths are due to the instrument response and we estimate the error bars to be 0.007 nm for the H I Ly α and 0.025 nm for the O VI lines. We found that the contributions to the total intensities due to stray light and interplanetary hydrogen (in the case of Ly α) are no more than 10%. We also found that the above corrections give only 2%–5% differences in the widths of the observed profiles for both Ly α and O VI lines (Dobrzycka *et al.* 1998). Thus, in our analysis, we ignore the stray light and interplanetary hydrogen corrections.

3. Results and Discussion

We found that the H I Ly α and O VI emission lines have similar characteristics in polar and low latitude coronal holes. Figure 1 plots latitudinal distributions of the H I Ly α and O VI (103.2 nm) line intensities and 1/e half widths, as observed on 21 August 1996. To show variations with radius we plotted these distributions at two different heights: $1.75 R_{\odot}$ and $2.25 R_{\odot}$. The polar coronal holes are clearly seen as areas of low, relatively constant intensity and increased O VI line 1/e width. The Elephant’s Trunk coronal hole appeared at about $PA = 100^{\circ}$ (dashed line) on that

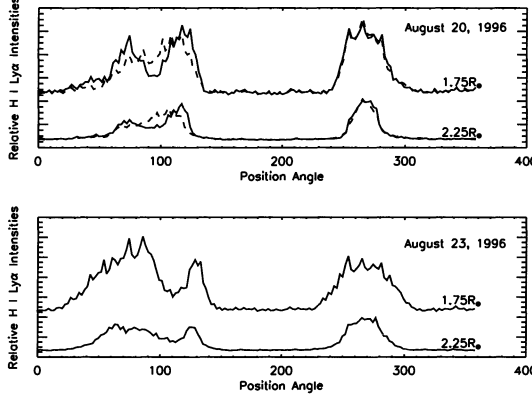


Figure 2. (Upper panel) Relative H I Ly α intensity distributions at $1.75 R_{\odot}$ and $2.25 R_{\odot}$ as seen on 20 August 1996. They are plotted in arbitrary units. The dashed line corresponds to the respective distributions observed a day earlier (19 August 1996), when the equatorial coronal hole was not clearly seen yet. (Lower panel) The H I Ly α intensities observed on different day: 23 August 1996. The Elephant's Trunk coronal hole was seen at about $PA = 110^{\circ}$ then.).

day. The H I Ly α and O VI (103.2 nm) line intensities decreased, but not to the polar coronal hole level ($I(\text{Ly}\alpha)_{ET} \approx 3-5 \times I(\text{Ly}\alpha)_{PH}$) most likely due to line-of-sight contamination by the brighter streamer. The O VI (103.2 nm) 1/e half widths are significantly (~ 2.5 times) higher in the polar coronal holes than in the streamers. The widths also slightly increased above the streamer level in the Elephant's Trunk hole, especially at $2.25 R_{\odot}$ (~ 1.5 times). The H I Ly α widths seem to decrease at the position of the equatorial hole. However, there is a big scatter of the H I Ly α widths in coronal holes and streamers, so this effect is less significant.

In previous analysis of the WSM data we found that the boundaries of the polar coronal holes have a superradial diverging geometry (Dobrzycka *et al.* 1998). Figure 2 shows evidence that boundaries of the equatorial coronal hole also diverge superradially. We plotted the H I Ly α intensity distribution at $1.75 R_{\odot}$ and $2.25 R_{\odot}$ as seen on 20 August 1996. On that day UVCS/SOHO observed the cross section of the low latitude part of the Elephant's Trunk that appeared on the east limb. We overplotted it with the respective distribution observed a day earlier (19 August 1996), when the equatorial coronal hole was not clearly seen yet. A decrease of intensity within the east streamer due to appearance of the Elephant's Trunk hole is wider at higher height ($\Delta PA \approx 22^{\circ}$ and 30° at $1.75 R_{\odot}$ and $2.25 R_{\odot}$ respectively). Also, on 23 August 1996 the decrease of intensity is significantly narrower at $1.75 R_{\odot}$ ($\Delta PA \approx 40^{\circ}$) than at $2.25 R_{\odot}$ ($\Delta PA \approx 50^{\circ}$) suggesting superradial divergence of the hole boundaries.

The polar coronal holes are known sources of the fast solar wind. To learn how the equatorial coronal hole contributes to the solar wind we plotted the O VI (103.2 nm) and O VI (103.7 nm) line intensity ratio (Figure 3), which is a good indicator of the O $^{+5}$ outflow velocities (Withbroe *et al.* 1982; Noci *et al.* 1987). The

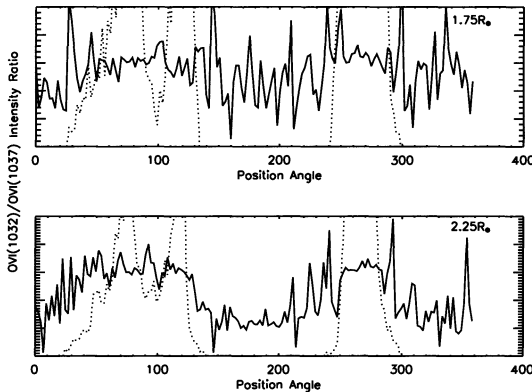


Figure 3. The O VI (103.2 nm) and the O VI (103.7 nm) line intensity ratio, as a function of the position angle, from 21 August 1996, at $1.75 R_{\odot}$ and $2.25 R_{\odot}$. The H I Ly α intensity distribution is overplotted to show the position of the equatorial coronal hole.

line ratio appears higher on the position of the Elephant's Trunk hole with respect to the ratio in the polar coronal holes and the streamers. This may indicate that the equatorial coronal holes have outflow velocities lower than in the polar coronal holes which would confirm similar results by, e.g., Nolte *et al.* (1976), Wang and Sheeley (1990), and Neugebauer *et al.* (1998). Unfortunately, the observed O VI line ratio enhancement is not very significant as there is a big scatter in the data. It also seems to occur at slightly different position angles at the two heights. Further careful modeling, including the 3-D reconstruction of the coronal model (Panasyuk 1998) to avoid the line-of-sight contamination, is necessary to determine the outflow velocities in the equatorial coronal hole.

This work is supported by the National Aeronautics and Space Administration under grant NAG5-3192 to the Smithsonian Astrophysical Observatory, by Agenzia Spaziale Italiana, and by the ESA PRODEX program (Swiss contribution).

References

- Dobrzycka, D., *et al.*: 1998, *J. Geophys. Res.*, in press.
- Gardner, L. D., *et al.*: 1996, *SPIE*, **2831**, 2.
- Kohl, J. L., *et al.*: 1997, *Solar Phys.*, **175**, 613.
- Neugebauer, M., *et al.*: 1998, *J. Geophys. Res.*, **103**, 14587.
- Noci, G., Kohl, J. L., and Withbroe, G. L.: 1987, *Ap. J.*, **315**, 706.
- Nolte, J. T., *et al.*: 1976, *Solar Phys.*, **46**, 303.
- Panasyuk, A. V.: 1998, *J. Geophys. Res.*, in press.
- Wang, Y.-M., and Sheeley, N. R. Jr.: 1990, *Ap. J.*, **355**, 726.
- Withbroe, G. L., Kohl, J. L., Weiser, H., and Munro, R. H.: 1982, *Space Sci. Rev.*, **33**, 17.

VARIATION OF POLAR CORONAL HOLE PROFILES WITH SOLAR CYCLE

D. DOBRZYCKA,* L. STRACHAN, M. P. MIRALLES, J. L. KOHL,
L. D. GARDNER and P. SMITH

Harvard-Smithsonian Center for Astrophysics, Cambridge, MA 02138, USA

M. GUHATHAKURTA and R. FISHER
NASA/GSFC, Greenbelt, MD 20771

Abstract. We compared the H I Ly α polar coronal hole profiles obtained during the three Spartan 201 flights (in 1993, 1994, and 1995) and during the more recent UVCS/SOHO mission. We found that at $2.1 R_\odot$ there are no significant variations of the line shape over the several years of the descending phase of the solar cycle. However, there may be some evidence for the $1.8 R_\odot$ profiles being broader towards solar minimum. The profiles at $2.1 R_\odot$ are different from profiles obtained at $1.8 R_\odot$; they have clearly narrower cores and wide wings. We fitted the profiles with single and/or multiple Gaussian functions and calculated their typical $1/e$ half widths.

Key words: corona, coronal holes, line profiles

1. Introduction

Three Spartan 201 flights in 1993, 1994, and 1995 provided us with H I Ly α observations in the north and south polar coronal hole regions. Together with the SOHO Ultraviolet Coronagraph Spectrometer (UVCS/SOHO) data (obtained near solar minimum) these data span several years of the declining phase of the solar cycle and allow us to characterize changes of the plasma properties in the polar coronal holes. Here we present preliminary results of our analysis of the Spartan data from the first three flights. Over the last several months, improved calibration and analysis of the Spartan Ultraviolet Coronal Spectrometer (UVCS/Spartan) gave us a more thorough understanding of instrumental effects on the observed profiles.

2. Observations

The UVCS/Spartan instrument is described Kohl *et al.* (1995). It is deployed from the shuttle and spends about 40 hours observing selected targets in the solar corona. Here we report preliminary analysis of the observations from the first three missions: Spartan 201-1 on 11–13 April 1993, Spartan 201-2 on 12–14 September 1994, and Spartan 201-3 on 8–10 September 1995. Improvements in the calibration (Gardner *et al.* 1999; Miralles *et al.* 1999) have resulted in a very self consistent set of data from these missions. Final results of the data analysis will be published elsewhere (Dobrzycka *et al.* 1999).

UVCS/Spartan obtained H I Ly α observations of the north and south polar coronal holes at different projected heliocentric heights, $1.5 R_\odot \leq \rho \leq 3.5 R_\odot$,

* Also: Copernicus Astronomical Center, Bartycka 18, 00-716 Warsaw, Poland



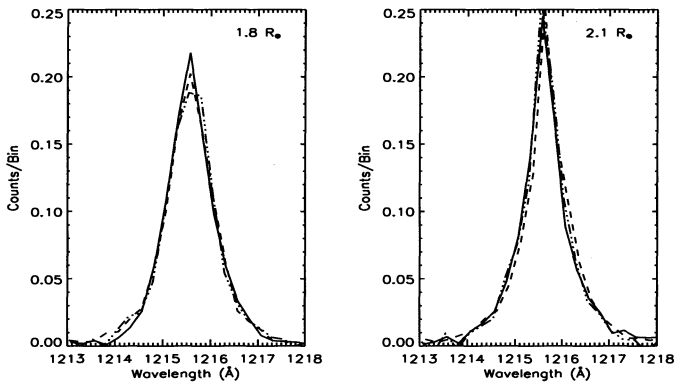


Figure 1. Examples of the H I Ly α UVCS/Spartan profiles obtained at $1.8 R_{\odot}$ and $2.1 R_{\odot}$ in the north polar coronal hole in 1993 (solid line), 1994 (dashed line), and 1995 (dashed-dotted line). The detector bins are 0.25 \AA . The profiles were normalized so their integrated area is unity.

and position angles, PA (measured counterclockwise from the north heliographic pole), ranging from -15° to 45° for the north and from 150° to 210° for the south coronal hole. During the third flight of Spartan 201, only the north coronal hole was observed. The data have been corrected for the background, detector cross-talk and the flat field. We fitted the profiles with single and/or multiple Gaussian functions and the best fit was determined by minimizing the reduced χ^2 :

$$\chi^2 = \frac{1}{\nu} \sum_{i=1}^N \left(\frac{y_i - y(x_i; a_1, \dots, a_M)}{\sigma_i} \right)^2 ,$$

where σ_i is a standard deviation for each data point (x_i, y_i) , N is the number of data points, M is the number of free parameters, and $\nu = N - M$ gives the number of degrees of freedom. The $1/e$ half widths translated from wavelengths to velocities correspond to the proton speed and kinetic temperature of the protons moving along the line-of-sight.

The H I Ly α coronal profiles contain additional components that account for scattering of disk H I Ly α and absorption of the coronal Ly α by the geocorona. The actual width of the geocoronal line is about 10 times smaller than the width of the instrumental profile, so it can not be resolved. The geocoronal contribution is both an absorption and emission feature. We estimated that the geocoronal emission component becomes significant in profiles obtained at heliocentric heights $\rho = 2.5$, 3.0 , and $3.5 R_{\odot}$ (Miralles *et al.* 1999). However, at lower heights (1.7 , $1.8 R_{\odot}$) the emission and absorption components reach a balance and the coronal H I Ly α emission dominates the observed profile. In our analysis we concentrate on the profiles obtained at $\rho = 1.8 R_{\odot}$ and $2.1 R_{\odot}$ where, at least in the case of the $1.8 R_{\odot}$ data, we assume that we can ignore the geocoronal contribution.

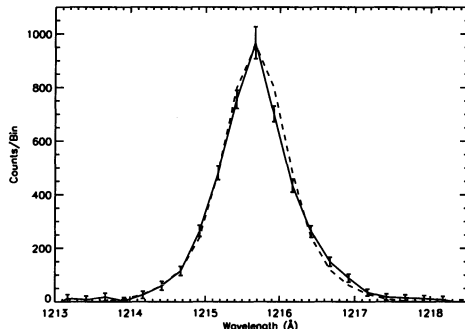


Figure 2. The 1993 H I Ly α UVCS/Spartan profile at $1.8 R_{\odot}$ in the north polar coronal hole (solid line), best fitted with a single Gaussian ($V_{1/e} = 129$ km/s, 0.52 \AA) convolved with the instrumental profile (dashed line).

3. Results and Discussion

Figure 1 shows examples of the H I Ly α UVCS/Spartan profiles obtained at $1.8 R_{\odot}$ and $2.1 R_{\odot}$ in the north polar coronal hole during three Spartan 201 flights. We estimated that the relative uncertainties in the corrected intensities are $\sim 5\%$ in the core of the line and increase towards the wings. The profiles were normalized so their integrated areas are unity. It appears that at $2.1 R_{\odot}$ there are no significant variations of the H I Ly α line shape over several years of the descending phase of the solar cycle. There may be some evidence for the $1.8 R_{\odot}$ profiles being broader towards solar minimum. Careful data analysis is necessary to confirm this. The profiles at $2.1 R_{\odot}$ appear to be different from profiles obtained at $1.8 R_{\odot}$; they have a clearly narrower core and wide wings.

For the data at $1.8 R_{\odot}$ we found that the single Gaussian convolved with the instrumental profile accounts for the observed profiles rather well in case of 1993, 1994, and 1995 data (Figure 2). The $1/e$ half widths of the Gaussians correspond to $0.51\text{--}0.57 \text{ \AA}$ (126–141 km/s, or 0.96–1.2 MK). This would be consistent with the narrow component reported in the 1993 data (Kohl *et al.* 1996). There is no significant difference between north and south polar coronal holes. In several cases of 1994 and 1995 data, there was a slight improvement of the fit (better reduced χ^2) if there was a second Gaussian with $1/e$ half width 1.1 \AA (267 km/s, 4.3 MK). The UVCS/SOHO observations obtained close to solar minimum in 1996 show $1/e$ half widths of the H I Ly α to be $\sim 0.7 \text{ \AA}$ (170 km/s, 1.8 MK; Kohl *et al.* 1997; Cranmer *et al.* 1999) for single Gaussian fits. Data obtained with UVCS/SOHO later in 1998 show $1/e$ half widths of $\sim 0.65\text{--}0.7 \text{ \AA}$ (160–170 km/s; Suleiman *et al.* 1999).

At $2.1 R_{\odot}$ the single Gaussian fit does not give satisfactory results. The double Gaussian fit gives better χ^2 for both north and south polar coronal holes in 1993 and 1994 (Figure 3). The narrow component has a $1/e$ half width of 0.36 \AA (89 km/s, or 0.5 MK) and the broad component of $1.0\text{--}1.1 \text{ \AA}$ (252–267 km/s, or 3.85–4.31 MK).

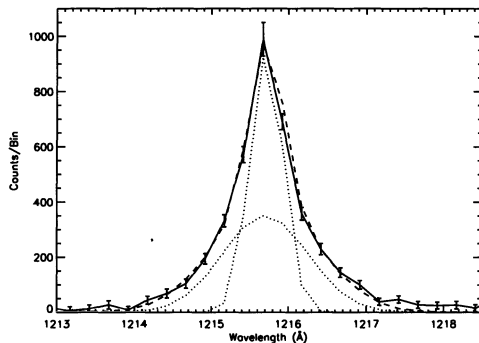


Figure 3. The 1993 H I Ly α UVCS/Spartan profile, from $\rho = 2.1 R_{\odot}$, is best fitted with two Gaussians ($Vn_{1/e} \sim 80$ km/s, and $Vb_{1/e} \sim 250$ km/s) (dotted line) convolved with the instrumental profile (dashed line).

This is consistent with the narrow and broad components in the north polar coronal hole reported by Kohl *et al.* (1996). Similar widths were found for 1993, 1994, and 1995 data. The solar minimum UVCS/SOHO data show $1/e$ half widths of ~ 0.85 Å (210 km/s) for single Gaussian fits (Kohl *et al.* 1997; Cranmer *et al.* 1999).

The results presented here are only preliminary and their interpretation is not clear yet. Nevertheless, the H I Ly α profiles at $1.8 R_{\odot}$ may indicate that the total velocity of neutral hydrogen atoms along the line of sight increases towards solar minimum in the polar coronal holes. The $2.1 R_{\odot}$ data are more difficult to interpret as they may contain a significant geocoronal contribution. Further data simulations and analysis will allow us to select best fits to the observed profiles, properly remove the geocoronal contribution, and identify sources of the narrow and broad components in the UVCS/Spartan H I Ly α profiles.

This work is supported by NASA under grants NAG5-613 and NAG5-3192 to the Smithsonian Astrophysical Observatory, by Agenzia Spaziale Italiana, and by the ESA PRODEX program (Swiss contribution).

References

- Cranmer, S. R., *et al.*: 1999, *ApJ*, **511**, 481.
- Dobrzycka, D., *et al.*: 1999, in preparation.
- Gardner, L. D., *et al.*: 1999, in preparation.
- Kohl, J. L., Gardner, L. D., and Strachan, L., 1995, *Space Sci. Rev.*, **72**, 29.
- Kohl, J. L., Strachan, L., and Gardner, L. D., 1996, *ApJL*, **465**, L141.
- Kohl, J. L., *et al.*: 1997, *Solar Phys.*, **175**, 613.
- Miralles, M. P., *et al.*: 1999, in preparation.
- Suleiman, R., *et al.*: 1999, *Space Sci. Rev.*, this volume.

LARGE-SCALE CORONAL HEATING, CLUSTERING OF CORONAL BRIGHT POINTS, AND CONCENTRATION OF MAGNETIC FLUX

D. A. FALCONER, R. L. MOORE, J. G. PORTER and D. H. HATHAWAY
Marshall Space Flight Center/NASA, Email: falcoda@ips1.msfc.nasa.gov

Abstract. By combining quiet-region Fe XII coronal images from SOHO/EIT with magnetograms from NSO/Kitt Peak and from SOHO/MDI, we show that the population of network coronal bright points and the magnetic flux content of the network are both markedly greater under the bright half of the large-scale quiet corona than under the dim half. These results (1) support the view that the heating of the entire corona in quiet regions and coronal holes is driven by fine-scale magnetic activity (microflares, explosive events, spicules) seated low in the magnetic network, and (2) suggest that this large-scale modulation of the magnetic flux and coronal heating is a signature of giant convection cells.

Key words: coronal heating, magnetic network, coronal bright points

The quiet corona shows spatial variations in brightness on sub-supergranular scales and on larger scales as well (Figure 1a). The sub-supergranular features comprise a coronal network that is rooted in the magnetic network lanes at the edges of the supergranules and that contributes only about 5% of the total Fe XII emission from the quiet corona (Falconer *et al.* 1998). Here we investigate the other 95% of the corona, the large-scale corona comprised of all features of the size of supergranules and larger.

We derive the large-scale corona from the Fe XII image (Figure 1a) by using a triple-pass, peak-clipping, picture-frame technique described in Falconer *et al.* (1999). This yields the large-scale corona shown in Figure 1b. We use the median brightness contour to divide the large-scale corona into bright and dim halves (Figure 1c). In either half there are features as small as supergranules (30,000 km wide), but most features are 2 to 4 supergranules wide. These features are not artifacts of our filter technique since the median contour of the filtered corona matches the median of the unfiltered image (Figure 1d). An order of magnitude more bright points occur in the bright half of the large-scale corona (Figure 1e). (“Bright points” are at least 10 DN s^{-1} per pixel brighter than the local large-scale corona. The average brightness of the dim half of the large-scale corona is 16 DN s^{-1} .) Moreover, the coronal network is about 3 times brighter in the bright half of the large-scale corona than in the dim half. Similarly, the photospheric magnetic flux is greater in the bright half than in the dim half by a factor of 1.3 to 1.5, about the same as the factor by which the Fe XII emission from the bright half exceeds that from the dim half (Figure 1f, Table I). To test whether these results were accidental, we looked at 6 other days and confirmed that the bright large-scale corona has more bright points, greater network emission, and greater magnetic flux than does the dim large-scale corona (Table I). As a control test case, we divided the area into 64 squares in a chessboard pattern with the squares assigned to be alternately bright or



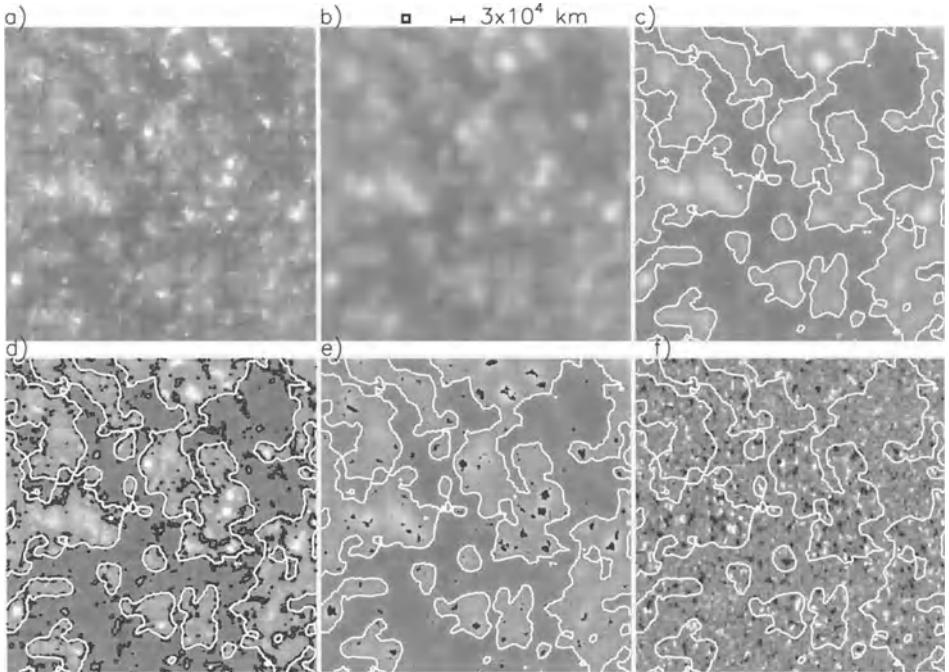


Figure 1. Images from 28 December 1996, centered on the disk and covering an area of 0.9 by 0.9 R_{\odot} . (a) EIT Fe XII image at 15:48 UT. (b) Large-scale corona derived from (a) using a picture-frame filter (the size and shape of which is shown above [b]) with a triple-pass clipping algorithm. The large-scale corona has dim and bright features of the size of supergranules (30,000 km) and larger. (c) Contour of the median brightness level (white) in the large-scale corona, dividing it into bright and dim halves. While some are supergranule-size, most regions in either half are multiple supergranules across. (d) Median contours of the large-scale corona (white) and of the unfiltered Fe XII corona (black), on the unfiltered Fe XII image, showing that the median contour of the large-scale corona is not an artifact of how the large-scale corona was derived. (e) Bright points (shown in black) are mostly in the bright half of the large-scale corona. (f) Median large-scale coronal brightness contour on a Kitt Peak magnetogram from 28 December 1996, 17:00 UT, showing that there is more magnetic flux in the bright half of the large-scale corona than in the dim half.

dim. In all parameters (average brightness, area covered by bright points, fraction of network emission, and magnetic flux), the values from the bright and dim halves of the chessboard differed by no more than 10% (Table I).

The large-scale corona evolves little in 6 hours and the concentration of magnetic flux under the bright half persists for longer than 6 hours (Figure 2). Most new network bright points occur at or near sites of previous bright points, producing clusters of accumulated bright points (Figure 2). These clusters are at sites of flux cancellation, or flux emergence, or both (Figure 2).

Because positive and negative fluxes are well mixed and nearly in balance throughout the quiet region in Figures 1 and 2, it is unlikely that the large-scale flux

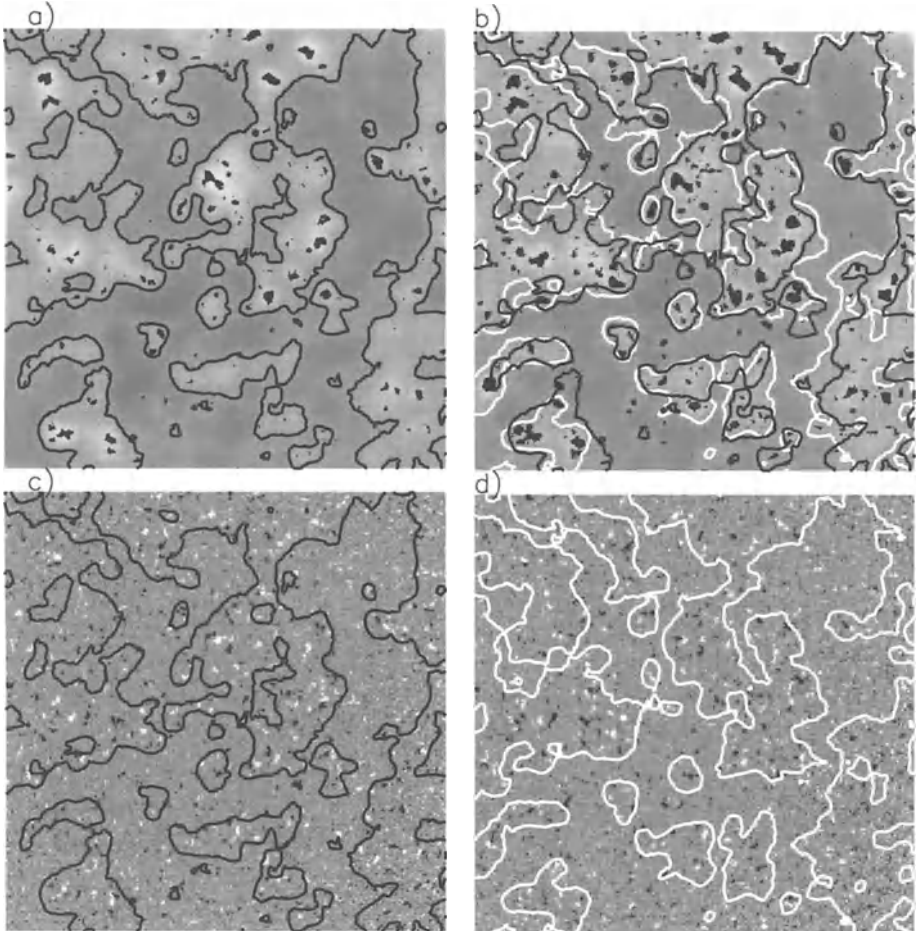


Figure 2. (a) Same as Figure 1e, but at 10:09 UT. The large-scale corona evolves little in 6 hours as can be seen in (b) where both contours (black for 10:09 UT; white for 15:48 UT) are plotted on the 15:48 large-scale corona, demonstrating that the lifetime of the large-scale corona is longer than 6 hours. The black areas in (b) are the accumulated bright pixels (those that were 10 DN s^{-1} or more above local background in two or more images taken between 10:09 and 15:48). During this interval the observation cadence was roughly once every fifteen minutes. MDI magnetograms from 9:39 UT (c) and 16:03 UT (d) show that the large-scale magnetic flux concentrations marking the bright half of the large-scale corona last longer than six hours. These two magnetograms also show that the bright points are at sites of local field concentrations, many of which have flux cancellation and/or emergence.

concentrations are merely old remnants of active regions. Instead, the enhancement of mixed magnetic flux on scales larger than supergranules indicates that something larger than a supergranule is at play, possibly giant-cell convection. Recently,

Table I
Comparison of the Bright and Dim Halves of the Large-Scale Corona

| | Brightness Half | 28 Dec 1996 15:48 UT | 28 Dec 1996 10:09 UT | Average 6 days | Chessboard Pattern |
|---|-----------------|-------------------------|-------------------------|-------------------|--------------------|
| Average Brightness (DN s^{-1}) | Bright Dim | 24 16 | 24 16 | 28 22 | 20 20 |
| % of Area in Bright Points | Bright Dim | 3.2% 0.31% | 3.7% 0.20% | 3.2% 0.33% | 2.0% 1.9% |
| Share of Coronal Network Emission | Bright Dim | 74% 26% | 78% 22% | 74% 26% | 47% 53% |
| Average Magnetic Flux Density (G) | Bright Dim | 4.2 2.7 | 4.1 2.9 | 4.3 2.9 | 3.4 3.6 |

helioseismology has provided evidence that such giant cells exist (Beck, Duvall, and Scherrer 1998).

We conclude that: (1) Magnetic flux in quiet regions is concentrated/diluted on scales larger than supergranules, perhaps by giant convection cells. (2) This clumping of magnetic field gives an enhanced, more active, magnetic network under the large-scale bright corona; the greater network activity produces an enhanced coronal network and enhanced heating of the large-scale corona. (3) The sites of locally strongest activity and heating are network bright points. (4) Rather than the activity in the bright points per se, similar activity, locally weaker but at more numerous sites more widely spread throughout the network, probably drives most of the heating of the large-scale corona. (5) The location of network coronal bright points on neutral lines, the presence of many other neutral lines throughout the network, and the flux emergence and cancellation observed in bright-point clusters all suggest that the drivers of most of the coronal heating on all scales are seated low in the network on neutral lines, i.e., the heating on all scales might be driven by active neutral-line core fields in the network.

This work is part of a SOHO Guest Investigation funded by the Solar Physics Branch of NASA's Office of Space Science.

References

- Beck, J. G., Duvall, T. L., Jr., and Scherrer, P. H.: 1998, *Nature*, **394**, 653.
- Falconer, D. A., Moore, R. L., Porter, J. G., and Hathaway D. H.: 1998, *Ap.J.*, **501**, 386.
- Falconer, D. A., Moore, R. L., Porter, J. G., and Hathaway D.H.: 1999, in preparation for submission to *Ap.J.*

EUV OBSERVATIONS ABOVE POLAR CORONAL HOLES

A. FLUDRA¹, G. DEL ZANNA² and B. J. I. BROMAGE²

¹*Rutherford Appleton Laboratory, Chilton, Didcot, OX11 0QX, UK*

²*University of Central Lancashire, Preston, UK*

Abstract. We derive electron temperature and density as a function of height up to $0.2 R_{\odot}$ above the limb in polar coronal holes, using five EUV data sets recorded by the SOHO Coronal Diagnostic Spectrometer between July 1997 and February 1998. Radial T_e and N_e distributions, averaged in a 2° to 10° range of position angles, are the same above the North and South coronal holes. They do not show any time variability over a period of seven months. Polar plumes are found to have lower electron temperature and higher density than the interplume lanes. The electron density slope suggests that the proton temperatures are twice as high as the electron temperatures.

Key words: solar corona, coronal holes, electron temperature, electron density

1. Introduction

Measurements of electron temperature and density above the polar coronal holes provide means to test the validity of models of coronal holes and solar wind acceleration. Particularly, the measurements made by EUV spectrometers at the base of the solar corona fill in the gap unavailable from white light coronagraph observations and provide the boundary conditions for solar wind models.

Fludra *et al.* (1997, 1999) presented observations of the lower corona made by the Coronal Diagnostic Spectrometer (CDS) on SOHO in August 1996. Electron temperature and density distributions above the limb have been compared for closed field regions and coronal holes. The coronal hole observations in Fludra *et al.* (1999) reached up to $1.1 R_{\odot}$.

In this paper we present the analysis of a new data set taken from regular weekly observations of the North and South polar coronal holes that have been carried out with the CDS since September 1997. We present results for the following five days: the North coronal hole (24 July 1997, 8 September 1997) and the South coronal hole (18 October 1997, 21 November 1997, 9 February 1998). Selected EUV spectral lines in the CDS Normal Incidence range were recorded up to 1.2 solar radii. Intensities of the coronal lines covering the temperature range from 7×10^5 to 2×10^6 K have been measured and used to derive the electron temperature and electron density as a function of the radial distance above the solar limb. Electron densities are derived from the density-sensitive lines of Si IX 342 and 350 Å, and the electron temperature is derived from the Mg X 625/Mg IX 368 Å line ratio as described by Fludra *et al.* (1999).

2. Results and Discussion

The electron temperature curves for all five observations are shown in Figure 1. The temperature behavior for individual coronal holes differs for locations on the disk



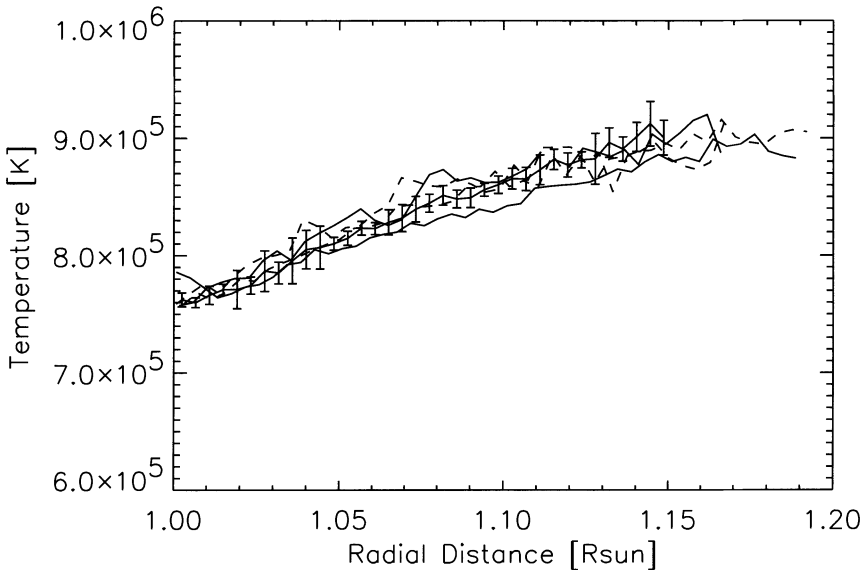


Figure 1. A comparison of electron temperatures derived from Mg X 625 Å to Mg IX 368 Å intensity ratios, measured above the North coronal hole (24 July 1997, 8 September 1997; dashed lines) and the South coronal hole (18 October 1997, 21 November 1997, 9 February 1998; solid lines). The line intensities were averaged over a range of position angles up to 10°. The statistical errors of individual temperature points are 1–4%. Only one of the data sets is shown with error bars.

(values $r < 1.0 R_{\odot}$) due to local features like the coronal hole boundary or bright points. In contrast, all the curves converge to one temperature distribution above the limb. The temperature increases from 7.5×10^5 K at the limb to 9.0×10^5 K at $1.2 R_{\odot}$. There is no asymmetry between the North and South coronal holes for the distances up to $1.2 R_{\odot}$. The data covers the period from July 1997 to February 1998, and no long-term time variability can be noticed during this time.

Coronal hole electron temperatures lower than 10^6 K have also been derived from O VI lines by David *et al.* (1998), who observe that the electron temperature reaches a peak between $1.15 R_{\odot}$ and $1.2 R_{\odot}$, then decreases with height. Our T_e observations reach up to $1.2 R_{\odot}$, and begin to show the flattening of the temperature curve. The two results are based on different spectral lines.

The low values of electron temperatures are consistent with the fact that the coronal holes selected for analysis in this paper have very little or no emission in the Si XII 520 Å line. Emission in this line originates in temperatures above 1.1×10^6 K and peaks at 1.8×10^6 K, and typically comes from closed magnetic loops. Its presence in coronal holes would be an indication that the coronal hole boundary partially obscures the coronal hole.

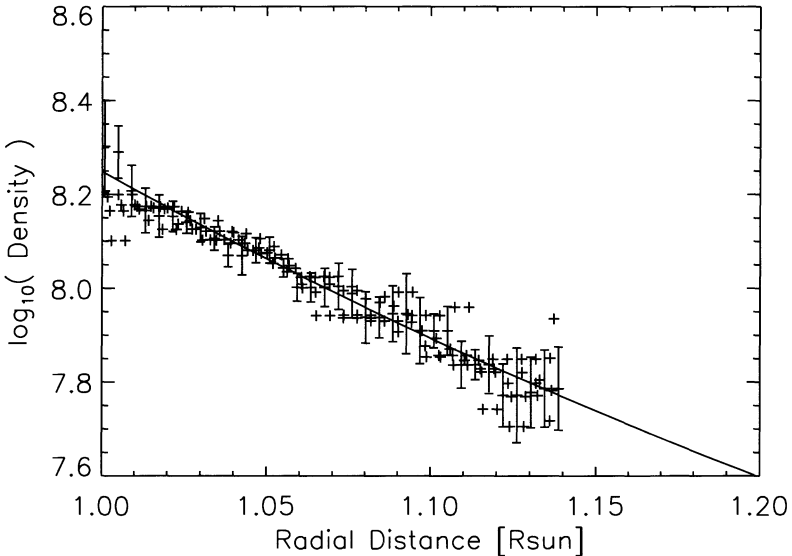


Figure 2. The electron density from the Si IX 350/342 Å ratio measured above the North coronal hole (24 July 1997, 8 September 1997) and the South coronal hole (18 October 1997, 21 November 1997, 9 February 1998). The data represent an angular average over a range of position angles up to 10°. The averaged area contains polar plumes. One of the data sets is shown with error bars; the remaining data are shown as crosses. Statistical errors of individual density values are 10–50%. A median filter has been applied to the data.

Electron densities derived from the Si IX 350/342 Å ratio are shown in Figure 2. All five coronal hole measurements give the same densities. They decrease from $1.6 \times 10^8 \text{ cm}^{-3}$ at $r = 1.0 R_\odot$ to $5.6 \times 10^7 \text{ cm}^{-3}$ at $1.14 R_\odot$. The density errors are between 10% and 50%. The density curves, within errors, are the same for the North and South coronal holes and do not change with time over seven months.

The results obtained in this paper extend further above the limb than the coronal hole measurements made in August 1996 by Fludra *et al.* (1998). The overlapping distance from $1.0 R_\odot$ to $1.1 R_\odot$ has similar results in this paper as in August 1996, showing that the average coronal hole temperature and density distributions with height remained constant for a period of 18 months.

The temperature and density in Figures 1 and 2 represent a spatial average over a range of position angles that varies from 2° to 10° between the data sets. This range usually includes both several plumes and the interplume lanes. Using the data from 18 October 1997 we identified a well defined plume with an adjacent dark interplume lane. We found that the plume temperature from the Mg X/Mg IX ratio was lower than the temperature in the interplume lane by about 10^4 K and that the

temperature difference persisted with height. Another observation, on 12 October 1997, was used to compare the plume and interplume density at the height of 40 to 60 arcseconds above the limb. The density in the interplume region is $1.5 \times 10^8 \text{ cm}^{-3}$, while the density across the plume is systematically higher, $2.5 \times 10^8 \text{ cm}^{-3}$. Temperatures and densities in plumes and interplume regions are also discussed by Wilhelm *et al.* (1998).

Both the solar wind models and recent SOHO/UVCS observations suggest that the ion temperatures can be significantly greater than the electron temperatures in the coronal holes, with, e.g., proton temperatures greater than $2 \times 10^6 \text{ K}$. The CDS electron density measurements can be used to estimate a *lower* limit on the proton temperatures T_p , by neglecting the $u \partial u / \partial r$ term in the momentum equation and using the hydrostatic approximation to the total density: $N(r) = N(R_\odot) \exp [-\mu m_H g_\odot R_\odot (1 - R_\odot/r)/(kT_{\text{eff}})]$, where $N = N_e + N_p$ and the effective temperature $T_{\text{eff}} = (T_p + T_e)/2$ (Guhathakurta *et al.* 1998). The mean atomic weight $\mu = 0.62$ for $N_{\text{He}}/N_{\text{H}} = 0.1$, m_H is the proton mass, k is the Boltzmann constant, R_\odot is the solar radius, and g_\odot is the solar gravity at the solar surface. A line fit as a function of $(1 - R_\odot/r)$ was made to all densities in Figure 2 in the radial range from 1.02 to 1.14 R_\odot , giving $T_{\text{eff}} = 1.6 \times 10^6 \text{ K}$, which gives $T_p \geq 2.3 \times 10^6 \text{ K}$. Values of T_{eff} obtained from fits to individual data sets vary from $1.4 \times 10^6 \text{ K}$ to $1.8 \times 10^6 \text{ K}$. These results suggest that proton temperatures are greater than $2 \times 10^6 \text{ K}$ even below $1.15 R_\odot$ above polar coronal holes. Since the areas where the CDS spectra were spatially averaged contain plumes, we have also derived T_{eff} from the electron density slope in plumes using N_e results from Wilhelm *et al.* (1998) in the radial range 1.06 to 1.20 R_\odot . We obtain a value of $T_{\text{eff}} = 1.9 \times 10^6 \text{ K}$ which is even higher than the one derived from our data.

In contrast, the electron density in the equatorial closed field regions (Fludra *et al.* 1999) falls off with distance more steeply than the coronal hole density in Figure 2. Therefore, T_{eff} is lower ($1.15\text{--}1.35 \times 10^6 \text{ K}$) and the proton temperatures in the equatorial regions are close to the electron temperatures.

This work was supported by the United Kingdom's PPARC.

References

- David, C., Gabriel, A. H., Bely-Dubau, F., Fludra, A., Lemaire, P., and Wilhelm, K.: 1998, *Astron. Astrophys.*, **336**, L90.
- Fludra, A., Del Zanna, G., Bromage, B. J. I., and Thomas, R.: 1997, *Proceedings of the Fifth SOHO Workshop*, ESA SP-404, p. 385.
- Fludra, A., Del Zanna, G., Alexander, D., and Bromage, B. J. I.: 1999, *J. Geophys. Res.*, in press.
- Guhathakurta, M., and Fisher, R.: 1998, *Astrophys. J.*, **499**, L215.
- Wilhelm, K., Marsch, E., Dwivedi, B. N., Hassler, D. M., Lemaire, P., Gabriel, A. H., and Huber, M. C. E.: 1998, *Astrophys. J.*, **500**, 1023.

UVCS/SOHO ION KINETICS IN CORONAL STREAMERS

R. A. FRAZIN,* A. CIARAVELLA, E. DENNIS, S. FINESCHI,** L. D. GARDNER,
J. MICHELS, R. O'NEAL, J. C. RAYMOND, C.-R. WU and J. L. KOHL
Harvard-Smithsonian Center for Astrophysics, 60 Garden St., Cambridge, MA 02138

A. MODIGLIANI*** and G. NOCI
Università di Firenze, I-50125 Firenze, Italy

Abstract. We made streamer observations with the Ultraviolet Coronagraph Spectrometer (UVCS) on the Solar and Heliospheric Observatory (SOHO) during the early part of 1998, which was a time of moderate solar activity. We present an empirical study of coronal ion kinetics using the line profiles from these observations. Our first and most striking result is that the mid-latitude (ML) streamers have much narrower O VI 1032 Å line profiles than the solar minimum equatorial (SME) streamers. Our second result is that the line profiles from a small collection of ions in ML streamers do not seem to be consistent with the ions having a single temperature and turbulent velocity. We discuss several interpretations, including line of sight (LOS) effects. This work is supported by the National Aeronautics and Space Administration under grant NAG-3192 to the Smithsonian Astrophysical Observatory.

1. O VI 1032 Å Line Widths

Figure 1 shows the measured $1/e$ velocities (i.e., the velocities corresponding to 60% of the full widths at half maximum) of the O VI 1032 Å line for a mid-latitude (ML) streamer during the time period 30 March 1998 to 5 April 1998 and the corresponding $1/e$ velocities for a solar minimum equatorial (SME) streamer presented by Kohl *et al.* (1997). According to Figure 1, the mid-latitude streamer has considerably smaller $1/e$ velocities above about $2.5 R_\odot$. Furthermore, unlike their counterparts in SME streamers, the SME OVI line widths do not approach those of the H I Ly α line for any observed height above the limb (Kohl *et al.* 1997). This indicates the ML and SME streamers have substantially different properties. There may be a connection between these two types of streamers and the large scale coronal temperature distributions discussed by Guhathakurta and Fisher (1994).

2. Ion Line Widths

The line widths depend primarily on the variance of the line-of-sight (LOS) velocity distribution, which we will denote as $\langle w_{i,\text{LOS}}^2 \rangle$. The LOS velocity distribution for the i^{th} ion may be divided into a microscopic part, which describes the velocity distribution in the frame of the fluid element, and a macroscopic part which

* Email: rfrazin@cfa.harvard.edu

** On leave from Osservatorio Astronomico di Torino, I-10025 Pino Torinese, Italy

*** Now at Space Division of Terma GmbH, Brunnenweg 19, 64331 Weiterstadt, Germany



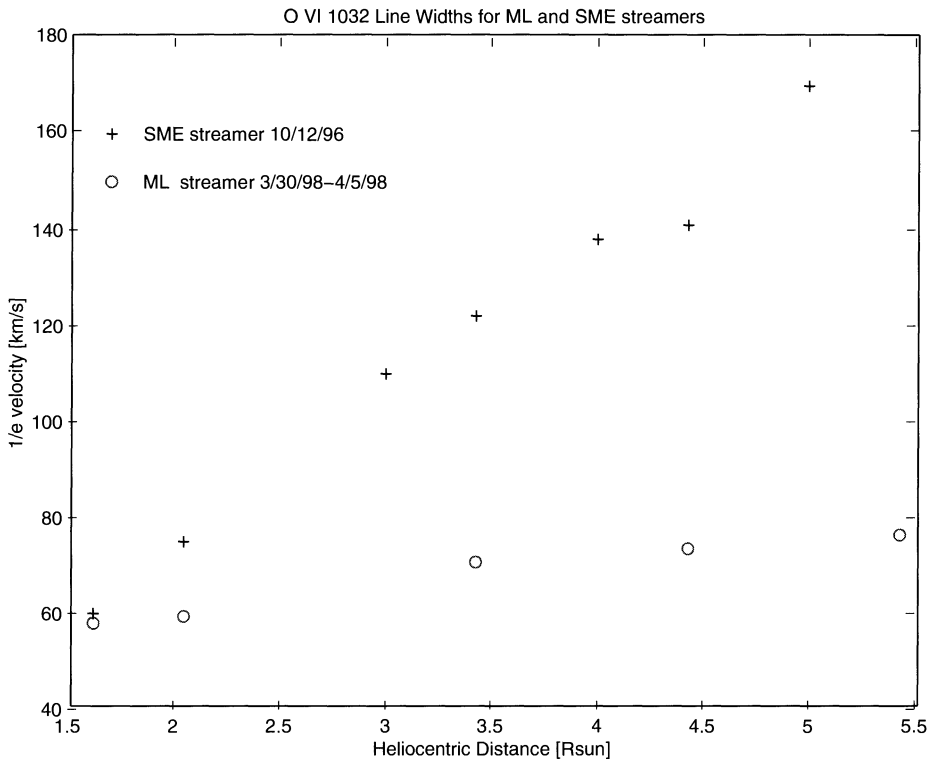


Figure 1. O VI 1032 Å line widths for a ML streamer and a SME streamer as a function of heliocentric distance. The observation dates are given in the figure. The sun was considerably more active in the spring of 1998 than it was during October of 1996.

describes the velocity distribution of the fluid element as a function of time and position along the LOS. We may define $kT_{\perp i}/m_i$ as the variance of the microscopic velocity distribution, where m_i is the ion mass, and $T_{\perp i}$ is called the perpendicular temperature. We define $\xi^2/2$ as the variance of the macroscopic part of the velocity distribution (the factor of 1/2 makes our definition of ξ correspond to that of Tu *et al.* 1998). Then we have

$$\langle w_{i,\text{LOS}}^2 \rangle = \frac{k}{m_i} T_{\perp i} + \frac{1}{2} \xi^2 . \quad (1)$$

The profile of a spectral line provides a probe of the velocity distribution projected onto the LOS. Let us consider a fully thermalized (i.e., $T_{\perp i} \equiv T$), statistically homogeneous, and optically thin plasma. The plasma produces spectral lines that come from ions with different masses m_i , and if we made a plot of $m_i \langle w_{i,\text{LOS}}^2 \rangle$ vs. m_i , we would find that graph to be a straight line with slope $\xi^2/2$ and intercept kT .

If the emission lines from a plasma that is statistically homogeneous along the LOS do not satisfy the linear relationship, it means that the plasma is nonthermal and cannot be described by a single temperature, implying that either flow-effects or wave-particle interactions are giving the ions independent velocity distributions. The situation for a plasma that is not statistically homogeneous along the LOS is more complicated. Consider M independent slabs of plasma, each with a thickness δx_k projected along the LOS, and a line-integrated emissivity (in the i^{th} spectral line) of j_{ik} . We denote the product $\delta I_{ik} \equiv j_{ik}\delta x_k$ and the sum $I_i \equiv \sum_{k=1}^M \delta I_{ik}$. The measured line width is given by the expression

$$\sigma_{i,\text{LOS}}^2(m_i) \approx \frac{1}{I_i} \sum_{k=1}^M \delta I_{ik} \left[\frac{k}{m_i} T_k + \frac{1}{2} \xi_k^2 \right], \quad (2)$$

where T_k is the temperature in the k^{th} slab. If the emitting plasma were statistically homogeneous we would have the relationship $\sigma_{i,\text{LOS}}^2 = \langle w_{i,\text{LOS}}^2 \rangle$. Equation (2) shows that the linear relationship between $m\sigma_{i,\text{LOS}}^2$ and m still holds if δI_k and $(T_k + \xi_k^2)$ are not correlated. If the spectral line widths do not satisfy the linear relationship described above, it is powerful evidence for either independent ion temperatures, statistical inhomogeneity along the LOS or both.

The line widths from the observations of 26 January 1998 to 1 February 1998 off the west limb, shown in Figure 2, make a fairly convincing case that the Si XII, the H I Lyman β and the O VI 1032 lines are not collinear. Instrumental effects are unlikely to cause this, because all of the spectral lines go through an identical optical path through the spectrometer.

Using the single plasma assumption, it is possible to use the plots in Figure 2 to place a reasonable upper limit on ξ^2 and lower limits on $T_{\perp i}$ in the plasma. It follows from equation (1) that the maximum value of ξ^2 is given by the minimum value of $(m_i\sigma_i^2 - m_p\sigma_p^2)/(m_i - m_p)$, assuming that none of the ions is cooler than the protons. Thus, we can extract the range of possible ion perpendicular temperatures by varying ξ^2 from 0 to its maximum value. Using the O VI and H I line widths, for data taken during 30 March 1998 to 5 April 1998 at 1.62 and 2.05 R_{\odot} (not shown here), we determined values of $\xi_{max}/\sqrt{2} \approx 17$ to 22 km/s, with the 1.62 R_{\odot} data clustering closer to 17 km/s and the 2.05 R_{\odot} data clustering closer to 22 km/s. The same analysis yields temperatures $T_{\perp} = 2$ to 2.3×10^6 K, which is substantially higher than the typical value of $T_e \approx 1.6 \times 10^6$ K assigned to a SME streamer (Raymond *et al.* 1997; Li *et al.* 1998). If it is true that the ion temperature is substantially greater than the electron temperature, we may infer that the resistive heating (e.g., van Ballegooijen 1986) is not the dominant heating process, because the energy from resistive heating goes directly into the electrons.

We note that similar work, using SUMER data, has been carried out by Tu *et al.* (1998), Banerjee *et al.* (1998), and Seely *et al.* (1997).

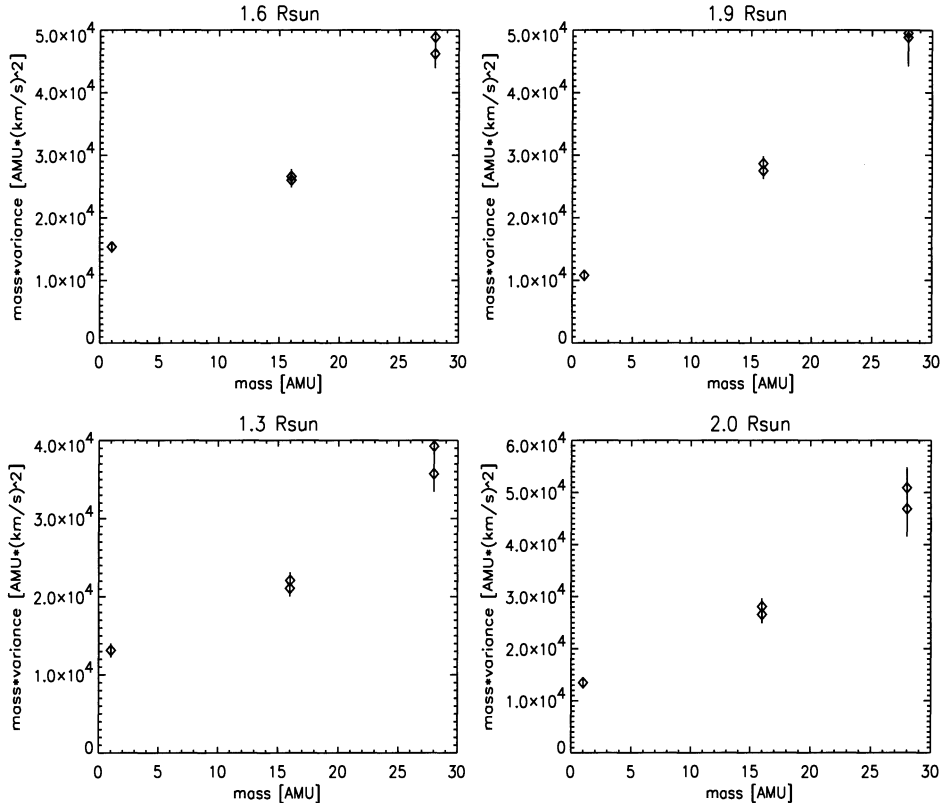


Figure 2. Plots of $m_i \langle \sigma_{i,\text{LOS}}^2 \rangle$ vs. m_i . The data points are H I (Lyman β), O VI (1032, 1037 Å), and Si XII (499, 520 Å). The error bars are about 2σ . The data were taken between 26 January 1998 and 1 February 1998 off the West limb. See text for more details.

References

- Banerjee, D., et al.: 1998, *A&A*, in press.
- Guhathakurta, M., and Fisher, R. R.: 1994, *Solar Physics*, **152**, 181.
- Kohl, J. L., et al.: 1997, *Solar Physics*, **175**, 613.
- Li, J., et al.: 1998, *Ap. J.*, in press.
- Raymond, J. C., et al.: 1997, *Solar Physics*, **175**, 645.
- Seely, J. F., et al.: 1997, *Ap. J.*, **484**, L87.
- Tu, C.-Y., et al.: 1998, *Ap. J.*, **503**, 475.
- van Ballegooijen, A.: 1986, *Ap. J.*, **311**, 1001.

A PARALLEL ADAPTIVE 3D MHD SCHEME FOR MODELING CORONAL AND SOLAR WIND PLASMA FLOWS

C. P. T. GROTH, D. L. DE ZEEUW and T. I. GOMBOSI

*Space Physics Research Laboratory, Department of Atmospheric, Oceanic and Space Sciences,
University of Michigan, Ann Arbor, MI 48109–2143, USA*

K. G. POWELL

Department of Aerospace Engineering, University of Michigan, Ann Arbor, MI 48109–2118, USA

Abstract. A parallel adaptive mesh refinement (AMR) scheme is described for solving the governing equations of ideal magnetohydrodynamics (MHD) in three space dimensions. This solution algorithm makes use of modern finite-volume numerical methodology to provide a combination of high solution accuracy and computational robustness. Efficient and scalable implementations of the method have been developed for massively parallel computer architectures and high performance achieved. Numerical results are discussed for a simplified model of the initiation and evolution of coronal mass ejections (CMEs) in the inner heliosphere. The results demonstrate the potential of this numerical tool for enhancing our understanding of coronal and solar wind plasma processes.

Key words: magnetohydrodynamics, parallel computing, adaptive mesh refinement, solar wind, coronal mass ejection

1. Introduction

Global models based on the numerical solution of the equations of magnetohydrodynamics (MHD) represent a very important component of efforts to understand coronal and solar wind plasma flows. While providing only a low-order approximation to the behavior of conducting fluids, MHD models have been used successfully to simulate and advance our understanding of many space plasma processes. Examples of the application of MHD models to the study of coronal and solar wind plasma flows include the studies by Mikić and Linker (1994), Linker and Mikić (1995), Wu and Guo (1997), Guo and Wu (1998), Lionello *et al.* (1998), Dryer (1998), and Odstrčil and Pizzo (1998). In this paper, the application of a new parallel solution-adaptive MHD model to the simulation of fully three-dimensional solar wind plasma flows is described. Numerical results are discussed for a coronal mass ejection (CME) driven by a local plasma density enhancement in order to demonstrate the potential of the approach.

2. Parallel Solution-Adaptive 3D MHD Model

In the last decade, several developments have led to a new paradigm for the numerical solution of partial differential equations (PDEs). They are: (1) advances in numerical methods, particularly for hyperbolic conservation laws, (2) the evolution of solution-adaptive techniques from a research topic to a practical tool, and (3) the advent of massively parallel computers. By capitalizing on these developments, a new, efficient, and reliable parallel solution-adaptive algorithm has been developed



for solving the hyperbolic PDEs of ideal MHD in three space dimensions. The main elements of this algorithm are now briefly outlined.

2.1. UPWIND FINITE-VOLUME SCHEME

A cell-centered upwind finite-volume formulation of the type first proposed by Godunov (1959) is adopted to solve the standard eight equations of ideal MHD in weak conservation or divergence form (Powell 1994; Powell *et al.* 1995).^{*} Two of the more popular approximate Riemann solvers—the Riemann solver due to Roe (1981) and a modified version of the method of Harten, Lax, Van Leer, and Einfeldt (Harten *et al.* 1983; Einfeldt *et al.* 1991)—are employed in the evaluation of the numerical flux. Originally devised for gas dynamics, these flux functions have been rederived for MHD to cope with the solenoidal condition and deal with degeneracies in the MHD eigenstructure (Powell 1994; Powell *et al.* 1995; Roe and Balsara 1996; Linde 1998). Limited linear reconstruction is used to achieve higher-order accuracy (Van Leer 1979) and multi-stage schemes (Van Leer *et al.* 1989), with point-implicit treatment of source terms, are used to integrate the ordinary differential equations that result from the spatial discretization of the governing PDEs. The finite-volume scheme solves the hydrodynamic and magnetic equations in a tightly coupled manner, provides accurate resolution of discontinuities, and works equally well across a range of plasma β , where β is the ratio of thermal and magnetic pressures.

2.2. BLOCK-BASED ADAPTIVE MESH REFINEMENT

Computational grids that automatically adapt to the solution of the governing PDEs are effective in treating problems with multiple length scales, greatly reducing the computing resources required for many problems. Borrowing from previous work by Berger (Berger 1984; Berger and Colella 1989), Quirk (Quirk 1991; Quirk and Hanebutte 1993), and De Zeeuw and Powell (1993) and keeping in mind the desire for high performance on parallel architectures, a block-based adaptive mesh refinement (AMR) technique has been developed for the preceding upwind finite-volume formulation. In this approach, the governing equations are integrated to obtain volume-averaged solution quantities within rectangular Cartesian computational cells. The cells are embedded in regular structured blocks with cells of equal size. The blocks are self-similar and all consist of $N_x \times N_y \times N_z$ cells. Computational grids are then taken to be composed of many blocks and mesh adaption is accomplished by dividing and coarsening the appropriate blocks, with changes in cell resolution by a factor of two permitted between adjacent blocks. In regions

* For the applications of interest here, the MHD equations are supplemented with additional source terms representing the effects of the solar gravitational force and plasma heating. In the case of the latter, an empirically formulated volumetric heating function is included to model micro-physical processes not represented by the ideal MHD description, such as coronal heating and heat transfer effects.

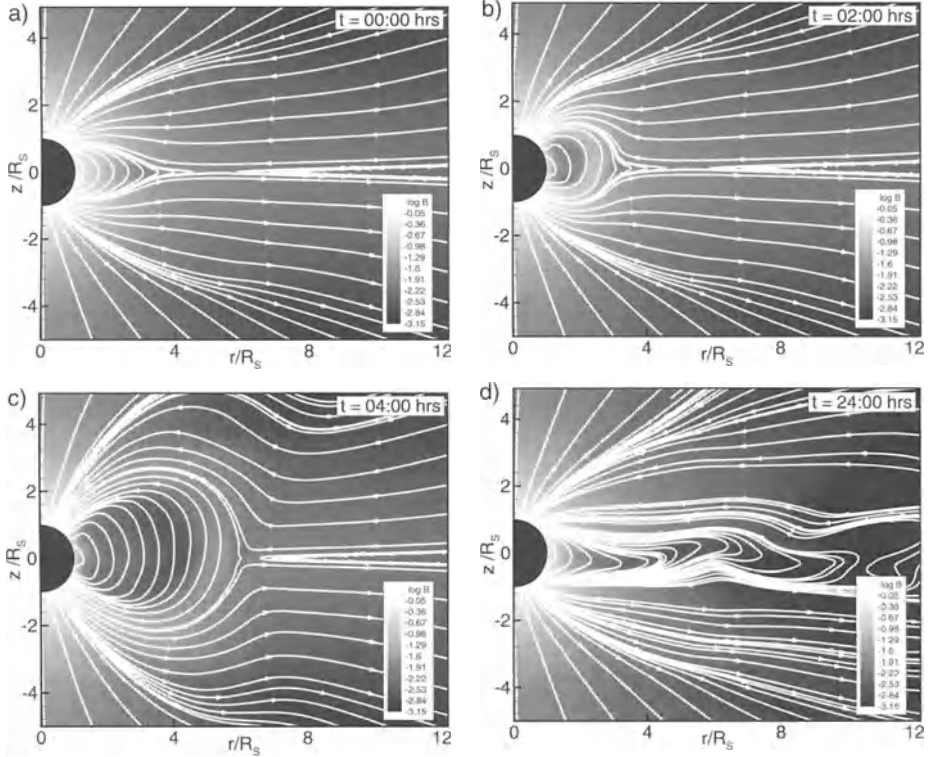


Figure 1. Four meridional snapshots of the computed CME solution depicting the initiation and evolution of the disturbance from $t = 0$ hours to $t = 24$ hours.

that require increased resolution, a block is refined by dividing, with each of its eight octants becoming a block having the same number of cells as the original. In regions that are deemed over-resolved, the refinement process is reversed and eight blocks are coarsened and coalesced into a single block with half the spatial resolution. Physics-based refinement criteria are used to direct coarsening and division of blocks. A hierarchical data structure is used to track mesh refinement and solution block connectivity (De Zeeuw *et al.* 1998).

2.3. PARALLEL IMPLEMENTATION

The preceding solution-adaptive scheme is designed to achieve high performance on massively parallel architectures. Parallel implementation of the algorithm has been carried out using FORTRAN 90 and the message passing interface (MPI) library on several multi-processor platforms, and 233 GFlops has been attained on a 1,024-processor Cray T3E with near-perfect scalability (De Zeeuw *et al.* 1998).

3. Simulation of Coronal Mass Ejections

Some initial studies of the formation and evolution of CMEs have been carried out using the parallel solution-adaptive MHD scheme described above. In these studies, a model of the nominal background solar wind for conditions during solar minimum was used to represent the initial state of the solar wind, and CMEs were initiated by localized isothermal density and pressure enhancements. While the magnetic field configuration and CME onset mechanism used in the simulations were somewhat oversimplified, these calculations represent initial steps towards developing more sophisticated models of the solar wind.

In the CME simulations, the “steady-state” solar wind was modeled by assuming that the inner solar corona is a large rotating reservoir of hot plasma with an embedded dipole field. The reservoir temperature and number density were taken to be 3.1 MK and 10^8 cm^{-3} , respectively, and the strength of the magnetic field at the poles was 1 G. A value of 5/3 was used for the specific heat ratio such that adiabatic cooling at large heliocentric distances was correctly modeled. The coronal plasma was heated by volumetric heating in the vicinity of the Sun where the latitude and radial dependence of the heat source was chosen to produce a reasonable solar wind, having both fast and slow streams.

Figure 1a shows a meridional cut through the calculated initial solar wind solution. The shading represents the logarithm of the magnitude of the magnetic field and the white lines correspond to field lines. It is evident that the solution, which is dictated by a complex balance between pressure, magnetic, gravitational, and inertial forces, has regions of open and closed field lines and is characterized by the now classical “helmet” streamer configuration with associated neutral point and equatorial current sheet similar to that obtained by Pneuman and Kopp (1971). However, unlike the Pneuman-Kopp model, the solution more correctly mimics the two-state nature of the solar wind (McComas *et al.* 1998). Fast solar wind (800 km/s) originating from polar coronal holes is produced above 30° in heliolatitude, slow solar wind (400 km/s) is produced near the solar equator at lower latitudes, and reasonable values for the plasma properties and interplanetary magnetic field are obtained at 1/2 AU. Refer to Figure 2. Shown is a polar diagram of the asymptotic values of the computed flow speed as a function of heliolatitude. The numerical solution is consistent with Ulysses/SWOOPS observations (McComas *et al.* 1998), also shown in the figure.

Using the preceding initial state, numerical results for a CME driven by an isothermal density enhancement are shown in Figures 1b–d. The solution at times $t = 2, 4$, and 24 hours after onset are shown. For this calculation, a 40:1 density enhancement was introduced with a duration of 16 hours at the solar surface just above the equatorial plane. The density enhancement first leads to the “filling” of closed magnetic field lines with additional plasma. This is followed by an expansion of the closed field line region. After a period of time, the closed field lines are unable to contain additional plasma and the streamer belt is disrupted. The resulting CME

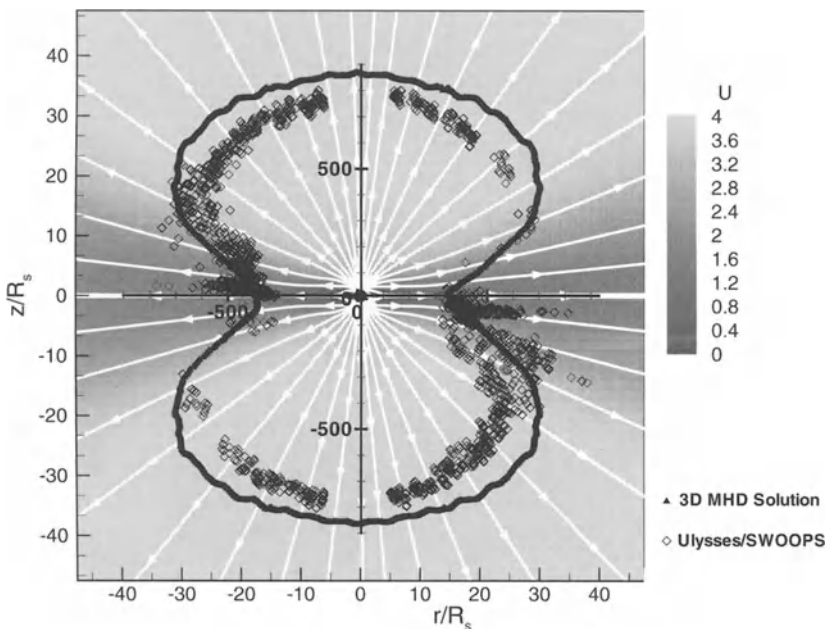


Figure 2. Predicted solar wind velocity and stream lines, and polar plot of computed solar wind speed compared to Ulysses/SWOOPS data (McComas *et al.* 1998).

moves rapidly through the inner corona and propagates outward, dragging out closed field lines with it and disrupting the heliospheric current sheet as it moves. A magnetic cavity propagates behind the front of the disturbance, which moves at velocities nearing 450 km/s. Between $t = 17$ and $t = 19$ hours, the density enhancement completely diminishes and CME field lines begin disconnecting from the solar surface. This results in the reformation of the current sheet. The solution at $t = 24$ hours of Figure 1d depicts this reformation process.

This work was supported by the NSF-NASA-AFOSR inter-agency grant NSF ATM-9318181 and by NASA HPCC CAN NCCS5-146.

References

- Berger, M. J.: 1984, Adaptive mesh refinement for hyperbolic partial differential equations, *J. Comput. Phys.*, **53**, 484.
- Berger, M. J., and Colella, P.: 1989, Local adaptive mesh refinement for shock hydrodynamics, *J. Comput. Phys.*, **82**, 67.
- De Zeeuw, D., and Powell, K. G.: 1993, An adaptively refined Cartesian mesh solver for the Euler equations, *J. Comput. Phys.*, **104**, 56.

- De Zeeuw, D. L., Groth, C. P. T., Marshall, H. G., Gombosi, T. I., Powell, K. G., and Stout, Q. F.: 1998, A parallel adaptive high-resolution scheme for MHD with applications in space plasma physics, *SIAM J. Sci. Comput.*, submitted.
- Dryer, M.: 1998, Multidimensional MHD simulation of solar-generated disturbances: Space weather forecasting of geomagnetic storms, *AIAA J.*, **36** (3), 365.
- Einfeldt, B., Munz, C. D., Roe, P. L., and Sjögreen, B.: 1991, On Godunov-type methods near low densities, *J. Comput. Phys.*, **92**, 273.
- Godunov, S. K.: 1959, Finite-difference method for numerical computations of discontinuous solutions of the equations of fluid dynamics, *Mat. Sb.*, **47**, 271.
- Guo, W. P., and Wu, S. T.: 1998, A magnetohydrodynamic description of coronal helmet streamers containing a cavity, *Astrophys. J.*, **494**, 419.
- Harten, A., Lax, P. D., and van Leer, B.: 1983, On upstream differencing and Godunov-type schemes for hyperbolic conservation laws, *SIAM Rev.*, **25** (1), 35.
- Linde, T. J.: 1998, *A Three-Dimensional Adaptive Multifluid MHD Model of the Heliosphere*, Ph.D. thesis, University of Michigan.
- Linker, J. A., and Mikić, Z.: 1995, Disruption of a helmet streamer by photospheric shear, *Astrophys. J.*, **438**, L45.
- Lionello, R., Mikić, Z., and Schnack, D. D.: 1998, Magnetohydrodynamics of solar coronal plasmas in cylindrical geometry, *J. Comput. Phys.*, **140**, 172.
- McComas, D., et al.: Ulysses' return to the slow solar wind, *Geophys. Res. Lett.*, **25**, 1.
- Mikić, Z., and Linker, J. A.: 1994, Disruption of coronal magnetic field arcades, *Astrophys. J.*, **430**, 898.
- Odstrčil, D., and Pizzo, V. J.: 1998, Three-dimensional propagation of a CME within a tilted-dipole background solar wind flow, *J. Geophys. Res.*, submitted.
- Pneuman, G. W., and Kopp, R. A.: 1971, Gas-magnetic field interactions in the solar corona, *Sol. Phys.*, **18**, 258.
- Powell, K. G.: 1994, An approximate Riemann solver for magnetohydrodynamics (that works in more than one dimension), Report 94-24, ICASE.
- Powell, K. G., Roe, P. L., Myong, R. S., Gombosi, T. I., and De Zeeuw, D. L.: 1995, An upwind scheme for magnetohydrodynamics, Paper 95-1704-CP, AIAA.
- Quirk, J. J.: 1991, *An Adaptive Grid Algorithm for Computational Shock Hydrodynamics*, Ph.D. thesis, Cranfield Institute of Technology.
- Quirk, J. J., and Hanebutte, U. R.: A parallel adaptive mesh refinement algorithm, Report 93-63, ICASE.
- Roe, P. L.: 1981, Approximate Riemann solvers, parameter vectors, and difference schemes, *J. Comput. Phys.*, **43**, 357.
- Roe, P. L., and Balsara, D. S.: 1996, Notes on the eigensystem of magnetohydrodynamics, *SIAM J. Appl. Math.*, **56** (1), 57.
- Van Leer, B.: 1979, Towards the ultimate conservative difference scheme. v. a second-order sequel to Godunov's method, *J. Comput. Phys.*, **32**, 101.
- Van Leer, B., Tai, C. H., and Powell, K. G.: 1989, Design of optimally-smoothing multi-stage schemes for the Euler equations, Paper 89-1933-CP, AIAA.
- Wu, S. T., and Guo, W. P.: 1997, A self-consistent numerical magnetohydrodynamic (MHD) model of helmet streamer and flux rope interactions: Initiation and propagation of coronal mass ejections (CMEs), in *Coronal Mass Ejections*, Geophysical Monograph 99, (American Geophysical Union, Washington).

SEMI-EMPIRICAL MHD MODEL OF THE SOLAR WIND AND ITS COMPARISON WITH ULYSSES

M. GUHATHAKURTA* and E. C. SITTLER
GSFC, Code 682, Greenbelt, MD 20771, USA

D. MCCOMAS
LANL, Los Alamos, NM

Abstract. We have developed a 2D semi-empirical model (Sittler and Guhathakurta 1999) of the corona and the interplanetary medium using the time independent MHD equations and assuming azimuthal symmetry, utilizing the SOHO, Spartan and Ulysses observations. The model uses as inputs (1) an empirically derived global electron density distribution using LASCO, Mark III and Spartan white light observations and *in situ* observations of the Ulysses spacecraft, and (2) an empirical model of the coronal magnetic field topology using SOHO/LASCO and EIT observations. The model requires an estimate of solar wind velocity as a function of latitude at 1 AU and the radial component of the magnetic field at 1 AU, for which we use Ulysses plasma and magnetic field data results respectively. The model makes estimates as a function of radial distance and latitude of various fluid parameters of the plasma such as flow velocity \mathbf{V} , temperature T_{eff} , and heat flux Q_{eff} which are derived from the equations of conservation of mass, momentum and energy, respectively, in the rotating frame of the Sun. The term “effective” indicates possible wave contributions. The model can be used as a planning tool for such missions as Solar Probe and provide an empirical framework for theoretical models of the solar corona and solar wind.

1. Introduction

Numerous theoretical models have been developed to describe the heating of the solar corona and acceleration of the solar wind. The more recent models have been 2D MHD codes such as that developed by Steinolfson *et al.* (1982), Wang *et al.* (1995), Mikic and Linker (1994), Linker and Mikic (1995), Suess *et al.* (1996), and Wang *et al.* (1998). The approach has been to include various physical mechanisms such as an *ad hoc* volumetric heat source as used in the Suess *et al.* (1996) model, and then to compare the model calculations to observations. Furthermore, the models may assume a polytrope for the gas which may not be valid and assume a dipole magnetic field for the Sun which is an oversimplification of the Sun’s surface magnetic field. Contrary to that previously done we have developed an empirical approach for modeling the solar corona and solar wind. Here we use empirically derived electron densities from white light coronagraph observations and empirically derived models of the magnetic field, also derived from white light coronagraph observations, to constrain the physics and combine these two pieces of information with the conservation equations of mass, momentum and energy. The model presented in this publication is a continuing effort of that initially done by Sittler and Guhathakurta (1999), for which Skylab data were used.

* Catholic University, Physics Department

2. MHD Model of the Solar Corona and Interplanetary Medium

The semi-empirical 2D MHD description of the coronal expansion for a polar coronal hole was recently presented in detail in Sittler and Guhathakurta (1999). This study was based on the Skylab observations reported by Munro and Jackson (1977) and Guhathakurta *et al.* (1996). This model assumes azimuthal symmetry and conservation of mass, momentum and energy. The basic equations governing the coronal expansion under steady state conditions and axial symmetry, transformed into the rotating frame of the Sun, are presented in Sittler and Guhathakurta (1999). In order to integrate these equations and solve for the flow speed \mathbf{V} , effective temperature T_{eff} and effective heat flux Q_{eff} , we must have knowledge of the mass density ρ and magnetic field \mathbf{B} as a function of radial distance and latitude. The effective temperature $T_{\text{eff}} = (T_p + T_e)/2 + T_{\text{wave}}$, where T_p is the proton temperature, T_e is the electron temperature, and T_{wave} is the temperature contribution due to waves. The effective heat flux $Q_{\text{eff}} = Q_{\text{cond}} + Q_{\text{wave}}$ is the conductive heat flux due to electrons and a wave contribution term, where near the Sun Q_{wave} may dominate while far from the Sun Q_{cond} will dominate.

The mass density is computed from the electron density profiles as described in Sittler and Guhathakurta (1999), which are derived from the white light coronagraph data and solar wind observations at 1 AU (from Ulysses plasma data). For the magnetic field we fit a multipole expansion to the boundary of the polar coronal hole defined by Guhathakurta *et al.* (1999). The only current present in this model is that occurring at the current sheet. This means that we neglect the effects of localized currents in polar coronal holes. There is at present no indication that such currents produce a large deviation of the coronal hole magnetic geometry from the one determined by us. Wolfson (1985) modeled the coronal magnetic field with volume and sheet currents. Comparison of his model with other MHD and source surface models suggested that the current sheet remains the dominant influence on the overall geometry of the coronal magnetic field; the inclusion of volume currents alters the field in a secondary fashion. The magnitude of the magnetic field at the base of the corona is fixed by the radial component of the magnetic field from spacecraft observations at 1 AU.

3. Magnetic Field Topology and Global Density Model

We have taken a non-traditional approach to obtaining the solar magnetic field geometry as introduced by Sittler and Guhathakurta (1999). We use coronal observations to determine the geometry of the large-scale magnetic field, while Ulysses observations of the radial component B_r fix the field strength at the coronal base. The solar magnetic field geometry is found by fitting a multipole expansion (monopole, dipole, quadrupole and octupole) of the magnetic field to the streamer topology as defined by the various observations as well as the divergence of polar

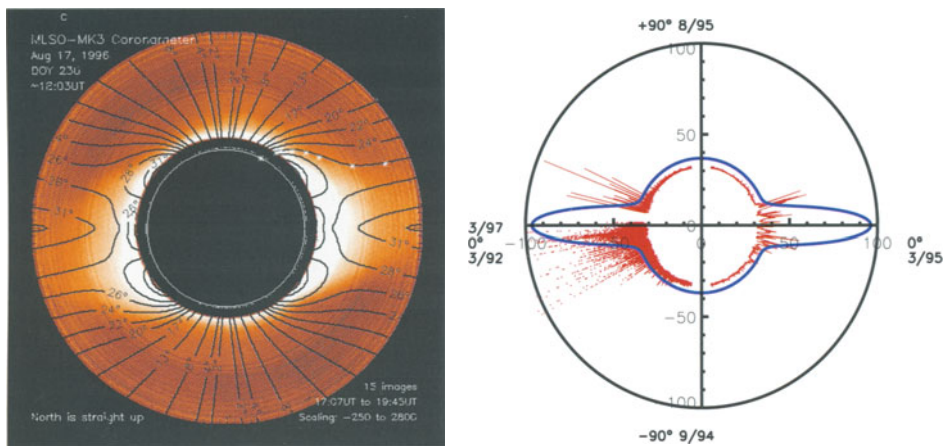


Figure 1. (a) The magnetic field modeled by a multipole expansion including monopole, dipole, quadrupole, and octupole terms. The monopole term includes a current sheet within the equatorial plane. The model is fit to the boundary of the polar coronal hole as reported by Guhathakurta *et al.* (1999) and is indicated by the symbols *. Superposition of field lines on pB observations from Mark III for 17 August 1996, outlining the boundary of the polar coronal hole. (b) Polar plot of Ulysses proton density N_p at 1 AU plus 30 ($(N_p + 30) \text{ cm}^{-3}$) in red, and our model inferred electron density, $N_{2.5}$, at a height of $2.5 R_\odot$ scaled by a factor ($(N + 3 \times 10^5)/10^4 \text{ cm}^{-3}$) in blue, during the Whole Sun Month period. The above scale factors were necessary to put the density at 1 AU and $2.5 R_\odot$ in the same plot.

plumes observed in SOHO/EIT data, which are the *only* structures in the corona that provide us with a glimpse of the geometry of the open magnetic field lines in the innermost corona (Guhathakurta and Sittler 1999).

Here the addition of the monopole term allows us to extend our calculations far from the Sun. The monopole term includes a current sheet in the equatorial plane. In Figure 1a we show an example of the least squares fit to the boundary of the polar coronal hole as defined by Guhathakurta *et al.* (1999). The model fit, which adjusts the relative strengths of the various multipole terms, found a dominant octupole term, and resulted in model field lines that accurately trace the plumes and streamers seen in this Mark III image (Figure 1a). The solar field found in this analysis of the solar minimum corona using SOHO data is very similar to that found for the Skylab solar minimum period.

These calculations are qualitatively different from the potential-field-source-surface-model (PFSS) or the MHD models where latitudinal gradients are maintained by volume currents. In our model the equatorial regions near the Sun are dominated by a large, disconnected open magnetic field line region. Such an ill-defined equatorial magnetic field is the primary limitation of this single current sheet magnetic field model close to the Sun (up to $2.5 R_\odot$). Topological incompatibility between the octupole term and the use of a single current sheet is the primary

cause of this problem. Thus we shall consider solutions only outside of $2.5 R_{\odot}$ for the streamer belt region.

The global electron density pattern is clearly visible in Figure 1b, which presents in a polar diagram the particle density observed by Ulysses and extrapolated to 1 AU (red) as a function of heliospheric latitude, and our model inferred density at $2.5 R_{\odot}$ (blue). Here N_p represents the measured proton density by the Ulysses spacecraft normalized to 1 AU. The model inferred density inside the polar coronal hole shows no variation with latitude, an observation that was made earlier by using Skylab and Mauna Loa K coronameter data by Guhathakurta *et al.* (1996) and Guhathakurta and Holzer (1994). The agreement between our model inferred electron density, $N_{2.5}$ at $2.5 R_{\odot}$ and Ulysses observations at 1 AU, with regard to the latitudinal constancy of the polar coronal hole density and the overall boundary between the fast and slow wind, is remarkable. Thus, white-light observations (in the range 2.5 – $5.0 R_{\odot}$) alone can provide the boundary between the quasi-steady fast and the slow solar wind. A recent study by Guhathakurta and Fisher (1998) showed that while the density inside the polar coronal hole is a constant with respect to latitude and longitude as well as in the high latitude Ulysses observations, there remains a factor of 1.5–1.8 constant variability at any given latitude in both data sets. This variability in the density in the polar coronal hole was attributed to structures such as rays/plumes by Guhathakurta and Fisher (1998). Finally, to obtain the mass density ρ we assume an ion composition primarily composed of protons with 5% contribution by number of alpha particles.

4. Results

Although the speed is an input to our model calculations at 1 AU, for which we use Ulysses data, the speed profile as a function of radial distance and latitude are derived from our model calculations. The speed plot (Figure 2a) shows that over the poles we infer a velocity of ~ 350 km/s at $2.5 R_{\odot}$ while the asymptotic velocity is around 770 km/s. At the equator the velocity is less than 100 km/s at $2.5 R_{\odot}$ reaching an asymptotic value of around 450 km/s (Figure 2a). Our inner coronal polar velocity estimates are in good agreement with the velocities inferred from UVCS and IPS observations (Breen *et al.* 1998; Strachan *et al.* 1997) during this time frame. The global solar wind flow pattern is clearly visible in Figure 3a, which presents in a polar diagram the wind speed (red) versus latitude from Ulysses observations (normalized to the fastest wind speed) and our model inferred normalized velocities at four different radial distances: 2.5 (magenta), 5.0 (green), 10.0 (black) and $215.0 R_{\odot}$ (blue). The sonic point in the coronal hole region is at $2.2 R_{\odot}$ while for the streamer belt it is at $8.5 R_{\odot}$. The Alfvén critical point over the poles is at $13.3 R_{\odot}$ and within the streamer belt region it is between 15.5 and $18.5 R_{\odot}$. We find that in our model at $1.16 R_{\odot}$, the fast solar wind (680–780 km/s observed at 1 AU) originates from the poles at $\pm 90^{\circ}$ and extends down to $\pm 70^{\circ}$ latitude, where the effective temperature is 9×10^5 K (Figure 2b) and density is

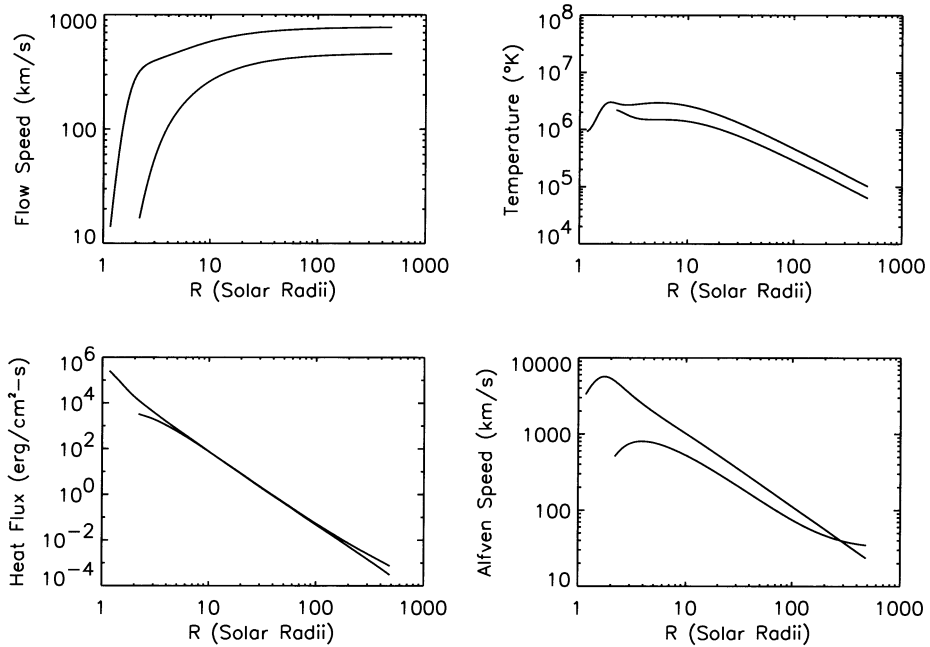


Figure 2. Radial plot of (a) flow speed, (b) effective temperature, T_{eff} , (c) effective heat flux, Q_{eff} and (d) Alfvén speed. The solid lines starting at $1.15 R_{\odot}$ are solutions for the polar most flow tube while the lines starting at $2.0 R_{\odot}$ are solutions for the equatorial region.

$2.4 \times 10^7 \text{ cm}^{-3}$. An enhanced temperature maximum ($3 \times 10^6 \text{ K}$) was observed between 1.8 and $6.0 R_{\odot}$ in this region (Figure 2b).

The model computed mass flux at 1 AU inside the polar coronal hole is constant with a value of $1.5 \times 10^8 \text{ cm}^{-2} \text{ s}^{-1}$ while the mass flux in the streamer belt is about a factor of 2 higher. The Ulysses mass flux data is scaled by a factor of $2.75 \times 10^8 \text{ cm}^{-2} \text{ s}^{-1}$ producing a mass flux varying from 1.5 – $2.2 \times 10^8 \text{ cm}^{-2} \text{ s}^{-1}$ in the high speed wind (Figure 3b). This variation of a factor of 1.5 in the mass flux as well as particle density was reported by Guhathakurta and Fisher (1998) in the high latitude high speed wind.

The model computes effective temperatures far from the Sun that can be compared with Ulysses plasma observations (Figure 2b, Figure 3c). In Figure 3c we compared T_{eff} from Ulysses with our model calculations at 1 AU and four other heights. The Ulysses observations were extrapolated to 1 AU by assuming $r^{-0.7}$ radial variation in the proton temperature. This choice tended to minimize the variance in the proton temperature with latitude and is different from that determined by Goldstein *et al.* (1996), who found $r^{-1.03}$ (northern hemisphere) and $r^{-0.81}$ (southern hemisphere). Once the proton temperature was extrapolated to 1 AU we

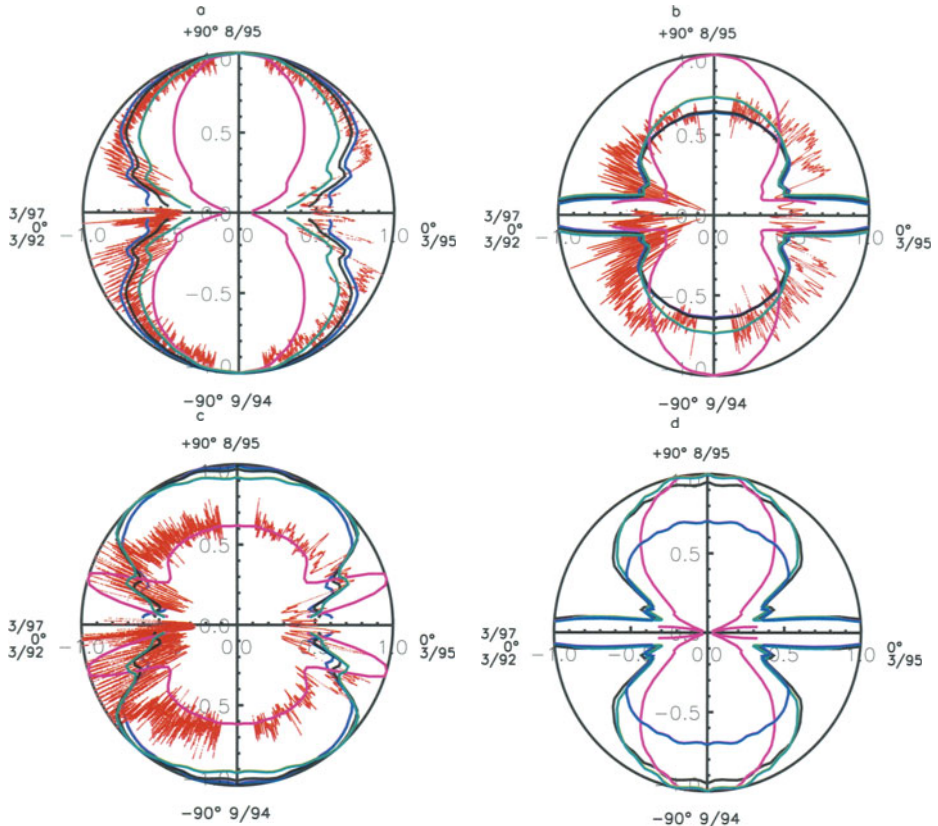


Figure 3. For all plots, Ulysses observations scaled and extrapolated to 1 AU are in red (March 1992 to March 1997). Normalized model inferred results are at distances of 2.5 (magenta), 5.0 (green), 10.0 (black) and 215.0 (blue). (a) Model inferred normalized velocities at above radial distances with normalizing constants, 276, 396, 528, 773 km/sec, respectively. The normalizing constant for Ulysses velocity was 822 km/sec. (b) Same as in (a) except the observations are for mass flux. The normalizing constants are: 2.08×10^{12} , 4.02×10^{11} , 1.04×10^{11} , 2.5×10^8 and Ulysses (2.75×10^8) in units of cm^2/sec , respectively. (c) Same as in (a) except the observations are for effective temperature. The normalizing constants are: 4.4, 3.2, 2.6, .23 and Ulysses (3.25) in units of 10^6 K, respectively. (d) Same as in (a) except the observations are for effective heat flux. The normalizing constants are, 8.18×10^3 , 6.41×10^2 , 73.1, 5.93×10^{-3} in units of $\text{erg}/\text{cm}^2/\text{sec}$, respectively.

used the relation $T_{\text{eff}} = (T_p + T_e)/2$ to compute T_{eff} and set $T_e = 10^5$ K in polar regions and $T_e = 1.5 \times 10^5$ K in equatorial regions. It is clear from Figure 3c that the boundary between the coronal hole and equatorial temperature is set by $5 R_\odot$.

We get a heat flux maximum of $5 \times 10^5 \text{ erg}/\text{cm}^2/\text{s}$ at $1.16 R_\odot$ over the poles (Figure 2c). For the polar most flow tube we inferred an effective heat flux of $\sim 8 \times 10^3 \text{ erg}/\text{cm}^2/\text{s}$ at $2.5 R_\odot$ while at 1 AU it is around $4 \times 10^{-3} \text{ erg}/\text{cm}^2/\text{s}$. At the equator the effective heat flux is around $3 \times 10^3 \text{ erg}/\text{cm}^2/\text{s}$ at $2.5 R_\odot$, reaching a value of around $6 \times 10^{-3} \text{ erg}/\text{cm}^2/\text{s}$ at 1 AU. We note that it can be shown that

wave contributions due to T_{eff} and Q_{eff} are negligible at 1 AU and our estimates for T_{eff} and Q_{eff} at 1 AU are characteristic of the gas. In Figure 3d we have presented a polar plot of the model calculated effective heat flux for four different heights. Again the sharp boundary between the high heat flux in the coronal hole is already established by $5 R_{\odot}$.

In summary, we have that a simple steady state, azimuthally symmetric MHD model of the solar corona/wind is able to reproduce some of the observed features of solar wind at 1 AU and close to the Sun. Some model results are:

1. The UVCS observations by Kohl *et al.* (1996) suggest that the proton temperature is $\sim 5 \times 10^6$ K over the poles. Assuming an electron temperature of 5×10^5 K we get $T_{\text{eff}} \sim 2.75 \times 10^6$ K from $1.8\text{--}3.5 R_{\odot}$. In this same radial range our model predicts $T_{\text{eff}} \sim 2.5\text{--}3.0 \times 10^6$ K.
2. In situ observations show $T_p \sim 2.5\text{--}3.0 \times 10^5$ K and $T_e \sim 10^5$ K (Feldman *et al.* 1976) at 1 AU or $T_{\text{eff}} \sim 2 \times 10^5$ K. The flow velocity V was estimated to be 820 km/s while the density was $\approx 1.8 \text{ cm}^{-3}$ (Guhathakurta and Fisher 1998). For high speed streams $Q_e \sim 3 \times 10^{-3} \text{ erg/cm}^2/\text{s}$ at 1 AU (Feldman *et al.* 1976). Our model estimates $N \approx 1.5 \text{ cm}^{-3}$, $V \approx 770 \text{ km/s}$, $T_{\text{eff}} \approx 2.6 \times 10^5$ K and $Q_{\text{eff}} \approx 3.7 \times 10^{-3} \text{ erg/cm}^2/\text{s}$ at 1 AU over the poles.
3. The model produces high speed flows over the poles with $V \sim 350 \text{ km/s}$ at $2.5 R_{\odot}$ and $V < 100 \text{ km/s}$ close to the equator. At 1 AU the asymptotic flow speed over the poles is $V \sim 770 \text{ km/s}$ and that close to the equator is $V \sim 450 \text{ km/s}$.
4. Over the poles the effective temperature is a minimum $T_{\text{eff}} \sim 9 \times 10^5$ K near the Sun ($r = 1.16 R_{\odot}$), while a large temperature maximum (3×10^6 K) extends from $1.8\text{--}6 R_{\odot}$.
5. The heat flux is maximum over the poles with $Q_{\text{eff}} \sim 5 \times 10^5 \text{ erg/cm}^2/\text{s}$ at $1.16 R_{\odot}$.

Acknowledgements

Madhulika Guhathakurta would like to thank the support of the NASA SR&T and the SOHO Guest Investigator programs.

References

- Breen, A. R., *et al.*: 1999, *J. Geophys. Res.*, in press.
 Feldman, W. C., Asbridge, J. R., Bame, S. J., Montgomery, M. D., and Gary, S. P.: 1975, *J. Geophys. Res.*, **80**, 4181.
 Feldman, W. C., *et al.*: 1976, *J. Geophys. Res.*, **81**, 5054.
 Goldstein, B. E., *et al.*: 1996, *Astron. & Astrophys.*, **316**, 296.
 Guhathakurta, M., *et al.*: 1999, *J. Geophys. Res.*, in press.
 Guhathakurta, M., and Holzer, T. E.: 1994, *Astrophys. J.*, **426**, 782.
 Guhathakurta, M., and Sittler, E. C., Jr.: 1998, submitted to *J. Geophys. Res.*
 Hundhausen, A. J.: 1972, *Coronal Expansion and Solar Wind*, (Springer-Verlag).

- Kohl, J. L., Strachan, L., and Gardner, L. D.: 1996, *Astrophys. J.*, **465**, L141.
Linker, J. A., and Mikic, Z.: 1995, *Astrophys. J.*, **438**, L45.
Mikic, Z., and Linker, J. A.: 1994, *Astrophys. J.*, **430**, 898.
Sittler, E. C., Jr., and Guhathakurta, M.: 1999, *Astrophys. J.*, in press.
Steinolfson, R. S., Suess, S. T., and Wu, S. T.: 1982, *Astrophys. J.*, **255**, 730.
Strachan, L., et al.: 1997, ESA SP-404, 691.
Suess, S. T., Wang, A. H., and Wu, S. T.: 1996, *J. Geophys. Res.*, **101**, 19957.
Wang, A. H., Wu, S. T., Suess, S. T., and Poletto, G.: 1995, *Solar Phys.*, **161**, 365.
Wang, A. H., Wu, S. T., Suess, S. T., and Poletto, G.: 1998, *J. Geophys. Res.*, **103**, 1913.
Wolfson, R.: 1985, *Astrophys. J.*, **288**, 769.

Address for correspondence: M. Guhathakurta, GSFC, Code 682, Greenbelt, MD 20771, USA.
Email: lika@tristang.gsfc.nasa.gov

PLASMA PROPERTIES IN CORONAL FUNNELS

P. HACKENBERG* and G. MANN

Astrophysikalisches Institut Potsdam, Potsdam, Germany

E. MARSCH

Max-Planck-Institut für Aeronomie, Katlenburg-Lindau, Germany

Abstract. A two dimensional model of the transition region and the lower corona, based on the idea that the magnetic flux is strongly concentrated at the boundaries of the supergranular convection cells, has been proposed by Gabriel in 1976. The plasma moves along the open magnetic field lines, which define the the so-called “funnel,” and eventually builds up the solar wind.

Based on a two dimensional funnel model we investigate the stationary plasma flow at its central line, taking heat conduction, radiative losses, and a heating function into account. The derived height profiles of the plasma properties within the funnel are presented.

Key words: coronal holes, magnetic network, solar wind

1. Introduction

We compose a 2-D model (in the x - z plane) of the magnetic network above two adjacent supergranules. Their boundary is located at $x = 0$ (where the magnetic field is compressed due to the convective supergranule plasma flow) and their centers are at $x = -L/2$ and $x = +L/2$ (see Figure 1). Since it is our aim to keep the model simple, we assume a high degree of symmetry: we impose four planes of symmetry which are defined by $x = -L/2$, $x = 0$, $x = +L/2$ and $y = 0$ respectively. Above the photosphere ($z > 0$, the region of our interest) the magnetic field recovers from its compression by becoming homogeneous with increasing height, since the low-beta plasma there no longer dominates the magnetic field. Moreover, the plasma flow must follow the magnetic field lines.

We describe the plasma with the stationary magnetohydrodynamic equations (Priest 1984). In the entropy equation a heating function, H , radiative losses, L_r , and thermal conductivity, q , are considered. The calculation of the 2-D potential magnetic field is done first, since the magnetic equations decouple. Afterwards, the remaining hydrodynamic equations are solved at the central field line of the funnel.

2. The Magnetic Field Structure

By examining the imposed symmetry conditions it can easily be shown that the magnetic field $\mathbf{B} = \nabla A(x, z) \times \mathbf{e}_y$ is a potential one ($j = 0$). We separate the homogeneous magnetic field from the funnel structure by $A(x, z) = A_0(x, z) + B_0x$ and solve the Laplace equation $\Delta A_0 = 0$. The Dirichlet boundary conditions are

* Supported by the DLR, Grant 50 OC 9702.



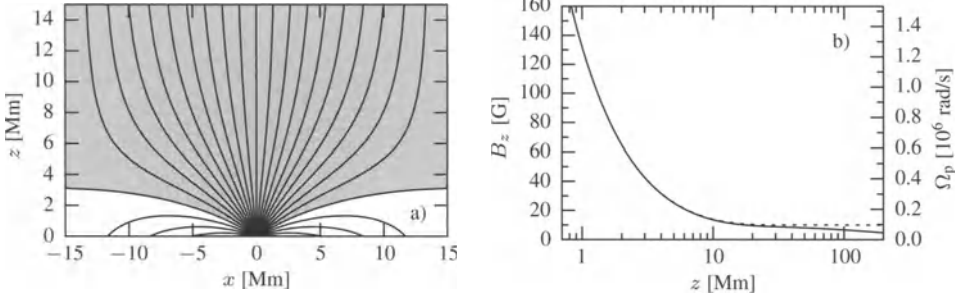


Figure 1. (Left) The magnetic field above two supergranules builds up the funnel structure. The region of open field lines is marked with gray color. The parameters are: $L = 30$ Mm, $d = 0.285$ Mm, $B_0 = 10$ G, $B_m = 1.5$ kG. The photospheric level is at $z = 0$. The supergranule boundary is at $x = 0$.

Figure 2. (Right) The magnetic field at the center of the funnel, i.e., at $x = 0$, with large scale decay (solid line) and without it (dotted line). On the right hand side the corresponding proton cyclotron frequency is shown.

$A_0 = 0$ except that at $z = 0$ (photospheric level) they are given by the compressed magnetic field which we assume to be

$$B_z(z=0) = \begin{cases} B_m & \text{for } -\frac{d}{2} \leq x \leq \frac{d}{2} \\ -\frac{B_m d - B_0 L}{L - d} & \text{elsewhere.} \end{cases} \quad (1)$$

Solving $\Delta A_0 = 0$ yields (see Figures 1 and 2)

$$B_z(x, z) = B_0 + (B_m - B_0) \left[-\frac{d}{L - d} + \frac{L}{L - d} \frac{1}{\pi} \times \left(\arctan \frac{\cosh \frac{2\pi}{L} z \sin \frac{\pi}{2L} d + \sin(\frac{\pi}{2L} d + \frac{2\pi}{L} x)}{\sinh \frac{2\pi}{L} z \cos \frac{\pi}{2L} d} \right. \right. \\ \left. \left. + \arctan \frac{\cosh \frac{2\pi}{L} z \sin \frac{\pi}{2L} d + \sin(\frac{\pi}{2L} d - \frac{2\pi}{L} x)}{\sinh \frac{2\pi}{L} z \cos \frac{\pi}{2L} d} \right) \right] \quad (2)$$

and

$$B_x(x, z) = \frac{B_m - B_0}{2\pi} \frac{L}{L - d} \ln \frac{\cosh \frac{2\pi}{L} z - \cos(\frac{\pi}{L} d + \frac{2\pi}{L} x)}{\cosh \frac{2\pi}{L} z - \cos(\frac{\pi}{L} d - \frac{2\pi}{L} x)}. \quad (3)$$

The magnetic field becomes nearly homogeneous at heights $\gtrsim 15$ Mm and takes the value B_0 there. At the central line of the funnel ($x = 0$) the magnetic field is given by

$$B_z(z) = \underbrace{B_0}_{\text{replace with}} + \frac{B_m - B_0}{L - d} \left[L \frac{2}{\pi} \arctan \left(\coth \frac{\pi}{L} z \tan \frac{\pi}{2L} d \right) - d \right]. \quad (4)$$

$B_0 \left(\frac{R_\odot}{R_\odot + z} \right)^3$ (decay of large-scale magnetic field)

For greater heights ($z \gtrsim 15$ Mm) it is necessary to take the r^{-3} decay of the coronal magnetic field, modeled as a dipole, into account.

3. Central Line of the Funnel

On the central line, conservation of magnetic and particle flux yields

$$\frac{\partial}{\partial x} B_x = - \frac{\partial}{\partial z} B_z \quad \text{and} \quad \frac{\partial}{\partial x} v_x = - \frac{v_z}{B_z} \frac{\partial}{\partial z} B_z , \quad (5)$$

and we obtain a system of *ordinary* differential equations:

$$v_z = \frac{\Phi_m B_z}{\varrho B_0} , \quad (6)$$

$$\varrho v_z \frac{\partial}{\partial z} v_z = - \frac{\partial}{\partial z} p - \varrho g , \quad (7)$$

$$\varrho v_z \frac{\partial}{\partial z} p - \gamma v_z p \frac{\partial}{\partial z} \varrho = (\gamma - 1) \varrho (H - L_r - \nabla \cdot \mathbf{q}) . \quad (8)$$

According to Marsch and Tu (1997) the plasma heating is done by cyclotron-damped Alfvén waves and the heating function becomes $H = -H_0 \Omega_p^{-1} \partial B_z / \partial z$ with $H_0 = 8.3 \times 10^8$ erg cm $^{-2}$ s $^{-1}$ G $^{-1}$. The radiation cooling is approximated by $L_r = n_e n_p Q(T)$ with $n_e n_p \approx 0.23 n^2$, and $Q(T) \approx 2 \times 10^{-22}$ erg cm 3 /s for $30\,000$ K $< T < 3\,000\,000$ K. Since heat conduction is most effective parallel to the magnetic field ($\kappa = 1 \times 10^{-6} T^{5/2}$ erg cm $^{-1}$ K $^{-7/2}$), we neglect the perpendicular conduction and obtain:

$$-\nabla \cdot \mathbf{q} \approx \frac{\partial}{\partial z} \kappa \frac{\partial}{\partial z} T - \frac{\kappa}{B_z} \left(\frac{\partial}{\partial z} B_z \right) \left(\frac{\partial}{\partial z} T \right) . \quad (9)$$

The results of the numerical integration (fifth order Runge-Kutta method) are shown in Figure 3. We have adjusted the free parameters and initial conditions to obtain an electron density $n_e = 1 \times 10^8$ cm $^{-3}$ at $z = 10$ Mm (Wilhelm *et al.* 1998), a maximum temperature $T_{\max} = 0.95 \times 10^6$ K at $z = 100$ Mm (David *et al.* 1998) and a mass flux $\Phi_m = 1 \times 10^{-10}$ g cm $^{-2}$ s $^{-1}$.

Since the electron and ion temperatures significantly differ at greater heights (Marsch and Tu 1997), it is not astonishing that we have not been able to reproduce the electron temperature profile found by David *et al.* (1998) with our one-fluid (one-temperature) model. A two-fluid model would be more appropriate and will be done next.

References

- David, C., Gabriel, A. H., Bely-Dubau, F., Fludra, A., Lemaire, P., and Wilhelm, K.: 1998, 'Measurement of the electron temperature gradient in a solar coronal hole,' *Astron. Astrophys.*, **336**, L90–L94.

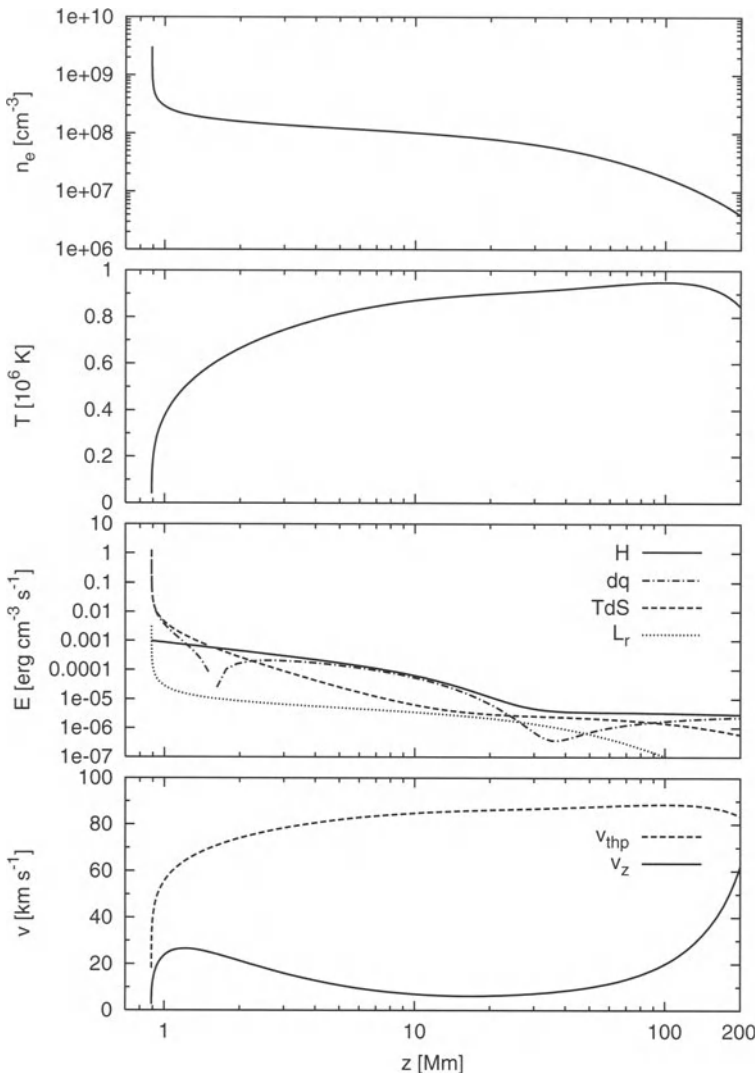


Figure 3. Height profiles in the coronal funnel. The displayed quantities are: electron number density n_e , temperature T , thermal energy generation and consumption due to the heating function (H), the divergence of the heat flux (dq), the change of gas entropy (TdS), and radiation cooling (L_r), and in the bottom panel the plasma flow speed v_z and the thermal proton velocity v_{thp} .

- Gabriel, A. H.: 1976, 'A magnetic model of the solar transition region,' *Phil. Trans. R. Soc. London*, **281**, 339–352.
 Marsch, E., and Tu, C.-Y.: 1997, 'Solar wind and chromospheric network,' *Sol. Phys.*, **176**, 87–106.
 Priest, E. R.: 1984, *Solar Magnetohydrodynamics*, Dordrecht: D. Reidel Publishing Company.
 Wilhelm, K., Marsch, E., Dwivedi, B. N., Hassler, D. M., Lemaire, P., Gabriel, A. H., and Huber, M. C. E.: 1998, 'The solar corona above polar coronal holes as seen by SUMER on SOHO,' *Astrophys. J.*, **500**, 1023–1038.

THE ROTATION OF THE Fe XIV SOLAR CORONA DURING THE RECENT SOLAR ACTIVITY MINIMUM

B. INHESTER, G. STENBORG, R. SCHWENN, N. SRIVASTAVA and B. PODLIPNIK
Max-Planck-Institut für Aeronomie, D-37191, Katlenburg-Lindau, Germany

Abstract. We analyze data observed by the LASCO C1 coronagraph on board the SOHO spacecraft during the solar minimum activity from April 1996 to March 1997. Using the phase dispersion technique, we investigate the periodicity and recurrence of Fe XIV emission structures with heliospheric latitude and distance above the Sun's surface with high spatial resolution. We find no significant deviation from a rigidly rotating Fe XIV corona with latitude or with distance from the Sun even on these small scales. In agreement with earlier work, the coronal rotation period at solar minimum is about 27.5 ± 1 days.

1. Introduction

The differential rotation of the photosphere has been firmly established by independent photospheric observations of Doppler shifts and drifts of sunspots (see e.g., Howard 1984). Roughly, the latitude dependence of the photospheric rotation period was found to be

$$T_{\text{rot}} \simeq 27 \text{ days} + 6 \text{ days } \sin^2 \lambda + \mathcal{O}(\sin^4 \lambda) \quad (1)$$

where λ is the heliographic latitude. Contrary to these measurements, the solar corona both in white light and in Fe XIV emission appears to rotate more or less rigidly at a period of about 27 days (e.g., Sime *et al.* 1989).

This discrepancy is difficult to understand, because the coronal plasma is dominated by the magnetic field which itself is widely assumed to be firmly anchored in the photosphere. An explanation that has been put forward is that the structures in the corona are only sensitive to large scale magnetic field variations and low multipole moments in the underlying photosphere (e.g., Wang *et al.* 1988). In this case, a gradual transition from rigid to differential rotation should be expected with decreasing distance from the photosphere and with increasing spatial resolution of the data.

The high quality of the LASCO C1 data allows us to investigate the variation of T_{rot} with good spatial resolution in bins of $dr = 0.1 R_{\odot}$ in radius and $d\lambda = 5^\circ$ in latitude. The coronagraph occulter, however, restricts the field of view to beyond $1.1 R_{\odot}$.

2. Method

We have scanned through more than 6000 flatfielded Fe XIV images taken between May 1996 and April 1997. The periodicity of the measured emission intensity $e(t)$ at some time t in each of the radius and latitude bins mentioned above was analyzed by



means of the phase dispersion method (Sterlingwerf 1978) In the simplest version of this method, first the overall rms scatter σ of $e(t)$, e.g.,

$$\sigma = \sum_t (e(t) - E)^2 / (N - 1) \quad (2)$$

is determined, where N and E are the number of data points and the average value of $e(t)$. In the next step, the rms scatter σ_i within M temporal phase bins i is found, where the phase of t is defined in the conventional way given an assumed time period T , i.e.,

$$\left. \begin{array}{l} N_i \\ E_i \\ \sigma_i \end{array} \right\} = \sum_{t \mid M \text{ frac}(\frac{t}{T}) \in [i - \frac{1}{2}, i + \frac{1}{2}]} \left\{ \begin{array}{l} 1 \\ e(t)/N_i \\ (e(t) - E_i)^2 / (N_i - 1) \end{array} \right. \quad (3)$$

Here, N_i , E_i are the number of data points within each phase bin and their average value, respectively; $\text{frac}()$ denotes the integer fraction of its argument. If the right period $T \simeq T_{\text{rot}}$ is chosen, the scatter ratio

$$S(T)/\sigma = 1/N_i \sum_{i=1}^{N_i} \sigma_i / \sigma \quad (4)$$

of the σ_i average $S(T)$ to the overall rms scatter σ assumes a minimum. For a period T far off T_{rot} the above ratio has a value close to unity. The width and depth of the minimum $S(T)/\sigma$ near T_{rot} depends, among other quantities, on the shape and the lifetime of the periodic signals in the time series $e(t)$.

In Figure 1, this ratio is shown for a low latitude $\lambda = 9^\circ$ and for a high latitude $\lambda = 63^\circ$. For both latitudes, the scatter ratios of the lowest radius bins are displayed in stacked diagrams. For low latitudes, the coronal emissivity in Fe XIV is intense enough to allow a fairly reliable determination of $T_{\text{rot}} \simeq 27$ days. Note that the identified minima are marked by a vertical line reaching from unity to the minimum value. Their length therefore corresponds to the depth of the minimum. At latitudes above 60° the coronal Fe XIV intensity becomes faint and the determination of T_{rot} more difficult. Inspection of the scatter ratio in Figure 1 provides some evidence that a periodicity with $T_{\text{rot}} < 30$ days is present at least close to the surface at $r = 1.15$ and $1.25 R_\odot$. There is no sign of a reduced rotation rate to be expected from equation (1).

3. Results and discussion

On the right half of Figure 2, the estimated rotation periods are shown wherever a reliable periodicity between 5 and 50 days could be found with an error less than ± 1.5 days. Clearly, all periods fall within the range 27 to 28 days. Some exceptions are found for period estimates at high latitudes; however, the increased scatter

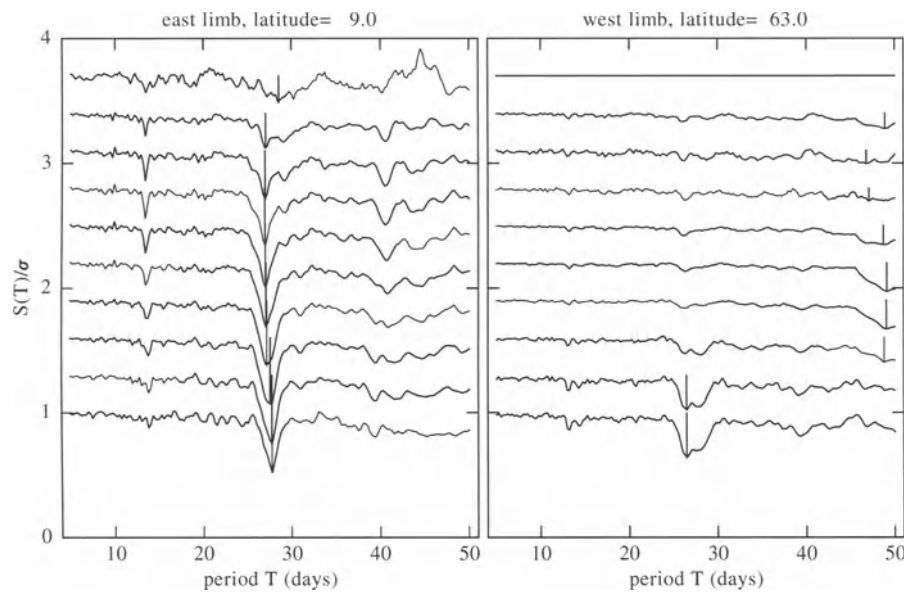


Figure 1. Scatter ratio (equation 4) with period estimate T for data from two selected latitudes and ten distances $r = 1.15$ to $2.05 R_\odot$, from bottom to top. The curves for the different distances, except for the lowest, are each shifted by 0.3 with respect to its lower neighbor to obtain the stacked diagram.

signals an enhanced uncertainty of the estimate. Neither do we find a remarkable systematic period change with distance from the Sun's surface, nor with latitude.

The shape of the $S(T)/\sigma$ minimum allows us to determine the error of the period estimate (not shown) and a statistical amplitude the T -periodic signal in $e(t)$ relative to the noise (see, e.g., Sterlingwerf 1978). A large value for this amplitude is indicative of either a strong intensity or a long duration of the periodic emission signal. On the left half of Figure 2, the amplitude/noise ratio is presented as it results from the analysis of the Fe XIV emission data. Remarkably, the maxima occur in the region of the high latitude streamer belts. These are not the region of strongest emission, but are the most persistent features in the Fe XIV observations. We also see some degradation close to the Sun's surface indicating a less stable and more transient Fe XIV emissivity there.

The Fe XIV line is emitted from hot coronal plasma of about 2×10^6 K on presumably closed field lines. Open field lines are much colder and practically show no Fe XIV emission (Schwenn *et al.* 1997). The period estimates presented in this paper should therefore be representative for the coronal streamer belt plasma. In agreement with previous and recent studies (Sime *et al.* 1989; Lewis *et al.* 1998), our analysis of one year of LASCO data during low solar activity shows no indication of a differential rotation of the Fe XIV corona. In extension of this

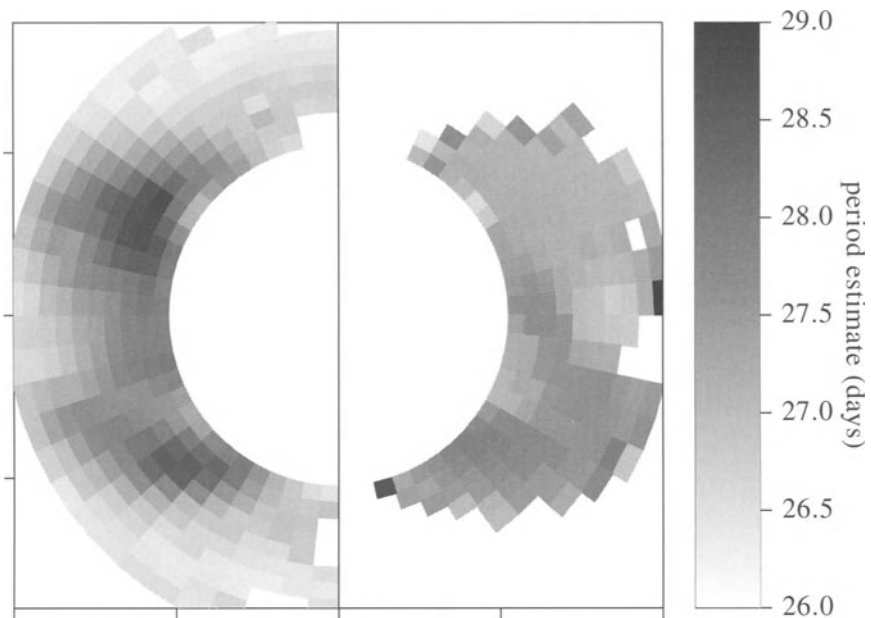


Figure 2. Estimated rotation periods (right half, grey scale code on the right) and amplitude/noise ratio of the periodic signal component in $e(t)$ (left half, grey scale in relative units) for the radius and latitude bins investigated.

previous work, our database allowed us to resolve periodicities on spatial scales as small as $\Delta\lambda = 6^\circ$ and $\Delta r = 0.1R_\odot$. However, even on these scales, we did not find a significant local deviation of the coronal rotation from a rigid rotation rate of 27.5 days/cycle.

We have also investigated the motion of individual high latitude streamers (Schwenn *et al.* 1997) above the poles. As we will report elsewhere, even these high latitude structures show a motion in agreement with the above rotation period.

References

- Howard, R.: 1984, 'Solar rotation,' *Ann. Rev. Astron. Astrophys.*, **22**, 131–155.
- Lewis, D. J. *et al.*: 1998, 'LASCO observations of the coronal rotation,' in preparation.
- Schwenn, R., *et al.*: 1997, 'First view of the green-line emission corona at solar activity minimum using the LASCO-C1 coronagraph,' *Solar Phys.*, **175**, 667–684.
- Sime, D. G., Fisher, R. R., and Altrock, R. C.: 1989, 'Rotation characteristics of the Fe XIV solar corona,' *Astrophys. J.*, **336**, 454–467.
- Sterlingwerf, R. F.: 1978, 'Period determination using the phase dispersion method,' *Astrophys. J.*, **224**, 953–960.
- Wang, Y. M., Sheeley, N. R., Nash, A. G., and Shampine, L. R.: 1988, 'The quasi-rigid rotation of coronal magnetic fields,' *Astrophys. J.*, **327**, 427–450.

A CDS OBSERVATION OF THE RELATIONSHIP BETWEEN A CORONAL HOLE AND CHROMOSPHERIC STRUCTURE

JUDE E. INSLEY

NASA/GSFC, Code 682.3, Greenbelt, MD 20771

Abstract. This paper studies the relationship between chromospheric structure and the location of the coronal hole boundary, using a SOHO-CDS observation made on 13 June 1996. The cell structure visible in the oxygen and helium data is smoothed and a basin algorithm is used to find the individual cells. As the smoothing scale increases, cells merge to form larger ones. A trade off between merging and smoothing was made, a scale of 5,000 km being used. There is good agreement between the edges of cells and the coronal hole boundary, as determined in Mg IX 368 Å, although it is not perfect. This preliminary analysis shows that the coronal hole boundary is located along chromospheric network cell edges in most places, as would be expected if the chromosphere is the source of the coronal structure and solar wind.

1. Introduction

Coronal holes are the source of the fast solar wind (Leer and Holzer 1985), and possibly the slow solar wind too (Bravo and Stewart 1997). A study of the coronal hole, visible in X-ray and certain EUV lines such as Mg IX 368 Å, and the structure in the chromosphere below it can lead to a possible understanding of solar wind acceleration mechanisms and coronal heating (McKenzie *et al.* 1998). In this paper, the relationship between the coronal hole boundary and the chromospheric network, as seen in SOHO-CDS observations, is examined.

2. Observations

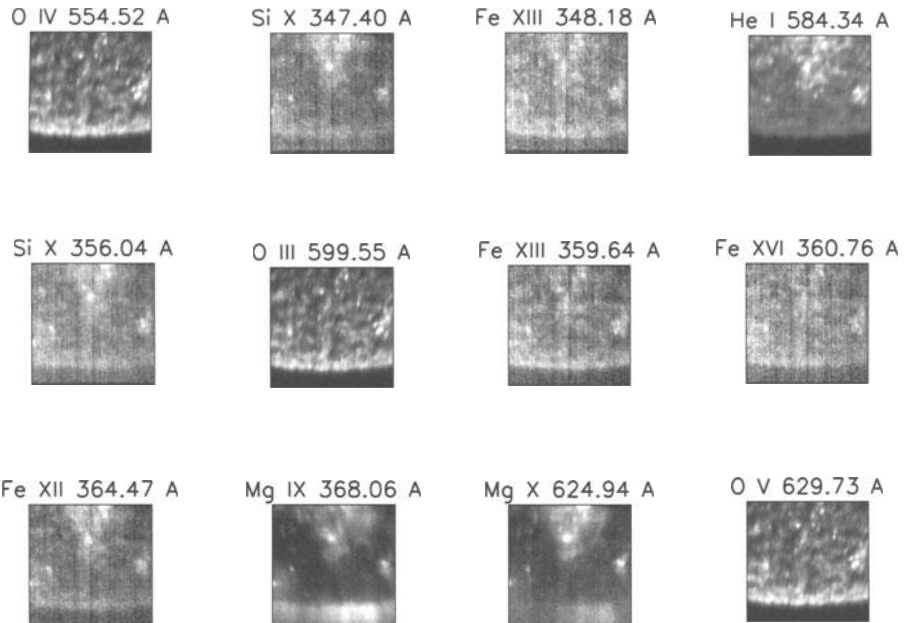
The coronal hole observations, shown in Figure 1, were made using the SOHO-CDS instrument on 13 June 1996. The lines of interest are the three oxygen lines, which all show essentially the same structure, the He I line, and the Mg IX line. The other lines are not used in this analysis. These data are comprised of a series of 120 exposures, rastered to produce an image, the duration of each exposure being 40 seconds. These data show a portion of the southern coronal hole, in a 4×4 arcmin area.

3. Analysis

Using a similar algorithm to Hagenaar *et al.* (1997) the network cell pattern in the O III 599 Å data was defined. This is a basin finding algorithm, and as such is sensitive to noise in the data. In order to compensate for some of the apparent noisiness of the original data was filtered.

A low pass Butterworth filter, in Fourier space, was applied to the data. The order of the filter was 2. Higher orders tend to smooth out edges further. The scale





SOHO/CDS NIS Raster, 13-Jun-1996 01:46:25

CHSTR_X -- Coronal Hole: Plumes -- s3159r00.fits
 Center = $(-3'', -876'')$, Size = $244'' \times 240''$

Figure 1. CDS observation of the southern coronal hole on 13 June 1996. These data show the coronal hole, and a portion of the quiet Sun in the center.

size of the filter was varied from 1,000 km to 20,000 km, with merging of cells apparent as the scale size increases. A scale size of 5,000 km was chosen as a tradeoff between smoothing and merging.

Using the Mg IX 368 Å data, a coronal hole boundary was defined, by determining where the line intensity changed significantly, from a low value to a high value. This boundary, taken at an intensity of 180 photons/cm²/sec/arcsec², is shown in Figure 2.

4. Results

The cell pattern as found using the above method is shown in Figure 3, alongside the original data (Figure 1). The pattern is in good agreement with a visual inspection of the raw data. The cell edges as shown are true edges, but some edges may have been lost due to merging of cells. The average cell size is approximately 10 Mm,

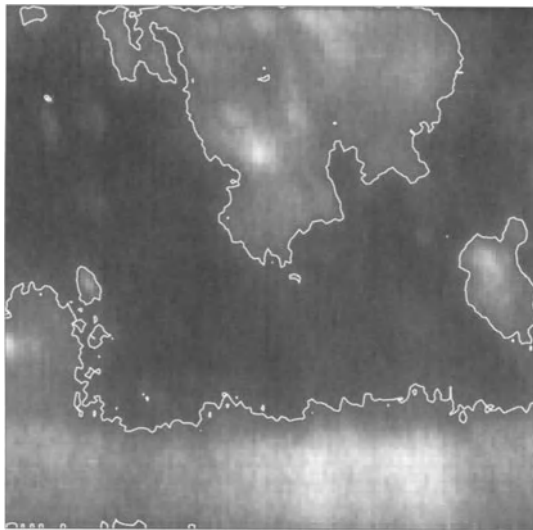


Figure 2. Mg IX 368 Å image with the coronal hole boundary overlaid. The boundary is taken at an intensity contour of 180.

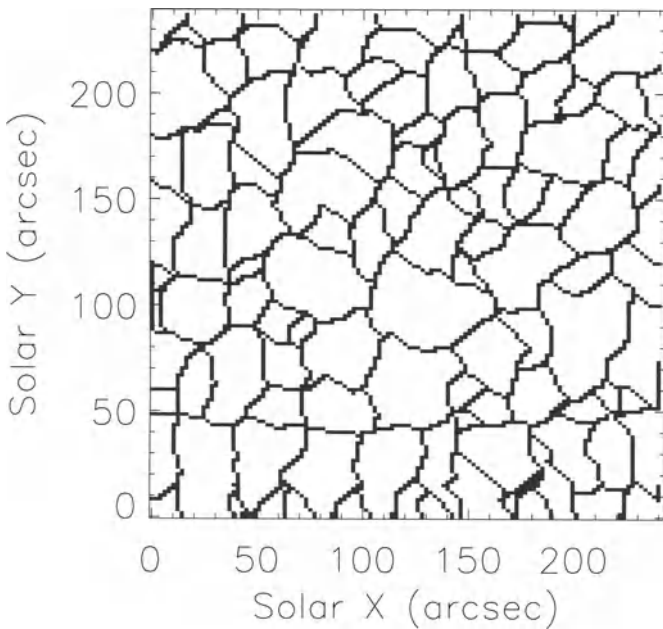


Figure 3. The chromospheric network in O III 599 Å, as determined using the basin finding algorithm.

which is smaller than normal, but not unexpected, due to geometric projection effects at the pole. Figure 4 shows the comparison between the network cells and

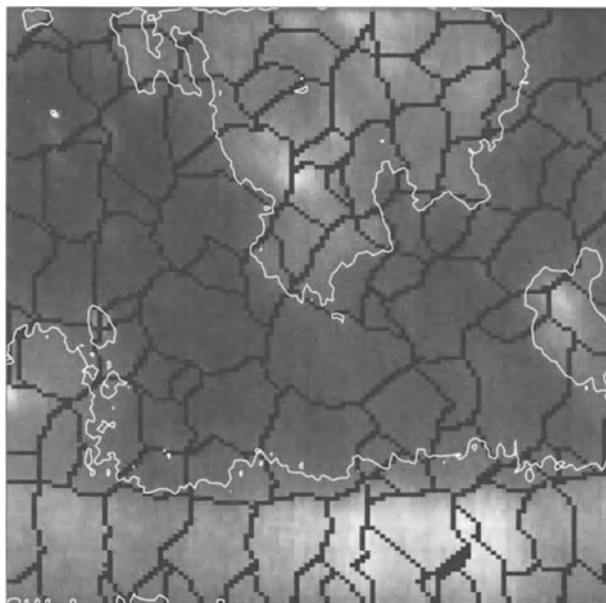


Figure 4. The coronal hole boundary overlaid on the chromospheric network cells, showing a close alignment of the two.

the boundary as derived from the Mg IX line. There is a good agreement along most of the boundary, but not complete.

5. Conclusions

These unique multi-wavelength observations of a coronal hole boundary enable the close comparison of the coronal hole boundary and underlying chromospheric network structure. The coronal hole boundary appears to lie along the edges of chromospheric network cells, or close to them. Possible reasons for the discrepancies include line of sight effects and the width of the coronal hole boundary. Further analysis of similar data is required.

References

- Bravo, S., and Stewart, G. A.: 1997, 'Fast and Slow Wind from Solar Coronal Holes,' *Astrophys. J.*, **489**, 992–999.
- Hagenaar, H. J., Schrijver, C. J., and Title, A. M.: 1997, 'The Distribution of Cell Sizes of the Solar Chromospheric Network,' *Astrophys. J.*, **481**, 988–995.
- Leer, E., and Holzer, T. E.: 1985, 'Solar Wind and Coronal Holes,' in *Future Missions in Solar, Heliospheric and Space Plasma Physics*, pp. 3–9.
- McKenzie, J. F., Sukhorukova, G. V., and Axford, W. I.: 1998, 'The source region of the fast solar wind,' *Astron. Astrophys.*, **330**, 1145–1148.

STUDY OF DYNAMICAL PROPERTIES OF CORONAL STRUCTURES IN THE POLAR REGIONS

MARGARITA KAROVSKA and BRIAN E. WOOD

Harvard-Smithsonian Center for Astrophysics, 60 Garden St., Cambridge, MA 02138

JOHN W. COOK, RUSSELL A. HOWARD and GUENTER E. BRUECKNER

Naval Research Laboratory, 4555 Overlook Av., SW, Washington DC, 20375-5320

Abstract. We present the results from a study of the dynamical properties of polar jets in the Sun's polar regions using LASCO C2 coronagraph and EIT observations. In the simplest impulsive acceleration scenarios for jets, gravity is expected to be the dominant force on the jet following the initial acceleration, especially in the Sun's polar regions where the open magnetic fields should not significantly impede the jet's motion. Our analysis shows that although at low heights the kinematics of the jets could be consistent with a gravitational deceleration of the ejected plasma, at higher heights their motions may simply follow the ambient solar wind outflow. If so, the polar jets can be used as tracers of the solar wind in coronal holes.

1. Introduction

White-light coronal images taken by LASCO have revealed a new type of solar ejection phenomena called "polar jets" (Wang *et al.* 1998). As seen in LASCO's C2 coronagraph, which images the corona from about $2 R_{\odot}$ to $6 R_{\odot}$, the jets are narrow, radially extended intensity enhancements that appear to move outwards from the Sun's polar regions in a nearly radial direction. We focused our study on several jets detected in two sequences of C2 images recorded on 1997 March 22 and on 1997 August 5–6.

On 1997 March 22 at 23:46 UT, a unique sequence of LASCO C2 images of the north polar region was recorded. This sequence lasted for about 41 hours. The average time between the 200 images taken during the sequence was 12 minutes, an improvement of about a factor of two over the time cadence normally attained by LASCO in its monitoring of the solar corona. Near the end of the polar imaging sequence, a series of three jets is seen originating from the same location near the north pole, appearing at 2–3 hour intervals. In addition to these jets, we studied six more jets that occurred on 1997 August 5–6, and were seen by both LASCO C2 and EIT. The cadence in this sequence is two times lower than in the 1997 March observations. Most of the EIT EUV (Fe XII $\lambda 195$) jets are narrow, radially extended features roughly analogous to their white-light appearance in the LASCO C2 field of view.

Using these two sequences we explore the kinematics of the jets, assuming that their observed apparent motion corresponds to plasma following a ballistic trajectory in the solar gravitational field.



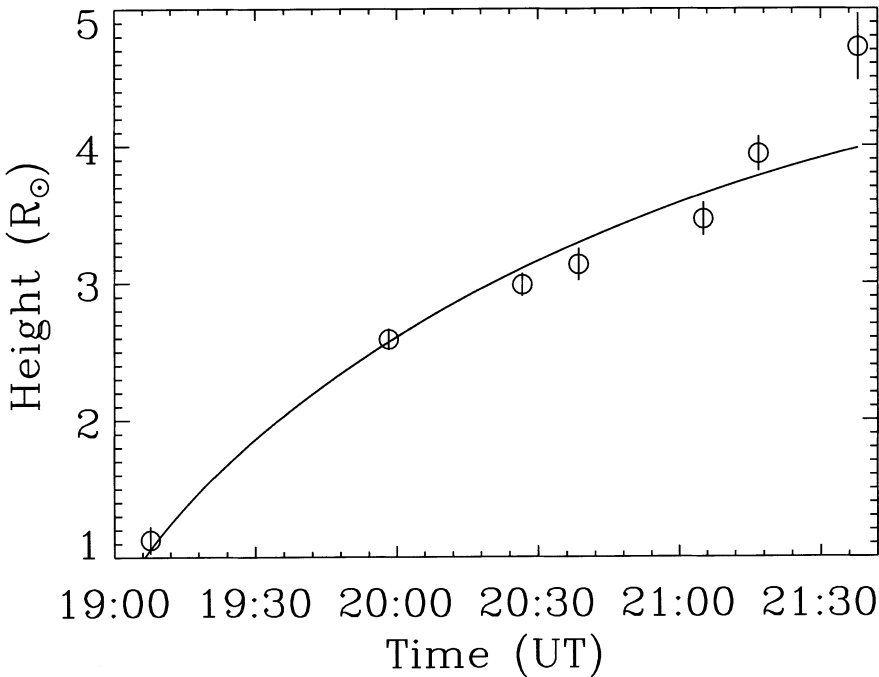


Figure 1. Motion of a polar jet observed by LASCO and EIT on 1997 August 5. We plot the centroid of the jet (circles) as a function of time, along with a best-fit ballistic trajectory curve (solid line).

2. Data Analysis

We selected thin sectors centered on the axis of the jets. These sectors were partitioned into numerous (~ 70) segments. We measured intensities along the axis of each sector by summing the pixels within individual segments. For each intensity tracing we had to make a nonlinear conversion from distance along the jet axis to distance from Sun center, because the axes of the jets are not precisely radial. It is at an angle such that an extension of the axis passes well above Sun center. This is not a surprise, since polar plumes show similar superradial expansion (DeForest *et al.* 1997). For each intensity tracing, we fitted a Gaussian to the intensity profile to determine the location of the centroid of the jet. In Figure 1 we show an example of the centroid motion as a function of time for one of the jets in our sample. The centroid measurements are displayed as circles, and are shown with the 2σ error bars.

The centroid points in our sample of polar jets indicate a deceleration of the ejected plasma. The simplest interpretation for this deceleration is that it is due to gravity. In order to test this hypothesis, we fitted the centroid data points with

ballistic trajectory curves, assuming the jet material is ejected from the solar surface with an initial velocity v_0 . Our best fits to the data demonstrate that the motion of the jets is roughly consistent with a ballistic trajectory. For example, the fit to the first of the 1997 March jets implies a decrease in velocity from 292 km s^{-1} at $3 R_\odot$ to 184 km s^{-1} at $5 R_\odot$. The initial ejection velocity of this jet is $v_0 = 584 \pm 4 \text{ km s}^{-1}$. This is slightly below the Sun's escape velocity of 619 km s^{-1} , suggesting that in the absence of other forces the jet material will fall back toward the Sun after reaching a height of $9.0 R_\odot$. The results for the second 1997 March jet that we analyzed are similar, with a somewhat lower ejection velocity of $v_0 = 551 \pm 5 \text{ km s}^{-1}$. In the absence of other forces the material of that jet would reach a height of $4.8 R_\odot$ before falling back to the Sun. As for the 1997 August jets, the initial data points, which include EIT data, also suggest significant deceleration at low heights. This is consistent with the kinematic scenario of impulsive acceleration followed by gravitational deceleration. For example, based on the purely ballistic trajectory fits to the brightest three of the six jets, we estimate initial velocities of 545 ± 4 , 571 ± 1 , and $545 \pm 4 \text{ km s}^{-1}$ for these jets. However, there are statistically significant discrepancies between the fits and the data, as seen for the jet shown in Figure 1.

These discrepancies suggest gravity may not be the only force acting on the jets. The initial velocities of the fitted ballistic trajectories provide another argument against purely ballistic motion. All of the ballistic trajectories suggest initial velocities in a narrow range of $540\text{--}590 \text{ km s}^{-1}$, as if the polar jets were tuned to a narrow range of initial velocities. In the gravitational deceleration scenario, jets with initial velocities below about 500 km s^{-1} will never reach the C2 field of view, so explaining the lower initial velocity limit is not a problem. The upper limit, however, is not easy to explain. If the impulsive acceleration followed by gravitational deceleration scenario is true, why are there no jets with initial velocities greater than 610 km s^{-1} and velocities in the C2 field of view greater than 300 km s^{-1} ? One possibility is that within the C2 field of view they may have been incorporated into the ambient solar wind flow. The average jet velocities in the C2 field of view do appear to be roughly consistent with the polar outflow velocities measured between $1.5 R_\odot$ and $4.0 R_\odot$ by the Ultraviolet Coronagraph Spectrometer (UVCS) instrument on *SOHO* (Kohl *et al.* 1998).

3. Conclusions

Our observations of several polar jets show significant deceleration at low heights that could be consistent with a gravitational deceleration of the ejected plasma. However, purely ballistic trajectories are unable to entirely explain the motions of the jets, implying that gravity may not be the only force acting on the jets. One possibility is that the ambient solar wind exerts a drag force on the polar jets that causes them to eventually approach the ambient solar wind motion above about

4 solar radii. Our detailed analysis shows that the jet centroid velocities above a few solar radii are in fact similar to the velocities of the background solar wind. Therefore at those heights, the jets might be used for studies of the outflow wind velocities in coronal holes.

Acknowledgements

This project is supported by the Naval Research Laboratory (NRL) contract N0014-97-1-G023. MK is a member of the AXAF Science Center, which is operated under NASA contract NAS-839073. JWC and RAH are supported by NASA and the Office of Naval Research. SOHO is a project of international cooperation between ESA and NASA.

References

- DeForest, C. E., *et al.*: 1997, *Solar Physics*, **175**, 393.
Kohl, J. L., *et al.*: 1998, *Ap. J.*, **501**, L127.
Wang, Y.-M., *et al.*: 1998, *Ap. J.*, **508**, 899.

NUMERICAL SIMULATIONS OF STELLAR WINDS

R. KEPPENS and J. P. GOEDBLOED

keppens@rijnh.nl, FOM-Institute for Plasma Physics Rijnhuizen, P.O. Box 1207, 3430 BE Nieuwegein, The Netherlands

Abstract. We discuss steady-state transonic outflows obtained by direct numerical solution of the hydrodynamic and magnetohydrodynamic equations. We make use of the Versatile Advection Code, a software package for solving systems of (hyperbolic) partial differential equations. We model thermally and magneto-centrifugally driven stellar outflows as generalizations of the well-known Parker and Weber-Davis wind solutions. To obtain steady-state solutions efficiently, we exploit fully implicit time stepping.

Wind solutions containing both a ‘wind’ and a ‘dead’ zone are presented. We emphasize the boundary conditions imposed at the stellar surface. For axisymmetric wind solutions, we use the knowledge of the flux functions to verify the numerical solutions.

1. Axisymmetric Transonic MHD Flows

We use cylindrical coordinates (R, Z, φ) and ideal MHD. For $\partial\varphi = 0$ and $\partial t = 0$, mass and flux conservation lead to a poloidal stream function $\chi(R, Z)$ and a poloidal flux function $\psi(R, Z)$ with $\chi(\psi)$. All axisymmetric stationary ideal MHD equilibria are derivable from a single variational principle $\delta L = \delta \int \mathcal{L} dV = 0$ with Lagrangian density (Goedbloed *et al.* 1998):

$$\mathcal{L}(M^2, \psi, \nabla \psi; R, Z) = \frac{1}{2R^2}(1 - M^2) |\nabla \psi|^2 - \frac{\Pi_1}{M^2} + \frac{\Pi_2}{\gamma M^{2\gamma}} - \frac{\Pi_3}{1 - M^2}$$

The minimizing Euler-Lagrange equations need to be solved simultaneously for the flux function $\psi(R, Z)$ and the squared poloidal Alfvén Mach number $M^2(R, Z) \equiv \rho v_p^2/B_p^2 = \chi'^2/\rho$. They describe force balance across poloidal streamlines and energy conservation along them. Integrating the axisymmetric, stationary ideal MHD equations, one obtains five flux functions. These enter in the profile expressions Π_i . The flux functions are the Bernoulli function (\sim energy) $H \equiv \frac{1}{2}v^2 + (\gamma/(\gamma - 1))p/\rho - GM_g/r - R\Omega v_\varphi$, the derivative of the stream function $\chi' \equiv \partial\chi/\partial\psi$, the entropy S , the total specific angular momentum $L \equiv Rv_\varphi - RB_\varphi/\chi'$, and the derivative of the electric field potential $\Omega \equiv R^{-1}(v_\varphi - (\chi'/\rho)B_\varphi)$. By an appropriate choice of the free flux functions, we can construct axisymmetric, stationary flows. Self-similar solutions can be analyzed further by analytic means. General solutions require a numerical solution procedure.



2. Versatile Advection Code

VAC (Tóth 1996) is a general purpose software package for solving a conservative system of partial differential equations with additional non-hyperbolic source terms. We solve the system on a finite volume structured grid. Particular systems available are the hydrodynamic (Euler and Navier-Stokes) and the magnetohydrodynamic (ideal and resistive) equations. The source code is dimension independent, so it can solve 1D, 2D, 2.5D, and 3D problems. A modular approach ensures the compatibility between the different code segments. As a result, several spatial and temporal (explicit, semi-implicit and fully implicit) discretizations are applicable to all physics modules.

3. Magnetized Winds Containing a ‘Dead’ Zone

With VAC, we can calculate steady-state transonic solutions to the MHD equations which mimic thermally and/or magneto-centrifugally driven stellar outflows. Under polytropic $p \sim \rho^\gamma$ conditions, analytic solutions are available for equatorial outflow from a magnetized, rotating star. In Keppens and Goedbloed (1998), we explain how we start from a hydrodynamic, non-rotating, spherically symmetric, isothermal outflow (Parker wind), and relax all assumptions to allow for magnetic fields, rotation and polytropic flows. The resulting Weber-Davis solution has slow r_s and fast r_f critical points, and an Alfvén point r_A where the radial velocity v_r equals the radial Alfvén speed A_r . Using modern numerical schemes, we generate Weber-Davis solutions. The positions of and velocities at these specific points can be verified to agree perfectly with analytic solutions *a posteriori*.

Extrapolating the Weber-Davis solution out of the equatorial plane yields polytropic, axisymmetric and transonic outflow from magnetized, rotating stars. One obtains critical surfaces, and a continuous acceleration from subslow flow at the surface to superfast flow at large distances. Poloidal streamlines of constant $\chi(R, Z)$ and poloidal field lines of constant (R, Z) are parallel. Specific angular momentum and all other flux functions are conserved along them.

By a suitable initialization of the time-marching procedure to obtain steady-state stellar wind solutions, we can find magnetized, rotating winds containing both a ‘wind’ and a ‘dead’ zone. Boundary conditions at the stellar surface impose the mass flux and ensure the correct rotational coupling of velocity and magnetic field. We let the density and all magnetic field components adjust freely at the base. This allows for the simultaneous and self-consistent modeling of both open and closed field line regions, thereby extending models presented by Sakurai (1985). Figure 1 shows the overall solution, described in detail in Keppens and Goedbloed (1998). Our method easily allows us to incorporate a latitudinal dependence of the stellar rotation rate, or the magnetic field strength. The latitudinal variation of the density and the velocity can be compared with Ulysses (SWOOPS) measurements (McComas *et al.* 1998).

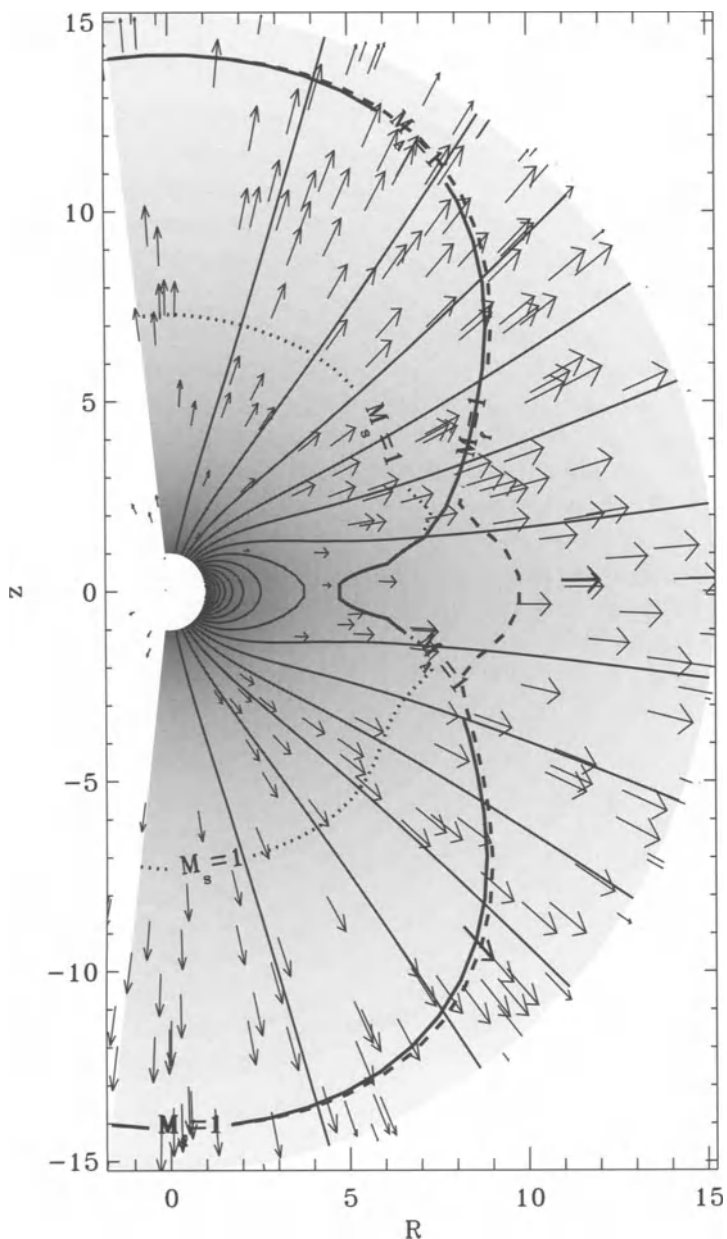


Figure 1. Axisymmetric magnetized wind containing a ‘wind’ and a ‘dead’ zone. Shown are the poloidal magnetic field lines and the poloidal flow field as vectors. Indicated are the three critical surfaces where $M_s^p = 1$ (dotted), $M_A^p = 1$ (solid line), and $M_f^p = 1$ (dashed). The density structure is shown in a grey scaling.

Clearly, the density is higher about the ecliptic and there is a decrease in wind speed associated with the equatorial ‘dead’ zone. Of particular interest is the way in which the outflow accelerates to superfast flow, thereby defining and crossing the critical surfaces where the poloidal flow exceeds the poloidal slow, Alfvén, and fast velocities.

4. Conclusions

A single variational principle governs all axisymmetric transonic MHD flows. While specific classes of self-similar flows can be studied analytically, general flow solutions are to be obtained by large-scale 3D MHD codes. VAC is such a general-purpose code, running on vector and parallel supercomputers, and we demonstrated its capacity to model stellar winds. So far, we presented steady-state transonic outflows in spherical and axisymmetry. In Keppens and Goedbloed (1998), we modeled: (i) isothermal, spherically symmetric Parker winds; (ii) polytropic, spherically symmetric Parker winds; (iii) polytropic, rotating Parker winds for the equatorial plane; (iv) Weber-Davis magnetized, polytropic, rotating winds for the equatorial plane; and finally axisymmetric, polytropic, rotating 2D winds, both (v) unmagnetized and magnetized, without (vi) and with (vii) a ‘dead’ zone. We can now meaningfully explore time-dependent 3D wind modeling. Extensions of such thermal and magneto-centrifugal MHD wind models could explore additional wave-driven phenomena, which presumably play a role in fast solar polar wind streams.

Acknowledgements

This work is sponsored by the NWO ‘Massaal Parallel Rekenen’ project and by NCF for use of supercomputer facilities.

References

- Goedbloed, J. P., Keppens, R. and Lifschitz, A. E.: 1998, “Axisymmetric Transonic MHD flows,” *Proceedings of 25th EPS conference on controlled fusion and plasma physics*, 29 June to 3 July, Prague, Czech Republic, in press.
- Keppens, R. and Goedbloed, J. P.: 1998, “Numerical simulations of stellar winds: polytropic models,” *Astron. & Astrophys.*, in press.
- McComas, D. J. *et al.*: 1998, “Ulysses’s return to the solar solar wind,” *Geophys. Res. Lett.*, **25**(1), 1.
- Sakurai, T.: 1985, “Magnetic stellar winds – a 2-D generalization of the Weber-Davis model,” *Astron. & Astrophys.*, **152**, 121.
- Tóth, G.: 1996, “A general code for modeling MHD flows on parallel computers: Versatile Advection Code,” *Astrophys. Lett. and Comm.*, **34**, 245.

ON THE ELECTRON TEMPERATURE AND CORONAL HEATING IN THE FAST SOLAR WIND CONSTRAINED BY IN-SITU OBSERVATIONS

Y.-K. KO

Harvard-Smithsonian Center for Astrophysics, Cambridge, MA 02138

C. P. T. GROTH

Department of Atmospheric, Oceanic and Space Sciences, University of Michigan, Ann Arbor, MI 48109

Abstract. The electron temperature profile in the polar coronal hole inferred by the ionic charge state data of the fast wind exhibits a local maximum of $\sim 1.5 \times 10^6$ K. This indicates the existence of electron heating in the source region of the fast solar wind. In this paper, a two-fluid solar wind model, which incorporates additional ‘mechanical’ heating, is used to investigate the heating of the electrons in the coronal hole. We find that the classical collision-dominated description for the electron conduction heat flux is not valid and needs to be severely limited in order for the electron temperatures predicted by the model to agree with constraints supplied by both the solar wind ionic charge state data and the solar wind plasma properties observed at 1 AU. The corresponding constraints on the coronal electron heating will also be discussed.

1. Introduction

Electron temperature is one of the important physical properties in the solar corona and the solar wind. The ionic charge state data of the fast wind measured by SWICS/Ulysses during its south polar pass have implied that the electron temperature in the south polar coronal hole has a maximum of around 1.5×10^6 K (Ko *et al.* 1997). At 1 AU, it was observed to have a mean value of $1.41 \pm 0.38 \times 10^5$ K (Newbury *et al.* 1998) with average heat flux of $2.8 \pm 0.9 \times 10^{-3}$ erg cm $^{-2}$ s $^{-1}$ (Feldman *et al.* 1976). It is commonly accepted that electrons decouple from protons very low in the corona, and thus they need to be treated as separate fluids in modeling the solar wind. Quite a few efforts have been devoted to the heating and acceleration of the solar wind using multi-fluid models (e.g., Hansteen and Leer 1995; Olsen and Leer 1996; Esser *et al.* 1997). In this paper, we use a two-fluid model with the aim of fitting the electron temperature both in the inner corona and at 1 AU to gain some insights into the heat transport and coronal heating of the solar wind electrons.

2. The Two-Fluid Model

The transport equations adopted for the one-dimensional proton-electron two-fluid model are ($s = p, e$):

$$\frac{\partial}{\partial t} \left(\frac{\rho_s}{B} \right) + u_s \left(\frac{\rho_s}{B} \right) + \frac{\rho_s}{B} \frac{\partial u_s}{\partial r} = \frac{\delta}{\delta t} \frac{\rho_s}{B} \quad (1)$$



$$\frac{\partial u_s}{\partial t} + u_s \frac{\partial u_s}{\partial r} + \frac{B}{\rho_s} \frac{\partial}{\partial r} \left(\frac{p_s + p_{w,s}}{B} \right) = \frac{\delta u_s}{\delta t} - \frac{p_s + p_{w,s}}{\rho_s} \frac{1}{B} \frac{dB}{dr} - \frac{GM}{r^2} + \frac{q_s}{m_s} E \quad (2)$$

$$\frac{\partial}{\partial t} \left(\frac{p_s}{B} \right) + \frac{5}{3} \frac{p_s}{B} \frac{\partial u_s}{\partial r} + u_s \frac{\partial}{\partial r} \left(\frac{p_s}{B} \right) + \frac{2}{3} \frac{\partial}{\partial r} \left(\frac{h_s}{B} \right) = \frac{\delta}{\delta t} \left(\frac{p_s}{B} \right) + \frac{2Q_s}{3B} + \frac{2}{3} u_s \frac{p_s}{B} \frac{1}{B} \frac{dB}{dr} \quad (3)$$

where ρ_s , u_s , p_s and h_s are the mass density, velocity, gas pressure ($= \rho_s k T_s / m_s$) and heat flux for species s . The magnetic flux tube geometry is given the form of super-radial expansion, $B_0/B(r) = f(r)(R_s^2/r^2)$, where B_0 is the magnetic field strength at one solar radius, R_s , and $f(r)$ takes the commonly adopted form from Kopp and Holzer (1976) with f_{\max} , r_1 and σ as free parameters. The Alfvén wave pressure is $p_{w,e} = 0$ for electrons, and for protons it is adopted from Habbal *et al.* (1994). The solar wind plasma is subject to the condition of quasi-neutrality $n_e = n_p$ and zero-current density $n_e u_e = n_p u_p$ where $n_s = \rho_s/m_s$ is the number density for species s . In conjunction with eq. (2) for electrons, we can solve for the electric field E . The source terms $\delta(\rho_s/B)/\delta t$, $\delta u_s/\delta t$, and $\delta(p_s/B)/\delta t$ represent the time rate of change due to electron-proton collisions, for which we adopt the forms in Schunk (1975).

Without the knowledge of specific heating mechanisms, the heating term Q_s in eq. (3) is generally given an *ad hoc* form of (e.g., Esser *et al.* 1997):

$$Q_p = Q_{p0} e^{-|(r-r_m)/H_m|} \quad \text{and} \quad Q_e = Q_{e0} e^{-|(r-r_m)/H_m|} - n_e n_p P(T_e). \quad (4)$$

Note that radiative cooling $n_e n_p P(T_e)$ (following Rosner *et al.* 1978) is included in the heating term for electrons.

It is well known that the classical description of the electron heat conduction (Spitzer and Härm 1953) in the solar wind is not valid when $\lambda_e/L_T \gtrsim 10^{-2}$, where $\lambda_e = (kT)^2/8\pi n_e e^4$ is the electron mean free path for $e-e$ and $e-p$ collisions and $L_T = |(1/T_e)(dT_e/dr)|^{-1}$ is the temperature scale height (e.g., Hollweg 1976). We find that this ‘collision-dominated’ description breaks down very close to the coronal base (cf. Figure 1b). We thus choose to describe the heat flux for protons and electrons as:

$$h_s = \begin{cases} \max \left(-k_s \frac{\partial T_s}{\partial r}, -\phi_s \frac{3}{2} p_s v_{th,s} \right) & \text{if } \frac{\partial T_s}{\partial r} > 0 \\ \min \left(-k_s \frac{\partial T_s}{\partial r}, \phi_s \frac{3}{2} p_s v_{th,s} \right) & \text{if } \frac{\partial T_s}{\partial r} < 0 \end{cases} \quad (5)$$

where k_s is the classical heat conductivity as derived by Schunk (1975). ϕ_s is a factor multiplied by the ‘free-streaming’ heat flux $h_{FS} = \frac{3}{2} p_s v_{th,s}$ where $v_{th,s} = \sqrt{5p_s/3\rho_s}$ is the thermal speed. The above transport equations are solved using a higher-order semi-implicit Godunov-type finite volume scheme. For the detailed numerical procedure, see Groth *et al.* (1999).

Figure 1a shows the proton and electron temperature profiles from our model in which we try to fit the model parameters with the observed values. Figure 1b compares λ_e with L_T in this model. We can see that $\lambda_e/L_T \gtrsim 10^{-2}$ for $r \gtrsim 2.2R_s$.

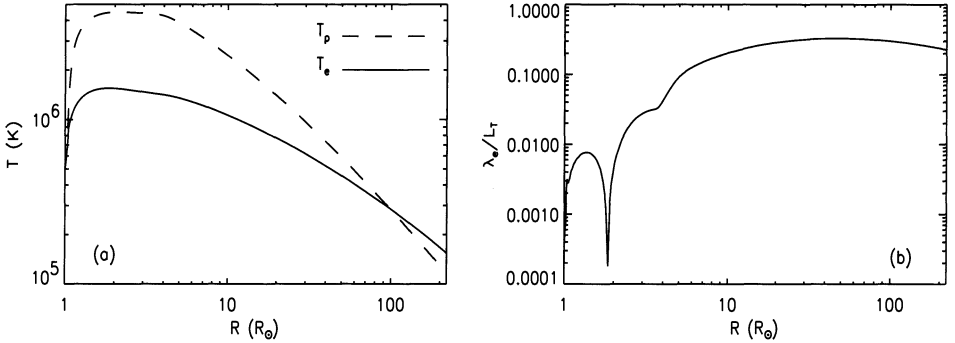


Figure 1. (a) Proton and electron temperature profiles. The input parameters for this particular model are: $f_{\max} = 10$, $r_1 = 1.5R_s$, $\sigma = 0.7R_s$, $n_p(1R_s) = n_e(1R_s) = 10^8 \text{ cm}^{-3}$, $T_p(1R_s) = T_e(1R_s) = 5 \times 10^5 \text{ K}$, $Q_{p0} = 3 \times 10^{-4} \text{ erg cm}^{-3} \text{s}^{-1}$, $Q_{e0} = 1.1 \times 10^{-4} \text{ erg cm}^{-3} \text{s}^{-1}$, $H_m = 0.4R_s$, $r_m = 1.0R_s$, $\phi_p = 2.0$, $\phi_e = 0.17$. The resulting solar wind parameters are: in the inner corona, $T_{p,\max} = 4.49 \times 10^6 \text{ K}$, $T_{e,\max} = 1.55 \times 10^6 \text{ K}$; and at 1 AU, $T_{p,E} = 1.18 \times 10^5 \text{ K}$, $T_{e,E} = 1.56 \times 10^5 \text{ K}$, $n_E = 3.1 \text{ cm}^{-3}$, $u_E = 818 \text{ km s}^{-1}$, $n_E u_E = 2.54 \times 10^8 \text{ cm}^{-2} \text{s}^{-1}$, $h_{p,E} = 6.1 \times 10^{-4} \text{ erg cm}^{-2} \text{s}^{-1}$, $h_{e,E} = 3.4 \times 10^{-3} \text{ erg cm}^{-2} \text{s}^{-1}$. (b) λ_e/L_T as a function of r in our model.

Therefore, the classical electron heat conduction already breaks down low in the corona. In this particular model, the heat flux for electrons takes the form of the ‘free-streaming’ flux (cf. eq. [5]) starting at $\sim 3.7 R_s$ and beyond.

3. Discussion

The main goal of this work is to look for coronal conditions in the fast wind source region (i.e., the physical parameters in the context of our two-fluid model) that can simultaneously satisfy the observed $T_{e,\max}$ in the coronal hole and $T_{e,E}$ at 1 AU. We find that the classical description of the electron heat conduction flux is not valid starting very low in the corona. Taking this form for the entire range will overestimate the electron heat flux and the electron temperature profile will be too flat to satisfy the observed values at both the inner corona and 1 AU (Hu *et al.* 1997). Furthermore, the electron heat flux at large r needs to be nearly an order of magnitude smaller than the ‘free-streaming’ flux ($\phi_e \sim 0.17$). This agrees with the observation that $\phi_e = 0.22 \pm 0.07$ at 1 AU (Feldman *et al.* 1976). Figure 2 shows $T_{e,\max}$, $T_{e,E}$ and $h_{e,E}$ as a function of ϕ_e , with other parameters fixed at values stated in Figure 1. Other observable solar wind quantities are very weak functions of ϕ_e . It is obvious that in order to fit the observed $T_{e,\max}$, $T_{e,E}$ and $h_{e,E}$ simultaneously, ϕ_e must be around 0.2. Note that increasing (or decreasing) the electron heating (i.e., Q_{e0} , H_m , r_m) moves all these curves up (or down), and we cannot find any values of Q_{e0} , H_m , r_m that fit with the observations if $\phi_e > 0.2$.

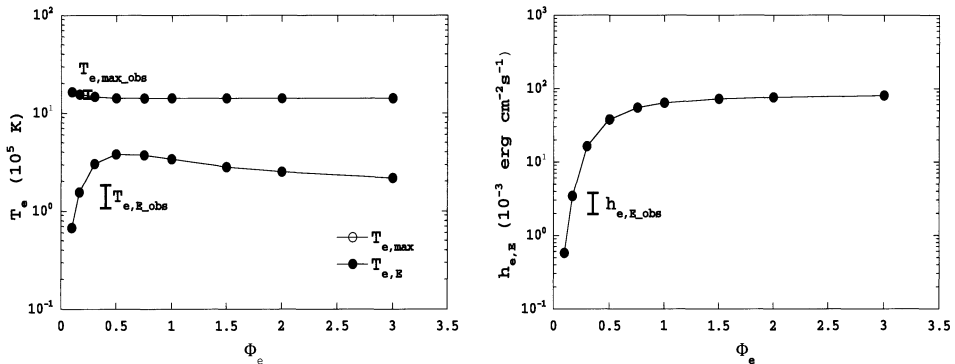


Figure 2. $T_{e,\max}$, $T_{e,E}$ and $h_{e,E}$ as a function of ϕ_e . The ranges of their observed values are also shown.

We also find that the implied $T_{e,\max}$ from the data requires an electron heating source other than heat conduction and electron-proton collisions. Our models show that $T_{e,\max} \propto Q_{e0}^{0.46} H_m^{1.7} r_m^{1.8}$ which is a strong function of these heating parameters. This would put a rather tight constraint on the possible magnitude of the electron heating in coronal heating models.

Olsen and Leer (1996) have shown from their 8-moment 2-fluid model that the electron heat conductivity can be well described by the Spitzer-Härm term. They also discussed that the 8-moment approximation breaks down if $h_s/h_{FS} \gtrsim 1$ which is the case here for $r > 9 R_s$ if we take h_e to be the classical heat conduction flux. The prime result of our work is that the model cannot produce an electron temperature profile that fits both the inner coronal value and that at 1 AU without having some sort of heating *and* much lower heat conduction fluxes than the classical values. Various coronal line ratios (e.g., Wilhelm *et al.* 1998; David *et al.* 1998) indicate that the coronal electron temperature is no higher than $\sim 8 \times 10^5$ K for $r \lesssim 1.6 R_s$ and is lower outward. This obviously contradicts with that inferred by the solar wind ionic charge states. We find that this discrepancy is hard to reconcile at this moment. The argument lies mainly on the observed Si charge states which indicate a freezing-in temperature $> 1.4 \times 10^6$ K. Owocki and Ko (1999) have shown that these Si ions are relatively insensitive to the non-thermal tail of electrons in the coronal temperature range. Thus, a non-thermal distribution of electrons may not explain this discrepancy between solar wind particles and coronal UV measurements.

When the classical description of the heat flux breaks down, the heat transport becomes non-local. Thus our prescription of the heat flux is not strictly valid because of the local nature of the ‘free-streaming’ flux. Non-local heat transport of electrons due to a steep temperature gradient has been widely studied in laser fusion studies (e.g., Krasheninnikov 1993). In general, the heat flux under a steep

temperature gradient is found to be a small fraction of the free-streaming flux. This is in agreement with our results. Although solar wind electrons have no strong effect on the bulk flow properties, we stress that it is necessary to incorporate adequate electron heat transport into the solar wind models to correctly model the heating of solar wind electrons.

Acknowledgements

Y.-K. Ko acknowledges the support by NASA/JPL contract 955460 to the University of Michigan and by NASA grant NAG5-3192 to the Smithsonian Astrophysical Observatory.

References

- David, C., et al.: 1998, *Astron. Astrophys.*, **336**, L90.
Esser, R., et al.: 1997, *J. Geophys. Res.*, **102**, 7063.
Feldman, W. C., et al.: 1976, *J. Geophys. Res.*, **81**, 5054.
Groth, C. P. T., Ko, Y.-K., and Gombosi, T. I.: 1999, in preparation.
Habbal, S. R., Hu, Y.-Q., and Esser, R.: 1994, *J. Geophys. Res.*, **99**, 8465.
Hansteen, V., and Leer, E.: 1995, *J. Geophys. Res.*, **100**, 21577.
Hollweg, J. V.: 1976, *J. Geophys. Res.*, **81**, 1649.
Hu, Y.-Q., Esser, R., and Habbal, S. R.: 1997, *J. Geophys. Res.*, **102**, 14661.
Ko, Y.-K., et al.: 1997, *Sol. Phys.*, **171**, 345.
Kopp, R. A., and Holzer, T. E.: 1976, *Sol. Phys.*, **49**, 43.
Krasheninnikov, S. I.: 1993, *Phys. Fluid B*, **5**, 74.
Newbury, J. A., et al.: 1998, *J. Geophys. Res.*, **103**, 9553.
Olsen, E. L., and Leer, E.: 1996, *J. Geophys. Res.*, **101**, 15591.
Owocki, S. P., and Ko, Y.-K.: 1999, in *Solar Wind 9*, in press.
Rosner, R., Tucker, W. H., and Vainu, G. S.: 1978, *Astrophys. J.*, **220**, 643.
Schunk, R. W.: 1975, *Planet. Space Sci.*, **23**, 437.
Spitzer, L., and Härm, R.: 1953, *Phys. Rev.*, **89**, 977.
Wilhelm, K., et al.: 1998, *Astrophys. J.*, **500**, 1023.

Address for correspondence: Code 682.3, NASA/GSFC, Greenbelt, MD 20771, Email:
kuen@uvcs14.nascom.nasa.gov

UVCS/SOHO OBSERVATIONS OF SPECTRAL LINE PROFILES IN POLAR CORONAL HOLES

J. L. KOHL, S. FINESCHI, R. ESSER, A. CIARAVELLA, S. R. CRANMER,
L. D. GARDNER and R. SULEIMAN

Harvard-Smithsonian Center for Astrophysics, Cambridge, MA 02138, USA

G. NOCI and A. MODIGLIANI
Università di Firenze, I-50125 Firenze, Italy

Abstract. Ultraviolet emission line profiles have been measured on 15–29 September 1997 for H I 1216 Å, O VI 1032, 1037 Å and Mg X 625 Å in a polar coronal hole, at heliographic heights ρ (in solar radii) between 1.34 and 2.0. Observations of H I 1216 Å and the O VI doublet from January 1997 for $\rho = 1.5$ to 3.0 are provided for comparison. Mg X 625 Å is observed to have a narrow component at $\rho = 1.34$ which accounts for only a small fraction of the observed spectral radiance, and a broad component that exists at all observed heights. The widths of O VI broad components are only slightly larger than those for H I at $\rho = 1.34$, but are significantly larger at $\rho = 1.5$ and much larger for $\rho > 1.75$. In contrast, the Mg X values are less than those of H I up to 1.75 and then increase rapidly up to at least $\rho = 2.0$, but never reach the values of O VI.

Key words: corona, solar wind, UV radiation, spectroscopy, line profiles

1. Introduction

Ultraviolet spectroscopy of the extended solar corona can provide detailed information about the physical conditions of the coronal plasma. Measurements of spectral line profiles for H I 1216 Å and the O VI doublet at 1032, 1037 Å (Kohl *et al.* 1997a, 1997b) and a self consistent empirical model derived from the observations (Kohl *et al.* 1998; Cranmer *et al.* 1999a) have provided strong evidence of anisotropic velocity distributions for protons and O⁵⁺ in polar coronal holes. This paper summarizes the observations of H I, O VI, and Mg X emission lines published recently by Kohl *et al.* (1999), and also presents several additional profiles that could not be included in that brief letter.

2. Observations and Instrumental Corrections

The observations for this paper were carried out with the Ultraviolet Coronagraph Spectrometer, UVCS (Kohl *et al.* 1995) on the *Solar and Heliospheric Observatory* (Domingo, Fleck, and Poland 1995). Observations of O VI and Mg X use the UVCS O VI Spectrometer Channel which includes its “Redundant Optical Path.” Observations of H I 1216 Å use both the UVCS Lyman Alpha Channel and the O VI Redundant Optical Path. All of the observations presented are for polar coronal holes. They sample a range of projected heights ρ (in solar radii, R_\odot) from 1.34 to 3.0. The observations were made during two time periods: 1997 January 25 to 1997 February 4, and 1997 September 15–29. The estimated angular extent of the coronal hole at $\rho = 1.34$ is 60° centered over the heliocentric north pole.



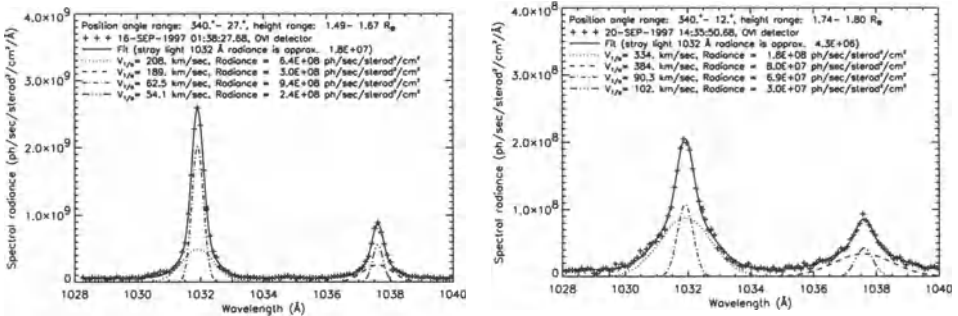


Figure 1. UVCS observations of O VI 1032, 1037 Å line profiles during 1997 September 16–22, for strips of the corona parallel to a limb tangent at a position angle of 0°. The projected radial heights of the strips are $\rho = 1.49\text{--}1.67$ (left) and $\rho = 1.74\text{--}1.80$ (right).

The procedure for correcting the UVCS observations for instrumental effects is described in more detail by Kohl *et al.* (1999) and Panasyuk *et al.* (1999). After the dark-count background is removed, the data are corrected for flat field and geometrical distortions, as well as for an instrument characteristic (described by Kohl *et al.* 1997a) that mislabels a small fraction of the photons so as to create an artificial line wing extending out about 4 Å on each side of the line center. Instrumental stray light, scattered from the solar disk, can account for a significant fraction of the line photons. The stray light background signal is derived from a measurement of the apparent radiance of the C III 977 Å line, which is assumed to arise only from the disk.

The observed line profiles are fitted with a standard algorithm that minimizes the reduced χ^2 (see Kohl *et al.* 1997a). Spectral lines are generally fitted to two component curves plus a constant background, which is believed to be instrumental in origin. In the case of H I 1216 Å, one component is taken to be stray light and is constrained to have the line profile of chromospheric H I 1216 Å convolved with instrumental broadening. A Gaussian shape is used for the coronal component. In the case of O VI and Mg X, two Gaussian curves are generally used and the radiance of the narrower component is compared with that expected from the stray light.

3. Discussion

Figures 1, 2, and 3 provide examples of line profiles, curve fits, and derived coronal line parameters. The particle speed $v_{1/e}$ corresponds to the $1/e$ half width, where the conversion from wavelength to velocity is made using $\Delta\lambda_{1/e}/\lambda_0 = v_{1/e}/c$, which holds for collisionally excited lines and resonant scattering at 90°. Figure 1 shows O VI profiles centered at $\rho = 1.49$ and 1.74 , Figure 2 shows O VI and Mg X profiles centered at $\rho = 1.99$, and Figure 3 shows Mg X profiles centered at $\rho = 1.34$ and 1.49 . For O VI, the stray light accounts for less than 10% of the

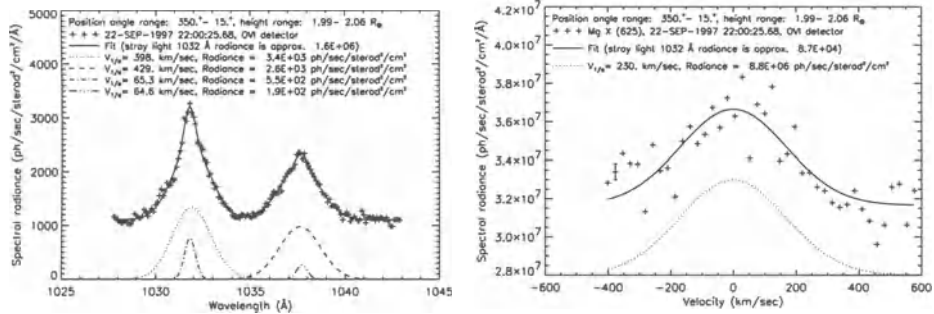


Figure 2. UVCS observations of O VI 1032, 1037 Å (left) and Mg X 625 Å (right) line profiles during 1997 September 16–22, for strips of the corona parallel to a limb tangent at a position angle of 0° . The projected radial height of the strip is $\rho = 1.99\text{--}2.06 R_\odot$.

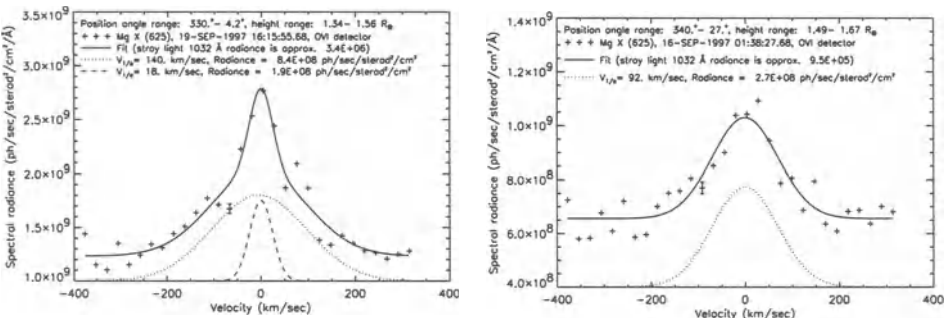


Figure 3. UVCS observations of Mg X 625 Å line profiles during 1997 September 16–22, for strips of the corona parallel to a limb tangent at a position angle of 0° . The projected radial heights of the strips are $\rho = 1.34\text{--}1.56$ (left) and $\rho = 1.49\text{--}1.67$ (right).

narrow fit component at $\rho = 1.49$, but by 1.99 stray light can account for the entire narrow component. (The stray light grows in relative importance with increasing height because the coronal intensity decreases more rapidly with radius than the stray light.) For Mg X at $\rho = 1.34$, the estimated stray light accounts for only 3% of the observed narrow component. For higher heights, the statistical accuracy for Mg X is not high enough to discern whether or not a narrow component exists.

Figure 4 provides a compilation of the $v_{1/e}$ velocities (after instrumental correction) as a function of height. Note that lines with low count rates (such as Mg X at large heights) are often fit with single Gaussians because the statistics are not sufficient to resolve multiple components. The $v_{1/e}$ for the narrow components of O VI and Mg X are smaller than those for H I 1216 Å at the same heights, and the narrow Mg X value is smaller than that of O VI. In the case of the broad components, it is

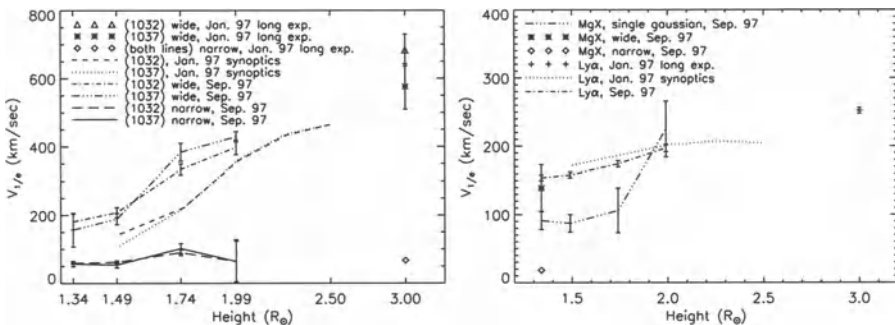


Figure 4. Compilation of line widths expressed as $v_{1/e}$ for broad and narrow components of the O VI 1032, 1037 Å lines (left), and the Mg X 625 Å and H I 1216 Å lines (right). Values for broad and narrow components of two-Gaussian fits to the other lines are plotted for all components with significant total radiance.

seen that the $v_{1/e}$ for O^{5+} are only slightly larger than that of H^0 at $\rho = 1.34$, but are significantly larger at 1.5 and much larger at 1.75 and higher heights. In contrast, the Mg^{9+} values are less than those for H^0 up to 1.75 and then increase rapidly up to at least $\rho = 2.0$. Since O^{5+} and Mg^{9+} have similar charge to mass ratios, one might expect their $v_{1/e}$ to behave similarly if ion-cyclotron resonance is responsible for their broadening (e.g., Tu *et al.* 1999; Cranmer *et al.* 1999b). The difference in both the height where the rapid increase in width begins and the fact that the Mg X width is narrower, both suggest that the Mg^{9+} may be more influenced by the expected proton collision rates which scale as q^2/m (see also Esser *et al.* 1999).

This work is supported by the National Aeronautics and Space Administration under grant NAG5-3192 to the Smithsonian Astrophysical Observatory, by Agenzia Spaziale Italiana, and by the ESA PRODEX program (Swiss contribution).

References

- Cranmer, S. R., *et al.*: 1999a, *Ap. J.*, **511**, 481.
- Cranmer, S. R., Field, G. B., and Kohl, J. L. 1999b, this volume.
- Esser, R., *et al.*: 1999, *Ap. J. Letters*, **510**, L63.
- Domingo, V., Fleck, B., and Poland, A.: 1995, *Solar Phys.*, **162**, 1.
- Kohl, J. L., *et al.*: 1995, *Solar Phys.*, **162**, 313.
- Kohl, J. L., *et al.*: 1997a, *Solar Phys.*, **175**, 613.
- Kohl, J. L., *et al.*: 1997b, *Adv. Space Res.*, **20**, no. 1, 3.
- Kohl, J. L., *et al.*: 1998, *Ap. J. Letters*, **501**, L127.
- Kohl, J. L., *et al.*: 1999, *Ap. J. Letters*, **510**, L59.
- Panasyuk, A., *et al.*: 1999, in preparation.
- Tu, C.-Y., Marsch, E., and Wilhelm, K.: 1999, this volume.

THE HIGHEST SOLAR WIND VELOCITY IN A POLAR REGION ESTIMATED FROM IPS TOMOGRAPHY ANALYSIS

M. KOJIMA, K. FUJKI, T. OHMI, M. TOKUMARU and A. YOKOBE
Solar-Terrestrial Environment Laboratory, Nagoya University, Toyokawa, Japan

K. HAKAMADA

Department of Engineering Physics, Chubu University, Kasugai, Japan

Key words: interplanetary scintillation, Ulysses, solar wind speed, latitudinal structure

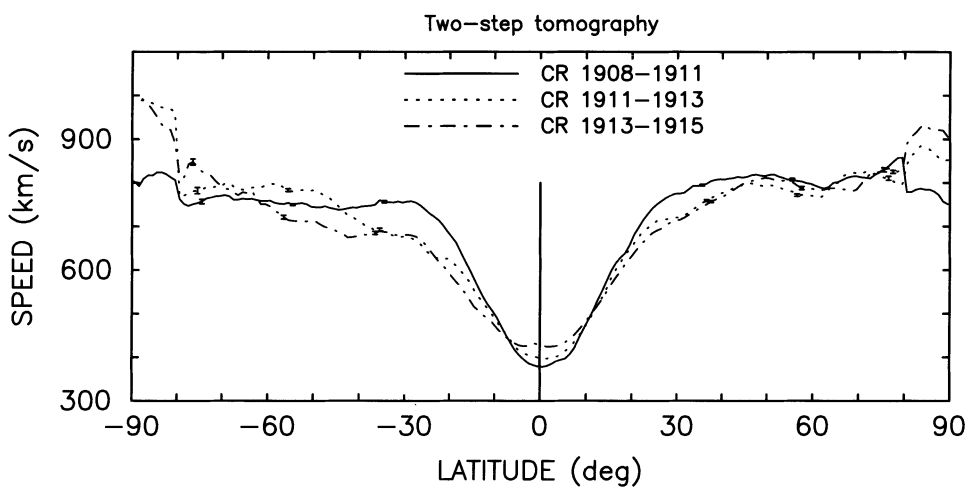
Abbreviations: IPS – interplanetary scintillation

1. Extended Abstract

The Ulysses spacecraft has revealed that the velocity of high-speed solar wind increases with latitude for latitudes $\geq 30^\circ$ (Woch *et al.* 1997; Goldstein *et al.* 1996). We have investigated this velocity increase up to the polar regions using a tomography method from interplanetary scintillation observations made in 1996. For this analysis the tomography method was modified from its previous version (Kojima *et al.* 1998) so that it has enough sensitivity for the observations at the polar regions, and the reliability and uniqueness of its solution was tested. The modified tomography method analyzes the latitudinal structure in two steps: first the structure within $\pm 80^\circ$ was derived, and then the latitudes of 80° – 90° are analyzed. Synoptic maps of velocity in Carrington longitude and heliographic latitude were derived with the modified tomography method, and latitudinal structures were obtained by averaging velocities along a longitude (Figure 1a). All analysis results show that the velocity increases with latitude in both hemispheres. In Carrington rotations 1911 to 1915, the velocities in the southern polar regions are 100–150 km/s larger than the velocity expected from the extrapolation of the observations at mid-latitudes, while in the northern polar region they were 35–75 km/s larger than the velocities similarly expected from mid-latitude observations. In rotations 1908 to 1911, the velocities in both polar regions were within ± 60 km/s of the expected velocity. A large velocity decrease was not seen in the polar regions. At mid-latitudes, the velocity in the northern hemisphere is higher than that in the southern hemisphere. This north-south asymmetry in latitudinal velocity structures at the mid-latitudes agrees qualitatively with that in the magnetic flux expansion factor (Figure 1b; see also Wang and Sheeley 1990). The expansion factor is defined as the factor by which a magnetic flux tube expands from the photosphere to the source surface at $2.5 R_\odot$ relative to R^2 expansion (i.e., $R_\odot^2 B_r$ [photosphere]/ $R_s^2 B_r$ [source surface]). The north-south asymmetry is stable structure existing during eight Carrington rotations of 1908 to 1915 and in the same sense as that Ulysses observed in 1995.



(a)



(b)

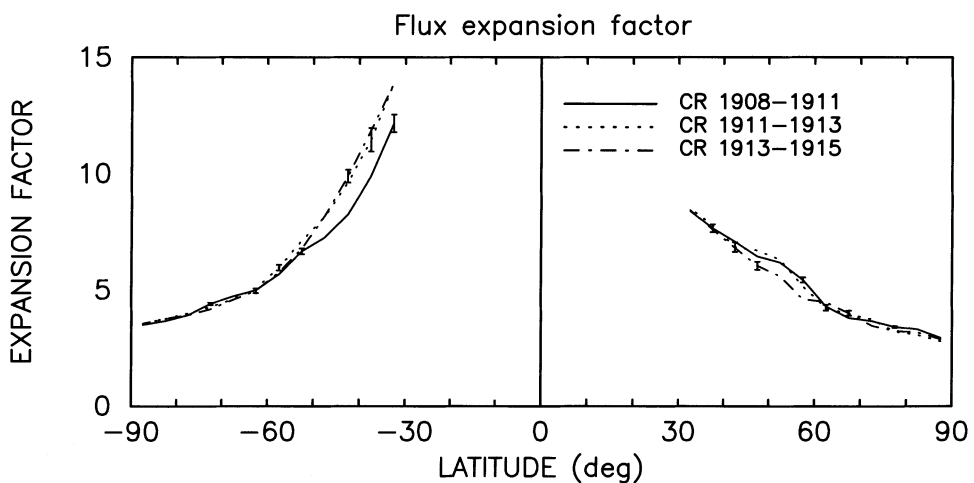


Figure 1. Latitudinal structures of (a) the velocity from the two-step tomography analysis, and (b) the magnetic flux expansion factor.

The full text of this paper will be submitted to the *Journal of Geophysical Research*.

Acknowledgements

NSO/Kitt Peak data used here are produced cooperatively by NSF/NOAO, NASA/GSFC, and NOAA/SEL.

References

- Goldstein, B. E., Neugebauer, M., Phillips, J. L., Bame, S., Gosling, J. T., McComas, D., Wang, Y.-M., Sheeley, N. R., and Suess, S. T.: 1996, "Ulysses plasma parameters: latitudinal, radial, and temporal variations," *Astron. Astrophys.*, **316**, 296.
- Kojima, M., Tokumaru, M., Watanabe, H., Yokobe, A., Asai, K., Jackson, B. V., and Hick, P. L.: 1998, "Heliospheric tomography using interplanetary scintillation observations, II, Latitude and heliocentric distance dependence of solar wind structure at 0.1–1 AU," *J. Geophys. Res.*, **103**, 1981.
- Wang, Y.-M., and Sheeley, N. R., Jr.: 1990, "Solar wind speed and coronal flux-tube expansion," *J. Geophys. Res.*, **355**, 726.
- Woch, J., Axford, W. I., Mall, U., Wilken, B., Livi, S., Geiss, J., Gloeckler, G., and Forsyth, R. J.: 1997, "SWICS/Ulysses observations: The three-dimensional structure of the heliosphere in the declining/minimum phase of the solar cycle," *Geophys. Res. Lett.*, **24**, 2885.

Address for correspondence: M. Kojima, Solar-Terrestrial Environment Laboratory, Nagoya University, 3-13 Honohara, Toyokawa 442-8507, Japan. Email: kojima@stelab.nagoya-u.ac.jp

OBSERVATION OF TRANSITION REGION FINE STRUCTURES WITH SOHO/SUMER

E. LANDI¹, H. E. MASON² and M. LANDINI¹

¹ Dipartimento di Astronomia e Scienza dello Spazio, Università di Firenze, Largo E. Fermi 5, 50124, Firenze, Italy

² DAMTP, University of Cambridge, UK

Abstract. We present a preliminary analysis of two quiet Sun transition region areas observed with the SOHO/SUMER spectrometer, using lines from oxygen, nitrogen and silicon. The average quiet Sun physical parameters are studied as a function of line intensity. Systematic variations of line position and width with increasing intensity are found. A large number of small-scale active points have been observed, and preliminary analysis of the physical properties and dynamics of these active features is presented. A jet-like structure, found in an active point, is also investigated and its velocity along the line of sight determined.

Key words: UV spectral emission lines, solar transition region

1. Observations and Quiet Sun Features

We have analyzed two different SUMER observations of quiet Sun regions: a $400'' \times 300''$ map at disk center, observed on 16 September 1996 with N V (1238.82 Å and 1242.80 Å) and O V (2×629.73 Å), and a $100'' \times 100''$ map at disk center, observed on 17 September 1996 with Si IV, O III,IV and S IV lines. The O IV lines allow density diagnostics using the CHIANTI package (Dere *et al.* 1997; Landi *et al.* 1999).

Observed line profiles have been fit with Gaussian functions, and intensity maps have been created using chromospheric and transition region lines. Fitted intensity maps reveal the presence of a lot of structures in the quiet Sun, at the limit of the instrumental spatial resolution (Figure 1, left). These structures seem to be overlying the chromospheric network, seen through a Si I line. Line position maps show the presence of relative motions across the whole observed region.

In several few-pixel wide areas on the network, profiles of strong, isolated lines are distorted and present secondary peaks. These profile distortions are due to dynamic events taking place in these locations, and they identify explosive events. Much stronger activity is found in two more extended areas, where line profile distortions are much larger; in one of them a jet-like structure is observed (Figure 1, right).

2. Quiet Sun Results

The maps of fitted intensities of each spectral line have been divided into 11 classes according to intensity and each observation has been divided in 11 different sub-



Space Science Reviews 87: 241–244, 1999.

©1999 Kluwer Academic Publishers.

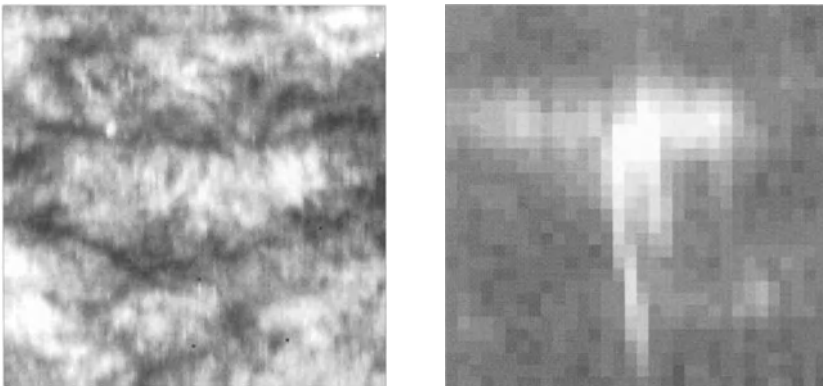


Figure 1. Left: O v $120'' \times 90''$ intensity map. Right: the jet structure ($32'' \times 24''$).

datasets selected using these intensity grids. In each sub-dataset, the spectrum has been spatially averaged and spectral lines fit. Resulting line positions and widths (the latter have also been corrected for the presence of relative motions inside each sub-dataset; dashed line) are displayed in Figure 2 for O v. Similar results are obtained with all the other lines. In all cases line positions are redshifted and line widths increase as the intensity increases. The redshifts correspond to velocities between 4.1 and 7.5 km s^{-1} , while line width variations are of the order of 11 to $35 \text{ m}\text{\AA}$.

Electron density and temperature have been measured inside each sub-dataset (Figure 2); the latter, measured through the O v/N v ratio, shows variations only for low values of line intensity, while the former increases as O v intensity increases although uncertainties are of the same order as the variations.

3. Explosive Events and a Jet-like Structure

The few-pixel wide active points overlying the network are quite common in the studied regions. The secondary peaks have been fitted for a small sample of these points with the assumption of Gaussian profiles, and the resulting positions and velocities relative to the average value are reported in Table I.

The fitted secondary lines are broadly symmetrical relatively to the rest position, with velocities of the order $40\text{--}60 \text{ km s}^{-1}$. The secondary lines are usually more intense and broader than the central, un-shifted component. Unfortunately, line blending has not allowed the determination of the electron density of the plasma emitting the secondary peaks.

In one explosive event location a large jet-like structure is visible with all the observed lines (Figure 1, right). The structure is $\simeq 700 \text{ km}$ wide along the solar x

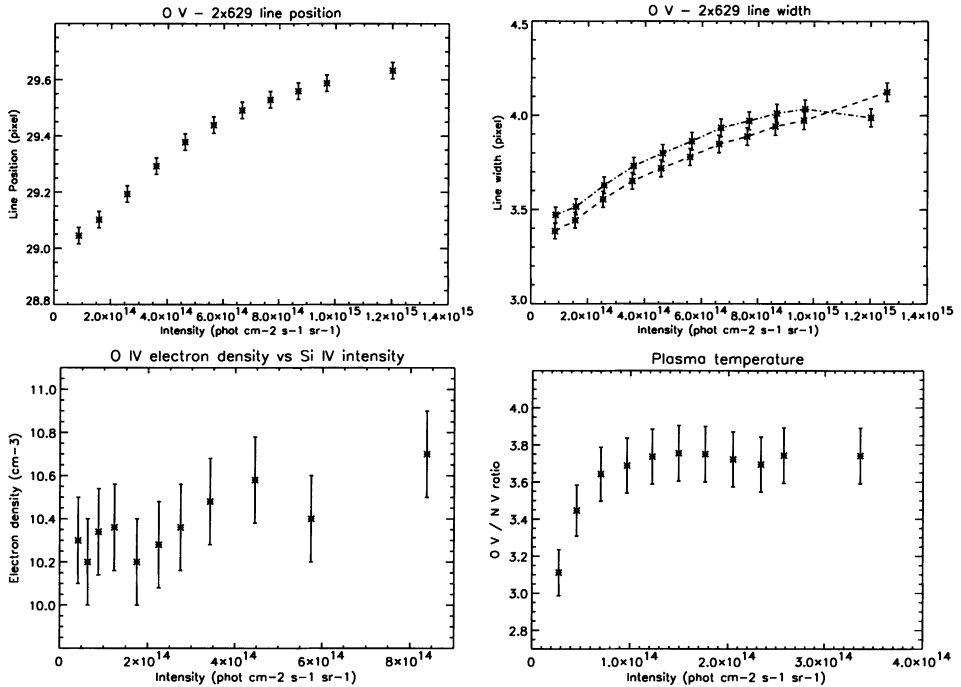


Figure 2. Top: O V line position (left) and width (right) as a function of line intensity. Bottom: electron density (left) and temperature (right) as a function of line intensity.

Table I
Velocities and line widths measured in some active points from Si IV

| Region | Pos (pxl) | Width (pxl) | Velocity (km s ⁻¹) | Region | Pos (pxl) | Width (pxl) | Velocity (km s ⁻¹) |
|---------|--------------|----------------|-----------------------------------|--------|--------------|----------------|-----------------------------------|
| Average | 418.414 | 3.526 | — | | | | |
| Reg. 1 | 412.009 | 5.160 | 58.6 | Reg. 3 | 413.945 | 5.823 | 40.8 |
| | 418.592 | 3.473 | -1.5 | | 418.717 | 2.730 | -2.8 |
| | 424.845 | 5.089 | -58.8 | | 425.026 | 3.837 | -60.4 |
| Reg. 2 | 411.931 | 5.716 | 59.2 | Reg. 4 | 413.209 | 3.962 | 47.6 |
| | 414.986 | 3.534 | 31.3 | | 418.904 | 3.197 | -4.5 |
| | 419.037 | 2.883 | -5.7 | | 424.153 | 3.579 | -52.4 |
| | 424.045 | 4.547 | -51.5 | | | | |

and $\simeq 4200$ km along the solar y direction. A second, smaller jet-like structure is also visible on the right.

The jet is observed in three consecutive raster positions (corresponding to three subsequent times of observation) and the line-of-sight velocity has been measured for all of them. The resulting values are 250 km s^{-1} (left position), 170 km s^{-1} (center and right positions).

4. Discussion

The analysis of SUMER observations at different wavelengths of the quiet Sun Transition Region at disk center has revealed the presence of a large number of structures at the limit of the spatial resolution overlying the chromospheric network, where most of the quiet Sun intensity is concentrated. Significant correlation has been found between quiet Sun line intensity and line width and position.

Explosive events have been observed with SUMER by Chae *et al.* (1998) and by Innes *et al.* (1997), reporting Doppler velocities around 70 km s^{-1} and 150 km s^{-1} respectively. These determinations are in agreement with the values found in the present work. These explosive events have been thought to be associated with bi-directional jets caused by magnetic reconnection; they seem also to be associated with H_{α} chromospheric upflows (Chae *et al.* 1998). The relatively large number of events observed in our dataset suggests that explosive events are a quite common feature in the “quiet” transition region. This activity is mostly found around chromospheric network.

Acknowledgements

We acknowledge the support of the SUMER team in obtaining these data and supplying analysis software. SOHO is a ESA/NASA project.

References

- Chae, J., Wang, H., Lee, Chik-Yin, and Goode, P. R.: 1998, *Ap. J.*, **504**, L123.
Dere, K. P., Landi, E., Mason, H. E., Monsignori Fossi, B. C., and Young, P. R.: 1997, *A&ASS*, **125**, 149.
Innes, D. E., Inhester, B., Axford, W. I., and Wilhelm, K.: 1997, *Nature*, **386**, 811.
Landi, E., Landini, M., Dere, K. P., Young, P. R., and Mason, H. E.: 1999, *A&A*, in press.

LOOP MODELS FROM SOHO OBSERVATIONS

M. LANDINI¹, A. BRKOVIĆ², E. LANDI¹, I. RÜEDI² and S. SOLANKI²

¹*Dipartimento di Astronomia e Scienza dello Spazio, Università di Firenze, Italy*

²*Institute of Astronomy, ETH-Zentrum, CH-8092 Zurich, Switzerland*

Abstract. The Coronal Diagnostic Spectrometer (CDS) on SOHO is a grazing/normal incidence spectrograph, aimed to produce stigmatic spectra of selected regions of the solar surface in six spectral windows of the extreme ultraviolet from 150 Å to 785 Å (Harrison *et al.* 1995). In the present work, CDS, EIT, MDI and Yohkoh observations of active region loops have been analyzed. These observations are part of JOP 54. CDS monochromatic images from lines at different temperatures have been co-aligned with EIT and MDI images, and loop structures have been clearly identified using Fe XVI emission lines. Density sensitive lines and lines from adjacent stages of ionization of Fe ions have been used to measure electron density and temperature along the loop length; these measurements have been used to determine the electron pressure along the loop and test the constant pressure assumption commonly used in loop modeling. The observations have been compared with a static, isobaric loop model (Landini and Monsignori Fossi 1975) assuming a temperature-constant heating function in the energy balance equation. Good agreement is found for the temperature distribution along the loop at the coronal level. The model pressure is somewhat higher than obtained from density sensitive line ratios.

Key words: atomic database, synthetic spectra, solar atmosphere, intensity calibration

1. The Observation

The observations were taken on 29 April 1997, between 8:20 and 10:40 AM on an active region on the solar disk centered at around ($-100''$, $-400''$). The CDS observations consist of several spectral windows located around selected wavelengths, in order to observe both transition region and coronal lines. The observed lines are formed in the chromosphere (He I), the transition region (O III, O IV, O V, Ne V, Mg VII) and the corona (Mg VIII, Mg IX, Si XI, Si XII, Fe XII, Fe XIII, Fe XIV, Fe XVI). These lines allow density determination (Fe XII, Fe XIII), and they sample the plasma up to temperatures around 2.5×10^6 K. The presence of consecutive stages of ionization for several elements allows the temperature to be diagnosed through intensity ratios of lines of different ions.

The CDS observations have been co-aligned by a cross-correlation technique with EIT and Yohkoh full-disk images. The theoretical intensity ratios for density and temperature diagnostics have been calculated using the CHIANTI database (Landi *et al.* 1999).

2. Results

2.1. MORPHOLOGY OF THE EMITTING REGION

The hottest emitting plasma is confined in a few loop-like regions whose footpoints correspond to photospheric enhancements of magnetic field of opposite polarity.



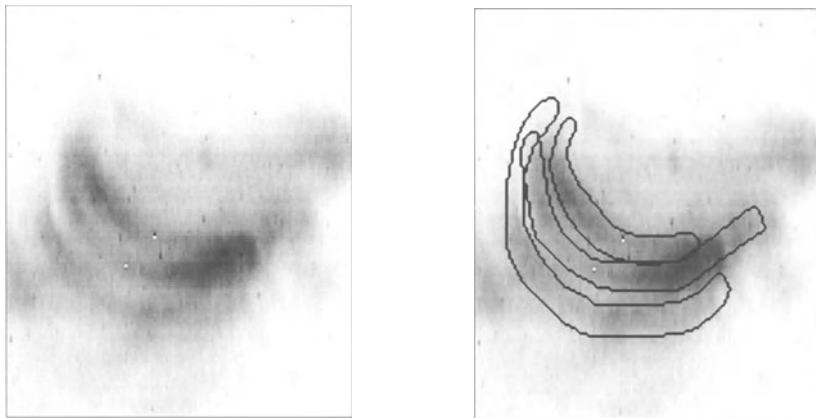


Figure 1. $4' \times 4'$ intensity map of the Fe XVI 335.4 Å line with adopted partition.

Using images in Fe XVI lines (Figure 1), EIT and MDI, the presence of three distinct structures is revealed. The outermost one is studied in the present work; it has been divided into 21 sections, and the relevant line emission has been integrated over each section. Lines from cooler ions (i.e., O V) are restricted to regions around the footpoints of the Fe XVI loops. Emission from transition region ions is confined in small areas, some of which correspond to the footpoints of the loops. Larger and fainter structures are visible from Mg IX emission, appearing completely uncorrelated with the Fe XVI loops.

2.2. DENSITY, TEMPERATURE AND PRESSURE DIAGNOSTICS

Density measurements for each section are performed by means of the intensity ratio of density sensitive pairs of lines. Lines of Fe XII (364.47 Å and 338.28 Å) and Fe XIII (359.64 Å, 359.84 Å and 348.18 Å) have been used. Background emission from regions adjacent to the loop structures has been subtracted. The density values are scattered within the experimental uncertainties around a constant value (Figure 2). Temperature measurements are performed through the Fe XVI/Fe XIV line ratio; temperatures increase slightly toward the loop center and tend to decrease at the two ends. This is broadly consistent with loop models in the literature. The changes are very small. The constant pressure assumption in loop models appears to be satisfied by the observations.

3. Comparison with the Loop Model

We have compared the observations with the Landini and Monsignori Fossi (1975) loop model. It describes a cylindrical loop with constant pressure P_0 ; temperature

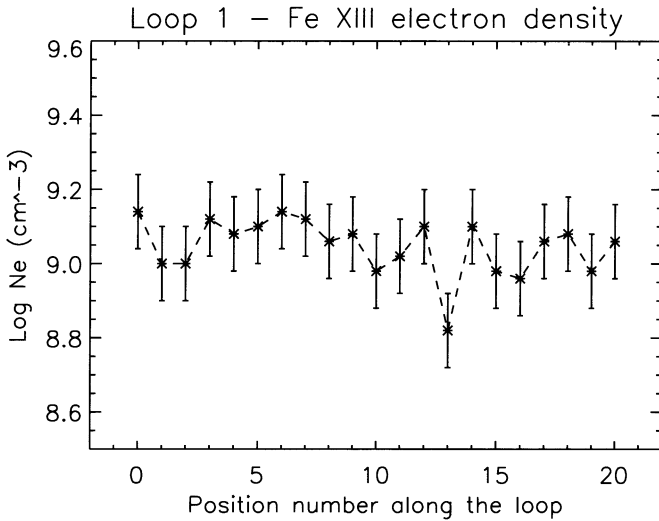


Figure 2. Density diagnostics for the outermost loop in Figure 1.

and density are obtained as a function of position along the loop by the balance of a constant input, radiative losses and divergence of thermal conduction.

The total power emitted by a loop in each optically thin line depends on two parameters: $P_0 S$, where S is the loop cross section, assumed to be constant, and the temperature T_M at which the conductive flux reaches its maximum value and radiative losses balance the input power. Each curve in Figure 3 displays the values of $P_0 S(T_M)$ that fits each observed line emission. The region of the plot where all the curves meet together allows $P_0 S$ to be estimated from the common crossing point Y_{cross} and T_M values, thus determining the loop model that fits all the observations. The following results have been obtained:

1. The loop top temperature T_{top} is evaluated from T_M as $\log T_{\text{top}} = 1.79 T_M = 2.2 \times 10^6$ K.
2. The measured values of T_M and the total loop length L (1.1×10^{10} cm) allow P_0 to be evaluated using the scaling law of the loop model: $L = 1.65 \times 10^{-10} (T_M^{3.25} / P_0)$ cm. The resulting pressure is $P_0 = 0.9$ dyne cm⁻²; this value is to be compared with the pressure P_{ratio} given by the intensity ratio measurements of temperature and density: $P_{\text{ratio}} = 0.3$ dyne cm⁻².
3. The crossing point Y_{cross} is given by $Y_{\text{cross}} = 2.1 \times 10^{-8} P_0 S$. Using a measured value of P_0 and Y_{cross} , a cross section $S = 2.6 \times 10^8$ km² is obtained, reasonably in agreement with the mean cross section measured on the maps.

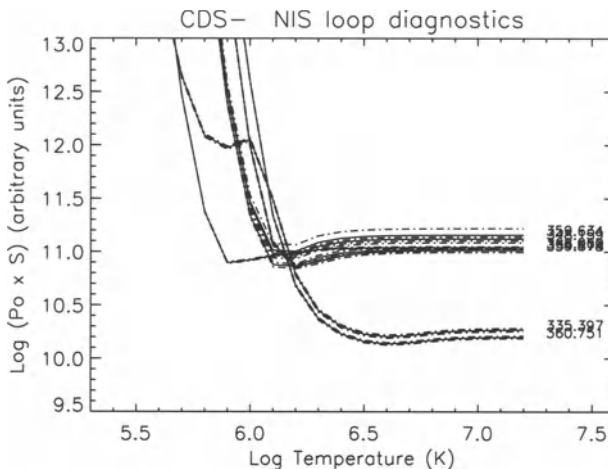


Figure 3. Values of P_0S as a function of temperature T_M for each spectral line.

4. Conclusions

In the present work, CDS, EIT, MDI and Yohkoh observations (JOP 54) of an active region loop are analyzed. The physical properties of the emitting plasma along the loop length have been determined and their values have been compared with the Landini and Monsignori Fossi (1975) loop model. The following results have been found:

1. Lines of different elements show different structures in the active region, and structures of ions formed at different temperature seem to be completely uncorrelated.
2. The maximum loop height is smaller than the scale height, and the loop pressure is expected to be constant along the loop. Measured temperature and density along the loop are in agreement with a constant pressure assumption; different loops show different pressures.
3. There is reasonable agreement between the predictions of the Landini and Monsignori Fossi (1975) loop model and the observations. The predicted loop length and top temperature are in agreement with the values determined from the observations, while the predicted loop pressure is higher than observed.

References

- Harrison, R. A., et al.: 1995, *Solar Physics*, **162**, 233.
 Landi, E., Landini, M., Dere, K. P., Young, P. R., and Mason, H. E.: 1999, *A&A*, in press.
 Landini, M., and Monsignori Fossi, B. C.: 1975, *A&A*, **42**, 213.

SEARCH FOR SIGNATURES OF A CORONAL HOLE IN TRANSITION REGION LINES NEAR DISK CENTER

P. LEMAIRE, K. BOCCIALINI and V. ALETTI

*Institut d'Astrophysique Spatiale, Unité mixte CNRS-Université Paris XI, F-91405 Orsay Cedex,
France*

D. HASSSLER

Southwest Research Institute, 1050 Walnut Street, Boulder, CO, 80302, USA

K. WILHELM

Max Planck Institute für Aeronomie, D-37189 Katlenburg-Lindau, Germany

Abstract. The analysis of data taken by SUMER near disk center, where a small coronal hole is observed in EIT images, is performed. From the measurements of Doppler non-thermal velocities and intensities, we search for the diagnostics and the signature of small scale structures in the coronal hole using transition region lines. Transition region lines in the range of 7×10^4 K to 2.5×10^5 K have a non-thermal velocity excess of 4.0 to 5.5 km s⁻¹ relative to the contiguous quiet Sun. While the average intensity is lower in the coronal hole than in the quiet area, this result shows an increase of turbulence at the base of the high speed solar wind.

Key words: Sun, coronal hole, transition region

1. Introduction

Measurements of coronal hole properties on the solar disk near the equator at the disk center are scarce in the chromosphere and the transition region. While coronal holes are clearly visible in the corona by the reduced line intensities, in the transition region and upper chromosphere there are few indications of such intensity variations (e.g., Bocchialini and Vial 1996). EIT/SOHO images in the He II 304 Å line show a reduced line emission in polar coronal holes. The same reduced emission near the disk center can be used as a coronal hole signature. Velocities along the line of sight in coronal holes have been detected in O V 62.9 nm (Rottman *et al.* 1982) with an upflow of 7 km s⁻¹. An inconclusive search has been performed with the C IV 154.8 nm line using SMM observations (Mullan and Waldron 1987). Recently, Hassler *et al.* (1998), analyzing O VI 103.2 nm at the border of a polar coronal hole, reported an upflow of a few km s⁻¹ (see also Patsourakos *et al.* 1997). But there is no published measurement of the line width which can be used to determine the non-thermal velocities or the broadening due to unresolved motions.

We report here an observation made simultaneously in several transition region lines across a small coronal hole near the equator taken by the SUMER spectrometer on 7 and 8 March 1997. After a description of the observations and the data analysis technique, we present and discuss the results.



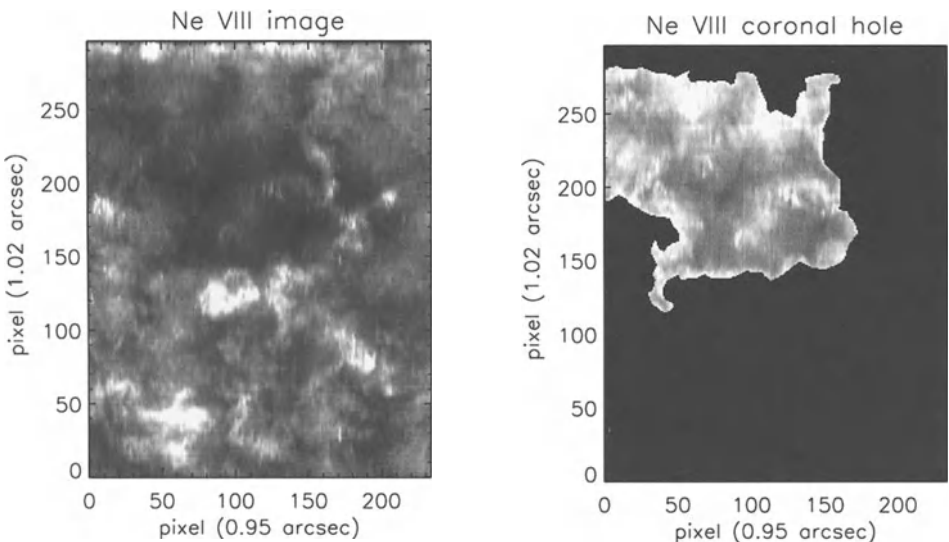


Figure 1. Ne VIII 77.0 nm intensity image obtained by the solar rotation across the slit during 24 hours. A small coronal hole (CH), also detected in EIT He II 30.4 nm, is visible in the upper left. The CH image is displayed on the right.

2. Observations and Data Analysis

The observations were performed with the SUMER spectrometer (Wilhelm *et al.* 1995) using the 1×300 arcsec 2 slit with a fixed wavelength recording range from 75.2 nm to 79.2 nm on the B detector. To cope with the telemetry limitations, only 6 detector windows of 50 spectral pixels width were transmitted during the 90 s exposure time. The windows were centered on 76.01 nm, 76.49 nm, 77.04 nm, 77.59 nm and 79.02 nm. The recorded lines are: Ne VIII 77.04 nm (6.3×10^5 K), O V 76.04 nm (2.4×10^5 K), O IV 78.77 nm (1.7×10^5 K), S IV 78.74 nm (1.7×10^5 K), N IV 76.51 nm (1.4×10^5 K), and N III 76.43 nm (1.0×10^5 K). The observation started on 7 March 1997 at 18:00 UT and ended on 8 March 1997 at 17:42 UT. The center of the north-south slit was pointed at $x = 0$ and $y = 279$ arcsec in solar/SOHO disk coordinates, and the solar rotation provided the scanning during the observation.

The data were processed using the usual SUMER procedures: flat field correction, destretching of the detector image and dead-time correction, that take into account the detector characteristics. To produce a set of data with a very good signal to noise ratio, to smooth rapid local variations of solar profiles and to obtain the same scale in x and y , we averaged the data over 4 exposures (or 6 min) which corresponds to a solar drift of about 0.95 arcsecond across the 1 arcsecond slit width. Along the slit the pixel size corresponds to 1.02 arcsecond.

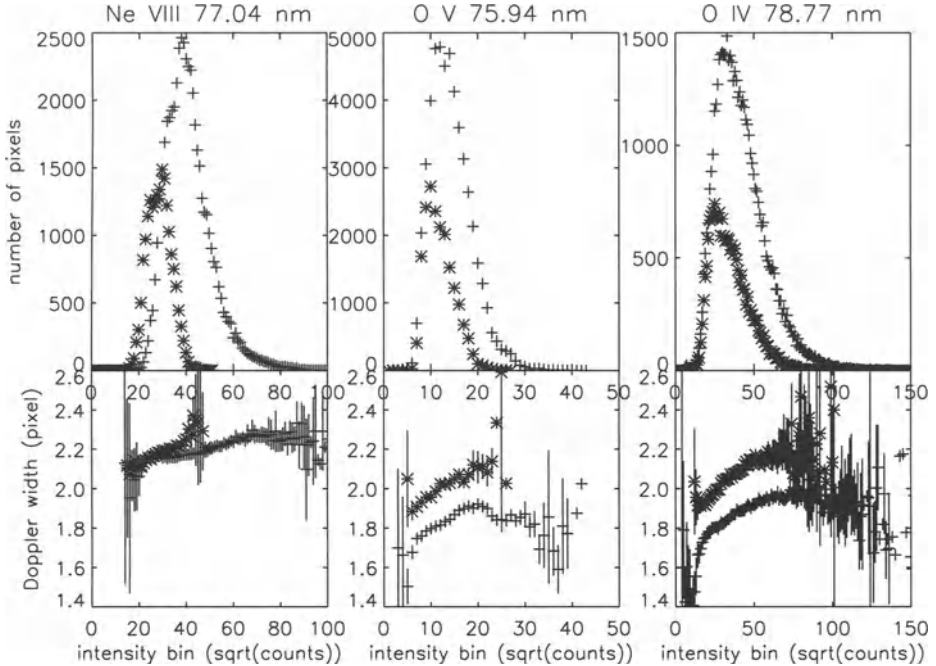


Figure 2. Upper part: Histograms of intensity for Ne VIII and O V lines in quiet area (+) and coronal hole (*); the abscissae are the square root of detector counts. Lower part: the corresponding Gaussian widths (σ) for the same lines with the same notations.

The Ne VIII intensity image produced by the solar rotation was used to locate the coronal hole (CH) by comparing with the EIT He II 30.4 nm image obtained during the observational run. In the upper part of the image, the edge of the CH was determined and a mask applied to separate quiet area (QA) and CH. Figure 1 displays the total Ne VIII intensity image and the extracted CH section (the intensity scale is enhanced in the extracted CH image to show the structures).

The mask has been applied to other wavelengths in order to compare the line intensities and the Doppler widths in QA and CH. For each pixel, the line profiles were fitted by one (or multiple) Gaussians (when several lines are in the same 50 pixel window) and the line widths were extracted. We have established the intensity histogram (Figure 2) for each line (in QA and CH) using a square root scale for the binned intensities (other binning scales will produce similar results).

3. Results and Conclusion

From the intensity histogram curves and from Table I we conclude:

Table I

Relationship between coronal hole (CH) and quiet area (QA) for decreasing temperatures (\bar{I} : average line intensity per pixel; ξ (CH-QA): differential non-thermal velocity at the peak of the histograms).

| ion | Ne VIII | O V | O IV | S V | N IV | N III |
|----------------------------------|---------|------|------|------|------|-------|
| \bar{I} (CH) / \bar{I} (QA) | 0.38 | 0.62 | 0.66 | 0.71 | 0.66 | 0.71 |
| ξ (CH-QA) km s ⁻¹ | 0.7 | 6.4 | 5.6 | 5.4 | 4.4 | 4.1 |

1. the coronal holes are detected in intensity in the transition region,
2. the average line widths in CH are larger than in QA (increased turbulence?), and the difference increases with the temperature of ionization of elements up to 2.4×10^5 K, and
3. the average line widths increase with intensity in CH and in QA.

This is the first measurement of non-thermal velocity in transition region coronal hole lines observed at disk center.

4. Acknowledgements

The SUMER project is supported by DARA, CNES, NASA and the ESA PRODEX program (Swiss contribution). SOHO is a mission of international cooperation between ESA and NASA.

References

- Bocchialini K., and Vial J.-C.: 1996, 'High chromosphere and low transition region network: a different organization in coronal holes,' *Sol. Phys.*, **168**, 37–45.
- Hassler, D. M., Dammasch, I., Lemaire, P., Brekke, P., Mason, H. E., Vial, J.-C., and Wilhelm, K.: 1999, 'Solar Coronal Hole Outflow Velocities and the Chromospheric Network,' *Science*, in press.
- Mullan, D. J., and Waldron, W. L.: 1987, 'Velocity Fields in a Low-Latitude Coronal Hole: Results from the Solar Maximum Mission,' *Astrophys. J.*, **317**, 487–501.
- Patsourakos, S., Bocchialini, K., and Vial, J.-C.: 1997, 'Low Transition Region Characteristics of Equatorial Coronal Holes,' in *The Corona and the Solar wind near minimum activity, Fifth SOHO workshop*, ESA SP-404, 577–582.
- Rottman, G. J., Orrall, F. Q., and Klimchuk, J. A.: 1982, 'Measurements of Outflow from the Base of Solar Coronal Holes,' *Astrophys. J.*, **260**, 326–337.
- Wilhelm, K., Curdt, W., Marsch, E., Schühle, U., Lemaire, P., Gabriel, A., Vial, J.-C., Grewing, M., Huber, M. C. E., Jordan, S. D., Poland, A. I., Thomas, R. J., Khüne, M., Timothy, J. G., Hassler, D. M., and Siegmund, O. H. W.: 1995, 'SUMER: Solar Ultraviolet Measurements of Emitted Radiations,' *Solar Phys.*, **162**, 189–231.

A 16-MOMENT FAST SOLAR WIND MODEL

XING LI

Harvard-Smithsonian Center for Astrophysics, Cambridge, MA 02138, Email: xli@cfa.harvard.edu

Abstract. A 16-moment fast solar wind model based on a bi-Maxwellian velocity distribution is presented. Although the proton heat flux density is found to be significantly smaller than the classical Spitzer-Härm value, it still plays a significant role in shaping the proton temperature anisotropy in the fast solar wind.

1. Introduction

In situ measurements between 0.3 and 1 AU (Marsch *et al.* 1982) and spectral line observations in the inner corona (Kohl *et al.* 1998) indicate that protons and heavier ions have strong temperature anisotropy. The proton heat flux density derived from in situ measurements between 0.3 and 1 AU is at least an order of magnitude smaller than the classical value (Marsch and Richter 1984). Since the heat flux density can significantly influence the proton temperature profile, a better knowledge of the proton heat flux density is critical for the understanding of the heating and acceleration processes of the solar wind.

While it is clear that the classical expression for the proton heat flux density (Spitzer and Härm 1953; Braginskii 1965) is not valid for the solar wind, it is still not known whether the proton heat flux can be completely ignored in the inner corona. To adequately explore the magnitude of the proton heat flux density, transport equations including higher moments of the distribution function must be taken into account. The first bi-Maxwellian based 16-moment solar wind models developed by Demars and Schunk (1991) started at $28 R_S$ and were typical of a slow solar wind. Hence, the key solar wind acceleration region—the first several solar radii—was not explored.

In this paper, we present a bi-Maxwellian velocity distribution based 16-moment fast solar wind model. The 16-moment description is applied to the protons only while the electrons are assumed to be isotropic.

2. Model Computation

The details of the one-dimensional, time-dependent bi-Maxwellian based 16-moment transport equations for the electron-proton solar wind, with anisotropic proton temperature and including the effect of the interplanetary spiral magnetic field, are given by Li (1999). The electron heat flux density q_e and the proton parallel and perpendicular heat flux densities $q_{p\parallel}$ and $q_{p\perp}$ are solved simultaneously with the



electron density n , the proton velocity v , the electron temperature T_e , and the proton parallel and perpendicular temperatures, $T_{p\parallel}$ and $T_{p\perp}$. The mean proton temperature is given by $T_p = (T_{p\parallel} + 2T_{p\perp})/3$. The proton total heat flux density is defined as $q_p = (q_{p\parallel} + 2q_{p\perp})/2$.

We assume that protons are heated only in the direction perpendicular to the magnetic field, i.e., $Q_{p\parallel} = 0$. The following ad hoc heating and momentum addition functions (e.g., Withbroe 1988; Hu *et al.* 1997)

$$\begin{aligned} Q_{p\perp} &= Q_{p1} e^{(R_s - r)/\sigma_p} + Q_{p2} \left[1 - e^{(R_s - r)/10R_s} \right] \frac{R_s^4}{r^4}, \\ Q_e &= Q_{e0} e^{(R_s - r)/\sigma_e}, \quad D = D_0 e^{(R_s - r)/\sigma_d}, \end{aligned} \quad (1)$$

are used in our calculation, where Q_{e0} , σ_e , Q_{p0} , σ_p , D_0 and σ_d are constants. The additional heating function $Q_{p\perp}$ consists of two parts: one corresponds to a local heating at the coronal base and the other to an extended heating similar to that used by McKenzie *et al.* (1997).

The following coronal base conditions ($r = 1 R_s$) are assumed in our model calculations: $n_e = 2.5 \times 10^8 \text{ cm}^{-3}$, $T_e = T_{p\parallel} = T_{p\perp} = 6 \times 10^5 \text{ K}$. Shown in Figure 1 as solid lines is an example of a model calculation with a rapidly diverging flux tube similar to that given by Munro and Jackson (1977). The input parameters are chosen to yield a high speed wind which matches, as closely as possible, currently available empirical constraints in the inner corona (Fisher and Guhathakurta 1995) and in interplanetary space (Marsch *et al.* 1989). The filled circles in Figure 1 represent the observed upper and lower perpendicular temperatures of neutral hydrogen derived from line-width measurements of H I Ly α in polar coronal holes (Kohl *et al.* 1998). The triangles and stars represent the perpendicular and parallel proton temperatures observed by Helios (Marsch *et al.* 1982).

Because of its rapid acceleration, the perpendicular cooling of the protons due to the radial expansion of the fast solar wind is only important in the inner corona (Hu *et al.* 1997; Li *et al.* 1999). Hu *et al.* (1997) demonstrated that the cooling effect of the spiral magnetic field is small too. Hence it is difficult to cool the proton parallel temperature in interplanetary space. This becomes even more difficult in the 16-moment model since the proton perpendicular heat flux density can conduct energy to or from the parallel degree of freedom because of the flow tube expansion. In 16-moment equations, $q_{p\perp}$ appears in the parallel energy equation too. Hence $q_{p\perp}$ can conduct thermal energy from the perpendicular to the parallel degree of freedom. In our model, a higher $T_{p\perp}$ in the inner corona leads to a greater q_{\perp} (see $T_{p\parallel}$ and $q_{p\perp}$ between 2 to 20 R_s in Figures 1b and 1c). That is why, as seen in Figure 1b, $T_{p\parallel}$ can increase from 2 R_s to about 50 R_s . This additional heating causes the proton parallel temperature to gain non-realistically high values beyond 0.3 AU. When both $T_{p\perp}$ and $T_{p\parallel}$ match observations in the fast solar wind, the total proton heat flux density can match observations as well (Li 1999). The heat flux densities can change sign in the near Sun region, since proton temperatures reach a maximum in this region.

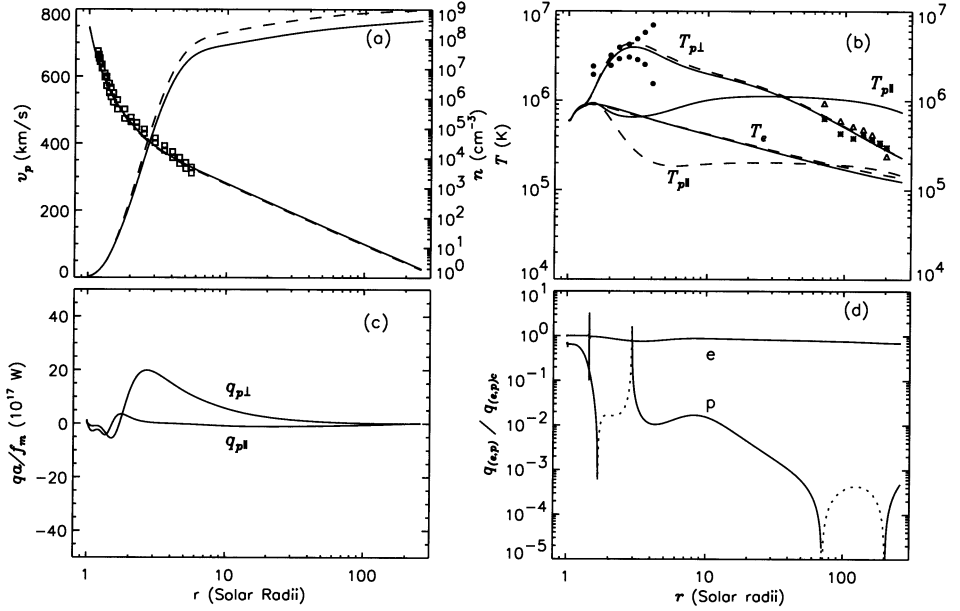


Figure 1. Parameters used in the model calculations are: $f_m = 6$, $r_a = 1.31 R_s$, $\sigma_a = 0.51 R_s$, $\sigma_e = 0.23 R_s$, $Q_{e0} = 1.9 \times 10^{-6} \text{ erg cm}^{-3} \text{ s}^{-1}$, $\sigma_p = 0.42 R_s$, $Q_{p1} = 8.2 \times 10^{-7} \text{ erg cm}^{-3} \text{ s}^{-1}$, $Q_{p2} = 1.64 \times 10^{-6} \text{ erg cm}^{-3} \text{ s}^{-1}$, $D_0 = 3.32 \times 10^{-15} \text{ g cm}^{-2} \text{ s}^{-2}$, $\sigma_d = 0.77 R_s$. See text for details.

In order to show the effect of the 16-moment heat flux densities, we also compute a model by keeping the input parameters the same but neglecting the proton heat flux. The result is shown in Figure 1 as dashed lines. The electron density and temperature profiles are almost the same. The flow speed at 1 AU increases by about 33 km/s while the mass flux at 1 AU decreases by less than 3%. The most striking difference is in the parallel temperature. The proton parallel temperature is only about 20% of that in the 16-moment model starting from $10 R_s$.

Shown in Figure 1d are the ratios between the electron and proton heat flux densities q_e and q_p computed from our model and the classical heat flux densities q_{ec} and q_{pc} defined by: $q_{ec} = 8 \times 10^{-7} T_e^{5/2} (dT_e/dr)$, $q_{pc} = 3.2 \times 10^{-8} T_p^{5/2} (dT_p/dr)$, with T_e and T_p taken from our 16-moment model. It is found that the electron heat flux density is very close to its classical value; the maximum relative difference is smaller than 25%. The small disturbances in Figure 1d are due to either the existence of a temperature maximum, where the classical heat flux density is zero, or a zero heat flux density. Hence the classical electron heat flux is still valid in our fast solar wind solutions. On the other hand, the classical Coulomb collision dominated concept of the proton heat flux completely breaks down in our model. Except at

the coronal base, q_p is found to be much smaller than its classical value. The ratio q_p/q_{pc} can have negative values (dotted lines), implying that the collisionless proton heat flux does not necessarily conduct thermal energy from high to low temperature regions. In most of the computational domain, the 16-moment proton heat flux density is more than 2 orders of magnitude smaller than the classical heat flux density. Only at the coronal base is the proton heat flux density close to its classical value. However, the proton heat flux density is still important as far as the proton anisotropy is concerned. The electron heat flux density on the other hand is only slightly different from its classical value.

Acknowledgements

I would like to thank Dr. Shadia Habbal for her helpful discussions and support. This work is supported by NASA grant NAG5-6271.

References

- Braginskii, S. I.: 1965, in *Reviews of Plasma Physics*, Vol. 1, (Consultant Bureau, New York), p. 205.
- Demars, H. G., and Schunk, R. W.: 1991, *Planet. Space Sci.*, **39**, 435.
- Fisher, R. R., and Guhathakurta, M.: 1995, *Astrophys. J.*, **447**, L139.
- Hu, Y. Q., Esser, R., and Habbal, S. R.: 1997, *J. Geophys. Res.*, **102**, 14661.
- Kohl, J. L., et al.: 1998, *Astrophys. J.*, **501**, L128.
- Li, X., Esser, R., Habbal, S. R., and Hu, Y. Q.: 1997, *J. Geophys. Res.*, **102**, 17419.
- Li, X., Habbal, S. R., Hollweg, J., and Esser, R.: 1999, *J. Geophys. Res.*, in press.
- Li, X.: 1999, *J. Geophys. Res.*, in preparation.
- Marsch, E., Muhlhäuser, K. H., Rosenbauer, H., Schwenn, R., and Neubauer, F. M.: 1982, *J. Geophys. Res.*, **87**, 35.
- Marsch, E., and Richter, A. K.: 1984, *J. Geophys. Res.*, **89**, 6599.
- Marsch, E., Philip, W. G., Thieme, K. M., and Rosenbauer, H.: 1989, *J. Geophys. Res.*, **94**, 6893.
- McKenzie, J. F., Banaszkiewicz, M., and Axford, W. I.: 1997, *Geophys. Res. Lett.*, **24**, 2877.
- Munro, R. H., and Jackson, B. V.: 1977, *Astrophys. J.*, **213**, 874.
- Spitzer, L., Jr., and Härm, R.: 1953, *Phys. Rev.*, **89**, 977.
- Withbroe, G. L.: 1988, *Astrophys. J.*, **325**, 442.

HYBRID SIMULATIONS OF WAVE PROPAGATION AND ION CYCLOTRON HEATING IN THE EXPANDING SOLAR WIND

PAULETT LIEWER, MARCO VELLI* and BRUCE GOLDSTEIN

Jet Propulsion Laboratory, California Institute of Technology, Pasadena, CA 91109

Abstract. We present results from hybrid (particle ions, fluid electrons) simulations of the evolution of Alfvén waves close to the ion cyclotron frequency in the solar wind, which take into account the basic properties of the background solar wind flow, i.e., the spherical expansion and the consequent decrease in magnetic field and cyclotron frequency with increasing distance from the Sun. We follow the evolution of a plasma parcel in a frame of reference moving with the solar wind using a 1D expanding box hybrid model; use of the hybrid model yields a fully self-consistent treatment of the resonant cyclotron wave-particle interaction. This model is related to a previous MHD model (Velli *et al.* 1992), which allows the use of a simple Cartesian geometry with periodic boundary conditions. The use of stretched expanding coordinates in directions transverse to the mean radial solar wind flow naturally introduces an anisotropic damping effect on velocity and magnetic field. We present results for the case of a single circularly polarized Alfvén wave propagating radially outward. Initially, the wave is below the cyclotron frequency for both the alpha particles and protons. As the wind expands, the wave frequency (as seen in the solar wind frame) decreases more slowly than the cyclotron frequencies and the wave comes into resonance. With only protons, heating occurs as the wave frequency approaches the proton cyclotron frequency. With both alphas and protons, the alphas, which come into resonance first, are observed to be preferentially heated and accelerated.

1. Introduction

The resonant interaction between ions and Alfvén waves near the ion cyclotron frequencies is important in determining the wave spectrum and plasma distribution functions in the expanding solar wind. Ion cyclotron damping is generally invoked as a source of dissipation in MHD turbulence theories. The interaction of Alfvén waves with solar wind ions may be the cause of the observed higher (relative to protons) heavy ion temperatures and speeds in the solar wind.

To study such effects, one needs a model that includes both the interaction between ions and Alfvén waves and the effects of solar wind expansion. Nonlinear effects of ion-cyclotron resonant interactions are included self-consistently in a hybrid (particle ion, fluid electron) model. In a hybrid code, the orbits of the individual ions and the wave fields are evolved self-consistently in time. The effects of the ions on the wave dispersion relation and the effect of the waves on the ion distribution functions are treated in a fully non-linear self-consistent manner. Because of the vast difference in scales between the cyclotron waves and the solar wind expansion, a standard hybrid code cannot include the effects of solar wind expansion.

* Permanent address: Dipartimento di Astronomia e Scienza dello Spazio, Università di Firenze, 50125 Firenze, Italy



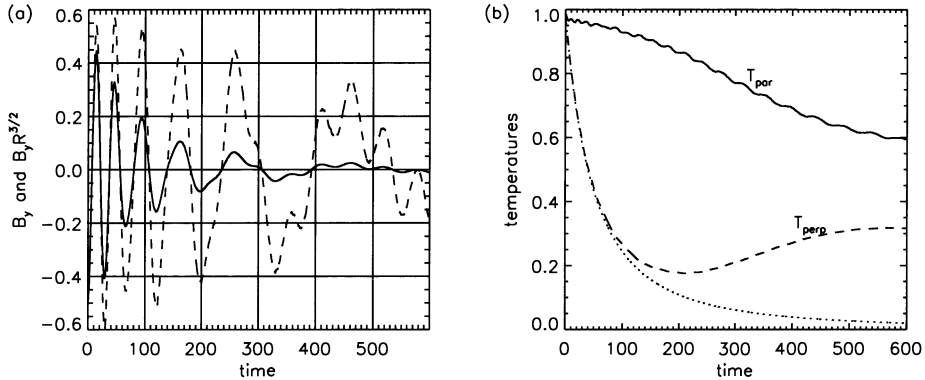


Figure 1. (a) Transverse magnetic field B_y of the Alfvén wave vs. time at a fixed grid point (solid line); $B_y R(t)^{3/2}$, the same field with the WKB scaling removed (dashed line) (b) Perpendicular (dashed line) and parallel (solid line) proton temperatures and scaled temperature, $T_{\perp}(0)/R^2$ (dotted line). Time is scaled as $t \Omega_p^0$.

2. The Expanding Box Hybrid Model

To include the effects of expansion in a 1D hybrid code, we have adopted the transformation used in the expanding box MHD model of Velli *et al.* (1992). Consider the evolution of a small parcel of plasma moving radially outward at a constant speed U_0 . The radial extent ΔR remains constant, but the transverse dimension a of the parcel expands as $a(t) = a_0(1 + U_0 t/R_0)$. We assume the parcel is thin ($\Delta R \ll R$) and that the initial transverse dimension a_0 is small ($a_0/R_0 \ll 1$) so that the spherical geometry effects can be neglected within and across the parcel. We thus can make a coordinate transformation from the initial spherical Sun-centered system to a local Cartesian system moving radially with the wind. The transformation is made in two steps (see Grappin and Velli 1996 for further details): (1) from the spherical system to a Cartesian system with x aligned along the radial direction, and (2) a Galilean transformation to a Cartesian frame centered at $R(t) = R_0 + U_0 t$. The transverse coordinates are renormalized to follow the expansion: $x' = x - R(t)$, $y' = y R_0/R(t)$, $z' = z R_0/R(t)$. This coordinate transformation is then applied to the standard hybrid code equations and terms second order or more in a_0/R_0 are neglected. In the transformed equations, the slow variations in space due to expansion have been transformed to variations in time and thus we can use periodic boundary conditions.

3. Simulation Results

The figures show results from the 1D expanding box hybrid code for two simulations which follow the evolution of a single Alfvén /ion cyclotron wave propagating out

from the Sun with $U_0/R_0 = 0.01\Omega_p^0$. (An unphysically rapid expansion rate is chosen to reduce the computation time; tests using half this expansion rate give the same results.) Case 1 has only protons while Case 2 has 4% alphas. All other parameters are the same: wave amplitude $\delta B/B = 0.05$, $\beta_e = \beta_i = 10^{-2}$, $T_p = T_{He}$, $x_{max}/\lambda = 3$, 1024 grid points and 40 particles/species/cell. For both cases, the wave is initialized with wavenumber $kV_a = 0.28\Omega_p^0$ and the frequency is initially below the ion cyclotron frequency. Note that although the wave frequency is constant in the frame of the Sun, the wave frequency decreases in the solar wind (simulation) frame. For low frequency Alfvén waves satisfying the linear dispersion relation $\omega = kV_a$, expansion causes V_a and thus the wave frequency to decrease as $1/R(t)$ where $R(t) = R_0 + U_0 t$. The cyclotron frequencies decrease as $1/R^2$, scaling as the radial magnetic field. For these parameters, the expansion would cause the wave to become resonant with the alpha particles by $t\Omega_p^0 \approx 60$ and with the protons by $t\Omega_p^0 \approx 230$.

Figure 1a shows results from Case 1 (protons only) for the evolution of the transverse magnetic field component $B_y(t)$ (solid line) and $R^{3/2}B_y(t)$ (dashed line) at a fixed point in the domain. Note the increase in the wave period with time and the decrease in wave amplitude, which is faster than $1/R^{3/2}$, the WKB scaling for Alfvén waves. The decrease in wave frequency is clearly visible until $t\Omega_p^0 \approx 200$, which is close to the time at which the wave frequency approaches the proton gyrofrequency and one would expect significant interaction between waves and particles to occur. After this time, a high frequency component appears superimposed on the initial low frequency frequency wave. Figure 1b shows the evolution of the proton perpendicular (dashed line) and parallel (solid line) temperatures, and also $T_{\perp}(0)/R^2$ (dotted line), the expected scaling if no wave-particle effects were present. It can be seen that the protons are being heated in the perpendicular direction by the ion cyclotron resonant interaction, especially for $t \geq 200\Omega_p^0$. Results showing the evolution of the distribution functions will be presented elsewhere.

Figure 2a shows the evolution of the transverse magnetic field component $B_y(t)$ (solid line) and $R^{3/2}B_y(t)$ (dashed line) for Case 2 (4% alphas) at a fixed point in the domain. For this case, the wave propagation is affected much earlier than in Case 1, consistent with the alpha ion cyclotron resonance affecting the wave propagation earlier than protons. Wave propagation is affected by $t\Omega_p^0 \approx 80$, close to the time at which the scaled linear wave frequency and alpha cyclotron frequencies become equal, $t\Omega_p^0 \approx 60$. Figure 2b shows the evolution of the perpendicular and parallel temperatures for both the alphas (He) and the protons (H) for Case 2. Clearly, the alphas are heated by the resonant interaction, while the proton temperature continues to fall for much longer times than in Case 1 (Figure 1b), although the decline appears to stop by time 400 and one sees perhaps a hint of subsequent heating for later times. It therefore seems that the presence of a 4% population of alpha particles has altered the wave propagation to the extent that no significant resonant wave proton interactions have occurred. The alphas were also accelerated relative to the protons by $\sim 0.1V_a$.

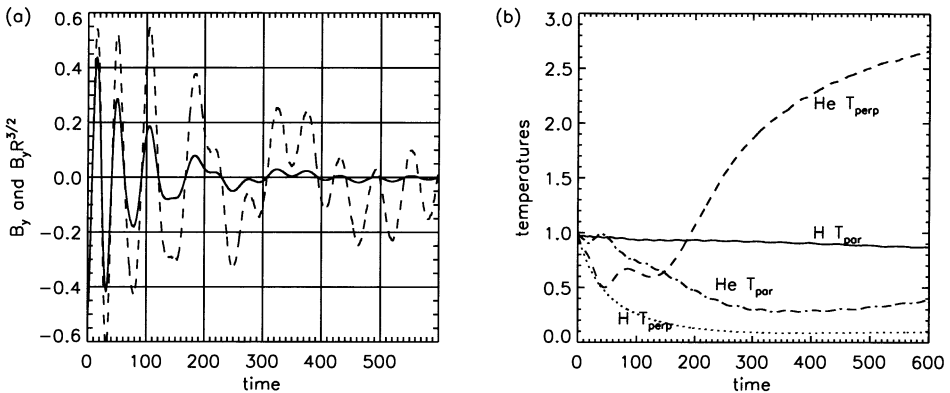


Figure 2. (a) Transverse magnetic field B_y of the Alfvén wave vs. time (solid); $B_y R(t)^{3/2}$, the same field with the WKB scaling removed (dashed) (b) Hydrogen (H) and helium (He) perpendicular and parallel temperatures.

Quasilinear theory with solar wind expansion effects was used by Marsch *et al.* (1982) to study ion heating and acceleration by cyclotron resonant interactions. A more detailed discussion of our results and a comparison with those of Marsch *et al.* (1982) will be presented elsewhere.

Acknowledgements

This research was performed at the Jet Propulsion Laboratory under a contract between the California Institute of Technology and the National Aeronautics and Space Administration. One of the authors (MV) held a National Research Council JPL Research Associateship.

References

- Grappin, R., and Velli, M.: 1996, *JGR*, **101**, 425.
- Marsch, E., Goertz, C. K., and Richter, K.: 1982, *JGR*, **87**, 5030.
- Velli, M., Grappin, R., and Mangeney, A.: 1992, *AIP Proc.*, **267**, 154.

MAGNETO-GRAVITY WAVES TRAPPED IN THE LOWER SOLAR CORONA

YU-QING LOU

*Department of Astronomy and Astrophysics, 5640 South Ellis Avenue,
The University of Chicago, Chicago, IL 60637 USA*

Abstract. The possibility of trapped magneto-gravity waves in the lower solar corona with an open magnetic field is discussed. Intensity variations and/or Doppler shifts of relevant UV, EUV and x-ray spectral lines in the chromosphere, transition region and lower corona may reveal the existence of such low-frequency modes (with periods longer than ~ 1.5 hour). The spectrum may be either discrete or continuous depending on the reflection property of the narrow transition region. These modes can be utilized to probe the dynamics of the upper chromosphere, transition region and lower corona; they may also play an important role in coronal heating.

Key words: coronal holes, coronal seismology, magneto-gravity waves, solar corona, spicules, supergranules, transition region

The basic physics of gravity waves in a gravitationally stratified atmosphere is well known (Hines 1960; Mihalas and Toomre 1981; Mihalas and Mihalas 1984; Lou 1995a, b). In short, gravity waves exist when the frequency of a small compressible perturbation is lower than the Brunt-Väisälä buoyancy frequency; for frequencies higher than the acoustic cutoff frequency, acoustic waves appear instead. What happens then for magnetohydrodynamic (MHD) waves in a gravitationally stratified atmosphere permeated with an open magnetic field (say, a large solar coronal hole)? In addition to incompressible transverse Alfvén waves (Lou and Rosner 1994), there are compressible MHD modes related to the conventional fast and slow waves (Lou 1996a, b). As a result of the background inhomogeneity, it is now inconvenient to simply refer to these compressible MHD wave modes as fast or slow because the corresponding wave speeds vary with height. There is one compressible MHD wave branch which is more magnetic in nature and there is another compressible MHD wave branch which contains magneto-acoustic waves in the high-frequency regime and magneto-gravity waves in a certain range of the low-frequency band.

Ferraro and Plumpton (1958) first studied MHD waves in a uniformly magnetized atmosphere stratified by a constant gravity in Cartesian geometry. In a certain parameter regime, the information about magneto-gravity waves is actually contained in their mathematical expressions; nonetheless, the relevant physical interpretation is not sufficiently explicit. The physics of MHD waves, including magneto-gravity waves, in a gravitationally stratified stellar atmosphere with an open magnetic field in spherical geometry has been explored in the past few years (Lou 1996a, b, c). Here, we specifically call attention to the possibility of low-frequency magneto-gravity waves trapped in the lower solar corona because data collected by various SOHO instruments may contain information about these modes. Similar to the role of p -modes in helioseismology, the existence of such



trapped coronal magneto-gravity modes would provide a powerful means of probing physical conditions in the upper chromosphere, transition region and lower corona.

We present a succinct model formulation for this MHD wave problem below and discuss qualifications. In spherical geometry, the background stellar atmosphere is taken to be static (assuming a sufficiently subsonic outflow near the stellar surface) and spherically symmetric with a radial magnetic field $B_0 \propto r^{-2}$ where r is the radial coordinate. For the present purpose, one can prescribe a radial temperature profile $T_0(r)$ to derive corresponding pressure and density profiles $p_0(r)$ and $\rho_0(r)$ from hydrostatic conditions. One can readily write out the standard three-dimensional ideal MHD perturbation equations using the polytropic approximation for the energy equation (Lou 1996a). Alfvén waves and compressible MHD waves decouple from each other in the linear regime. By a suitable angular and temporal separation of variables in the form of $Y_{lm}(\theta, \phi) \exp(i\omega t)$, one can reduce the compressible MHD wave equations to a set of ordinary differential equations in terms of r . For an isothermal atmosphere which crudely represents the lower solar corona above the transition region, one can derive asymptotic solutions at sufficiently large r and close to the stellar surface. By imposing the condition for outward propagating MHD waves at large r , one can integrate radially inward to examine solution behaviors (Lou 1996b).

Shown in Figure 1 is such a numerical solution with an outgoing magneto-acoustic wave specified sufficiently far above the stellar surface (Lou 1996a, b). The parameters adopted are $\gamma = 5/3$, $\bar{\omega} = 1$, $\delta = 2$ and $l = 2$ where γ is the polytropic index, $\Lambda \equiv GM\mu m_H/(k_B T_0)$ defines a length scale (r^2/Λ is the actual scale height), G is the gravitational constant, M is the stellar mass, μ is the mean molecular weight, m_H is the proton mass, k_B is the Boltzmann constant, $x \equiv 2r/\Lambda$ is the dimensionless radius, $\delta \equiv 4(\gamma - 1)^{1/2}C_S/(\Lambda\gamma\omega)$, C_S is the sound speed, $\bar{\omega}^2 \equiv 4\pi\rho_*\omega^2 \exp(-2/x_*) (\Lambda/2)^6/A_B^2$, ρ_* is the gas mass density at the stellar surface, $A_B \equiv B_0 r^2$ is the constant magnetic flux, and x_* is the dimensionless stellar radius. Panel (a) shows radial variations of the real (solid line) and imaginary (dotted line) parts of the dimensionless transverse divergence of the velocity perturbation $(\nabla_\perp \cdot \mathbf{v}_\perp)^* \equiv -i\bar{\omega}x^2\tilde{b}_r$ where $\tilde{b}_r \equiv b_r/B_0(x_*)$ and b_r is the radial magnetic field perturbation. Panel (b) shows radial variations of the real and imaginary parts of the scaled dimensionless transverse divergence of the magnetic field perturbation $(\nabla_\perp \cdot \mathbf{b}_\perp)^* x \exp[-1/(2x)]$ where $(\nabla_\perp \cdot \mathbf{b}_\perp)^* \equiv -x^{-2}d(x^2\tilde{b}_r)/dx$. Panel (c) shows the real and imaginary parts of the dimensionless radial velocity perturbation $\tilde{v}_r \equiv v_r(4\pi\rho_*)^{1/2} \exp(-1/x_*)/B_0(x_*)$. The constant energy flux due to a tiny magneto-acoustic leakage is represented by the dash-dotted line. Panel (d) shows the real and imaginary parts of the scaled dimensionless pressure perturbation $\bar{p} \equiv \exp(-2/x)(\Lambda/2)^2 4\pi p/[A_B B_0(x_*)]$. For a larger value of l , the signature of trapped magneto-gravity waves near the stellar surface is more prominent with more radial nodes and the signature of magneto-acoustic waves appears further above the stellar surface. Note that in both (a) and (c), the real and imaginary parts

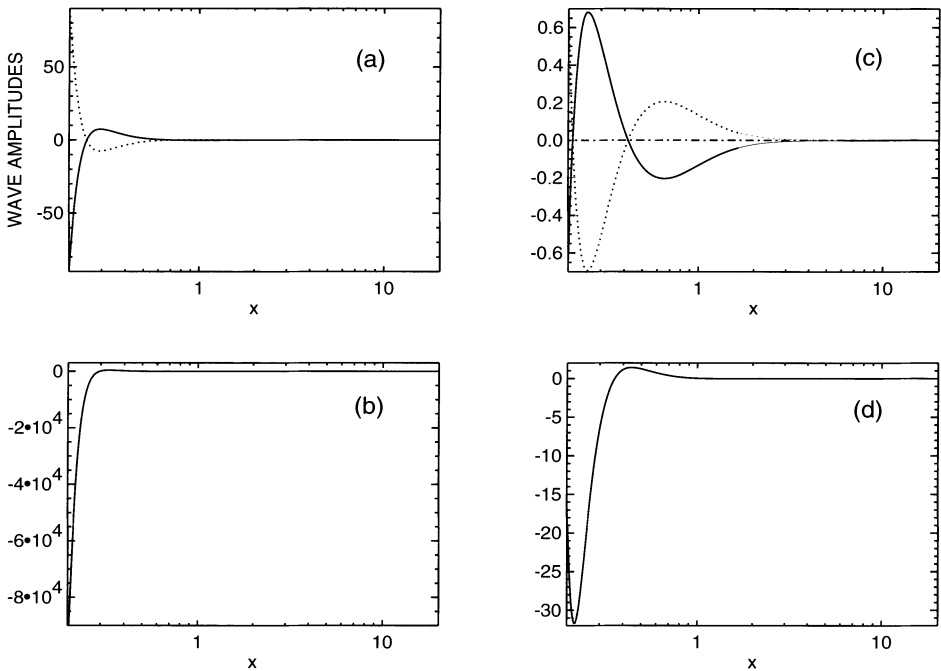


Figure 1. An illustrating example of a trapped magneto-gravity wave (see text).

are of opposite sign, while, in both (b) and (d), the real and imaginary parts *nearly* coincide for the trapped magneto-gravity wave. Magneto-gravity waves must tunnel through an effective barrier in the mid-atmosphere to emerge in the form of magneto-acoustic waves. This involves the process of MHD wave transformation in an inhomogeneous atmosphere (Thomas 1983; Zhugzhda 1984).

Coronal magneto-gravity waves are effectively trapped from above because of the gradual decrease of the buoyancy frequency with increasing height and the presence of a strong magnetic field. The narrow transition region may be treated as a discontinuity when the radial wavelength is sufficiently long (Lou 1993). Strong wave reflection is thus expected across the transition region. Given these conditions, discrete magneto-gravity modes may exist in the lower solar corona. Otherwise, a continuous spectrum should appear instead. Oscillation periods of coronal magneto-gravity waves should be longer than the timescale corresponding to the buoyancy frequency at the coronal base which is estimated to be ~ 1.5 hour.

Besides various sporadic activities, the most likely sources of persistent excitation of magneto-gravity waves are protruding spicules along supergranule boundaries and random structural variations of supergranules over much longer timescales

of a few days. Whether random processes could completely swamp signals of trapped coronal magneto-gravity waves is unclear at this stage. Although the solar convection zone is messy enough, millions of small-amplitude p -modes persist with distinct characteristics; this empirical fact offers an encouraging prospect of finding coronal magneto-gravity waves. The best place to search for signals of trapped magneto-gravity waves is in large coronal hole regions. Since magneto-gravity waves involve both radial and transverse velocity perturbations as well as density and pressure perturbations, it is possible to examine Doppler shifts and/or intensity variations of appropriate spectral lines in UV, EUV and x-ray bands at the transition region and coronal base; both limb and disk center observations should be carried out for consistency.

Acknowledgements

This research has been supported in part by grants from U.S. National Science Foundation (ATM-9320357 and AST-9731623), National Aeronautics & Space Administration (Space Physics Theory and Supporting Research & Technology programs) and a SOHO/UVCS subcontract to the University of Chicago, and by the Visiting Scientist Program of the International Space Science Institute, Bern, Switzerland.

References

- Ferraro, V. C. A., Plumpton C.: 1958, *Astrophysical Journal*, **127**, 459.
Hines, C. O.: 1960, *Canadian Journal of Physics*, **38**, 1441.
Lou, Y. Q.: 1993, *Astrophysical Journal Letters*, **414**, L141.
Lou, Y. Q.: 1995a, *Astrophysical Journal*, **442**, 401.
Lou, Y. Q.: 1995b, *Monthly Notices of Royal Astronomical Society*, **276**, 769.
Lou, Y. Q.: 1996a, *Monthly Notices of Royal Astronomical Society*, **281**, 750.
Lou, Y. Q.: 1996b, *Monthly Notices of Royal Astronomical Society*, **281**, 761.
Lou, Y. Q.: 1996c, *Science*, **272**, 521.
Lou, Y. Q., Rosner, R.: 1994, *Astrophysical Journal*, **424**, 429.
Mihalas, D., Mihalas, B. W.: 1984, *Foundation of Radiation Hydrodynamics* (Oxford: Oxford University Press).
Mihalas, B. W., Toomre, J.: 1981, *Astrophysical Journal*, **249**, 349.
Thomas, J. H.: 1983, *Annual Review of Fluid Mechanics*, **15**, 321.
Zhugzhda, Y. D.: 1984, *Monthly Notices of Royal Astronomical Society*, **207**, 731.

LY- α OBSERVATION OF A CORONAL STREAMER WITH UVCS/SOHO

L. MACCARI¹, G. NOCI¹, S. FINESCHI², A. MODIGLIANI¹, M. ROMOLI¹ and
J. L. KOHL³

¹ Dipartimento di Astronomia e Scienza dello Spazio, Università di Firenze, Firenze, Italy

² Osservatorio Astronomico di Torino, Pino Torinese, Italy

³ Harvard-Smithsonian Center for Astrophysics, Cambridge, MA, USA

Abstract. In this paper we discuss some characteristics of an equatorial streamer observed by UVCS in July 1997. We determine the height distribution of the Ly- α total intensity and of its width. We focus our attention, in particular, on the time variability of these parameters.

1. The Data

We analyze a set of data obtained by the UVCS instrument on board the SOHO spacecraft on 23–27 July 1997. The instrument is described in Kohl *et al.* (1995). A review of the results of the first period of operation of UVCS is given in Kohl *et al.* (1997a), Kohl *et al.* (1997b), Noci *et al.* (1997), and Raymond *et al.* (1997).

Our data concern a streamer at the West limb of the Sun, scanned at heliocentric heights running from 1.25 to 5.0 R_{\odot} (the instrument was in the offset-pointing mode for the observations at heights lower than 1.5 R_{\odot}). The spectral lines falling in the observed range are, for the Ly- α channel, H I Ly- α , Si II λ 1264, N V λ 1239, λ 1243, Fe XII λ 1242, Si III λ 1206 and C III λ 1175; for the O VI channel, H I Ly- β , Ly- γ , O VI λ 1032, λ 1037, Si XII λ 499 (2nd order) and C III λ 977. The lines of Si II, Si III, and C III are used for stray light evaluation.

The data have been calibrated and flat field corrected in the standard way (see Gardner *et al.* 1996). The other instrumental effects that we considered are stray light, instrumental profile, finite slit width, and detector broadening. For the total (i.e., integrated over the line profile) intensity, the first one only is relevant. The stray light correction was made by assuming that the ratio of stray light intensity to disk intensity is the same for Ly- α and Si III λ 1206, and that the latter is, in the coronal data, due entirely to stray light.

For what concerns the profiles, we corrected them, as a first step, for the detector broadening, applying a procedure of deconvolution described by Kohl *et al.* (1997a). Secondly, we did the stray light correction, for which we used the Ly- α disk profile from Gouttebroze *et al.* (1978) convolved with the instrument and slit profile. The obtained $I(\lambda)$ curves were then compared with the result of a convolution of a first guess Gaussian coronal profile with the instrument and slit profile; consequently, the parameters of the coronal profile were varied until a χ^2 best fit was reached. This gives the coronal Ly- α width. The FWHM of the instrumental profile has been assumed to be 0.28 Å (Gardner *et al.* 1996). The slit is 50 μm wide for all the observations, except for the lowest, at 1.25–1.35 R_{\odot} , where its width is 35 μm .

The observations have been made with the purpose of determining some physical parameters which characterize the observed streamer. We started with the Ly- α total



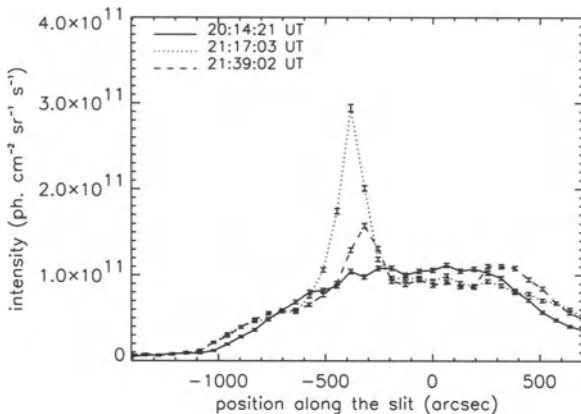


Figure 1. Total intensity of the Ly- α line, plotted as a function of the position along the slit at different times (25 July). The slit is perpendicular to the equatorial plane, with the position 0 (equator) distant $1.8 R_{\odot}$ from Sun's center. Moving away from 0 there is a heliocentric distance increase and a latitude increase; both contribute to the intensity decline.

intensity and line width; we report, in this preliminary analysis, on the height distribution of these parameters on the equatorial plane. Since the observations take a time interval of some days, we give particular attention to the time variability in the data to establish how significant the results obtained will be.

2. Total Intensities

Let us start with the short temporal variations (time scale of $\simeq 10$ minutes) of the Ly- α total intensity. One slit image is composed of n consecutive exposures, each one 5 minutes long, where n depends on the slit width, heliocentric distance and statistical significance required. Hence, analyzing consecutive exposures, one can detect time variations with a 5 minute time scale.

The result of our analysis, for the observations listed above and the synoptic observations of the same period (22–27 July), is that there are no short time variations larger than the statistical errors, with the exception of those due to a CME which occurred on 25 July. This event was detected at the heliocentric distances of 1.8 and $1.9 R_{\odot}$. Figure 1 shows the Ly- α total intensity at $1.8 R_{\odot}$ before the transient, at the time of maximum intensity enhancement, and when the contribution of the transient was fading. As can be seen in the figure, the phenomenon seems to have affected only a limited region of space, and its effects on the total intensity of the line must be considered important only in a comparatively narrow portion of the slit. The rest of the slit (that is, an interval of 6–7 bins, corresponding to 4–5 tenths of solar radius in the equatorial region) appears to have been affected slightly by

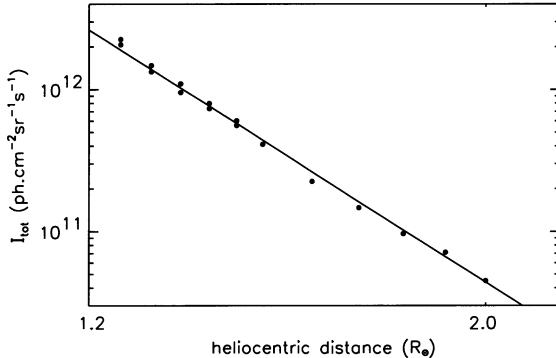


Figure 2. Ly- α total intensity vs. heliocentric height in the equatorial plane. The solid curve is a fit with a function having the form: $I(r) = I_0 r^{-b}$, with a resulting value for b equal to 8.01. Errors (statistical) are $\leq 10\%$.

the transient (10–15%), and thus the value corresponding to the equator has been used in our fit of Figure 2 (see below).

At a distance of $1.9 R_\odot$, the intensity profiles show a similar behavior. The observation, starting at 21:50:16 UT, is subsequent to the one at $1.8 R_\odot$; the main contribution of the transient has already passed beyond the field of view (which puts a lower limit of 35 km/s to the transient speed) and the strong short-time variations are relevant only in the earlier exposures of the sequence. The portion of the slit that is affected by rapid variations of intensity is, again, limited in space.

Variations with longer time scales (days) can be studied with the use of the synoptic observations (made every day), and with special observations. These variations are considerably larger than the short time ones, being of the order of 10–15% for consecutive days, but reaching, in some cases, 40% if we compare observations three or four days apart. Ly- α total intensities in the equatorial plane from the special observations made on 23, 24, 25 July are given in Figure 2. The discrepancies between the values found at the same height on two consecutive days (23 and 24 July, below $1.5 R_\odot$) are in agreement with the variability rate obtained from the synoptic observations ($\simeq 10\%$).

3. Profile Widths

The evaluation of the Ly- α widths has been made with the procedure described in section 1. The results are shown in Figure 3. The points with error bars represent the values obtained in this analysis for the random velocity, expressed as $c\sigma/\lambda_o$, where σ is the $1/e$ half width of the profile which best fits the corrected Ly- α data, and λ_o the wavelength of the transition. In the plot we also report, as a comparison, the values obtained in different measurements some months before our observations.

We can confirm, generally, for the profile width, the same trend we detected for the total intensities: relatively small fluctuations on the time scale of one day (5–10%) and wider (20–25%) variability if we consider the whole week.

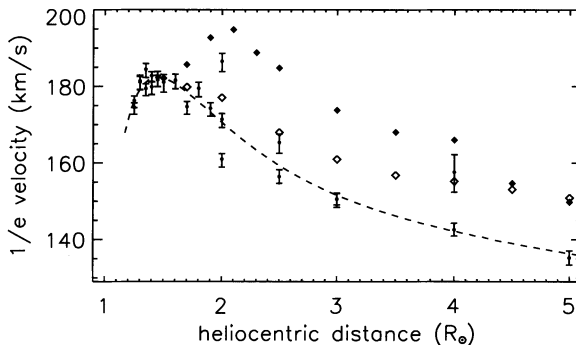


Figure 3. $1/e$ half width of the Ly- α line, plotted as a function of the heliocentric distance. Points with error bars: our results; full and open diamonds: 12 October 1996 and 5 February 1997, respectively (Kohl *et al.* 1997a). Dashed curve: fit of our points with a 3rd degree polynomial curve, plus a term of the form: const. $/\sqrt{r}$.

4. Conclusions

We have studied the Ly- α total intensity and profile in the equatorial streamer belt at the West limb of the Sun on 22–27 July 1997. The total intensity shows a rapid decline with the heliocentric distance, as expected; the profile width also decreases beyond $r \simeq 1.6 R_\odot$, but from $r = 1.25 R_\odot$ to $r = 1.5 R_\odot$ our data suggest the profile width to increase with height.

For what concerns the variability, we could not determine any in the time scale range of a few minutes, except when a CME occurred. On larger time scales (one day), 10–15% variations were observed in the total intensity; on even longer scales (3–4 days) the variations could be as large as 40%. The relative variations of the Ly- α profile width were about a factor of 2 smaller. Even among observations months apart, the width differences are less than 20% (Figure 3). We have not examined enough data, yet, to establish whether the width decrease from October 1996 to July 1997 indicates a temporal trend.

The variations observed on the daily time scale, both for line intensity and profile width, are consistent with the picture of long lived (weeks or more) structures, a few tens of degrees wide, which change position because of the solar rotation.

References

- Gardner, L. D., Kohl, J. L., Daigneau, P. S., *et al.*: 1996, *Proc. SPIE*, **2831**, 2.
- Gouttebroze, P., Lemaire, P., Vial, J. C., and Artzner, G.: 1978, *ApJ*, **225**, 665.
- Kohl, J. L., Esser, R., Gardner, L. D., *et al.*: 1995, *Solar Phys.*, **162**, 313.
- Kohl, J. L., Noci, G., Antonucci, E., *et al.*: 1997a, *Solar Phys.*, **175**, 613.
- Kohl, J. L., Noci, G., Antonucci, E., *et al.*: 1997b, *Adv. Space Res.*, **20**, 3.
- Noci, G., Kohl, J. L., Antonucci, E., *et al.*: 1997, *ESA SP-404*, 75.
- Raymond, J. C., Kohl, J. L., Noci, G., *et al.*: 1997, *Solar Phys.*, **175**, 645.

FLUCTUATIONS, DISSIPATION AND HEATING IN THE CORONA

W. H. MATTHAEUS, G. P. ZANK, R. J. LEAMON, C. W. SMITH and D. J. MULLAN
Bartol Research Institute, University of Delaware

S. OUGHTON

Department of Mathematics, University College London, London WC1E 6BT, UK

Abstract. Mechanisms for the deposition of heat in the lower coronal plasma are discussed, emphasizing recent attempts to reconcile the fluid and kinetic perspectives. Structures at the MHD scales are believed to act as reservoirs for fluctuation energy, which in turn drive a nonlinear cascade process. Kinetic processes act at smaller spatial scales and more rapid time scales. Cascade-driven processes are contrasted with direct cyclotron absorption, and this distinction is echoed in the contrast between frequency and wavenumber spectra of the fluctuations. Observational constraints are also discussed, along with estimates of the relative efficiency of cascade and cyclotron processes.

1. Introduction

A recurring theme in recent studies of the physics of the corona has been the issue of the mechanism by which heat is deposited within two or three solar radii of the photosphere (Holzer 1977; Habbal *et al.* 1995) in sufficient quantities to both accelerate the solar wind and to account for high temperatures inferred from recent SOHO observations. One of the models which has been proposed to explain these observational constraints (McKenzie *et al.* 1995; Axford and McKenzie 1997) relies upon the cyclotron absorption of relatively high frequency (\sim kHz) waves propagating upward in the lower solar atmosphere. There is no observational evidence for waves of such high frequency. Here we will discuss several physical and observational issues of relevance to this model as well as alternatives that would involve MHD cascade as an essential feature. We will emphasize the possibility that magnetic fluctuations with high transverse wavenumber may be dynamically driven in a way that allows heating to occur without requiring a pre-existing reservoir of high frequency waves. The possible importance of Landau damping and cyclotron absorption of highly oblique structures will be discussed, especially in view of recent observational evidence from solar wind data. These discussions motivate the development of models based upon anisotropic, reduced MHD equations, in which quasi-two dimensional (2D) turbulence plays a central role in the dissipation of fluctuations and the subsequent heating of the corona.

2. Damping of High Frequency Alfvén Waves

The Axford-McKenzie model (McKenzie *et al.* 1995; Axford and McKenzie 1997) of coronal heating envisions generation of broadband waves due to disturbances in or near the chromospheric network. In this model the waves are launched upwards at the Alfvén speed (perhaps thousands of km/s) and within 1–2 solar radii the



waves dissipate, heating the corona and imposing signatures of cyclotron damping in the form of a high perpendicular temperature (T_{\perp}) for protons and minor ions. The hot coronal plasma produces an outward flow at altitudes sufficiently low to satisfy constraints on radial acceleration of the solar wind inferred from remote sensing observations (Grall *et al.* 1996). Recently Tu and Marsch (1997) elaborated upon the cyclotron wave damping model, investigating the upward propagation, transport, and dissipation of a flux of Alfvén waves generated at the base of a model corona. Their study lends support to the direct cyclotron heating model, provided that sufficient wave power is supplied at high enough frequencies. This appears to require a spectrum no steeper than $1/f$ (C.-Y. Tu, private communication) extending out to kHz frequencies.

This coronal dissipation scenario descends conceptually from earlier work on collisionless damping of MHD waves (Barnes 1969), and even earlier work on thermal excitation of instabilities through cyclotron resonance (e.g., Rowlands *et al.* 1966; Kennel and Engelmann 1966). Based upon linear theory, one concludes typically that fast and slow mode waves are very heavily damped through kinetic processes. If one observes a broad persistent spectrum of MHD waves, as one does in the solar wind (Tu and Marsch 1995), there is an expectation that these fluctuations would be in the Alfvén mode. Direct observations frequently support this conclusion (Belcher and Davis 1971). The same predisposition exists in coronal physics, but is less well bolstered by observations than is the solar wind case. The perspective of Tu and Marsch (1995) is that coronal Alfvén waves propagate upwards until reaching an altitude at which the height-dependent cyclotron frequency is low enough to absorb them. This mechanism might be called “cyclotron resonance sweeping,” or simply “cyclotron sweeping,” given that the absorption sweeps towards lower frequency, progressively eating away the spectrum of fluctuations. This idea appeared earlier in several contexts, including solar wind particle anisotropies (Schwartz *et al.* 1981) and acceleration of He^{++} (Hollweg and Turner 1978).

3. Frequency vs. Wavenumber: Transfer in k-space

If one focuses upon the dynamics of parallel propagating MHD Alfvén waves, it is tempting to assume tacitly that frequency ω and wavenumber k are in a one-to-one correspondence. For the slab model with wave vector \mathbf{k} parallel to the large scale mean magnetic field \mathbf{B}_0 , and for Alfvén waves having $\omega \sim \mathbf{k} \cdot \mathbf{B}_0 \equiv k_{\parallel} B_0$, the correspondence is accurate. However, the perpendicular component of wavenumber k_{\perp} is unaccounted for in this assumption. If one talks about a “cascade in frequency,” there is an assumption that nonlinear transfer is to higher k_{\parallel} with no implied transfer in k_{\perp} . Conversely, a cascade in wavenumber may imply various possibilities in the frequency domain.

This distinction seems not have been fully appreciated in the past. For example, the assumption of a steady spectral distribution in parallel wavenumber is indeed useful in estimating cyclotron effects on minor ions (Isenberg and Hollweg 1983)

or other test particles in which only small fractions of the total fluctuation energy may be involved. It is quite a different story to assume that the rate of replenishment of fluctuation energy by cascade to higher parallel wavenumber is sufficient to heat the thermal plasma. However, this assumption is implicit in the solar wind theory of Tu (1988) in which cyclotron sweep was neglected in favor of a large cascade rate computed in terms of an *isotropic* Kolmogoroff-like inertial range phenomenology. This theory assumes a strong cascade, but one equally strong in all directions. At this point one must ask what simulations and MHD theory have to say about transfer of energy in wavenumber space.

Numerical simulations show that a strong, large-scale magnetic field \mathbf{B}_0 produces relatively enhanced spectral transfer in the directions transverse to \mathbf{B}_0 . This is a consequence of the suppression of spectral transfer in the parallel direction because of Alfvénic propagation effects. This phenomenon has been seen in two-dimensional, three-dimensional, incompressible and compressible MHD (Shebalin *et al.* 1983; Oughton *et al.* 1994; Matthaeus *et al.* 1996). The expectation that non-linear activity preferentially involves high transverse wavenumber is also implicit in the structure of “reduced MHD” (Strauss 1976; Montgomery 1982), which is widely believed to be a leading order low frequency dynamical description of laboratory plasmas at low plasma beta. There are also a variety of indications that the spectrum of observed solar wind turbulence is highly anisotropic, containing what appears to be a rather large admixture of high k_{\perp} fluctuations (e.g., Matthaeus *et al.* 1995). This anisotropy has sometimes been idealized as a two component mixture (Matthaeus *et al.* 1990) of so-called 2D fluctuations (varying k_{\perp} with $k_{\parallel} = 0$) and slab fluctuations (varying k_{\parallel} with $k_{\perp} = 0$). When parameterized in this way, fits to Helios data (Bieber *et al.* 1996) suggest that 80% of the energy is in 2D modes, and the remaining 20% in slab modes.

Such evidence represents a strong break with the more traditional view that solar wind fluctuations are pure slab (or, isotropic), and a corollary is that the simple correspondence of frequency and wavenumber discussed above may be strongly violated. 2D turbulence may emerge from a variety of causes, including the anisotropic spectral transfer alluded to above. Several studies (Kinney and McWilliams 1998; Matthaeus *et al.* 1998) support the view that spectral transfer purely transverse to the mean field, i.e., purely in the k_{\perp} direction, is a reasonable first approximation. In this case spectral transfer of Alfvén modes may occur at *constant* frequency, while something resembling a Kolmogoroff-type nonlinear cascade occurs in k_{\perp} .

4. Cyclotron Absorption vs. Cascade

In evaluating the possible roles of the cyclotron sweep mechanism and the anisotropic nonlinear cascade mechanism in coronal heating, it is useful to estimate directly their respective heating rates. Let us denote the cascade heating rate as ϵ_{\perp} and the cyclotron sweep heating rate as ϵ_c . The cascade heating rate is estimated in the standard way (Zank *et al.* 1996) as $\epsilon_{\perp} = \delta u^3 / \lambda_{\perp}$ where δu is the rms turbulent

velocity and λ_{\perp} is the similarity scale, or energy containing scale of the quasi-2D fluctuations, often taken to be the perpendicular correlation length. Note that this is a *perpendicular* heating rate and that the concomitant transfer rate into high parallel wavenumbers is much smaller.

The cyclotron sweep damping rate (Tu and Marsch 1997; Schwartz *et al.* 1981) may be estimated as $\epsilon_c \sim (U + V_A) P(f_c) df_c/dr$ where U is the flow speed, V_A the Alfvén speed, $P(f)$ the frequency dependent power spectrum of the fluctuations, and f_c is the local proton gyrofrequency, varying with radius r . Defining λ_h as the scale height for gyrofrequency variation, and δu_{diss}^2 to be the energy in dissipation range fluctuations (Leamon *et al.* 1998a, b), we find that $\epsilon_c \sim (U + V_A) \delta u_{\text{diss}}^2 / \lambda_h$. Regrouping terms, we estimate that the ratio of cascade heating rate to gyrofrequency sweep heating rate is

$$\frac{\epsilon_{\perp}}{\epsilon_c} = \left(\frac{\delta u^2}{\delta u_{\text{diss}}^2} \right) \left(\frac{\delta u}{V_A} \right) \left(\frac{\lambda_h}{\lambda_{\perp}} \right). \quad (1)$$

The first of these factors expresses essentially the ratio of fluctuation energy at the correlation length scale to that at the cyclotron dissipation scale. Thus, it is large for a broadband inertial range, perhaps $\sim 10^3$ unless the spectrum is very flat, say $1/f$ as assumed by Tu and Marsch (1997). In the latter case this factor is ≈ 1 . The second factor is unknown for the corona, but (simply guessing) it may be “small,” say 10^{-2} , or up to a “saturated” value, ≈ 1 . The final factor is also hard to estimate, since the transverse correlation scale of coronal fluctuations is unknown. However, based upon remote sensing of anisotropic density fluctuations (Grall *et al.* 1997), and our knowledge of solar wind anisotropies, we might expect that $\lambda_{\perp} \ll 1R_{\odot}$. The scale height for gyrofrequency variation (see Tu and Marsch 1997) is typically assumed to be a few tenths of a solar radius or more. Thus the third factor may be, say, 10^2 or perhaps much larger. On balance one concludes that the cascade mechanism may be dominant, and almost certainly cannot be neglected.

Tu and Marsch (1997) reached the opposite conclusion, examining only the cyclotron sweep mechanism for coronal parameters, while discarding the direct cascade. However, the cascade model they employed was one in which the total energy transfer rate is inversely proportional to V_A . This type of model (see, e.g., Galtier *et al.* 1997) is based upon the isotropic inertial range theory of Kraichnan (1965) and does not take strong anisotropy into account. In addition a decay rate $\propto V_A^{-1}$ is apparently inconsistent with MHD simulations at moderate Reynolds number (Hossain *et al.* 1995). Tu and Marsch present no quantitative support for their approximation and, on the basis of the estimates above, we can see no reason why the perpendicular cascade should be neglected for coronal parameters.

5. Dissipation Mechanisms

In either the cascade model or the cyclotron sweep model, the net dissipation rate

of energy depends crucially on the full three dimensional energy spectrum $E(\mathbf{k})$ (energy here refers to flow kinetic energy plus magnetic energy). For example, if the dissipation function is of the form $(dE(\mathbf{k})/dt)_{\text{diss}} = -\gamma(\mathbf{k})E(\mathbf{k})$, then the dissipation rate for the total energy E is

$$\frac{dE}{dt} = - \int d^3k \gamma(\mathbf{k})E(\mathbf{k}) \quad (2)$$

where the integral extends over all wave vectors. Clearly, $\gamma(\mathbf{k})$ alone does not determine the dissipation rate, as the integral also involves the distribution of energy. Thus, in the cyclotron sweep picture one must specify a spectrum of noninteracting waves that is supplied to the corona. The nature of the spectrum is then deferred to a discussion about wave generation at the base of the corona. The cascade picture might also retain some sensitivity to the boundary or input spectrum, but the spectrum sufficiently far from the boundary may be almost fully determined by local nonlinear interactions, i.e., by spectral transfer.

In this perspective, we need to simultaneously confront the issues of MHD spectral transfer, governed by large scale dynamics, and kinetic dissipation mechanisms, controlled by microphysics. MHD spectral transfer, which we suspect to be highly anisotropic in coronal conditions, most likely sends energy vigorously to high transverse wave numbers. The net dissipative effect will be determined by whatever absorption rate $\gamma(\mathbf{k})$ is afforded by available kinetic processes. Several issues, some raised by recent solar wind work, warrant mention:

1. On the basis of linear theory, a very large $|\gamma|$ is expected for fluctuations with polarizations corresponding to the fast or slow mode (Barnes 1969). However, little seems to be known at present regarding how rapidly a strong nonlinear cascade of Alfvén modes supplies energy to the magnetosonic polarizations. If such rates are large, this would have important consequences for the existence of an inertial range, and might affect the dissipation range.
2. Recent investigation of $\gamma(\mathbf{k})$ associated with the Alfvén mode (Leamon *et al.* 1999) in the solar wind reveals that there is angular dependence of damping rates computed from linear Vlasov theory. Comparison with inferred spectral anisotropy (at 1 AU) leads to the conclusion that most of the energy damps at oblique angles.
3. Analysis of dissipation range magnetic helicity (Leamon *et al.* 1998b) suggests that both cyclotron resonant and non-cyclotron resonant processes (e.g., Landau damping) operate in the solar wind dissipation range.
4. For dissipation at highly oblique angles, where k_\perp is important, the relevant length scale is likely to be the ion inertial scale ρ_i rather than the gyroradius λ_{ci} which enters more naturally into cyclotron absorption of high k_\parallel structures. In the low- β corona, this distinction is significant.
5. Nonlinear kinetic mechanisms need to be considered as well as linear Vlasov results. Various possibilities exist for nonlinear effects which might contribute significantly to damping at oblique wave vectors, e.g., driving of magnetosonic

modes (mode conversion), dissipation at reconnection sites, and secondary instabilities associated with parallel electron beams.

6. Possibility of a Reduced MHD Model

Based in part on the considerations above, we recently proposed a model to examine the implications of a highly anisotropic nonlinear cascade in the corona (Matthaeus *et al.* 1999). In its simplest form the model consists of propagating Alfvén waves and quasi-2D MHD turbulence. The waves drive the turbulence and the latter dissipates the energy at small perpendicular scales. Specifically, we assume that the continual energy supply for the turbulent heating arises from (approximately) Alfvénic fluctuations generated in the chromosphere. These propagate into the corona where some fraction experience non-WKB reflection off the large-scale density and field gradients (Hollweg 1996; Velli 1993). When sufficient fluctuation energy resides in low frequency quasi-2D MHD modes, whose wavevectors are almost perpendicular to the (average) coronal magnetic field \mathbf{B}_0 , then the waves can drive the turbulence (Shebalin *et al.* 1983; Matthaeus *et al.* 1996; Matthaeus *et al.* 1998). At large Reynolds numbers, the quasi-2D fluctuations engage in a transverse cascade involving successive reconnection of poloidal flux structures, thereby transferring energy to small (perpendicular) scales where it is dissipated.

Two preliminary implementations of this model have been examined. In the first, the turbulence is modeled by a simple one point phenomenology (e.g., Zank *et al.* 1996) and the reflections are modeled by reflection coefficients. In the second implementation, the turbulence is modeled as reduced MHD. In each case the results show that a significant fraction of the input energy in the form of propagating waves is converted to heat by dissipation of the 2D turbulence. The process is efficient ($\sim 50\%$) and the initial seed 2D turbulence is robustly regenerated. So far only scalar dissipation coefficients, incompressible MHD, and modeled reflection coefficients have been employed. However, the results are encouraging with regard to further exploration along these lines.

Research supported by NASA grant NAG5-7164.

References

- Axford, W. I., and McKenzie, J. F.: 1997, *Cosmic Winds and the Heliosphere*, (U. Arizona Press), p. 31.
- Barnes, A.: 1969, *Astrophys. J.*, **155**, 311.
- Belcher, J. W., and Davis, Jr., L.: 1971, *J. Geophys. Res.*, **76**, 3534.
- Bieber, J. W., Wanner, W., and Matthaeus, W. H.: 1996, *J. Geophys. Res.*, **101**, 2511.
- Galtier, S., Politano, H., and Pouquet, A.: 1997, *Phys. Rev. Lett.*, **79**, 2807.
- Grall, R. R., Coles, W. A., Klingsmith, M. T., Breen, A. R., Williams, P. J. S., Markkanen, J., and Esser, R.: 1996, *Nature*, **379**, 429.

- Grall, R. R., Coles, W. A., Spangler, S. R., Sakurai, T., and Harmon, J. K.: 1997, *J. Geophys. Res.*, **102**, 263.
- Habbal, S., Esser, R., Guhathakurta, M., and Fisher, R.: 1995, *Geophys. Rev. Lett.*, **22**, 1465.
- Hollweg, J. V., and Turner, J. M.: 1978, *J. Geophys. Res.*, **83**, 97.
- Hollweg, J. V.: 1996, in *Solar Wind Eight*, ed. D. Winterhalter, J. T. Gosling, S. R. Habbal, W. S. Kurth, and M. Neugebauer, (New York: AIP), p. 327.
- Holzer, T.: 1977, *J. Geophys. Res.*, **82**, 23.
- Hossain, M., Gray, P. C., Pontius, Jr., D. H., Matthaeus, W. H., and Oughton, S.: 1995, *Phys. Fluids*, **7**, 2886.
- Isenberg, P. A., and Hollweg, J. V. 1983, *J. Geophys. Res.*, **88**, 3923.
- Kennel, C. F., and Engelmann, F.: 1966, *Phys. Fluids*, **9**, 2377.
- Kinney, R., and McWilliams, J. C.: 1998, *Phys. Rev. E*, **57**, 7111.
- Kraichnan, R. H.: 1965, *Phys. Fluids*, **8**, 1385.
- Leamon, R. J., Smith, C. W., Ness, N. F., Matthaeus, W. H., and Wong, H. K.: 1998a, *J. Geophys. Res.*, **103**, 4775.
- Leamon, R. J., Matthaeus, W. H., Smith, C. W., and Wong, H. K.: 1998b, *Astrophys. J.*, **507**, L181.
- Leamon, R. J., Smith, C. W., Ness, N. F., and Wong, H. K.: 1999, *J. Geophys. Res.*, submitted.
- McKenzie, J., Banaszkiewicz, M., and Axford, W. I.: 1995, *Astron. Astrophys.*, **303**, L45.
- Matthaeus, W. H., Goldstein, M. L., and Roberts, D. A.: 1990, *J. Geophys. Res.*, **95**, 20673.
- Matthaeus, W. H., Bieber, J. W., and Zank, G. P.: 1995, *Rev. Geophys. Supp.*, **33**, 609.
- Matthaeus, W. H., Ghosh, S., Oughton, S., and Roberts, D. A.: 1996, *J. Geophys. Res.*, **101**, 7619.
- Matthaeus, W. H., Oughton, S., Ghosh, S., and Hossain, M.: 1998, *Phys. Rev. Lett.*, **81**, 2056.
- Matthaeus, W., Zank, G., and Oughton, S.: 1999, in *Solar Wind Nine*, in press.
- Montgomery, D. C.: 1982, *Physica Scripta*, **T2/1**, 83.
- Oughton, S., Priest, E. R., and Matthaeus, W. H.: 1994, *J. Fluid Mech.*, **280**, 95.
- Rowlands, J., Shapiro, V. D., and Shevchenko, V. I.: 1966, *Soviet Phys. JETP*, **23**, 651.
- Schwartz, S. J., Feldman, W. C., and Gary, S. P.: 1981, *J. Geophys. Res.*, **86**, 541.
- Shebalin, J. V., Matthaeus, W. H., and Montgomery, D.: 1983, *J. Plasma Phys.*, **29**, 525.
- Strauss, H. R.: 1976, *Phys. Fluids*, **19**, 134.
- Tu, C.-Y.: 1988, *J. Geophys. Res.*, **93**, 7.
- Tu, C.-Y., and Marsch, E.: 1995, *Space Sci. Rev.*, **73**, 1.
- Tu, C.-Y., and Marsch, E.: 1997, *Solar Phys.*, **171**, 363.
- Velli, M.: 1993, *Astron. Astrophys.*, **270**, 304.
- Zank, G. P., Matthaeus, W. H., and Smith, C. W.: 1996, *J. Geophys. Res.*, **101**, 17093.

Address for correspondence: Bartol Research Institute, University of Delaware, Newark, DE 19716

PROPERTIES OF CORONAL HOLE/STREAMER BOUNDARIES AND ADJACENT REGIONS AS OBSERVED BY SPARTAN 201

M. P. MIRALLES, L. STRACHAN, L. D. GARDNER, P. L. SMITH and J. L. KOHL
Harvard-Smithsonian Center for Astrophysics, Cambridge, MA 02138, USA

M. GUHATHAKURTA and R. R. FISHER
NASA Goddard Space Flight Center, Code 682, Greenbelt, MD 20771

Abstract. The Spartan 201 flights from 1993 to 1995 provided us with observations in H I Lyman- α of several coronal hole/streamer boundaries and adjacent streamers during the declining phase of the current solar cycle. Analysis of the latitudinal dependence of the line intensities clearly shows that there is a boundary region at the coronal hole/streamer interface where the H I Lyman- α intensity reaches a minimum value. Similar results are also found in UVCS/SOHO observations. We also discuss differences in the coronal hole/streamer boundaries for different types of streamers and their changes over the three year period of Spartan 201 observations.

1. Introduction

Coronal streamers have been studied for many years, yet we do not have an adequate three-dimensional picture which describes their morphology and physical conditions. Streamers overlie active regions as well as more stable regions like filaments in the case of helmet streamers. The slow speed solar wind is believed to originate in streamers (e.g., Gosling *et al.* 1981; Feldman *et al.* 1981), and also at the boundaries of the coronal hole according to observational results (Antonucci *et al.* 1997; Habbal *et al.* 1997) and theoretical models (Bravo *et al.* 1998; Neugebauer *et al.* 1998). The relative contribution of streamers and boundaries to the overall solar wind is still uncertain. The streamers and boundaries may be the key to understanding the physical causes of variations in the slow speed wind.

The study of ultraviolet emission lines adds enormously to our empirical knowledge of streamers. The Ultraviolet Coronal Spectrometer (UVCS) on Spartan 201 is designed for ultraviolet spectroscopy of the extended solar corona. UVCS/Spartan observes primarily the profile and intensity of H I Ly- α . By making scans in the radial direction at several position angles, UVCS/Spartan can be used to map the spectroscopic properties (intensities and line widths) of streamers from 1.5 to 3.5 R_{\odot} (from near the base of the arcade to the streamer cusp). The spectral line profiles of H I Ly- α in streamers provide direct measurement of the velocity distributions of neutral hydrogen along the line of sight. A preliminary comparison of UVCS/Spartan streamer/boundary observations at different stages of the current solar cycle is presented here.

2. Observations and Data Analysis

Streamer and boundary observations were made using the UVCS instrument (Kohl *et al.* 1994) aboard the Spartan 201 satellite during three flights, each one lasting



~ 40 hours. UVCS/Spartan measured the intensity and spectral line profile of H I Ly- α (1215.67 Å) in the solar corona during 11–13 April 1993, 12–14 September 1994, and 8–10 September 1995. Observations were made at projected heliocentric heights between 1.5 to 3.5 R_\odot . The shortest integration times were typically 1.0 minute (for 1.5 and 1.8 R_\odot) and the longest 8.5 minutes (for 3.5 R_\odot). The field of view of the entrance slit was 2.5×0.5 . The White Light Coronagraph (WLC) also aboard Spartan 201 provided polarized brightness observations that were co-registered with the UV spectroscopic observations.

Observations of a southeast (SE) streamer in 1993, a northeast (NE) streamer in 1994, and a southwest (SW) streamer in 1995, and their respective boundaries, are presented here. The data were corrected for detector background, cross-talk, and flat field. The detector characterization was consistent for all flights. The laboratory radiometric calibration indicates that the instrument has retained its sensitivity during the three missions (Gardner *et al.* 1998; Miralles *et al.* 1998). This allows us to make a reliable comparison of UVCS/Spartan data from 1993 to 1995.

To determine the “true” profile for the solar coronal radiation, each observed profile is fitted by the sum of two Gaussians. A narrow Gaussian, which has a $1/e$ half-width that is the same as the instrument profile (~ 0.18 Å), is normalized so that its intensity equals the net geocoronal H I Ly- α contribution. This consists of an exospheric emission minus an absorption component of the coronal H I Ly- α by exospheric hydrogen (see Withbroe *et al.* 1982). The emission component is based on UVCS/Spartan coronal observations at 3.5 R_\odot where geocoronal emission dominates. The second Gaussian is an approximation of the true coronal profile corrected for instrumental broadening assuming that the instrumental profile is Gaussian. Total integrated intensities are calculated from the corrected coronal profile.

3. Integrated Intensity Profiles vs. Position Angle

Figure 1 shows, in detail, H I Ly- α integrated intensity measurements for a subset of streamers and their boundaries observed by UVCS/Spartan between 1.8 and 3.5 R_\odot as function of position angle (hereafter PA). One streamer region from each Spartan 201 mission is shown. The uncertainty in the streamer intensities is lower than the boundary region intensities because the signal to noise ratios are better in the streamer.

In the case of the helmet streamer that was observed on the SE limb during the Spartan 201-01 flight, the H I Ly- α intensity drops sharply from the axis of the streamer ($PA = 120^\circ$ – 130°) toward the southern boundary ($PA \sim 160^\circ$), by about one and a half orders of magnitude. For example, the integrated intensity (in units of photons $s^{-1} cm^{-2} sr^{-1}$), plotted on a log scale, changes from 11.4 to 9.9 when going from the center of the helmet structure toward the boundary with the south coronal hole at 1.8 R_\odot . For each observed height, we found an intensity minimum ($PA = 132^\circ$ – 157°) near the boundary between the streamer and the south coronal hole. This intensity minimum seems to be outside of the streamer edge as observed

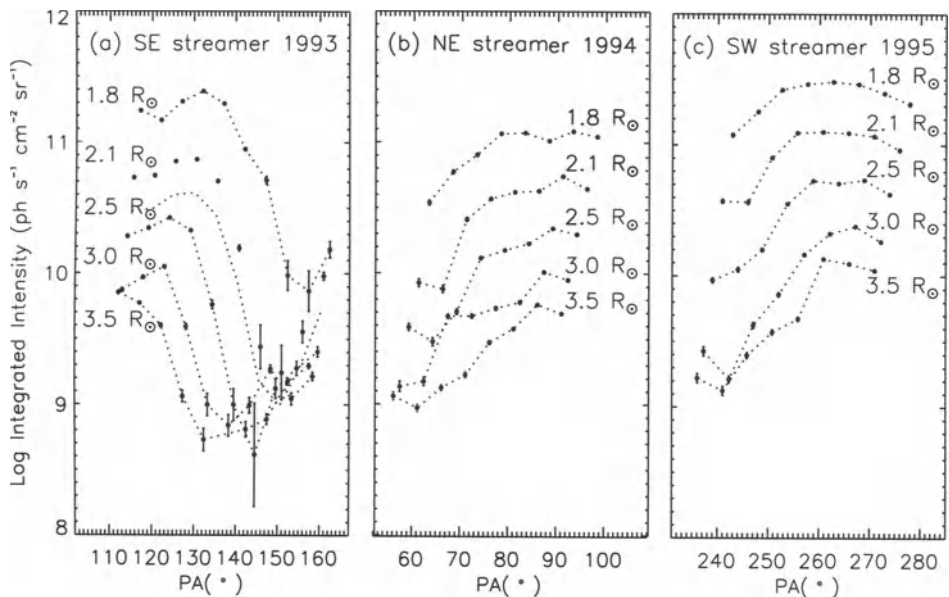


Figure 1. Variation of the logarithm of the integrated intensity as function of position angle (measured counterclockwise from the north heliographic pole) for selected streamers and their boundary regions observed during Spartan 201-01 (a), -02 (b), -03 (c).

in polarized brightness (pB) by the WLC/Spartan instrument (Guhathakurta and Fisher 1995). The north boundary ($\text{PA} \sim 115^\circ$) of the streamer is less well defined due to the presence of a second streamer in the NE.

Figure 1b shows the streamer observed above the NE limb during the Spartan 201-02 flight. There is a clear difference between the intensity profile of this streamer and the one observed in 1993. The 1994 NE streamer seems to present a combination of active region and quiescent streamer(s). More than one streamer axis was observed in this structure. The multiple axes could be due to one complex structure or the projections of separate streamers in the foreground and/or background (Miralles *et al.* 1999). The transition from the streamer axes (e.g., $\text{PA} = 86^\circ$ – 93°) to the north coronal hole ($\text{PA} \sim 50^\circ$) is less pronounced than the 1993 streamer, by about half an order of magnitude at a height of $1.8 R_{\odot}$. The intensity minimum ($\text{PA} = 61^\circ$ – 66°) in the boundary is also present for heliographic heights from 2.1 to $3.5 R_{\odot}$. WLC/Spartan pB data were not available for this flight.

Figure 1c shows that the intensity profiles of the streamer present on the SW limb during the Spartan 201-03 flight are similar to the ones observed in 1994. Multiple streamer axes are also present. The transition from the streamer axis (or maximum) ($\text{PA} = 265^\circ$ – 272°) toward the south coronal hole ($\text{PA} \sim 230^\circ$) presents about half an order of magnitude decrease in the intensity at a height of $1.8 R_{\odot}$. A minimum ($\text{PA} = 241^\circ$ – 245°) in the integrated intensity vs. polar angle is also observed for the scans at 2.1 to $3.5 R_{\odot}$.

4. Discussion

The H I Ly- α observations play a key role in providing information about the large scale coronal structure. Since the H I Ly- α intensity depends on electron temperature and outflow velocity as well as density, such observations provide information about those quantities. Recent observational results (Antonucci *et al.* 1997; Habbal *et al.* 1997) and theoretical models (e.g., Bravo *et al.* 1998) suggest that the slow wind at low latitude originates from the bordering regions of the coronal holes. The minima near the boundary of the observed streamers may be evidence of Doppler dimming caused by increasing outflow velocities. It might also be evidence for a reduced number of polar plumes along the line of sight.

Preliminary analysis of the Spartan 201 flight observations of mid-latitude solar coronal structures shows that different streamer orientations and types may influence the kind of transition found between the streamer and the coronal hole. The common features are a drop of the integrated intensity of about 0.5 to 1.5 orders of magnitude and the presence of an intensity minimum near the boundary region with the adjacent coronal hole for all the streamers observed during the three flights. The intensity minimum is more noticeable in 1993 than in the period closer to solar minimum (1994 and 1995). The 1993 streamer was a stable structure while the streamers in 1994 and 1995 were more variable and complex structures. The lowest intensity values in the boundaries occur at $3.0\text{--}3.5 R_{\odot}$, where the gradients in the intensity profiles are steeper. In general, the boundaries seem to expand away from the center of the coronal hole as a function of height. For example, in 1993 the intensity minimum changes by 25° (in PA) away from the coronal hole and in 1994 and 1995 the minimum changes by 5° .

Similar intensity minima are present in data taken with UVCS/SOHO during solar minimum (Figures 4 and 5 of Strachan *et al.* 1997; Figure 3 of Antonucci *et al.* 1997) when the dominant structure on the limb was a quiescent streamer. In the first case, the intensity minima in the boundary regions with the coronal holes are at heliographic latitudes of $\pm 40^{\circ}$. In the latter case, the intensity minimum in the boundary region with the south coronal hole is at PA = $110^{\circ}\text{--}115^{\circ}$. Such data typically show a latitudinal intensity variation of ~ 1 order of magnitude (H I Ly- α) and ~ 0.5 order of magnitude (O VI 1032) between the streamer belt and the coronal hole for latitudinal scans at heliographic heights of 1.75, 2.25, and $2.3 R_{\odot}$.

Additional analysis of the UVCS/Spartan Ly- α line profiles is required to determine the physical properties (densities, outflow velocities, and velocity distributions) of the boundaries before solar minimum that can be compared with results from UVCS/SOHO during and after solar minimum.

Further characterization is necessary to investigate if the streamer boundary properties found here depend on factors such as the sampling of the observations (5° intervals in PA) or possibly foreground/background coronal structures (like plumes, etc.) that intercept the line of sight.

Acknowledgements

This work is supported by NASA under grants NAG 5-613 and 5-3192 to the Smithsonian Astrophysical Observatory. M. G. and R. F. acknowledge grant from NASA suborbital research program of the Space Physics Division and NASA grant 5-2881 to the Catholic University of America.

References

- Antonucci, E., et al.: 1997, in *Fifth SOHO Workshop*, ESA SP-404, p. 175.
Bravo, S., Blanco-Cano, X., and Stewart, G. A.: 1998, in *Solar Wind Nine*, in press.
Feldman, W. C., et al.: 1981, *J. Geophys. Res.*, **86**, 5408.
Gardner, L. D., et al.: 1998, in preparation.
Gosling, J. T., et al.: 1981, *J. Geophys. Res.*, **86**, 5438.
Guhathakurta, M., and Fisher, R. R.: 1995, *Geophys. Res. Letters*, **22**, 1841.
Habbal, S. R., et al.: 1997, *Astrophys. J.*, **489**, L103.
Kohl, J. L., Gardner, L. D., Strachan, and Hassler, D. M.: 1994, *Space Sci. Rev.*, **70**, 253.
Miralles, M. P., et al.: 1998, *Applied Optics*, in preparation.
Miralles, M. P., et al.: 1999, in *Solar Wind Nine*, in press.
Neugebauer, M., et al.: 1998, *Geophys. Res. Letters*, **103**, 14587.
Strachan, L., et al.: 1997, in *Fifth SOHO Workshop*, ESA SP-404, p. 691.
Withbroe, G. L., Kohl, J. L., Weiser, H., and Munro, R. H.: 1982, *Space Sci. Rev.*, **33**, 17.

Address for correspondence: Mari Paz Miralles, Harvard-Smithsonian Center for Astrophysics, 60 Garden Street, Mail Stop 50, Cambridge, MA 02138, USA. Email: mmiralles@cfa.harvard.edu

CORONAL HEATING BY MAGNETIC EXPLOSIONS

R. L. MOORE, D. A. FALCONER, J. G. PORTER and S. T. SUESS
Marshall Space Flight Center/NASA, Email: ron.moore@msfc.nasa.gov

Abstract. From magnetic fields and coronal heating observed in flares, active regions, quiet regions, and coronal holes, we propose that exploding sheared core magnetic fields are the drivers of most of the dynamics and heating of the solar atmosphere, ranging from the largest and most powerful coronal mass ejections and flares, to the vigorous microflaring and coronal heating in active regions, to a multitude of fine-scale explosive events in the magnetic network, driving microflares, spicules, global coronal heating, and, consequently, the solar wind.

Key words: coronal heating, magnetic field, magnetic shear, magnetic explosion

The strongest coronal heating that happens on the Sun occurs transiently in flares in the strong magnetic fields rooted in and around sunspots (Moore *et al.* 1980; Moore 1990, 1992). Every flare is seated in an initially closed magnetic field configuration composed of either a single dipole or two or more impacted dipoles (Machado *et al.* 1988). Usually, the greater the flare energy release and heating in a flaring dipole, the greater the preflare store of nonpotential magnetic energy in the dipole. This energy is usually in the form of shear in the magnetic field along the neutral line in the core of the dipole (Moore and Rabin 1985; Moore 1988; Machado *et al.* 1988). In the frequently occurring situation of a small active dipole (having strong sheared core field) embedded in one polarity of a much larger passive dipole (having relatively little nonpotential magnetic energy), the flare event is of the type known as a surge, flaring arch, or X-ray jet (Tandberg-Hanssen 1977; Zirin 1988; Fontenla *et al.* 1991; Shibata 1998). In these events, energy release in the embedded sheared-core dipole injects energetic particles, multi-temperature plasma, and MHD disturbances up the impacted leg of a loop of the large passive dipole, strongly heating this loop so that it becomes much brighter in coronal X-ray images, but not as bright as the driving active dipole at its foot (Tang and Moore 1982; Machado *et al.* 1988). For any flare event rooted in a sheared-core dipole, whether or not the event is isolated and confined within that dipole or instead ejects a plasmoid (coronal mass ejection) or otherwise strongly disturbs the active dipole's surroundings, the total energy (in mass motion, energetic particles, and heat) of the event is plausibly supplied by an explosion (eruptive expansion and untwisting) of the sheared core field (Moore 1988, 1998). (See Moore and Rabin 1985; Moore *et al.* 1999, and references therein for discussion of the origin of sheared core fields and how they explode.)

Falconer *et al.* (1997) and Porter *et al.* (1998) have found that large, persistently bright coronal loops rooted in the outskirts of active regions stem from around islands of included polarity, and that the core fields encircling these islands are strongly sheared and continually microflare. From analysis of coronal X-ray images from the Yohkoh Soft X-ray Telescope and MSFC vector magnetograms, we have estimated the thermal and magnetic energetics of typical extended bright coronal



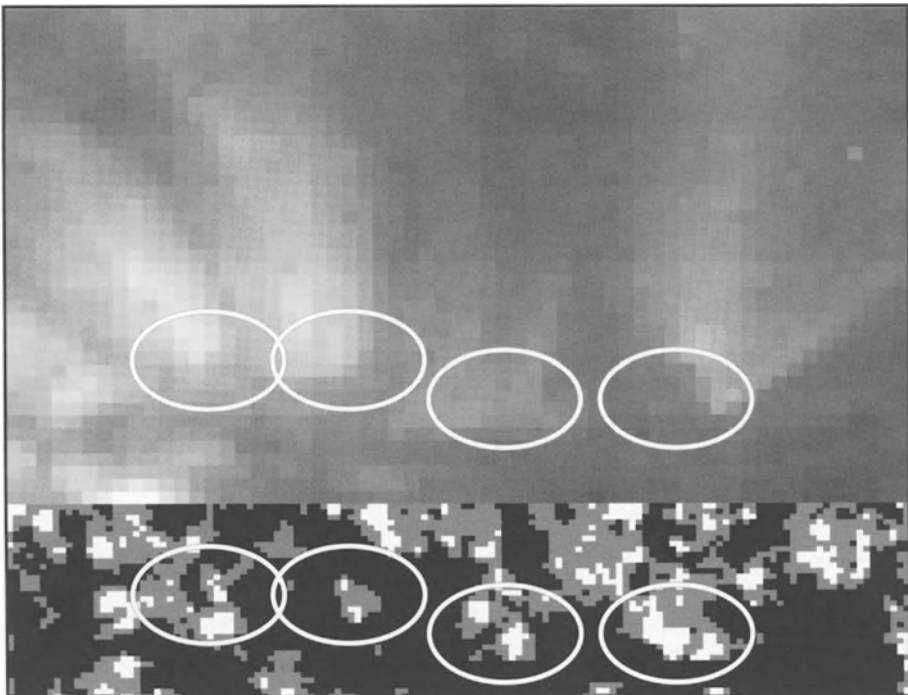


Figure 1. Nonpolar coronal plumes rooted around islands of positive (white) magnetic flux in an enhanced magnetic network of predominantly negative (black) polarity. *Top:* SOHO/EIT Fe XII coronal image showing four bright plume clusters rooted in the diffused remnant magnetic flux from decayed active regions. *Bottom:* Magnetic polarity map derived from an NSO/Kitt Peak magnetogram taken a few hours before the coronal image. Each circle is about the size of a supergranule, encloses the foot of a plume cluster in the coronal image, and has the same heliographic location in the magnetic map. The similarity of the appearance of these nonpolar plumes to polar plumes and to giant loops arising from active regions, and the similar magnetic rooting of all these enhanced extended coronal features at sites of mixed polarity, suggest that all are heated in the same way via active core fields at their feet.

loops and the microflares in the sheared core fields at their feet (Moore *et al.* 1999). We find (1) that the sheared core fields have enough nonpotential magnetic energy to supply the coronal heating within themselves and in the large coronal loops stemming from them for about a day, a typical time scale for buildup of core-field shear in active regions, and (2) that the energy can be released via a staccato of magnetic micro-explosions in the core fields—one micro-explosion for each microflare—each being an expansion and/or untwisting of the microflaring strand of core field of only a few percent at most. Thus, we find that it is energetically feasible for low-lying, microflaring, sheared core fields to drive all of the enhanced coronal heating in active regions and in the large coronal loops extending out of active regions.

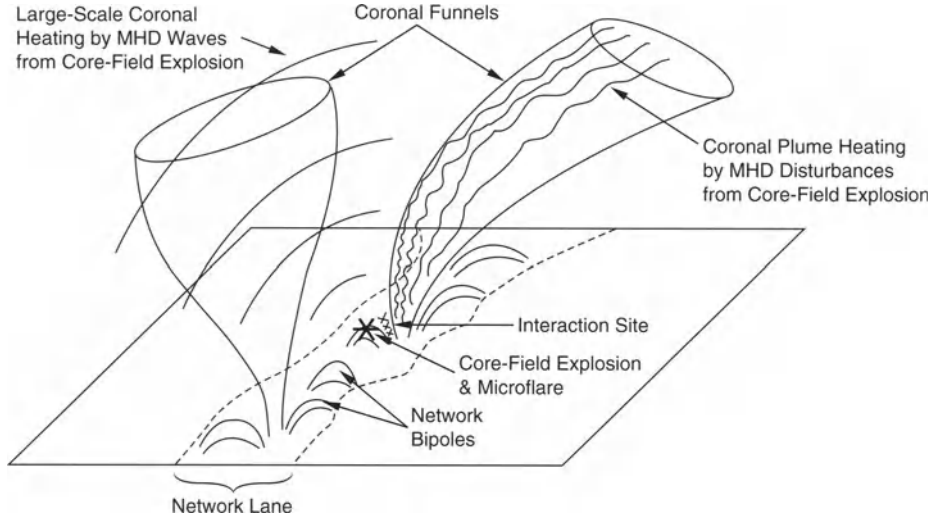


Figure 2. Depiction of our scenario for heating the coronal network and the extended corona in quiet regions and coronal holes by core-field explosions low in the magnetic network (modified from Porter and Moore 1988).

Porter *et al.* (1987) found that the magnetic network in quiet regions is continually thickly populated by localized microflares, and that each network microflare is seated on a network neutral line, i.e., in a network core field. Wang *et al.* (1997) have shown that polar coronal plumes in coronal holes are rooted in mixed-polarity magnetic flux concentrations. Figure 1 shows an example of nonpolar coronal plumes rooted around islands of included polarity in a region of enhanced magnetic network. Falconer *et al.* (1998a, 1998b) have found that at the base of the quiet corona there is a faint coronal network rooted in the magnetic network, that small coronal bright points sit on neutral lines in the magnetic network, and that (averaged over regions larger than a supergranule) where the magnetic network has enhanced magnetic flux, both the coronal network and the extended corona have enhanced brightness. These observational results for quiet regions and coronal holes, along with our above cited quantitative estimates of the coronal heating energetics in active regions, suggest, as sketched in Figure 2, that exploding sheared core fields seated on neutral lines low in the magnetic network are the main drivers of both the numerous fine-scale explosive events (including spicules) in the network and the extended coronal heating in quiet regions and coronal holes.

Acknowledgements

This work is supported by NASA's Office of Space Science by funding through its Solar Physics Branch.

References

- Falconer, D. A., Moore, R. L., Porter, J. G., Gary, G. A., and Shimizu, T.: 1997, *Ap.J.*, **482**, 519.
- Falconer, D. A., Moore, R. L., Porter, J. G., and Hathaway, D. H.: 1998a, *Ap.J.*, **501**, 386.
- Falconer, D. A., Moore, R. L., Porter, J. G., and Hathaway, D. H.: 1998b, "Large-Scale Coronal Heating, Clustering of Coronal Bright Points, and Concentration of Magnetic Flux," this volume.
- Fontenla, J. M., Svestka, Z., Farnik, F., and Tang, F. Y.: 1991, *Solar Phys.*, **134**, 145.
- Machado, M. E., Moore, R. L., Hernandez, A. M., Rovira, M. G., Hagyard, M. J., and Smith, J. B., Jr.: 1988, *Ap.J.*, **326**, 425.
- Moore, R., et al.: 1980, in *Solar Flares*, ed. P. A. Sturrock, (Boulder: Colorado Associated University Press), 341.
- Moore, R. L.: 1988, *Ap.J.*, **324**, 1132.
- Moore, R. L.: 1990, *Memorie della Societa Astronomica Italiana*, **61** (2), 317.
- Moore, R. L.: 1992, in *The Astronomy and Astrophysics Encyclopedia*, ed. S. P. Maran, (Van Nostrand Reinhold: New York), 637.
- Moore, R.: 1998, "Solar Prominence Eruption," in *Encyclopedia of Astronomy and Astrophysics*, (Institute of Physics Publishing: London), in press.
- Moore, R. L., Falconer, D. A., Porter, J. G., and Suess, S. T.: 1999, "On Heating the Sun's Corona by Magnetic Explosions: Feasibility for Active Regions and Prospects for Quiet Regions and Coronal Holes," *Ap.J.*, submitted.
- Moore, R., and Rabin, D.: 1985, *Ann. Rev. Astron. Astrophys.*, **23**, 239.
- Porter, J. G., Falconer, D. A., and Moore, R. L.: 1998, in *Solar Jets and Coronal Plumes*, ESA 421, ed. T.-D. Guyene (ESA Publ. Div., ESTEC: Noordwijk), 147.
- Porter, J. G., and Moore, R. L.: 1988, in *Solar and Stellar Coronal Structure and Dynamics*, ed. R. C. Altrock (National Solar Observatory: Sacramento Peak Observatory, Sunspot, New Mexico), 125.
- Porter, J. G., Moore, R. L., Reichmann, E. J., Engvold, O., and Harvey, K. L.: 1987, *Ap.J.*, **323**, 380.
- Shibata, K.: 1998, in *Solar Jets and Coronal Plumes*, ESA 421, ed. T.-D. Guyenne (ESA Publ. Div., ESTEC: Noordwijk), 137.
- Tandberg-Hanssen, E.: 1977, in *Illustrated Glossary for Solar and Solar-Terrestrial Physics*, ed. A. Bruzek and C. J. Durrant (Dordrecht: Reidel), 97.
- Tang, F., and Moore, R. L.: 1982, *Solar Phys.*, **77**, 263.
- Wang, Y.-M., et al.: 1997, *Ap.J.*, **484**, L75.
- Zirin, H.: 1988, *Astrophysics of the Sun* (Cambridge University Press: Cambridge), 278.

SOHO OBSERVATIONS OF DENSITY FLUCTUATIONS IN CORONAL HOLES

L. OFMAN

Raytheon ITSS and NASA GSFC, Code 682, Greenbelt, MD 20771, USA

M. ROMOLI and G. NOCI

Dept. of Astronomy, University of Florence, Largo Fermi 5, I-50125 Florence, Italy

G. POLETTA

Arcetri Observatory, Largo Fermi 5, I-50125 Florence, Italy

J. L. KOHL

Harvard Smithsonian CfA, 60 Garden St, Cambridge, MA 02138, USA

R. A. HOWARD

Naval Research Lab., Code 7660, Washington, DC 20375, USA

C. ST. CYR

Naval Research Lab and NASA GSFC, Code 682, Greenbelt, MD 20771, USA

C. E. DEFOREST

Stanford University and NASA GSFC, Code 682, Greenbelt, MD 20771, USA

Abstract. In recent UVCS/SOHO White Light Channel (WLC) observations we found quasi-periodic variations in the polarized brightness (pB) in the polar coronal holes at heliocentric distances of 1.9 to 2.45 solar radii. The motivation for the observation is the 2.5D MHD model of solar wind acceleration by nonlinear waves, that predicts compressive fluctuations in coronal holes. In February 1998 we performed new observations using the UVCS/WLC in the coronal hole and obtained additional data. The new data corroborate our earlier findings with higher statistical significance. The new longer observations show that the power spectrum peaks in the 10–12 minute range. These timescales agree with EIT observations of brightness fluctuations in polar plumes. We performed preliminary LASCO/C2 observations in an effort to further establish the coronal origin of the fluctuations.

1. Introduction

The exact mechanism that provides the additional momentum input necessary to obtain the high speed solar wind streams is still unknown. A possible source of the additional acceleration in coronal holes are nonlinear MHD waves that must get their energy from photospheric motions.

Recently Ofman and Davila (1997a, 1997b, 1998) have developed a self-consistent nonlinear 2.5D MHD model of solar wind acceleration by waves and found that nonlinear compressional MHD waves are generated in a model coronal hole via Alfvén waves. These waves contribute to solar wind acceleration and can account for the additional energy input required to obtain the high-speed solar wind streams.

A viable observational goal is to test the above model by detecting the presence (or absence) of compressional waves in the solar wind. The detection of waves can be accomplished by observing time-dependent density fluctuations and determining



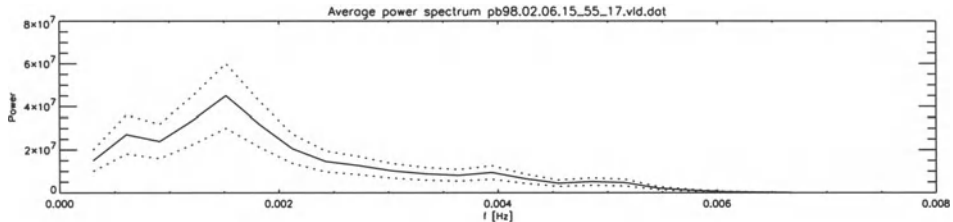


Figure 1. Power spectrum of the pB obtained with the WLC on 6 February 1998 in the south coronal hole interplume region.

whether the amplitude and propagation speed of these waves are consistent with the model predictions.

We present the results from the SOHO UVCS White Light Channel (WLC) (Kohl *et al.* 1995, 1997) that indicate the presence of density fluctuations in a polar coronal hole—a possible signature of compressional waves (Ofman *et al.* 1997, 1998). We discuss EIT and LASCO observations.

2. Observational results

The first WLC observation of the milliHertz frequency density fluctuations far from the solar limb (in the range $1.9\text{--}2.45 R_{\odot}$) obtained in February 1997 were confirmed by longer observations in February 1998. Recent observations with EIT in plumes and LASCO C2 in coronal holes show signatures of compressional waves in the milliHertz range that support the WLC observations.

Each WLC observing sequence was 3 to 10 hours long and consisted of alternating exposures of 45 s or 60 s at two different polarizer positions that correspond to tangent and radial directions. Two polarizer positions are enough to determine the polarized brightness (pB) in the assumption that the polarization angle is known. The corona-K polarization plane is tangent to the limb, to a good approximation.

Several of the WLC observing sequences exhibit spectra of fluctuations in pB with distinct peaks in the power spectrum. The fluctuations in pB may indicate possible periodicities consistent with the presence of nonlinear compressional waves propagating in the coronal hole.

WLC observations in February 1998 confirm the presence of the low frequency fluctuation found by Ofman *et al.* (1997, 1998). In Figure 1 we show the results of an FFT power spectrum of the pB fluctuations observed by the WLC on 6 February 1998 in the south coronal hole interplume region. The largest peak in Figure 1 appears at a frequency of 1.5 mHz or a period of 11 minutes with additional smaller peaks at about 0.6 mHz. The dashed lines show the confidence intervals of the power spectrum obtained by dividing the observing sequence into nine segments and computing the power spectrum of each windowed segment.

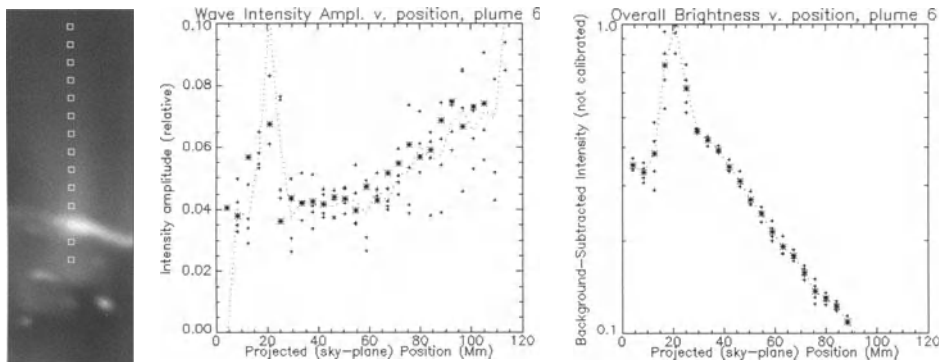


Figure 2. EIT observations of waves in a plume (see text).

On 20 and 24 March 1998 we obtained a sequence of high cadence LASCO C2 observations over a limited part of its field of view. The images were taken at a cadence of ~ 90 s for about two hours. The images were recalibrated to eliminate the effects of small exposure variations, and difference movie sequences were generated. The movies show evidence of outward propagating small scale structures.

We obtained time-series of brightness fluctuations in various part of the LASCO C2 images and performed a power spectrum analysis. To increase the statistical confidence of the power spectra we averaged the power spectra of 9 adjacent pixels at each observational location. Preliminary analysis of the images shows fluctuations with strong peaks at 5–20 minutes. The power spectra peaks are about 2–3 times stronger than the background noise in the spectrum. Longer sequences of high cadence observations are needed to improve the statistical significance of the LASCO C2 observations.

DeForest and Gurman (1998) demonstrated that there are coherent outwardly propagating brightness structures that propagate at ~ 75 – 150 km s $^{-1}$ and recur quasi-periodically on timescales of ~ 10 – 15 minutes. Ofman, Nakariakov, and DeForest (1999) identified these fluctuations as slow magnetosonic waves.

In Figure 2 we show the background-subtracted intensity dependence on the height in a plume observed by EIT (right panel) and the relative wave amplitude dependence on the height in the plume (left panel). The relative wave amplitude was calculated by subtracting the intensity fluctuations from the smoothed intensity and dividing by the intensity. The data are plotted with asterisks; the estimates of the upper and the lower limits are marked by crosses. Half the locations of the observations in the plume are marked by the squares in the plume image. It is evident that the relative wave amplitude in the plume increases with height. This increase is in qualitative agreement with the theory of slow magnetosonic waves in gravitationally stratified magnetized atmosphere (Ofman, Nakariakov, and DeForest 1999).

3. Conclusions

Observations with the UVCS WLC indicate that the density in a coronal hole at $1.9 R_{\odot}$ fluctuates on a time scale of about 10–12 minutes, with possibly longer time scale fluctuations. It is likely that these fluctuations are generated by compressional waves propagating from the Sun.

Observations with EIT show that there are magnetosonic waves low in the plumes (up to $1.3 R_{\odot}$). The observations agree with theoretical properties of slow magnetosonic waves (Ofman, Nakariakov, and DeForest 1999). LASCO C2 observation indicate the presence of fluctuations in the 5–20 minute range farther in the corona. Longer observations are needed to improve the statistical significance of the LASCO results.

The UVCS, EIT, and LASCO observations strongly suggest that low frequency compressional waves are present throughout the coronal holes. These waves are possible signatures of the heating and fast solar wind acceleration mechanisms.

References

- DeForest, C. E., and J. B. Gurman: 1998, *Astrophys. J.*, **501**, L217.
Kohl, J. L. *et al.*: 1995, *Sol. Phys.*, **162**, 313.
Kohl, J. L. *et al.*: 1997, *Sol. Phys.*, **175**, 613.
Ofman, L., Davila, J. M.: 1997a, *Astrophys. J.*, **476**, 357.
Ofman, L., Davila, J. M.: 1997b, *Astrophys. J.*, **476**, L51.
Ofman, L., Davila, J. M.: 1998, *J. Geophys. Res.*, **103**, 23677.
Ofman, L., Romoli, M., Poletto, G., Noci G., Kohl, J. L.: 1997, *Astrophys. J.*, **491**, L111.
Ofman, L., Romoli, M., Poletto, G., Noci G., Kohl, J. L.: 1998, *Astrophys. J.*, **507**, L189.
Ofman, L., Nakariakov, V., and DeForest, C. E.: 1999, *Astrophys. J.*, in press.

Address for correspondence: L. Ofman, NASA GSFC, Code 682, Greenbelt, MD 20771, USA

OUTFLOW VELOCITIES AT THE BASE OF A POLAR CORONAL HOLE DURING THE 1998 TOTAL ECLIPSE

S. PATSOURAKOS and J.-C. VIAL

I.A.S., Université Paris XI-CNRS, Bât 121, 91405 Orsay Cedex, France

J.-R. GABRYL

Observatoire Royal De Belgique, Avenue Circulaire 3, 1180 Bruxelles, Belgium

S. KOUTCHMY

I.A.P., CNRS, 98 Bis Bd Arago, 75014 Paris, France

U. SCHÜHLE

Max-Planck-Institut fur Aeronomie, D-37189 Katlenburg-Lindau, Germany

Abstract. Polar coronal holes represent the most convincing site from which the high-speed solar wind originates. Here we report high-accuracy Doppler shifts measured in the O VI (1037.6 Å) line obtained by SUMER on SOHO inside an interplume region within the south polar coronal hole. We infer limits on the outflow velocity and draw hints about the flow geometry.

Key words: Sun, corona, coronal holes, flows

1. Introduction

Polar coronal holes are the birth-place of the permanent fast solar wind. They are characterized by essentially open field-lines as well as electron densities and temperatures lower than in the quiet regions. Coronal holes are made of two components: bright threads presumably rooted at the boundaries of the chromospheric network, known as polar plumes (e.g., DeForest *et al.* 1997), and dark lanes which fill the interplume volume. However, there exists some controversy on the kind of structure—plume, interplume, or both—that gives rise to the observed outflow above 1 R_s (e.g., Hassler *et al.* 1997, and references herein).

A precise knowledge of the physical conditions at the coronal hole base is of vital importance for constructing realistic wind models. For example, it is very important to know the outflow velocity and the flow geometry at low heights within the corona. This, among others, could provide the variation with distance of the solar wind velocity.

In order to tackle these issues we carried out a synergetic program involving the SUMER spectrometer on board SOHO and eclipse observations performed during the 26 February 1998 total solar eclipse. Here we report some results of the SUMER part of this investigation. This paper has the following organization: in Section 2 we briefly describe our observations, and Section 3 contains some preliminary results and our conclusions.

2. Observations and Data Reduction

In order to derive flow velocities at coronal temperatures we used the SUMER spectrometer on board SOHO (Wilhelm *et al.* 1995). Our observations were carried



Space Science Reviews 87: 291–294, 1999.

©1999 Kluwer Academic Publishers.

out on 26 February 1998 (the day of the 1998 total eclipse) from 19:21–19:46 UT with the center of the $0.3'' \times 120''$ slit at $(0'', -970'')$ within the south polar coronal hole. Our dataset includes 16 readouts of SUMER's detector with an exposure time of 90 s in the wavelength range 1020–1060 Å. The superimposition of the SUMER slit on a Fe IX/X EIT (171 Å) image taken the same day at 21:00 UT led us to conclude that we observed in an interplume region.

Before further analysis, corrections accounting for inhomogeneities of the detector response (flat field), geometric distortion of detector images (destretching), and finally conversion of the obtained count-rates into physical units (intensity calibration) have been applied (Wilhelm *et al.* 1997).

The well-known O VI limb brightening permitted us to determine the photospheric limb position at pixel 63 along the slit. We determined the stray light contribution to the O VI signal by using an identical sequence carried out just after our actual observations at $(0'', -1500'')$. For this we assumed that at the given position, the O VI signal is dominated by the stray light and that the stray light ratio of O VI and the nearby chromospheric C II 1036 Å line is constant. The stray light has been found to amount to $\simeq 9\%$ of the observed O VI signal and it has been neglected.

Since there is no wavelength reference on SUMER we made use of 5 O I lines at 1027.4307, 1028.4307, 1028.1571, 1039.2304, 1040.9425, and 1041.6876 Å for determining the dispersion relation, assuming that those chromospheric lines are not Doppler shifted. Since these lines are relatively faint we produced a time and space averaged profile and via a Gaussian fit we calculated the line centers of these 5 lines. The dispersion relation was then derived by fitting the calculated line center positions to the corresponding laboratory wavelengths with a linear relation.

By fitting the time-averaged O VI 1037 Å profiles at each spatial position with a Gaussian, we derived (via the dispersion relation) the solar wavelengths λ_{sol} for each of them. Doppler velocities have been obtained by the relation $v_{\text{dopp}} = c \Delta\lambda/\lambda_{\text{sol}}$, where $\Delta\lambda$ is the difference between λ_{sol} and the laboratory wavelength λ_{lab} of the line.

The uncertainties on the Doppler velocities are of the order of 1.5–2 km/s, which is the average deviation between the calculated and the corresponding laboratory wavelengths. However, this number should be better for the O VI line because of its much higher photon statistics.

3. Results and Conclusions

On the disk (Figure 1a) there is no signature of an outflow. The sudden increase of velocity around pixel 15 is due to an explosive event which is the subject of an ongoing study. Outside the limb the O VI line is red-shifted.

In Figure 1b one can readily distinguish three different regimes of the O VI doublet ratio. Inside the disk, the ratio is about 2 (with the exception of some pixels

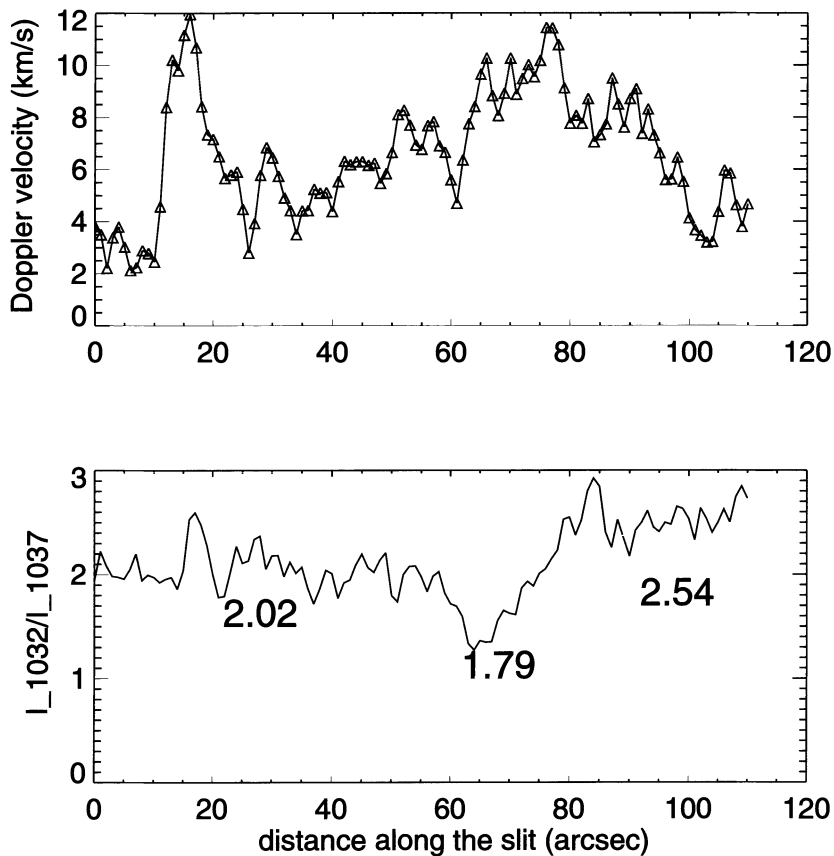


Figure 1. Variation of (a) the Doppler velocity (*top*), and (b) the O VI 1032 to 1037 Å intensity ratio (*bottom*), with distance along the slit (pixel 63 corresponds to the photospheric limb).

around pixel 15 which belong to the observed explosive event); from the limb until about pixel 75 it is lower than 2; and finally for the rest of the slit it is significantly larger than two. The dip of the intensity ratio at the limb could be seen as an indirect confirmation of our limb-position determination.

The observed interplume region seems to contain predominantly plasma flowing at relatively low velocities ($\simeq 7$ km/s along the line of sight [l.o.s.]) away from SOHO. This could be interpreted as a hint that the major part of the interplume lies behind the plane of the sky, and consequently that we observe plasma flowing out of the Sun. We note here that interplumes have been proposed by various authors as the main source of the solar wind in coronal holes (e.g., Hassler *et al.* 1997, and references herein).

The O VI intensity ratio of about 2 on the disk indicates collisionally dominated emission (e.g., Kohl and Withbroe 1982) while values lower than 2 close to the limb

indicate that the two lines are optically thick and thus any conclusion concerning outflows should be considered cautiously.

For the outer region (pixels 75–110) the derived ratio of $\simeq 2.5$ implies an optically thin emission. Moreover, the radiative contribution to line formation is important and comes into play close to the disk indeed. This ratio value is about the same as the one observed at about $1.5 R_s$ by UVCS (see for example Figure 5 in Poletto *et al.* 1998). Doppler dimming (e.g., Kohl and Withbroe 1982) gives at these distances (e.g., Figure 8 in Poletto *et al.* 1998) low radial solar wind velocities of the order of 20–40 km/s. Thus we can put limits on the outflow velocity. The lower limit is when considering only the l.o.s. velocity of about 7 km/s. An upper limit can be derived by combining the observed l.o.s. velocity with the above mentioned radial velocity at $1.5 R_s$, which gives a value of 40.6 km/s. In the second case one finds a significant inclination angle (~ 10 degrees). This inclination angle is opposite to the B_0 angle of the Sun. So, if we assume that the l.o.s. is not “polluted” by emission from non-coronal hole regions, this means that the mass flow in the polar interplume region in question is inclined by (at least) 10 degrees with respect to the radial direction.

As a next step, we plan to use the electron densities derived from our eclipse observations in order to deduce the flux of matter at the coronal base. It is also appealing to see how our observations compare with in-situ ones.

4. Acknowledgements

The work of S. Patsourakos is financed by the ERB4001GT964067 contract of the EU Training and Mobility of Researchers program. The SUMER project is financially supported by DARA, CNES, NASA and the ESA Prodex program (Swiss contribution). SOHO is a mission of international cooperation between ESA and NASA.

References

- DeForest, C. E., Hoeksema, J. T., Gurman, J. B., Thompson, B., Howard, R., Plunkett, S., P., Harrison, R., and Hassler, D. M.: 1997, *Solar Phys.*, **175**, 375.
- Hassler, D., M., Wilhelm K., Lemaire, P., and U., Schühle.: 1997, *Solar Phys.*, **175**, 349.
- Kohl, J. L., and Withbroe G. L.: 1982, *Astrophys. J.*, **256**, 263.
- Poletto, G., Corti, G., Romoli, M., Kohl, J. L., and Noci, G.: 1998, in *Proc. Solar Jets and Coronal Plumes*, ESA 421, 69.
- Wilhelm, K., Curdt, W., Marsch, E., Schühle, U., Gabriel, A.-H., Lemaire, P., Vial, J.-C., Grewing, M., Timothy, J. G., and Siegmund, O. H. W.: 1995, *Solar Phys.*, **162**, 189.
- Wilhelm, K., Lemaire, P., Curdt, W., Schühle, U., Marsch, E., Poland A. I., Jordan, SD. D., Thomas, R. J., Hassler, D. M., Huber, M. C. E., Vial, J.-C., Kühne, M., Siegmund, O. H. W., Gabriel, A., Timothy, J. G., Grewing, M., Feldman, U., Hollandt, J., and Brekke, P.: 1997, *Solar Phys.*, **170**, 75.

VELOCITY SHEAR INDUCED PHENOMENA IN SOLAR ATMOSPHERE

S. POEDTS* and A. D. ROGAVA **

CPA, K. U. Leuven, Celestijnenlaan 200B, 3001 Heverlee, Belgium

S. M. MAHAJAN ***

Inst. for Fusion Studies, The Univ. of Texas at Austin, Austin, TX 78712, USA

Abstract. We present a brief overview of the probable velocity-shear induced phenomena in solar plasma flows. Shear-driven MHD wave oscillations may be the needed mechanism for the generation of solar Alfvén waves, for the transmission of fast waves through the transition region, and for the acceleration of the solar wind.

Key words: shear flow, linear MHD, non-modal analysis

Recently, the non-modal analysis of shear flows has revealed some non-exponential effects, induced by the sheared character of plasma (fluid) motion, that have been overlooked in the classical normal mode approach: (1) waves acquire a slow (adiabatic) temporal variation of their frequencies (Chagelishvili *et al.* 1994), and compressible waves can extract/add energy from/to the mean flow; (2) waves become coupled and their reciprocal transformations take place in the flows sustaining $n > 1$ modes of wave motion (Chagelishvili *et al.* 1996); (3) nonperiodic patterns (“shear vortices”) arise, characterized by vortical motions of plasma particles (Rogava *et al.* 1998); (4) in moderate and high shear flows, vortex-wave conversion processes can occur (Chagelishvili *et al.* 1997).

The solar atmosphere seems to provide a fertile ground for the appearance of these processes; the solar wind, corona, transition region, and chromosphere are observed to be in constant oscillatory, transient, and/or *systematic* motion with essentially sheared rates (Pneuman and Orrall 1986). Thus the velocity shear induced effects may play an important, possibly dominant, role in the generation of solar MHD waves and the acceleration of the solar wind. In Poedts *et al.* (1998) we made a first attempt to study this broad unexplored area. A rather simple physical model was taken: we assumed a uniform magnetized plane slab plasma, embedded in a constant magnetic field $\mathbf{B}_0 = B_0 \mathbf{e}_z$, and flowing along the magnetic field with a linear velocity profile, $\mathbf{V}_0 = Ax \mathbf{e}_z$. Small perturbations in this model shear flow obey the following linearized MHD equations:

$$(\partial_t + Ax\partial_z)\hat{d} + \nabla \cdot \mathbf{u} = 0, \quad \nabla \cdot \mathbf{b} = 0, \quad (1)$$

$$(\partial_t + Ax\partial_z)u_i = -V_s^2 \partial_i \hat{d} + V_A^2 [\partial_z \hat{b}_i - \partial_i \hat{b}_z], \quad (2a)$$

* Research Associate of the Fund for Scientific Research, Flanders (Belgium)

** On leave from Abastumani Astrophysical Observatory and Department of Physics, Tbilisi State University, Tbilisi, Rep. of Georgia

*** Abdus Salam International Centre for Theoretical Physics, 34014 Trieste, Italy



$$(\partial_t + Ax\partial_z)u_z = -V_s^2\partial_z\hat{d} - Au_x, \quad (2b)$$

$$(\partial_t + Ax\partial_z)\hat{b}_i = \partial_z u_i, \quad (3)$$

where $i = x, y$ denotes the longitudinal components of the vector quantities, while the constants V_s and V_A refer to the sound and the Alfvén speeds, respectively. Following the standard path of the nonmodal method (Chagelishvili *et al.* 1994, 1996) we affect a change of variables: $x' = x, y' = y, z' = z - Axt, t' = t$, then take a *spatial* Fourier transformation of the perturbed quantities $F = \int \hat{F}(\mathbf{k}) \exp(i\mathbf{k} \cdot \mathbf{x}') d\mathbf{k}$ and reduce the problem to the analysis of linear *ordinary* differential equations governing the *nonexponential* temporal dynamics of perturbations, affected by the nonzero shearing ($A \neq 0$) of the flow. We adopted the dimensionless variables $D \equiv i\hat{d}$, $b_x \equiv i\hat{b}_x$, $b_y \equiv i\hat{b}_y$, $R \equiv A/(V_A k_{x'})$, $\varepsilon \equiv V_s/V_A$, $\tau \equiv V_A k_{x'} t'$, $K_x(\tau) \equiv k_{x'}/k_{z'} - R\tau \equiv K_0 - R\tau$, $K_y \equiv k_{y'}/k_{z'}$, $v_i \equiv u_i/V_A$ ($i = x, y, z$); introduced an auxiliary function $\hat{\psi} \equiv D + K_x(\tau)b_x + K_y b_y$, and reduced the problem to three coupled, second-order ordinary differential equations:

$$\hat{\psi}^{(2)} + \omega_1^2 = \mathcal{C}_1(\tau)b_x + \mathcal{C}_2 b_y, \quad (4a)$$

$$b_x^{(2)} + \omega_2^2(\tau)b_x = \mathcal{C}_1(\tau) + \mathcal{C}_3(\tau)b_y, \quad (4b)$$

$$b_y^{(2)} + \omega_3^2 b_y = \mathcal{C}_2 + \mathcal{C}_3(\tau)b_x, \quad (4c)$$

with $\omega_1 \equiv \varepsilon$, $\omega_2^2(\tau) \equiv 1 + (1 + \varepsilon^2)K_x^2(\tau)$, $\omega_3^2 \equiv 1 + (1 + \varepsilon^2)K_y^2$, $\mathcal{C}_1(\tau) \equiv \varepsilon^2 K_x(\tau)$, $\mathcal{C}_2 \equiv \varepsilon^2 K_y$, and $\mathcal{C}_3(\tau) \equiv -(1 + \varepsilon^2)K_y K_x(\tau)$.

We heavily exploited the notable analogy of this system with that of coupled linear oscillators (Rogava *et al.* 1998; Poedts *et al.* 1998) and considered two specific subclasses (FMW-AW and FMW-SMW) of the MHD wave transformation phenomena. The effectiveness of the *FMW-AW transformations* in a cold (“zero- β ,” $\epsilon = 0$) plasma (Figure 1a shows corresponding dispersion curves) depends mainly on the wave characteristics (K_0 and K_y) and *not explicitly* on the intrinsic physical characteristics of the flow (Poedts *et al.* 1998). Figure 1b displays the solution for $b_y(\tau)$; the conversion of an initially pure FMW (fast magnetosonic wave) into an AW (Alfvén wave) around the time $\tau = \tau_* \equiv K_0/R$ is visible. We found that the initial FMW was only partially converted into the AW. Transformations are quite abrupt with a time-scale of the order of R^{-1} .

The shear-induced coupling generally allows for *mutual* wave transformations (Rogava *et al.* 1998), i.e., the opposite transformation regime (AW-FMW) is also realized. Figure 1c is an illustration of this process.

As regards *FMW-SMW transformations*, for two-dimensional ($K_y = 0$) perturbations it was shown (Poedts *et al.* 1998) that effective transformations of FMW to SMW (slow magnetosonic waves) should happen in those regions of the solar wind where the magnetic and the acoustic Mach numbers are approximately equal, i.e., where $V_A \simeq V_s$ ($\varepsilon \simeq 1$). We presented estimates showing that the conditions for FMW-SMW transformations are favorable beyond ~ 0.5 AU.

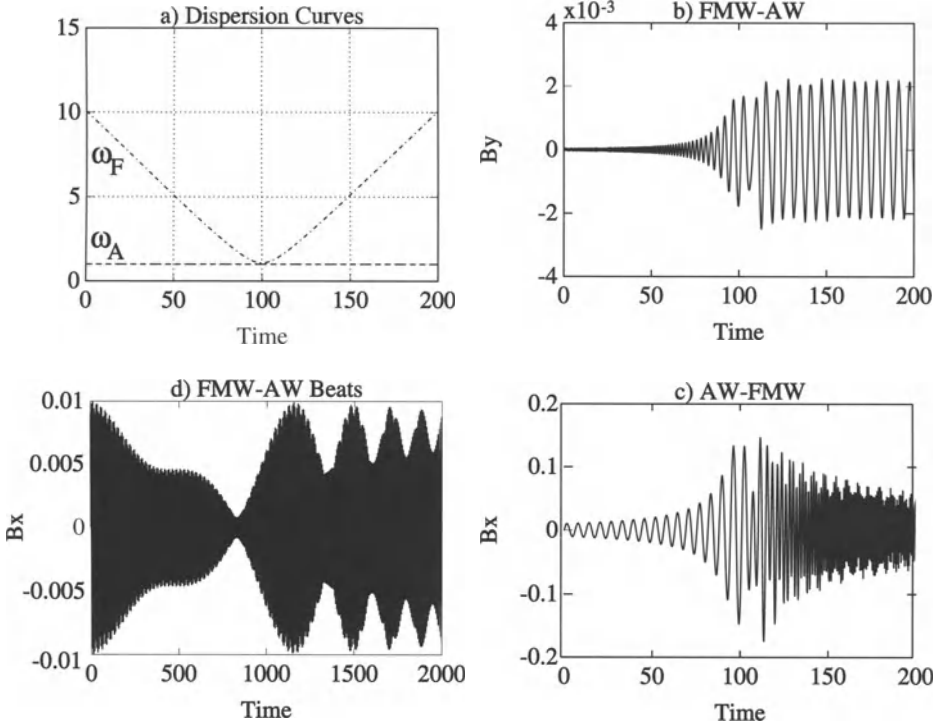


Figure 1. Examples of velocity shear induced processes (see text).

We found that the velocity shear induces yet another impressive phenomenon: the excitation of *beat modes*. Like in the hydrodynamical case (Rogava and Mahajan 1997), this regime is realized when $R \ll K_0 \ll 1$ for both the cold plasma example (FMW-AW case) and in the 2-D setup (FMW-SMW case with $\varepsilon \simeq 1$). A representative example of such a solution (FMW-AW case) is shown in Figure 1d for $K_0 = K_y = 0.1$, and $R = 2 \times 10^{-4}$.

These processes are likely to take place not only in the solar wind but also in the inner (chromosphere, transition region, corona) layers of the solar atmosphere. In particular, we argue that the fast magnetosonic waves that are amply produced by high-frequency photospheric motions become subject to shear-induced FMW-AW transformations (partial) in the chromosphere. The Alfvén waves, being weakly dissipative, are able to penetrate through the transition region and to reach those heights of the solar corona where the main bulk of the solar wind acceleration processes are generally believed to take place. The principal source of the acceleration may turn out to be the compressive damping of “secondary” fast waves—the outcome of the opposite (AW-FMW) transformation processes—evoked again by the velocity shear of the coronal flows. The main advantage of this scenario is that it seems to *remove* the well-known problem with solar fast waves: the difficulty

of their transmission throughout the transition region. Specifically, that part of the FMWs which is converted into AWs *below* the transition region passes through this region without any losses and later gives birth to secondary (internally generated) fast waves *above* the transition region. In this respect one may say that the velocity shear induces a remarkable series of mutual transformations of the MHD waves—shear-driven MHD wave oscillation phenomena—which bears a frail but attractive analogy with the oscillations of solar neutrinos. We anticipate also that for both the FMW-AW and FMW-SMW regimes, if certain conditions are favored, peculiar shear patterns—shear-beat modes—become launched. These beat waves, due to their prolonged lifetime and distinctive outward appearance, may serve as *bona fide* observable signatures of the shear-induced processes going on in the solar atmosphere.

One may be curious whether the other two shear-induced phenomena (viz. the appearance of the “shear vortices” and the vortex-wave conversion processes) also occur in the solar plasma flows. We are inclined to believe that it is quite probable. Actually, high-resolution observations of the transition region and low corona suggest that these layers of the solar atmosphere exhibit explosive-like radial motions, both upward and downward, rather than wave like motions (Pneuman and Orrall 1986). It is tempting to argue that these mysterious motions are associated with hydromagnetic shear vortices, which are just characterized by non-periodic, vortical motion of the plasma particles (Rogava *et al.* 1998). Moreover, if the shear vortices happen to arise in the moderate-shear or high-shear layers (e.g., in the adjacent layers of low-speed and high-speed streams) then the physical conditions will be ideal for the ignition of the shear-induced vortex-wave conversion processes (Chagelishvili *et al.* 1997). This means that the shear vortices will be converted into MHD waves providing yet another channel for the MHD wave generation, associated with the presence of the velocity shear in the solar atmosphere.

References

- Chagelishvili, G. D., Rogava, A. D., and Segal, I. N.: 1994, *Phys. Rev. E*, **50**, 4283.
- Chagelishvili, G. D., Rogava, A. D., and Tsiklauri, D. G.: 1996, *Phys. Rev. E*, **53**, 6028.
- Chagelishvili, G. D., Tevzadze, A. G., Bodo, G., and Moiseev, S. S.: 1997, *Phys. Rev. Lett.*, **79**, 3178.
- Pneuman, G. W., and Orrall, F. Q.: 1986, in *Physics of the Sun, Vol. II*, ed. P. A. Sturrock, (D. Reidel), p. 71.
- Poedts, P., Rogava, A. D., and Mahajan, S. M.: 1998, *Ap. J.*, **505**, 369.
- Rogava, A. D., Chagelishvili, G. D., and Mahajan, S. M.: 1998, *Phys. Rev. E*, **57**, 7103.
- Rogava, A. D., and Mahajan, S. M.: 1997, *Phys. Rev. E*, **55**, 1185.

SIGNATURES OF CORONAL HOLE SPECTRA BETWEEN 660° Å AND 1460 Å MEASURED WITH SUMER ON SOHO

U. SCHÜHLE, W. CURDT and K. WILHELM

Max-Planck-Institut für Aeronomie, D-37191 Katlenburg-Lindau, Germany

S. K. SOLANKI and K. STUCKI

Institute of Astronomy, ETH-Zentrum, CH-8092 Zürich, Switzerland

Abstract. Spectra of the northern polar coronal hole measured with the SUMER spectrometer on SOHO on 25 October 1996 are analyzed. We present spectra taken at locations on the solar disk where part of the spectrometer slit intersects a polar coronal hole region and an area of brighter emission from outside of the coronal hole area. By comparing the line intensities between the parts of the spectrum taken inside the “dark” area of the coronal holes and the brighter regions, we work out the signatures of the specific coronal hole in the chromosphere, transition region and lower corona. We find that emissions of neutral atom lines, of which there are many in the spectrum of SUMER, show no difference between the coronal hole and the bright boundary areas, whereas all ionized species show strong intensity enhancements, including the continuum emissions of carbon and hydrogen. These enhancements are larger than in normal quiet Sun areas.

1. Introduction

With the SUMER spectrometer on SOHO a spectral atlas of the full spectral range of the instrument is performed regularly in quiet Sun areas on the solar disk. More rarely such an atlas has been measured at coronal hole locations. While coronal holes observed on the solar disk show very clear intensity deficiencies in coronal emission lines, the signatures in the transition region and chromosphere are less significant and less well known. The SUMER spectrometer covers the spectral range of most chromospheric and transition region lines, as well as the lines from the lower corona. In search of signatures in the spectral emission from the base of the coronal holes, we have analyzed SUMER spectra in the spectral range from 660 Å to 1460 Å at locations on the solar disk where the spectrometer slit intersects areas with a clear deficiency of coronal emission, identified as coronal holes in the SUMER spectra in the emission of the Ne VIII lines at 770 Å and 780 Å and by comparison with images of the Fe XII window at 195 Å of the Extreme Ultraviolet Imaging Telescope (EIT) on SOHO. On 25 October 1996 the northern polar coronal hole was inclined towards the Earth. Bright emission at 195 Å extended across the coronal hole from its boundaries and was probably caused by the polar crown filament present in the field-of-view at that time. A SUMER spectral atlas was acquired with the spectrometer slit extending across the coronal hole and part of it outside the hole.

2. Data Acquisition and Reduction

The SUMER spectral atlas was acquired with the $1'' \times 300''$ slit crossing the northern polar coronal hole from the limb to the hole boundary. The data consist of



Space Science Reviews **87**: 299–302, 1999.

©1999 Kluwer Academic Publishers.

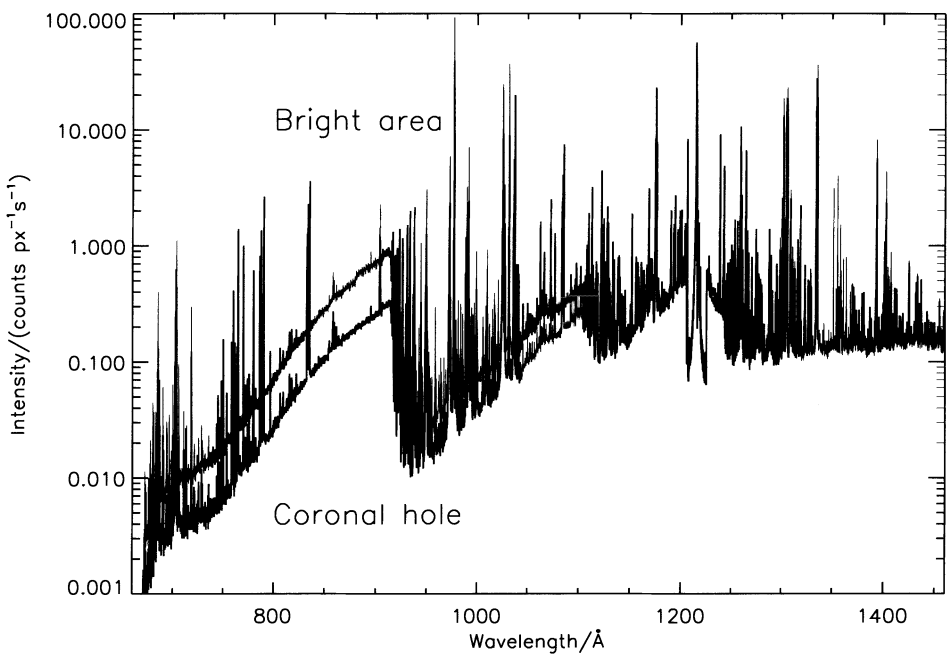


Figure 1. SUMER spectra of the polar coronal hole and the brighter boundary on 25 October 1996. Note the effect of the attenuator at the Lyman- α line.

60 exposures of 5 minutes each with overlapping wavelength ranges to cover the whole spectral range from 660 Å to 1460 Å in first order using the B-Detector. Thus, the time required to record the whole spectrum was 5 hours. The position of the slit was selected in such a way as to include some brighter emission from the coronal hole boundary. The EIT images of this day show that the coronal emission from the polar crown was brighter than “normal” quiet Sun emission. The SUMER data arrays were treated with standard routines for decompression, flat field correction, and geometrical distortion correction, before the entire spectrum was built up by concatenating appropriate sections from the KBr part of each exposure (see Wilhelm *et al.* 1997 for details). Then the part of the slit intersecting the coronal hole was selected by identifying the typical deficiency in the intensity of the Ne VIII lines at 770 Å and 780 Å. Next the intensity was averaged over 50''. For comparison, a similar section was selected from the part of the image outside the coronal hole. An overview of the full spectrum is given in Figure 1. By comparing the emission from two sections not far apart along the slit, we minimize the influence of the center-to-limb differences. Line identification and wavelength calibration could be done automatically by reference to a comprehensive line list determined previously (Curdt *et al.* 1997).

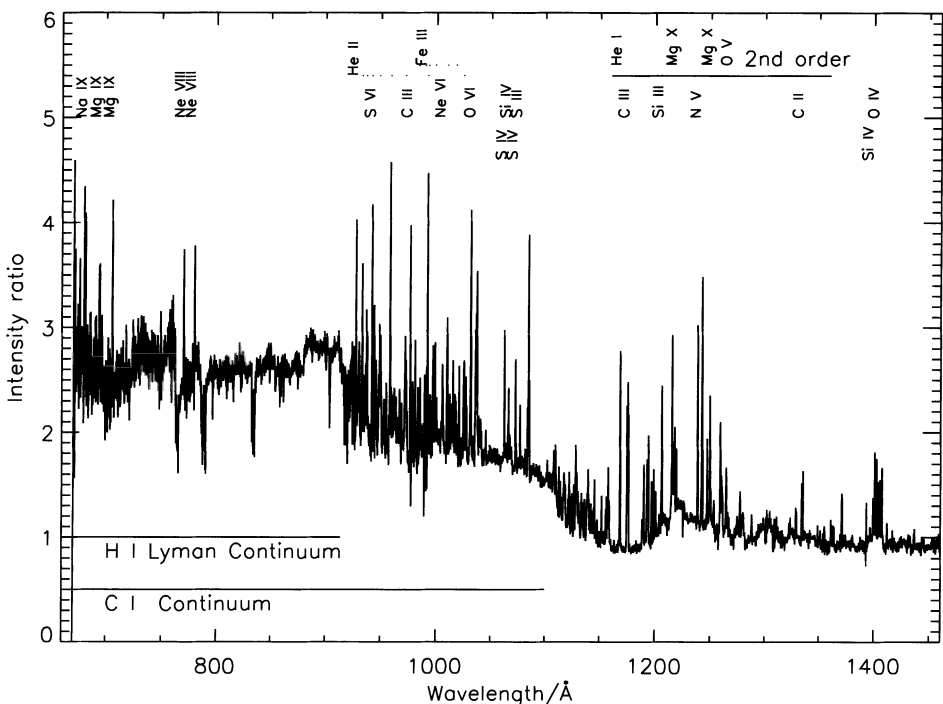


Figure 2. Ratio of the bright emission divided by the coronal hole spectra shown in Figure 1.

3. Results and Discussion

In Figure 1 we show the spectra of the bright area and the polar coronal hole superimposed, not converted to radiometric units for this purpose. At first sight, there are only small differences between both spectra except for the generally lower emission in the coronal hole. This distinction seems to be more pronounced in the Lyman continuum emission below 912 Å than in the longer wavelength range. To work out more clearly the signatures of the coronal hole spectrum, we simply took the ratio of both spectra. Since both spectra have been produced in exactly the same way, we have no shifts (other than of solar origin) between the two which could reduce the correlation and, thus, adversely affect their ratio.

In Figure 2 we show the ratio of the bright emission divided by the coronal hole spectrum. This simple treatment gives some striking results. First, many of the several hundred lines of the SUMER spectrum disappear in this ratio spectrum. Upon closer inspection, we see that almost all of the neutral lines give a ratio close to unity. Second, the ratio of the spectra shows a step at the edge of the H I Lyman continuum and another step at the edge of the C I continuum. At longer

wavelengths, the ratio of the continuum is close to unity. Third, pronounced intensity enhancements in the bright areas are found in almost every line of ionized species with ratios ranging from 1.7 up to 5. Pronounced differences between the coronal hole and the bright area spectra are seen in the lines of the He II Balmer series. The lines showing enhancements in the coronal hole boundary area are, together with the measured ratios: He I λ 584: 3.0; Mg X λ 609, 624: 2.4; O V λ 629: 2.2; Mg IX λ 694, 706: 4.7; Ne VIII λ 770, 780: 3.5; He II λ 928, 930, 933, 937, 942, 949, 959, 972, 992, 1025, 1085: 2 - 5; S VI λ 933, 944: 4.0; C III λ 977: 4.5; Fe III λ 981, 984, 986, 990, 991, 993, 997, 999, 1010, 1017, 1018: 3.5; N III λ 990: 3.5; Ne VI λ 1006, 1010: 3.0; O VI 1032, 1037: 4.0; S IV λ 1063, 1073: 3.3; Si IV λ 1067: 3.0; S III λ 1077: 2.8; N II λ 1084: 3.0; C III λ 1175: 2.5; Si III λ 1206: 2.5; N V λ 1238, 1242: 3.5; C II λ 1334, 1335: 1.8; O IV λ 1401, 1404: 1.8; Si IV λ 1393, 1402: 1.7. Since the compensation for the solar rotation was not invoked during this measurement, a change of solar conditions during the five hour period cannot be excluded. But the ratios we derive are measured strictly simultaneously, and the smooth ratio of the continuum and the ratio of all of the neutral lines above 1200 Å being precisely unity provides evidence that no dramatic changes occurred. The intensity ratios found here are larger than those of normal quiet Sun and coronal hole ratios as reported by Stucki *et al.* (1999), Lemaire *et al.* (1999), and Dammasch *et al.* (1999). Thus we conclude that the bright emission related to the coronal hole boundary is not identical with the normal quiet Sun spectrum but rather influenced by the polar crown filament. Further studies are necessary to characterize these differences.

Acknowledgements

The SUMER project is financially supported by DLR, CNES, NASA, and the PRODEX program (Swiss contribution).

References

- Curdt, W., Feldman, U., Laming, J. M., Wilhelm, K., Schühle, U., and Lemaire, P.: 1997, *A&A Suppl. Ser.*, **126**, 281.
- Dammasch, I. E., Hassler, D. M., Curdt, W., and Wilhelm, K.: 1999, "Statistical analysis of EUV and UV lines inside and outside of solar coronal holes," this volume.
- Lemaire, P., Bocchialini, K., Aletti, V., Hassler, D. M., and Wilhelm, K.: 1999, "Search for signatures of a coronal hole in transition region lines near disk center," this volume.
- Stucki, K., Solanki, S. K., Rüedi, I., Stenflo, J. O., Brković, A., Schühle, U., Wilhelm, K., and Huber, M. C. E.: 1999, "Coronal Holes versus normal quiet Sun observed with SUMER," this volume.
- Wilhelm, K., Lemaire, P., Curdt, W., Schühle, U., Marsch, E., Poland, A. I., Jordan, S. D., Thomas, R. J., Hassler, D. M., Huber, M. C. E., Vial, J.-C., Kühne, M., Siegmund, O. H. W., Gabriel, A., Timothy, J. G., Grewing, M., Feldman, U., Hollandt, J., and Brekke, P.: 1997, *Sol. Phys.*, **170**, 75.

ACCELERATION PROFILE OF THE SLOW SOLAR WIND AS INFERRRED FROM GRADUAL MASS EJECTIONS OBSERVED BY LASCO

NANDITA SRIVASTAVA, RAINER SCHWENN, BERND INHESTER,
GUILLERMO STENBORG and BORUT PODLIPNIK
Max-Planck-Institut für Aeronomie, 37191, Katlenburg-Lindau, Germany

Abstract. The slow solar wind ($< 400 \text{ km s}^{-1}$) appears to initiate from the regions in the corona where magnetic fields are closed, or from the interface between streamers and other coronal regions. The nature of the acceleration of slow solar wind is not yet well known. LASCO observations of gradually evolving mass ejections offer us a good opportunity to study the speed and acceleration profiles of the slow solar wind from a distance of 1.1 up to $30 R_{\odot}$. We present speed and acceleration profiles of slow solar wind, derived on the basis of measurements of mass flows in several cases of gradual mass ejections and present them in perspective of earlier work.

1. Introduction

The fast (700 km s^{-1}) and slow solar wind ($< 400 \text{ km s}^{-1}$) are now well known to originate and accelerate differently. While the fast solar wind is believed to come from the coronal holes and is observed to accelerate close to the sun, the slow solar wind is highly variable and most likely originates from streamers and interfaces between streamers and other coronal regions. Sheeley *et al.* (1997) suggested that the acceleration of the slowly moving blobs as observed by LASCO starts at 3 to $4 R_{\odot}$ above the cusps of streamers, and they then move radially outward at speeds from 150 km s^{-1} to 300 km s^{-1} . Since the features are small and accelerate in a similar fashion, they appear to trace out the slow solar wind.

In our quest for slowly moving blobs or blob-like features in the inner corona (i.e., the C1 field of view), no such small-scale features could be detected, although we could identify a distinct class of slow CMEs that were relatively less frequent in occurrence. During its 2.5 years of operation aboard SOHO, LASCO has recorded several of these gradual coronal mass ejections that have been tracked from 1.1 to $30 R_{\odot}$ using its three coronagraphs. These CMEs can be classified as gradually rising balloon-type events. They are structurally distinct and evolve as a low-lying loop for several hours in the C1 field of view before crossing gradually the entire field of view of the C2 and C3 coronagraphs in several hours (of the order of a day). In the past, only a few observations of similar type slow CMEs have been reported by, e.g., Fisher and Garcia (1984), based on data of the K-III coronameter within the range of 1.24 to $2.31 R_{\odot}$. We present a study of a few cases of slowly evolving or gradual CMEs as observed by LASCO and compare their flow speed and acceleration profiles to those of the slow solar wind as obtained by Sheeley *et al.* (1997).



2. Observations

Several cases of balloon-type events were analyzed for this study. We analyzed the entire range of observations covered by C1 (Fe XIV or 5303 Å green and Fe X or 6374 Å red emission lines) from 1.1 to 3 R_{\odot} , and the white light coronagraphs C2 (2 to 6 R_{\odot}) and C3 (3.7 to 30 R_{\odot}). The leading or frontal edge was identified and tracked in the field of view of all three coronagraphs. Measurements were also made for the prominence or core material in some cases where they could be uniquely identified and tracked. An example of a balloon-type CME is shown in Figure 1 as observed by the LASCO C1 coronagraph in the Fe XIV emission line on 19 October 1997 in the northwest (NW) quadrant. This CME was associated with an eruptive prominence. The time-lapse images show a slow rising loop (marked by an arrow) from 03:10 UT until 07:04 UT when the top of the loop reaches the edge of the field of view in C1. This CME was followed up in the C2 and C3 fields of view until 16:05 UT (19 October) and 06:02 (20 October) respectively. Thus, the leading edge was observed for approximately 28 hours. The other events also lasted for more than 24 hours.

From the measured height-time profiles of several such gradual events, the speeds were calculated. It is found that the range of the projected speeds lie between 10 and 500 km s^{-1} . The initial speeds of these CMEs are less than 100 km s^{-1} , and sometimes even less than 50 km s^{-1} in the range of 1.1–3 R_{\odot} . The terminal speeds around 25 R_{\odot} range between 300 and 400 km s^{-1} . Figure 2 shows a plot of speed versus distance for the CMEs analyzed with an overplot of the speed profile obtained by Sheeley *et al.* (1997) for slowly moving blobs. The estimated uncertainties for the speeds are approximately $\pm 5 \text{ km s}^{-1}$ (C1), $\pm 10 \text{ km s}^{-1}$ (C2) and $\pm 50 \text{ km s}^{-1}$ (C3). The values of the acceleration were also determined from the calculated speeds and it is found that the range of acceleration lies between 5 and 25 m s^{-2} for these CMEs.

3. Conclusion

Gradual CMEs are observed by the C1 coronagraph to originate close to the limb at around 1.5 R_{\odot} , near the large-scale streamers. These balloon-type events are seen to change the nearby large-scale streamers and may be considered “streamer blowouts” (Howard *et al.* 1985). They start rising slowly with a speed $< 100 \text{ km s}^{-1}$, with a majority even less than 50 km s^{-1} . The terminal speeds beyond 20 R_{\odot} range between 300 and 400 km s^{-1} . The speed versus distance profile is similar to that obtained by Sheeley *et al.* (1997) for slowly moving density enhanced blobs. It may also be noted that in some cases, a two step speed profile is found. The CME accelerates initially until reaching a certain height and then it moves with almost constant speed for some time before finally drifting away with the slow solar wind. The acceleration for balloon-type events increases gradually from 1.1 R_{\odot} reaching a maximum value ranging between 5 and 25 m s^{-2} . The lower limit

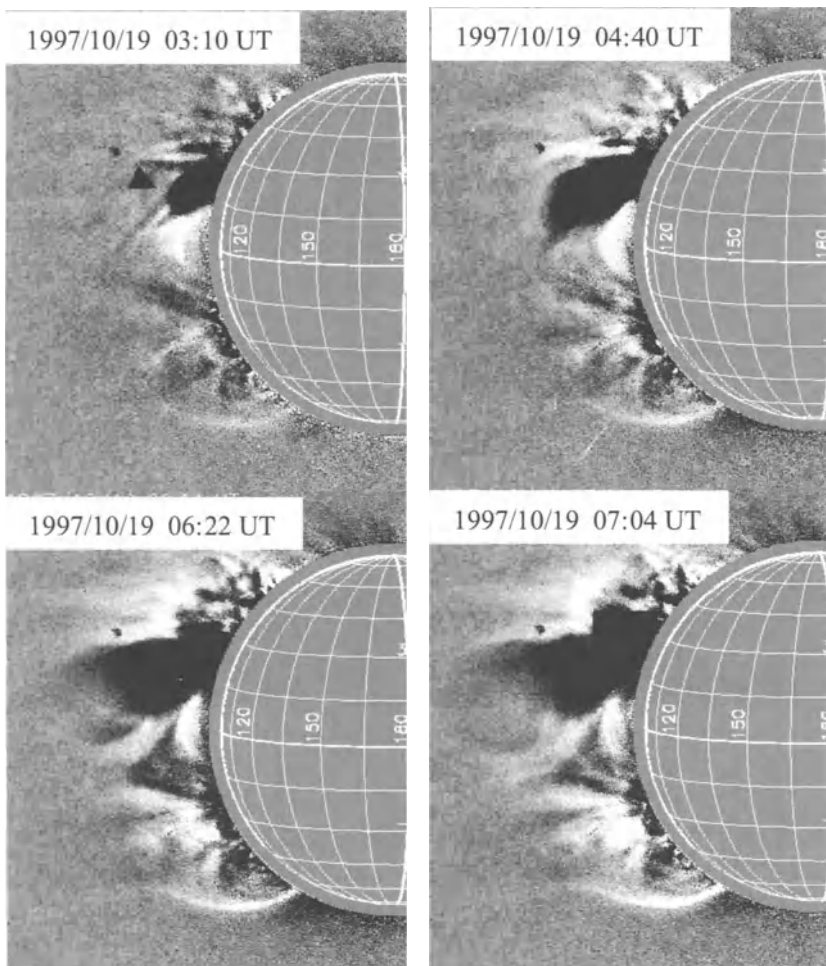


Figure 1. Time-lapse images of a gradual mass ejection observed by LASCO C1 coronagraph on 19 October 1997, showing evolution of a loop structure (arrow) from 03:10 to 07:04 UT.

coincides with the average value (4 m s^{-2}) measured for slowly moving blobs. The maximum acceleration for balloon-type CMEs occurs between 3 and $6 R_{\odot}$. Beyond this distance, acceleration decreases, approaching low values similar to those for slowly moving blobs around $15 R_{\odot}$. Further, the acceleration ends around a distance of $20 R_{\odot}$, in agreement with results obtained by Breen *et al.* (1997) using IPS EISCAT observations of the slow solar wind. There also seems to be an indication of deceleration beyond $20 R_{\odot}$ in some balloon-type events. This needs to be confirmed, as uncertainties in the measurement near the outer edge of the field of view are large due to low intensity. We conclude, since the magnitude of

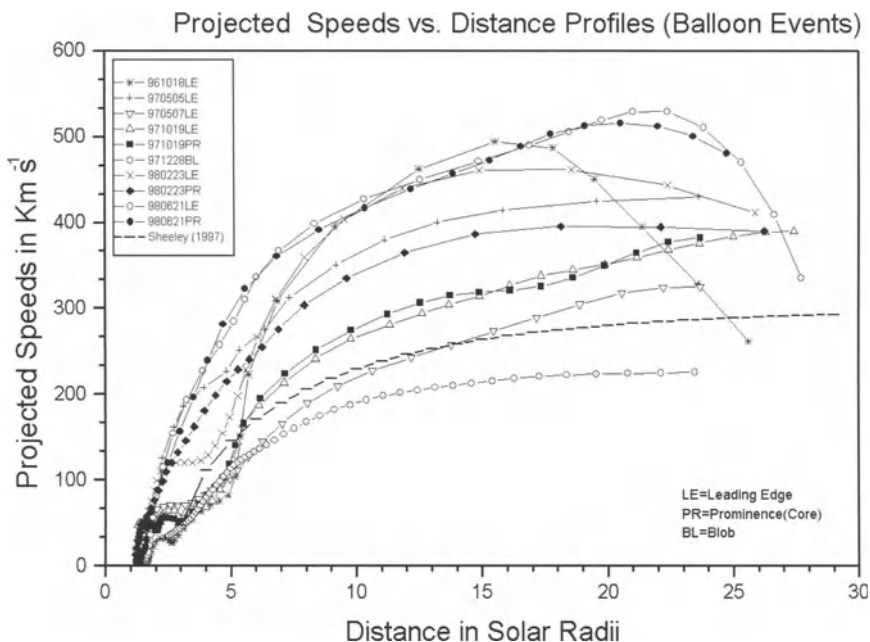


Figure 2. Speed versus distance profiles for gradual CMEs observed by LASCO. For comparison, the speed profile obtained for slowly moving blobs (Sheeley *et al.* 1997) is also overplotted with a dashed line.

the speeds of the slowly evolving balloon-type events is comparable to that of slow solar wind as traced by the “leaves in the wind,” it appears that they then drift away in the slow solar wind.

References

- Breen, A. R., Coles, W. A., Grall, R. R., Harrison, R. A., Mckenzie, J. F., Markkanen, J., Moran, P. J., Varley, C. A., and Williams, P. J. S.: 1997, “Ground and space-based studies of solar wind acceleration,” in *The Corona and Solar Wind near Minimum Activity, Proc. Fifth SOHO Workshop*, ESA-SP 404, 223.
- Fisher, R., and Garcia, C.: 1984, “Detection of a slowly moving coronal transient,” *Astrophys. J.*, **282**, L35.
- Howard, R. A., Sheeley, N. R., Jr., Koomen, M. J., Michels, D. J.: 1985, “Coronal Mass Ejections: 1979–1981,” *J. Geophys. Res.*, **90**, No. A9, 8173.
- Sheeley, N. R., Jr., Wang, Y. M., Hawley, S. H., *et al.*: 1997, “Measurements of flow speeds in the corona between 2 and 30 R_{\odot} ,” *Astrophys. J.*, **484**, 472.

MICA: THE MIRROR CORONAGRAPH FOR ARGENTINA

G. STENBORG, R. SCHWENN, N. SRIVASTAVA, B. INHESTER and B. PODLIPNIK
Max-Planck-Institut für Aeronomie, Max-Planck-Str. 2, (37191) Katlenburg-Lindau, Germany

M. ROVIRA

Instituto de Astronomía y Física del Espacio, C.C. 67 - Suc. 28, (1428) Buenos Aires, Argentina

C. FRANCILE

*Observatorio Astronómico Félix Aguilar, Benavidez 8175 Oeste, (5413) Chimbás, San Juan,
Argentina*

Abstract. As part of the new German-Argentinian Solar Observatory in El Leoncito, San Juan, Argentina, a new ground-based solar telescope (MICA) began to operate in August 1997. MICA is an advanced mirror coronagraph, its design being an almost exact copy of the LASCO-C1 instrument. Since its installation, it has been imaging the inner solar corona (1.05 to 2.0 solar radii) in two spectral ranges corresponding to the emission lines of the Fe XIV and Fe X ions. The instrument can image the corona as fast as every minute. Thus, it is ideally suited to study fast processes in the inner corona. In this way, it is a good complement for the LASCO-C1 instrument. After a brief review of the instrument, we present some recent observations showing the capabilities of the instrument.

Key words: corona, coronagraph

Abbreviations: MICA – Mirror Coronagraph for Argentina

1. Introduction

One of the basic limitations in the externally occulted coronagraph is that of poor spatial resolution in the inner corona due to the very small effective aperture. Also, residual instrumental stray light and scattered light in the terrestrial atmosphere make the detection of faint coronal structures out to large distances above the solar limb difficult. Newkirk and Bohlin (1963) pointed out in the 1960s that instrumental stray light can be considerably reduced by using mirror optics instead of lenses. LASCO-C1 on SOHO and a prior prototype (Epple and Schwenn 1995) were the first internally occulted coronagraphs designed with reflecting optics. Following this line, MICA incorporates all the advantages of internal occulting and mirror design such as compactness, a low level of instrumental scattered light and optical achromacy, to name the most important.

MICA is a ground-based solar telescope, installed in the Prof. Ulrico Sesco Observing Station of OAFA at El Leoncito (69.3 W, 31.8 S), San Juan, Argentina, at an altitude of 2400 m, 50 km eastwards from the Argentinian “Cordillera de los Andes.” It is part of a bilateral science program between Argentina and Germany. The participating institutions are: Instituto de Astronomía y Física del Espacio (IAFE) and Observatorio Astronómico “Félix Aguilar” (OAFA), San Juan University, on the Argentinian side, and Max-Planck-Institut für Aeronomie (MPAE) and Max-Planck-Institut für Extraterrestrische Physik (MPE), on the German side.



Space Science Reviews 87: 307–310, 1999.

©1999 Kluwer Academic Publishers.

2. The Instrument

The MICA system is almost identical to the LASCO-C1 instrument (Brueckner *et al.* 1995). It is designed to produce filtergrams of the emission line corona. MICA uses a set of narrow-band interference filters using a specifically designed mechanism. MICA's field of view ranges from 1.05 to 2.0 solar radii, one pixel subtending 3.7 arcsec, limiting the spatial resolution to ~ 8 arcsec. Since MICA is not constrained by telemetry, the temporal resolution is extremely high as compared to LASCO-C1. Typical exposure times are 40 seconds for the on-line images and 15 seconds for the off-line ones, the time gap between images being ~ 10 seconds. It uses a 1280×1024 CCD array coded on 12 bits. The whole telescope is enclosed in a lightweight thermal canister which maintains thermal stabilization of MICA during operations in all seasons at El Leoncito.

MICA observes two emission lines of iron. The well-known green coronal line is obtained with a 0.9 Å wide interference filter at a wavelength of 5303 Å. Subtraction of reference images taken in the nearby continuum (at 5260 Å) are necessary in order to reveal the structures of the hot corona (~ 1.8 MK). Similarly, the coronal red line (6374 Å, ~ 1.0 MK) is achieved by subtraction of continuum images at 6340 Å (Schwenn *et al.* 1997). Observing sequences in MICA require frequent reference images in order to avoid changes in the sky brightness, this feature being the main constraint for MICA.

A newly developed sky tester (Epple 1997) is mounted close to MICA along with a sun tester (details will be presented in a future paper) in order to continuously register the sky (aureola) and solar disk brightness, respectively. These values are then used by the control software of the telescope (in conjunction with the wind speed as obtained by a weather station) to automatically decide whether the conditions are good for starting (continuing, stopping) coronal observations.

3. Observations

Some images obtained by MICA are presented in Figures 1 and 2. The orientation of all frames show equatorial north at top, west at right. The emission line corona in two different emission lines at nearly the same time on 23 August 1997 is shown in Figure 1. Comparison of these two images shows that although the structures have their origin in the same active region, there exist some regions with Fe XIV but not Fe X emission and vice versa. In Figure 2 a comparison of MICA and LASCO-C1 is shown. Note the internal edge of MICA's field of view (1.05 solar radii) as compared to LASCO-C1's (1.10 solar radii). The LASCO-C1 image is the result of subtracting a nearby continuum image from the respective on-line. Only the constant camera offset bias has been taken out. However, MICA images are corrected not only for the offset bias but also flat fielded and calibrated in terms of the solar disc intensity, although a precise photometric study is still under way.

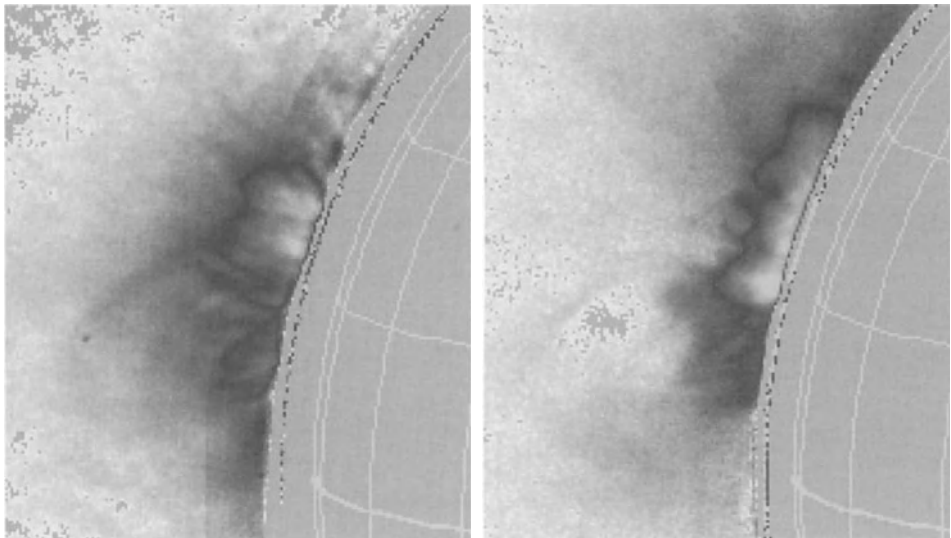


Figure 1. Observation of the green line (left) at 15:52:44 UT and the red line (right) at 16:18:53 UT on 23 August 1997 by MICA (40 second exposure time in both cases).

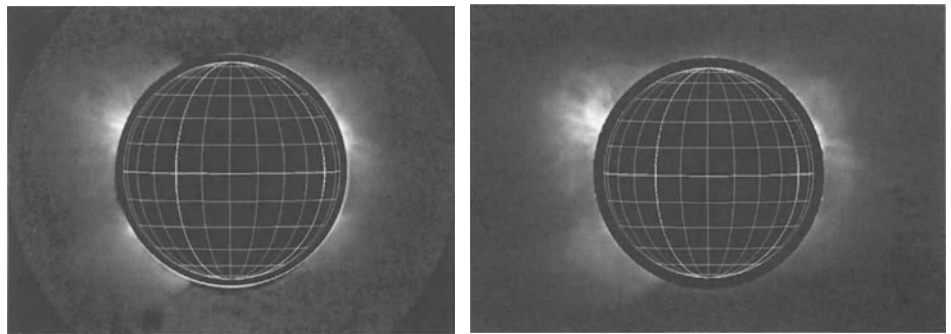


Figure 2. Green coronal emission line on 26 November 1997 as observed by MICA (left) and LASCO-C1 (right) at 12:15:10 UT and 12:24:14 UT respectively. The C1 image has been scaled to the spatial resolution of the MICA image.

4. Discussion

MICA, a low scattered light mirror coronagraph, has been in operation since August 1997. Several test and calibration sequences were run during the first months. In particular, the working temperature of the filters was adjusted and algorithms for the automatic control of the instrument were developed. Although mainly limited by the brightness and temporal variability of the sky, recent observations made by

MICA have shown a very detailed view of transient phenomena in both temporal and spatial scales. We are able to detect the coronal emission corresponding to the Fe XIV and Fe X ions out to 1.6 solar radii, using tools for image treatment and background correction.

The instrument is very well suited to study the processes that occur in coronal transients and the conditions that trigger them. In the future we will exploit the high temporal resolution of MICA in order to study fast processes in the inner solar corona, and take advantage of the high sensitivity of the instrument in order to study the temporal evolution of the transparency of the earth's atmosphere.

Acknowledgements

This study is based on data obtained in the framework of the German-Argentinian HASTA/MICA Project at OAFA (El Leoncito, San Juan, Argentina), in a collaborative effort by IAFE, OAFA, MPAe and MPE.

References

- Brueckner, G. E., *et al.*: 1995, 'The Large Angle Spectroscopic Coronagraph (LASCO),' *Solar Phys.*, **162**, 357.
Epple, A., and Schwenn, R.: 1995, 'PICO: A Mirror Coronagraph on Pic Du Midi,' *Proc. 15th National Solar Observatory/Sacramento Peak Summer Workshop*, **1**, 233.
Epple, A.: 1997, 'Erdgebundene Beobachtungen der Sonnenkorona mit einem Spiegelkoronographen,' *Ph.D. Thesis*, Göttingen University, Germany, pp. 42–47.
Newkirk G., and Bohlin, D.: 1963, 'Reduction of Scattered Light in the Coronagraph,' *Appl. Opt.*, **2**, 131.
Schwenn, R., *et al.*: 1997, 'First View of the Extended Green-Line Emission Corona at Solar Activity Minimum using the LASCO-C1 Coronagraph on SOHO,' *Solar Phys.*, **175**, 667.

CONSTRAINTS ON CORONAL OUTFLOW VELOCITIES DERIVED FROM UVCS DOPPLER DIMMING MEASUREMENTS AND IN-SITU CHARGE STATE DATA

L. STRACHAN, Y-K. KO, A. V. PANASYUK, D. DOBRZYCKA and J. L. KOHL
Harvard-Smithsonian Center for Astrophysics, Cambridge, MA 02138, USA

M. ROMOLI and G. NOCI
Università di Firenze, I-50125 Firenze, Italy

S. E. GIBSON*
NASA Goddard Space Flight Center, Greenbelt, MD 20771, USA

D. A. BIESECKER **
University of Birmingham, Edgbaston, Birmingham, B15 2TT, UK

Abstract. We constrain coronal outflow velocity solutions, resolved along the line-of-sight, by using Doppler dimming models of H I Lyman alpha and O VI 1032/1037 Å emissivities obtained with data from the Ultraviolet Coronagraph Spectrometer (UVCS) on SOHO. The local emissivities, from heliocentric heights of 1.5 to 3.0 solar radii, were determined from 3-D reconstructions of line-of-sight intensities obtained during the first Whole Sun Month Campaign (10 August to 8 September 1996). The models use electron densities derived from polarized brightness measurements made with the visible light coronagraphs on UVCS and LASCO, supplemented with data from Mark III at NCAR/MLSO. Electron temperature profiles are derived from ‘freezing-in’ temperatures obtained from an analysis of charge state data from SWICS/Ulysses. The work concentrates on neutral hydrogen outflow velocities which depend on modeling the absolute coronal H I Ly α emissivities. We use an iterative method to determine the neutral hydrogen outflow velocity with consistent values for the electron temperatures derived from a freezing-in model.

Key words: corona, solar wind, UV radiation, spectroscopy, line profiles

1. Introduction

The determination of coronal outflow velocities from the Doppler dimming method (Withbroe *et al.* 1982; Strachan *et al.* 1993) relies on an independent knowledge of key plasma parameters for the region being probed. For example, the neutral hydrogen density distribution is needed in order to calculate the expected emergent H I Ly α intensity from the plasma. The neutral H density is routinely calculated as the product of the electron density and the ionization balance for neutral hydrogen. The ionization balance is the ratio of neutral H to the total H (atoms plus protons) in the plasma. In the past this fraction has been estimated based solely on the electron temperature of the plasma. However, it has been well known that the ionization states of coronal ions are affected by the bulk outflow of the plasma (Hundhausen 1972). The outflow velocity of the plasma causes the ionization state to become ‘frozen in’ at the height where the characteristic expansion time is much shorter than the times for ionization or recombination. In this paper we present H outflow

* Also: The Catholic University of America

** Now at Space Applications Corporation, NASA/GSFC, Greenbelt, MD 20771, USA



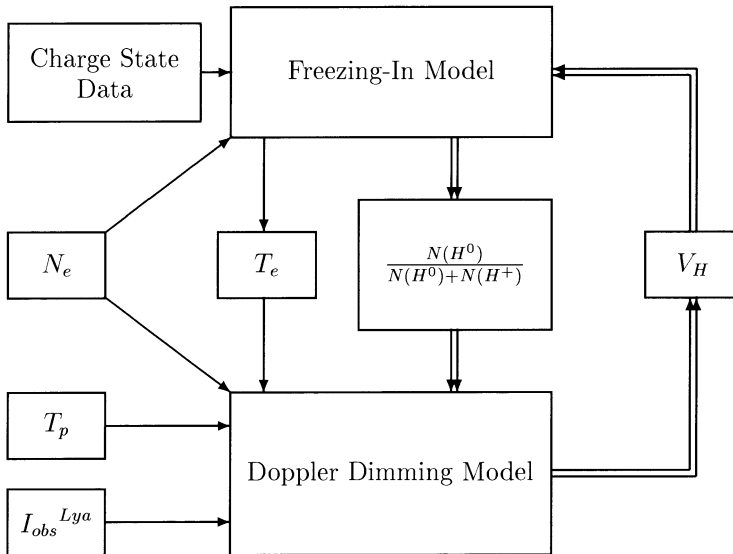


Figure 1. Iteration scheme for using self-consistent values of electron temperatures derived from the freezing-in model and outflow velocities derived from the Doppler dimming model. Double arrows show the repeated loop in the iteration.

velocities that are determined from the Doppler dimming of H I Ly α using new ionization balance calculations that include the freezing-in process.

2. Models and Observational Constraints

We describe the Doppler dimming model and freezing-in models next. Figure 1 shows how the H outflow velocities, V_H are determined from the observational and modeling constraints.

The Doppler dimming model uses electron density, N_e ; hydrogen ionization balance; and electron and hydrogen (or proton) temperatures (T_e and T_p), each as a function of heliocentric height, to model the observed H I Ly α intensity, $I_{obs}^{Ly\alpha}$. The modeled H outflow velocity, V_H , is found when the observed Ly α intensities are matched by the model (Strachan *et al.* 1993). In general the hydrogen small scale velocity distributions are not the same in the directions parallel and perpendicular to the radial direction. For convenience we use ‘temperature’ to parameterize the velocity distributions and assume that the protons and hydrogen have the same temperatures. We let the observed Ly α profile widths constrain the perpendicular T_p and assume the parallel T_p is equal to the value for T_e at the observed heights. Note that the perpendicular T_p probably contains a nonthermal component due to waves (e.g., Kohl *et al.* 1998).

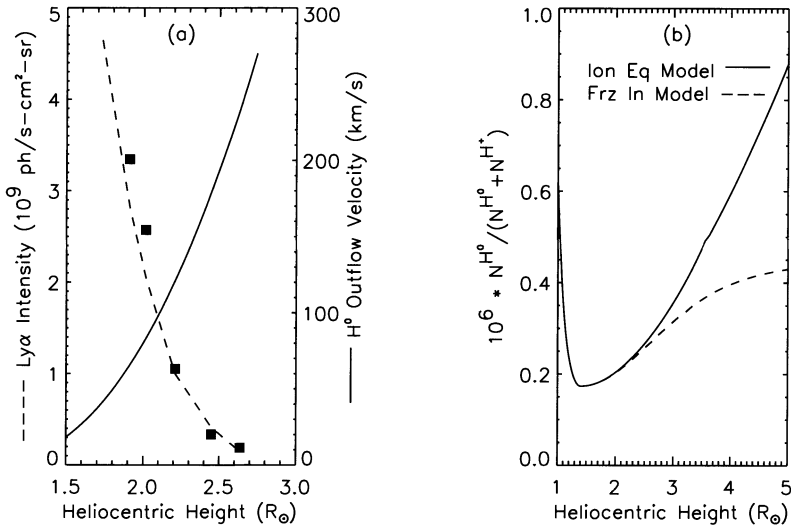


Figure 2. (a) H I Ly α intensities from a 3-D coronal reconstruction (points) and results from a Doppler dimming model (dashes) using the outflow velocities (solid line) shown on the right scale. (b) Neutral hydrogen ionization balance models assuming outflow (dashed) and no outflow (solid line).

The coronal hole electron densities, N_e , are based on WLC/Spartan and HAO/MLSO Mark III K-coronameter data obtained at the time of the Ulysses South Polar Passage (Guhathakurta and Fisher 1998). These are similar to the coronal hole densities derived from Whole Sun Month observations.

A freezing-in model using charge states from several ions was used to calculate the coronal hole electron temperatures, T_e , used in our model. The charge state data were obtained from the SWICS/Ulysses experiment during the time of the Ulysses South Polar Passage (Ko *et al.* 1997). We compute an initial hydrogen ionization balance ratio, $N(H^0)/[N(H^0) + N(H^+)]$, using the given values for T_e and the first guess for the H outflow velocity, V_H . The ionization balance ratio is used to produce a better estimate for the H number density and this is put back into the Doppler dimming model. The iteration is continued until the outflow velocity converges after only a few iterations.

3. Model Results

The H outflow velocity as a function of height is shown as the solid line in Figure 2a. The velocity steadily increases from about 20 to 270 km/s (right scale) in the height range 1.5 to $2.75 R_\odot$. The velocities have the same functional form as those in Ko *et al.* (1997) and start from zero velocity at $1 R_\odot$. These velocities are

used to produce the dashed curve for the modeled H I Ly α intensities (left scale). The modeled intensities compare favorably to the empirically determined H I Ly α intensities shown by the solid square symbols. The intensities (emissivities times the LOS dimension) were derived from the reconstructed UVCS intensities based on Whole Sun Month observations (Panasyuk 1999). These particular data points are from position angle 210° in the south coronal hole on 17 August 1996.

Figure 2b shows the neutral hydrogen fraction based on two different assumptions: (i) (solid curve) hydrogen is in ionization equilibrium, and (ii) (dashed curve) the H⁰ ionic fraction is calculated including the effects of the outflow velocity in the ionization/recombination processes for hydrogen. The models are nearly the same below 2 R_{\odot} but diverge rapidly at higher heights.

4. Discussion

While this is the first time that we have combined the Doppler dimming models and the SWICS/Ulysses freezing-in models, only an example is presented here. Neither the uniqueness of the results nor the characterization of the errors associated with the models have been analyzed. We would like to make the models more realistic by also including the electron temperature (which depends on the freezing-in analysis of several ionic charge states) in the iteration process. In addition we want to automate the search in parameter space to find the optimum parameters for the outflow velocity.

Other directions of research using similar methods include extending the UVCS/SOHO H I Ly α observations to larger distances from the Sun in order to explore the effects of higher outflow velocities on the freezing-in process. O VI 1032/1037 Doppler dimming measurements may also be included to add additional constraints on the hydrogen outflow velocities.

This work is supported by the National Aeronautics and Space Administration under grant NAG5-3192 to the Smithsonian Astrophysical Observatory, by Agenzia Spaziale Italiana, and by the ESA PRODEX program (Swiss contribution).

References

- Guhathakurta, M., and Fisher, R.: 1998, *Astrophys. J.*, **499**, L215.
- Hundhausen, A. J.: 1972, *Coronal Expansion and Solar Wind*, (Springer-Verlag, New York), p. 114.
- Ko, Y.-K., Fisk, L. A., Geiss, J., Gloeckler, G., and Guhathakurta, M.: 1997, *Solar Phys.*, **171**, 345.
- Kohl, J. L., *et al.*: 1998, *Astrophys. J.*, **501**, L127.
- Panasyuk, A. V.: 1999, *J. Geophys. Res.*, in press.
- Strachan, L., Kohl, J. L., Weiser, H., Withbroe, G. L., and Munro, R. H.: 1993, *Astrophys. J.*, **412**, 410.
- Withbroe, G. L., Kohl, J. L., Weiser, H., and Munro, R. H.: 1982, *Space Sci. Rev.*, **33**, 17.

CORONAL HOLE PROPERTIES OBSERVED WITH SUMER

K. STUCKI, S. K. SOLANKI, I. RÜEDI, J. O. STENFLO and A. BRKOVIĆ
Institute of Astronomy, ETH-Zentrum, CH-8092 Zürich, Switzerland

U. SCHÜHLE and K. WILHELM
Max-Planck-Institut für Aeronomie, D-37191 Katlenburg-Lindau, Germany

M. C. E. HUBER
European Space Agency, Space Science Department, ESTEC, PO Box 299, 2200 AG Nordwijk, The Netherlands

Abstract. We analyze SUMER spectra of 14 lines belonging to 12 ions, obtained on both sides of the boundary of polar coronal holes as well as at other locations along the limb. We compare line intensities, shifts and widths in coronal holes with values obtained in the quiet Sun. We find that with increasing formation temperature, spectral lines show an increasingly stronger blueshift in coronal holes relative to the quiet Sun at an equal heliospheric angle. The width of the lines is generally larger (by a few km/s) inside the coronal hole. Intensity measurements show the presence of the coronal hole in Ne VIII lines as well as in Fe XII, with evidence for a slightly enhanced emission in polar coronal holes for lines formed below 10^5 K.

1. Introduction

Coronal holes are the source of the fast solar wind and the primary example of coronal heating in regions with an excess of one magnetic polarity, but are not yet well understood. SUMER on board SOHO provides us with the capability of observing full line profiles at high spatial resolution, and thus determining line intensities, flows, and turbulent velocities in the chromosphere, transition region, and lower corona.

Distinctive differences in the center-to-limb intensity variations of lines between coronal holes and quiet Sun regions have been reported earlier by, e.g., Wilhelm *et al.* (1998). Here, we report on a comparison of high spatial and spectral resolution data of coronal hole and quiet Sun regions by comparing Gaussian-fit parameters of spectral lines measured at different locations along the limb.

2. Observations

Three sets of observations from SUMER were used. The first set consists of a series of 14 different spectral frames, each frame exposed for 300 seconds using the $1'' \times 300''$ slit placed on the central meridian. This slit crossed either the northern or the southern coronal hole (JOP055). The second set is very similar to the first one, but was taken 10 months later when the solar rotation compensation could be used (JOP055-TR).

The third set consists of a series of 12 different spectral frames taken during one of SOHO's roll maneuvers at different locations along the limb, with emphasis on the equator (slit $1'' \times 300''$, exposure time 150 s).



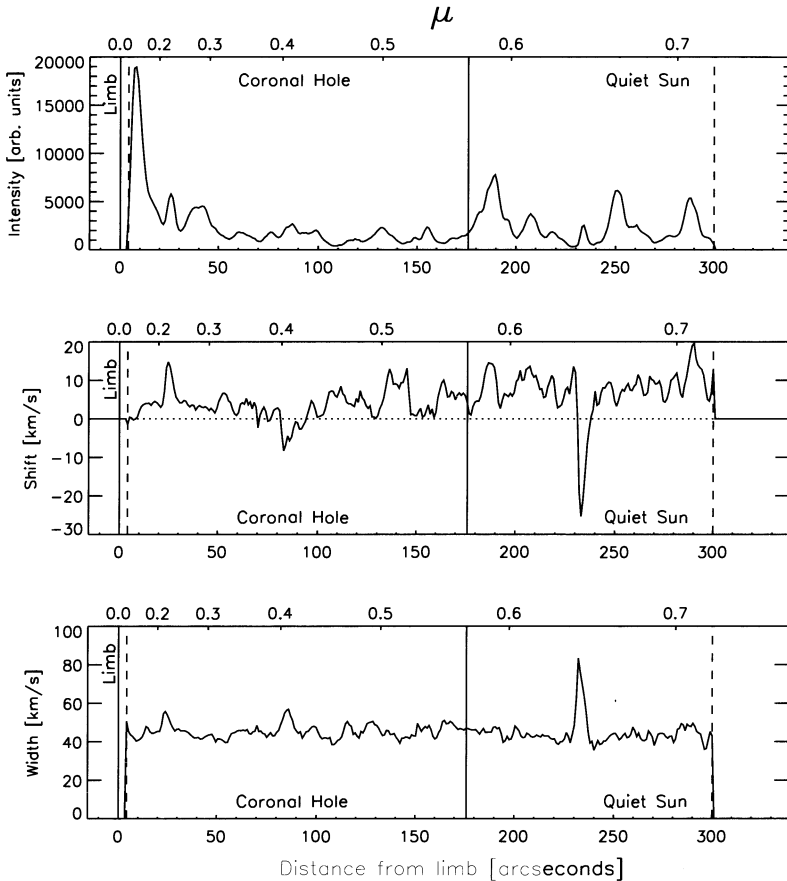


Figure 1. Example of the fit parameters (intensity, shift and width) using the spectral profiles of S VI at 933.39 Å, obtained from the first set of observations with SUMER (JOP055). The coronal hole boundary is located approximatively 176'' from the limb (vertical line). The vertical line (solid line on the left) representing the position of the limb is located just outside the limits of the image on the detector (dashed vertical lines) in this data set. The scale at the top of each frame indicates $\mu = \cos \vartheta$, where ϑ is the heliocentric angle. The increased width near 230'' marks the presence of an explosive event. Negative shifts signify blue shifts.

A group of spectral lines common to all observations was selected, and the intensity, shift, and width parameters were calculated at each spatial pixel using a Gaussian fitting method. The selected lines belong to: Si I, O I, N I, C II, Ni II, Si III, Si IV, N IV, O V, S VI, Ne VIII, and Fe XII. An example of the variation of line parameters along the slit is shown in Figure 1 for S VI 933.39 Å.

3. Results

In total we had about 25 exposures of each spectral line at our disposal. In each exposure, we averaged the fit parameters in a sector corresponding to the position

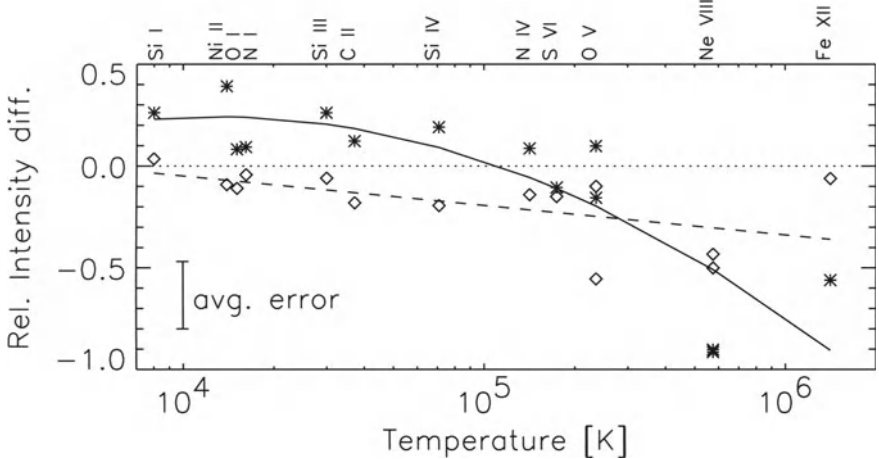


Figure 2. Relative intensity difference vs. ion temperature. The relative intensity difference was calculated using the expression: $2 \cdot (I_{\text{meridian}} - I_{\text{other locations}})/(I_{\text{meridian}} + I_{\text{other locations}})$. Diamonds: large μ sector (only quiet Sun); Stars: small μ sector (including coronal hole). The solid line shows a second order fit of the small μ sector points, while the dashed line shows a first order fit of the large μ sector points.

of the coronal hole (“small μ sector”), and in a sector corresponding to the quiet Sun (“large μ sector”). Those values were then averaged over all exposures taken at the meridian (containing northern or southern coronal hole regions), and over all exposures taken at other locations (roll data taken around the disk). The line parameters found are then related to the temperatures of maximum abundance of the ions taken from Arnaud and Rothenflug (1985).

In Figure 2 we plot the relative intensity difference between the meridian and the other locations, once for the “small μ sector” (stars) and once for the “large μ sector” (diamonds). The “small μ sector” consists of coronal hole data at the meridian and quiet Sun data at the other locations, while the “large μ sector” consists of quiet Sun data in all regions. Only the high temperature lines Ne VIII and Fe XII show reduced emission in the coronal hole. The large μ sector, which is outside the hole for every location, shows a smaller emission for the meridian data. The reason for this behavior is unknown. The influence of the FIP effect is currently being examined. Element fractionation is not apparent, possibly because it is covered by other effects.

The line shift displays a distinct trend towards larger blueshifts for higher ion temperatures in the coronal hole, which may be evidence of solar wind outflow at low altitudes in coronal holes (see Figure 3).

Figure 4 shows slightly increased line widths in the coronal hole, indicating higher non-thermal velocities for almost all lines except for Fe XII. The apparently contradictory result for Fe XII could be due to blends from cooler ions in its wings, which may contribute to its anomalous behavior.

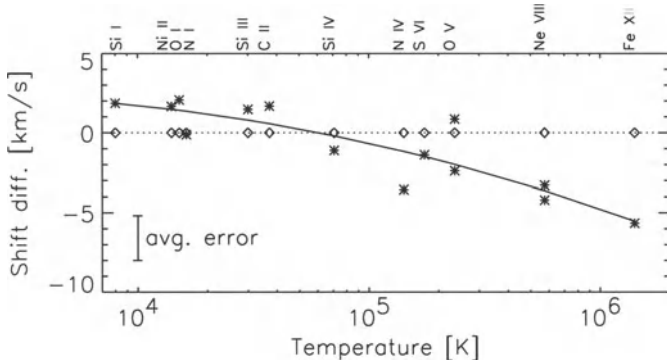


Figure 3. Wavelength shift difference in velocity units vs. formation temperature. The “shift difference” represents the difference between the shifts observed on the meridian and the ones observed at other locations at the same μ . Since the wavelength scale is not absolute, we equalized the shifts between meridian and equator outside the hole. *Diamonds*: large μ sector (identically zero due to shift equalization); *Stars*: small μ sector (i.e., shift of hole profiles relative to non-hole profiles). The solid curve shows a second order fit of the small μ sector points.

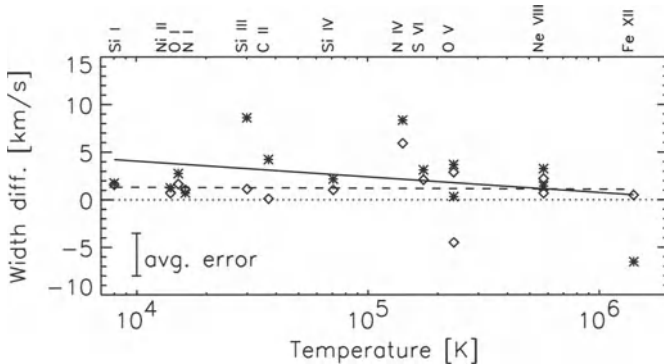


Figure 4. Width difference vs. formation temperature. The “width difference” represents the difference between the line width observed on the meridian and that at other locations. *Diamonds*: large μ sector; *Stars*: small μ sector (i.e., widths of hole profiles relative to non-hole profiles). The solid line shows a first order fit of the small μ sector points, while the dashed line shows a fit of the large μ sector points.

Acknowledgements

The SUMER project is financially supported by DLR, CNES, NASA, and the ESA PRODEX program (Swiss contribution). This work was partly supported by the Swiss National Science Fundation, grant no. 21-45083.95, and by a grant from the ETH-Zürich which is gratefully acknowledged.

References

- Arnaud, M., and Rothenflug, R.: 1985, *A&A*, **60**, 425.
 Wilhelm, K., Lemaire, P., Dammasch, I. E., Hollandt, J., Schühle, U., Curdt, W., Kucera, T., Hassler, D. M., and Huber, M. C. E.: 1998, *A&A*, **334**, 685.

ULYSSES-UVCS COORDINATED OBSERVATIONS

S. T. SUESS

NASA Marshall Space Flight Center, Huntsville, AL, USA

G. POLETTO and G. CORTI

Osservatorio Astrofisico di Arcetri, Firenze, Italy

G. SIMNETT

University of Birmingham, United Kingdom

G. NOCI and M. ROMOLI

Università di Firenze, Italy

J. KOHL

Harvard-Smithsonian Center for Astrophysics, Cambridge, MA, USA

B. GOLDSTEIN

Jet Propulsion Laboratory, Pasadena, CA, USA

Abstract. We present results from SOHO/UVCS measurements of the density and flow speed of plasma at the Sun and again of the same plasma by Ulysses/SWOOPS in the solar wind. UVCS made measurements at 3.5 and 4.5 solar radii and Ulysses was at 5.1 AU. Data were taken for nearly 2 weeks in May–June 1997 at 9–10 degrees north of the equator in the streamer belt on the east limb. Density and flow speed were compared to see if near Sun characteristics are preserved in the interplanetary medium. By chance, Ulysses was at the very northern edge of the streamer belt. Nevertheless, no evidence was found of fast wind or mixing of slow wind with fast wind coming from the northern polar coronal hole. The morphology of the streamer belt was similar at the beginning and end of the observing period, but was markedly different during the middle of the period. A corresponding change in density (but not flow speed) was noted at Ulysses.

Key words: SOHO, Ulysses, streamers

1. The Observations

On 26 May 1997 (Day of Year [DoY] 146) the Ulysses–Sun–SOHO angle was 90°, presenting an opportunity to observe a solar wind limb source with SOHO and later observe the same solar wind *in situ* at Ulysses. This opportunity occurs only about twice a year. Ulysses was at 5.1 AU, 10° north of the heliographic equator and off the east limb. It was near sunspot minimum so the streamer belt was confined to low latitudes.

LASCO/C2 images and Ulysses data are shown in Figure 1. At 400 km/s, it takes solar wind three weeks to reach 5 AU. Therefore, we analyzed data for two weeks centered on 16 June (DoY 167). These were extrapolated backwards in time to the solar source assuming constant speed. Since the uncertainty in such extrapolations is $\sim \pm 10$ degrees and the Ulysses–SOHO angle changes by $\sim 1^\circ/\text{day}$, the plasma from this entire period can be approximated as having originated at the limb. Extrapolation results are in Figure 2, where the small forward shock on DoY 168 has resulted in the gap in the extrapolated flow speed.

The flow speed in Figure 2 is constant from DoY 141 to 154 (22 May to 1 June). This is unusual for slow wind (McComas *et al.* 1998) and reflects the quiet



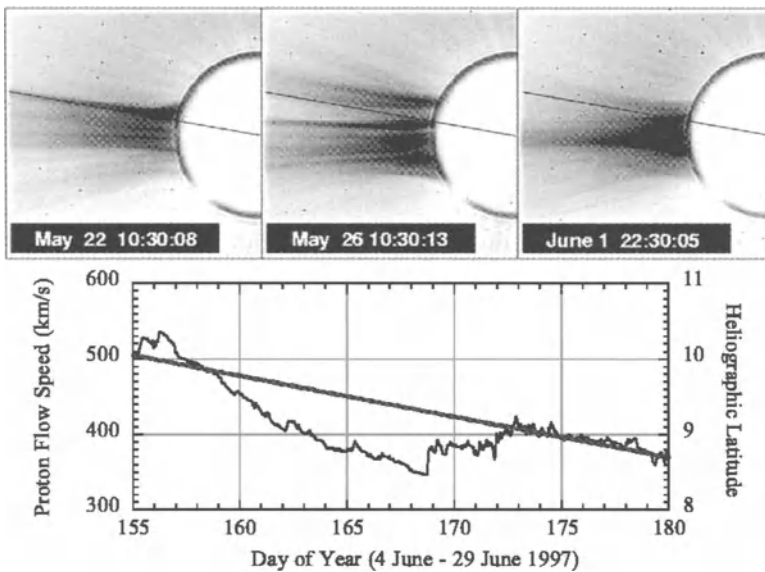


Figure 1. Top: Negative, edge enhanced LASCO/C2 images on 22 May, 26 May, and 1 June 1997. The black line shows the direction to Ulysses. Bottom: SWOOPS solar wind speed and Ulysses latitude over the interval when wind from 22 May to 1 June 1997 would have reached Ulysses.

conditions in the corona. Comparing this with the LASCO images in Figure 1, it is seen that the latitude of Ulysses was always inside the streamer (barely inside on 22 May). However, the appearance of the corona underwent large changes. First, the streamer belt was narrow, well defined, and had a sharp northern boundary. Next, the streamer belt fanned out to a wide angle. Finally, the streamer belt returned to being thin with a sharp northern boundary. UVCS detected similar streamer morphology at this time.

The UVCS O⁵⁺ 1032 to 1037 Å line ratio, \mathcal{R} , gives an estimate for the plasma outflow speed without the modeling necessary to compute quantitative speeds (Kohl *et al.* 1997). These ratios are shown in Figure 2. At $3.5 R_S$, $\mathcal{R} = 2.6\text{--}2.7$ (except on 23 May) while at $4.5 R_S$, $1.8 < \mathcal{R} < 2.0$. The range $2 < \mathcal{R} < 4$ implies $v < 100$ km/s while $\mathcal{R} \leq 2$ implies $v > 100$ km/s from Doppler dimming. Therefore, Figure 2 implies $v < 100$ km/s at $3.5 R_S$ and $v > 100$ km/s at $4.5 R_S$. The data (except on 23 May) are also consistent with no time variation, as observed at Ulysses. However, we note that the 1σ error bars shown in Figure 2, especially those on DoY 149/150, imply considerable uncertainty in these results.

SWOOPS density extrapolated to the Sun is shown in Figure 3. This is compared with UVCS Ly- α intensity, which is a density proxy (Ly- α intensity is not directly equivalent to density since it is convolved with flow speed and kinetic temperature). The uncertainty in $I_{\text{Ly-}\alpha}$ is $< 5\%$ and therefore not displayed in this figure. $I_{\text{Ly-}\alpha}$

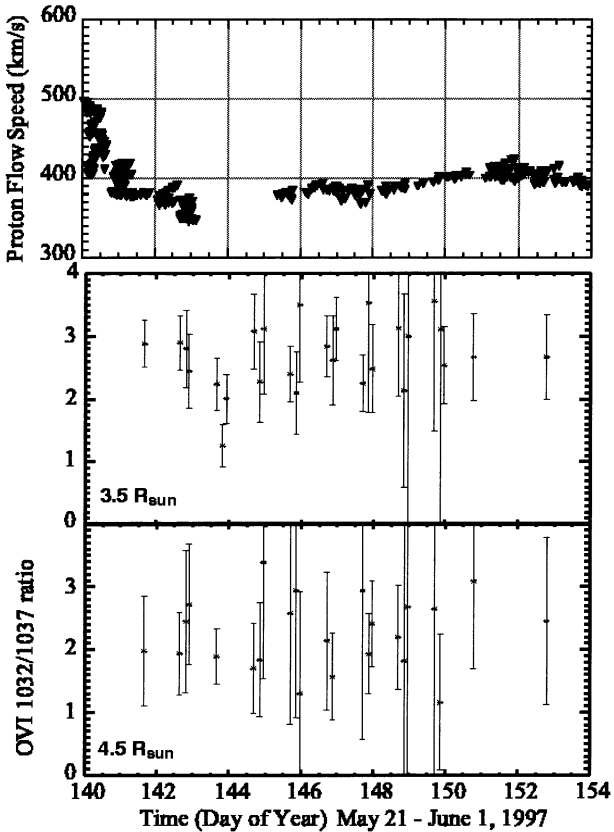


Figure 2. Top: Solar wind flow speed extrapolated to the Sun using the constant velocity approximation. *Bottom:* UVCS O VI 1032/1037 Å ratio at 3.5 and 4.5 R_S and 9–10° latitude over the interval Ulysses was off the Solar limb.

changes over the target interval by less than a factor of two, but there are definite “sub-intervals” that seem distinct from each other. Sub-intervals I1, I2, and I3 correspond in time with the LASCO/C2 visual changes in Figure 1. The sub-intervals also seem to have a counterpart in the density at Ulysses in Figure 3.

2. Summary & Conclusions

1. If it is assumed that the bright streamer boundary is the fast/slow wind boundary, then the solar wind moves little in latitude between a few R_S and 5 AU. Also, there is no obvious mixing due to shear instabilities.
2. The slow wind has the same speed independent of the visual streamer appearance, both near the Sun and at 5 AU.

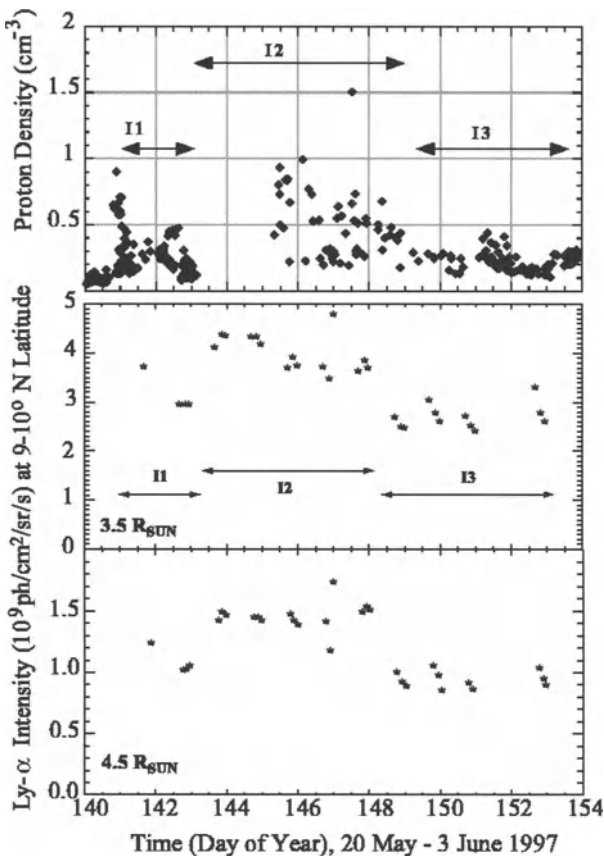


Figure 3. Top: SWOOPS density extrapolated to the Sun. Bottom: UVCS Ly- α intensity at several times over the interval Ulysses was off the Solar limb.

3. The broadening of the streamer corresponds both to enhanced $I_{\text{Ly-}\alpha}$ and to enhanced solar wind density.

This research has been supported by the Ulysses/SWOOPS and SOHO/UVCS projects.

References

- Kohl, J. L., et al.: 1997, *Sol. Phys.*, **175**, 613–644.
 McComas, D. J., et al.: 1998, *Geophys. Res. Lett.*, **25**, 1–4.

Address for correspondence: S. T. Suess, NASA Marshall Space Flight Center, Mail Stop ES82, Huntsville, AL 35812, USA

STREAMER EVAPORATION

S. T. SUESS

NASA Marshall Space Flight Center, Huntsville, AL, USA

A.-H. WANG and S. T. WU

University of Alabama in Huntsville, USA

S. F. NERNEY

Ohio University in Lancaster, USA

Abstract. Streamer evaporation is the consequence of heating *in ideal MHD models* because plasma is weakly contained by the magnetic field. Heating causes inflation, opening of field lines, and release of solar wind. It was discovered in simulations and, due to the absence of loss mechanisms, the ultimate end point is the complete evaporation of the streamer. Of course streamers do not behave in this way because of losses by thermal conduction and radiation. Heating is also expected to depend on ambient conditions. We use a global MHD model with thermal conduction to examine the effect of changing the heating scale height. We also extend an analytic model of streamers developed by Pneuman (1968) to show that *steady* streamers are unable to contain plasma for temperatures near the cusp greater than $\sim 2 \times 10^6$ K.

Key words: corona, streamers, magnetohydrodynamics

1. MHD Models

In ideal, polytropic, MHD models of coronal structure, the energy equation used is (1) where γ is the polytropic index and $1 \leq \gamma \leq 5/3$. If volumetric heating, Q , is added then the equation is generalized to (2).

$$\left(\frac{\partial}{\partial t} + \mathbf{v} \cdot \nabla \right) \left(\frac{p}{\rho^\gamma} \right) = 0 \quad (1)$$

$$\left(\frac{\partial}{\partial t} + \mathbf{v} \cdot \nabla \right) \left(\frac{p}{\rho^\gamma} \right) = \frac{\gamma - 1}{\rho^\gamma} Q \quad (2)$$

When $\mathbf{v} \neq 0$, $\gamma < 5/3$ in (1) implies heating and the equivalent heat source can be found by setting $\gamma = 5/3$ in (2) and solving for Q . However, in magnetostatic structures, such as was presumed to be the case in streamers, $\mathbf{v} \equiv 0$ and the *only permissible heat source is* $Q = 0$, even when $\gamma < 5/3$. Steinolfson (1988) showed that $Q \neq 0$ in (1) therefore results in a time-dependent global solution in which streamers become hotter, expand, and slowly open from the top to release new solar wind. In the absence of thermal conduction and radiative losses, this process continues until streamers have completely evaporated. We later generalized this result (Wang *et al.* 1998, *op cit.*) by showing that thermal conduction reduces, but does not eliminate evaporation, permitting a small, stable streamer core only after physical times of several months.

This clarifies the physics of streamer confinement by showing that in streamers the ratio of thermal to magnetic pressure (β) is greater than unity above $\sim 1.2 R_S$,



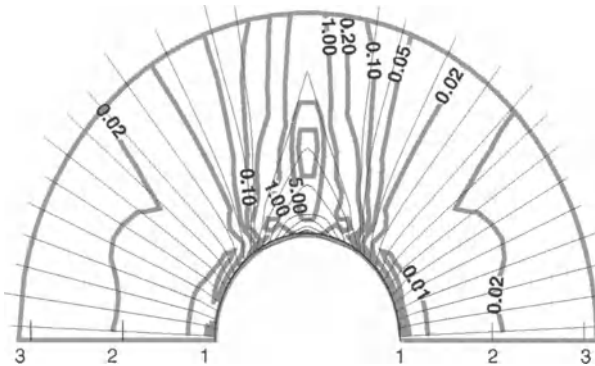


Figure 1. β in a model with volumetric heat and momentum sources (Wang *et al.* 1998). Thin lines are magnetic field lines, thick gray lines are β contours.

with confinement provided by the magnetic fields outside streamers, in adjacent coronal holes, pressing against the flanks of streamers. This contradicts the widely held idea that $\beta < 1$ in streamers and that a $\beta \ll 1$ prominence cavity is an essential component of streamers (e.g., Low 1996). However, it is supported by other numerical models (Steinolfson *et al.* 1982) and SOHO and Yohkoh empirical results (Li *et al.* 1998). Figure 1 reproduces β from a recent simulation with heat and momentum sources and thermal conduction, showing that $\beta > 1$ in the streamer and $\beta \ll 1.0$ in adjacent coronal holes (Wang *et al.* 1998). We used this MHD model to see the effect of varying the heat source scale height with a source term given by

$$Q = Q_o(\theta) \exp(-|r - a(\theta)|/L) \quad (3)$$

$$a(\theta) = 2.88 [1 - 0.3 \cot^{-1}(5(j - 18))] / [1 + 0.3 \tan^{-1}(5(j - 18))] \quad (4)$$

$$Q_o(\theta) = Q_o [\rho(r, \theta)/\rho_o(\theta)] [1 - 0.25 \tan^{-1}(5(j - 18))] \quad (5)$$

where $j = 1, 18$ from the pole to the equator and Q_o is in units of 10^{-8} ergs/cm³/s. We tried three cases: (1) $Q_o = 10.75$, $L = 2 R_S$, (2) $Q_o = 7.00$, $L = 5 R_S$, (3) $Q_o = 5.80$, $L = 10 R_S$. The functional form for (3)–(5) is based on empirical requirements and earlier models (Wang *et al.* 1998). By adjusting the magnitude of the heating while changing the scale height, we find that the solution can be made independent of the scale height over the above range of parameters. In all cases, the streamer evaporation continued in much the same way, significantly reducing the height of the streamer over 1–2 months.

2. Analytic Models

To evaluate evaporation without the ambiguity of numerical solutions, we apply Pneuman's (1968) analytic model. Given that $\beta > 1.0$ in streamers, it divides a

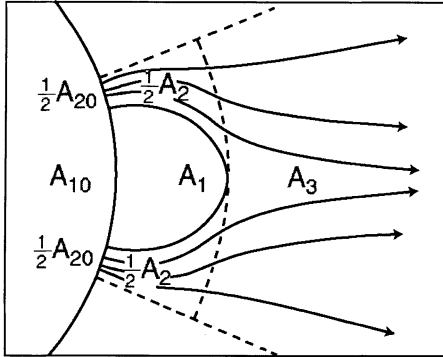


Figure 2. Definitions of the three regions in Pneuman's (1968) analytic model of coronal structures (see text).

streamer and adjacent coronal holes into the three regions shown in Figure 2: (1) A_1 where $\beta > 1$ and there is no flow, (2) A_2 where $\beta \ll 1$ and there is a Parker thermal wind, approximated here by radial flow, and (3) A_3 , occupying the entire region above the helmet. This model assumes the coronal hole magnetic field provides the $\mathcal{O}[1]$ confining force for streamers. The parameters are the base area ratio, A_{20}/A_{10} , the height above which $\beta_1 > 1$, the temperatures in regions 1 and 2, the density at the base of regions 1 and 2, and the magnetic field strength at the base of region 2. The field is ignored in region 1 and Pneuman assumed isothermal flow. The governing equations are

$$N_1 = N_{10} \exp \left\{ -\frac{\mu G M_S m_p}{r_o k T_1} (1 - r_o/r) \right\} \quad (6)$$

$$\frac{1}{2} V^2 + \frac{k T_2}{\mu m_p} \ln \left(\frac{N_2}{N_{20}} \right) + \frac{G M_S}{r_o} (1 - r_o/r) = \frac{1}{2} V_{20}^2 \quad (7)$$

$$N_2 V_2 A_2 = N_{20} V_{20} A_{20} \quad (8)$$

$$B_2 A_2 = B_{20} A_{20} \quad (9)$$

$$A_1 + A_2 = (r^2/r_o^2)(A_{10} + A_{20}) \quad (10)$$

$$k N_1 T_1 = k N_2 T_2 + (B_2^2/2\mu_o) \quad (11)$$

While this invokes an isothermal, hydrostatic atmosphere in A_1 , hydrostatic solutions with additional physical processes such as thermal conduction, wave heating, and radiative losses are easily incorporated.

Figure 3 shows some of Pneuman's solutions. It is apparent (left and center panels) that they look just like numerical solutions, with low temperatures producing rounded streamers and higher temperatures producing sharply cusped streamers. Pneuman then showed that above a specific temperature *no closed solution exists*. In the right panel, for $A_{20}/A_{10} = 0.5$ there is no closed solution for $T > 1.62 \times 10^6$ K, close to the temperature measured by Li *et al.* (1998)! This implies an upper bound

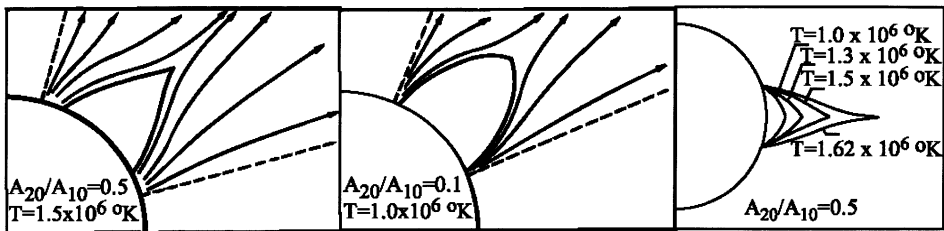


Figure 3. Left and Center: Streamer geometry for two different area ratios and temperatures. Right: Solutions for varying temperature with constant area ratio.

for the temperature in steady coronal streamers and evaporation in the presence of increasing temperature.

What Pneuman did not realize is that because $\beta \ll 1$ in coronal holes, the solution to (6)–(11) is, to $\mathcal{O}[1]$, independent of plasma conditions in the coronal hole and it is not necessary to solve for the flow field to find the streamer geometry. This suggests a very simple mathematical approach to streamer analysis. First, any 1D static atmosphere solution can be used in the streamer above heights where $\beta > 1$. Many such models have been published that incorporate radiative losses, thermal conduction, and various forms of heating (e.g., Priest *et al.* 1998). This is where the most important physical processes come into in this model. Second, the simplicity of the equations admits analytic analysis of slow streamer evolution and of streamer stability. Finally, it will be possible to unambiguously analyze the effects of different physical processes for heating streamers.

To conclude, this provides a way for improved modeling of streamer confinement, evolution, and of the source of the observed small releases of mass.

References

- Li, J., *et al.*: 1998, ‘Physical Structure of a Coronal Streamer in the Closed-Field Region as Observed from UVCS/SOHO and SXT/Yohkoh,’ *Ap. J.*, **506**, 431.
- Low, B. C.: 1996, ‘Solar Activity and the Corona,’ *Sol. Phys.*, **167**, 217.
- Pneuman, G.: 1968, ‘Some General Properties of Helmeted Coronal Structures,’ *Sol. Phys.*, **3**, 578.
- Priest, E. R., *et al.*: 1998, ‘Nature of the Heating Mechanism for the Diffuse Solar Corona,’ *Nature*, **393**, 545.
- Steinolfson, R. S.: 1988, ‘Density and White-Light Brightness in Looplike Coronal Mass Ejections: Importance of the Preevent Atmosphere,’ *J. Geophys. Res.*, **93**, 14261.
- Steinolfson, R. S., Suess, S. T., and Wu, S. T.: 1982, ‘The Steady Global Corona,’ *Ap. J.*, **255**, 730.
- Wang, A.-H., Wu, S. T., Suess, S. T., and Poletto, G.: 1998, ‘Global Model of the Corona with Heat and Momentum Addition,’ *J. Geophys. Res.*, **103**, 1913.

UVCS/SOHO OBSERVATIONS OF H I LYMAN ALPHA LINE PROFILES IN CORONAL HOLES AT HELIOCENTRIC HEIGHTS ABOVE $3.0 R_{\odot}$

R. M. SULEIMAN,* J. L. KOHL, A. V. PANASYUK, A. CIARAVELLA,**
S. R. CRANMER, L. D. GARDNER, R. FRAZIN, R. HAUCK and P. L. SMITH
Harvard-Smithsonian Center for Astrophysics, 60 Garden St., Cambridge, MA 02138, USA

G. NOCI
Università di Firenze, I-50125 Firenze, Italy

Abstract. The Ultraviolet Coronagraph Spectrometer (UVCS) on the Solar and Heliospheric Observatory (SOHO) has been used to measure spectral line profiles for H I Ly α in the south polar coronal hole at projected heliocentric heights from 3.5 to $6.0 R_{\odot}$ during 1998 January 5–11. Observations from 1.5 to $2.5 R_{\odot}$ were made for comparison. The H I Ly α profile is the only one observable with UVCS above $3.5 R_{\odot}$ in coronal holes. Within this region the outflowing coronal plasma becomes nearly collisionless and the ionization balance is believed to become frozen.

In this paper, the $1/e$ half widths of the coronal velocity distributions are provided for the observed heights. The velocity distributions include all motions contributing to the velocities along the line of sight (LOS). The observations have been corrected for instrumental effects and interplanetary H I Ly α . The half widths were found to increase with projected heliographic height from 1.5 to $2.5 R_{\odot}$ and decrease with height from 3.5 to $5 R_{\odot}$.

Key words: corona, coronal holes, solar wind, UV radiation, spectroscopy, line profiles

1. Introduction

The H I Ly α line is formed predominately by resonant scattering of chromospheric photons by the few neutral hydrogen atoms remaining in the extended corona, and negligibly by collisionally excited atoms (Gabriel 1971). In polar coronal holes, H I Ly α is the most intense spectral line and the only line profile observable with UVCS above $3.5 R_{\odot}$. At high heights in the extended corona the H 0 is believed to decouple from protons (Allen, Habbal and Hu 1998) and the ionization balance becomes frozen at about $5 R_{\odot}$ (e.g., Ko *et al.* 1997). Hence the H 0 velocity distribution may not fully reflect the proton transverse wave motions or the effects of wave damping. However, the relative drift velocity between H 0 and protons can induce a preferential “frictional” heating of the H 0 atoms (Olsen *et al.* 1994).

Observations of H I Ly α line profiles at projected heliographic heights above $3 R_{\odot}$ in polar coronal holes provide an interesting test of solar wind models aimed at identifying the physical processes involved in the acceleration of high speed solar wind streams. This paper provides $1/e$ half widths of H 0 velocity distributions derived from line profile measurements.

* Email: rsuleiman@cfa.harvard.edu

** Visiting Scientist, Smithsonian Astrophysical Observatory



2. Polar Coronal Hole Observations

The spectral line profiles discussed in this paper were obtained with the Ultraviolet Coronagraph Spectrometer, UVCS (Kohl *et al.* 1995) on the Solar and Heliospheric Observatory, SOHO (Domingo, Fleck and Poland 1995). The UVCS/SOHO has been described previously in detail by Kohl *et al.* (1995).

The south polar coronal hole was observed during 1998 January 5–11 by both the UVCS Ly α channel and the redundant optical path of the O VI channel. The south polar coronal hole subtends a range of position angles of 50 degrees at $2 R_{\odot}$ centered at a position angle of 180 degrees, and appears to be similar to the configuration observed by SOHO (Cranmer *et al.* 1999) in 1996 near solar minimum. During the period of observation the south polar coronal hole was observed from 3.5 to $6 R_{\odot}$ for \sim 47 hours. Lower heights (1.5 – $2.5 R_{\odot}$) were observed with the Ly α channel using a standard synoptic sequence. The Ly α instantaneous field of view (FOV) was $14'' \times 40'$. The width of the spectrometer slit of the Ly α channel was $50 \mu\text{m}$ which provides an effective $1/e$ half width of the instrument profile (see Panasyuk *et al.* 1999) of 0.46 \AA . The detector binning for the Ly α channel was 0.28 \AA in the spectral direction and $21''$ in the spatial direction. The fields of view of the two instrument channels are slightly offset. The redundant path FOV was $14'' \times 40'$ and the spectrometer slit of the redundant path was $50 \mu\text{m}$ with an effective $1/e$ half width of the instrument profile of about 0.13 \AA . The detector binning for the redundant path was 0.185 \AA in the spectral direction and $14''$ in the spatial direction.

3. H I Ly α Line Profile Analysis

The line profiles presented in this paper are averaged over a $10.5'$ segment of the length of the entrance slit and centered on the projection of the south solar pole axis. The observed region is expected to include contributions from both polar plumes and interplume regions. The observed coronal line profiles were first corrected for a detector effect that redistributes photon counts from the line core to the line wing. This produces an artificial broad line wing with an amplitude of 1–3% of the line peak. The removal of this effect is described by Kohl *et al.* (1997). The observations are corrected for flat field effects and geometrical distortion effects, and are wavelength and radiometrically calibrated using a procedure described by Panasyuk *et al.* (1999). The corrected profiles were curve-fit with a standard algorithm that minimizes the χ^2 . The stray light and F corona have the same profile as that of the disk convolved with the instrument profile. Constrained curve fits were used to identify and remove those contributions to the observed profiles. For observations with the Ly α channel at heights of 1.5 – $6 R_{\odot}$, a combination of stray light and F corona intensities were determined using in-flight measurements (not simultaneously) of the H I Ly α disk intensity and the ratio of the Si III 1206 \AA intensity at the observed heights in the coronal hole to its disk intensity. The

coronal intensity of Si III 1206 Å is expected to be negligible in coronal holes at the observed heights and so the observed intensity is expected to be a combination of stray light and F corona. For observations with the redundant optical path at heights of 3.5–6 R_{\odot} , C III 977 Å was used to determine the stray light to disk intensity ratio. The in-flight stray light plus F corona for H I Ly α at 2 R_{\odot} was found to be equivalent to $7.1 \times 10^7 \text{ ph s}^{-1} \text{ cm}^{-2} \text{ sr}^{-1}$ which is consistent with laboratory values (Gardner *et al.* 1996). The stray light for both channels was estimated to be equivalent to $\sim 1 \times 10^7 \text{ ph s}^{-1} \text{ cm}^{-2} \text{ sr}^{-1}$ for observed heights $\geq 3.5 R_{\odot}$. Removal of interplanetary H I Ly α will be discussed later in this §. The detector dark count was identified and subtracted by taking exposures of the same duration with a 3 density filter inserted near the entrance slit. The dark rate is about 2.5×10^{-5} counts per second per pixel.

The contribution from interplanetary H I Ly α for all profiles was determined from the observed profile at 6 R_{\odot} . We first removed the F corona and all instrumental effects (except the instrument profile width) from the coronal profile at 6 R_{\odot} . Judging from the shape of the resulting profile at 6 R_{\odot} , we have assumed that it includes contributions from only the interplanetary H I Ly α (i.e., no coronal component). We then used the intensity and width of this profile to constrain the contribution from interplanetary H I Ly α at other heights. The integrated intensity of interplanetary H I Ly α was found to be $3.2 \times 10^7 \text{ ph s}^{-1} \text{ cm}^{-2} \text{ sr}^{-1}$.

The observed coronal line profile widths resulting from the curve fits were corrected for the instrumental profile using a procedure described by Panasyuk *et al.* (1999) and converted to a velocity distribution using the usual Doppler formula:

$$v_{1/e} = \frac{\Delta\lambda_{1/e}}{\lambda_o} c \quad (1)$$

where $\Delta\lambda_{1/e}$ is the observed ($1/e$) half-width in wavelength and λ_o is the wavelength of the spectral line (Ly α in our case). This formula holds for 90 degree resonant scattering and is expected to be accurate to about $\pm 10\%$ for the observed coronal hole. The $v_{1/e}$ along the LOS includes all motions of the H 0 atoms. For example, no correction has been made for line broadening due to outflow velocity.

Figure 1 shows the $v_{1/e}$ for the observed coronal profiles. There is an increase in $v_{1/e}$ up to 2.5 R_{\odot} and gradual decrease from 3.5 to 5 R_{\odot} . This behavior is generally consistent with previously reported UVCS/SOHO results at projected heliographic heights up to 4 R_{\odot} (Kohl *et al.* 1997; Kohl *et al.* 1998), but uncertainties for heights at and above 3.5 R_{\odot} are now much smaller. It is also a different time in the solar cycle.

4. Discussion

We have measured H I Ly α spectral line profiles at projected heliographic heights from 1.5 to 6 R_{\odot} in the south polar coronal hole during 1998 January 5–11. The resulting coronal line widths, converted to $v_{1/e}$, increase from 1.5 to 2.5 R_{\odot} and

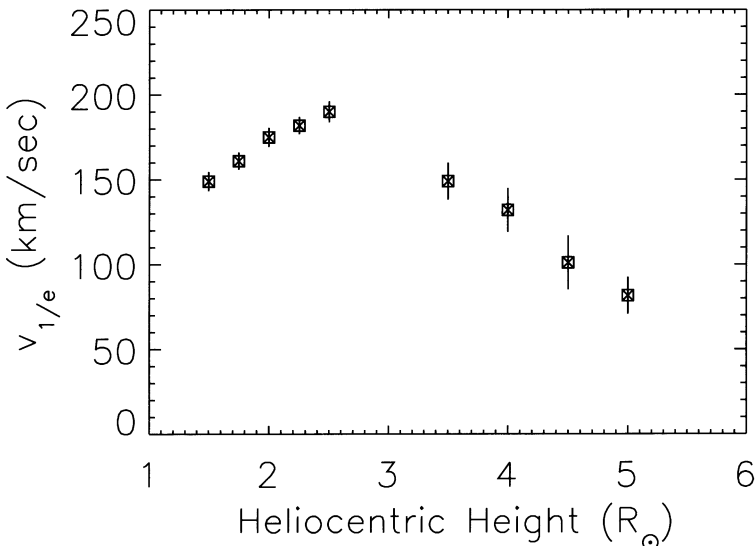


Figure 1. Plot of the $1/e$ half width of the H^0 velocity distribution averaged along the line of sight versus projected heliocentric height of the observations. The velocities are derived from H I Ly α line profile measurements in the south polar coronal hole during 1998 January 5–11. Error bars designate 1 standard deviation.

decrease with distance from sun center at observed heights above $3.5 R_{\odot}$. The statistical accuracy is high. Uncertainties at 1σ (1 standard deviation) in $v_{1/e}$ due to statistics and the removal of instrument effects and interplanetary H I Ly α are estimated, for example, at 3% at $2 R_{\odot}$ and 9.8% at $4 R_{\odot}$ (see Figure 1).

We are grateful to Egil Leer for the original suggestion to measure neutral hydrogen line profiles in coronal holes at high heights. This work is supported by NASA under Grant NAG5-3192 to the Smithsonian Astrophysical Observatory, by the Italian Space Agency, and by the ESA PRODEX program (Swiss contribution).

References

- Allen, L. A., Habbal, S. R., and Hu, Y. Q.: 1998, *J. Geophys. Res.*, **103**, 6551.
- Cranmer, S. R., et al.: 1999, *Ap. J.*, **511**, 481.
- Domingo, V., Fleck, B., and Poland, A., eds.: 1995, *The SOHO Mission*, *Solar Phys.*, **162**, 1–531.
- Gabriel, A. H.: 1971, *Solar Phys.*, **21**, 392.
- Gardner, L. D., et al.: 1996, *SPIE*, **2831**, 2–24.
- Ko, Y.-K., Fisk, L. A., Geiss, J., Gloeckler, G., and Guhathakurta, M.: 1997, *Solar Phys.*, **171**, 345.
- Kohl, J. L., et al.: 1995, *Solar Phys.*, **162**, 313.
- Kohl, J. L., et al.: 1997, *Solar Phys.*, **175**, 613.
- Kohl, J. L., et al.: 1998, *Ap. J. Letters*, **501**, L127.
- Olsen, E. L., Leer, E., and Holzer, T. E.: 1994, *ApJ*, **420**, 913.
- Panasyuk, A. V., et al.: 1999, in preparation.

ION TEMPERATURES AS OBSERVED IN A SOLAR CORONAL HOLE

C.-Y. TU* E. MARSCH and K. WILHELM

Max-Planck-Institut für Aeronomie, D-37191 Katlenburg-Lindau, Germany

Abstract. From the widths of the extreme ultraviolet (EUV) lines measured by the SUMER instrument on SOHO, it was found previously (Tu *et al.* 1998) that the average temperature of Ne^{+7} , at heights (relative to h_0) above the southern solar limb from $17''$ to $64''$, ranges between 1.3 and 5×10^6 K and of Ne^{+6} between 1 and 4×10^6 K. For mass-per-charge numbers greater than 4 the temperatures of the ions increase slightly with increasing mass-per-charge, while the thermal speed reveals no clear trend. We present a new data set with exposure times much longer than the ones in the previous study. The results obtained from line width analysis of Fe XII (1242 Å), Mg X (1249 Å), Mg VIII (772 Å) Ne VIII (770 Å), and Si VIII (1445 Å) support our previous study. In this case, the trend of increasing temperature begins at a mass-per-charge number of 3 . A qualitative explanation based on ion-cyclotron-resonance heating within linear kinetic theory is suggested.

1. Data Analysis and Results

Tu *et al.* (1998) presented an analysis of ion temperatures and the turbulence amplitude in solar coronal holes by using SUMER EUV emission line data. We present here a new data set supporting our previous analysis and suggest an explanation for the heating of the heavy ions. From the line width of an EUV emission line, one can estimate the effective ion speed $V_{i,\text{eff}}$ in the source region of the radiation, which consists of two components as described by the following equation:

$$V_{i,\text{eff}}^2 = \frac{2k_B T_{i,\text{eff}}}{m_i} = \frac{2k_B T_i}{m_i} + \xi^2 \quad (1)$$

Here T_i is the temperature of the ions of species i along the line of sight, m_i is their mass, and ξ the turbulent speed. The present study is based on a data set obtained by SUMER with long exposure times. The observation dates and instrument parameters for data sets 1, 2, 3 are as follows: 6 November, 7 December, and 10 December 1996, slit size: $1'' \times 300'', 4'' \times 300'', 1'' \times 300''$; center of the slit, Sun y (''): $-1160.31, -1129.69, 1120.19$, Sun x : 0; exposure time \times number of images: $720\text{ s} \times 28, 320\text{ s} \times 19, 1800\text{ s} \times 1$. The five emission lines chosen for this study are listed in Table I.

Figure 1(a) shows the five line profiles, with the measurements given by crosses and the fits given by the continuous interpolation curves. The results obtained for $V_{i,\text{eff}}$ and $T_{i,\text{eff}}$ at about $r = 1.15 R_S$ in the polar corona are listed in Table I and shown in Figure 1(b).

For the off-limb observations an acceptable assumption is that the contribution by a turbulent velocity, ξ , to the line widths is the same for different ion emission lines (Feldman and Laming 1993; Seely *et al.* 1997). From Table I we see that the

* Also: Department of Geophysics, Peking University, Beijing, 100871, China



Table I

Emission lines, wavelengths, normalized mass per charge ratios, full widths at half maximum (FWHM), effective temperatures, effective speeds and formation temperatures (Mg X in second order)

| λ | Fe XII (1242 Å) | Mg X (1249 Å) | Mg VIII (772 Å) | Ne VIII (770 Å) | Si VIII (1445 Å) |
|-----------------------------------|--------------------|------------------|--------------------|--------------------|---------------------|
| A_i/Z_i | 5.1 | 2.7 | 3.5 | 2.9 | 4.0 |
| FWHM (mÅ) | 289 | 343 | 195 | 189 | 385 |
| $\log(T_{i,\text{eff}}/\text{K})$ | 6.8 | 6.6 | 6.5 | 6.4 | 6.6 |
| $V_{i,\text{eff}}$ (km/s) | 42 | 50 | 46 | 44 | 48 |
| $\log(T_f/\text{K})$ | 6.2 | 6.1 | 5.9 | 5.8 | 5.9 |

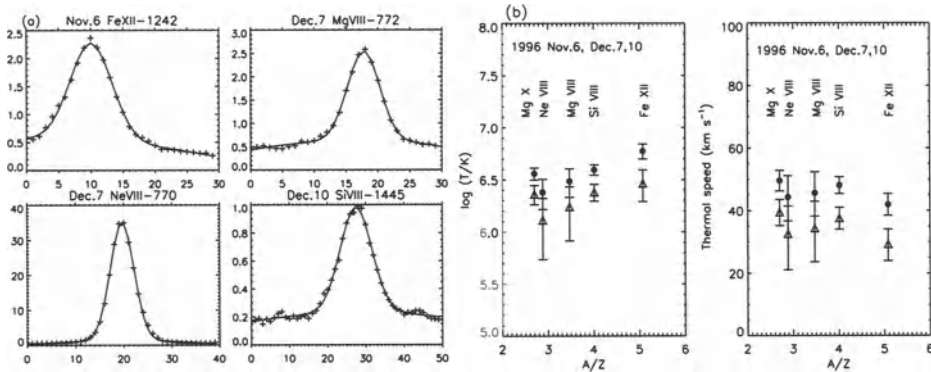


Figure 1. (a) Examples of observed averaged line profiles (crosses) and their Gaussian fits. The vertical axis corresponds to the averaged counting rate in count $\text{px}^{-1} \text{s}^{-1}$ and the horizontal axis to wavelengths in pixel units of the detector. (b) The left panel shows the logarithm of the ion temperature, $\log(T_i/\text{K})$, versus the A_i/Z_i ratio of the ions. The right panel shows the thermal speed of the ions derived from EUV emission from $140''$ to $180''$ above the limb, as defined by the brightening of the N IV line. Filled dots represent the results for $\xi = 0$, while triangles are for $\xi = 30 \text{ km s}^{-1}$. The uncertainties correspond to a ± 0.2 pixel variation of the Gaussian-fit standard deviation, σ , for each line.

heaviest ion, iron, has the smallest effective speed, 42 km s^{-1} . Since the iron kinetic temperature must not be negative, a zero value of that temperature will produce a $V_{i,\text{eff}}$ which is solely due to turbulence and thus places an upper limit on ξ . The upper limit on ξ is about 40 km s^{-1} in this data set. Assuming a relatively large value of $\xi = 30 \text{ km s}^{-1}$ we can then calculate for each of the lines studied lower limits of the ion kinetic temperatures. In Figure 1(b) we show our results (triangles), giving lower limits for the ion temperatures.

On the other hand, we may put ξ equal to zero, in which case the line broadenings would be of a thermal nature only. Accordingly, the $T_{i,\text{eff}}$ resulting from equation (1) will set an upper limit on T_i for each line (filled dots in Figure 1[b]). We see that

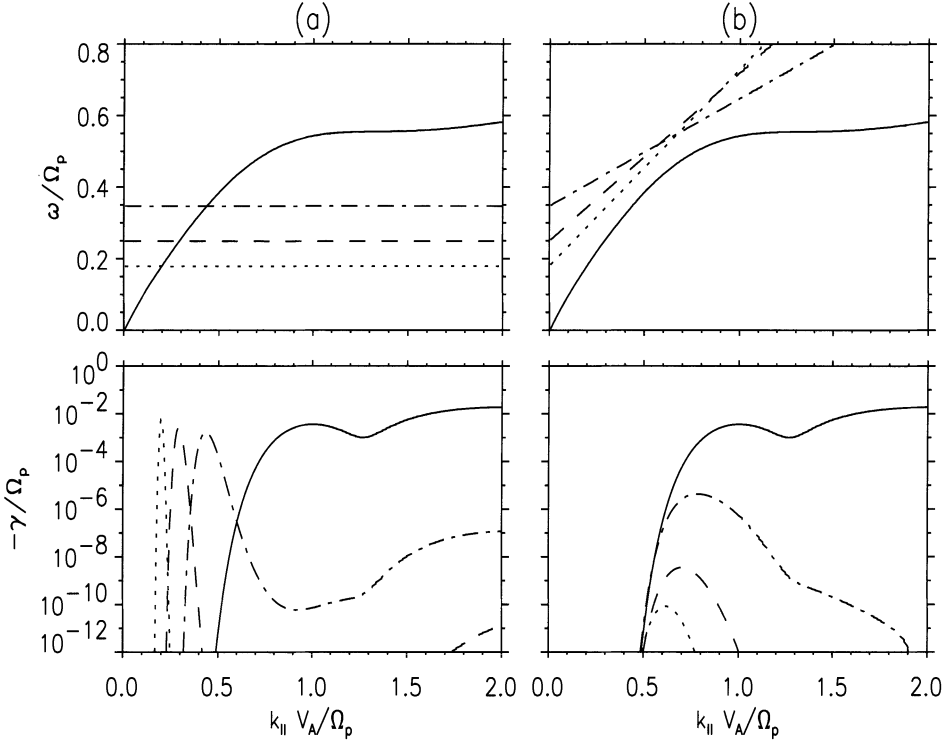


Figure 2. (a) The upper panel shows the dispersion relations and the lower one the normalized damping rates ($-\gamma$). The solid line in the upper panel shows the dispersion relation with $\beta_p = 0.056$, $\beta_\alpha = 0.014$, relative abundance $\eta_\alpha = 0.1$, and $\hat{U}_i = 0$. In the lower panel the solid line shows the damping rate contributed only by protons. The three dashed lines show the dispersion relations (upper panel) and the damping rates (lower panel), respectively, for Ne^{+7} , Si^{+7} and Fe^{+10} with $\hat{U}_i = 0$. (b) Same as (a), but $\hat{U}_{Fe} = 0.38$, $\hat{U}_{Si} = 0.30$, $\hat{U}_{Ne} = 0.15$, where \hat{U}_i is the ion drift speed normalized to the Alfvén speed.

the temperature for Si^{+7} and Mg^{+9} ranges from 2.5×10^6 to 5.0×10^6 K. We also see a slight trend of an ion temperature increase with increasing mass-per-charge number. Since the uncertainties are large, the trend needs to be confirmed by further studies.

2. A Possible Explanation

We suggest the following process to explain the data: in the first step, heavy ions resonate with waves at a frequency much lower than the resonant frequency of protons. Figure 2(a) illustrates this situation. The equations used in the calculation of the linear damping rate are all described in Marsch *et al.* (1982). The heavy ions have no or only small drift speeds. The resonant frequency, ω , is near Ω_i .

Therefore, the heavy ions absorb almost all the energy of the waves propagating outwards from the base of the corona. This absorption leads to an extremely high heating and acceleration of heavy ions.

In the second step, both heavy ions and protons absorb simultaneously the wave energy at wave vectors very near the resonant k_{\parallel} . Figure 2(b) illustrates this situation. At this stage, the ion resonance frequencies (in the wind frame) finally reach the high-frequency range, where a considerable amount of protons are also in resonance with the waves, since the ion plasma beta, $\beta_i = 2k_B T_i / m_i V_A^2$, in the corona is small but finite.

From Figure 2(b) we see that the normalized drift speed \hat{U}_i increases from 0.0 to 0.28, when increasing the mass-per-charge of the three heavy ions. Apparently, the acceleration and heating are related. This may qualitatively explain the observed slight trend of the heavy ion temperature increasing with mass-per-charge.

Acknowledgements

The SUMER project is financially supported by DLR, CNES, NASA and the ESA PRODEX program (Swiss contribution). We thank the SUMER operation team and the staff at the Experiment Operations Facility (EOF) of SOHO at GSFC in Greenbelt, USA, for their support in obtaining the observations. Part of C.-Y. Tu's work was supported by the National Natural Science Foundation of China and by Peking University.

References

- Feldman, U., and Laming, J.M.: 1993, *Ap.J.*, **404**, 799.
- Marsch, E., Goertz, C. K., and Richter, K.: 1982, *J. Geophys. Res.*, **87**, 5030.
- Seely, J. F., Feldman, U., Schühle, U., Wilhelm, K., Curdt, W., and Lemaire, P.: 1997, *Ap.J.*, **484**, L87.
- Tu, C.-Y., Marsch, E., Wilhelm, K., and Curdt, W.: 1998, *Ap.J.*, **503**, 475.

UVCS OBSERVATIONS AND MODELING OF STREAMERS

A. M. VÁSQUEZ, J. C. RAYMOND and A. A. VAN BALLEGOOIJEN

*Harvard-Smithsonian Center for Astrophysics, 60 Garden St. MS 15, Cambridge, MA 02138, Email:
avasquez@cfa.harvard.edu*

Abstract. We present results derived from the analysis of an equatorial streamer structure as observed by the UVCS instrument aboard SOHO. From observations of the H I Ly α and Ly β lines we infer the density and temperature of the plasma. We develop a preliminary axisymmetric, magnetostatic model of the corona which includes the effects of gas pressure gradients on the magnetic structure. We infer a coronal plasma $\beta > 1$ in the closed field regions and near the cusp of the streamer. We add to the model a parallel velocity field assuming mass flux conservation along magnetic flux tubes. We then compute the Ly α emissivity and the line-of-sight integrals to obtain images of Ly α intensity, taking into account projection effects and Doppler dimming. The images we obtain from this preliminary model are in good general agreement with the UVCS observations, both qualitatively and quantitatively.

1. UVCS Streamer Observations

The Ultraviolet Coronagraph Spectrometer instrument (UVCS/SOHO) is designed to measure many different UV coronal lines with high spectral and spatial resolution (maximum resolutions are about 0.15 Å and 12'' respectively; Kohl *et al.* 1995). The equatorial streamer image shown in Figure 1 has been constructed from observations of the solar west limb on 26 and 27 July 1996, near solar minimum. Close to minima the corona presents a relatively simple morphology: low latitudes are dominated by the equatorial streamer belt, and high latitudes by the polar coronal holes. Coronal UV lines are the result of a combination of collisional excitation and radiative scattering. The observed intensities for each contribution are roughly given by the following line-of-sight (LOS) integrals (e.g., Withbroe *et al.* 1982; Noci *et al.* 1993)

$$\begin{aligned} I_{\text{coll}}^{(\lambda)} &\propto \int_{\text{LOS}} n_e^2 (n_i/n_e) q_{ex}^{(\lambda)} dl \\ I_{\text{rad}}^{(\lambda)} &\propto \int_{\text{LOS}} n_e (n_i/n_e) I_{\odot}^{(\lambda)} B_{12} D^{(\lambda)} dl \end{aligned} \quad (1)$$

where n_e and n_i are the electron and emitting ion number densities, respectively, $q_{ex}^{(\lambda)}$ is the collisional excitation rate, B_{12} is the Einstein absorption coefficient, $I_{\odot}^{(\lambda)}$ is the chromospheric intensity for the line, and $D^{(\lambda)}$ accounts for Doppler dimming as well as dilution effects.

From the ratio of H I Ly α and Ly β intensities one can determine the collisional and radiative components for each line (see Raymond *et al.* 1997). Using the above integrals and assuming some radial dependence for electron density, we infer the electron density as a function of height along the axis of the streamer. From the width of the Ly α line we infer the H I temperature. For the streamer shown in



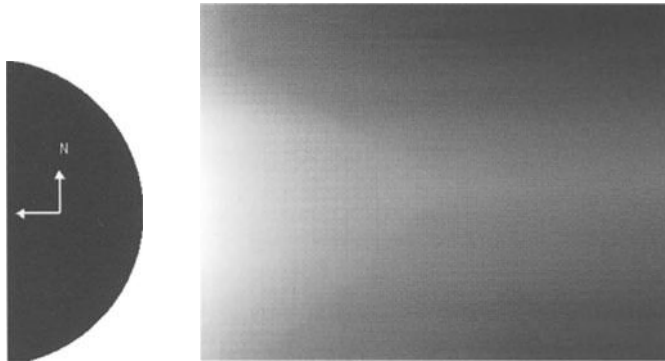


Figure 1. UVCS Ly α intensity image of equatorial streamer belt, in log scale.

Figure 1 we find, between 1.5 and 3.0 R_{\odot} , $n_e(r) \sim 6.5 \times 10^7 (r/R_{\odot})^{-4.3} \text{ cm}^{-3}$ and $T_H \sim 1.6 \times 10^6 \text{ K}$. Assuming $T_H \sim T_e$ in this region and a 10% He abundance, we obtain for the gas pressure $p \sim 0.03 (r/R_{\odot})^{-4.3} \text{ dyn cm}^{-2}$. These results are in agreement with previous analyses of this particular structure (see Raymond *et al.* 1997; Li *et al.* 1998).

2. Theoretical Modeling

To describe the general structure of the streamer belt, we assume stationarity (this structure existed for several months) and axisymmetry (roughly valid close to solar cycle minima). As a first step of this modeling, we neglect the effect of the solar wind on the coronal magnetic structure. Then, the force balance on the coronal plasma is described by

$$0 = -\nabla p + \rho \mathbf{g} + \frac{1}{4\pi}(\nabla \times \mathbf{B}) \times \mathbf{B}, \quad (2)$$

where $p(r, \theta)$ is the pressure, $\rho(r, \theta)$ is the density, \mathbf{g} is the acceleration of gravity, \mathbf{B} is the magnetic field, and θ is the polar angle. Let $A \equiv A_{\phi} r \sin \theta$, where $A_{\phi}(r, \theta)$ is the azimuthal component of the vector potential ($\mathbf{B} \equiv \nabla \times \mathbf{A}$); note that $A(r, \theta)$ is constant along field lines. The photospheric magnetic field is given by $B_r(R_{\odot}, \theta) = 10 \cos^7 \theta \text{ Gauss}$. We assume that 80% of the surface flux is open, i.e., the boundary between open and closed fields is given by $A_{\text{crit}} = 0.8 A_{\text{eq}}$, where A_{eq} is the value of A at the solar equator. We assume that the polar coronal hole boundary is at $A_{\text{bound}} \equiv 0.7 A_{\text{eq}}$.

The pressure and density are written as combinations of power laws:

$$p = \sum_{n=1}^3 p_n(A) \tilde{r}^{-k_n}, \quad \rho = \frac{R_{\odot}}{GM_{\odot}} \sum_{n=1}^3 k_n p_n(A) \tilde{r}^{1-k_n}, \quad (3)$$

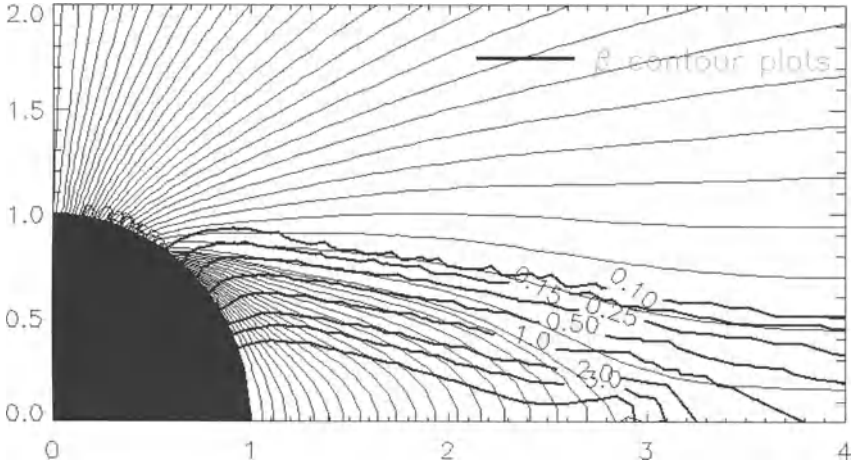


Figure 2. Magnetic field lines (thin lines) and contours of β (thick lines) in the meridional plane.

where $\tilde{r} \equiv r/R_\odot$ (we use $k_1 = 10$, $k_2 = 3.73$ and $k_3 = 3.63$). Note that equation (3) satisfies the component of equation (2) parallel to \mathbf{B} . We adjust the $p_n(A)$ to roughly match semiempirically derived densities in the equatorial region (from the above observations) and in the polar region (Cranmer *et al.* 1999). The functions $p_n(A)$ are constant within the coronal hole region ($0 < A < A_{\text{bound}}$), and increase with A within the streamer ($A_{\text{bound}} < A < A_{\text{eq}}$). To solve the perpendicular force balance we use an energy-minimization technique: we vary $A_\phi(r, \theta)$ until the volume integral of $B^2/(8\pi) - p(r, A)$ reaches a minimum. It can be shown that the solutions of this minimization problem are also solutions of equation (2). As a result of this procedure, we obtain the coronal magnetic field \mathbf{B} as well as pressure and density fields. Figure 2 shows selected field lines and contours of β , the ratio of gas pressure and magnetic pressure. Note the high β values in the closed region of the streamer and near the cusp (located at a radius of about $3 R_\odot$).

We add to this structure a parallel velocity field v_{out} using mass flux conservation and $n_p v_{\text{out}} \sim 2 \times 10^8 \text{ cm}^{-2}\text{s}^{-1}$ at 1 AU. Assuming ionization equilibrium to estimate the H I density, we compute the Ly α emissivity at each point of the corona. Then we compute the LOS integrals, given by equations (1), to obtain the Ly α intensity, accounting for Doppler dimming. We allow for an arbitrary angle α between the LOS and the meridional plane. Figure 3 shows the resulting images for two values of α .

3. Conclusions and Further Work

We have developed an axisymmetric and magnetostatic model of the corona, accounting for the effects of gas pressure gradients on the coronal magnetic struc-

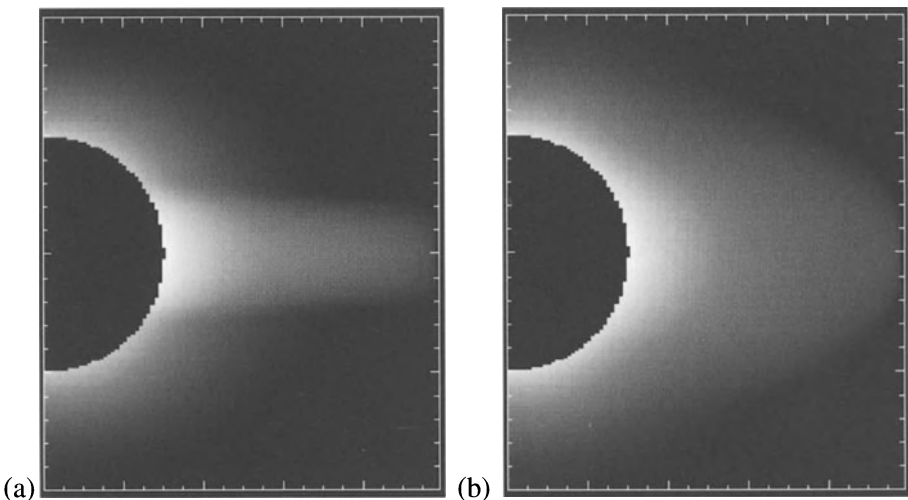


Figure 3. Ly α intensity as derived from the model (in log scale). The dark disk represents $1.5 R_{\odot}$. (a) $\alpha = 90^\circ$ (edge-on view); (b) $\alpha = 70^\circ$.

ture. The model predicts high plasma β values in the core and cusp of the streamers in accordance with recent global coronal models (e.g., Wang *et al.* 1998). We find that the streamer core is narrower than in the corresponding potential-field model. The predicted coronal Ly α intensities are in qualitative and quantitative agreement with UVCS observations at cycle minimum. For a small change in the direction of the LOS, the resulting images are noticeably different, illustrating very clearly the importance of projection effects in UV coronal observations.

Streamers are believed to be the source region of the slow solar wind. We are working on a second model, relaxing the static assumption to include a self-consistent velocity field. Also, we are working on a model for the minor ions, including the effects of gravitational settling in the streamer core. Using methods similar to the ones used in this work, we will compute O VI 1032, 1037 Å intensity images to compare with UVCS observations.

References

- Cranmer, S. R., *et al.*: 1999, *Astrophys. J.*, **511**, 481.
- Kohl, J. L., *et al.*: 1995, *Solar Phys.*, **162**, 313.
- Li, J., Raymond, J. C., and Acton, L. W.: 1998, *Solar Phys.*, submitted.
- Noci, G., *et al.*: 1993, *Solar Phys.*, **147**, 73.
- Raymond, J. C., *et al.*: 1997, *Solar Phys.*, **175**, 645.
- Wang, A. H., *et al.*: 1998, *J. Geophys. Res.*, **103**, 1913.
- Withbroe, G. L., Kohl, J. L., and Weiser, H.: 1982, *Space Science Rev.*, **33**, 17.

ALFVÉN WAVE GENERATION IN PHOTOSPHERIC VORTEX FILAMENTS, MACROSPICULES, AND “SOLAR TORNADOES”

MARCO VELLI* and PAULETT LIEWER

Jet Propulsion Laboratory, California Institute of Technology, Pasadena, CA 91109

Abstract. The properties of Alfvén waves generated in the photosphere by field lines trapped in vortex sinks and propagating upwards through the transition region and corona are discussed and contrasted to those of waves generated via reconnection in transition region explosive events, or rather via untwisting reconnecting flux tubes. An outline for future simulations and theoretical advances necessary to understand the dynamics of spicules and macrospicules is described, and a detailed search for photospheric velocity patterns underlying macrospicules is suggested.

1. Introduction

Spicules and macrospicules are a ubiquitous feature of the solar atmosphere outside active regions. Recently, Pike and Mason (1998) have shown that macrospicules may contain a significant rotational component (≥ 40 km/s) and dubbed their observed events “solar tornadoes.” They also suggested that the mechanism proposed by Shibata and Uchida (1986) of a reconnecting untwisting magnetic jet might be an appropriate model for the observed structures. Here we propose an alternative scenario which does not necessarily contradict but rather completes the previous one: the direct generation of such jets via the dynamics of photospheric vortices. Though this is not an entirely new proposition (see, e.g., the introduction to the papers on torsional Alfvén waves of Hollweg *et al.* 1982 and Hollweg 1992), a comparison of the reconnection/direct generation scenarios is worthwhile in order to determine the relative importance of the two phenomena in determining the observed dynamic features of the chromosphere-corona transition region. In the subsequent paragraphs we attempt such a comparison on the basis of analytical results and published simulations of Alfvén wave propagation and magnetic reconnection relevant to the solar atmosphere.

2. A Synopsis of Observations

Observations of the chromosphere in H α show the ubiquitous presence of spicules. These are jets of material outlining the chromospheric network, with diameters of about 10^3 km, that extend up to 6×10^3 to 10^4 km in the corona. Their lifetime is of order 5–10 min, vertical velocities are typically $v_z \simeq 20$ –30 km/s and the jets are observed to fade out, diffuse or fall back down. Characteristic electron temperatures and densities are of order $T_e \simeq 1.5 \times 10^4$ K, $n_e \simeq 1$ – 2×10^{11} cm $^{-3}$. Observations

* Permanent address: Dipartimento di Astronomia e Scienza dello Spazio, Università di Firenze, 50125 Firenze, Italy



by Pasachoff *et al.* (1968) and subsequently Cook (1991) seemed to show torsional motions in spicules, possibly up to speeds of order 50 km/s.

Macrospicules are larger versions of H α spicules with diameters up to 10^4 km, that extend higher up, from $2\text{--}4 \times 10^4$ km into the corona, have longer lifetimes, up to about 45 min, and higher vertical velocities, up to about 150 km/s. They are seen in lines formed between 6×10^4 K and 3×10^5 K and in radio observations (6 cm) where they appear to tilt and expand at their tops. Moore *et al.* (1977) established that macrospicules seen in the EUV are associated with H α macrospicules, and they also suggested an association with coronal X-ray bright points. Pike and Harrison (1997) reported observations of a macrospicule using the CDS instrument on SOHO and found relative Doppler velocities of up to 150 km/s in O V emission, which they interpreted as an outward flow possibly accelerating into the solar wind.

Pike and Mason (1998) found that CDS macrospicules observed on the limb show red and blue shifts on opposing sides of the macrospicule axis. The estimated velocities are just about symmetric with respect to the axis and increase from 0–10 km/s at the surface to about 20–50 km/s at heights of 1.5×10^4 km. They interpret such structures as rotating features, with rotational velocities increasing with height, possibly superimposed on an overall axial plasma acceleration. As to the structure of the rotating jet, observation of a dark lane in the O V emission led them to conclude that it is made of a cooler material core (presumably emitting in H α) surrounded by a transition region sheath of hotter material. The authors suggest the reconnection of emerging twisted flux tubes with pre-existing fields as the cause for the formation of such “tornadoes,” along the lines of work reviewed in Shibata (1997). A twisted magnetic loop reconnecting with an open field line and unwinding does so principally by emitting torsional Alfvén waves. However, such waves are also generated directly by photospheric turbulent velocity fields and the waves may only differ in the overall duration of individual packets as well as intrinsic frequencies excited. To clarify this point, we begin by discussing relevant theoretical modeling and numerical simulations.

3. Unwinding of Twisted Flux Tubes and Simulations of Alfvén Wave Propagation: Reconnection or Vorticity Emission?

The propagation of waves generated in the photosphere/chromosphere up through the transition region and corona has been the subject of extensive investigations in both linear and non-linear regimes (see, e.g., Velli 1993 and Hollweg 1992 for summaries of linear and non-linear investigations). A linear wave propagating upwards from the photosphere suffers significant reflection in the higher chromosphere and transition region, if one assumes horizontal homogeneity and the radial density stratification described by standard one dimensional (Vernazza, Avrett, and Loeser 1981) models of the solar atmosphere; in this respect, generation via magnetic reconnection at transition region heights would circumvent the transmission problem by shifting the generation height of the waves, as well as creating higher

frequency waves as will be shown below. On the other hand, the stratification in magnetic regions of the solar atmosphere probably deviates significantly from the one described above, so that the Alfvén velocity gradient as observed while moving upwards within a thin expanding photospheric flux tube could be significantly weaker than the corresponding gradient in the weakly magnetized atmosphere outside the flux tubes, allowing a significant energy flux to enter the corona.

Shibata and Uchida (1986) first proposed the reconnected, untwisting jet mechanism for the solar atmosphere and carried out 2D cylindrically symmetric simulations of a two-temperature atmosphere (representing the chromosphere and corona) with gravitational stratification. They started with a field twisted in its inner core extending from the chromospheric layer into the lower corona. As the twist is released it creates a jet propagating upwards and fanning out with height, attaining speeds that are a significant fraction of the ambient Alfvén speed when the twist of the initial tube is high (i.e., they always considered azimuthal field strengths of the same order of magnitude or larger than the axial field strengths).

Hollweg *et al.* (1982) and subsequently Hollweg (1992) carried out detailed 1D simulations of the propagation of a torsional pulse (of 90 s duration) within a fixed axially symmetric magnetic field geometry, and observed the formation of a fast and slow shock as the pulse propagated upward, as well as reflection at the transition region and upwelling of the latter, which was tentatively interpreted as formation of a spicule. More recently, Kudoh and Shibata (1997) carried out a 1D simulation similar in spirit, but with a continuously varying random azimuthal velocity at the base of the flux tube. The given flux tube geometry is such that the flux tube expands from a 280 km width and a 1600 G field intensity in the photosphere, to a diameter of 4×10^3 km, with a 7.8 G field intensity in the corona, while the photospheric density is 3×10^{-7} g/cm³ and falls to 10^{-15} g/cm³ in the corona. As a result, the Alfvén speed varies from 8.25 km/s in the photosphere to 695 km/s in the corona. The initial rms photospheric azimuthal velocity of ≈ 1 km/s becomes an rms velocity of ≈ 20 km/s in the corona, a factor of 5 less than expected from a WKB (zero reflection, conserved energy flux) estimate of the velocity. The variations in amplitude of the driver, combined with the background stratification, create a wave-associated force which drives a slow (sound) wave upwards as well as a jet. The rms axial coronal velocity is found to be 9.62 km/s. The azimuthal forcing drives the transition region upwards from 2×10^3 km to 5×10^3 km and higher. Concerning the time-scale of the driver, the variations in azimuthal velocity were composed of a rapid (less than 1 minute period) variation superimposed on a more regular 5 minute oscillation of 2 km/s amplitude. Remark that although the calculated coronal velocities are of the correct order of magnitude for observed spicules, the flux tube model used may underestimate the transmitted power. The reason is that a 1600 G flux tube is close to equipartition with the photospheric pressure, and must therefore be significantly evacuated. If this is the case, the Alfvén speed in the tube is much higher than the estimate given above, and therefore the overall Alfvén speed gradient is greatly reduced, allowing for improved wave transmission. This implies that 20–40 km/s

speeds in the corona might result from photospheric velocity fields with an rms amplitude well below 1 km/s.

Let us now consider the characteristics of an Alfvén wave generated by reconnection. If a twisted flux tube of radius r and length L emerges with a winding angle $N = LB_\phi/2\pi rB_z \geq 1$, (where B_ϕ, B_z are the poloidal and axial magnetic fields respectively), and reconnects, a wave-packet with typical period $\tau = L/NV_a$ and overall duration $T = L/V_a$ is emitted. One may estimate dimensionally the amplitude of the wave to be the greater of $B_\phi, R_c B_z/L$ where R_c was the original curvature of the emerging flux tube. For reconnection to be considered as a trigger type process, it must occur on a time scale not appreciably greater than the times mentioned above, which for a length of order 10^3 – 10^4 km and Alfvén speeds in the range $V_a \sim 10^2$ – 10^3 km/s translate into $T \sim 10$ – 100 s. This is close to the wave periods considered in the papers described above, and is within the time frame of spicules and chromospheric jets. Macrospicules however last appreciably longer, and one must invoke either much longer flux tubes (unlikely) or a very slow reconnection rate to increase T . An alternative may be given by the dynamics of photospheric vorticity.

Photospheric supergranulation flows concentrate magnetic flux at the network boundaries, where the resulting flux tubes exceed dynamic pressure equipartition and are close to evacuation pressure balance. Vorticity obeys the same equation as magnetic induction, and it is therefore plausible that vorticity and magnetic flux concentrations coincide. Vorticity filaments are the natural dissipative structures of 3D hydrodynamic turbulence and are observed to form in simulations of the solar convection zone (see, e.g., Brandenburg *et al.* 1991). Simon and Weiss (1997) have given several examples of vorticity sinks, associated with photospheric downdrafts, at mesogranular scales. They fit the observed vorticity with a profile

$$\omega(r) = (V/R) \exp(-r^2/R^2) ,$$

where V is the characteristic rotational velocity associated with the vortex and R its characteristic radius. A typical photospheric vortex lasts several hours and takes about two hours to develop. The strongest vortex they observed had $|\omega| \simeq 1.4 \times 10^{-3}$ s⁻¹, a size $R \simeq 2.5 \times 10^3$ km and a maximum azimuthal velocity of order 0.5 km/s. Such a vortex would produce an Alfvén wave packet, as the magnetic field lines are entrained by the rotational motion, whose frequency is given by the vorticity itself, and whose duration coincides with the life of the vortex. It is an intriguing coincidence that the lower bound of the so called Alfvénic range of turbulence in the solar wind resides at frequencies comparable to the intensity, i.e., vorticity or frequency, of the vortex filament found above.

4. Conclusions

We have compared the typical characteristics of reconnection generated Alfvén waves with those which should arise naturally above photospheric downdrafts with

associated vorticity sinks, and have shown that the latter typically have longer durations and lower frequencies than waves emitted during reconnection processes. The macrospicule jet would in our scenario be associated with the establishment of a vorticity sink, which could however last much longer than the associated macrospicule. The macrospicule jet which might decay, depending on the details of the magnetic geometry and thermodynamics, even though torsional Alfvén waves are being emitted until the vortex filament disrupts. This is because the spicule is associated with the initial piston provided by the development of the Alfvén wave packet as the vortex filament develops. Depending on the overall geometry (i.e., the nozzle shape) and temperature profile, such a jet might never reach a stationary state or provide the source of a “funnel wind flow” as envisaged by Tu and Marsch (1997), a topic which we are presently investigating. From a numerical point of view, simulations of Alfvén waves generated by a discrete set of vortex filaments with a somewhat simplified description of the photosphere, chromosphere and transition region in 2 and 3 dimensions are also being planned to provide a quantitative evaluation of the ideas described here. From an observational point of view, it would clearly be of interest to determine the photospheric velocity fields at the same time and place where a macrospicule is occurring, to verify whether or not an association with vortex filaments exists.

This research was performed at the Jet Propulsion Laboratory under a contract between the California Institute of Technology and the National Aeronautics and Space Administration. One of the authors (MV) held a National Research Council JPL Research Associateship.

References

- Brandenburg, A., Jennings, R. L., Nordlund, A., Rieutord, M., and Cook, J. W.: 1991, in *Mechanisms of Chromospheric and Coronal Heating*, ed. P. Ulmschneider, E. R. Priest and R. Rosner, (Springer Verlag), p. 93.
- Hollweg, J.: 1992, *ApJ*, **389**, 731.
- Hollweg, J., Jackson, S., and Galloway, D.: 1982, *Sol. Phys.*, **75**, 35.
- Kudoh, T., and Shibata, K.: 1997, in *Fifth SOHO Workshop: The Corona and Solar Wind near Minimum Activity*, ESA SP-404, p. 477.
- Moore, R. L., Tang, F., Bohlin, J. D., and Golub, L.: 1977, *ApJ*, **218**, 286.
- Pasachoff, J. M., Noyes, R. W., and Beckers, J. M.: 1968, *Sol. Phys.*, **5**, 131.
- Pike, C. D., and Harrison, R.: 1997, *Sol. Phys.*, **175**, 457.
- Pike, C. D., and Mason, H. E.: 1998, *Sol. Phys.*, in press.
- Shibata, K.: 1997, in *Fifth SOHO Workshop: The Corona and Solar Wind near Minimum Activity*, ESA SP-404, p. 103.
- Shibata, K., and Uchida, Y.: 1986, *Sol. Phys.*, **103**, 299.
- Simon, G. W., and Weiss, N. O.: 1997, *ApJ*, **489**, 960.
- Stein, R. F., and Tuominen, I.: 1996, *J. Fluid Mech.*, **306**, 325.
- Tu, C. Y., and Marsch, E.: 1997, *Sol. Phys.*, **176**, 87.
- Velli, M.: 1993, *A&A*, **270**, 304.
- Vernazza, J. E., Avrett, E. H., and Loeser, R.: 1981, *ApJS*, **45**, 635.

COMPARING QUIET SUN AND CORONAL HOLE REGIONS WITH CDS/SOHO

P. R. YOUNG

Department of Applied Mathematics and Theoretical Physics, Cambridge U.K.

R. ESSER

Smithsonian Astrophysical Observatory, Cambridge, Massachusetts, USA

Abstract. Spectra from the Coronal Diagnostic Spectrometer on board SOHO are used to compare density and temperature in coronal hole and quiet Sun regions.

Key words: coronal hole, quiet Sun, density, temperature

The Coronal Diagnostic Spectrometer (CDS) is an instrument on board SOHO that measures extreme ultraviolet emission lines (Harrison *et al.* 1997). The upper panel of Figure 1 shows three of these lines in quiet Sun and coronal hole conditions, while the lower panel shows the contribution functions of these ions, illustrating the temperatures at which they are most abundant. In the transition region, quiet Sun and coronal hole are not distinguished, and so the O V line has a similar intensity in each. The Mg IX line is representative of the “quiet corona,” and has a lower, but non-zero intensity in the coronal hole, while the Si XII line is more representative of the “active corona” and has zero intensity in the hole. The absence of Si XII implies that there is very little plasma with temperatures ≥ 1 million K.

The coronal hole spectrum in Figure 1 is from a “quiet coronal hole” area such as that highlighted in the EIT image of Figure 2. This image clearly shows that even for extended coronal holes such regions are difficult to isolate on account of contamination from plumes, bright points and loops in the coronal hole. The best place to find these quiet coronal hole areas is close to the quiet Sun/coronal hole boundary. Can the spectra be contaminated by high-lying quiet Sun plasma in the line of sight, however? The spectrum comparison of Figure 1 shows the Si XII 520.7 line to be absent in the coronal hole, but CDS observations of the quiet Sun above the limb (Fludra *et al.* 1997) show that an increasing amount of Si XII emission is expected with height. It is these high-lying regions that would be expected to contribute to the coronal hole spectrum, and the absence of the Si XII line confirms that the contamination is negligible.

Based on the consideration of many different coronal hole observations from CDS, it is possible to *define* quiet coronal hole regions as those where there is no Si XII emission, and where the Mg IX line has a signal of $50\text{--}100 \text{ erg cm}^{-2}\text{s}^{-1}\text{sr}^{-1}$. In terms of the Mg IX line a comparison of such regions with coronal hole bright points (CHBPs), “quiet” quiet Sun areas (QQS), average quiet Sun (QS) and quiet Sun bright points (QSBPs) is presented in Figure 3. The QCH regions are found to be between 5 and 9 times weaker than average quiet Sun areas.

With the use of the Mg IX line as a guide in the choice of solar region, the 349.9/345.1 density diagnostic of Si IX can be used to compare densities in quiet



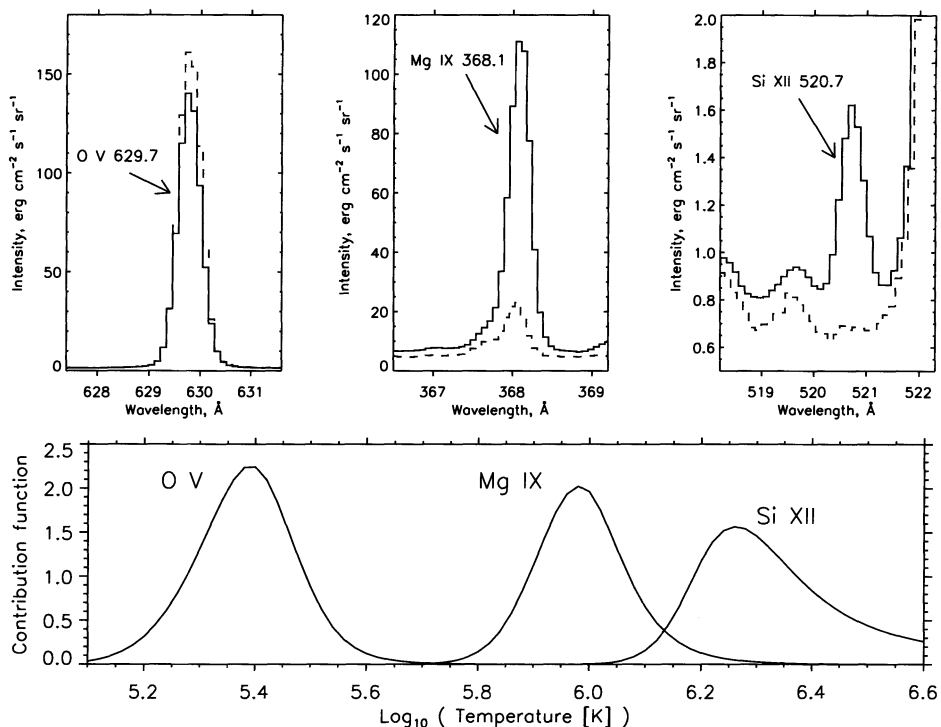


Figure 1. The upper plot shows CDS spectra from a quiet Sun area (solid line) and a coronal hole area (dashed line). The emission lines are O V 629.7 Å, Mg IX 368.1 Å and Si XII 520.7 Å, and the temperatures at which the lines are emitted are illustrated in the lower plot where the contribution functions of the ions are shown.

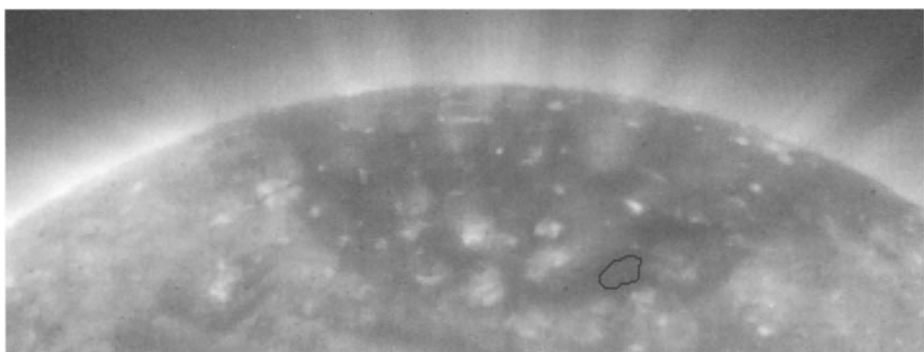


Figure 2. EIT Fe IX/X image of the north coronal hole from 01:00 UT, 21 October 1996. The black contour indicates a “quiet coronal hole” area.

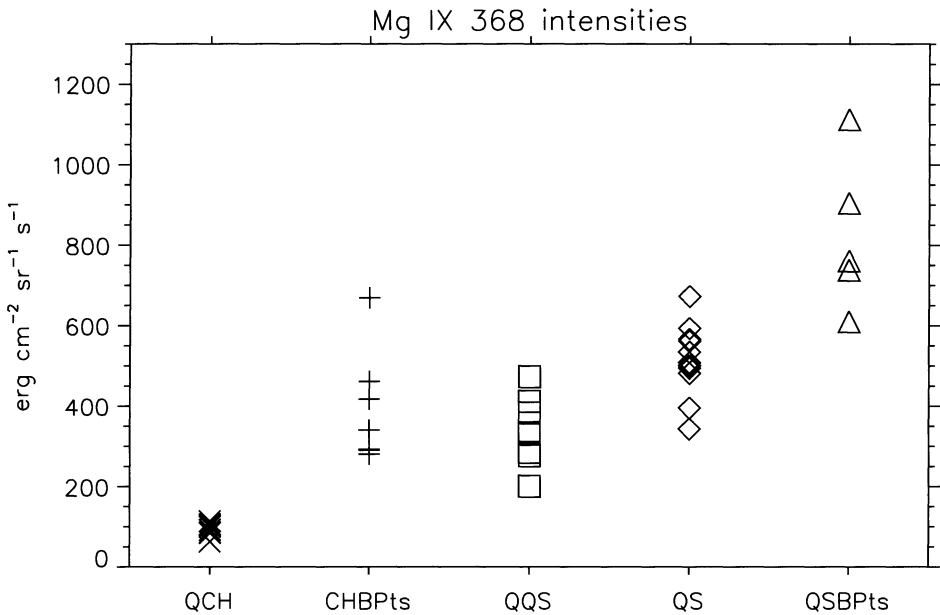


Figure 3. Mg IX 368.1 Å intensities for selected regions: quiet coronal hole (QCH), coronal hole bright points (CHBPs), “quiet” quiet Sun (QQS), average quiet Sun (QS) and quiet Sun bright points (QSBPs).

Sun and coronal hole regions. Si IX has an almost identical temperature of formation to Mg IX, and this is confirmed by Figure 4(a) which shows the 345.1+349.9 intensity plotted against the Mg IX intensity for several data-sets, revealing a linear correlation. In Figure 4(b) the 349.9/345.1 ratios are plotted against the Mg IX intensities. The conversion of the Si IX ratios to the densities in Figures 4(c) and 4(d) was performed by supplementing the *Chianti* ion model (Landi *et al.* 1998) with photoexcitation and stimulated emission rates, following Flower and Pineau des Forets (1973). The incident photons are assumed to be from a 6000 K photosphere, and it is necessary to specify the distance above the surface of the Si IX-emitting region through the *radiative dilution factor* (W). The values used here are 0.0 and 0.43, which correspond to the region being at infinity (equivalent to neglecting the extra processes) and 10 arc sec above the surface. The densities are lowered by the photon processes, with the differences being greatest at low densities: a density of 10^9 electrons/cm³ falls by only 3%, but a density of 10^8 electrons/cm³ falls by 61%.

Figure 4(d) shows that the quiet coronal hole regions have an order of magnitude lower density than the quiet Sun, and the values of $\approx 0.9\text{--}2.0 \times 10^7$ electrons/cm³ are considerably lower than those found previously. For example, Esser *et al.* (1998) derive $7\text{--}20 \times 10^7$ electrons/cm³ from *Skylab* data. The difference is largely due to the inclusion of the photon processes.

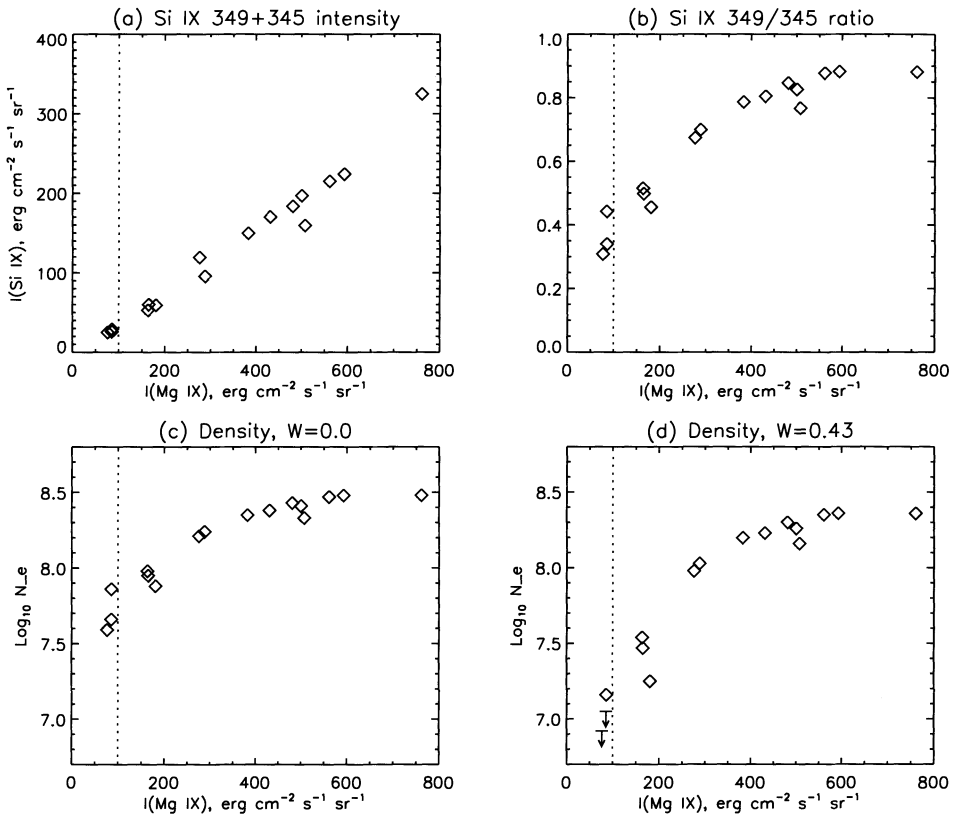


Figure 4. In each plot the x -axis gives the intensity of the Mg IX 368.1 Å line for a number of data-sets. In (a), the y -axis gives the Si IX 345.1+349.9 Å summed intensity; (b) the 349.9/345.1 ratio; (c) the derived electron number density (N_e) for $W = 0.0$; (d) the density for $W = 0.43$. Quiet coronal hole areas lie below Mg IX intensities of 100 erg cm⁻² s⁻¹ sr⁻¹ (the dashed line).

References

- Esser, R., Edgar, R. J., and Brickhouse, N. S.: 1998, *ApJ*, **498**, 448–457.
 Flower, D. R., and Pineau des Forets, G.: 1973, *Astronomy and Astrophysics*, **24**, 181–192.
 Fludra, A., Del Zanna, G., Bromage, B. J. I., and Thomas, R. J.: 1997, *Proc. of the 5th SOHO Workshop*, ESA SP-404, 385–389.
 Harrison, R. A., Fludra, A., Pike, C. D., et al.: 1997, *Sol. Phys.*, **170**, 123–141.
 Landi, E., Landini, M., Dere, K. P., Young, P. R., and Mason, H. E.: 1998, *Astronomy and Astrophysics*, in press.

ON THE LYMAN α AND O VI LINE PROFILES IN STREAMERS AND CORONAL HOLES

L. ZANGRILLI and P. NICOLOSI

Dipartimento di Ingegneria Elettronica ed Informatica, Università degli Studi di Padova, I-35131 Padova, Italy, Istituto Nazionale per la Fisica della Materia, Unità di Padova, Italy

G. POLETTO

Osservatorio Astrofisico di Arcetri, I-50125 Firenze, Italy

G. NOCI

Università di Firenze, I-50125 Firenze, Italy

Abstract. The profiles of the Ly α line at 1215.6 Å and of the O VI doublet at 1031.9 Å and 1037.6 Å in the extended solar corona have been analyzed vs. latitude and radial direction, performing observations with the Ultraviolet Coronagraph Spectrometer (UVCS) on board the ESA-NASA solar satellite SOHO (Solar and Heliospheric Observatory). The results show that these lines behave differently with latitude: the H I Ly α line has larger full width at half maximum (FWHM) values in the streamer region and narrower values towards the pole, while the FWHM of O VI lines has a minimum at the center of the streamer and slightly increases towards the polar regions. We briefly discuss the impact of the results on coronal heating theories.

Key words: Sun: corona, Sun: UV radiation, line profiles, Sun: solar wind

In the present research we study some properties of the H I Ly α and O VI line profiles in the extended solar corona as a function of latitude and heliocentric distance. The coronal Ly α emission originates from resonant scattering of the chromospheric radiation, while the O VI doublet also has a significant collisional contribution (Noci, Kohl, and Withbroe 1987). Spectroscopic observations have been performed with UVCS/SOHO (see Kohl *et al.* 1995; Domingo, Fleck, and Poland 1995), on 5–11 August 1996. We observed the North-East sector of the solar corona at $1.5 R_{\odot}$, at 0° (East), 90° (North), and 30° and 60° of roll angle in two days. Slit widths of $50 \mu\text{m}$ for the Ly α channel and $75 \mu\text{m}$ for the O VI channel have been selected to optimize both spectral resolution and photon flux. The exposure times were 9000, 14400, 18000, and 25200 s, respectively for 0° , 30° , 60° , and 90° . Different points along the slit correspond to different heliocentric distances, from $1.5 R_{\odot}$ up to $2.0 R_{\odot}$. Special effort has been taken to improve the confidence in the derived data through a careful evaluation of the statistical and experimental uncertainties of the measures. We identified the following sources of uncertainty: (i) uncertainty in the stray light contribution; (ii) flat-field correction; (iii) uncertainty in the instrumental function; (iv) the line profile fitting procedure; and (v) fluctuations of the coronal emission. The uncertainty due to changes of the coronal emission with time and the statistics has been estimated by arbitrarily combining the exposures of the whole week into three data sets. We assumed that the variations between the full widths at half maximum (FWHMs) and intensities measured for each group are representative of this uncertainty. The corresponding sigma values are shown as error bars. Our analysis showed that the stray light



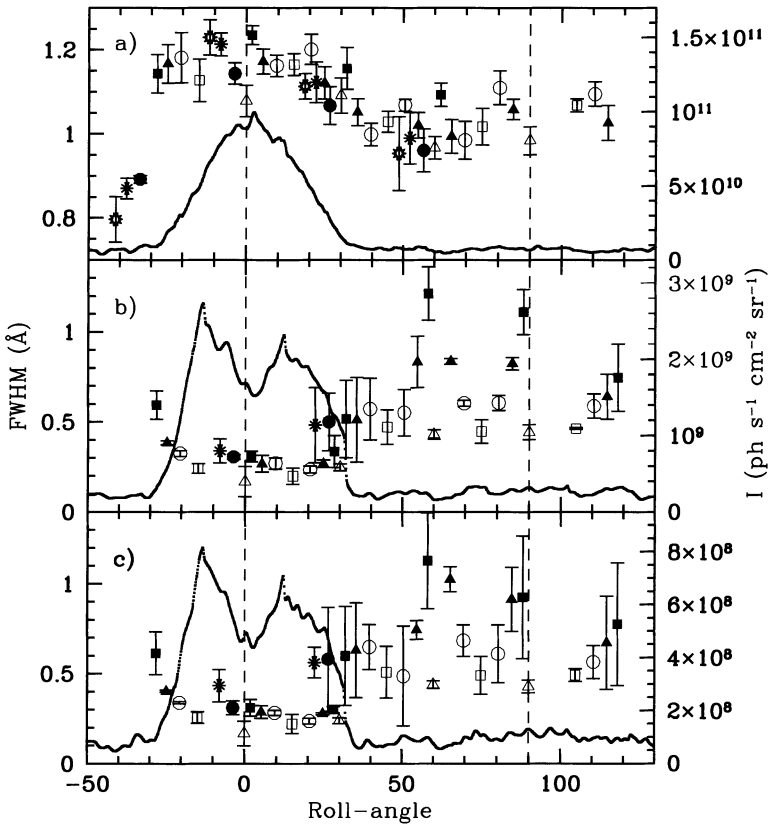


Figure 1. Representation of the latitude behavior of the line widths vs. roll angle for Ly α (a), O VI at 1031.9 Å (b), and O VI at 1037.6 Å (c), integrated over the whole observational week. Values at 1.5, 1.55, 1.6, 1.65, 1.7, 1.8, 1.9, and 2.0 R_{\odot} are represented, respectively, by open triangles, open squares, open circles, full triangles, full squares, full circles, asterisks, and stars. A continuous line represents the line intensity at 1.6 R_{\odot} . Two vertical dashed lines mark the equator (0) and the North pole (90).

correction affects heavily the profiles of O VI at higher heliocentric distances, but the qualitative behavior of the results is not affected. For a detailed description of the data analysis procedure see Zangrilli *et al.* (1999). The values shown in the following figures have been derived from spectra integrated over the whole week.

In Figure 1a the FWHM values of the Ly α spectral profiles are reported vs. roll angle for different heliocentric distances. These values show the presence, in the streamer region, of relatively wide profiles, which become narrower towards higher latitudes. This tendency is more evident in measures taken at higher distances, and is in contrast with the O VI behavior. Furthermore, the line widths slightly increase

with the distance. For reference purposes the intensity vs. latitude profile at $1.6 R_{\odot}$, obtained from the synoptic observations, is shown as a solid line in Figure 1. In Figure 1a the comparison between the line widths and the intensity reveals a correlation with the latitude, with both line widths and intensity decreasing towards the North pole. The O VI lines show a different behavior, both in intensity and in line width. The corresponding values are reported in Figures 1b and 1c. The coronal emission in the streamer region exhibits a double peaked spatial configuration with a deep minimum at the center (solid line) and the narrowest values of FWHM of the line profiles are in correspondence with the minimum of intensity at the center of the streamer region. Then the decrease of intensity near the streamer boundary (at about 40°) corresponds to an increase of the line widths. Moving towards the North pole we can appreciate an almost steady increase of the line widths with latitude at any heliocentric distance. Moreover, lines observed at higher distances are systematically wider than those at lower distances. The line width behavior is just the opposite to that of the line intensity, which decreases both with latitude and distance. We did not find evidence for a particular feature in correspondence with the double peak in intensity at about -20° and $+20^{\circ}$. The behavior of the O VI profiles is consistent with the ion-cyclotron coronal heating interpretation and the properties of the Alfvén waves with latitude (Ulysses observations revealed that Alfvén waves are continuously present in the polar region of the sun while at lower latitudes they become increasingly scarce and intermittent; Smith *et al.* 1995), as we expect wider profiles in the polar region. The results for Ly α are apparently inconsistent with this scenario, as narrower profiles are seen in the polar region. This can be explained by the lower efficiency of this mechanism for lighter ions, possibly masked by other effects.

In this context, we compared the kinetic temperatures, T_k , derived from the width values of the Si XII line at 1041.2 \AA (520.6×2) with those of the O VI line at 1031.9 \AA . In the center of the streamer the T_k of Si XII appears to be larger than the O VI value, while between 20° and 30° the two ions seem to have the same T_k . Because the ion-cyclotron resonance dissipation mechanism depends on the ratio A/Z (A is the atomic mass and Z is the ion charge) (see, e.g., Kohl *et al.* 1998 and references therein) we would expect the O VI lines to be wider than Si XII lines, a behavior which does not comply with present data. We conclude that observations need to be analyzed on a more quantitative basis (for instance, also taking into account processes by which ions lose energy to the ambient plasma) before drawing any conclusion about the role of the ion-cyclotron mechanism in coronal heating. Another issue that we would like to point out is the bimodal characteristic of the FWHM of O VI line profiles (Figures 1b and 1c): narrow profiles in the streamer and larger ones outside, possibly consistent with the Alfvén waves' behavior. Also, there is some evidence for a peculiar feature at the streamer-coronal hole boundary. In Figure 1a we see a local minimum in the Ly α line widths between 50° and 60° , followed by an increase towards the pole, particularly evident in data at 1.5, 1.6 and

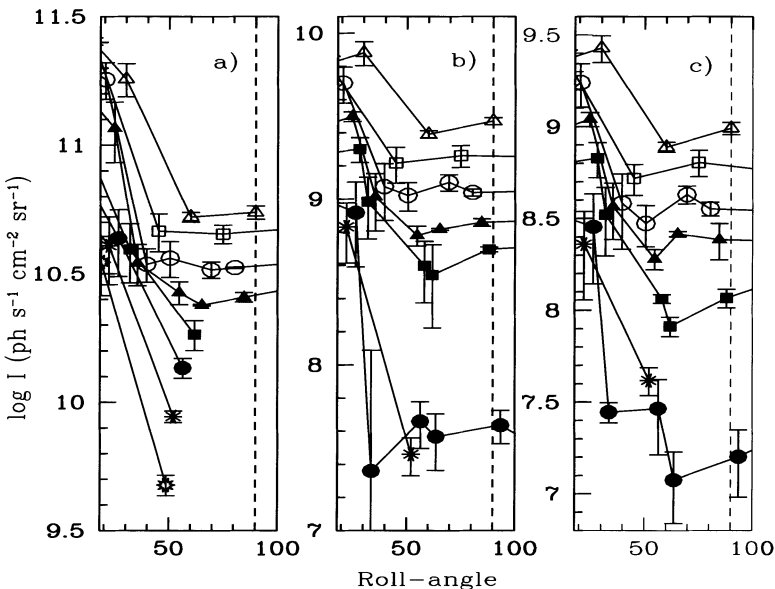


Figure 2. Intensity vs. roll angle for Ly α (panel a), O VI at 1031.9 Å (panel b), and O VI at 1037.6 Å (panel c), with the same meaning of the symbols as in Figure 1.

$1.65 R_{\odot}$. In the corresponding region the O VI widths (Figures 1b and 1c) do not show any particular characteristics.

In Figure 2 the intensity values obtained from our observations are shown. These data allow better statistics than the synoptic ones. In Figure 2a there is a hint for an inflection in the Ly α intensity at about 40° to 60° (data at $1.65 R_{\odot}$). In Figures 2b and 2c, O VI data show, in the same region, more clear evidence for a local minimum. These features may be related to a local maximum in the flux-tube expansion factor which occurs at the streamer-coronal hole boundary (Wang and Sheeley 1990). In this case, a local minimum of the density or plasma speed would be revealed by a lower intensity of the emission lines. It is beyond our purposes to check this interpretation on a more quantitative basis.

References

- Domingo, V., Fleck, B., and Poland, A. I.: 1995, *Solar Phys.*, **162**, 1–37.
- Kohl, J. L., et al.: 1995, *Solar Phys.*, **162**, 313–356.
- Kohl, J. L., et al.: 1997, *Solar Phys.*, **175**, 613–644.
- Kohl, J. L., et al.: 1998, *Astrophys. J.*, **501**, L127–L131.
- Noci, G., Kohl, J. L., and Withbroe, G. L.: 1987, *Astrophys. J.*, **315**, 706–715.
- Smith, E. J., et al.: 1995, *Geophys. Res. Lett.*, **22**, 3381–3384.
- Wang, Y.-M., and Sheeley, N. R.: 1990, *Astrophys. J.*, **355**, 726–732.
- Zangrilli, L., et al.: 1999, *Astron. Astrophys.*, in press.

THE TRANSITION BETWEEN FAST AND SLOW SOLAR WIND FROM COMPOSITION DATA

T. H. ZURBUCHEN, S. HEFTI, L. A. FISK, G. GLOECKLER* and
R. VON STEIGER**

Department of Atmospheric, Oceanic and Space Sciences, University of Michigan, Ann Arbor, USA

Abstract. The transition between coronal hole associated fast solar wind and slow solar wind is studied using data from the high resolution mass spectrometer SWICS on ACE. We discuss the data in the framework of a recent theory about the global heliospheric magnetic field and conclude that the data are consistent with magnetic connections between field-lines in the fast and in the slow wind.

Key words: coronal holes, solar wind, ion composition, elemental fractionation, Ulysses, ACE

1. Introduction

The transition between fast and slow solar wind is determined close to the Sun, at the boundaries of coronal holes. Even though the kinetic properties of the streams may be changed due to the dynamic interaction between fast and slow wind, the elemental and charge composition remains unchanged in the heliosphere. It therefore carries valuable information about the small-scale properties of coronal hole boundaries close to the Sun.

It has been pointed out by Geiss *et al.* (1996) that during the mid-latitude phase of Ulysses from 1992 to mid-1993, the average compositional patterns clearly indicated the qualitative difference between fast and slow wind. Figure 1 has been reproduced from Geiss *et al.* (1994). It shows a superposed-epoch analysis of SWICS-Ulysses data. Slow solar wind is observed to have a higher oxygen freeze-in temperature than fast, coronal hole associated wind. Additionally, slow wind shows an enrichment of Mg/O, with Mg enhanced due to its low first ionization potential (FIP). Possible reasons for this difference in composition have recently been discussed by Schwadron *et al.* (1998). For a short summary, see also Zurbuchen *et al.* (1998). Other differences in the two types of flow, such as a greater variability in the composition, were previously suggested by Axford (1977) based on the magnetic field configuration in the low corona. In the superposed epoch analysis of Ulysses data, the average transition time from one solar wind type to the other (τ_{s-f} from slow to fast, τ_{f-s} from fast to slow wind) is an upper limit to the actual transition time in any one case. Figure 1 shows that $\tau_{f-s} < 1$ day and $\tau_{s-f} < 4$ days for this data-set.

Traditionally, compositional studies have concentrated on the leading edge of the high speed streams (see, e.g., Wimmer-Schweingruber *et al.* 1997). There, the

* Also at Department of Physics and IPST, University of Maryland, College Park, USA

** On leave from International Space Science Institute, Bern, CH



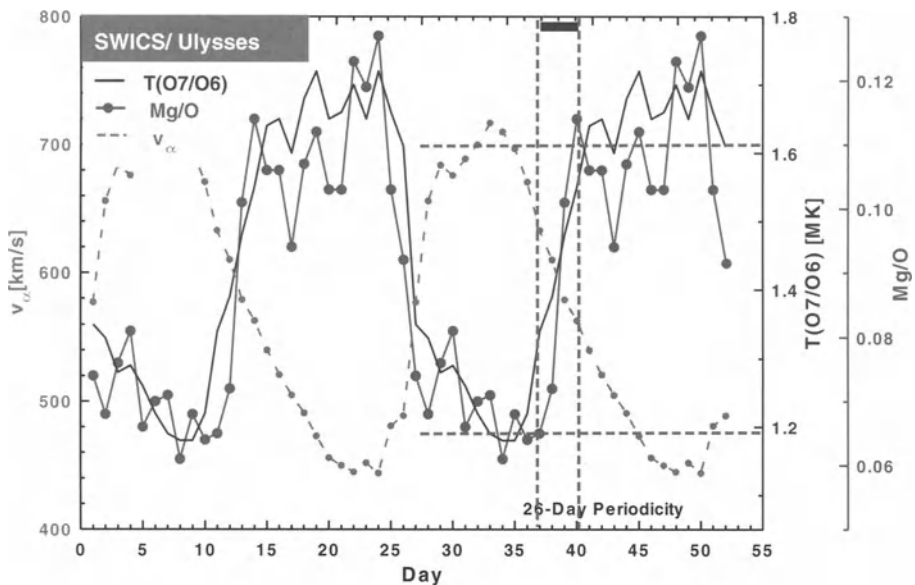


Figure 1. Superposed epoch analysis showing compositional variations derived from 1992 day 191 to 1993 day 98. The solar wind composition reflects a qualitative difference between slow and fast wind. The transition times in this analysis are upper limits to the transition time in any particular event (Figure adapted from Geiss *et al.* 1994).

density is large and therefore statistically accurate results are more easily obtained. Data from the trailing edge, however, provide a much more sensitive measure for the actual small-scale processes relevant for the transition between solar wind streams because all the geometrical quantities are literally *stretched out*.

In this paper we use high-resolution composition data from SWICS-ACE (for instrumental details, see Gloeckler *et al.* 1998) to further explore the transition times between different solar wind streams, in particular between fast and following slow solar wind. We then discuss the result in the framework of the Fisk *et al.* theory described in this volume.

2. Fast-Slow Transitions from SWICS-ACE

We use SWICS-ACE data during the period from day 203 to 210 in 1998. In Figure 2 we show V_α , Fe/O and T_O in the same format as presented in Figure 1. The time-resolution for V_α and T_O is 13 minutes, for Fe/O \sim 1 hour. First, ACE was immersed in low speed solar wind with high variability in the freeze-in temperature and elemental composition. During day 203 a transition occurs into fast solar wind originating from a low-latitude coronal hole. After a period of steady coronal hole

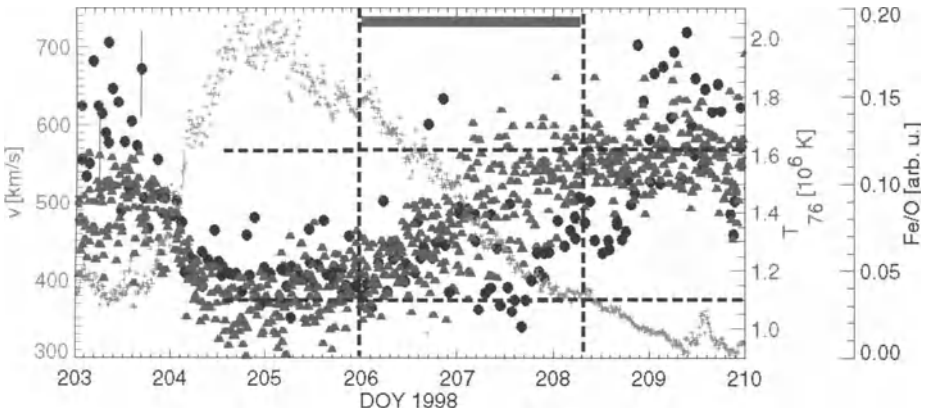


Figure 2. SWICS-ACE data during a fast solar wind stream in 1998. The format is adapted to Figure 1. The triangles denote the freeze-in temperature of O, the solid circles denote Fe/O, and crosses the solar wind speed. The typical uncertainties are mostly given by the counting statistics.

associated wind, the compositional signatures gradually turn back to a slow solar wind composition. Notice that even though there is a great deal of structure in both Fe/O and T_O , there is nowhere a clear step between *fast* and *slow* compositions. The transition time from fast to slow solar wind occurs on a scale of $\tau_{f-s} \sim 50$ hrs. consistent with the upper limits of Geiss *et al.* (1994) in case of the polar coronal hole.

Generally, for a total number of eight fast-slow transitions measured by SWICS-ACE we found no example of a clear step transition between *fast* and *slow* compositions in the trailing edge of fast streams. Interestingly, the transitions in elemental and charge state compositions sometimes do not occur at exactly the same time or have even more structure than shown in Figure 2.

3. Discussion and Conclusions

During the first months of the SWICS-ACE measurements, transitions between fast and slow solar wind have been observed. Generally, they are associated with solar wind emanating from low-latitude coronal holes as described by Burlaga *et al.*, in this volume. The compositional patterns of those holes seem to be very much comparable with the observations of high-latitude, polar coronal holes as shown in Figure 1. The transitions between the two states do not necessarily appear to occur on the shortest time-scale. We find fast transitions from fast to slow wind on the time-scale of $\tau_{s-f} \sim$ hours or sometimes from one measurement time to the next. In the trailing edge of the fast stream, where no dynamic steepening can take place, we find a rather steady transition on a time-scale of $\tau_{f-s} \sim 40$ hrs or more. These

transition times are consistent with the previous analysis by Geiss *et al.* (1994) shown in Figure 1.

In a paper by Fisk *et al.* in this volume, a theory of the magnetic nature of fast and slow solar wind has been presented. It is pointed out that the expansion of magnetic field-lines from the differentially rotating photosphere into a pressure-equilibrated corona puts constraints on the solar magnetic field. In particular, it leads to a transport of open field from coronal holes into a region with predominantly closed magnetic field, thereby causing reconnection between field-lines carrying *fast* and *slow* solar wind. If this reconnection process occurs, *slow* and *fast* solar wind composition can be found in one and the same field-line. Very likely, this reconnection also occurs within the sonic point, where the thermal speed is larger than the bulk speed of the plasma, allowing for mixing of the plasma along magnetic field-lines. This would lead to a steady transition as shown in Figure 2.

Notice that the solar wind plasma can only be efficiently mixed along the magnetic field and not perpendicular to it. If fast and slow solar wind streams flow in magnetically disconnected flux-tubes, the transition is expected to have a more step-like character which is clearly not observed in Figure 2.

This steady transition has been observed in all unperturbed fast-slow transitions observed by ACE-SWICS during a 200 day period. However, it is important to keep in mind that transitions between fast and slow solar wind are not always identical and also, effects dependent on the solar cycle may be important (see, e.g., Schwenn 1990). Only a study based on the combined analysis of solar, compositional, and plasma data is expected to provide a conclusive picture.

This work was supported, in part, by NASA contracts NAG5-2810, NAG5-7111 and JPL contract 955460. THZ was also supported, in part, by NSF grant ATM 9714070.

References

- Axford, W. I.: 1977, in *Study of Traveling Interplanetary Phenomena*, eds. M. A. Shea, *et al.*, (Dordrecht: D. Reidel), p. 145.
- Fisk, L. A.: 1996, *J. Geophys. Res.*, **101**, 15547.
- Fisk, L. A., Zurbuchen, T. H., and Schwadron, N. A.: 1998, *Astrophys. J.*, submitted.
- Geiss, J., Gloeckler, G., and von Steiger, R.: 1994, *Space Sci. Rev.*, **72**, 49.
- Geiss, J., *et al.*: 1996, *Science*, **268**, 1033.
- Gloeckler, G., *et al.*: 1998, *Space Sci. Rev.*, **86**, 495.
- Schwadron, N. A., Fisk, L. A., and Zurbuchen, T. H.: 1998, *Astrophys. J.*, submitted.
- Schwenn, R.: 1990, in *Physics of the Inner Heliosphere I*, eds. R. Schwenn and E. Marsch, (Springer Verlag), p. 99.
- Wimmer-Scheingruber, R. F., von Steiger, R., and Paerli, R.: 1997, *J. Geophys. Res.*, **102**, 17407.
- Zurbuchen, T. H., Fisk, L. A., Gloeckler, G., and Schwadron, N. A.: 1998, *Space Sci. Rev.*, **85**, 397.